Schweizerische Eidgenossenschaft
Confédération suisse
Confederazione Svizzera
Confederaziun svizra

Eidgenössisches Departement für Umwelt, Verkehr, Energie und Kommunikation UVEK
Département fédéral de l'environnement, des transport, de l'énergie et de la communication DETEC
Dipartimento federale dell'ambiente, dei trasporti, dell'energia e delle communication DATEC

Bundesamt für Strassen
Office fédéral des routes
Ufficio federale delle Strade

Tragverhalten und Bemessung von Tübbingfugen

Comportement et dimensionnement des joints de voussoirs de tunnel

Behaviour and design of segmental tunnel lining joints

ETH Zürich, Institut für Baustatik und Konstruktion
Dr. Fabian Morger
Prof. Dr. Walter Kaufmann

Forschungsprojekt AGT2019/001
auf Antrag des Bundesamtes für Strassen ASTRA
Juli 2026 | 1827

Der Inhalt dieses Berichtes verpflichtet nur den (die) vom Bundesamt für Strassen unterstützten Autor(en). Dies gilt nicht für das Formular 3 "Projektabschluss", welches die Meinung der Begleitkommission darstellt und deshalb nur diese verpflichtet. Bezug: Schweizerischer Verband der Strassen- und Verkehrsfachleute (VSS)

Le contenu de ce rapport n'engage que les auteurs ayant obtenu l'appui de l'Office fédéral des routes. Cela ne s'applique pas au formulaire 3 « Clôture du projet », qui représente l'avis de la commission de suivi et qui n'engage que cette dernière. Diffusion : Association suisse des professionnels de la route et des transports (VSS)

La responsabilità per il contenuto di questo rapporto spetta unicamente agli autori sostenuti dall'Ufficio federale delle strade. Tale indicazione non si applica al modulo 3 "conclusione del progetto", che esprime l'opinione della commissione d'accompagnamento e di cui risponde solo quest'ultima. Ordinazione: Associazione svizzera dei professionisti della strada e dei trasporti (VSS)

The content of this report engages only the author(s) supported by the Federal Roads Office. This does not apply to Form 3 'Project Conclusion' which presents the view of the monitoring committee. Distribution: Swiss Association of Road and Transportation Experts (VSS)

Tragverhalten und Bemessung von Tübbingfugen

Comportement et dimensionnement des joints de voussoirs de tunnel

Behaviour and design of segmental tunnel lining joints

ETH Zürich, Institut für Baustatik und Konstruktion
Dr. Fabian Morger
Prof. Dr. Walter Kaufmann

Forschungsprojekt AGT2019/001
auf Antrag des Bundesamtes für Strassen ASTRA
Juli 2026 | 1827

Impressum

Forschungsstelle und Projektteam

Projektleitung
Prof. Dr. Walter Kaufmann

Mitglieder
Dr. Fabian Morger

Begleitkommission

Präsident
Remo Crapp

Mitglieder
Prof. Em. Dr. Georgios Anagnostou
Sebastian Bischoff
Alessandro Castelli
Paul Freudiger
Dr. Federica Sandrone

Ko-Finanzierung des Forschungsprojekts

Bundesamt für Verkehr
ETH Zürich

Antragsteller

Bundesamt für Strassen ASTRA

Bezugsquelle

Das Dokument kann kostenlos von
https://www.mobilityplatform.ch/
heruntergeladen werden.

Juli 2026

Inhaltsverzeichnis

Abbildungsverzeichnis 7

Zusammenfassung 9

Résumé 19

Summary 29

1 Einleitung 37
1.1 Hintergrund 37
1.2 Projektziel und Abgrenzung 38
1.3 Methodik 39
1.4 Aufbau des Berichts 39

2 Stand der Technik und offene Fragestellungen 41
2.1 Längsfugen 41
2.2 Ringfugen 43
2.3 Forschungsschwerpunkte und -ziele 44
2.3.1 Längsfugen 44
2.3.2 Ringfugen 45

3 Durchgeführte Untersuchungen und Erkenntnisse 47
3.1 Umschnürung 47
3.1.1 Umschnürungsmodell 47
3.1.2 Vergleich mit bestehenden Modellen und Validierung 49
3.2 Geschweisste Leiterbewehrung 51
3.2.1 Experimentelle Untersuchungen mit faseroptischen Messungen 51
3.3 Kombination von Lastausbreitung und Umschnürungsbewehrung für die Streifenbelastung von Beton 52
3.3.1 Experimentelle Untersuchungen 52
3.3.2 Modellierung 54
3.3.3 Validierung und Vergleich mit anderen Modellierungsansätzen 56
3.4 Tübbinglängsfugen 57
3.4.1 Experimentelle Untersuchungen 57
3.4.2 Modellierung 59
3.4.3 Validierung und Vergleich mit anderen Modellierungsansätzen 61
3.5 Streifenbelastung und Tübbinglängsfugen – Stahlfaserbewehrter Beton 63
3.5.1 Experimentelle Untersuchungen 63
3.5.2 Modellierung 65
3.5.3 Validierung 66

3.6 Ringfugen 66
3.6.1 Krafteinleitung 67
3.6.2 Scheibenbeanspruchung 67
3.6.3 Versätze 70
3.6.4 Bemessungsvorschlag 71

4 Zusammenfassung und Schlussfolgerungen 73
4.1 Zusammenfassung 73
4.2 Empfehlungen 75
4.3 Forschungsbedarf 76

Literaturverzeichnis 78

Datenverwendung 80

Anhänge 81
A. ETH-Dissertation 31577: Passive Confinement and Strip Loading in Longitudinal Tunnel Lining Segment Joints 81
B. Ringfugen – Ungerissene linear elastische Modellierung (Cedrus) 279
C. Ringfugen – Nichtlineare Modellierung (IDEA StatiCa Detail) 285

Projektabschluss 295

Abbildungsverzeichnis

Abbildung 1: Gestapelte Tübbinge (links) und Tübbingausbau mit ausgefahrenen Vortriebspressen einer TBM, die sich in der Ringfugen paarweise auf den zuletzt eingebauten Tübbingring abstützen (rechts). 37
Abbildung 2: Definition der Parameter der Tübbinge und der Längsfuge. 38
Abbildung 3: Umschnürungsmodell – (a) und (b) Definition der Paraboloide, (c) umschnürtes Betonvolumen und (d) Kraftfluss. 48
Abbildung 4: Massgebender Querschnitt – (a) umschnürte Fläche und (b) vereinfachte umschnürte Fläche. 49
Abbildung 5: Vergleich der Umschnürungsspannung nach dem neuem Modell ($\sigma_{conf,mod}$) mit dem Ansatz bestehender Normen (σ_{conf}). 50
Abbildung 6: Vergleich des Effektivitätsfaktors (A_{conf}/A_{cs}) der verschiedenen Modelle in Funktion des vertikalen Bewehrungsabstandes s_x – (a) variable Querschnittsgrösse mit einem Bügel und (b) konstanter Querschnitt mit unterschiedlicher Bewehrungsanzahl. 50
Abbildung 7: Instrumentierung der Leiterbewehrung – (a) geschweisster Kreuzungsstoss mit faseroptischem Sensor in Nut und geschützt mit einem Epoxidharz und (b) schematische Zeichnung der Sensoranordnung. 51
Abbildung 8: Blockversuche – (a) Geometrie Versuchskörper [mm], (b) Versuchsaufbau und (c) geprüfter Versuchskörper. 52
Abbildung 9: Verschiedene Bewehrungstypen. (a) geschweisste Leiterbewehrung, (b) Bügelbewehrung und (c) Dübelbewehrung. 53
Abbildung 10: Tragverhalten und Rissentwicklung eines Blockversuchs. 54
Abbildung 11: Dual-Wedge Spannungsfeld. 55
Abbildung 12: Vergleich der Modellvorhersagen mit den experimentellen Versuchsresultaten geplottet in Funktion von (a) Last-Konzentrations-Verhältnis, (b) transversalem mechanischem Bewehrungsgehalt und (c) Betondruckfestigkeit. 57
Abbildung 13: Geometrie der Fugenversuche [mm]. 58
Abbildung 14: Fugenversuche – (a) Geschweisste Leiterbewehrung, (b) Fugenausbildung mit Aussparung für Führungsstab und (c) Versuchsaufbau. 59
Abbildung 15: Modellierung der Längsfugen – (a) Multi-Wedge Spannungsfeld, (b) Dual-Wedge Spannungsfeld und (c) zugehöriges Bewehrungslayout. Es ist jeweils nur eine Symmetriehälfte dargestellt und die lateralen und vertikalen Spannungen sind unterschiedlich skaliert. 60
Abbildung 16: (a) Longitudinale Lastausbreitung und (b) horizontaler Schnitt mit belasteten Flächen durch Lastausbreitung. 61
Abbildung 17: Verschiedene Varianten zur Berücksichtigung einer Fugenaussparung aufgrund eines Führungsstabes basierend auf dem Multi-Wedge Spannungsfeld. 62
Abbildung 18: Vergleich der Modellvorhersagen mit den experimentellen Resultaten der Fugenversuche ohne Fugenaussparung geplottet in Funktion von (a) Last-Konzentrations-Verhältnis, (b) transversalem mechanischen Bewehrungsgehalt und (c) Betondruckfestigkeit. 63
Abbildung 19: Vergleich der Blockversuche mit stahlfaserbewehrtem Beton (lila) und konventionellem Beton (schwarz). (a) Belastungsbreite 140 mm; (b)

Belastungsbreite 210 mm. Mechanischer Bewehrungsgehalt in Klammern (für hybrid bewehrte Versuchskörper Summe aus konventioneller Bewehrung und residualer Zugfestigkeit). Abkürzungen: FO = fibres only (keine konventionelle Bewehrung), WG = Welded grids (geschweisste Leiterbewehrung und BT = Bent ties (Bügelbewehrung). 64
Abbildung 20: Vergleich der Fugenversuche mit stahlfaserbewehrtem Beton (lila) und konventionellem Beton (schwarz). (a) Belastungsbreite 140 mm; (b) Belastungsbreite 210 mm. Mechanischer Bewehrungsgehalt in Klammern (für hybrid bewehrte Versuchskörper Summe aus konventioneller Bewehrung und residualer Zugfestigkeit). Abkürzungen: FO = fibres only (keine konventionelle Bewehrung) und WG = Welded grids (geschweisste Leiterbewehrung). Im Vergleich zu [1] wurde Versuchskörper TLJ-60-WG2p-B5 zusätzlich in der Grafik integriert. 65
Abbildung 21: Bewehrungsspannungen ermittelt mit Idea StatiCa Detail im Grenzzustand der Tragsicherheit (GZT). 69
Abbildung 22: Rissbreiten ermittelt mit Idea StatiCa Detail im Grenzzustand der Gebrauchstauglichkeit (GZG)..... 70

Zusammenfassung

Tübbinge – vorfabrizierte Tunnelauskleidungssegmente aus Stahlbeton – sind im modernen Tunnelbau weit verbreitet. Bei ihrer Bemessung spielen die Längs- und Ringfugen eine wesentliche Rolle. Dieses Projekt untersucht beide Fugentypen, mit Schwerpunkt auf den Längsfugen.

Die Kontaktflächen der Längsfugen der Tübbinge sind normalerweise kleiner als der Regelquerschnitt. Dadurch werden die Längsfugen insbesondere bei Tunnels unter hohem hydrostatischem Druck oder im druckhaften oder quellenden Gebirge, mit den damit verbundenen hohen Ringnormalkräften, massgebend für die Abmessung der Tübbingdicke. Stahlbetontübbinge mit kräftiger Umschnürungsbewehrung sind eine vielversprechende Option, um hohen Beanspruchungen in den Längsfugen ohne Vergrösserung der Tübbingstärke standzuhalten. Heute ist dieser Ansatz im Tunnelbau jedoch wenig verbreitet, da Normvorschriften weitgehend fehlen – was hauptsächlich daran liegt, dass keine experimentell validierte mechanische Modelle existieren.

Das Tragverhalten der Längsfugen entspricht im Wesentlichen einer Streifenbelastung, bei welcher die aufgebrachten Spannungen die einachsige Betondruckfestigkeit bekanntlich deutlich überschreiten können. Diese höhere Druckfestigkeit ist auf laterale (d.h. quer zur Beanspruchungsrichtung wirkende) Umschnürungsspannungen zurückzuführen, die durch die Lastausbreitung (geometrische Umschnürung) oder Umschnürungsbewehrung (passive Umschnürung) hervorgerufen werden. Um Tübbinglängsfugen effizient zu bemessen, sind somit sowohl die geometrische als auch die passive Umschnürung zu berücksichtigen. Zu diesem Zweck wird im vorliegenden Bericht das mechanische Verhalten von Stahlbeton unter Streifenbelastung mit ausgeprägter passiver Umschnürung theoretisch und experimentell untersucht, um schliesslich Bemessungsansätze vorzuschlagen. Die Untersuchungen der Längsfugen lassen sich grob in drei Teile gliedern.

Der erste Teil gibt einen Überblick über den Wissensstand im Bereich der passiven Umschnürung und präsentiert ein mechanisches Modell für die lokale dreidimensionale Lastausbreitung aktivierter Umschnürungsbewehrung, das anschliessend erfolgreich validiert wird. Die passive Umschnürung infolge der lateralen Bewehrung wird bei der Bemessung von Stahlbetonbauteilen unter hoher Druckbeanspruchung, wie z. B. Stützen, Pfeilern oder Tübbingen, berücksichtigt. In aktuellen Richtlinien existieren bereits verschiedene Modelle zur Berücksichtigung dieses vorteilhaften Effekts. Allerdings fehlt es diesen Ansätzen an mechanischer Konsistenz hinsichtlich der dreidimensionalen Ausbreitung der Umschnürungskräfte. Das neue mechanische Modell trägt dazu bei, diese Lücke zu schliessen, indem der dreidimensionale Kraftfluss mit parabolischen, ausschliesslich druckbelasteten Schalen berücksichtigt wird. Weiter werden die Gleichgewichts- und Fliessbedingungen berücksichtigt, wodurch das Modell einen unteren Grenzwert der Traglast nach der Plastizitätstheorie darstellt.

Weiterführend wird das neue Modell mit aktuellen Ansätzen zur Bemessung der Umschnürung von Stahlbetonbauteilen verglichen und erfolgreich anhand experimentel-

ler Ergebnisse validiert. Im Vergleich zu bestehenden Ansätzen zur Bemessung (Eurocode 2 - EN 1992-1-1:2023 (EC2:2023), SIA 262:2013 und *fib* Model Code 2010 (MC2010)) weist das neue Modell mehrere wesentliche Vorteile auf: (i) Die Abstände der Umschnürungsbewehrung, sowohl lateral als auch in Belastungsrichtung, werden konsistent berücksichtigt, (ii) das Modell basiert auf einer mechanischen Grundlage, (iii) verfolgt den Kraftfluss konsequent und (iv) kann das Umschnürungsverhalten von rechteckigen und kreisförmigen Querschnitten konsistent erklären. Trotz der mechanischen Konsistenz des neuen Modells und des dadurch verbesserten Verständnisses des Verhaltens passiv umschnürten Betons ist es aufgrund der Komplexität bei der Bestimmung der massgebenden umschnürten Betonfläche für die Ingenieurpraxis nur begrenzt nutzbar. Durch eine vereinfachte Bestimmung dieser Fläche konnte ein angepasstes Modell entwickelt werden, welches ebenfalls erfolgreich anhand experimenteller Daten validiert werden konnte. Es ist zudem noch einfacher anzuwenden als die bestehenden Modelle in aktuellen Normen, was es zu einer wertvollen Alternative für die Bemessungspraxis macht.

Darüber hinaus wird im Rahmen des ersten Teils der Untersuchung der Längsfugen das Tragverhalten von geschweisster Leiterbewehrung als Umschnürungsbewehrung untersucht. Bei der Herstellung von Stahlbetontübbingen wird zunehmend geschweisste Leiterbewehrung eingesetzt, da diese die Bewehrungsmontage vereinfachen, Zeit und Kosten im Vorfertigungsprozess reduzieren, ressourceneffizient sind und das Betonieren durch die geringere Bewehrungsmenge erleichtern. Während ihre Vorteile bekannt sind, ist ihr Tragverhalten noch nicht vollständig erforscht. Um diese Forschungslücke zu schliessen, wurden faseroptische Messungen an mehreren Bewehrungsstäben der geschweissten Leiterbewehrung eines streifenbelasteten Stahlbetonprüfkörpers durchgeführt. Die Schweissverbindungen entsprachen der Qualität SF50. Zwei Quer- und vier Längsbewehrungsstäbe des Prüfkörpers wurden mit faseroptischen Sensoren versehen. Auf Grundlage der faseroptischen Dehnungsmessungen und der Materialeigenschaften der nakten Bewehrungsstäbe konnten die Normalspannungen und die Krümmung der Bewehrungsstäbe ermittelt werden. Dadurch konnte gezeigt werden, dass zwei Längsbewehrungsstäbe ausreichen, um die Querbewehrungsstäbe über die Länge zwischen den inneren geschweissten Kreuzungspunkten vollständig zu aktivieren (Querbewehrung fliesst). Ergänzend lieferten die Messungen Erkenntnisse über die Lastübertragung zwischen der Bewehrung und dem umliegenden Beton, was zur Quantifizierung des Effekts der geschweissten Leiterbewehrung als passive Umschnürung notwendig ist. Neben der direkten Lasteinleitung an den Kreuzungspunkten werden die Längsbewehrungsstäbe auf Biegung beansprucht, was die beobachteten Querkrümmungen verdeutlichen. Dennoch ist die Längsbewehrung in der Lage, eine Umschnürungswirkung in Längsrichtung zu gewährleisten. Weitere Untersuchungen wären erforderlich, um zu beurteilen, ob die Ergebnisse auch für unterschiedliche Bewehrungs- oder Lastanordnungen gelten. Trotzdem erweitert die hier durchgeführte Untersuchung das Verständnis des Tragverhaltens geschweisster Leiterbewehrung und belegt, dass diese eine vielversprechende Alternative zur konventionellen Bügelbewehrung für die Herstellung von Tübbingen aus Stahlbeton darstellt.
Der zweite Teil der Untersuchungen der Längsfugen erforscht das Tragverhalten von streifenbelastetem Stahlbeton anhand einer Kombination aus experimentellen und theoretischen Untersuchungen. Zu diesem Zweck werden zwei experimentelle Serien an Stahlbetonblöcken und an grossmassstäblichen Prüfkörpern mit Längsfugen vorge-

stellt und die Ergebnisse diskutiert. Auf Grundlage der experimentellen Ergebnisse werden mechanisch konsistente Spannungsfeldmodelle entwickelt, welche die kombinierte Wirkung von Lastausbreitung und Umschnürungsbewehrung berücksichtigen.

Stahlbeton unter Streifenbelastung stellt ein häufiges Problem in der Ingenieurpraxis dar. Die erhöhte Betondruckfestigkeit bei der Lasteinleitung lässt sich auf geometrische und passive Umschnürungsspannungen zurückführen, die durch die Lastausbreitung und die Bewehrung verursacht werden. Aktuelle Bemessungsvorschriften erlauben jedoch keine Kombination dieser beiden Umschnürungseffekte, was zu konservativer Bemessung führt. Zudem ist die experimentelle Datenlage für streifenbelastete Stahlbetonbauteile mit ausgeprägter passiver Umschnürung und moderaten Lastkonzentrationsverhältnissen, wie sie beispielsweise in Längsfugen von Tübbingen vorkommen, dünn. Zunächst werden verschiedene Modelle für die Streifenbelastung sowie eine experimentelle Serie von 15 streifenbelasteter Betonblöcke mit ausgeprägter passiver Umschnürung und moderaten Lastkonzentrationsverhältnissen vorgestellt. Die untersuchten Parameter waren (i) der Bewehrungsgrad und -typ, (ii) die Breite und Lage der belasteten Fläche sowie (iii) die Betondruckfestigkeit. Die Ergebnisse zeigen, dass Prüfkörper mit einem ausreichenden mechanischen Bewehrungsgrad ein duktiles Verhalten aufweisen und dass die Tragfähigkeit durch höhere Mengen an Umschnürungsbewehrung wesentlich gesteigert werden kann, was für verschiedene Bewehrungstypen (Bügelbewehrung, geschweisste Leiterbewehrung und Dübelbewehrung) validiert wurde. Die Tragfähigkeit der verschiedenen Bewehrungstypen variierte nicht wesentlich, was darauf hindeutet, dass geschweisste Leiterbewehrung eine praktikable Alternative zu Bügeln darstellen kann. Darüber hinaus bestätigen die Versuche, dass die geometrische Umschnürung mit zunehmender belasteter Breite oder exzentrischer Belastung abnimmt und sich dadurch die maximal aufnehmbare Kontaktspannung an der Lasteinleitung verringert. Schliesslich zeigen die Ergebnisse, dass hochfeste Prüfkörper im Vergleich zu normalfesten tendenziell geringere normierte Tragwiderstände aufweisen, die zudem möglicherweise nicht vollständig ausgenutzt werden können, da die Rissbreiten, die in den Versuchen mittels digitaler Bildkorrelation bestimmt wurden, die Bemessung massgebend beeinflussen. Jedoch wurden lediglich drei Prüfkörper aus hochfestem Beton hergestellt, wobei weitere experimentelle Daten erforderlich sind um diese vorläufigen Schlussfolgerungen zu bekräftigen.

Neben der experimentellen Serie werden vier verschiedene Modelle – Dual-Wedge-Spannungsfeld (DW-cc), eine Vereinfachung des Spannungsfelds (DW-s), das geometrische und passive Umschnürungsmodell (GPC) und der Bemessungsansatz gemäss der Richtlinie des Deutschen Ausschusses für unterirdisches Bauen (DAUB:2024)) – zur Bemessung von streifenbelasteten Stahlbetonbauteilen vorgestellt. Zudem wird erläutert, wie die Umschnürungsspannungen und die umschnürte Betonfläche für regelmässige und unregelmässige Bewehrungsabstände bestimmt werden können. Die verschiedenen Modelle werden mit experimentellen Daten, einschliesslich der 15 Betonblockversuche, verglichen. Es zeigt sich, dass die Modelle, welche die Effekte von Lastausbreitung und passiver Umschnürung kombinieren (DW-cc, DW-s und GPC) den Tragwiderstand im Durchschnitt ähnlich und mit guter Genauigkeit vorhersagen, mit vergleichbaren Streuungsniveaus, und im Allgemeinen auf der sicheren Seite liegen. Der DAUB:2024-Ansatz, der lediglich die Lastausbreitung berücksichtigt, erweist sich in den meisten Fällen als sehr konservativ. Die erfolgreiche Validierung der drei Mo-

delle, welche die passive Umschnürung einbeziehen, bestätigt indirekt, dass die vorgeschlagenen Ansätze zur Bestimmung der Umschnürungsspannungen und der umschnürten Betonfläche plausibel sind. Unter diesen Modellen untersucht das GPC-Modell lediglich zwei Querschnitte, um die Tragfähigkeit von streifenbelasteten Stahlbetonbauteilen zu bestimmen: Einen an der Lasteinleitung und einen an der Stelle, an der die Last vollständig verteilt ist. Dagegen erfasst das Dual-Wedge-Spannungsfeld den gesamten Kraftfluss und ermöglicht die Analyse der Tragfähigkeit jedes horizontalen Schnitts des Lastausbreitungsbereichs sowie die konsistente Bestimmung der Bewehrungsposition. Darüber hinaus entspricht es dem EC2:2023, der die Kombination von passiver und geometrischer Umschnürung für die Bemessung von teilbelasteten Flächen zulässt, sofern dreidimensionale Spannungsfelder angewendet werden. Während die Anwendung des DW-cc in der Bemessung relativ aufwändig ist, zeichnet sich das vereinfachte DW-s, das aus einer parametrischen Studie des Dual-Wedge-Spannungsfelds (DW-cc) abgeleitet wurde, durch seine direkte Formulierung und den geringsten Variationskoeffizienten aus, was darauf hinweist, dass es trotz seiner Einfachheit die verschiedenen Einflüsse auf die Tragfähigkeit am besten abdecken kann.

Es wird daher vorgeschlagen, streifenbelastete Stahlbetonbauteile gemäss der Vereinfachung des Dual-Wedge-Spannungsfelds (DW-s) zu bemessen, wobei die Eingabeparameter auf Grundlage des im ersten Teil der Untersuchungen entwickelten passiven Umschnürungsmodells bestimmt werden. Das mechanisch konsistente DW-cc-Modell kann weitere Erkenntnisse hinsichtlich der Bewehrungsanordnung liefern und ist das einzige Modell, das in der Lage ist, variierende Umschnürungsspannungen in den Umschnürungs- und Spaltzugbereichen zu berücksichtigen. Folglich wird das DW-cc für detaillierte Betrachtungen vorgeschlagen und ist insbesondere für die Beurteilung bestehender Tragwerke geeignet.

Während sich die Blockversuche auf vollständig umschnürte, streifenbelastete Betonelemente konzentrierten, wurde mit den grossmassstäblichen Versuchen an Prüfkörpern mit Längsfuge das Tragverhalten von vorgefertigten Stahlbetontübbingen untersucht. Stahlbetontübbinge mit ausgeprägter Umschnürungsbewehrung im Lastausbreitungsbereich neben den Fugen stellen eine praktikable Möglichkeit dar, um hohe Ringdruckkräfte aufnehmen zu können. Diese Lösung hat sich jedoch bisher nicht weitreichend im Tunnelbau etabliert, was hauptsächlich mit der unzureichenden Abdeckung in bestehenden Richtlinien und fehlender experimenteller Validierung zu begründen ist. Diese Problematik wird folgendermassen adressiert: (i) Die Ergebnisse einer Versuchskampagne zur Untersuchung des Tragverhaltens von Tübbingen mit Längsfugen an neun Stahlbetonprüfkörpern mit ausgeprägter passiver Umschnürung werden vorgestellt, (ii) ein auf einer anwendungsspezifischen Spannungsfeldlösung basierender Modellierungsansatz für die Bemessung von Längsfugen, der das vollständige Verfolgen des Kraftflusses ermöglicht wird vorgeschlagen und (iii) das Spannungsfeld wird auf die Berücksichtigung des Effekts von Aussparungen für Führungsstäbe erweitert.

Die untersuchten Parameter der Versuchskampagne waren (i) der Querbewehrungsgehalt, (ii) die Bewehrungskonfiguration und (iii) die Fugengeometrie der Stahlbetonprüfkörper mit geschweisster Leiterbewehrung. Die experimentellen Ergebnisse zeigen, dass bei einem grössenen Lastkonzentrationsverhältnis (grössere Fugenbreite)

die Kontaktspannung an der Fuge aufgrund der begrenzten geometrischen Umschnürung abnimmt, jedoch die Normalkraft aufgrund der grösseren Fugenfläche weiterhin zunimmt. Umschnürungsbewehrung trägt zur Tragfähigkeit von Längsfugen bei. Die mögliche Laststeigerung durch das Einbringen von Umschnürungsbewehrung ist jedoch begrenzt, wenn die Tübbinge neben der umschnürten Zone an der Fuge eine nicht umschnürte Zone aufweisen. In der nicht umschnürten Zone kann lediglich die einachsige Betondruckfestigkeit aktiviert werden, und zwar auf einer kleineren Fläche als dem Tübbingquerschnitt, da sich in der umschnürten Zone entstehende Abplatzungsrisse in die nicht umschnürte Zone ausbreiten. Folglich sind Tübbinge mit hohen Bewehrungsgraden und breiten Fugen, die hohe Axialkräfte aufnehmen können, anfällig für ein Versagen in der nicht umschnürten Zone. Prüfkörper, die in der nicht umschnürten Zone versagten, zeigten ein weniger duktiles Verhalten als jene die in der umschnürten Zone versagten. Um die Tragfähigkeit von Tübbingen mit massgebender nicht umschnürter Zone zu steigern, kann in dieser Zone eine Umschnürungsbewehrung mit reduziertem Bewehrungsgehalt im Vergleich zur umschnürten Zone an der Fuge eingelegt werden. Vollständig umschnürte Tübbinge können insbesondere für Tunnels mit variierenden Lastkombinationen entlang ihrer Länge sinnvoll sein, da sie zur lokalen Verstärkung der am stärksten beanspruchten Tübbingringe eingesetzt werden können und damit eine konstante geringere Dicke über die gesamte Tunnellänge ermöglichen. Darüber hinaus zeigen die auf zwei Seitenflächen jedes Prüfkörpers durchgeführten digitalen Bildkorrelationsmessungen, dass Rissbreiten die Bemessung nicht massgebend beeinflussen. Somit kann die volle Tragfähigkeit ausgenutzt werden.

Das Multi-Wedge-Spannungsfeld (MW-Spannungsfeld), das auf dem zuvor vorgestellten DW-cc-Spannungsfeld aufbaut und die Last von der Fuge auf den Bereich innerhalb der Bewehrung in der umschnürten Zone verteilt, wird eingeführt und gewährleistet dadurch einen konsistenten Übergang zu einer angrenzenden nicht umschnürten Zone. Hinsichtlich der Festigkeit der letzten wird vorgeschlagen, lediglich die einachsige Betondruckfestigkeit innerhalb der Fläche der Umschnürungsbewehrung anzusetzen. Mit diesen zwei Ansätzen kann das Tragverhalten von Tübbinglängsfugen auf mechanisch konsistente Weise untersucht werden, wobei die Verfolgung des gesamten Kraftflusses möglich ist. Darüber hinaus wird das MW-Spannungsfeld auf die Berücksichtigung des Effekts einer Aussparung für Führungsstäbe erweitert. Es werden drei verschiedene Varianten vorgestellt, wobei für die Variante, die eine Lastausbreitung nach innen (in Richtung der Aussparung) ermöglicht, die höchste vorhergesagte Tragfähigkeit resultiert.

Der Vergleich der experimentellen Daten mit dem MW-Spannungsfeld und drei bestehenden sowie zuvor eingeführten Bemessungsansätzen (DW-cc, GPC und DAUB:2024) für die Versuche ohne Aussparung für Führungsstäbe zeigt, dass die Modelle, die Effekte von Lastausbreitung und passiver Umschnürung in der umschnürten Zone kombinieren (MW, DW-cc und GPC), die Tragfähigkeit ähnlich und mit guter Genauigkeit vorhersagen, sofern die nicht umschnürte Zone ebenfalls berücksichtigt wird. Andernfalls können unkonservative Vorhersagen resultieren. Der DAUB:2024-Ansatz, der keine Umschnürungsbewehrung berücksichtigt, ist am konservativsten. Die MW-Spannungsfeldvariante für Aussparungen aufgrund von Führungsstäben. Welche die höchste Tragfähigkeit vorhersagt, zeigt im Vergleich mit dem Versuchsergebnis gute Übereinstimmung. Das Modell ist vielversprechend. Allerdings ist ein ein-

ziger Versuch als Grundlage für den Vergleich nicht ausreichend für eine aussagekräftige Überprüfung, weshalb weitere Versuche dafür notwendig sind.

Zusammenfassend lässt sich festhalten, dass (i) die vorgestellte experimentelle Serie an grossmassstäblichen Prüfkörpern mit Längsfugen die Aktivierung einer starken Umschnürungsbewehrung bestätigt und damit eine praktikable Möglichkeit zur Steigerung des axialen Widerstands der Längsfugen von Tübbingen darstellt und (ii) das MW-Spannungsfeld der einzige Bemessungsansatz ist, der den Kraftfluss auf eine mechanisch konsistente Weise erklären kann. Zudem zeigt sich eine gute Übereinstimmung mit den Versuchsresultaten, was das Modell erfolgreich validiert.

Im letzten Teil der Untersuchungen der Längsfugen wird das Tragverhalten von stahlfaserbewehrtem Beton (SFRC) unter Streifenbelastung mit und ohne konventioneller Stabstahlbewehrung näher untersucht. Es werden auf den Spannungsfeldern basierende Bemessungsansätze vorgeschlagen.

Faserbewehrter Beton wird in der Ingenieurpraxis aufgrund seiner hohen Robustheit, seines Nachrissverhaltens und seiner Rissbreitenbegrenzung zunehmend beliebter. Für Streifenbelastungen, wie sie beispielsweise in Längsfugen von Tübbingen vorkommen, bietet die Verwendung von faserbewehrtem Beton das Potenzial, konventionelle Bewehrung zu reduzieren. Allerdings kombiniert kein bestehender Bemessungsansatz die Effekte von Lastausbreitung, Umschnürungsbewehrung und Faserbewehrung, und die experimentelle Datenlage ist dünn. Das Tragverhalten von streifenbelastetem SFRC mit und ohne zusätzliche Stabbewehrung wird daher untersucht. Es werden elf Experimente an streifenbelasteten SFRC-Prüfkörpern aus zwei Serien vorgestellt, die die Streifenbelastung an Blockprüfkörpern und Prüfkörpern mit Längsfuge untersuchen. Davon enthielten sieben Prüfkörper zusätzliche konventionelle Umschnürungsbewehrung (hybrid bewehrte Prüfkörper), während die verbleibenden vier ausschliesslich faserbewehrt waren. Die experimentellen Ergebnisse zeigen unterschiedliche Versagensmodi für die hybrid bewehrten und die rein faserbewehrten Prüfkörper. Die hybrid bewehrten Prüfkörper versagten duktil, während die rein faserverstärkten Prüfkörper trotz weggesteuerter Belastung in einer steifen Prüfmaschine ein annähernd linear elastisches Verhalten mit ausgeprägter Entfestigung (Blockversuch) bzw. ein sprödes Versagen (Fugenversuche) zeigten. Während die rein faserbewehrten Prüfkörper spröde versagten, wurden Versagenslasten beobachtet, die höher als die Last lagen, bei der erstmals oberflächliche Risse auftraten. Dies deutet darauf hin, dass die Fasern aktiviert wurden und damit mutmasslich das Wachstum anfänglicher (Mikro-)Risse hemmten. Im Vergleich zu Stahlbetonblockprüfkörpern wiesen die meisten hybrid bewehrten SFRC-Blockprüfkörper höhere Tragfähigkeiten in Verbindung mit gesteigerter Duktilität auf. Gleiches gilt für die Fugenversuche, solange nicht die nicht umschnürte Zone für das Versagen massgebend war. Es sei angemerkt, dass mit einem höheren Anteil an konventioneller Bewehrung der Einfluss der Fasern abnimmt. Die Rissbreiten wurden mittels digitaler Bildkorrelation auf der Prüfkörperoberfläche gemessen. Die bewehrten SFRC-Prüfkörper wiesen bei gleichem Lastniveau geringere Rissbreiten auf als vergleichbare Stahlbetonprüfkörper mit moderaten konventionellen Umschnürungsbewehrungsgraden. Bei grösserer Umschnürung wurde kein günstiger Einfluss der Fasern auf die Rissbreiten beobachtet.

Darüber hinaus werden Modellierungsansätze für hybrid bewehrten und rein stahlfaserbewehrten Beton unter Streifenbelastung vorgestellt. Für hybrid bewehrte Prüfkörper wird vorgeschlagen, die durch konventionelle Bewehrung bereitgestellten Umschnürungsspannungen mit der gerissenen Restzugfestigkeit des SFRC zu superponieren. Diese Spannungen werden anschliessend auf mechanisch fundierte Modelle für Stahlbetonelemente unter Streifenbelastung angewendet, die die Lastausbreitung und passive Umschnürung berücksichtigen, so wie das Multi-Wedge- oder Dual-Wedge-Spannungsfeld. Basierend auf standardisierten Materialversuchen mit prismatischen SFRC-Balken in Dreipunktbiegeversuchen gemäss EN 14651 wird die Restzugfestigkeit für eine Rissbreite von 1 mm gemäss dem linearen Modell des *fib* Model Code 2020 bestimmt. Der Vergleich der experimentellen Ergebnisse mit den Vorhersagen der zwei Spannungsfelder zeigt gute Übereinstimmungen. Obwohl lediglich sieben Versuche verfügbar sind, beinhaltet der Datensatz zwei verschiedene Bewehrungstypen (Bügelbewehrung und geschweisste Leiterbewehrung), unterschiedliche konventionelle Bewehrungsgrade sowie variierende Lasteinleitungsbreiten, was eine hinreichende Validierung ermöglicht. Zudem zeigten alle hybrid bewehrten Prüfkörper ein duktiles Versagen. Folglich können die Modelle als Grundlage für die Bemessung empfohlen werden.

Für die SFRC-Prüfkörper ohne zusätzliche konventionelle Bewehrung zur Kontrolle des Rissbreitenwachstums wird das einfachste Dual-Wedge-Spannungsfeld zur Erfassung der Lastausbreitung vorgeschlagen, welches keine passive Umschnürung berücksichtigt. Es wird angenommen, dass die Restzugfestigkeit des SFRC, die hier für eine Rissbreitenöffnung von 0.5 mm bestimmt wird, die Spaltzugspannungen aufnimmt. Die Modellvorhersagen liegen unter Betrachtung der experimentellen Ergebnisse auf der sicheren Seite, während das Spannungsfeld ein nützliches Werkzeug zur Verfolgung des Kraftflusses darstellt. Dennoch erfordern die spröde Versagensart der Fugenversuche und ein damit verbundener möglicher Massstabseffekt weitere Untersuchungen für eine erfolgreiche Validierung des Modells. Dies könnte eine Begrenzung der Höhe des Spannungsfelds umfassen, bis zu welcher gleichmässige Restzugspannungen angenommen werden, um eine begrenzte Lastverteilung und variierende Rissöffnungen über die Prüfkörperhöhe zu berücksichtigen, was zu niedrigeren Tragfähigkeitsvorhersagen führt.

Es sei darauf hingewiesen, dass alle vorgeschlagenen Modellierungsansätze auf einer angemessenen Beschreibung der mechanischen Eigenschaften des SFRC innerhalb des Bauteils beruhen. Für die Restzugfestigkeit spielen die Orientierung und Verteilung der Fasern eine bedeutende Rolle. Dementsprechend müssen geeignete Abminderungsfaktoren auf die Restzugfestigkeit angewendet werden, wenn die Faserorientierung oder -verteilung in den Prüfkörpern von jener in den Materialcharakterisierungsversuchen abweicht, die zur Bestimmung der mechanischen Eigenschaften verwendet wurden.

Zusammenfassend lässt sich festhalten, dass SFRC das Tragverhalten von Beton unter Streifenbelastung verbessern und Rissbreiten minimieren kann. SFRC ist besonders effizient bei hybrid bewehrten Prüfkörpern in Kombination mit geringen konventionellen Umschnürungsbewehrungsgraden. Folglich stellt SFRC eine praktikable Möglichkeit für die Bemessung von vorfabrizierten Tübbingen dar, da es den erforderlichen

konventionellen Bewehrungsgehalt der Längsfugen reduzieren kann und gleichzeitig weitere günstige Effekte, wie eine höhere Robustheit, bietet. Die Tragfähigkeit der hybrid bewehrten Prüfkörper kann mithilfe des vorgeschlagenen Modellierungsansatzes zuverlässig bestimmt werden. Dagegen erfordert die Anwendung von streifenbelasteten SFRC-Prüfkörpern ohne zusätzliche konventionelle Stabbewehrung in der Bemessung weitere Untersuchungen, insbesondere hinsichtlich eines möglichen Massstabseffekts im Zusammenhang mit der spröden Versagensart, trotz der vielversprechenden Modellierungsansätze.

Für die Ringfugen ist der Bauzustand relevant, bei dem die Druckkräfte der Vortriebszylinder in den zuletzt installierten Ring eingeleitet werden. Die Übertragung der Vortriebszylinderdruckkräfte durch die Ringfugen führt zu hohen lokalen Spannungen in den Tübbingen und kann bei mangelhafter Bemessung zu Schäden führen. Obwohl solche Schäden die Tragsicherheit i. d. R. nicht beeinträchtigen, können sie zu erforderlichen Instandsetzungsarbeiten führen, um beispielsweise die Anforderungen an die Wasserdichtigkeit bei unzulässig hohen Rissbreiten zu erfüllen.

Für die Bemessung relevant sind (i) die Druckspannungen während der Kraftübertragung über die Vortriebszylinderschuhe, (ii) die Spaltzugkräfte, die aus der dreidimensionalen Lastausbreitung resultieren sowie (iii) die Randzugkräfte zwischen den einzelnen Vortriebszylinderschuhen. Die Spaltzugkräfte (ii) und die Randzugkräfte (iii) resultieren aus Verträglichkeitsbedingungen, wobei erstere, falls erforderlich, die Aufnahme von Druckspannungen (i) ermöglichen, die die einachsige Betondruckfestigkeit überschreiten (Teilflächenpressung). Weiterführend können erhebliche Spannungen durch Versätze in der Auskleidungsanordnung entstehen, wobei Zugspannungen besonders relevant sind, da sie Risse verursachen und die Rissbreiten massgebend beeinflussen.

Die Lasteinleitung der Vortriebszylinderdruckkräfte wird anhand von linear elastischen und nichtlinearen Finite-Elemente-Analysen untersucht und verglichen. Darüber hinaus wird der Einfluss von Versätzen in der Tübbinganordnung diskutiert. Die Untersuchungen ergaben, dass aufgrund der Rissentwicklung erhebliche Unterschiede zwischen einer ungerissen linear elastischen und einer nichtlinearen Analyse bestehen. Aufgrund der zusätzlichen Unsicherheit hinsichtlich der Versätze empfiehlt es sich, beide Analysen durchzuführen und die Bewehrung für die massgebenden Spannungen aus beiden Analysen zu bemessen, wobei lediglich anhand der nichtlinearen Analyse Rückschlüsse auf die Rissbreiten gezogen werden können. Die zu erwartenden Rissbreiten infolge von Versätzen können anhand bestehender geometrischer Überlegungen abgeschätzt werden, wobei jedoch bei der Ausführung sorgfältig auf die Einbaugenauigkeit geachtet werden muss, da die Bewehrung die Rissbreiten zwar begrenzen, aber Risse nicht verhindern kann.

Die in diesem Bericht vorgestellten theoretischen und experimentellen Untersuchungen liefern relevante neue Erkenntnisse über das Tragverhalten von Stahlbeton unter Streifenbelastung. Zudem bieten die vorgeschlagenen Modelle eine solide Grundlage für eine mechanisch konsistente Berücksichtigung der kombinierten Wirkung von Lastausbreitung und Umschnürungsbewehrung bei der Bemessung von Längsfugen, was effiziente Tübbinge ermöglicht. Hinsichtlich der Ringfugen verdeutlicht der Be-

richt, dass im Vergleich zur üblichen linear elastischen Bemessung relativ einfache, jedoch mechanisch konsistente nichtlineare Analysen einen Mehrwert bieten, indem sie Risse berücksichtigen und zusätzlich die Bestimmung von Rissbreiten ermöglichen. Es zeigt sich auch, dass der Einfluss von Versätzen in Ringfugen nur bis zu einem gewissen Grad durch eine dichte Bewehrung kompensiert werden kann, was die Bedeutung eines präzisen Einbaus hervorhebt.

Résumé

Les revêtements par voussoirs préfabriqués en béton armé sont couramment utilisés dans la construction contemporaine de tunnels. Dans leur conception, les joints longitudinaux et circonférentiels jouent un rôle majeur. Ce projet étudie les deux types de joints, en mettant l'accent sur les joints longitudinaux.

Les joints longitudinaux de ces revêtements présentent généralement une surface de contact réduite, souvent déterminante pour le dimensionnement – notamment dans les tunnels soumis à une forte pression hydrostatique ou traversant des terrains poussants ou gonflants, avec des efforts de compression circonférentiels correspondants élevés. Les voussoirs en béton armé, avec une armature de frettage importante dans les zones d'introduction des charges, constituent une option viable pour résister à des charges élevées aux joints de voussoirs sans augmenter l'épaisseur du revêtement. Cependant, cette solution n'a pas encore été largement adoptée dans la pratique de la construction de tunnels, principalement en raison d'une couverture limitée dans les normes existantes, elle-même due au manque de modèles mécaniques validés expérimentalement.

Le comportement structurel des joints longitudinaux des revêtements de tunnel correspond essentiellement à un chargement uniforme sur une bande. La résistance d'un béton armé soumis à un chargement uniforme sur une bande peut être plusieurs fois supérieure à sa résistance à la compression uniaxiale. L'augmentation de la résistance peut être attribuée aux contraintes de confinement latérales (c'est-à-dire perpendiculaires à la direction de chargement), qui résultent soit de la diffusion des charges (confinement géométrique), soit de l'armature de frettage (confinement passif). Par conséquent, pour dimensionner efficacement les joints longitudinaux des revêtements, le confinement géométrique et le confinement passif doivent tous deux être pris en compte. À cet effet, ce rapport étudie le comportement mécanique fondamental sous chargement uniforme sur une bande, avec un confinement passif important, au moyen d'analyses théoriques et expérimentales, afin de proposer, en définitive, des méthodes de dimensionnement. Les études sur les joints longitudinaux peuvent, dans les grandes lignes, être divisées en trois parties.

La première partie passe en revue les travaux de recherche existants sur le confinement passif dans le béton armé, propose un modèle mécanique prenant en compte la diffusion tridimensionnelle locale des charges par les armatures de frettage activées, et valide avec succès ce modèle. Le confinement passif assuré par l'armature transversale est pris en compte dans le dimensionnement des structures en béton armé soumises à des charges de compression élevées, telles que les colonnes, les piles ou les voussoirs de revêtement de tunnel. Dans les directives actuelles, plusieurs modèles existent pour prendre en compte cet effet bénéfique. Cependant, ces approches manquent de cohérence mécanique concernant la diffusion tridimensionnelle des forces de confinement. L'introduction d'un nouveau modèle contribue à combler cette lacune. Le nouveau modèle tient compte du flux tridimensionnel des forces par des coques paraboliques en

compression pure et prend en compte les conditions d'équilibre et de plasticité, correspondant ainsi à une borne inférieure selon la théorie de la plasticité.

Le nouveau modèle est comparé aux approches de dimensionnement actuelles pour le confinement des structures en béton armé et validé avec succès par rapport aux données expérimentales. Comparé aux méthodes de dimensionnement existantes (Eurocode 2 - EN 1992-1-1:2023 (EC2:2023), SIA 262:2013 et *fib* Model Code 2010 (MC2010)), le nouveau modèle présente plusieurs avantages clés: (i) les espacements de l'armature de frettage dans la direction latérale et la direction de chargement sont pris en compte de manière cohérente, (ii) le modèle repose sur une base mécanique, (iii) fournit une solution permettant de suivre le flux des forces, et (iv) peut expliquer de manière cohérente le comportement au confinement de sections rectangulaires et circulaires. Bien que le nouveau modèle soit mécaniquement cohérent et améliore la compréhension du comportement du béton confiné, son utilisation dans la pratique est limitée en raison de la complexité de la caractérisation de la surface de béton confiné déterminante. En simplifiant la caractérisation de la surface de béton confiné déterminante, il a été possible de présenter une adaptation du modèle, également validée avec succès par rapport aux données expérimentales. Ce modèle est plus facile à appliquer que les modèles existants des directives actuelles, s'avérant être une alternative intéressante pour la pratique du dimensionnement.

De plus, dans le contexte de la première partie de l'étude sur les joints longitudinaux, le comportement de treillis soudés agissant comme armature de frettage est étudié expérimentalement. Les treillis soudés sont de plus en plus utilisés dans la fabrication des voussoirs de revêtement de tunnel en béton armé car ils simplifient l'assemblage des armatures, réduisent le temps et le coût de préfabrication, sont économes en ressources et facilitent la mise en œuvre en évitant la congestion. Bien que leurs avantages soient connus, leur comportement sous charge n'est pas encore entièrement élucidé. Pour combler cette lacune, des mesures par fibre optique ont été réalisées le long de plusieurs barres d'armature du treillis soudé, avec des connexions soudées de qualité SF50, sur une éprouvette en béton armé soumise à un chargement uniforme sur bande,. Deux barres transversales et quatre barres longitudinales par éprouvette ont été instrumentées avec des capteurs à fibre optique. Sur la base des mesures de déformation par fibre optique et des caractéristiques des barres d'armature nues, les contraintes normales et la courbure des barres d'armature ont pu être déterminées. Il a ainsi pu être démontré que deux barres longitudinales sont suffisantes pour activer pleinement (jusqu'à la plastification) les barres transversales sur la distance entre les nœuds de soudure intérieurs. De plus, les mesures ont fourni des informations sur le transfert de charge entre l'armature et le béton environnant, nécessaire pour déterminer l'effet des treillis soudés agissant comme confinement passif. Outre l'introduction directe de charge aux nœuds de soudure, les barres longitudinales sont sollicitées en flexion, comme en témoignent les courbures transversales observées. Elles sont néanmoins capables d'assurer un confinement dans la direction longitudinale. Des études supplémentaires seraient nécessaires afin de vérifier si les résultats s'appliquent également à d'autres dispositions d'armatures ou de configurations de chargement différentes. Néanmoins, l'étude approfondit la compréhension du comportement des treillis soudés et démontre qu'ils constituent une alternative prometteuse aux étriers conventionnels pour la fabrication des voussoirs de revêtement de tunnel.

La deuxième partie des études sur les joints longitudinaux explore le comportement du béton armé soumis à un chargement uniforme sur une bande, au moyen d'une combinaison d'études expérimentales et théoriques. À cette fin, deux campagnes d'essais sur des blocs en béton armé et sur des voussoirs à grande échelle munis de joints longitudinaux sont présentées, et leurs résultats sont discutés. Sur la base des résultats expérimentaux, des modèles de champs de contraintes mécaniquement cohérents prenant en compte l'effet combiné de la diffusion des charges et de l'armature de frettage sont développés.

Le chargement uniforme sur une bande pour du béton armé est un problème courant pour la pratique de l'ingénierie. L'augmentation de la résistance à la compression du béton au droit de l'introduction des charges peut être attribuée aux contraintes de confinement géométriques et passives, causées respectivement par la diffusion des charges et par l'armature. Cependant, les dispositions constructives actuelles ne permettent pas de combiner ces deux effets de confinement, ce qui conduit à des dimensionnements excessivement conservateurs. De plus, les données expérimentales sur les éléments en béton soumis à un chargement uniforme sur bande avec confinement passif prononcé et des taux de concentration de charge modérés – courants, par exemple, dans les joints longitudinaux des revêtements par voussoirs – sont rares. Dans un premier temps, différents modèles de chargement uniforme sur bande, ainsi qu'une campagne d'essais de 15 blocs en béton, avec un confinement passif prononcé et des taux de concentration de charge modérés, testés jusqu'à la rupture, sont présentés. Les paramètres étudiés étaient (i) le taux et le type d'armature, (ii) la largeur et la position de la surface chargée, et (iii) la résistance du béton. Les résultats montrent que les éprouvettes avec un taux mécanique d'armatures suffisant présentent un comportement ductile et que la résistance peut être substantiellement augmentée avec des quantités plus importantes d'armatures de frettage, ce qui a été validé pour différents types d'armatures (étriers, treillis soudés et armatures à double tête d'ancrage). Les performances des différents types d'armatures ne variaient pas substantiellement, indiquant que les treillis soudés peuvent être une alternative viable aux étriers. De plus, les essais confirment que le confinement géométrique diminue avec une largeur de chargement plus importante ou un chargement excentré, réduisant ainsi la contrainte de contact maximale à la rupture au droit de l'introduction des charges. Enfin, les résultats révèlent que, par rapport aux éprouvettes de résistance normale, les éprouvettes à haute résistance tendent à présenter des résistances normalisées plus faibles, qui, de surcroît, peuvent ne pas être pleinement exploitées, car l'ouverture des fissures, déterminée par corrélation d'images numériques lors des essais, est déterminante. Cependant, seules trois éprouvettes étaient constituées de béton à haute résistance, et davantage de données expérimentales sont nécessaires pour étayer ces conclusions préliminaires.

Outre la campagne d'essais, quatre modèles différents – le champ de contraintes Dual-Wedge (DW-cc), une simplification du champ de contraintes (DW-s), le modèle de confinement géométrique et passif (GPC), et l'approche selon la directive du Deutscher Ausschuss für unterirdisches Bauen (DAUB:2024) –pour le dimensionnement des éléments en béton armé soumis à un chargement sur bande sont présentés, et la manière de déterminer les contraintes de confinement et la surface de béton confiné pour des espacements d'armature réguliers et irréguliers est introduite. Les différents modèles sont comparés aux données expérimentales, y compris les 15 essais sur les blocs. Il est

montré que les modèles associant les effets de la diffusion des charges et du confinement passif (DW-cc, DW-s et GPC) prédisent, en moyenne, une résistance similaire, avec une bonne précision, des niveaux de variabilité comparables et, généralement, du côté de la sécurité. L'approche DAUB:2024, qui ne considère que la diffusion des charges, s'avère très conservatrice dans la majorité des cas. La validation, réalisée avec succès, des trois modèles intégrant le confinement passif confirme indirectement que les approches proposées pour déterminer les contraintes de confinement et la surface de béton confinée sont raisonnables. Parmi ces modèles, le modèle GPC n'examine que deux sections pour déterminer la résistance des éléments en béton armé soumis à un chargement uniforme sur une bande: l'une à l'introduction des charges et l'autre à la position où la charge est entièrement diffusée. En revanche, le champ de contraintes Dual-Wedge capture l'intégralité du flux des forces, permettant d'analyser la résistance de chaque section horizontale de la zone de diffusion et de déterminer de manière cohérente la position des armatures. De plus, il est conforme à l'EC2:2023, qui permet la combinaison du confinement passif et géométrique pour le dimensionnement des zones partiellement chargées, si des champs de contrainte tridimensionnels sont appliqués. D'autre part, alors que l'application du DW-cc pour le dimensionnement soit assez complexe, le modèle simplifié (DW-s), obtenu à partir d'une étude paramétrique du champ de contraintes Dual-Wedge, se distingue par sa formulation directe et par le coefficient de variation le plus faible, ce qui indique qu'il est le mieux à même de traiter les différentes influences sur la résistance malgré sa simplicité.

Les auteurs proposent donc de dimensionner les éléments en béton armé soumis à un chargement uniforme sur bande selon la simplification du champ de contraintes Dual-Wedge (DW-s), avec les paramètres déterminés sur la base du modèle de confinement passif développé dans la première partie de l'étude. Le modèle DW-cc, mécaniquement cohérent, peut fournir des informations supplémentaires sur la disposition de l'armature et est le seul modèle capable de prendre en compte la variation des contraintes de confinement dans les zones de confinement et d'éclatement. Par conséquent, le modèle DW-cc est proposé pour les évaluations détaillées et s'avère particulièrement utile pour l'évaluation des structures existantes.

Alors que les essais sur les blocs se concentraient sur des éléments en béton entièrement confinés soumis à un chargement uniforme sur bande, les essais à grande échelle sur des éprouvettes à joint longitudinal ont étudié le comportement sous charge de revêtements à voussoirs préfabriqués en béton armé. Les voussoirs en béton armé avec une armature de frettage importante dans la zone de diffusion des charges adjacente aux joints constituent une option viable pour résister aux efforts de compression circonférentiels élevés correspondants. Cependant, cette solution n'a pas encore été largement utilisée dans la construction de tunnels, principalement en raison d'une couverture limitée des directives existantes et d'un manque de validation expérimentale. Cette lacune est adressée comme suit: (i) les résultats d'une campagne d'essais étudiants le comportement structurel des voussoirs de revêtement de tunnel avec joints longitudinaux à l'aide de neuf éprouvettes en béton armé avec un confinement passif prononcé sont présentés, (ii) une approche de modélisation basée sur un champ de contraintes spécifique pour le dimensionnement des joints longitudinaux permettant de suivre l'intégralité du flux des forces est proposée et (iii) ce champ de contraintes est étendu pour couvrir l'effet des rainures de guidage.

Les paramètres étudiés lors de la campagne d'essais étaient (i) le taux d'armature transversale, (ii) la disposition de l'armature et (iii) la géométrie du joint des éprouvettes en béton armé renforcées par des treillis soudés. Les résultats expérimentaux soulignent qu'avec un rapport de concentration de charge plus élevé (largeur de joint plus grande), la contrainte de contact au joint diminue en raison du confinement géométrique limité, mais l'effort normal augmente tout de même en raison de la surface de joint plus grande. L'armature de frettage contribue à la résistance des joints longitudinaux. Cependant, l'augmentation de charge possible en fournissant une armature de frettage est limitée si les voussoirs contiennent, en plus de la zone confinée au joint, une zone non confinée. Dans la zone non confinée, seule la résistance à la compression uniaxiale du béton peut être mobilisée, sur une surface inférieure à la section du voussoir, en raison de la fissuration associée à l'éclatement du béton, qui se produit dans la zone confinée et se propage dans la zone non confinée. Par conséquent, les voussoirs à taux d'armature élevé et à joints larges, capables de résister à des efforts normaux élevés, sont susceptibles aux ruptures dans la zone non confinée. Les éprouvettes présentant une rupture dans la zone non confinée ont montré un comportement moins ductile que celles présentant une rupture dans la zone confinée. Afin d'augmenter la résistance des voussoirs avec zone non confinée déterminante, une armature de frettage peut être placée dans cette zone, avec un taux d'armature réduit par rapport à la zone confinée au niveau du joint. Les voussoirs entièrement confinés peuvent être particulièrement utiles pour les tunnels soumis à des chargements variables le long de leur tracé, car ils permettent de renforcer localement les voussoirs des anneaux les plus sollicités et de maintenir ainsi une épaisseur constante et plus faible sur l'intégralité de la longueur du tunnel. De plus, les mesures par corrélation d'images numériques utilisées pour étudier la fissuration sur les deux faces latérales de chaque éprouvette indiquent que la largeur des fissures n'est pas déterminante pour le dimensionnement; l'intégralité de leur résistance peut donc être exploitée.

Le champ de contraintes Multi-Wedge (MW), qui s'appuie sur le champ de contraintes DW-cc précédemment présenté et diffuse la charge depuis le joint vers la zone à l'intérieur de l'armature dans la zone confinée, est introduit, assurant ainsi une transition cohérente vers une zone non confinée adjacente. Concernant la résistance de cette dernière, il est proposé de considérer uniquement la résistance à la compression uniaxiale du béton à l'intérieur de la zone de l'armature de frettage. Avec ces deux approches, le comportement des joints longitudinaux des voussoirs de revêtement de tunnel peut être étudié de manière mécaniquement cohérente tout en suivant l'intégralité du flux des forces. De plus, le champ de contraintes MW est étendu pour tenir compte de l'effet d'une rainure de guidage. Trois variantes sont présentées dont la variante permettant la diffusion des charges vers l'intérieur (vers la rainure de guidage) qui conduit à la prédiction de la résistance la plus élevée.

La comparaison des données expérimentales avec le champ de contraintes MW et trois approches de dimensionnement existantes, précédemment introduites (DW-cc, GPC et DAUB :2024) pour les essais sans rainure de guidage révèle que les modèles combinant l'effet de la diffusion des charges et l'effet du confinement passif dans la zone confinée (MW, DW-cc et GPC) prévoient une résistance similaire, avec une bonne précision, à condition que la zone non confinée soit également prise en compte. Dans le cas contraire, des prédictions non conservatrices peuvent en résulter. L'approche

DAUB:2024, qui ne prend pas en compte l'armature de frettage, est la plus conservatrice. La comparaison de la variante du champ de contraintes MW pour les rainures de guidage, qui prédit la résistance la plus élevée, avec les résultats expérimentaux montre que le modèle est prometteur. Cependant, ne disposer que d'un seul essai à comparer n'est pas suffisant pour le valider avec succès, d'autres essais sont donc nécessaires.

En conclusion, (i) la campagne d'essais présentée sur les éprouvettes à grande échelle avec joints longitudinaux confirme qu'une armature de frettage importante peut être activée, constituant ainsi une option viable pour augmenter la résistance à l'effort normal des joints longitudinaux des voussoirs de revêtement de tunnel et (ii) le champ de contraintes MW est la seule approche de dimensionnement capable d'expliquer le flux des forces de manière mécaniquement cohérente. Il présente un bon accord avec les données expérimentales, ce qui valide le modèle avec succès.

La dernière partie de l'étude sur les joints longitudinaux approfondit l'étude d'un chargement sur bande avec du béton fibré, pourvu ou non d'armature conventionnelle, et propose des approches de dimensionnement basées sur les champs de contraintes.

Le béton fibré devient de plus en plus populaire dans la pratique de l'ingénierie en raison de sa grande robustesse, de son comportement après fissuration et de son contrôle de la fissuration. Pour un chargement uniforme sur une bande, courant dans les joints longitudinaux des voussoirs de revêtement de tunnel, par exemple, l'utilisation du béton fibré a le potentiel de réduire le taux d'armature conventionnelle. Cependant, aucune approche de dimensionnement existante ne combine les effets de la diffusion des charges, de l'armature de frettage et du renforcement par fibres, de plus, les données expérimentales sont rares. Le comportement du béton fibré soumis à un chargement sur une bande, avec et sans armatures supplémentaires, est étudié. Onze essais sur des éprouvettes en béton fibré, soumises à un chargement uniforme sur bande, issues de deux campagnes étudiant ce chargement sur des blocs et des joints longitudinaux de voussoirs de revêtement de tunnel, sont présentés. Sept éprouvettes contenaient une armature de frettage conventionnelle supplémentaire (éprouvettes renforcées de manière hybride), tandis que les quatre restantes étaient uniquement renforcées par des fibres. Les résultats expérimentaux mettent en évidence différents modes de rupture pour les éprouvettes hybrides et uniquement renforcées par fibres. Les éprouvettes hybrides ont présenté une rupture ductile, tandis que les éprouvettes uniquement renforcées par fibres ont présenté un comportement approximativement linéaire-élastique avec un adoucissement prononcé (essai sur les blocs) ou une rupture fragile (essais sur joints), malgré un chargement en contrôle de déplacement sur une machine d'essai rigide. Alors que les éprouvettes uniquement renforcées par fibres aient présenté une rupture fragile, des charges de rupture supérieures à la charge d'apparition des premières fissures en surface ont été observées, indiquant que les fibres étaient activées, entravant probablement la croissance des (micro-) fissures initiales. Par rapport aux éprouvettes constituées de blocs de béton armé, la plupart des éprouvettes constituées de blocs de béton renforcés de manière hybride ont présenté des résistances plus élevées et une ductilité accrue. Il en va de même pour les essais sur joints tant que la zone non confinée n'est pas déterminante pour la rupture. Notons qu'avec un taux d'armature conventionnelle plus élevé, l'effet des fibres diminue. Les largeurs de fissures en surface des éprouvettes ont été mesurées par corrélation d'images numériques. Les

éprouvettes en béton fibré armé ont présenté des ouvertures de fissures plus faibles au même niveau de charge que les éprouvettes en béton armé similaires avec des taux d'armature de frettage conventionnelle modérés. Pour un confinement plus élevé, aucun effet bénéfique des fibres sur l'ouverture des fissures n'a été observé.

De plus, des approches de modélisation pour le béton renforcé de manière hybride et uniquement fibré, soumis à un chargement uniforme sur une bande, sont présentées. Pour les éprouvettes hybrides, il est proposé de superposer linéairement les contraintes de confinement fournies par l'armature conventionnelle à la résistance résiduelle à la traction post-fissuration du béton fibré. Ces contraintes sont ensuite appliquées aux modèles mécaniquement cohérents établis pour les éléments en béton armé soumis à un chargement uniforme sur une bande qui prennent en compte la diffusion des charges et le confinement passif, tels que les champs de contraintes Multi-Wedge ou Dual-Wedge. La résistance résiduelle à la traction est déterminée pour une largeur de fissure de 1 mm selon le modèle linéaire du *fib* Model Code 2020, sur la base d'essais de matériaux standard sur des poutres prismatiques en béton fibré soumises à une flexion en trois points selon l'EN 14651. La comparaison des résultats expérimentaux avec les prédictions des deux champs de contraintes montre une bonne correspondance. Bien que seuls sept essais soient disponibles, l'ensemble de données contenait deux types d'armatures (étriers et treillis soudés), différents taux d'armatures conventionnelles et des largeurs d'application de charge variables, ce qui offre une validation substantielle. De plus, toutes les éprouvettes hybrides ont présenté des ruptures ductiles. Par conséquent, les modèles peuvent être recommandés comme base valable pour le dimensionnement.

Pour les éprouvettes en béton fibré sans armature conventionnelle supplémentaire contrôlant l'ouverture des fissures, le champ de contraintes Double-Wedge le plus simple, qui ne considère aucun confinement passif, est proposé pour tenir compte de la diffusion des charges. La résistance résiduelle à la traction du béton fibré, déterminée ici pour une ouverture de fissure de 0,5 mm, est supposée équilibrer les contraintes d'éclatement. Les prédictions du modèle sont du côté de la sécurité par rapport aux résultats expérimentaux, et le champ de contraintes est un outil utile pour suivre le flux des forces. Néanmoins, le mode de rupture fragile des essais sur joints et un possible effet d'échelle associé nécessitent des études supplémentaires pour une validation complète du modèle. Cela pourrait inclure la limitation de la hauteur du champ de contraintes jusqu'à celle où les contraintes résiduelles de traction uniformes sont présumées tenir compte d'une diffusion de charge limitée et d'ouvertures de fissures variables sur la hauteur de l'éprouvette, aboutissant à des prédictions de résistance plus faibles.

Notons que toutes les approches de modélisation proposées reposent sur une description pertinente des propriétés mécaniques du béton fibré au sein de l'élément de structure. Pour la résistance résiduelle à la traction, l'orientation et la distribution des fibres revêtent une grande importance. En conséquence, des facteurs de réduction adéquats doivent être appliqués à la résistance résiduelle à la traction si l'orientation ou la distribution des fibres dans les éprouvettes diffère de celles des essais de matériau utilisés pour déterminer les propriétés mécaniques.

En conclusion, le béton fibré peut améliorer le comportement du béton soumis à un chargement uniforme sur une bande et réduire l'ouverture des fissures. Le béton fibré est particulièrement efficace pour les éprouvettes à renforcement hybride lorsqu'il est combiné à de faibles taux d'armature de frettage conventionnelle. Par conséquent, le béton fibré est une option viable pour le dimensionnement des voussoirs de revêtement de tunnel préfabriqués, car il permet de réduire le taux d'armature conventionnelle requis pour les joints longitudinaux tout en offrant d'autres avantages, tels qu'une robustesse accrue. La résistance des éprouvettes à renforcement hybride peut être déterminée de manière fiable à l'aide de l'approche de modélisation proposée. Cependant, l'application au dimensionnement d'éprouvettes en béton fibré soumises à un chargement uniforme sur une bande, sans armature conventionnelle supplémentaire, nécessite des études supplémentaires, notamment quant à un possible effet d'échelle lié au mécanisme de rupture fragile, malgré les approches de modélisation prometteuses.

Dans la dernière partie du rapport, les joints circonférentiels sont étudiés. Pour ceux-ci, la phase de construction est importante, car ils transmettent les forces des vérins de poussée à l'anneau le plus récemment installé. La transmission des forces de poussée à travers les joints circonférentiels engendre des contraintes locales élevées sur les voussoirs et peut entraîner des dommages si leur dimensionnement est inadapté. Bien que de tels dommages n'affectent généralement pas la sécurité structurelle, ils peuvent nécessiter des travaux de réparation, par exemple pour garantir les exigences d'étanchéité en cas de fissures plus larges que permis.

Les éléments pertinents pour le dimensionnement sont (i) les contraintes de compression lors de la transmission des forces via les sabots de vérin, (ii) les forces d'éclatement résultant de la distribution généralement tridimensionnelle des charges, et (iii) les forces de traction en bordure entre les sabots de vérin. Les forces d'éclatement (ii) et les forces de traction en bordure (iii) résultent de la compatibilité, les premières permettant, si nécessaire, l'absorption des contraintes de compression (i) dépassant la résistance à la compression uniaxiale du béton (chargement uniforme sur bande). De plus, des contraintes irrégulières importantes peuvent apparaître en raison de décalages dans la disposition du revêtement, les contraintes de traction étant particulièrement pertinentes, car elles provoquent des fissures et influencent significativement leur ouverture.

L'introduction des forces de poussée est étudiée et comparée au moyen d'analyses par éléments finis élastiques-linéaires et non linéaires. De plus, l'influence des décalages dans la disposition des voussoirs est discutée. Les études ont révélé qu'en raison du développement de fissures, il existe des différences considérables entre une analyse élastique-linéaire non fissurée et une analyse non linéaire. En raison de l'incertitude supplémentaire liée aux décalages, il est conseillé d'effectuer les deux analyses et de dimensionner l'armature pour les contraintes déterminantes apparaissant dans chacune d'elles, bien que seule l'analyse non linéaire permette de tirer des conclusions sur la largeur des fissures. La largeur des fissures attendues dues aux décalages peut être estimée à l'aide de considérations géométriques existantes, bien qu'il convienne de faire preuve de vigilance lors de la construction pour assurer la précision de la pose, car les armatures peuvent limiter l'ouverture des fissures mais ne peuvent pas empêcher leur apparition.

Les études théoriques et expérimentales présentées dans ce rapport fournissent de nouvelles informations pertinentes sur le comportement du béton armé soumis à un chargement uniforme sur une bande. De plus, les modèles proposés constituent une base solide pour une prise en compte mécaniquement cohérente de l'effet combiné de la diffusion des charges et de l'effet de l'armature de frettage dans le dimensionnement des joints longitudinaux du revêtement de tunnel, permettant la réalisation de voussoirs efficients. En ce qui concerne les joints circonférentiels, le rapport souligne que, par rapport au dimensionnement élastique-linéaire couramment utilisé, des analyses non linéaires relativement simples mais mécaniquement cohérentes apportent une valeur ajoutée en tenant compte de la fissuration et permettent également de déterminer les largeurs des fissures. Il démontre également que l'influence des décalages dans les joints de couronne ne peut être considérée que de manière limitée, même avec une disposition dense d'armature, soulignant l'importance d'une pose précise.

Summary

Precast reinforced concrete segmental linings are commonly used in modern tunnelling. In their design, the longitudinal and ring joints play a major role. This project investigates both joint types, with the main focus on the longitudinal joints.

The longitudinal joints in these linings typically have a reduced contact cross-section, which often governs the design – particularly in tunnels under high hydrostatic pressure or crossing squeezing or swelling ground, with correspondingly high circumferential compressive forces. Reinforced concrete segments with substantial confining reinforcement at the load introduction are a viable option for resisting high loads at segment joints without increasing the lining thickness. However, this solution has not yet been widely adopted in tunnelling practice, mainly due to limited coverage by existing standards, which is in turn caused by the lack of experimentally validated mechanical models.

The structural behaviour of longitudinal tunnel lining joints essentially corresponds to strip loading. The load-bearing capacity of strip-loaded reinforced concrete can be several times higher than the uniaxial concrete compressive strength. The strength increase can be attributed to lateral (i.e., perpendicular to the loading direction) confining stresses, which result either from load dispersion (geometrical confinement) or confining reinforcement (passive confinement). Consequently, in order to design the longitudinal joints of segmental linings efficiently, both geometrical and passive confinement must be considered. For this purpose, this report fundamentally investigates the mechanical behaviour under strip loading with substantial passive confinement using theoretical and experimental analyses to ultimately propose design approaches. The investigations of the longitudinal joints can be roughly divided into three parts.

The first part reviews existing research on passive confinement in reinforced concrete, proposes a mechanical model considering the local three-dimensional load dispersion of activated confining reinforcement, and successfully validates the model. Passive confinement provided by transverse reinforcement is taken into account in the design of reinforced concrete structures subjected to high compressive loading such as columns, piers or tunnel lining segments. In current guidelines, several models exist to account for this beneficial effect. However, these approaches lack mechanical consistency regarding the three-dimensional load dispersion of the confining forces. The introduction of a new model contributes to bridging this gap. The new model accounts for the three-dimensional force flow by parabolic compression-only shells and considers equilibrium and the yield conditions, thereby corresponding to a lower-bound solution according to the theory of plasticity.

The new model is compared to current design approaches for the confinement of RC structures and is successfully validated against experimental data. Compared to existing design approaches (Eurocode 2 - EN 1992-1-1:2023 (EC2:2023), SIA 262:2013, and *fib* Model Code 2010 (MC2010)), the new model has several key advantages: (i) the confining reinforcement spacings in lateral and loading directions are considered

coherently, (ii) the model builds on a mechanical basis, (iii) it provides a solution that allows following the force flow, and (iv) the model can consistently explain the confining behaviour of rectangular and circular cross-sections. While the new model is mechanically consistent and improves the understanding of the behaviour of confined concrete, it is of limited use for engineering practice due to the complexity of determining the governing confined concrete area. By simplifying the determination of the governing confined concrete area, it was possible to present a model adaptation that can be successfully validated against experimental data and is even easier to apply than the existing models in current guidelines, proving to be a valuable alternative for design practice.

Moreover, in the context of the first part of the investigation on the longitudinal joints the load-bearing behaviour of welded grid reinforcement acting as confining reinforcement is experimentally investigated. Welded reinforcement grids are increasingly used in the production of reinforced concrete tunnel lining segments, since they simplify the reinforcement assembly, reduce time and cost in the prefabrication process, are resource-efficient and facilitate casting by avoiding congestion. While their advantages are known, their load-bearing behaviour is not yet fully understood. To close this research gap, fibre optical measurements of several reinforcing bars of the welded reinforcement grid with welding connections with quality SF50 of a strip loaded reinforced concrete specimen were conducted. Two transverse and four longitudinal reinforcing bars per specimen were instrumented with fibre optical sensors. Based on the fibre optical strain measurements and the characteristics of the bare reinforcing bars, the normal stresses and the curvature of the reinforcing bars could be inferred. Thereby, it could be shown that two longitudinal reinforcing bars are sufficient to fully activate (reaching yielding) the transverse reinforcing bars over the length between the inner welded cross joints. Furthermore, the measurements yielded insight into the load transfer between reinforcement and the surrounding concrete, which is required to determine the effect of the welded grids acting as passive confinement. Besides direct load introduction at the cross joints, the longitudinal reinforcing bars are activated in bending, as highlighted by the observed transverse curvatures. Nonetheless, they are able to provide confinement in the longitudinal direction. Further research would be needed to validate if the results also apply to varying reinforcement layouts or loading configurations. Nevertheless, the study increases the understanding of the load-bearing behaviour of welded reinforcement grids and proves that they are a promising alternative to conventional stirrup reinforcement for the production of tunnel lining segments.

The second part of the investigations of the longitudinal joints explores the load-bearing behaviour of strip-loaded reinforced concrete through a combination of experimental and theoretical investigations. To this end, two experimental campaigns on reinforced concrete blocks and on large-scale segments with longitudinal joints are presented and the results are discussed. Based on the experimental findings, mechanically sound stress field models that consider the combined effect of load dispersion and confining reinforcement are developed.

Strip loading of reinforced concrete is a common problem in engineering practice. The increased concrete compressive strength at the load introduction can be attributed to

geometrical and passive confining stresses caused by load dispersion and reinforcement, respectively. However, current design provisions do not allow combining these two confining effects, leading to overly conservative designs. Furthermore, experimental data on strip-loaded concrete members with pronounced passive confinement and moderate load concentration ratios, common e.g. in longitudinal joints of segmental tunnel linings, are scarce. Firstly, different models for strip loading as well as an experimental campaign on 15 strip-loaded concrete blocks with pronounced passive confinement and moderate load concentration ratios tested to failure are presented. The investigated parameters were (i) the reinforcement ratio and type, (ii) the width and position of the loaded area and (iii) the concrete strength. The results show that specimens with a sufficient mechanical reinforcement ratio experience a ductile behaviour and that the load-bearing capacity can be substantially increased with higher amounts of confining reinforcement, which was validated for different reinforcement types (bent ties, welded grids, and double-headed bars). The performance of the different reinforcement types did not vary substantially, indicating that welded grids can be a viable alternative to bent ties. Furthermore, the tests confirm that the geometrical confinement decreases with a larger loaded width or eccentric loading, thereby reducing the maximum bearable contact stress at the load introduction. Finally, the results reveal that compared to normal strength specimens, high strength specimens tend to have lower normalised load-bearing capacities, which in addition may not be fully utilised as the crack width, determined by digital image correlation in the experiments, governs the design. However, only three specimens were made of high strength concrete, and more experimental data is required to substantiate these preliminary conclusions.

Besides the experimental campaign four different models (Dual-Wedge stress field (DW-cc), a simplification of the stress field (DW-s), the geometric and passive confinement model (GPC), and the modelling approach according to the guideline of Deutscher Ausschuss für unterirdisches Bauen (DAUB:2024)) to design RC members subjected to strip loading are presented and it is introduced how to determine the confining stresses and confined concrete area for regular and irregular reinforcement spacings. The different models are compared to experimental data, including the 15 block tests. It is shown that the models combining the effects of load dispersion and passive confinement (DW-cc, DW-s and GPC) predict the load-bearing capacity similarly on average and all with good accuracy, comparable levels of scatter and generally on the safe side. The DAUB:2024 approach, which considers load dispersion only, is found to be highly conservative in the majority of cases. The successful validation of the three models incorporating passive confinement indirectly confirms that the proposed approaches to determine the confining stresses and the confined concrete area are reasonable. Among these models, the GPC model only investigates two sections to determine the load-bearing capacity of strip-loaded RC members: one at the load introduction and one at the position where the load is fully spread. In contrast, the Dual-Wedge stress field captures the entire load path, allowing for the analyse of the load-bearing capacity of every horizontal section of the load dispersion area and to consistently determine the reinforcement position. Furthermore, it complies with EC2:2023, which allows the combination of passive and geometrical confinement for the design of partially loaded areas if three-dimensional stress fields are applied. On the other hand, while the application of the DW-cc in design is rather cumbersome, the simpli-

fied DW-s, obtained from a parametric study of the Dual-Wedge stress field, stands out because of its straightforward formulation and the lowest coefficient of variation, which indicates that it is best able to cover the different influences on the load-bearing capacity despite its simplicity.

The authors thus propose to design strip-loaded RC members according to the simplification of the Dual-Wedge stress field (DW-s) with the input parameters determined based on the passive confinement model developed in the first part of the investigations. The mechanically consistent DW-cc model can provide further insight regarding the reinforcement layout and is the only model that is capable of accounting for varying confining stresses in the confining and bursting regions. Consequently, the DW-cc is proposed for detailed evaluations and is particularly useful for the evaluation of existing structures.

While the block tests focused on fully confined strip-loaded concrete blocks, the large-scale tests of specimens with a longitudinal joint investigated the load-bearing behaviour of precast reinforced concrete segmental linings. Reinforced concrete segments with substantial confining reinforcement in the load dispersion zone next to the joints are a viable option to resist high circumferential compressive forces. However, this solution has not been widely used in tunnelling yet, mainly due to limited coverage by existing guidelines and lack of experimental validation. This knowledge gap is addressed as follows: (i) the results of an experimental campaign investigating the structural behaviour of tunnel lining segments with longitudinal joints in nine reinforced concrete specimens with pronounced passive confinement is presented, (ii) a modelling approach based on a bespoke stress field solution for the design of longitudinal joints allowing the entire load path to be followed is proposed and (iii) this stress field is extended to cover the effect of guiding rod grooves.

The investigated parameters of the experimental campaign were (i) the transverse reinforcement ratio, (ii) the reinforcement configuration, and (iii) the joint geometry of RC specimens reinforced with welded grids. The experimental results highlight that with a higher load concentration ratio (larger joint width), the contact stress at the joint decreases due to the limited geometrical confinement, but the axial force still increases because of the larger joint area. Confining reinforcement contributes to the load-bearing capacity of longitudinal joints. However, the possible load increase by providing confining reinforcement is limited if the segments contain – besides the confined zone at the joint – an unconfined zone. In the unconfined zone, only the uniaxial concrete compressive strength can be activated, and on an area smaller than the segment cross-section due to spalling cracks occurring in the confined zone propagating into the unconfined zone. Consequently, segments with high reinforcement ratios and wide joints that can sustain high axial forces are prone to fail in the unconfined zone. Specimens failing in the unconfined zone exhibited a less ductile behaviour than those failing in the confined zone. In order to increase the load-bearing capacity of segments with a governing unconfined zone, confining reinforcement can be placed in that zone with reduced reinforcement content compared to the confined zone at the joint. Fully confined segments can particularly be useful for tunnels with varying loading scenarios along their length, as they can be used to strengthen the most heavily loaded segment rings locally and thereby maintain a constant, smaller thickness throughout the tunnel.

Furthermore, the digital image correlation measurements used to investigate the cracks on two lateral sides of each specimen indicate that crack widths do not govern the design; thus the full load-bearing capacity can be utilised.

The Multi-Wedge (MW) stress field, which builds on the previously presented DW-cc stress field and disperses the load from the joint to the area within the reinforcement in the confined zone is introduced, thereby ensuring a consistent transition to an adjoining unconfined zone. Regarding the strength of the latter, it is proposed to consider the uniaxial concrete compressive strength only within the area of the confining reinforcement. With these two approaches, the load-bearing behaviour of longitudinal joints of tunnel lining segments can be investigated in a mechanically consistent manner while following the entire load path. In addition, the MW stress field is extended to account for the effect of a guiding rod groove. Three different variants are presented, whereas the variant that allows for load dispersion towards the inside (towards the guiding rod groove) results in the highest predicted load-bearing capacity.
The comparison of the experimental data with the MW stress field and three existing and previously introduced design approaches (DW-cc, GPC, and DAUB) for the tests without guiding rod groove reveals that models combining the effect of load dispersion and passive confinement in the confined zone (MW, DW-cc, and GPC) predict the load-bearing capacity similarly and with good accuracy as long as the unconfined zone is considered as well. Otherwise, unconservative predictions can result. The DAUB:2024 approach, which does not account for confining reinforcement, is the most conservative. The comparison of the MW stress field variant for guiding rod grooves with the highest load-bearing capacity prediction with the experimental results shows that the model is promising. However, having only one test to compare with is not sufficient to successfully validate it, and further tests are thus required.

In conclusion, (i) the presented experimental campaign on the large-scale specimens with longitudinal joints confirms that substantial confining reinforcement can be activated thereby being a viable option to increase the axial force resistance of the longitudinal joints of tunnel lining segments and (ii) the MW stress field is the only design approach that can explain the force flow in a mechanically consistent manner. It shows good agreement with the experimental data, which successfully validates the model.

The last part of the investigations of the longitudinal joints further investigates the load-bearing behaviour of strip loading with steel fibre reinforced concrete with and without conventional bar reinforcement and proposes design approaches based on the stress fields.

Fibre reinforced concrete is becoming increasingly popular in engineering practice due to its high robustness, post-cracking behaviour and crack control. For strip loading, as common, for example, in longitudinal joints of tunnel lining segments, the use of fibre reinforced concrete has the potential to reduce conventional reinforcement. However, no existing design approaches combine the effects of load dispersion, confining reinforcement and fibre reinforcement, and experimental data is scarce. The load-bearing behaviour of strip-loaded SFRC with and without additional reinforcement is investigated. Eleven experiments on strip-loaded SFRC specimens out of two campaigns investigating strip loading in block specimens and longitudinal joints of tunnel lining

segments are presented. Seven specimens contained additional conventional confining reinforcement (hybrid-reinforced specimens), while the remaining four were purely fibre-reinforced. The experimental results highlight different failure modes for the hybrid and purely fibre-reinforced specimens: The hybrid-reinforced specimens failed in a ductile manner, while the purely fibre-reinforced specimens experienced a roughly linear elastic behaviour with pronounced softening (block test) or brittle failure (joint tests) despite displacement-controlled loading in a stiff testing machine. Although the purely fibre-reinforced specimens exhibited brittle failure, failure loads higher than the load at which surface cracks first appeared were observed, indicating that the fibres were activated, and likely hindering the growth of initial (micro-)cracks. Compared to RC block specimens, most hybrid-reinforced SFRC block specimens exhibited higher load-bearing capacities and increased ductility. The same holds for the joint tests as long as the unconfined zone did not govern failure. Note that with a higher content of conventional reinforcement, the effect of the fibres reduces. The crack widths on the specimen surface were measured with digital image correlation. The reinforced SFRC specimens experienced smaller crack widths at the same load level than similar RC specimens with moderate conventional confining reinforcement ratios. For higher confinement, no beneficial effect of the fibres on the crack widths was observed.

Furthermore, modelling approaches for strip-loaded hybrid and purely steel fibre reinforced concrete are presented. For hybrid-reinforced specimens, it is proposed to linearly superimpose the confining stresses provided by conventional reinforcement with the post-cracked residual tensile strength of the SFRC. These stresses are subsequently applied to mechanically sound models established for RC elements subjected to strip loading that account for load dispersion and passive confinement, such as the Multi-Wedge or Dual-Wedge stress fields. The residual tensile strength is determined for a crack width of 1 mm according to the linear model of *fib* Model Code 2020, based on standard material tests with prismatic SFRC beams subjected to three-point bending according to EN 14651. The comparison of the experimental results with the predictions of the two stress fields shows good agreement. Even though only seven tests were available, the data set contained two different reinforcement types (bent ties and welded grids), different conventional reinforcement ratios, and varying load application widths, providing a substantial validation. In addition, all hybrid-reinforced specimens exhibited ductile failures. Consequently, the models can be recommended as a valid basis for design.

For the SFRC specimens without additional conventional reinforcement controlling crack growth, the simplest Dual-Wedge stress field, which does not consider any confinement, is proposed to account for load dispersion. The residual tensile strength of the SFRC, determined here for a crack width opening of 0.5 mm, is assumed to equilibrate the bursting stresses. The model predictions are on the safe side compared to the experimental results, and the stress field is a useful tool to trace the force flow. Nevertheless, the brittle failure mode of the joint tests and a related possible size effect require further investigation for successful model validation. This might include limiting the height of the stress field up to which uniform residual tensile stresses are assumed to account for limited load distribution and varying crack openings over the specimen height, resulting in lower predictions of the load-bearing capacity.

Note that all proposed modelling approaches rely on a pertinent description of the mechanical properties of the SFRC within the structural member. For the residual tensile strength, the orientation and distribution of the fibres are of great importance. Accordingly, adequate reduction factors must be applied to the residual tensile strength if the fibre orientation or distribution in the specimens differs from that in the material characterisation tests used to determine the mechanical properties.

In conclusion, SFRC can enhance the load-bearing behaviour of strip-loaded concrete and minimise crack widths. SFRC is particularly efficient for hybrid-reinforced specimens when combined with low conventional confining reinforcement ratios. Consequently, SFRC is a viable option for the design of precast tunnel lining segments, as it allows the required conventional reinforcement of the longitudinal joints to be reduced while providing further beneficial effects, such as higher robustness. The load-bearing capacity of the hybrid-reinforced specimens can be reliably determined using the proposed modelling approach. However, the application of strip-loaded SFRC specimens without additional conventional reinforcement in design requires further investigation, particularly regarding a potential size effect related to the brittle failure mechanism, despite the promising modelling approaches.

In the last part of the report, the ring joints are investigated. For these, the construction stage is of relevance, transferring the thrust jack forces into the most recently installed ring. The transmission of thrust forces through the ring joints results in high local stresses on the segments and can cause damage if the design is inadequate. Although such damage does not generally affect structural safety, it may necessitate repair work, for example to ensure watertightness requirements are met in the event of cracks that are wider than permitted.

Relevant for the design are (i) the compressive stresses during force transmission via the jacking shoes, (ii) the bursting forces resulting from the generally three-dimensional load distribution, and (iii) the edge tensile forces between the jacking shoes. The bursting forces (ii) and the edge tensile forces (iii) result from compatibility, whereby the former, if necessary, allow for the absorption of compressive stresses (i) that exceed the uniaxial concrete compressive strength (partial area loading). In addition, significant irregular stresses may arise due to misalignments in the lining arrangement, with tensile stresses being particularly relevant as they cause cracks and significantly influence crack widths.

The load introduction of the thrust forces is investigated and compared using linear-elastic and nonlinear finite-element analyses. Furthermore, the influence of offsets in the segment arrangement is discussed. The investigations revealed that, due to crack development, there are considerable differences between an uncracked linear-elastic analysis and a nonlinear one. Due to the additional uncertainty regarding offsets, it is advisable to carry out both analyses and to design the reinforcement for the governing stresses occurring in both analyses, although only the nonlinear analysis allows any conclusions to be drawn regarding the crack widths. The expected crack widths due to offsets can be estimated using existing geometric considerations, although care must be taken during construction to ensure the accuracy of the installation, as the reinforcement can limit the crack widths but cannot prevent them from occurring.

The theoretical and the experimental investigations presented in this report provide relevant new insights into the load-bearing behaviour of strip-loaded reinforced concrete. Furthermore, the proposed models provide a solid basis for a mechanically consistent consideration of the combined effect of load dispersion and confining reinforcement in the design of longitudinal tunnel lining joints, enabling efficient tunnel lining segments. With regard to the ring joints, the report highlights that, compared to the commonly used linear-elastic design, relatively simple yet mechanically consistent nonlinear analyses provide added value by accounting for cracks, also enabling the determination of crack widths. It also demonstrates that the influence of offsets in ring joints can at most be covered to a limited extent even by dense reinforcement, highlighting the importance of precise installation.

1 Einleitung

1.1 Hintergrund

Für den Vortrieb von langen und tiefliegenden Tunnels kommen heute aufgrund der Zeit- und Kosteneffizienz, wie auch der Arbeitssicherheit, immer häufiger Tunnelbohrmaschinen (TBM's) zum Einsatz. Dabei werden bei Schild-TBM's oft vorfabrizierte Betontübbinge zur Ausbruchssicherung verwendet (siehe Abbildung 1). Die Tübbinge übernehmen den Lastabtrag im Bauzustand und für Tunnels mit einschaligem Ausbau auch während der gesamten Nutzungsdauer. Mehrere Tübbinge bilden zusammen einen Ring, wodurch Längs- und Ringfugen zwischen den Segmenten entstehen. Die Längsfugen verlaufen ungefähr parallel zur Tunnelachse, während die Ringfugen zwischen aufeinanderfolgenden Ringen senkrecht zur Tunnelachse orientiert sind (siehe Abbildung 2). Die Fugen übernehmen eine zentrale Rolle bei der Bemessung der Betontübbinge.

Abbildung 1: Gestapelte Tübbinge (links) und Tübbingausbau mit ausgefahrenen Vortriebspressen einer TBM, die sich in der Ringfugen paarweise auf den zuletzt eingebauten Tübbingring abstützen (rechts).

In den Längsfugen werden Normalkräfte, Biegemomente und Querkräfte übertragen, welche aus Gebirgs- und Wasserdrücken, dem Eigengewicht der Segmente und Tunnelinstallationen resultieren. Die Längsfugen werden typischerweise mit reduzierter Kontaktfläche im Vergleich zur vollen Querschnittsfläche der Tübbinge ausgebildet. Die reduzierte Kontaktfläche vereinfacht den Einbau, reduziert das Risiko von Abplatzungen und ermöglicht es Dichtungsprofile anzubringen. Zudem weisen die Längsfugen häufig eine Aussparung für Führungsstäbe (sogenannte Guiding Rods) auf, welche als Zentrierhilfen verwendet werden.
Im Gegensatz zu den Längsfugen sind die Ringfugen hauptsächlich Belastungen im Bauzustand ausgesetzt. Um die Vorschubkraft zu generieren, stützen sich die Pressen der TBM auf dem nachlaufenden Tübbingausbau ab (siehe Abbildung 1). Die über den Umfang angeordneten Pressenschuhe leiten die Vorschubkraft über die Ringfugen in die Segmente ein.
Aufgrund des hohen Wiederholungsgrad bei Tunnelprojekten – speziell bei langen Tunnels – bietet sich eine Optimierung der Tübbinge an. Dünnere Tübbinge reduzie-

ren nicht nur das Betonvolumen, sondern gleichzeitig den erforderlichen Ausbruchsquerschnitt und somit das Ausbruchsvolumen, was einen grossen Einfluss auf die Kosten aber auch auf die Umweltbelastung des Tunnelprojekts hat. Aus diesem Grund ist eine effiziente Bemessung der Tübbinge notwendig, wozu das vorliegende Forschungsprojekt beitragen soll.
Der Hauptfokus des Forschungsprojekts liegt auf den Längsfugen. Bei Tunnels mit hohen Wasserdrücken oder im druckhaften oder quellenden Gestein treten grosse Ringnormalkräfte und vergleichsweise kleine Biegemomente auf. Für dieses Belastungsszenario werden häufig die Längsfugen in der Bemessung massgebend für die Dicke der Tübbinge. Umschnürungsbewehrung bietet die Möglichkeit, den Tragwiderstand der Längsfugen zu erhöhen, ohne dafür die Dicke der Segmente zu vergrössern. Diese bis jetzt kaum in der Praxis eingesetzte Möglichkeit wird in diesem Forschungsprojekt detailliert untersucht, mit einem zusätzlichen Fokus auf geschweisster Leiterbewehrung. Ergänzend wird neben konventionellem Beton auch der Einfluss von stahlfaserbewehrtem Beton auf den Tragwiderstand der Längsfugen betrachtet.
Die Ringfugen werden nicht in der gleichen Tiefe wie die Längsfugen untersucht. Dabei wird vor allem der Unterschied zwischen einer Modellierung mit ungerissen linear elastischem Materialverhalten respektive nichtlinearem Materialverhalten auf die Bemessung aufgezeigt.

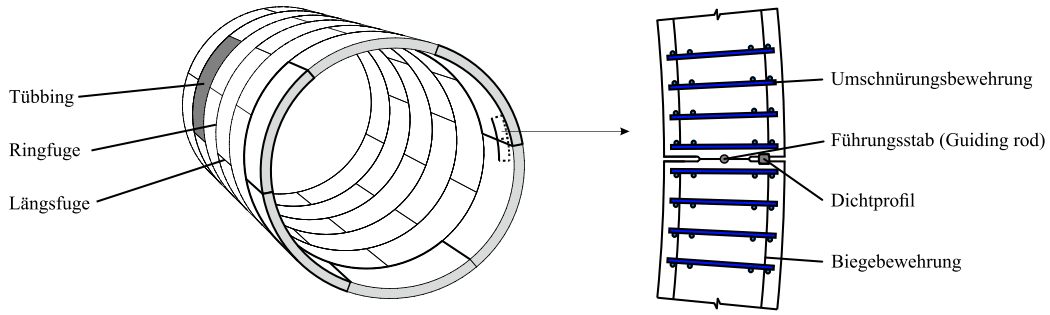

Abbildung 2: Definition der Parameter der Tübbinge und der Längsfuge.

1.2 Projektziel und Abgrenzung

Ziel dieses Forschungsprojekts ist die Untersuchung des Tragverhaltens von Betontübbingfugen, so dass effizientere Bemessungsvorschläge ausgearbeitet werden können. Dabei werden theoretische und experimentelle Untersuchungen für die Längsfugen sowie numerische Untersuchungen für die Ringfugen durchgeführt. Die spezifischen Ziele sind in Kapitel 2.3 aufgeführt.
Bei den Längsfugen konzentriert sich das Projekt auf das Tragverhalten von Tübbingen mit ausgeprägter Umschnürungsbewehrung für Stahlbeton und stahlfaserbewehrter Beton. Es werden ausschliesslich flache Fugen ohne kraftschlüssige Verbindungselemente, wie z.B. Dübel, untersucht. Des Weiteren werden zentrische und leicht exzentrische Normalkraftbelastungen untersucht; Querkräfte und Biegemomente mit damit verbundenen Fugenrotationen werden nicht berücksichtigt. Die Bestimmung der auf die Segmente einwirkenden Lasten sowie die Wechselwirkung zwischen Segmenten verschiedener Ringe oder dem angrenzenden Boden liegen ausserhalb des Rahmens dieses Forschungsprojekts. Die experimentellen Untersuchungen fokussieren auf das

Kurzzeitverhalten bei der Höchstlast. Langzeiteinwirkungen aufgrund von Kriechen werden experimentell am Rand untersucht, während Ermüdungsbeanspruchungen vollständig vernachlässigt werden. Die Versuche an den Längsfugen werden an Blöcken ohne Krümmung durchgeführt. Die theoretische Modellierung konzentriert sich auf die Vorhersage des Tragwiderstands. Das Verhalten unter Gebrauchslasten wird experimentell untersucht; der Fokus liegt dabei auf Oberflächenrissbreiten und der Fugenschliessung. In den theoretischen Modellierungen werden Mittelwerte der Materialeigenschaften verwendet. Sicherheitsfaktoren oder statistische Schwankungen der Materialparameter sind nicht Gegenstand dieser Arbeit.
Bei den Ringfugen beschränkt sich die Untersuchung – in Absprache mit der Begleitkommission – auf Finite-Elemente-Analysen für Stahlbeton an ebenen Tübbingen ohne Pressenexzentrizität, jeweils für eine spezifische Laststellung.

1.3 Methodik

Das Tragverhalten der Längsfugen wird durch theoretische und experimentelle Untersuchungen für bewehrten, faserbewehrten und gemischtbewehrten Beton erforscht. Die theoretischen Untersuchungen beinhalten die Entwicklung mechanisch konsistenter Modelle (Spannungsfelder) basierend auf dem unteren Grenzwert der Plastizitätstheorie, wodurch Gleichgewicht erfüllt wird während die Fliessbedingungen der Materialen nicht verletzt werden. Die Spannungsfelder benötigen als Eingabeparameter nur die Geometrie und die Eigenschaften der verwendeten Materialen (Beton und Bewehrungsstahl), wodurch die Anwendung möglichst einfach und verständlich ist. Die entwickelten Modelle werden mit den Resultaten der durchgeführten Versuche validiert und mit anderen Modellierungsansätzen verglichen. Aufgrund der mechanischen Grundlage können die erfolgreich validierten Modelle auch ausserhalb der Testparameter angewendet werden. Zusätzlich geben die Versuche einen vertieften Einblick in das Tragverhalten der Tübbinglängsfuge und den Einfluss verschiedener Parameter. Die Versuche sind so aufgebaut, dass in einem ersten Schritt zuerst das Zusammenspiel zwischen Umschnürung und Lastausbreitung an Betonblöcken untersucht wird und in einem zweiten Schritt Versuchskörper mit typischen Geometrien für Tübbinge und einer effektiven Fugenausbildung untersucht werden.
Die Ringfugen werden mittels Finite-Elemente-Analysen untersucht.

1.4 Aufbau des Berichts

Dieser Bericht fasst die durchgeführten Untersuchungen, die wichtigsten Erkenntnisse und die daraus abgeleiteten Schlussfolgerungen für die Praxis zusammen. Die verwendeten Methoden, entwickelten Modelle, und detaillierte Erläuterungen zu den Ergebnissen der Längsfugen-Untersuchungen sind in der ETH-Dissertation „Passive Confinement and Strip Loading in Longitudinal Tunnel Lining Segment Joints“ [1] von F. Morger enthalten, welche diesem Bericht angehängt ist. Der Anhang enthält weiter die Dokumentation der Finite-Elemente-Analysen zu den Ringfugen.

2 Stand der Technik und offene Fragestellungen

2.1 Längsfugen

In Tübbingen im druckhaften oder quellfähigen Gebirge oder bei hohen Wasserdrücken treten hohe Ringnormalkräfte auf, welche aufgrund der reduzierten Kontaktfläche zu hohen Spannungen in den Längsfugen führen. Allgemein wird die Situation der Längsfugen als Teilflächenbelastung betrachtet. Bei Teilflächenpressung können aufgrund der Lastausbreitung und den damit verbundenen lateralen Druckspannungen bei der Krafteinleitung (geometrische Umschnürung) Kontaktpressungen aufgenommen werden, die die einachsige Betondruckfestigkeit deutlich übersteigen. Zentral ist dabei, dass (i) die Druckspannungen bei der Krafteinleitung in beiden zur Lasteinleitungsrichtung lateralen Richtungen wirken, beziehungsweise Lastausbreitung in zwei Richtungen auftritt – so dass sich ein dreiachsiger Spannungszustand einstellt – und (ii) die in einem bestimmten Abstand von der Lasteinleitung resultierenden Zugkräfte aufgenommen werden können, wofür meist eine Querbewehrung erforderlich ist. Unzählige Versuche (z.B. [2], [3]) bestätigen eine erhöhte Betondruckfestigkeit bei räumlicher Lastausbreitung, so dass in heutigen Normenwerken für Betonbau (SIA 262:2025 [4], Eurocode 2 – EN 1992-1-1:2023 [5] (EC2:2023) oder *fib* Model Code 2020 [6] (MC2020)) bei der Teilflächenpressung auch eine Erhöhung der Betondruckfestigkeit erlaubt ist. Dazu wird häufig der Quadratwurzelansatz verwendet, der die Erhöhung der Betondruckfestigkeit als Quadratwurzel des Verhältnisses aus der zur Lastausbreitung verfügbaren Fläche und der belasteten Teilfläche ermittelt.
Der Quadratwurzelansatz geht auf Spieth [2] zurück und wurde empirisch an unbewehrten teilflächenbelasteten Betonprüfkörpern mit räumlicher Lastausbreitung ermittelt. Aufgrund der empirischen Natur ist dessen Anwendung durch zahlreiche Voraussetzungen und Einschränkungen begrenzt, welche sich je nach Normenwerk unterscheiden. Bei allen gängigen Normen (SIA 262:2025, EC2:2023, MC2020) ist die Festigkeitserhöhung auf den Faktor 3 limitiert und die anrechenbare Fläche zur Lastausbreitung wird begrenzt, wobei die Lastausbreitungsfläche denselben Schwerpunkt wie die belastete Teilfläche besitzen muss (symmetrische Lastausbreitung bzgl. den zwei Hauptachsen). Die Lastausbreitungsfläche wird dabei eingeschränkt, um den geometrischen Bedingungen in den der Quadratwurzel zugrunde liegenden Experimenten Rechnung zu tragen. Am restriktivsten diesbezüglich war der Eurocode 2 – EN 1992-1-1:2011 (EC2:2011), welcher geometrische Ähnlichkeit zwischen der Teilfläche und der Lastausbreitungsfläche forderte. In den neusten Versionen der SIA 262:2025 und dem EC2:2023 ist die Lastausbreitung in beiden Richtungen gleich anzusetzen, so dass die Seite mit dem geringeren Randabstand massgebend wird. Zur Bestimmung der erforderlichen Querbewehrung kann ein simples Fachwerkmodell verwendet werden, welches auf Mörsch [7] zurückgeht und z.B. im EC2:2023 [5] aufgeführt ist. Die resultierende Bewehrung ist in einem gewissen Abstand zur Kontaktfläche einzulegen. Eine Bewehrung im unmittelbaren Lasteinleitungsbereich hat nach diesen Modellen

keinen Einfluss auf den rechnerischen Tragwiderstand, obwohl ihr günstiger Einfluss bekannt ist.

Die Definition der Lastausbreitungsfläche bei der Behandlung resp. Bemessung als Teilflächenpressungsproblem ist für Tübbinglängsfugen sehr einschränkend, was jedoch in Anbetracht der primär ebenen Lastausbreitung (Abmessung der Fugen in Längsrichtung entspricht praktisch der Tübbinglänge) und der damit weitgehend fehlenden geometrischen Umschnürung in Längsrichtung gerechtfertigt ist. Diese spezifische Teilflächenbelastung wird als Streifenbelastung bezeichnet. Im theoretischen Fall einer reinen Streifenbelastung – Belastung über die gesamte Körperlänge – kann die Betondruckfestigkeit nach Kupfer [8] maximal um ca. 25% erhöht werden (entsprechend der Betonfestigkeit unter zweiachsigem Druck). In Versuchen erzielte höhere Festigkeiten können durch Umschnürung aufgrund der Aktivierung der Zugfestigkeit in den unbelasteten Schultern der Körper oder durch steife Lasteinleitplatten begründete werden. Diese Effekte sollten in der Bemessung jedoch nicht berücksichtigt werden. Trotzdem empfiehlt die für den Tunnelbau spezifische Richtline des DAUB (Deutscher Ausschuss für unterirdisches Bauen e.V., DAUB:2024) [9] die Anwendung des Quadratwurzelansatzes zur Bemessung der Längsfugen, ohne jegliche Begrenzung der Lastausbreitungsfläche, solange die Betondruckfestigkeitsklasse nicht über C50/60 liegt. In der vorherigen Version aus dem Jahr 2013 war hingegen noch, wie im EC2:2011, geometrische Ähnlichkeit der beiden Flächen gefordert. Zwar empfiehlt die aktuelle DAUB:2024-Richtlinie neben der zur Aufnahme der Querzugkräfte notwendigen Bewehrung eine konstruktive Randbewehrung bei der Lasteinleitungszone; diese wird jedoch weder in der Bemessung effektiv berücksichtigt, noch wird genauer auf ihre konstruktive Ausbildung eingegangen (wie sie zur Gewährleistung einer Umschnürung nötig wäre). Die Limitierung auf eine maximale Festigkeitserhöhung mit Faktor 3 gilt auch nach der neuen DAUB:2024-Richtlinie. Um höhere Tragfestigkeiten, z.B. bei sehr schmalen belasteten Teilflächen aufgrund von Lastexzentrizitäten, zu berücksichtigen, empfiehlt die DAUB projektbezogene Versuche.

Neben dem günstigen Einfluss der Lastausbreitung kann jedoch die Betondruckfestigkeit bei einer Lasteinleitung auch mittels Umschnürungsbewehrung (passive Umschnürung) erhöht werden. Dieser Effekt wurde bereits vor über 100 Jahren zum ersten Mal untersucht [10], [11]. Richart et al. [12], [13] zeigten 1929, dass bei allseitigem Querdruck die Betondruckfestigkeit etwa um den vierfachen Betrag der kleineren Querdruckspannung erhöht werden kann, und zwar unabhängig davon, ob der Querdruck aktiv aufgebracht oder durch Umschnürungsbewehrung passiv erzeugt wird. Umschnürungsbewehrung ist auch in heutigen Normenwerken (z.B. SIA 262:2025, EC2:2023, oder MC2020) enthalten (wenn auch nicht in der DAUB-Richtlinie).

Die Anwendung einer Umschnürungsbewehrung bei Tübbingen ohne gleichzeitige Berücksichtigung einer Lastausbreitung widerspricht allerdings dem erwarteten Tragverhalten und würde Umschnürungsbewehrung über die ganze Tübbinglänge (d.h. den gesamten Tunnelumfang) erfordern, was nicht sinnvoll ist. Die Kombination des Quadratwurzelansatzes und der Umschnürungsbewehrung ist andererseits nach den bestehenden Normenwerke explizit ausgeschlossen. Die SIA 262:2025 sowie der EC2:2023 erlauben zwar die Kombination der beiden Effekte, wenn dreidimensionale Spannungsfelder verwendet werden, ohne aber dazu genauere Angaben zu machen. Das Dual-Wedge Spannungsfeld [14] erfüllt zwar diese Bedingungen. Es wurde jedoch für sehr schmale Belastungsbreiten – wie typisch bei Betongelenken – entwickelt und validiert. Bei solchen Verhältnissen überwiegt der Einfluss der Lastausbreitung gegen-

über der Umschnürungsbewehrung klar. Bei den im Vergleich zu Betongelenken wesentlich breiteren Tübbinglängsfugen trifft dies jedoch nicht zu. Die Anwendung des Dual-Wedge Spannungsfelds für Tübbinglängsfugen ohne zusätzliche Untersuchungen wäre daher mit beträchtlicher Unsicherheit verbunden.
Das Fehlen ausreichend validierter mechanischer Modelle resp. darauf basierender normativer Vorschriften sind hauptsächlich dafür verantwortlich, dass eine Umschnürungsbewehrung bisher kaum zur Erhöhung des Tragwiderstands von Längsfugen mit ausgeprägter Normalkrafteinwirkung eingesetzt wurde und stattdessen – bei ungenügendem Bemessungswiderstand gemäss Quadratwurzelansatz – die Tübbingdicke vergrössert oder höherfester Beton eingesetzt wurde. Zudem bestehen Vorbehalte gegenüber der Aktivierung einer Umschnürungsbewehrung, da der Überdeckungsbeton aufgrund (i) der lateralen Betonausdehnung und (ii) der grösseren Bruchstauchung des umschnürten Betons zumindest bei hohem Umschnürungsbewehrungsgehalt im Gebrauchstauglichkeitszustand unzulässig grosse Rissbreiten aufweisen oder gar abplatzen könnte, jedoch liegen keine experimentellen Daten mit systematischer und ausgeprägter Umschnürungsbewehrung für Tübbinglängsfugen vor. Zusätzlich stellt sich die Frage, über welche Lasteinleitungszone Umschnürungsbewehrung angeordnet werden muss, bis die Normalkraft einzig über einachsigen Betondruck abgetragen werden kann. Ferner ist spezifisch für die im Tunnelbau immer populärer werdende geschweisste Leiterbewehrung die Endverankerung der Stäbe herausfordernd, und ihre Verwendung als Umschnürungsbewehrung wurde bisher weder experimentell noch theoretisch untersucht.
Faserbewehrter Beton wird ebenfalls häufig im Tunnelbau verwendet. Auch hier ist keine normative Abdeckung vorhanden, die die Kombination von konventioneller Stabbewehrung und faserbewehrtem Beton als Umschnürungsbewehrung erlaubt und so die Reduktion der konventionellen Bewehrung ermöglicht und allenfalls die Abplatzproblematik reduziert.

2.2 Ringfugen

Für die Einleitung der Vortriebspressenkräfte sind nach der DAUB:2024-Richtlinie [9] die Teilflächenpressung bei den Pressenschuhen sowie die Zugkräfte, die durch die Lastausbreitung und die Scheibenbeanspruchung mit oder ohne Versätzen in den Fugen resultieren, zu berücksichtigen. Bei der Teilflächenpressung wird auf den Quadratwurzelansatz ohne Ähnlichkeitskriterium verwiesen, und zur Ermittlung der auftretenden Zugkräfte ohne Berücksichtigung von Versätzen werden Tafelwerte [15] oder Finite-Element-Analysen empfohlen.
Die Finite-Element-Analysen werden häufig mit ungerissen linear elastischem Materialverhalten durchgeführt, was jedoch nur realitätsnahe Vorhersagen liefert, solange der Beton ungerissen ist, denn durch die Rissbildung treten in der Regel signifikante Schnittkraftumlagerungen auf. Eine Bemessung der Bewehrung auf Basis der ungerissen linear elastisch ermittelten Schnittgrössen ist daher inkonsistent, da die Bewehrung die Rissbildung nicht verhindert und die Steifigkeit selbst bei kräftiger Bewehrung bei Rissbildung markant abfällt. Weiter können keine Angaben zur Rissbreite gemacht werden. Die Verwendung allgemeiner nichtlinearer Finite-Element-Analysen ist dagegen sehr aufwändig und erfordert die Festlegung diversere Materialkennwerte

und Modellparameter, die häufig in der Planung nicht bekannt sind, wodurch solche Untersuchungen selten durchgeführt werden.
Versätze der Tübbinge in den Ringfugen führen beim Vortrieb zu ausgeprägten Randzugkräften mit damit verbunden Schäden (Längsrissen) an den Tübbingen. Behnen et al. [15] zeigen eine geometrische Abschätzungsformel für die auftretenden Rissbreiten infolge von Versätzen auf, empfehlen jedoch, den Einfluss von Versätzen bei der Tübbingbemessung zu vernachlässigen und stattdessen strikte geometrisch-konstruktive Vorgaben beim Tübbingzusammenbau zu machen, welche in der Ausführung entsprechend zu kontrollieren sind.

2.3 Forschungsschwerpunkte und -ziele

2.3.1 Längsfugen

Sowohl die Lastausbreitung als auch eine Umschnürungsbewehrung können, wie einleitend erwähnt, zum Normalkraftwiderstand von Tübbinglängsfugen beitragen. Jedoch sind diese Einflüsse für die bei Tübbinglängsfugen vorliegenden Verhältnisse bisher weder experimentell noch analytisch ausreichend untersucht worden, womit auch keine entsprechende Normvorschriften existieren. Dadurch werden die Anwendung in der Praxis sowie eine effiziente Bemessung erschwert.
Um dieses Problem zu beheben, werden in diesem Forschungsprojekt neue Bemessungsansätze für die Längsfugen vorgeschlagen. Zu diesem Zweck wird das mechanische Verhalten von streifenbelastetem Stahlbeton und stahlfaserbewehrtem Beton, jeweils mit relativ grosser Breite der belasteten Fläche und ausgeprägter Umschnürungsbewehrung, grundlegend untersucht. Theoretische und experimentelle Analysen werden kombiniert und als Grundlage für die Entwicklung mechanisch fundierter und experimentell validierter Modellierungsansätze verwendet. Die Untersuchungen lassen sich in drei Schwerpunkte einteilen.
Der erste Teil (Kapitel 3.1 und 3.2) befasst sich mit dem mechanischen Verhalten der passiven Umschnürung mit folgenden Zielen:

- Aufzeigen eines Überblicks über den aktuellen Wissensstand der passiven Umschnürung;
- Entwicklung eines mechanisch konsistenten Modells zur Beschreibung der dreidimensionalen Lastausbreitung von aktivierter Umschnürungsbewehrung;
- Validierung des Umschnürungsmodells mit experimentellen Daten aus der Literatur;
- Erarbeitung einer Empfehlung für die Definition der Umschnürungsspannung und der umschnürten Fläche;
- Experimentelle Untersuchung des Tragverhaltens geschweisster Leiterbewehrung, die als Umschnürungsbewehrung verwendet wird;
- Definition praktischer Empfehlungen für die Verwendung geschweisster Leiterbewehrung als Umschnürungsbewehrung.

Nachdem das Tragverhalten der Umschnürungsbewehrung untersucht wurde, wird dieses Wissen auf streifenbelasteten Stahlbeton angewendet, mit Schwerpunkt auf den Längsfugen von Tübbingen. Die Hauptziele dieses zweiten Teils der Untersuchungen (Kapitel 3.3 und 3.4) sind:

- Experimentelle Untersuchung des Tragverhaltens von streifenbelasteten umschnürten Blöcken mit Fokus auf dem Bewehrungsgehalt und -typ, der Breite und Position der belasteten Teilfläche und der Betondruckfestigkeit;
- Entwicklung eines mechanisch konsistenten Modells zur Tragwiderstandsvorhersage von streifenbelasteten Stahlbetonblöcken mit breiter Belastungsfläche und ausgeprägter Umschnürungsbewehrung durch Weiterentwicklung des bereits bestehenden Dual-Wedge Spannungsfeldes, welches sowohl Lastausbreitung als auch Umschnürungsbewehrung berücksichtigt;
- Ausarbeitung einer Vereinfachung des Spannungsfelds, um die Anwendung in der Praxis zu erleichtern;
- Validierung der Tragwiderstandsvorhersage der Modelle mit den Versuchsdaten und Vergleich mit bestehenden Bemessungsansätzen;
- Experimentelle Untersuchung des Tragverhaltens von Tübbinglängsfugen mit Grossversuchen;
- Weiterentwicklung der Spannungsfelder um (i) den Übergang von der umschnürten Zone zur nicht umschnürten Zone zu berücksichtigen und (ii) den Einfluss von Führungsstäben zu beachten;
- Validierung der angepassten Modelle und Vergleich mit bestehenden Bemessungsansätzen;
- Untersuchung des Zusammenhangs der auftretenden Rissbreiten und Fugenschliessung, welche für den Gebrauchszustand relevant sind, mit dem Tragwiderstand;
- Entwicklung praktischer Empfehlungen für eine sichere und effiziente Bemessung von Tübbinglängsfugen.

Zusätzlich wird das Tragverhalten von streifenbelastetem stahlfaserbewehrtem Beton untersucht (Kapitel 3.5). Die Ziele in diesem dritten Teil sind:

- Experimentelle Untersuchung des Einflusses von Stahlfasern bei streifenbelasteten Versuchskörpern mit und ohne konventioneller Umschnürungsbewehrung;
- Vergleich zwischen streifenbelastetem (i) Stahlbeton und (ii) stahlfaserbewehrtem Beton;
- Berücksichtigung der Stahlfasern in den Modellen und Validierung mit den experimentellen Daten.

2.3.2 Ringfugen

Bei den Ringfugen stellt sich die Frage, ob die in der Praxis häufig verwendete ungerissene linear elastische Materialmodellierung zielführend ist, oder ob eine nichtlineare Berechnung notwendig ist. In diesem Projekt werden dazu die beiden Modellierungsansätze verglichen, und auf dieser Grundlage wird eine Empfehlung zur Bemessung der Ringfugen unter zusätzlicher Berücksichtigung von der Teilflächenpressung und dem Einfluss von Versätzen ausgearbeitet. Für die nichtlinearen Analysen wird dabei eine Software eingesetzt, die gezielt für die normkomforme Untersuchung von Stahlbetontragwerken entwickelt wurde und im Unterschied zu den meisten nichtlinearen Finite-Elemente-Programmen ausschliesslich Standard-Inputparameter verwendet.

3 Durchgeführte Untersuchungen und Erkenntnisse

Dieses Kapitel fasst die durchgeführten Untersuchungen und die wichtigsten Erkenntnisse zusammen. Die Unterkapitel 3.1 bis 3.5 befassen sich mit den Längsfugen und sind gleich aufgebaut wie die Dissertation „Passive Confinement and Strip Loading in Longitudinal Tunnel Lining Segment Joints“ [1] von F. Morger, die diesem Bericht (in Englisch) angehängt ist. In Unterkapitel 3.6 sind die Ringfugenuntersuchungen aufgeführt.

3.1 Umschnürung

Um den günstigen Einfluss einer Umschnürungsbewehrung (passive Umschnürung) für die Bemessung der Längsfugen anzusetzen und mit dem ebenfalls günstigen Einfluss der Lastausbreitung (geometrische Umschnürung) zu kombinieren, ist ein mechanisch fundiertes Umschnürungsmodell essentiell. Für die Ermittlung der Umschnürungswirkung der Bewehrung sind dabei sowohl (i) die Grösse der Umschnürungsspannungen als auch (ii) die Grösse des umschnürten Volumens, in welchem ein dreiachsiger Spannungszustand mit der damit verbundenen höheren Betondruckfestigkeit herrscht, wobei die kleinste Querschnittsfläche massgebend ist, relevant. Beide Faktoren sind von der räumlichen Ausbreitung der durch die Aktivierung der Umschnürungsbewehrung resultierenden diskreten (d.h. bei den Abbiegungen resp. Verankerungen der Umschnürungsbewehrung wirkenden) Umschnürungskräfte abhängig. Daher wurde ein mechanisches Modell entwickelt, das die Lastausbreitung der Umschnürungskräfte berücksichtigt und mit dem somit die Umschnürungsspannung und die massgebende umschnürte Fläche konsistent ermittelt werden können.

3.1.1 Umschnürungsmodell

Das neue Umschnürungsmodell beschreibt die Lastausbreitung der aktivierten Umschnürungskräfte (F_y und F_z) für bewehrte Betondruckglieder durch Paraboloide (siehe Abbildung 3a und b), welche als reine Druckschalen zwischen den Lasteinleitungspunkten ausgebildet sind. Durch die Krümmung der Schalen resultieren Umlenkkräfte, welche den Umschnürungsspannungen entsprechen, und die Geometrie der Paraboloide definiert das umschnürte Betonvolumen (siehe Abbildung 3c). Die Geometrie ist durch die Bewehrungsabstände in lateraler Richtung (s_y und s_z) und axialer Richtung (s_x) sowie durch die initiale Neigung der quadratischen Parabeln in lateraler als auch in diagonaler Richtung, eindeutig definiert. Diese Neigungen könnten grundsätzlich beliebig angepasst werden, z.B. um unterschiedliche Bewehrungsabstände zu berücksichtigen, wobei Anpassungen jeweils die Umschnürungsspannungen und die umschnürte Fläche beeinflussen. Für homogene Umschnürungskräfte und -abstände wird die Neigung hier jedoch konstant zu $\pi/4$ (45 Grad) festgelegt (siehe Abbildung 3a und b). Abbildung 3d zeigt den Kraftfluss auf: Die Umschnürungskräfte werden mittels den lateralen Parabeln entlang des Bewehrungsumfangs in y- resp. z-Richtung aus-

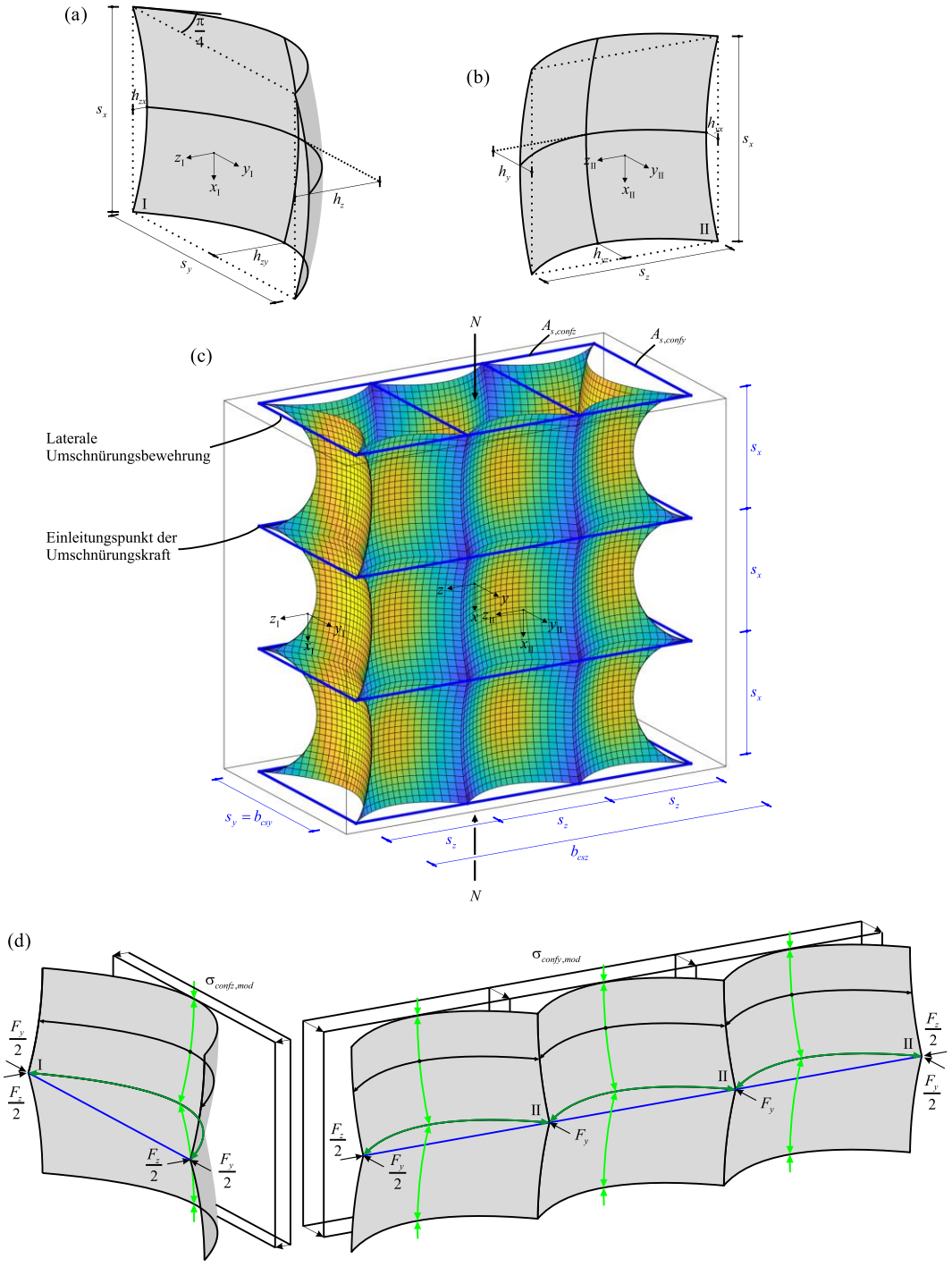

Abbildung 3: Umschnürungsmodell – (a) und (b) Definition der Paraboloide, (c) umschnürtes Betonvolumen und (d) Kraftfluss.

gebreitet. Die resultierenden Umlenkkräfte werden in axialer *x*-Richtung ebenfalls mit Parabeln abgetragen, deren Umlenkkräfte dann den gleichmässigen Umschnürungsspannungen $\sigma_{conf,mod}$ entsprechen. Der Kraftfluss zeigt auf, dass zur Aufnahme des lateralen Bogenschubs der Paraboloide in den Bewehrungsecken bereits Bewehrung (teil-)aktiviert werden muss, die sodann nicht zur Bestimmung der Umschnürungsspannungen angesetzt werden kann. In axialer *x*-Richtung kann der Bogenschub hingegen durch die aufgebrachte Last ausgeglichen werden. Die Umschnürungs-spannun-

gen in den zwei lateralen Richtungen können für homogene Umschnürungskräfte und -abstände folgendermassen bestimmt werden:

$$\sigma_{confy,mod} = \frac{A_{s,confy} \cdot f_{sy,conf}}{s_x \cdot s_z} = \frac{F_y}{s_x \cdot s_z} \tag{1}$$

$$\sigma_{confz,mod} = \frac{A_{s,confz} \cdot f_{sy,conf}}{s_x \cdot s_y} = \frac{F_z}{s_x \cdot s_y} \tag{2}$$

Das umschnürte Betonvolumen in Abbildung 3c zeigt, dass der massgebende Querschnitt jeweils zwischen zwei Bewehrungslagen zu liegen kommt (z.B. $x = 0$). Aus der Geometrie der Paraboloide kann die massgebende umschnürte Fläche $A_{conf,mod}$ ermittelt werden. Abbildung 4a zeigt den massgebenden Querschnitt mit der umschnürten Fläche für das Druckglied in Abbildung 3. Das Vorgehen zur Bestimmung der umschnürten Fläche ist jedoch sehr aufwändig und nicht für die Praxis geeignet. Aus diesem Grund wurde ein vereinfachtes Verfahren vorgeschlagen: Die umschnürte Fläche $A_{conf,mod}$ kann durch die Fläche $A_{conf,simp}$, welche dem grösstmöglichen Rechteck innerhalb von $A_{conf,mod}$ entspricht, angenähert werden (siehe Abbildung 4b). $A_{conf,simp}$ kann in geschlossener Form als Funktion der Bewehrungsabstände (s_x, s_y, s_z) und der äusseren Abmessung der Umschnürungsbewehrung (b_{csy} und b_{csz}) angegeben werden:

$$A_{conf,simp} = \left(b_{csy} - 2 \cdot h_y\right) \cdot \left(b_{csz} - 2 \cdot h_z\right) \tag{3}$$

$$= \left(b_{csy} - \frac{\sqrt{s_x^2 + s_z^2}}{2}\right) \cdot \left(b_{csz} - \frac{\sqrt{s_x^2 + s_y^2}}{2}\right)$$

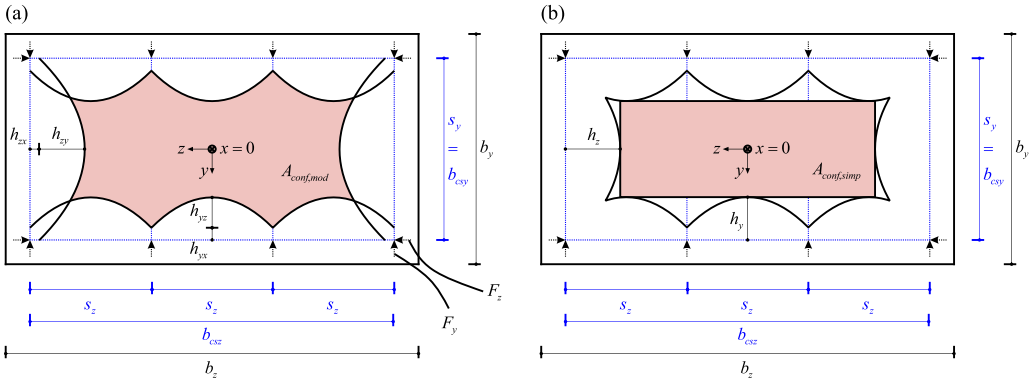

Abbildung 4: Massgebender Querschnitt – (a) umschnürte Fläche und (b) vereinfachte umschnürte Fläche.

3.1.2 Vergleich mit bestehenden Modellen und Validierung

Abbildung 5 vergleicht die Umschnürungsspannung nach dem neuen Modell ($\sigma_{conf,mod}$) mit dem Bemessungsansatz nach bestehenden Normen (σ_{conf}) wie dem Eurocode 2 – EN 1992-1-1:2023 [5], der SIA 262:2013 [16] resp. SIA 262:2025 [4] oder dem *fib* Model Code 2020 [6], welcher die Umschnürungsspannungen durch globales Gleichgewicht ermittelt, jedoch keine lokalen Effekte der Lastausbreitung (z.B. Bogenschub) berücksichtigt. Der Vergleich veranschaulicht, dass im extremen, jedoch bei Stützen häufigen Fall einer Umschnürungsbewehrung, die nur aus einem Bügel besteht ($n_{s,conf} = 2$, da zwei Bewehrungsschenkel) $\sigma_{conf,mod}$ nur 50% von σ_{conf} beträgt. Mit zu-

nehmender Anzahl Bewehrungseisen resp. Bügelschenkel ($n_{s,conf}$ ↑), wie bei Tübbingen in Querrichtung üblich, nimmt der Unterschied jedoch stark ab.

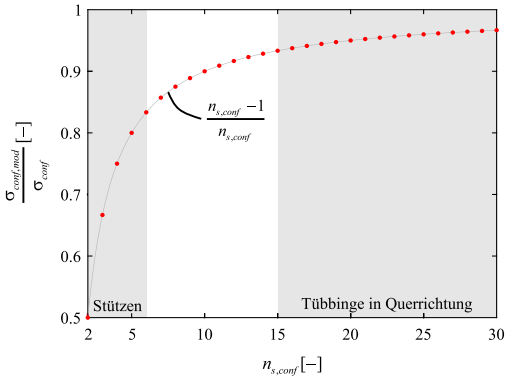

Abbildung 5: Vergleich der Umschnürungsspannung nach dem neuem Modell ($\sigma_{conf,mod}$) mit dem Ansatz bestehender Normen (σ_{conf}).

Abbildung 6 vergleicht die Grösse der massgebenden umschnürte Fläche der unterschiedlichen Modellierungsansätze. Dabei ist auf der Ordinate der Effektivitätsfaktor k als Verhältnis von A_{conf} zu $A_{cs} = b_{csy} \cdot b_{csz}$ dargestellt, und die Abszisse zeigt den axialen Bewehrungsabstand s_x. Alle Modellierungsansätze, mit Ausnahme der inzwischen revidierten SIA 262:2013 [16] (gemäss welcher der laterale Bügelabstand keine Rolle spielte), zeigen ein ähnliches Verhalten.

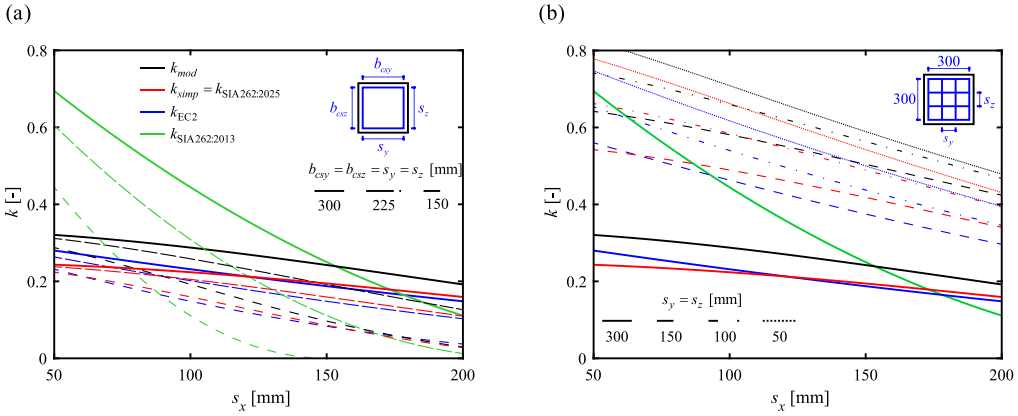

Abbildung 6: Vergleich des Effektivitätsfaktors (A_{conf}/A_{cs}) der verschiedenen Modelle in Funktion des vertikalen Bewehrungsabstandes s_x – (a) variable Querschnittsgrösse mit einem Bügel und (b) konstanter Querschnitt mit unterschiedlicher Bewehrungsanzahl.

Das neue Umschnürungsmodell (originales und vereinfachtes Modell) wurde erfolgreich validiert. Die Validierung wurde mittels 40 Versuchsdaten an Druckgliedern aus der Versuchsdatenbank von Moccia et al. [17] durchgeführt (für die detaillierten Ergebnisse siehe Dissertation in Anhang A). Die Definition der massgebenden umschnürten Fläche $A_{conf,simp}$ ist zudem bereits in der SIA 262:2025 [4] enthalten. In den folgenden Modellierungen wird für die Berücksichtigung der passiven Umschnürung die Umschnürungsspannung nach dem neuen Modell ($\sigma_{conf,mod}$) und die umschnürte Fläche nach der Vereinfachung ($A_{conf,simp}$) bestimmt.

3.2 Geschweisste Leiterbewehrung

Geschweisste Leiterbewehrung wird immer häufiger in der Produktion von Tübbingen verwendet. Dies liegt einerseits daran, dass Schweiss-Roboter autonom die Leiterbewehrung mit einer vorgegebenen Qualität herstellen können und andererseits daran, dass Leiterbewehrungen im Vergleich zu konventioneller Bewehrung den Bewehrungseinbau vereinfachen, den Betoniervorgang erleichtern und den Materialverbrauch reduzieren, letzteres durch Einsparung der Überlappungs- und Verankerungslängen, welche 10-20% des gesamten Stahlgewichts ausmachen. Die einzelnen Stäbe der Leiterbewehrung werden durch die angeschweissten Querstäbe verankert, wobei aufgrund der erreichbaren Schweissqualität häufig mindestens zwei Querstäbe erforderlich sind, um einen Stab komplett zu verankern (SF < 1.0, siehe [18]). Das Zusammenspiel der einzelnen Stäbe führt zu einem nicht trivialen Kraftfluss, der für die Anwendung der Leiter als Umschnürungsbewehrung Fragen aufwirft. Dabei ist von zentralem Interesse, (i) ob die Stäbe voll aktiviert werden können (Erreichen der Fliessspannung der Bewehrung), (ii) wo die Umschnürungskräfte in den Beton eingeleitet werden, da dadurch die umschnürte Fläche definiert wird und (iii) ob die Wirkung der zur Verankerung verwendeten Leiteräste als Umschnürungsbewehrung durch die Schweissung resp. Verankerung beeinträchtigt wird.

3.2.1 Experimentelle Untersuchungen mit faseroptischen Messungen

Mittels faseroptischer Messungen mehrerer Bewehrungsstäbe (in transversaler und longitudinaler Richtung) eines streifenbelasteten Betonkörpers wurde das Tragverhalten der Leiterbewehrung untersucht. Pro Bewehrungsstab wurden jeweils zwei Fasern auf gegenüberliegenden Seiten angebracht, so dass nicht nur die axiale, sondern auch die laterale Belastung ermittelt werden konnte (siehe Abbildung 7).
Die faseroptischen Messungen zeigten, dass geschweisste Leiterbewehrung effektiv als Umschnürungsbewehrung verwendet werden kann. Die transversalen Stäbe konnten bis zur Fliessspannung aktiviert werden, während die Stäbe in longitudinaler Richtung neben der Verankerung der transversalen Stäbe auch die notwendigen Umschnürungsbewehrung in Längsrichtung (siehe Erklärung in Unterkapitel 3.3) sicherstellen konnten. Die Umschnürungskräfte wurden teilweise lokal an den Kreuzungsstössen in den Beton eingeleitet, andererseits aber auch kontinuierlich entlang der longitudinalen Stäbe, die dadurch ausgeprägte Krümmungen erfuhren. Vereinfachend wird vorgeschlagen, den äusseren der beiden Kreuzungsstösse pro Stabseite als konzentrierten Lasteinleitungspunkt für die Modellierung der Umschnürungswirkung anzunehmen, was auch in den folgenden Modellierungen so angewendet wird.

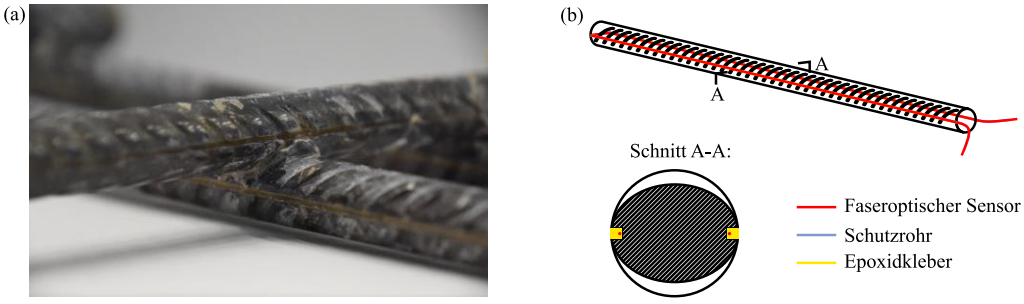

Abbildung 7: Instrumentierung der Leiterbewehrung – (a) geschweisster Kreuzungsstoss mit faseroptischem Sensor in Nut und geschützt mit einem Epoxidharz und (b) schematische Zeichnung der Sensoranordnung.

3.3 Kombination von Lastausbreitung und Umschnürungsbewehrung für die Streifenbelastung von Beton

Das Zusammenspiel zwischen Lastausbreitung und Umschnürungsbewehrung bei der Streifenbelastung von Beton wurde experimentell und theoretisch untersucht, um das erlangte Wissen in einem nächsten Schritt auf Tübbinglängsfugen anwenden zu können.

3.3.1 Experimentelle Untersuchungen

Das Tragverhalten von Betonkörpern mit Streifenbelastung wurde mittels einer Versuchsserie an 15 Betonblöcken mit Abmessung 350·550·525 mm³ (siehe Abbildung 8, im weiteren als Blockversuche bezeichnet), welche über die gesamte Höhe bewehrt waren, untersucht. Dabei wurden folgende Parameter variiert:

- Breite der belasteten Fläche (b_{ly} = 140 mm oder b_{ly} = 210 mm);
- Lage der belasteten Fläche (zentrisch e_y = 0 oder exzentrisch e_y = 29…58 mm);
- Bewehrungstyp (Leiter-, Bügel oder Dübelbewehrung, siehe Abbildung 9);
- Bewehrungsgehalt in transversaler und longitudinaler Richtung (ω_y = 0.07…0.37, ω_z = 0.03…0.40);
- Betondruckfestigkeit (normalfest f_{co} = 46.5…50.8 MPa oder hochfest f_{co} = 76.6 MPa).

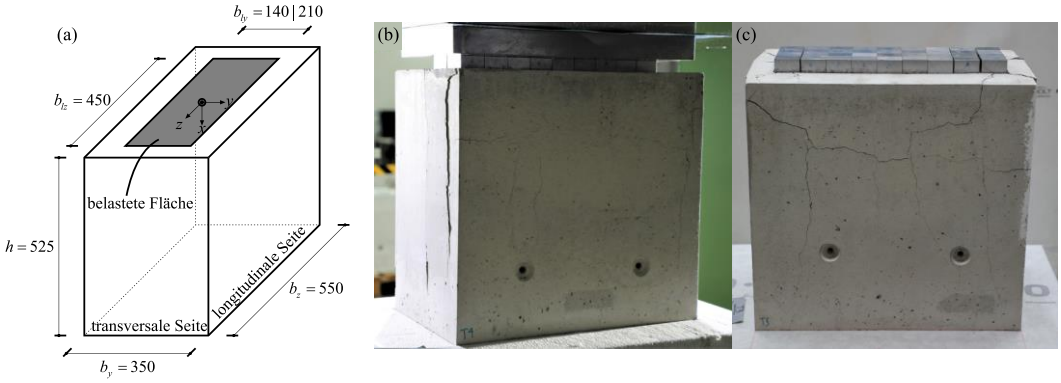

Abbildung 8: Blockversuche – (a) Geometrie Versuchskörper [mm], (b) Versuchsaufbau und (c) geprüfter Versuchskörper.

Die Streifenbelastung wurde weggesteuert über kleine Stahlklötze (zur Minimierung unerwünschter Querbehinderungen durch die Lasteinleitung) auf die Versuchskörper aufgebracht. Der Versuchsaufbau ist in Abbildung 8 abgebildet. Jeweils eine transversale und longitudinale Seite wurde mit digitaler Bildkorrelation (DIC = digital image correlation) untersucht, um die Rissentwicklung mit zunehmender vertikaler Zusammendrückung und Bewehrungsaktivierung zu verfolgen.
Die Versuchskörper zeigten allgemein ein duktiles Tragverhalten bis zur Höchstlast, mit zunehmendem vertikalem Eindrücken der Stahlklötze bei kleiner Laststeigerung, mit Ausnahme eines hochfesten Versuchskörpers, der sich praktisch bis zur Höchstlast näherungsweise linear elastisch verhielt. Abbildung 10 veranschaulicht exemplarisch das Tragverhalten und die Rissentwicklung für einen Versuchskörper.

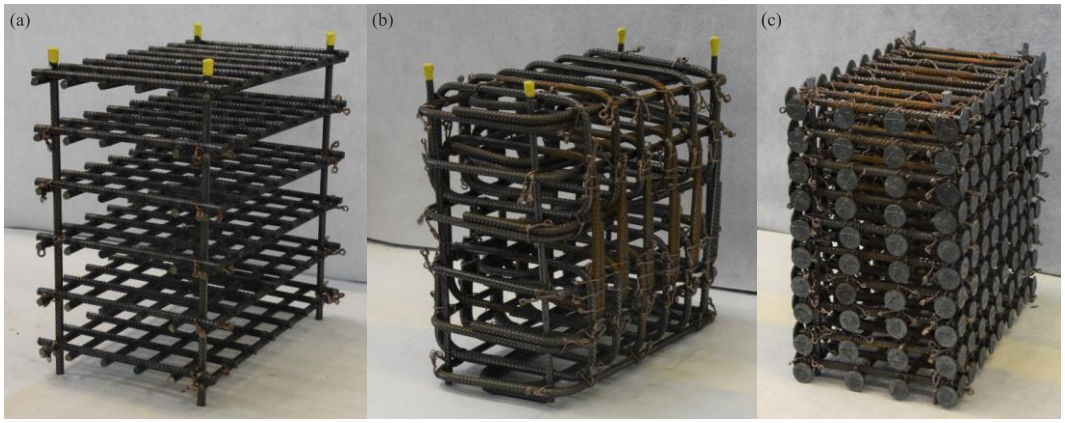

Abbildung 9: Verschiedene Bewehrungstypen. (a) geschweisste Leiterbewehrung, (b) Bügelbewehrung und (c) Dübelbewehrung.

Aus den Blockversuchen konnten folgende Erkenntnisse gewonnen werden:

- Mit zunehmender Belastungsbreite b_{ly} reduzierte sich die geometrische Umschnürung was dazu führte, dass die Betondruckfestigkeit bei der Lasteinleitung sank (= tiefere mittlere Spannung unter Höchstlast), wobei aber die Normalkraft (= Integral der Spannung) aufgrund der grösseren belasteten Fläche trotzdem zunahm;
- Eine exzentrische Belastung bewirkte bei gleicher Abmessung der belasteten Fläche eine Reduktion der aufnehmbaren Spannung und dementsprechend auch eine geringere Normalkraft, was ebenfalls durch reduzierte geometrische Umschnürung begründet ist;
- Der Vergleich der unterschiedlichen Bewehrungstypen zeigte keinen wesentlichen Unterschied zwischen Versuchskörpern mit sonst gleichen Parametern, was bestätigt, dass die geschweisste Leiterbewehrung voll aktiviert werden konnte;
- Mit höherem transversalem Bewehrungsgehalt konnte der Tragwiderstand erhöht werden, solange ausreichend Bewehrung in Längsrichtung vorhanden war, wobei aber eine grössere Eindrückung erforderlich war, um die stärkere Bewehrung zu aktivieren;
- Hochfeste Versuchskörper zeigten gegenüber normalfesten Versuchskörpern mit ähnlichem mechanischem transversalem Bewehrungsgehalt tendenziell leicht reduzierte normierte Tragwiderstände;
- Mit den DIC-Messungen und den daraus ermittelten Rissbreiten konnte gezeigt werden, dass für normalfeste umschnürte Versuchskörper die Tragfähigkeit voll ausgenutzt werden kann, ohne dass die Rissbreiten auf Gebrauchstauglichkeitsniveau ($w_{r,max}$ <= 0.2 mm, Gebrauchslast ermittelt unter Berücksichtigung der gängigen Sicherheitsfaktoren für die Einwirkungen und die Materialien aus der Höchstlast) massgebend werden; für die hochfesten Versuchskörper deutete sich hingegen an, dass die Rissbreite im Gebrauchszustand massgebend werden kann.

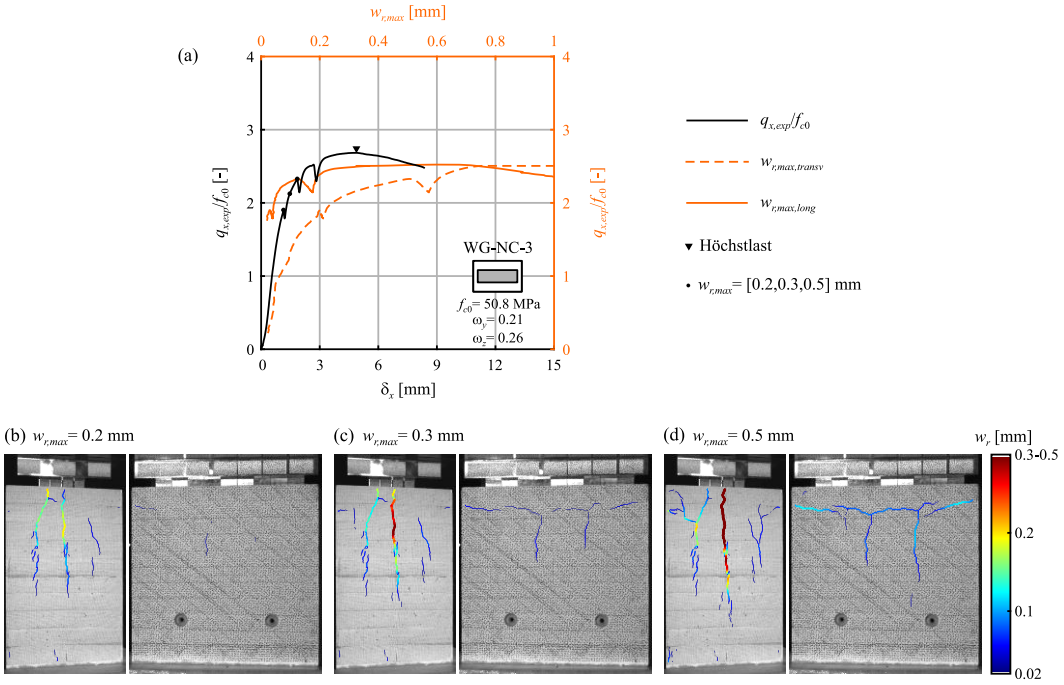

Abbildung 10: Tragverhalten und Rissentwicklung eines Blockversuchs.

3.3.2 Modellierung

Abbildung 11 zeigt das Dual-Wedge Spannungsfeld [14] (nur eine symmetrische Hälfte ist abgebildet), das ursprünglich für Betongelenke (Streifenbelastung mit schmaler belasteter Breite) entwickelt und erfolgreich validiert wurde [19]. Das Spannungsfeld berücksichtigt für den Beton das modifizierte Versagenskriterium nach Coulomb (mit $c = f_{co}/4$, $\tan\varphi = 0.75$ und $f_{ct} = 0$), wobei die longitudinale z-Richtung (aus der Ebene des Spannungsfeldes) eine Hauptspannungsrichtung ist, in die bei Streifenbelastung keine Lastausbreitung erfolgt und somit nur Umschnürungsbewehrung Druckspannungen erzeugen kann. Die mit dem Spannungsfeld ermittelte Spannung σ_{xo} kann daher – basierend auf dem Coulomb Versagenskriterium – nur aktiviert werden, wenn in longitudinaler Richtung ausreichend Bewehrung vorhanden ist, so dass die daraus resultierende Umschnürungsspannung der mittleren Hauptspannung entspricht und somit nicht massgebend wird.

Für die Modellierung von Streifenbelastung mit breiter Belastungsfläche, wie sie für Tübbinglängsfugen typisch ist, wurde das Dual-Wedge Spannungsfeld wie folgt weiterentwickelt: Die Umschnürungsspannungen (σ_{confy} resp. σ_{sy}, wobei für die Bemessung $\sigma_{confy} = \sigma_{sy}$ empfohlen und auch so in diesem Bericht berücksichtigt wird) werden nach dem Umschnürungsmodell (siehe 3.1.1) bestimmt, und als verfügbare Breite für die Lastausbreitung d_2 wird die umschnürte Breite nach der Vereinfachung des Umschnürungsmodells angesetzt:

$$d_2 = b_{ccy} = b_{csy} - 2 \cdot e_y - \frac{\sqrt{s_x^2 + s_z^2}}{2} \tag{4}$$

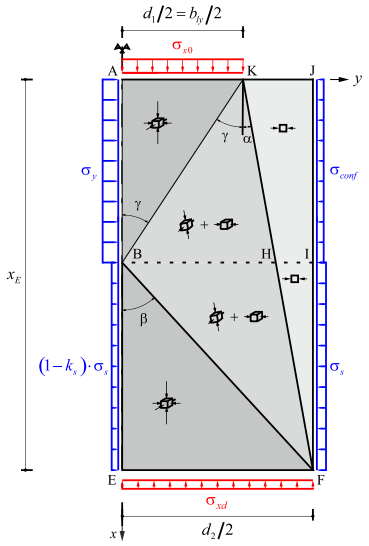

Abbildung 11: Dual-Wedge Spannungsfeld.

Die Erweiterung des Spannungsfelds wird hier als DW-cc bezeichnet (cc da nur der *c*onfined *c*oncrete (umschnürter Beton) zur Lastausbreitung berücksichtigt wird); in Kapitel 3.4 wird dann nur noch DW als Bezeichnung verwendet. Zudem wird vorgeschlagen, dass bei unregelmässigen Bewehrungsabständen die Umschnürungsspannungen mit dem Mittelwert der Abstände ermittelt werden darf, während für die umschnürte Fläche der maximale Bewehrungsabstand berücksichtigt werden soll.
Der mit dem Dual-Wedge Spannungsfeld ermittelte Tragwiderstand σ_{x0} kann in longitudinaler Richtung nur innerhalb der umschnürten Länge (b_{ccz}) angesetzt werden. Falls die belastete Fläche darüber hinausragt ($b_{lz} > b_{ccz}$), kann ausserhalb von b_{ccz} nur die einachsige Betondruckfestigkeit f_{c0} angesetzt werden, wodurch der Tragwiderstand $q_{x,u,\text{DW-cc}}$, bezogen auf die Lasteinleitfläche, resultiert:

$$q_{x,u,\text{DW-cc}} = \frac{\sigma_{x0,\text{DW-cc}} \cdot b_{ccz} + f_{c0} \cdot (b_{lz} - b_{ccz})}{b_{lz}} = f_{c0} \cdot \left(1 + \frac{b_{ccz}}{b_{lz}} \cdot \left(\frac{\sigma_{x0,\text{DW-cc}}}{f_{c0}} - 1\right)\right) \tag{5}$$

Die umschnürte Länge b_{ccz} kann dabei nach der Vereinfachung des Umschnürungsmodells ermittelt werden:

$$b_{ccz} = b_{csz} - \frac{\sqrt{s_x^2 + s_y^2}}{2} \tag{6}$$

Für gegebene Geometrie und Umschnürungsbewehrung wird die Spannung σ_{x0} mit dem Dual-Wedge Spannungsfeld iterativ bestimmt. Um eine geschlossene und einfache Formel zu erhalten, wurde eine Parameterstudie durchgeführt. Daraus resultierte folgende Vereinfachung, die als DW-s bezeichnet wird (s für *s*implified):

$$\sigma_{x0,\mathrm{DW-s}} = \left(\frac{d_2}{d_1}\right)^{\frac{2}{5}} \cdot \left(f_{c0} + 4 \cdot \sigma_{confy}\right) \leq \frac{5}{2} \cdot \left(f_{c0} + 4 \cdot \sigma_{confy}\right) \tag{7}$$

Mit dieser semi-empirischen Formel kann dann analog zu Gleichung (5) der Tragwiderstand ermittelt werden. Auf Basis der Parameterstudie können auch die erforderliche Umschnürungsspannung in Längsrichtung ($\sigma_{confz,req,\mathrm{DW\text{-}s}}$) sowie die Höhe der umschnürten Zone (x_E) abgeschätzt werden:

$$\sigma_{confz,req,\mathrm{DW-s}} = \frac{d_1}{\left(b_{csy} - 2 \cdot e_y\right)} \cdot \left(1.75 - 0.75 \cdot \frac{d_1}{d_2}\right) \cdot \sigma_{confy} \tag{8}$$

$$x_E = d_1 + d_2 \leq 1.5 \cdot d_2 \tag{9}$$

3.3.3 Validierung und Vergleich mit anderen Modellierungsansätzen

Der vorgeschlagene erweiterte Modellierungsansatz mit dem Dual-Wedge Spannungsfeld und die daraus abgeleitete Vereinfachung wurden mit den experimentellen Resultaten der Blockversuche validiert. Zusätzlich enthielt der Vergleich die Bemessungsempfehlung der DAUB:2024-Richtlinie [9], welche nur die Lastausbreitung berücksichtigt, sowie das semi-empirische GPC-Modell [20], welches sowohl die Lastausbreitung als auch die Umschnürungsbewehrung zur Ermittlung des Tragwiderstands anrechnet. Abbildung 12 zeigt, dass das erweiterte Dual-Wedge Spannungsfeld (DW-cc) und die Vereinfachung (DW-s) sehr ähnliche Tragwiderstände prognostizieren und diese gut mit den Versuchsresultaten übereinstimmen. Insbesondere der Einfluss des mechanischen Bewehrungsgehalts wird mit diesen beiden Ansätzen ausgezeichnet abgebildet (Abbildung 11b). In diesem Punkt unterscheiden sie sich von der DAUB:2024-Richtlinie und dem GPC-Modell: Da in der DAUB:2024-Richtlinie der Einfluss der Umschnürungsbewehrung vernachlässigt wird, resultieren mit zunehmendem Bewehrungsgehalt konservativere Prognosen, während für geringere Bewehrungsgehalte sogar eine Tendenz zu unsicheren Vorhersagen besteht. Dasselbe trifft auf das GPC-Modell zu, jedoch wesentlich schwächer ausgeprägt. Alle Modellierungsansätze zeigen eine Tendenz zur Überschätzung des Tragwiderstands der hochfesten Versuchskörper. Dabei ist anzumerken, dass für die Nachrechnungen die einachsige Betondruckfestigkeit f_{c0}, ohne Abminderung mittels Sprödigkeitsfaktor, z.B. $\eta_{cc} = (30/f_{c0})^{(1/3)}$ nach SIA 262 [16], berücksichtigt wurde. Dies wird auch in allen folgenden Nachrechnungen so gehandhabt. Die zwei neuen Modellierungsansätze konnten mit den experimentellen Versuchen erfolgreich validiert werden. Sie können somit für die Bemessung von streifenbelasteten und komplett umschnürten Betonkörpern vorgeschlagen werden.

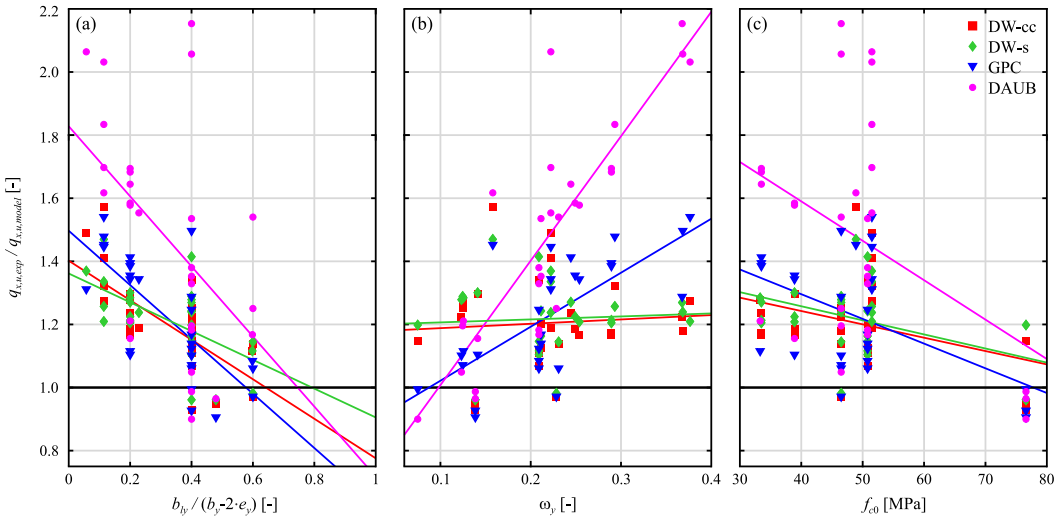

Abbildung 12: Vergleich der Modellvorhersagen mit den experimentellen Versuchsresultaten geplottet in Funktion von (a) Last-Konzentrations-Verhältnis, (b) transversalem mechanischem Bewehrungsgehalt und (c) Betondruckfestigkeit.

3.4 Tübbinglängsfugen

Die Anordnung von Umschnürungsbewehrung entlang des gesamten Tunnelumfangs ist aufgrund des sehr hohen Bewehrungsverbrauchs in den meisten Fällen nicht praktisch. Die Umschnürungsbewehrung konzentriert sich stattdessen auf die Lasteinleitungszonen bei den Längsfugen. Somit kann jeder Tübbing in zwei umschnürte Zonen bei den Längsfugen und eine nicht umschnürte Zone dazwischen eingeteilt werden. Die zusätzliche nicht umschnürte Zone ist der wesentliche Unterschied zu den im vorherigen Kapitel präsentierten Untersuchungen und wird in diesem Kapitel mittels experimenteller und theoretischer Überlegungen vertieft untersucht. Ein weiterer Unterschied zu den vorherigen Untersuchungen besteht in der Krümmung und radialen Belastung der Tübbinge. Diese Einflüsse werden in dieser Arbeit nicht weiter untersucht.

3.4.1 Experimentelle Untersuchungen

Die experimentellen Untersuchungen der Längsfugen („Fugenversuche“) beinhalteten neun Versuche, bei denen jeweils zwei Versuchskörperhälften mit gleichen Eigenschaften aufeinandergestellt wurden, wobei die Kontaktfläche als Fuge ausgebildet war. Die Abmessung der Versuchskörperhälften betrug 350·750·825 mm³ (siehe Abbildung 13). Die Fugenhöhe (neben der Kontaktfläche) betrug 7 mm, was zu einer Öffnung zwischen den Versuchskörperhälften von 14 mm führte, und die Fugenlänge 650 mm. Die Fugenversuche wurden ausschliesslich mit geschweisster Leiterbewehrung (siehe Abbildung 14) und normalfestem Beton (f_{co} = 42.1…55.2 MPa) ausgebildet. Wie bei den Blockversuchen wurde jeweils eine transversale und eine longitudinale Seite mittels DIC (siehe Abbildung 13) untersucht, um die Rissbreiten zu bestimmen. Die Versuche wurden zunächst kraftgesteuert durchgeführt; ab ca. 70% der erwarteten Versagenslast wurde die Regelung auf Wegsteuerung umgestellt.

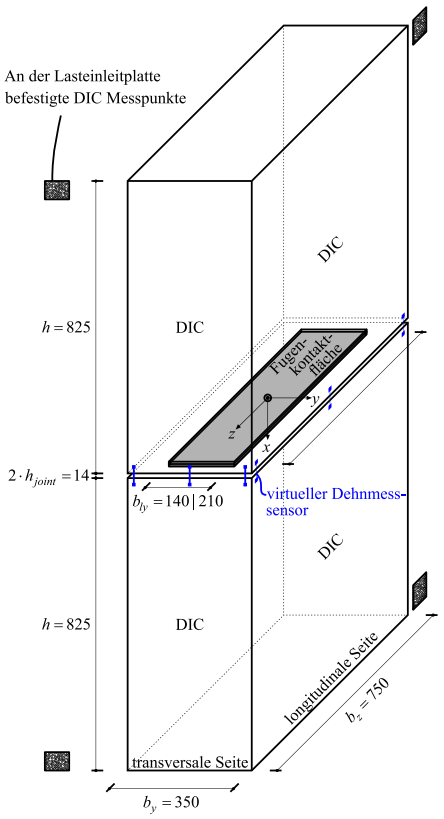

Abbildung 13: Geometrie der Fugenversuche [mm].

Bei den Fugenversuchen wurden folgende Parameter variiert:

- Fugengeometrie (b_{ly} = 140 oder b_{ly} = 210 mm, zusätzlich bei einem Versuch Aussparung in Fugenmitte für einen Führungsstab, siehe Abbildung 14b);
- Transversaler Bewehrungsgehalt (ω_y = 0.10…0.26);
- Anordnung der Umschnürungsbewehrung in Belastungsrichtung (umschnürte und nicht umschnürte Zone oder nur umschnürte Zone).

Aus den Fugenversuchen konnten folgende Erkenntnisse gewonnen werden:

- Für Tübbinglängsfugen kann das Versagen in der umschnürten oder nicht umschnürten Zone auftreten, und beim Vorhandensein einer Aussparung zudem auch lokal bei der Fuge;
- Die unterschiedlichen Versagensmechanismen zeigen vor allem nach Erreichen der Höchstlast ein unterschiedliches Verhalten: bei Versagen in der nicht umschnürten Zone oder lokal bei der Fuge kam es zu einem deutlich ausgeprägteren Lastabfall als bei Versagen in der umschnürten Zone, bei denen vereinzelt sogar ein Lastplateau beobachtet werden konnte;
- Eine Steigerung des Tragwiderstands durch höheren Umschnürungsbewehrungsgehalt ist nur möglich, solange die nicht umschnürte Zone Tragreserven besitzt und somit nicht massgebend wird. Bei hohen Normalkräften – was bei hohen Umschnürungsgehälter und/oder breiten Fugen auftritt – wird die umschnürte Zone massgebend;
- Bei Längsfugen mit gleichen Fugenaussenabmessungen ($b_{ly} \cdot b_{lz}$) führten sowohl ein Versatz in transversaler Richtung (simulierte fehlerhafte Ausrichtung) als auch eine Aussparung für einen Führungsstab zu einer höheren aufnehmbaren Kon-

taktspannung in der Fuge (aufgrund stärker ausgeprägter geometrischer Umschnürung), die aufnehmbare Normalkraft war jedoch aufgrund der reduzierten Kontaktfläche kleiner. Derselbe Effekt trat bei einer Reduktion der Belastungsbreite ($b_{ly}\downarrow$) auf;
- Abplatzungen des Überdeckungsbetons entlang der Bewehrung beschränkten sich nicht nur auf die umschnürte Zone, sondern setzten sich in die nicht umschnürten Zone fort; der Überdeckungsbeton kann somit in keiner Zone als tragend berücksichtigt werden;
- Die Rissbreiten wurden bei den untersuchten Versuchskörpern für den Gebrauchstauglichkeitsnachweis nicht massgebend (Gebrauchslast ermittelt unter Berücksichtigung der gängigen Sicherheitsfaktoren für die Einwirkungen und die Materialien aus der Höchstlast), so dass der volle, durch die Umschnürung erhöhte Tragwiderstand für die Bemessung berücksichtigt werden kann. Diese Aussage ist jedoch nur für die spezifischen Randbedingungen (z.B. Bewehrungsüberdeckung, Betonfestigkeit, Geometrie der Fuge) der untersuchten Versuchskörper gültig. Für weitere Informationen zur Rissthematik, wie z.B. die Rissentwicklung in Funktion der einwirkenden Belastung, wird auf die Dissertation in Anhang A verwiesen.

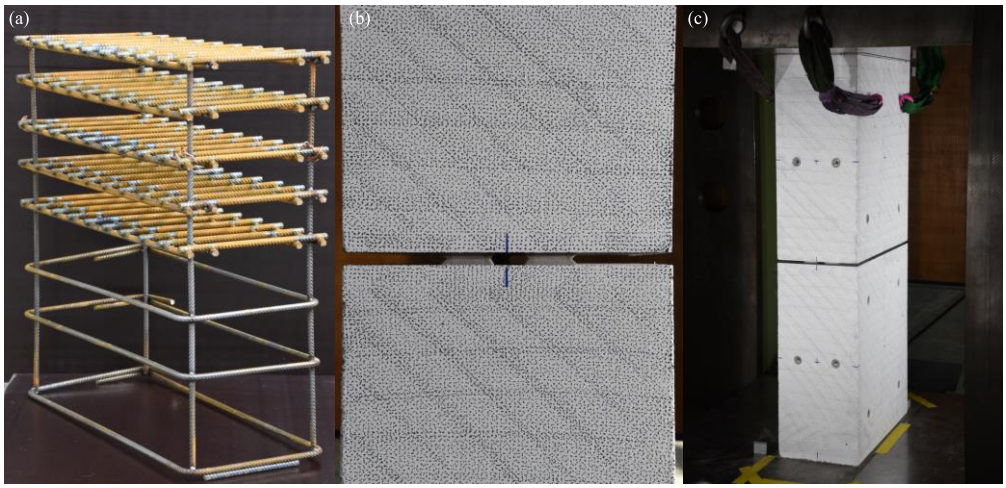

Abbildung 14: Fugenversuche – (a) Geschweisste Leiterbewehrung, (b) Fugenausbildung mit Aussparung für Führungsstab und (c) Versuchsaufbau.

3.4.2 Modellierung

Für die Modellierung der Längsfugen muss neben dem Tragwiderstand der umschnürten Zone ($q_{x,u,conf}$) auch – falls vorhanden – derjenige der nicht umschnürten Zone ($q_{x,u,unconf}$) ermittelt werden, wobei der kleinere Wert den Tragwiderstand der Fuge resp. des Tübbings bestimmt:

$$q_{x,u} = min\left(q_{x,u,conf}, q_{x,u,unconf}\right) \tag{10}$$

In der nicht umschnürten Zone ist keine weitere Lastausbreitung möglich, und es herrscht ein einachsiger Druckspannungszustand. Aufgrund der in den Versuchen beobachteten Fortsetzung der Abplatzungen des Überdeckungsbetons von der umschnürten in die nicht umschnürte Zone wird vorgeschlagen, für die Ermittlung des Tragwiderstands der nicht umschnürten Zone die einachsige Betondruckfestigkeit f_{co}

nur innerhalb der Bewehrung ($b_{csy} \cdot b_{csz}$) anzusetzen. Der Tragwiderstand der nicht umschnürten Zone, bezogen auf die Fugenkontaktfläche, beträgt somit:

$$q_{x,u,unconf} = \frac{f_{c0} \cdot b_{csy} \cdot b_{csz}}{(b_{ly} - b_{rod}) \cdot b_{lz}} \tag{11}$$

Für die Modellierung der umschnürten Zone bietet sich das weiterentwickelte Dual-Wedge Spannungsfeld (siehe 3.3.2, hier nur noch als DW anstatt DW-cc bezeichnet) an. Mit diesem Spannungsfeld kann jedoch nur eine Lastausbreitung innerhalb der umschnürten Breite (b_{ccy}) erfolgen, was zu einer statischen Diskontinuität am Übergang zur nicht umschnürten Zone führt, in welcher wie zuvor ausgeführt Betondruckspannungen innerhalb der Breite der Bewehrung (b_{csy}) angesetzt werden. Somit bedarf das Dual-Wedge Spannungsfeld einer weiteren Anpassung: Last kann auch zum Bereich zwischen b_{csy} und b_{ccy} geleitet werden, indem die Bewehrung die auftretenden Spreizzugkräfte aufnimmt, wobei die Betonspannungen die einachsige Festigkeit f_{c0} nicht überschreiten dürfen. Mit diesem zusätzlichen Lastpfad, welcher dem bestehenden Dual-Wedge Spannungsfeld superponiert werden muss, resultiert das Multi-Wedge Spannungsfeld. Abbildung 15 zeigt sowohl das Multi-Wedge als auch Dual-Wedge Spannungsfeld mit dem dazugehörenden Bewehrungslayout.

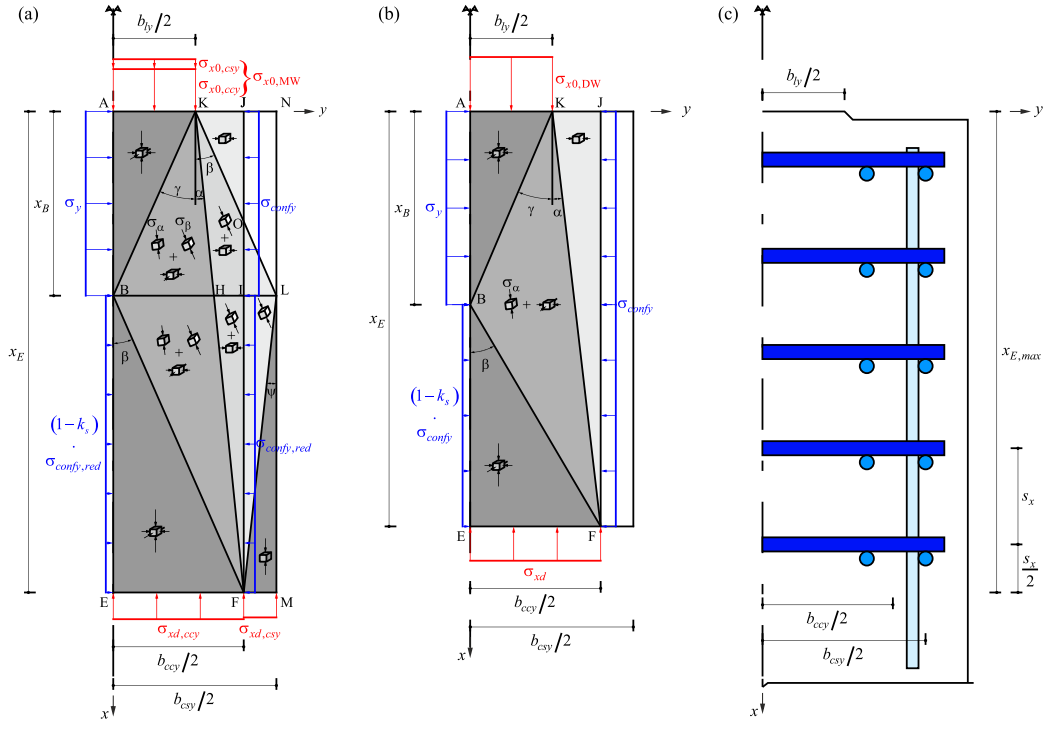

Abbildung 15: Modellierung der Längsfugen – (a) Multi-Wedge Spannungsfeld, (b) Dual-Wedge Spannungsfeld und (c) zugehöriges Bewehrungslayout. Es ist jeweils nur eine Symmetriehälfte dargestellt und die lateralen und vertikalen Spannungen sind unterschiedlich skaliert.

Durch zusätzliche Lastausbreitung in longitudinaler Richtung mit Aktivierung der Bewehrung zur Aufnahme der Spreizkräfte – siehe Abbildung 16 – ist es möglich, auch für den Teil der Kontaktfläche in der Längsfuge, der ausserhalb der umschnürten Länge liegt ($b_{lz} > b_{ccz}$), Kontaktspannungen ($\sigma_{x0,csz}$) grösser als f_{c0} zu erreichen. Die

Spannung $\sigma_{x0,csz}$ kann mit der einfachsten Form des Dual-Wedge Spannungsfeld ermittelt werden, siehe Abbildung 16a.
Abbildung 16b zeigt einen horizontalen Schnitt nach der Lastausbreitung mit farblich hervorgehobenen unterschiedlich belasteten Flächen aus der Lastausbreitung. Durch die unabhängige Betrachtung der 2D-Lastausbreitung in transversaler und longitudinaler Richtung kann das Modell keinen Kraftfluss zur kompletten Fläche innerhalb der Bewehrung ($A_{cs} = b_{csy} \cdot b_{csz}$) abdecken: Die Ecken von A_{cs} (in weisser Farbe) sind unbelastet. Um eine Normalkraft von $f_{co} \cdot A_{cs}$ (die dem Tragwiderstand der nicht umschnürten Zone entspricht) zu erreichen, wird vorgeschlagen, dass die Spannung $\sigma_{xd,ccy}$, welche mit dem Multi-Wedge Spannungsfeld ermittelt wird, entsprechend etwas grösser als f_{co} sein darf. Streng genommen wird dadurch das Bruchkriterium von unbewehrtem Beton verletzt; durch die sonst unberücksichtigte günstige Lastausbreitung in die unbelasteten Ecken kann der Vorschlag jedoch gerechtfertigt werden.
Der Tragwiderstand der umschnürten Zone, bezogen auf die Fugenkontaktfläche beträgt somit:

$$q_{x,u,conf} = \frac{\sigma_{x0,\mathrm{MW}} \cdot b_{ccz} + \sigma_{x0,csz} \cdot (b_{lz} - b_{ccz})}{b_{lz}} \tag{12}$$

Das Multi-Wedge Spannungsfeld wurde zudem weiterentwickelt, um den Effekt einer Aussparung in der Fuge für einen Führungsstab zu berücksichtigen. Abbildung 17 zeigt die drei entwickelten Varianten.

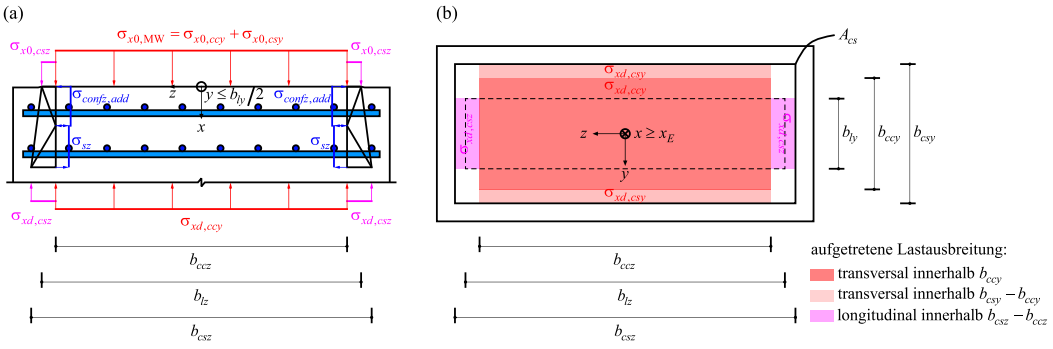

Abbildung 16: (a) Longitudinale Lastausbreitung und (b) horizontaler Schnitt mit belasteten Flächen durch Lastausbreitung.

3.4.3 Validierung und Vergleich mit anderen Modellierungsansätzen

Die Versuchsdaten und die Vorhersagen des Tragwiderstands der verschiedenen Modellierungsansätzen werden in Abbildung 18 in Funktion verschiedener Versuchsparameter verglichen. Die ausgefüllten Marker zeigen jeweils den Vergleich unter Berücksichtigung der massgebenden Zone (umschnürt oder nicht umschnürt), während die Marker ohne Füllung nur den Vergleich mit der Vorhersage des Widerstands der umschnürten Zone abbilden. Die Prognosen der Modelle, die sowohl die Lastausbreitung als auch die Umschnürungsbewehrung berücksichtigen (Multi-Wedge (MW) und Dual-Wedge (DW) Spannungsfeld sowie GPC), sind sehr ähnlich und liegen – ohne übermässig konservativ zu sein – auf der sicheren Seite, während nach der DAUB:2024-Richtlinie vorwiegend konservative Vorhersagen resultieren. Zusätzlich wird ersichtlich, dass der Tragwiderstand sowohl der umschnürten als auch der nicht umschnürten Zone berücksichtigt werden muss, da eine ausschliessliche Berücksich-

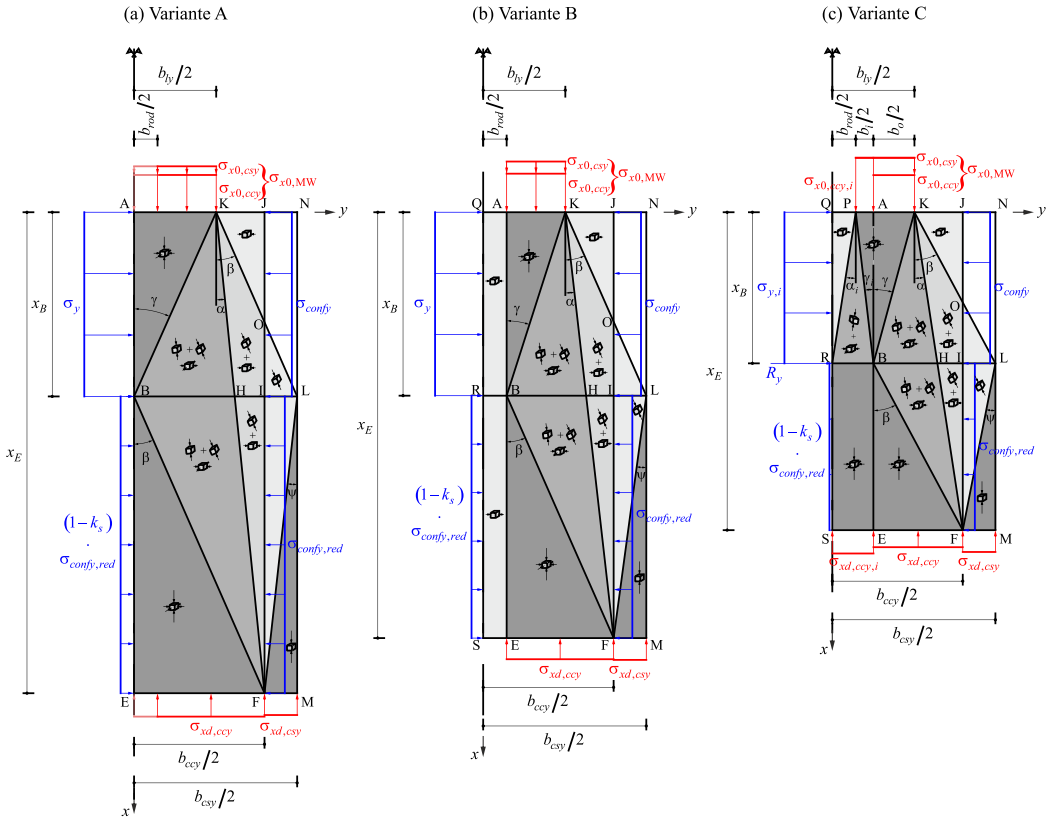

Abbildung 17: Verschiedene Varianten zur Berücksichtigung einer Fugenaussparung aufgrund eines Führungsstabes basierend auf dem Multi-Wedge Spannungsfeld.

tigung der umschnürten Zone zu unsicheren Vorhersagen führen kann. Der Modellierungsvorschlag für die nicht umschnürte Zone erweist sich dabei als geeigneter Ansatz. Mit den Versuchen konnten die beiden Spannungsfelder erfolgreich validiert und für die Praxis vorgeschlagen werden. Das Multi-Wedge Spannungsfeld sticht zudem als einziges Model heraus, das den gesamten Kraftfluss – auch zwischen umschnürter und nicht umschnürter Zone – konsistent berücksichtigen kann. Die verschiedenen Modellvorhersagen zur Berücksichtigung der Aussparung in der Fuge liegen alle auf der sicheren Seite. Jedoch ist der einzige durchgeführte Versuch nicht ausreichend, um die Modelle ausreichend zu validieren.

Ein direkter Vergleich der Tragwiderstandsvorhersagen für die Fugenversuche mit dem neu vorgestellten Multi-Wedge Spannungsfeld in Kombination mit dem Modellierungsansatz für die nicht umschnürte Zone und dem Bemessungsansatz nach der DAUB:2024 Richtlinie zeigt den Einfluss der Berücksichtigung einer Umschnürungsbewehrung in der Bemessung auf: Für die Fugenversuche mit einer nicht umschnürten Zone, die mutmasslich am relevantesten für die Tunnelbaupraxis sind, resultiert für die schmalen Fugen (b_{ly} = 140 mm) eine prognostizierte Tragwiderstandserhöhung von 16% bis 22% mit dem Multi-Wedge Spannungsfeld gegenüber der DAUB:2024 Richtlinie. Für die breiteren Fugen (b_{ly} = 210 mm) ist aufgrund des begrenzten Tragwiderstands der nicht umschnürten Zone der Effekt der Umschnürungsbewehrung kleiner, so dass mit dem DAUB:2024 Ansatz sogar etwas höhere prognostizierte Trag-

widerstände (0%...4%) auftreten. Dieser Vergleich verdeutlicht den Einfluss der nicht umschnürten Zone, unterstreicht aber auch das Optimierungspotential mittels Umschnürungsbewehrung. Es ist zu beachten, dass der Vergleich für die spezifischen Eigenschaften der untersuchten Fugenversuche gilt und nicht a priori auf andere Konfigurationen übertragen werden kann.

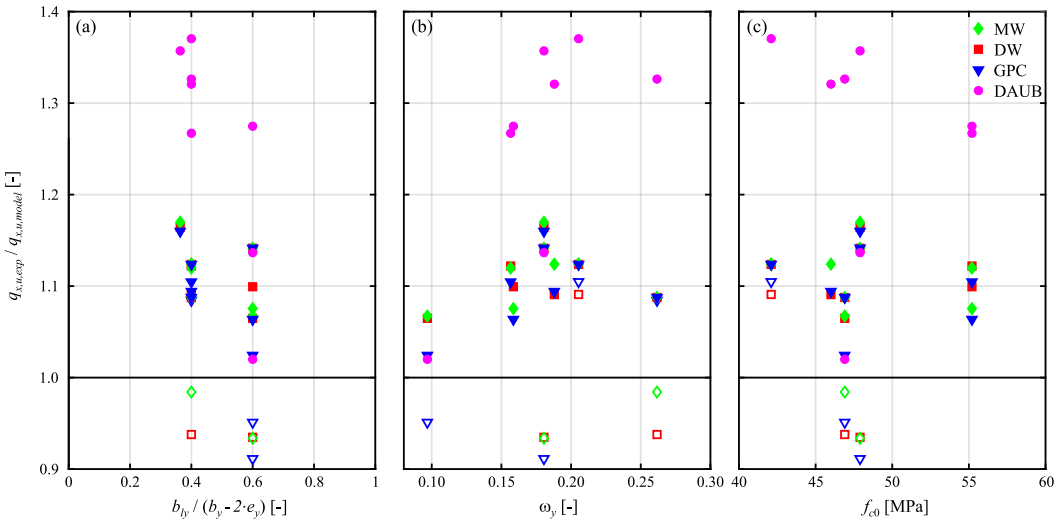

Abbildung 18: Vergleich der Modellvorhersagen mit den experimentellen Resultaten der Fugenversuche ohne Fugenaussparung geplottet in Funktion von (a) Last-Konzentrations-Verhältnis, (b) transversalem mechanischen Bewehrungsgehalt und (c) Betondruckfestigkeit.

3.5 Streifenbelastung und Tübbinglängsfugen – Stahlfaserbewehrter Beton

Stahlfaserbewehrter Beton geniesst im Tunnelbau durch seine Robustheit, das weniger spröde Nachriss-Verhalten und die Risskontrolle zunehmende Beliebtheit. Diese Eigenschaften erleichtern den Bau und bieten Vorteile bezüglich Wasserdichtigkeit. Wenn Fasern ohnehin bereits verwendet werden, ist es naheliegend, sie ebenfalls an den Tragwiderstand der Längsfugen anzurechnen. Dabei sind zwei Anwendungen möglich: (i) rein faserbewehrte Tübbinge und (ii) hybrid bewehrte Tübbinge, die neben den Fasern eine konventionelle Stabbewehrung enthalten. Beide Anwendungen wurden theoretisch und experimentell in Block- und Fugenversuchen – analog zu den vorgängig beschriebenen Versuchsserien an konventionell bewehrtem Beton – untersucht.

3.5.1 Experimentelle Untersuchungen

Für alle stahlfaserbewehrten Versuchskörper wurde Beton mit 40 kg/m³ der Dramix 3D 80/30BGP-Stahlfasern verwendet. Abgesehen davon waren die Versuchskörper in den Block- und Fugenversuchen identisch (Bewehrungslayout und Geometrie) wie die Versuchskörper in konventionell bewehrtem Beton, und wurden auch analog hergestellt (einzig die Betonierrichtung wurde angepasst, um eine optimale Faserorientierung zu erreichen) und geprüft, um einen direkten Vergleich zu ermöglichen.

Abbildung 19 zeigt den Vergleich zwischen den Blockversuchen mit faserbewehrtem Beton und konventionell bewehrtem Beton. Für die meisten hybrid bewehrten Versuchskörper erhöhte die Zugabe der Fasern den Tragwiderstand. Der positive Effekt der zusätzlichen Fasern war bei Versuchskörpern mit geringem konventionellem Bewehrungsgehalt am ausgeprägtesten, nahm hingegen mit zunehmendem konventionellem Bewehrungsgehalt ab. Die Zugabe der Stahlfasern führte zudem zu einer stärkeren Eindrückung bei der Höchstlast, veränderte das Last-Verformungsverhalten aber sonst nicht massgebend. Der einzige rein stahlfaserbewehrte Versuchskörper erfuhr hingegen ein bis fast zur Höchstlast annähernd linear elastisches Verhalten mit anschliessender stark ausgeprägter Entfestigung.

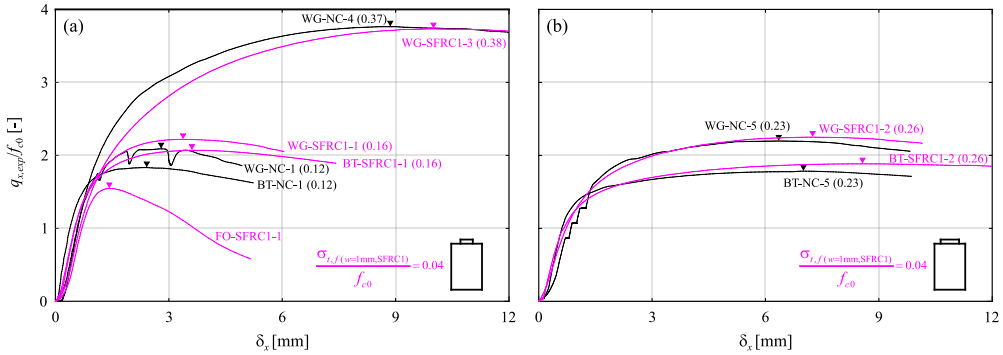

Abbildung 19: Vergleich der Blockversuche mit stahlfaserbewehrtem Beton (lila) und konventionellem Beton (schwarz). (a) Belastungsbreite 140 mm; (b) Belastungsbreite 210 mm. Mechanischer Bewehrungsgehalt in Klammern (für hybrid bewehrte Versuchskörper Summe aus konventioneller Bewehrung und residualer Zugfestigkeit). Abkürzungen: FO = fibres only (keine konventionelle Bewehrung), WG = Welded grids (geschweisste Leiterbewehrung und BT = Bent ties (Bügelbewehrung).

Der Vergleich der Fugenversuche mit faserbewehrtem Beton resp. konventionellem Beton ist in Abbildung 20 veranschaulicht. Wie bei den Blockversuchen konnte der Tragwiderstand der gering konventionell bewehrten Versuchskörper mittels Fasern erhöht werden. Der Einfluss der Fasern bei höheren konventionellen Bewehrungsgehalten war hingegen geringer, auch infolge der Begrenzung des Tragwiderstands durch die nicht umschnürte Zone. Herauszustreichen ist der Unterschied zwischen den rein faserbewehrten und den hybrid bewehrten Versuchen: Die rein faserbewehrten Versuche zeigten – wie der Blockversuch – ein annähernd linear elastisches Last-Verformungsverhalten bis fast zur Höchstlast, mit sehr starkem Lastabfall nach der Höchstlast oder sogar einem spröden Spreizzugversagen. Aufgrund dieses ungünstigen Verhaltens scheint die Anwendung von rein faserbewehrten Tübbingen für Tunnelausbauten nicht sinnvoll, obwohl höhere Tragwiderstände als mit nur konventionell bewehrten Versuchskörpern erreicht werden konnten. Vielmehr ist der Einsatz rein faserbewehrter Tübbinge – basierend auf den Kennwerten aus kleinen Standardversuchen nach EN 14651 [21]– unter diesem Gesichtspunkt kritisch zu beurteilen.

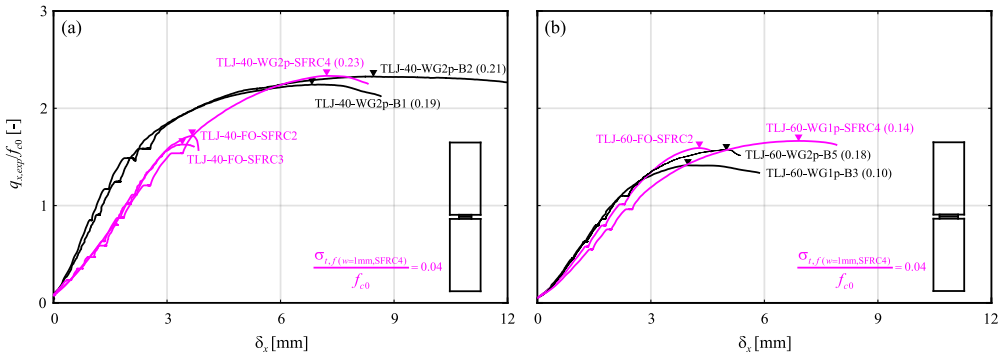

Abbildung 20: Vergleich der Fugenversuche mit stahlfaserbewehrtem Beton (lila) und konventionellem Beton (schwarz). (a) Belastungsbreite 140 mm; (b) Belastungsbreite 210 mm. Mechanischer Bewehrungsgehalt in Klammern (für hybrid bewehrte Versuchskörper Summe aus konventioneller Bewehrung und residualer Zugfestigkeit). Abkürzungen: FO = fibres only (keine konventionelle Bewehrung) und WG = Welded grids (geschweisste Leiterbewehrung). Im Vergleich zu [1] wurde Versuchskörper TLJ-60-WG2p-B5 zusätzlich in der Grafik integriert.

Die Fasern bewirkten bei geringen konventionellen Bewehrungsgehalten kleinere Rissbreiten bei gleicher Beanspruchung. Dieser Effekt reduzierte sich mit zunehmendem konventionellem Bewehrungsgehalt.

3.5.2 Modellierung

Für die Modellierung wird zwischen (i) hybrid bewehrten und (ii) rein faserbewehrten streifenbelasteten Betonkörpern unterschieden. Für beide Fälle wird die residuale Zugfestigkeit ($\sigma_{t,f}$) des faserbewehrten Betons als Parameter verwendet. $\sigma_{t,f}$ kann mittels Drei-Punkt-Biegeversuchen nach EN 14651 [21] und dem linearen Modell nach dem *fib* Model Code 2020 [6] als Funktion der Rissbreite (w) ermittelt werden. Weiter sind ein Faserorientierungs- resp. Faserverteilungsfaktor zu berücksichtigen, welche die residuale Zugfestigkeit abmindern, falls die Faserorientierung oder Faserverteilung im Bauteil (Tübbing) nicht derjenigen der Biegebalken entspricht. Die Bestimmung dieser Faktoren ist nicht Teil dieses Projekts.

Zur Ermittlung des Tragwiderstands von hybrid bewehrten streifenbelasteten Betonkörpern (i) wird für die Zone mit konventioneller Bewehrung vorgeschlagen, die Umschnürungsspannung der konventionellen Bewehrung mit der residualen Zugfestigkeit des faserbewehrten Betons zu einer hybriden Umschnürungsspannung ($\sigma_{conf,hyb}$) zu superponieren:

$$\sigma_{conf,hyb} = \sigma_{conf} + \sigma_{t,f}(w) \tag{13}$$

Die hybride Umschnürungsspannung kann sodann als Eingabeparameter für die bereits entwickelten Spannungsfelder (Multi-Wedge und Dual-Wedge) verwendet werden.

Für die nicht umschnürte Zone wird auch bei den faserbewehrten Tübbingen nur die einachsige Betondruckfestigkeit f_{co} berücksichtigt, so dass der Tragwiderstand nach Gleichung (11) – analog zum Modellierungsansatz für konventionell bewehrte Tübbinge – ermittelt werden kann.

Für rein faserbewehrte streifenbelastete Betonkörper (ii) wird die residuale Zugfestigkeit zur Aufnahme der Spreizzugkräfte aktiviert. Ein Einfluss der residualen Zugfestigkeit auf die Betondruckfestigkeit – analog einer Umschnürungsbewehrung – wird hingegen nicht berücksichtigt. Zur Modellierung wird das Dual-Wedge Spannungsfeld so-

mit ohne Ansatz von Umschnürungsspannungen und nur der residualen Zugfestigkeit vorgeschlagen, wobei aber für die Lastausbreitung die gesamte Körperbreite (b_y) und nicht nur der Bereich innerhalb der Bewehrung (b_{csy}, Multi-Wedge Spannungsfeld) resp. die umschnürte Breite (b_{ccy}, Dual-Wedge Spannungsfeld) eingesetzt werden kann.
Die unterschiedliche Berücksichtigung der Fasern bei hybriden und rein faserbewehrten Betonkörpern ist dadurch begründet, dass durch die konventionelle Bewehrung das Risswachstum kontrolliert wird und die Fasern somit in hybrid bewehrten Körpern eine Umschnürungswirkung ausbilden können, während ohne konventionelle Bewehrung – wie experimentell beobachtet– ein sprödes Zugversagen auftritt, weshalb nur die residuale Zugfestigkeit als Spreizbewehrung aktiviert werden kann.

3.5.3 Validierung

Der Vergleich des Tragwiderstands der hybrid bewehrten Versuchskörper mit den Modellvorhersagen der beiden Spannungsfelder (Multi-Wedge und Dual-Wedge Spannungsfeld) zeigt eine gute Übereinstimmung, so dass der Ansatz zur Bestimmung der hybriden Umschnürungsspannung sowie dessen Verwendung als Eingabeparameter für die Spannungsfelder erfolgreich validiert und für die Praxis empfohlen werden kann.
Für die rein faserbewehrten Versuchskörper liegen die Modellvorhersagen auf der sicheren Seite. Aufgrund des Risikos von sprödem Versagen sind jedoch weitere experimentelle Untersuchungen notwendig, bevor der Modellansatz ausreichend validiert ist, um für die Praxis vorgeschlagen werden zu können.

3.6 Ringfugen

Im Endzustand werden Tunnelausbauten primär quer zur Tunnelachse beansprucht, was für die Bemessung der in den vorhergehenden Kapiteln untersuchten Längsfugen massgebend ist. Die Beanspruchung der Ringfugen ist in diesem Zustand hingegen meist von untergeordneter Bedeutung. Für ihre Bemessung ist jedoch der Bauzustand zu beachten, in dem sich die Vortriebspressen der Tunnelbohrmaschine – üblicherweise über Pressenschuhe, die beispielsweise in den Viertelspunkten eines Tübbings angeordnet sind (siehe Abbildung 1) – lokal auf den zuletzt eingebauten Tübbingring abstützen.
Die Ein- und Durchleitung der Vortriebskräfte an den Ringfugen führt zu hoher örtlicher Beanspruchung der Tübbinge und kann bei unzureichender Bemessung Schäden verursachen. Diese sind zwar in der Regel nicht tragsicherheitsrelevant, können jedoch Sanierungen erforderlich machen, beispielsweise um bei unzulässig breiten Rissen die Anforderungen an die Wasserdichtigkeit zu gewährleisten.
Für die Bemessung relevant sind (i) die Druckspannungen bei der Krafteinleitung durch die Pressenschuhe, (ii) die Spreizzugkräfte infolge der allgemein dreidimensionalen Lastausbreitung und (iii) die Randzugkräfte zwischen den Pressenschuhen. Die Spreizzugkräfte (ii) und die Randzugkräfte (iii) resultieren aus Verträglichkeit, wobei erstere bei Bedarf die Aufnahme von Druckspannungen (i) ermöglichen, welche die einachsige Betondruckfestigkeit f_{co} überschreiten (Teilflächenpressung). Randzugkräfte treten auch zwischen den Pressenschuhen und den Tübbingrändern (bei den Längsfugen) auf; diese sind aber aufgrund des freien Randes und der damit einherge-

henden Verformungsmöglichkeit wesentlich geringer. Zusätzlich können durch Versätze in der Tübbinganordnung ausgeprägte unplanmässige Beanspruchungen auftreten, wobei vor allem die Zugkräfte relevant sind, da sie Risse verursachen und die Rissbreiten massgeblich beeinflussen.
Die Beanspruchung der Tübbinge wird in den folgenden Unterkapiteln untersucht. Die realistische, gemeinsame Betrachtung der Beanspruchungen (i)-(iii) würde dreidimensionale Analysen unter Berücksichtigung der Rissentwicklung erfordern. Darauf wird im Rahmen des vorliegenden Projekts verzichtet, da einerseits keine geeigneten Programme für mechanisch konsistente nichtlineare dreidimensionale Analysen existieren und andererseits nichtlineare dreidimensionale Finite-Elemente-Analysen mit kommerzieller Software selbst mit sehr grossem Aufwand – der den Rahmen des Projekts übersteigt – kaum aussagekräftigere Resultate liefern würden. Stattdessen werden in Kapitel 3.6.1 die lokale dreidimensionale Krafteinleitung und in Kapitel 3.6.2 die Scheibenbeanspruchung in Tübbingebene durch die Spreizzugkräfte (ii) sowie die Randzugkräfte (iii) gesondert betrachtet. Die Tübbingkrümmung wird dabei vernachlässigt, und es wird angenommen, dass die Lagerung auf der pressenabgewandten Ringfuge die gleichen Abmessungen und Positionen aufweist wie die Pressenschuhe.

3.6.1 Krafteinleitung

Zur Gewährleistung der lokalen Einleitung der Pressenkräfte können grundsätzlich die Abmessungen der Pressenschuhe so gewählt werden, dass die einachsige Betondruckfestigkeit f_{c0} nicht überschritten wird. Wird die Krafteinleitung hingegen als Teilflächenpressung behandelt, sind kleinere Pressenschuhe möglich. Dabei wird die höhere dreiachsige Betondruckfestigkeit infolge der Lastausbreitung (geometrische Umschnürung) berücksichtigt, wobei aufgrund der eingeschränkten Lastausbreitungsmöglichkeit in Dickenrichtung nur eine moderate Festigkeitssteigerung möglich ist. Höhere Druckfestigkeiten wären zwar durch die Anordnung einer Umschnürungsbewehrung in Dickenrichtung theoretisch möglich, jedoch wäre dies sehr aufwändig für eine Belastung, die nur im Bauzustand auftritt.
Zur Berücksichtigung der dreidimensionalen Lastausbreitung kann die Quadratwurzelformel verwendet werden, wobei die Lastausbreitungsfläche nach SIA 262:2025 [4] bzw. EN 1992-1-1:2023 [5] ermittelt wird. Dieser Ansatz berücksichtigt die begrenzte Lastausbreitung in Dickenrichtung – und somit die limitierte geometrische Umschnürung – durch eine gleichermassen reduzierte Lastausbreitung in Tunnelumfangsrichtung, auch wenn die Modellierungen in Kapitel 3.6.2 zeigen, dass die Lastausbreitung in dieser Richtung effektiv ausgeprägter ist. Zusätzlich ist eine Bewehrung zur Aufnahme der Spaltzugkräfte in beide Lastausbreitungsrichtungen anzuordnen. Dies ist insbesondere für die Dickenrichtung relevant, da Tübbinge ansonsten üblicherweise nicht verbügelt werden. Weiter ist anzumerken, dass die Krafteinleitung auch auf der den Pressen gegenüberliegenden Tübbingseite gewährleistet werden muss, so dass dort gegebenenfalls auch eine Bewehrung vorzusehen ist.

3.6.2 Scheibenbeanspruchung

Wird die Krafteinleitung durch die Pressenschuhe vereinfacht als gleichmässig über die gesamte Tübbingdicke und Breite der Pressenschuhe verteilte Belastung berücksichtigt, kann die Beanspruchung mit einer zweidimensionalen Berechnung untersucht werden, in welcher der Tübbing als Scheibe modelliert wird. Mit einer solchen

Scheibenberechnung können insbesondere die Spaltzugkräfte (ii) in Tübbingebene und die Randzugkräfte (iii) ermittelt werden.
Da die Spaltzugkräfte primär und die Randzugkräfte ausschliesslich aus der Verträglichkeit resultieren, hängt ihre Grösse stark von der Steifigkeit des Tübbings ab, welche wiederum massgeblich durch die Rissbildung beeinflusst wird. Für die Ermittlung der Beanspruchungen werden trotzdem häufig ungerissen linear elastische Finite-Elemente-Analysen oder daraus abgeleitete Tafelwerke (z.B. [15]) verwendet, die den Einfluss der Rissbildung auf die Steifigkeit nicht berücksichtigen. Die Bewehrung wird anschliessend so gewählt, dass die auftretenden Betonzugspannungen abgedeckt werden. Aus einer solchen Bemessung resultieren aufgrund der Vernachlässigung der Rissbildung mutmasslich unrealistische Beanspruchungen, und Aussagen über die Rissbreiten sind nur indirekt möglich.
Eine realistischere Ermittlung der Beanspruchungen, inklusive Rissbreiten, ist mit einer Scheibenberechnung möglich, welche die Rissbildung explizit berücksichtigt. Dafür eignet sich insbesondere die Compatible Stress Field Method (CSFM), die an der ETH Zürich entwickelt wurde [22]. Dabei wird eine spezifisch für Stahlbetontragwerke entwickelte nichtlineare Finite-Elemente-Analyse durchgeführt, die ausschliesslich Standard-Materialparameter verwendet und die Zugfestigkeit des Betons – mit Ausnahme der Zugversteifung, die mechanisch konsistent auf Basis des Zuggurtmodells [24] berücksichtigt wird – vernachlässigt. Somit können CSFM-Analysen mit verhältnismässig bescheidenem Aufwand durchgeführt werden und liefern normkomforme, nachvollziehbare Ergebnisse. Anzumerken ist, dass im Unterschied zu einer ungerissenen linear elastischen Berechnung die Bewehrung vor der CSFM-Analyse bestimmt werden muss.
Zur Illustration wird an einem praxisnahen Beispiel der Unterschied zwischen einer ungerissenen linear elastischen und einer nichtlinearen Modellierung mittels CSFM unter Berücksichtigung der Rissbildung aufgezeigt. Der für die Beispielberechnung untersuchte Tübbing besitzt folgende Eigenschaften:

- Abwicklung: 3.6·1.8 m²
- Dicke: 27 cm
- Beton: C55/67
- Bewehrung: B500B
- Anzahl Pressenschuhe: 2
- Länge Pressenschuhe: 900 mm
- Randabstand Pressenschuhe: 450 mm
- Pressenkräfte:
  - Regelvortrieb: 3.7 MN pro Pressenschuh (Doppelpresse)
  - Sondervortrieb: 4.6 MN pro Pressenschuh (Doppelpresse)
    NB: Für die Pressenkräfte wird kein zusätzlicher Lastfaktor in der Bemessung berücksichtigt.

Für den Vergleich der beiden Modellierungsvarianten wurde der Tübbing in einem ersten Schritt ungerissen linear elastisch bemessen (Software: Cedrus-9, Release 251, Firma Cubus AG). Anschliessend wurde mit der ermittelten Bewehrung eine nichtlineare Analyse (Software: IDEA StatiCa Detail, Version 25.0.4.1234, Firma IDEA StatiCa, basierend auf CSFM [23]) durchgeführt. Die detaillierten Berechnungen sind in Anhang B und C zu finden.
Die Bewehrung wurde für den massgebenden Lastfall aus Regelvortrieb und Sondervortrieb nach der DAUB:2024-Richtlinie [9] ermittelt, wobei für die Belastung des Re-

gelvortriebs die materialseitigen Teilsicherheitsbeiwerte berücksichtigt, beim Sondervortrieb hingegen vernachlässigt wurden. Trotzdem wurde in diesem Beispiel der Sondervortrieb für die ungerissene linear elastische Modellierung massgebend. Als Mindestbewehrung wurde eine Netzbewehrung mit 2xØ10@150 nach der DAUB:2024-Richtlinie berücksichtigt, so dass nur entlang der Ringfugenränder jeweils Zulagen 2x2Ø10 benötigt wurden (siehe Anhang B).
In der nichtlinearen Analyse wurde der Gebrauchstauglichkeitsnachweis (GZG: Rissbreiten < 0.15...0.30 mm, je nach Norm und Randbedingung) mit der Regelvortriebsbelastung geführt, während für den Nachweis der Tragsicherheit (GZT: Bewehrungsspannungen ≤ 500 MPa) die Beanspruchung unter Sondervortriebslast berücksichtigt wurde. Die vorhandene Bewehrung wurde mit voller Verankerung modelliert, und zeitliche Effekte wurden vernachlässigt. Durch die Idealisierung der Pressenschuhabmessungen (ganze Tübbingdicke) kann die Druckbelastung bei der Lasteinleitung mit diesem Vorgehen nicht untersucht werden.

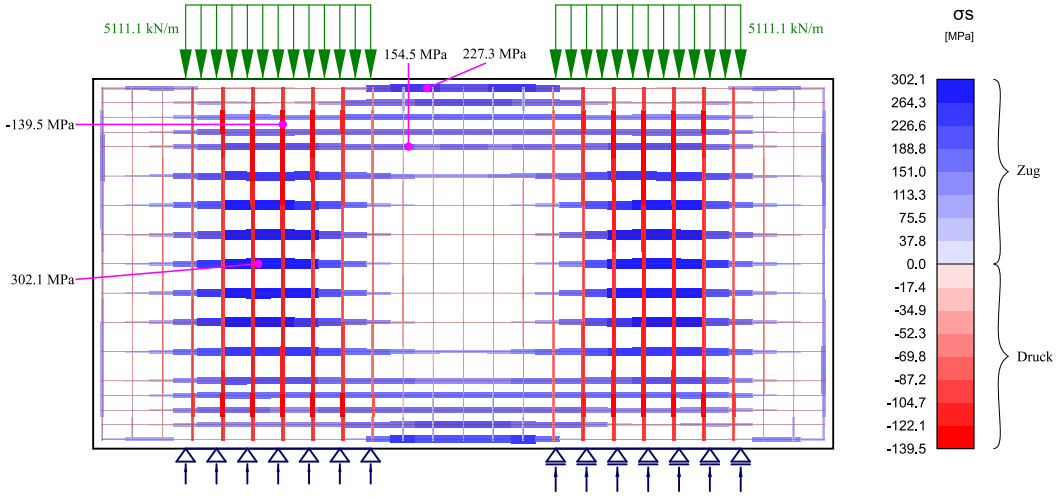

Abbildung 21: Bewehrungsspannungen ermittelt mit Idea StatiCa Detail im Grenzzustand der Tragsicherheit (GZT).

Aus der nichtlinearen Analyse konnten folgende Erkenntnisse gezogen werden:

- Durch die Berücksichtigung der Risse und der damit einhergehenden ausgeprägten Steifigkeitsänderungen trat eine andere Beanspruchung auf als nach der ungerissenen linear elastischen Modellierung. Im untersuchten Beispiel mit den gemäss der linear elastischen Bemessung notwendigen Zulagen entlang der Ringfugenränder wurden nicht die Randzugkräfte massgebend, sondern die Spreizzugkräfte in der Tübbingmitte (siehe Bewehrungsspannungen in Abbildung 21). Dies galt sowohl für den GZT als auch für den GZG. Dies verdeutlicht den Einfluss der Rissentwicklung, der sich günstig auswirkte, indem die Ränder durch die Rissbildung entlastet wurden. Dies unterstreicht, dass auch die Spreizzugkräfte in der Bemessung zu berücksichtigen sind;
- Für den GZT waren die mittels CSFM ermittelten Bewehrungsspannungen wesentlich tiefer als nach der ungerissenen linear elastischen Analyse erwartet. Die Bewehrung besass dadurch wesentliche Tragsicherheitsreserven (σ_{max} = 302.1 MPa << 500 MPa, siehe Abbildung 21). Durch die Rissbildung wurde die Randzugkraft von mehreren Bewehrungseisen aufgenommen, was den für die linear elastische Bemessung gewählten Ansatz (die aus den integrierten Zugspannungen resultierende Zugkraft wird gleichmässig auf die in der Zugzone liegende Bewehrung auf-

geteilt, auch wenn die Zugspannungen einen ausgeprägten Gradienten aufweisen, siehe Anhang B) bestätigt;
- Die im GZG auftretende maximale Spannung (243.5 MPa) lag deutlich im elastischen Bereich, so dass auch die maximalen Rissbreiten von w_{max} = 0.12 mm (siehe Abbildung 22) im vorliegenden Beispiel nicht massgebend wurden ($w_{max} \leq$ 0.15…0.30 mm).

Würde nur die Mindestbewehrung ohne Zulagen in der nichtlinearen Berechnung berücksichtigt, resultierte die massgebende Stelle weiter in Tübbingmitte, die Nachweise wären jedoch weiterhin erfüllt. Bei einer Optimierung ist zu beachten, dass bei der nichtlinearen Modellierung die Tübbingdicke bei gleichbleibender Bewehrung den Kraftfluss beeinflusst, da die unterschiedlichen Steifigkeitsverhältnisse eine Rolle spielen.

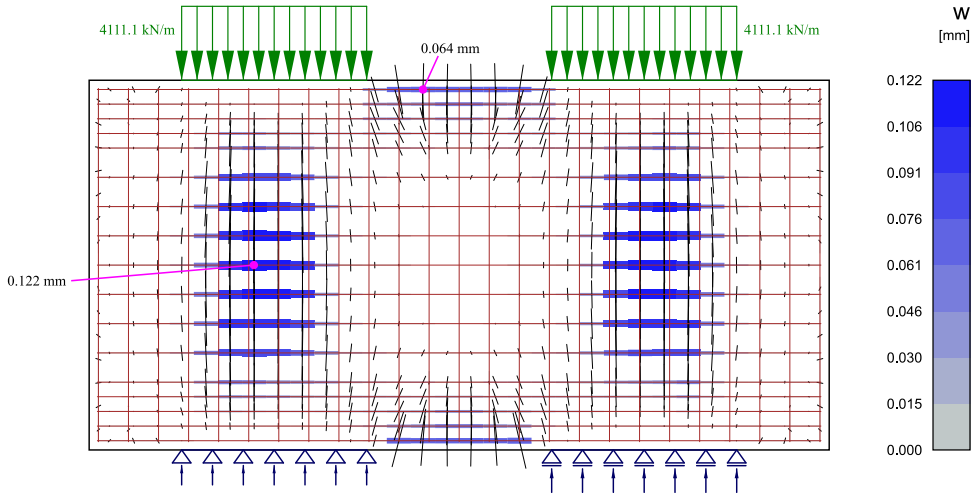

Abbildung 22: Rissbreiten ermittelt mit Idea StatiCa Detail im Grenzzustand der Gebrauchstauglichkeit (GZG).

3.6.3 Versätze

Beim Einbau der Tübbinge können kleine Versätze zwischen den Tübbingen unterschiedlicher Ringe auftreten, so dass die Lagerungsbedingungen (insbesondere auf der den Pressen gegenüberliegenden Seite des zuletzt eingebauten Tübbingrings) stark von der planmässigen Lage abweichen können. Durch die in der Praxis übliche Kraftsteuerung (Pressen parallel in einem Hydraulikkreis, somit abgesehen von Reibungsunterschieden gleiche Kräfte) sind die Pressenkräfte von den Versätzen nicht betroffen, aber je nach Ausmass der Versätze und der Anordnung der Pressen können grosse zusätzliche Randzugkräfte und damit verbundene Risse auftreten. Bei grösseren Versätzen können die Tübbinge zudem nicht mehr einzeln betrachtet werden (wie in den vorherigen Untersuchungen), da grössere Verformungen durch Rissbildung und Starrkörperrotationen auftreten, wodurch die betroffenen Tübbinge mit den umliegenden Ausbauten auch in den Längsfugen interagieren.

Eine realistische Modellierung dieses komplexen Verhaltens müsste somit nicht nur Versätze verschiedener Grösse, sondern auch Änderungen des statischen Systems inklusive der Interaktion zwischen den Tübbingen sowie die Rissentwicklung berücksichtigen. Dies wäre äusserst aufwändig und aufgrund der zahlreichen unbekannten Parameter mit beträchtlicher Unsicherheit verbunden, insbesondere hinsichtlich der Aussagekraft der Resultate. Aus diesem Grund wird in diesem Bericht die Modellie-

rung von Versätzen nicht weiter untersucht, und es werden auch keine Vorschläge zur Berücksichtigung allfälliger Ansätze unterbreitet.
Als pragmatische Alternative bietet sich an, die durch Versätze verursachten Rissbreiten auf Basis geometrischer Betrachtungen abzuschätzen und, darauf basierend, Grenzwerte für die beim Einbau zulässigen Abweichungen von der planmässigen Lage zu definieren. Bei diesem von Behnen et al. [15] vorgeschlagen Vorgehen ist die Anzahl Risse im massgebenden Bereich ein entscheidender Parameter, da die durch den Versatz verursachte Verformung durch die Summe der entsprechenden Rissöffnungen aufgenommen werden muss. Das Verhalten kann somit durch die Anordnung eines höheren Bewehrungsgehalts entlang der Tübbingränder verbessert werden: Dies führt gemäss Zuggurtmodell [24] zu einem kleineren Rissabstand und bewirkt somit eine grössere Anzahl an Rissen und letztlich kleinere Rissbreiten. Selbst mit kräftiger Bewehrung kann die Rissbildung jedoch nicht verhindert werden.
Es ist somit empfehlenswert, die Randbereiche der Tübbinge in einem wirtschaftlichen Masse verstärkt zu bewehren. Um unzulässig grosse Rissbreiten infolge von Versätzen zu vermeiden muss beim Einbau trotzdem darauf geachtet werden, dass Versätze begrenzt bleiben, resp. beim Überschreiten eines zulässigen Werts geeignete Massnahmen getroffen werden. Allerdings sind solche Risse in der Regel nicht tragsicherheitsrelevant und können im Bauzustand saniert werden. Die Rissbreiten im Bauzustand infolge von Vortriebskräften müssen somit nicht unter allen Umständen limitiert werden.

3.6.4 Bemessungsvorschlag

Als Bemessungsvorschlag für die Ringfugen wird empfohlen, die Teilflächenpressung und die Scheibenbeanspruchung entsprechend den in den vorherigen Kapiteln beschriebenen Vereinfachungen getrennt zu untersuchen.
Für die Bemessung wird folgender Ablauf vorgeschlagen:

1. Untersuchung der Krafteinleitung unter Berücksichtigung der Teilflächenpressung mit der Quadratwurzel-Formel;
2. Analyse der Scheibenbeanspruchung mithilfe eines ungerissenen linear elastischen Modells und Festlegung der erforderlichen Bewehrung, um die ermittelten Zugspannungen (gemittelt über die Zugzone) abzudecken;
3. Überprüfung der Ergebnisse der ungerissenen linear elastischen Modellierung durch eine nichtlineare Berechnung sowie allfällige Korrektur, wobei eine konservative Randbewehrung beibehalten werden sollte, da sie sich positiv auf mögliche Versätze beim Tübbingausbau auswirkt;
4. Festlegung der erforderlichen Baugenauigkeit basierend auf geometrischen Überlegungen, um Versätze zu begrenzen.

4 Zusammenfassung und Schlussfolgerungen

4.1 Zusammenfassung

In diesem Bericht wurden das Tragverhalten und die Bemessung von Tübbingfugen untersucht. Der Fokus lag dabei auf Längsfugen, die vorwiegend mit grosser Normalkraft belastet werden. Ergänzend wurden auch die Ringfugen betrachtet.
Für die Längsfugen wurde der Einfluss einer Umschnürungsbewehrung detailliert untersucht. Umschnürungsbewehrung kann zur Erhöhung des Tragwiderstands der Tübbinge beitragen, wodurch schlankere Tunnelausbauten möglich werden. In den meisten Fällen ist die Anordnung einer Umschnürungsbewehrung nur in der Zone direkt bei der Längsfuge sinnvoll. Dadurch kann der Tübbing in eine umschnürte und eine nicht umschnürte Zone eingeteilt werden, wobei der kleinere Tragwiderstand der beiden Zonen denjenigen des Tübbings bestimmt. Bei der Modellierung der umschnürten Zone sind sowohl der günstige Einfluss der Lastausbreitung (resultierend aus der im Vergleich zur Tübbingbreite reduzierten Fugenbreite) als auch der Umschnürungsbewehrung zu berücksichtigen. Dazu können die beiden im Rahmen der Arbeit entwickelten, mechanisch konsistenten Spannungsfelder (Multi-Wedge und Dual-Wedge Spannungsfeld) verwendet werden; damit können die Effekte der Lastausbreitung und der Umschnürungsbewehrung konform mit den aktuellen Normen (SIA 262:2025 [4] oder EC2:2023 [5]) überlagert werden. Zur Berücksichtigung der Umschnürungswirkung werden als Eingabeparameter der Spannungsfelder sowohl die Umschnürungsspannung als auch die umschnürte Breite benötigt. Diese können mit dem ebenfalls entwickelten Umschnürungsmodell und dessen Vereinfachung einfach und mechanisch begründet ermittelt werden. Die Modellierungsansätze wurden mit Versuchen an streifenbelasteten Betonblöcken mit über die gesamte Höhe angeordneter Umschnürungsbewehrung erfolgreich validiert („Blockversuche“). Weitere experimentelle Untersuchungen wurden an Versuchen aus zwei Betonblöcken mit einer Fuge als Kontaktfläche durchgeführt („Fugenversuche“). Dabei wurde die Umschnürungsbewehrung vorwiegend im Bereich direkt bei der Fuge angeordnet, während der restliche Bereich keine Umschnürung enthielt. Die Versuchsresultate zeigten, dass sowohl die umschnürte als auch die nicht umschnürte Zone massgebend werden kann, wobei hohe Normalkräfte – resultierend durch hohe Umschnürungsgehalte oder breite Fugen – zum Versagen der nicht umschnürten Zone führen. Weiter zeigte sich, dass sich Abplatzungen des Überdeckungsbetons von der umschnürten in die nicht umschnürte Zone fortsetzten und so die anrechenbare Betonquerschnittsfläche in der nicht umschnürten Zone begrenzten. Es wird daher vorgeschlagen, dass für die nicht umschnürte Zone nur die Betonfläche innerhalb der Bewehrung mit ihrer einachsigen Betondruckfestigkeit berücksichtigt werden soll. Weiter wurde das Multi-Wedge Spannungsfeld für die umschnürte Zone entwickelt, welches das einzige existierende Modell ist, das den gesamten Lastpfad und den Übergang zur nicht umschnürten Zone berücksichtigen kann. Das Spannungsfeld und der Modellierungsansatz der nicht umschnürten Zone wurden erfolgreich mit den Fugenversuchen validiert. Zusätzlich wurde das

Multi-Wedge Spannungsfeld weiterentwickelt, um den Einfluss eines Führungsstabs innerhalb der Fuge zu berücksichtigen. Eine Erhöhung des Tragwiderstands bei gleichbleibender Tübbingdicke ist mit zusätzlicher Umschnürungsbewehrung möglich, solange die nicht umschnürte Zone nicht massgebend wird. Mit grösser werdender Breite der Fuge reduziert sich der aktivierbare Umschnürungsgehalt und somit der Einfluss der Umschnürungsbewehrung. Bei der Nachrechnung der Fugenversuche zeigt sich, dass die Modellierung mit den Spannungsfeldern – im Vergleich zum Modellierungsansatz in der DAUB:2024-Richtlinie [9], der nur die Lastausbreitung berücksichtigt – eine um maximal 22% höhere Vorhersage des Tragwiderstands ermöglicht. Diese Aussage kann nicht pauschal auf jegliche Tübbinglängsfugen übertragen werden. Das Optimierungspotenzial einer Umschnürungsbewehrung kann projektspezifisch mit den in diesem Projekt entwickelten Spannungsfeldern, welche im Gegensatz zum empirischen Modellierungsansatz in der DAUB:2024-Richtlinie mechanisch fundiert sind, ermittelt werden. Speziell für kürzere Abschnitte mit erhöhter Belastung in einem Tunnel kann es sich lohnen, die gesamten Tübbinge zu umschnüren, um einen nochmals deutlich höheren Widerstand zu erreichen und damit eine schmale Dicke der Tübbinge über die gesamte Tunnellänge beizubehalten. Des Weiteren haben die experimentellen Untersuchungen gezeigt, dass geschweisste Leiterbewehrung in der Lage ist, als Umschnürungsbewehrung aktiviert zu werden, mit mindestens gleichwertiger Effizienz wie konventionelle Bügel- oder Dübelbewehrung.

Faserbewehrter Beton zeigte in Kombination mit konventioneller Stabbewehrung im Vergleich zu konventionellem Beton eine Erhöhung des Tragwiderstands und eine günstigere Rissentwicklung. Dies trat vor allem auf die Kombination mit moderater Stabbewehrung zu. Die Modellierung von faserbewehrten Tübbingen kann analog mit den Spannungsfeldern erfolgen, wobei die Umschnürungsspannungen aus der linearen Superposition der Umschnürungsspannung der Stabbewehrung mit der residualen Zugfestigkeit des faserbewehrten Betons ermittelt werden kann. Dieser Ansatz wurde erfolgreich mit den Block- und Fugenversuchen validiert. Rein faserbewehrte Tübbinge zeigten andererseits ein ungünstiges sprödes Bruchverhalten, was weitere Untersuchungen bedingt, bevor Anwendungen in der Praxis empfohlen werden können.

Zusammenfassend zeigten die Untersuchungen der Längsfugen, dass Umschnürungsbewehrung zur Erhöhung des Tragwiderstands von Tübbinglängsfugen beitragen kann. Die entwickelten Modelle ermöglichen zudem, dies in der Bemessung konform nach aktuellen Normen zu berücksichtigen.

Die Untersuchungen zu den Ringfugen zeigten auf, dass für die Einleitung der Pressenkräfte aufgrund der Rissentwicklung beträchtliche Unterschiede zwischen einer ungerissenen linear elastischen und der nichtlinearen Bemessung bestehen. Aufgrund der zusätzlichen Unsicherheit bezüglich Versätzen empfiehlt es sich, beide Analysen durchzuführen und die Bewehrung auf die in beiden Analysen auftretenden massgebenden Beanspruchungen festzulegen, wobei nur die nichtlineare Analyse überhaupt Aussagen zu den unter planmässiger Belastung durch die Vortriebspressen auftretenden Rissbreiten ermöglicht. Die erwarteten Rissbreiten aufgrund von Versätzen können mit bereits bestehenden geometrischen Überlegungen abgeschätzt werden, wobei in der Ausführung auf die Genauigkeit des Einbaus zu achten ist, da mit der Bewehrung zwar die Rissbreiten begrenzt, nicht aber die Rissbildung verhindert werden kann.

4.2 Empfehlungen

Für die Bemessung der Längsfugen von Tübbingen mit grosser Normalkrafteinwirkung ist der Tragwiderstand der umschnürten Zone und, falls vorhanden, der Widerstand der nicht umschnürten Zone zu ermitteln. Für die umschnürte Zone können als erste Abschätzung – zum Beispiel in der Vorbemessung – mit der Vereinfachung des Dual-Wedge Spannungsfelds unter Berücksichtigung der Standard Sicherheitsfaktoren für die Bewehrung (γ_s) und Beton (γ_c) (i) der Tragwiderstand für eine gegebene transversale Umschnürungsbewehrung abgeschätzt und (ii) die erforderliche longitudinale Bewehrung sowie die Höhe der umschnürten Zone festgelegt werden. Die Umschnürungsparameter (Umschnürungsspannung und umschnürte Fläche) können nach dem Umschnürungsmodell und dessen Vereinfachung bestimmt werden.
Zur besseren Übersicht sind die notwendigen Formeln für die Bemessung mit konventionellem Beton hier nochmals zusammengestellt:

$$q_{x,u,\mathrm{conf}} = \frac{\sigma_{x0,\mathrm{DW-s}} \cdot b_{ccz} + f_{c0} \cdot (b_{lz} - b_{ccz})}{b_{lz}} \tag{14}$$

mit

$$b_{ccz} = b_{csz} - \frac{\sqrt{s_x^2 + s_y^2}}{2} \tag{15}$$

$$\sigma_{x0,\mathrm{DW-s}} = \left(\frac{d_2}{d_1}\right)^{\frac{2}{5}} \cdot \left(f_{c0} + 4 \cdot \sigma_{confy}\right) \leq \frac{5}{2} \cdot \left(f_{c0} + 4 \cdot \sigma_{confy}\right) \tag{16}$$

$$d_1 = b_{ly} \tag{17}$$

$$d_2 = b_{ccy} = b_{csy} - 2 \cdot e_y - \frac{\sqrt{s_x^2 + s_z^2}}{2} \tag{18}$$

$$\sigma_{confy} = \sigma_{confy,mod} = \frac{A_{s,confy} \cdot f_{sy,conf}}{s_x \cdot s_z} \tag{19}$$

$$\sigma_{confz,req,\mathrm{DW-s}} = \frac{d_1}{\left(b_{csy} - 2 \cdot e_y\right)} \cdot \left(1.75 - 0.75 \cdot \frac{d_1}{d_2}\right) \cdot \sigma_{confy} \tag{20}$$

$$x_E = d_1 + d_2 \leq 1.5 \cdot d_2 \tag{21}$$

In einer späteren Projektphase können mit dem Multi-Wedge Spannungsfeld der effektive Tragwiderstand, die erforderliche Längsbewehrung und die Bewehrungsanordnung normkonform nach SIA 262:2025 und EC2:2025 unter Berücksichtigung der Standard Sicherheitsfaktoren für die Bewehrung (γ_s) und Beton (γ_c) bestimmt werden. Auf der Webseite der Professur (https://concrete.ethz.ch/applikationen) ist eine Applikation zur Anwendung des Multi-Wedge Spannungsfeldes geplant, wodurch die Anwendung vereinfacht werden sollte.
Für die nicht umschnürte Zone kann der Tragwiderstand bezogen auf die Längsfuge unter Berücksichtigung der einachsigen Betondruckfestigkeit (f_{c0}) innerhalb der Bewehrung ermittelt werden:

$$q_{x,u,unconf} = \frac{f_{c0} \cdot b_{csy} \cdot b_{csz}}{\left(b_{ly} - b_{rod}\right) \cdot b_{lz}} \tag{22}$$

Der Tragwiderstand der Tübbinglängsfuge (resp. des Tübbings) entspricht dem kleineren Widerstand der umschnürten resp. nicht umschnürten Zone:

$$q_{x,u} = min\left(q_{x,u,conf}, q_{x,u,unconf}\right) \tag{23}$$

Diese Empfehlungen beziehen sich auf die Ermittlung der Traglast der Längsfuge. Die Gebrauchstauglichkeit ist gesondert nachzuweisen. Dabei ist, basierend auf den experimentellen Untersuchungen in diesem Projekt, nur bei hohen Umschnürungsgehalten oder hochfestem Beton zu erwarten, dass der Gebrauchszustand massgebend werden kann. Empfehlungen für den Gebrauchszustand sind jedoch nicht Teil dieses Projekts.

Die Bemessungsempfehlung für die Ringfugen sind in Kapitel 3.6.4 aufgeführt.

4.3 Forschungsbedarf

Einige für die Tübbingbemessung relevante Punkte bedingen weitere Forschung. Für die Längsfugen wurden folgende offene Punkte identifiziert:

- In aktuellen Normen wird der Bemessungswert der Betondruckfestigkeit (f_{cd}) unter anderem als Funktion des sogenannten Sprödigkeitsfaktors η_{cc} ermittelt, z.B. $\eta_{cc} = (30/f_{ck})^{(1/3)} \leq 1$ nach SIA 262:2013 [16]. Für typische charakteristische Betondruckfestigkeiten im Tübbingbau von 50…60 MPa bewirkt der Sprödigkeitsfaktor somit bereits eine Reduktion der Betondruckfestigkeit von 15…20%. Die in diesem Projekt durchgeführten Versuche wurden ohne Berücksichtigung von η_{cc} in der überwiegenden Mehrheit der Fälle auf der sicheren Seite liegend nachgerechnet. Lediglich bei effektiv hochfesten Versuchen traten unkonservative Vorhersagen auf, die die Existenz des Sprödigkeitsfaktors rechtfertigen. Dies deutet darauf hin, dass der momentan verwendete Sprödigkeitsfaktor zumindest für die Streifenbelastung von umschnürtem und nicht umschnürtem Beton konservativ ist. Weitere Forschung die eine Reduktion des Faktors bei moderat erhöhtem Druckfestigkeiten bewirkte, hätte somit einen erheblichen Einfluss auf die Bemessung druckbelasteter Betonbauten, wie z.B. Tübbingfugen. Dazu wären zusätzliche Versuche mit Streifenbelastung und unterschiedlichen Betondruckfestigkeiten notwendig.
- Die Interaktion der einzelnen Stäbe einer geschweissten Leiterbewehrung ist nicht vollends geklärt, weshalb keine Bemessungsvorschläge dazu erarbeitet wurden. Weitere Versuche mit geschweisster Leiterbewehrung, die mit faseroptischen Sensoren ausgestattet ist, würde die Datengrundlage vergrössern, so dass Bemessungsgrundlagen erstellt werden könnten.
- Die Gebrauchstauglichkeit bezüglich Rissbreiten und Fugenschliessung wurde nur experimentell untersucht. Ein einfaches Bemessungsmodell für die Rissbreitenabschätzung (analytisch oder empirisch), das sowohl die Betonzugfestigkeit und dessen Streuung, die Dicke des Überdeckungsbetons und den Einfluss des Bewehrungsgehalts berücksichtigt, wäre für die Praxis sehr nützlich. Die Fugenschliessung könnte analytisch mittels Berücksichtigung der Spannungs-Dehnungsbeziehung von umschnürtem Beton und der Annahme linearere Lastausbreitung über die Höhe der umschnürten Zone abgeschätzt werden.

- Langzeiteffekte wie Kriechen und Relaxation wurden nicht detailliert untersucht. Es stellt sich die Frage, ob diese Effekte für umschnürte Tübbinge berücksichtigt werden müssen, und wenn ja, in welcher Form.
- Der Einfluss eines Führungsstabes wurde mittels eines einzigen Versuches untersucht. Zur Validierung der entwickelten Modelle sind weitere Versuche notwendig.
- Die rein faserbewehrten Fugenversuche zeigten ein ungünstiges sprödes Verhalten. Dieses Verhalten und der Einfluss möglicher Grösseneffekte sind weiter zu untersuchen.

Für die Ringfugen spielt die Beanspruchung aufgrund von Versätzen eine grosse Rolle. Es stellt sich die Frage, ob dieses Problem auch durch bautechnischen Fortschritt reduziert oder behoben werden kann. Eine Möglichkeit wäre, bei den Pressen eine servohydraulische Regelung einzuführen, so dass bei Pressen mit zu grossem Weg (bei gleicher Kraft) aufgrund geringen Widerstands – ausgelöst durch einen Versatz auf der gegenüberliegenden Seite – die Vortriebskraft reduziert und auf die umliegenden Pressen verteilt würde. Dazu müssten die Tübbinge für die Einleitung der entsprechend höheren Kräfte bemessen werden, was in der Regel problemlos möglich wäre.

Literaturverzeichnis

[1] F. Morger, «Passive Confinement and Strip Loading in Longitudinal Tunnel Lining Segment Joints», Doctoral thesis, ETH Zurich, Zurich, Switzerland, 2025.

[2] H. P. Spieth, «Das Verhalten von Beton unter hoher örtlicher Pressung», *Beton- und Stahlbetonbau*, Bd. 56, Nr. 11, S. 257–263, 1961.

[3] P. Wurm und F. Daschner, «Versuche über Teilflächenbelastung von Normalbeton». DAfStb, no. 286, 1977.

[4] Schweizerischer Ingenieur- und Architektenverein, *SIA 262:2025 Betonbau*, Zürich., 2025.

[5] EN 1992-1-1:2023, «Eurocode 2 - Design of concrete structures - Part 1-1: General rules and rules for buildings, bridges and civil engineering structures», Brussels, 2023.

[6] International Federation for Structural Concrete (fib), *Model Code for Concrete Structures 2020*, 2024.

[7] E. Mörsch, «Über die Berechnung der Gelenkquader», *Beton Eisen*, Bd. 23, Nr. 12, S. 156–161, 1924.

[8] H. Kupfer, «Das Verhalten des Betons unter zweiachsiger Beanspruchung». Lehrstuhl für Massivbau, Technische Universität München, Report No. 78, 1969.

[9] German Tunnelling Committee (ITA-AITES), *Empfehlungen für den Entwurf, die Herstellung und den Einbau von Tübbingringen*. Deutscher Ausschuss für unterirdisches Bauen e. V. (DAUB), 2024.

[10] A. Considère, «Étude expérimentale de la résistance à la compression du béton fretté», in *Comptes rendus des séances de l'académie des sciences*, Paris, 1902, S. 415–419.

[11] A. Considère, «Étude théorique de la résistance à la compression du béton fretté», in *Comptes rendus des séances de l'académie des sciences*, Paris, 1902, S. 365–368.

[12] F. E. Richart, A. Brandtzaeg, und R. L. Brown, «A Study of the Failure of Concrete under Combined Compressive Stresses», University of Illinois Engineering Experimental Station, Bulletin 185, 1928.

[13] F. E. Richart, A. Brandtzaeg, und R. L. Brown, «The failure of plain and spirally reinforced concrete in compression», University of Illinois Engineering Experimental Station, 1929.

[14] T. Markić, F. Morger, und W. Kaufmann, «Partially loaded areas in reinforced concrete: Mechanical modelling», *Engineering Structures*, Bd. 271, Nov. 2022, doi: 10.1016/j.engstruct.2022.114938.

[15] G. Behnen, O. Fischer, und G. Schmidt-Thrö, «Scheibenbemessung der Pressenkraftdurchleitung bei TVM-Vortrieben», *Beton- und Stahlbetonbau*, Bd. 111, Nr. 11, S. 694–705, Nov. 2016, doi: 10.1002/best.201600045.

[16] Schweizerischer Ingenieur- und Architektenverein, *SIA 262:2013 Betonbau*, Zürich., 2013.

[17] F. Moccia, Q. Yu, M. Fernández Ruiz, und A. Muttoni, «Concrete compressive strength: From material characterization to a structural value», *Structural Concrete*, Bd. 22, Nr. S1, Jan. 2021, doi: 10.1002/suco.202000211.

[18] ISO 17660-1:2006, *Welding - Welding of reinforcing steel - Part 1: Load-bearing welded joints*, Geneva., 2006.

[19] T. Markić, F. Morger, und W. Kaufmann, «Partially loaded areas in reinforced concrete: experimental campaign and model validation», *Engineering Structures*, Bd. 273, Dez. 2022, doi: 10.1016/j.engstruct.2022.114905.

[20] C. Proksch-Weilguni, M. Decker, und J. Kollegger, «Load distribution and passive confinement in reinforced concrete: Development of a mechanical model», *Engineering Structures*, Bd. 304, S. 117562, Apr. 2024, doi: 10.1016/j.engstruct.2024.117562.

[21] EN 14651:2005, *Test method for metallic fibered concrete - Measuring the flexural tensile strength (limit of proportionality (LOP), residual)*, Brussels, Belgium., 2005.
[22] J. Mata-Falcón, D. T. Tran, W. Kaufmann, und J. Navrátil, «Computer-aided stress field analysis of discontinuity concrete regions», in *Proceedings of the Conference on Computational Modelling of Concrete and Concrete Structures*, Bad Hofgastein, Austria: CRC Press, 2018, S. 641–650. [Online]. Verfügbar unter: http://hdl.handle.net/20.500.11850/259589
[23] W. Kaufmann *u. a.*, *Compatible Stress Field Design of Structural Concrete: Principles and Validation*. Zurich; Brno: ETH Zurich, Institute of Structural Engineering (IBK); IDEA StatiCa s.r.o., 2020. [Online]. Verfügbar unter: https://www.research-collection.ethz.ch/handle/20.500.11850/411585
[24] P. Marti, M. Alvarez, W. Kaufmann, und V. Sigrist, «Tension Chord Model for Structural Concrete», *Structural Engineering International*, Bd. 8, Nr. 4, S. 287–298, Nov. 1998, doi: 10.2749/101686698780488875.

Datenverwendung

Die in diesem Projekt verwendeten Daten stammen entweder von experimentellen Untersuchungen, mechanischen Modellierungen, der Anwendung kommerzieller Software oder aus der Literatur. Die Rohdaten der Versuche (DIC-Bilder, faseroptische Messungen, Kraftmessungen) sind bei der Professur abgelegt und werden auf begründetes Ersuchen ausgehändigt. Für die mechanischen Modellierungen sind alle notwendigen Formeln entweder direkt aufgeführt oder referenziert. Die verwendete kommerzielle Software ist aufgeführt und die verwendeten Daten aus der Literatur sind referenziert und zusammenfassend aufgeführt.

Anhänge

A. ETH-Dissertation 31577: Passive Confinement and Strip Loading in Longitudinal Tunnel Lining Segment Joints

DISS. ETH NO. 31577

Passive Confinement and Strip Loading in Longitudinal Tunnel Lining Segment Joints

A thesis submitted to attain the degree of

DOCTOR OF SCIENCES

(Dr. sc. ETH Zurich)

presented by

FABIAN NICOLA MORGER

born on 08.10.1992

accepted on the recommendation of

Prof. Dr. Walter Kaufmann

Prof. Dr. Albin Kenel

Prof. em. Dr. Johann Kollegger

Prof. Dr. Peter Mark

2025

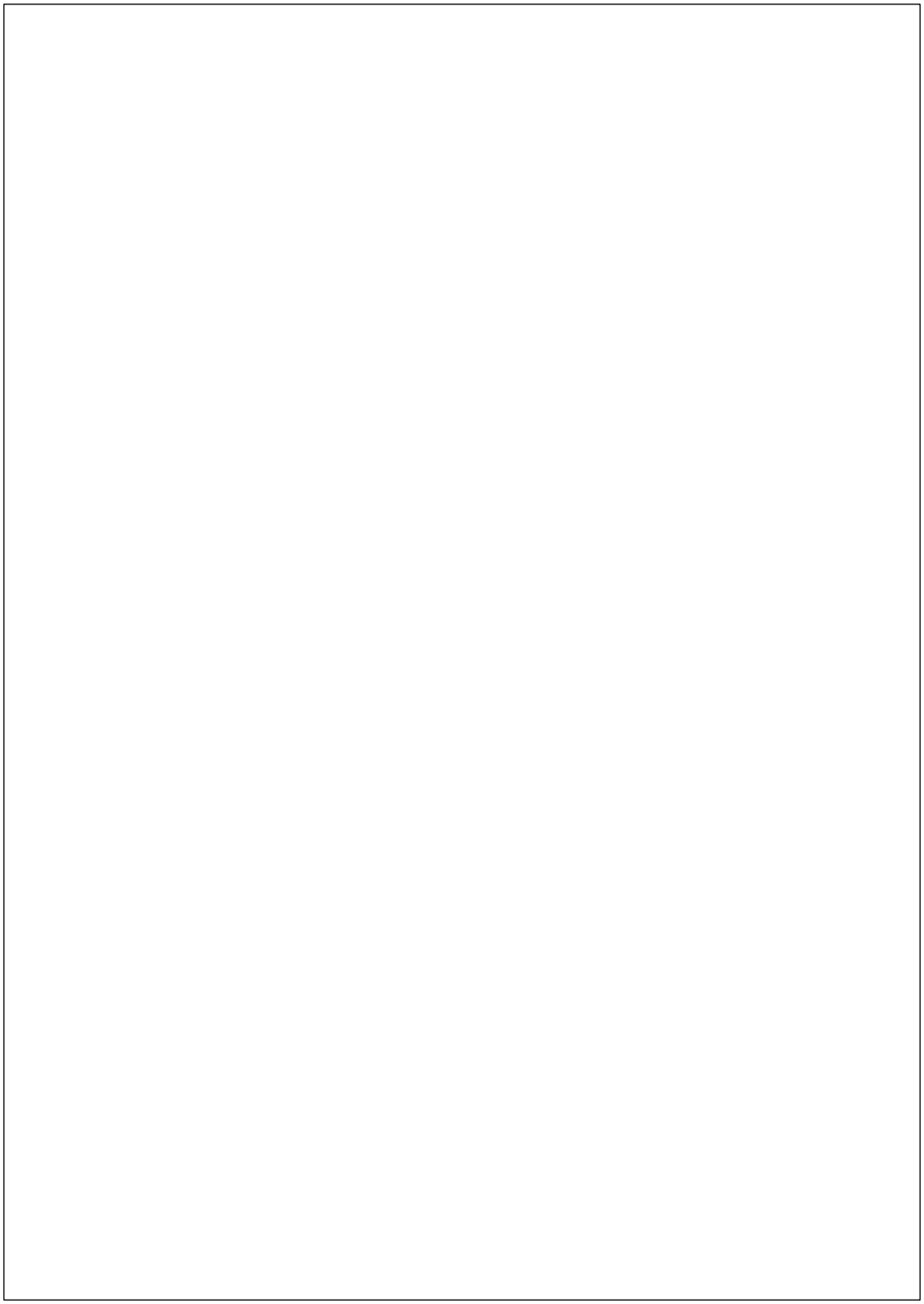

To grandma.

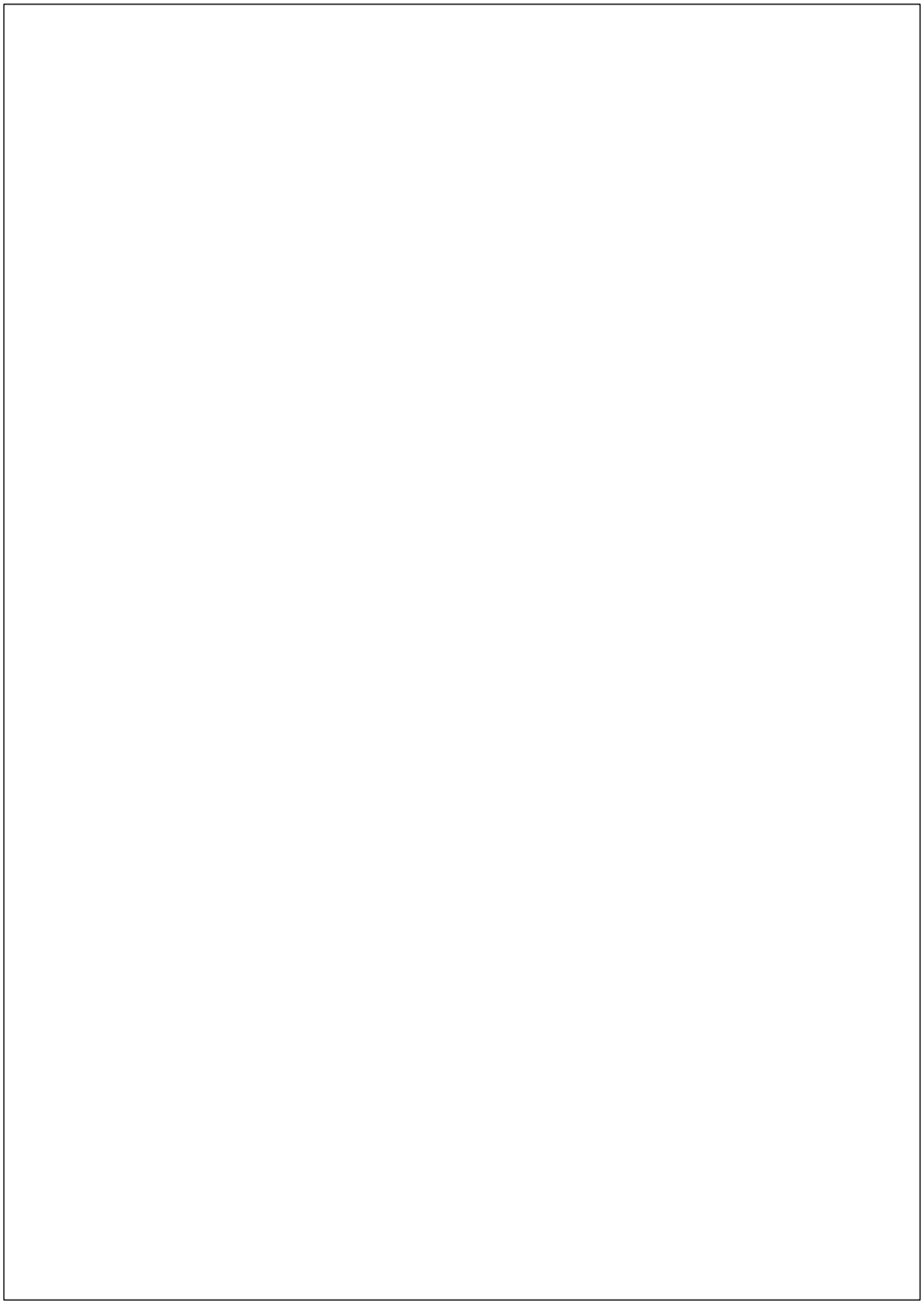

Abstract

Precast reinforced concrete segmental linings are commonly used in modern tunnelling. The longitudinal joints in these linings typically have a reduced contact cross-section, which often governs the design – particularly in tunnels under high hydrostatic pressure or crossing squeezing or swelling ground with correspondingly high circumferential compressive forces. Reinforced concrete segments with substantial confining reinforcement at the load introduction are a viable option for resisting high loads at segment joints. However, this solution has not yet been widely adopted in tunnelling practice, mainly due to limited coverage by existing standards, which is in turn caused by the lack of experimentally validated mechanical models.

The structural behaviour of longitudinal tunnel lining joints essentially corresponds to strip loading. The load-bearing capacity of strip-loaded reinforced concrete can be several times higher than the uniaxial concrete compressive strength. The strength increase can be attributed to lateral confining stresses, which result either from load dispersion (geometrical confinement) or reinforcement (passive confinement). Consequently, in order to design the longitudinal joints of segmental linings efficiently, both geometrical and passive confinement must be considered. For this purpose, this thesis fundamentally investigates the mechanical behaviour under strip loading with substantial passive confinement using theoretical and experimental analyses to ultimately propose design approaches.

The first part of this thesis reviews existing research on passive confinement in reinforced concrete, proposes a mechanical model considering the local three-dimensional load dispersion of activated confining reinforcement, and successfully validates the model. Moreover, the load-bearing behaviour of welded grid reinforcement acting as confining reinforcement is experimentally investigated using fibre optical measurements.

The second part explores the load-bearing behaviour of strip-loaded reinforced concrete through a combination of experimental and theoretical investigations. To this end, two experimental campaigns on reinforced concrete blocks and on large-scale specimens with longitudinal joints representing tunnel lining segments are presented and the results are discussed. Based on the experimental findings, mechanically sound stress field models that consider the combined effect of load dispersion and confining reinforcement are developed.

The last part further investigates the load-bearing behaviour of strip loading with steel fibre reinforced concrete with and without conventional bar reinforcement and proposes design approaches based on the stress fields.

The theoretical and the experimental investigations presented in this thesis provide relevant new insights into the load-bearing behaviour of strip-loaded reinforced concrete. The proposed models provide a solid basis for a mechanically consistent consideration of the combined effect of load dispersion and confining reinforcement in the design of longitudinal tunnel lining joints, enabling efficient tunnel lining segments.

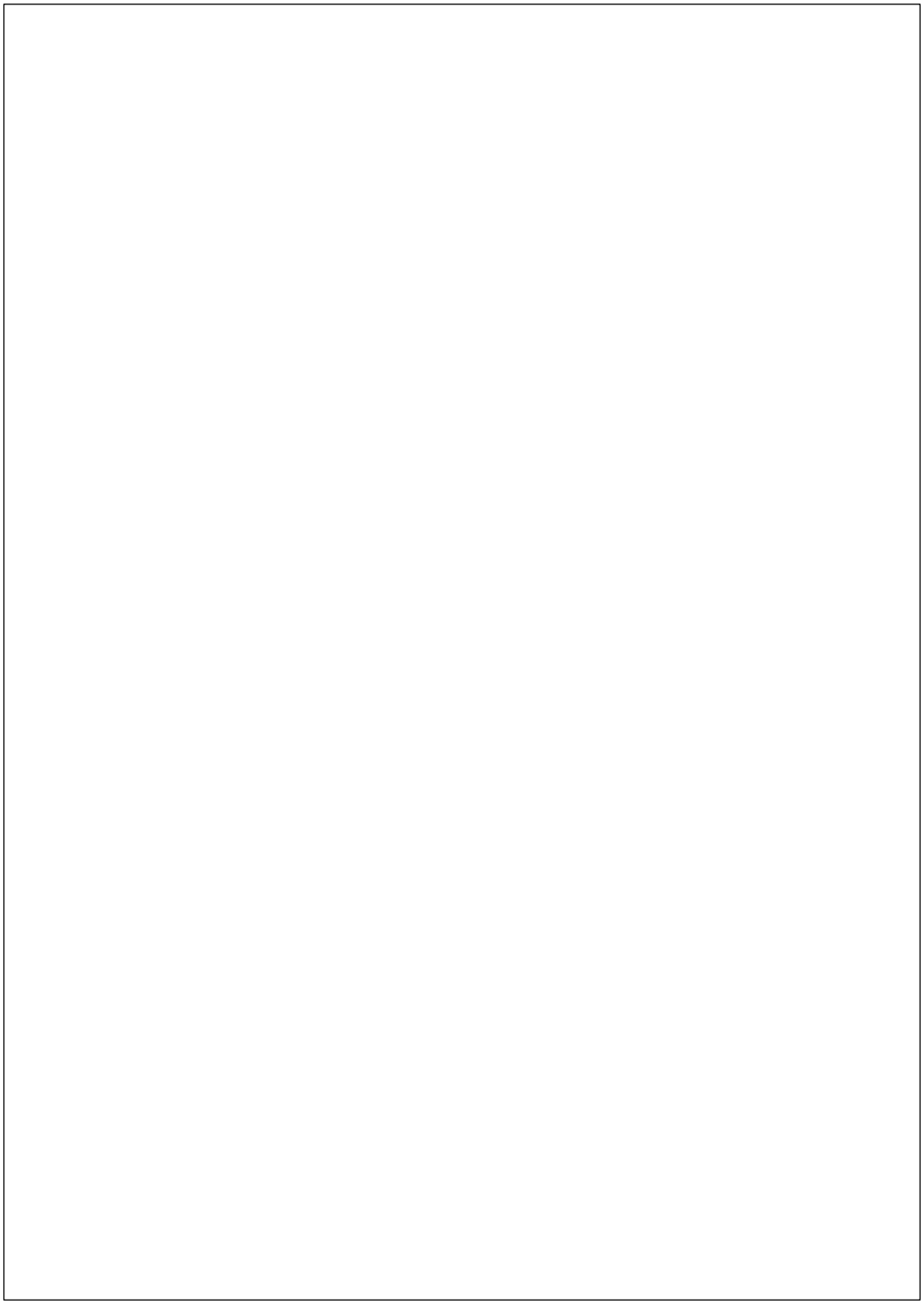

Kurzfassung

Im modernen Tunnelbau werden häufige vorfabrizierte Stahlbetontübbinge eingesetzt. Die Kontaktflächen der Längsfugen der Tübbinge sind normalerweise kleiner als der Regelquerschnitt. Dadurch werden die Längsfugen insbesondere bei Tunnels unter hohem hydrostatischem Druck oder im druckhaften oder quellenden Gebirge und den damit verbundenen hohen Ringnormalkräften massgebend für die Abmessung der Segmentdicke. Stahlbetontübbinge mit kräftiger Umschnürungsbewehrung sind eine vielversprechende Option, um hohen Beanspruchungen in den Längsfugen standzuhalten. Heute ist dieser Ansatz im Tunnelbau jedoch wenig verbreitet. Dies liegt hauptsächlich an nicht vorhandenen Normvorschriften – was auf dem Fehlen experimentell validierter mechanischer Modelle beruht.

Das Tragverhalten der Längsfugen entspricht im Wesentlichen einer Streifenbelastung, bei welcher die aufgebrachten Spannungen die einachsige Betondruckfestigkeit bekanntlich deutlich überschreiten können. Diese höhere Festigkeit ist auf laterale Umschnürungsspannungen zurückzuführen, die durch die Lastausbreitung (geometrische Umschnürung) oder Bewehrung (passive Umschnürung) hervorgerufen werden. Um Tübbinglängsfugen effizient zu bemessen, sind somit sowohl die geometrische als auch die passive Umschnürung zu berücksichtigen. In der vorliegenden Dissertation wird daher das mechanische Verhalten von Stahlbeton unter Streifenbelastung mit ausgeprägter passiver Umschnürung theoretisch und experimentell untersucht, um schliesslich Bemessungsansätze vorzuschlagen.

Der erste Teil der Arbeit gibt einen Überblick über den Wissensstand im Bereich der passiven Umschnürung und präsentiert ein mechanisches Modell für die lokale dreidimensionale Lastausbreitung aktivierter Umschnürungsbewehrung, das erfolgreich validiert wird. Zusätzlich wird das Tragverhalten geschweisster Leiterbewehrung mittels faseroptischer Messungen untersucht.

Im zweiten Teil wird das Tragverhalten von Stahlbeton unter Streifenbelastung experimentell und theoretisch untersucht. Dazu werden zwei Versuchskampagnen an Betonblöcken und Tübbingelementen mit Längsfuge präsentiert und die Resultate diskutiert. Basierend auf den experimentellen Erkenntnissen werden mechanisch konsistente Spannungsfelder entwickelt, die die kombinierte Wirkung von Lastausbreitung und Umschnürungsbewehrung berücksichtigen.

Der letzte Teil der Arbeit untersucht Streifenbelastung an stahlfaserbewehrtem Beton mit und ohne konventioneller Stabbewehrung und schlägt Bemessungsansätze auf Grundlage der Spannungsfelder vor.

Diese Arbeit liefert durch theoretische und experimentelle Untersuchungen wesentliche neue Erkenntnisse zum Tragverhalten von Stahlbeton unter Streifenbelastung. Darüber hinaus bilden die vorgeschlagenen Modelle eine solide Grundlage zur mechanisch konsistenten Berücksichtigung der kombinierten Wirkung von Lastausbreitung und Umschnürungsbewehrung bei der Bemessung von Tübbinglängsfugen, wodurch effizientere Stahlbetontübbinge möglich werden.

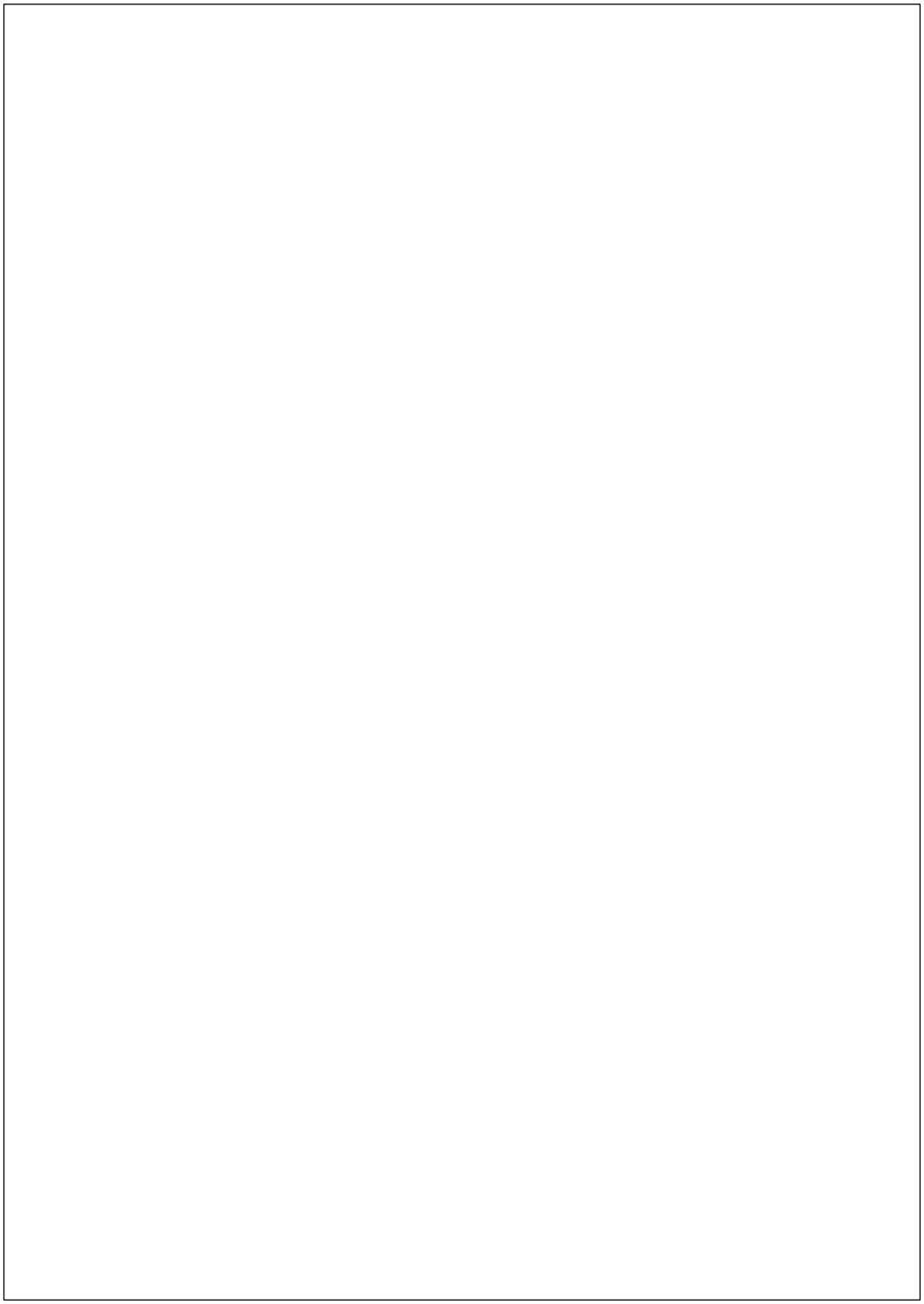

Acknowledgements

My doctoral thesis would not have been possible without the support of the people who accompanied me through this journey. Before turning to the technical parts, I would like to express my sincere appreciation to those who have supported me along the way.

First and foremost, I am deeply grateful to my supervisor Prof. Dr. Walter Kaufmann for granting me the opportunity to pursue the doctorate at the Chair of Concrete Structures and Bridge Design, supporting me with his impressive competence whenever needed but also entrusting me with freedom to follow my own research interests.

I am also deeply grateful to my second advisor, Prof. Dr. Albin Kenel for his interest in my work and his valuable inputs, the numerous fruitful discussions that several times went into detail and motivated me to keep going.

Furthermore, I would like to extend my gratitude to my co-examiners Prof. em. Dr. Johann Kollegger and Prof. Dr. Peter Mark for accepting to serve on my doctoral committee and for reviewing this thesis.

Conducting experiments was a significant part of my doctorate. I am especially grateful to Robert Widman from the Structural Engineering lab at Empa, who supported me with the handling of the 20 MN testing machine. Working with you was a pleasure! I am also thankful to the lab engineers and technicians at the Structural Engineering Laboratory at IBK and Empa for their support: Dominik Werne, Christoph Gisler, Pius Herzog, Thomas Jaggi, Andreas Reusser and Slavko Tudor, Dimitri Ott, Giovanni Saragoni, Kilian Strasser. Furthermore, I want to thank Rolf Bieri, Paul Freudiger and the team of Marti Tunnel AG for producing the specimens for the experimental campaign on the longitudinal joints. I also want to thank Remo Crapp for his valuable inputs from a practitioner's point of view.

I also thank all the students who wrote their Project thesis in the broader context of my research, in particular: Nino Hasler, Federico Somaini, Monica di Vincenzo and Marcel Roth.

I greatly appreciated the collegial and supportive working atmosphere at the Chair of Concrete Structures and Bridge Design. I am especially thankful to my PAL Tomislav Markić for introducing me to the topic of partial area loading (PAL) and for the many stimulating discussions we had about our stress fields. I am also greatly thankful to Simon Karrer, for discussing problems of our research and finding solutions together but also the enjoyable daily banter in the office. I am also thankful to my other colleagues, in particular Minu Lee, Tena Galkovski, Andreas Näsbom, Nathalie Reckinger, Lukas Gebhard, Severin Häfliger, Nicola Gehri, Yasmin Lemcherreq, Angela Sequeira Lemos and Yannick Kummer for the technical exchange and your support in the lab.

Finally, I would like to express my deepest gratitude to my parents and my sister for the unlimited support, my close friends outside ETH for always being there along the way, and Minnea for her understanding, encouragement, and love.

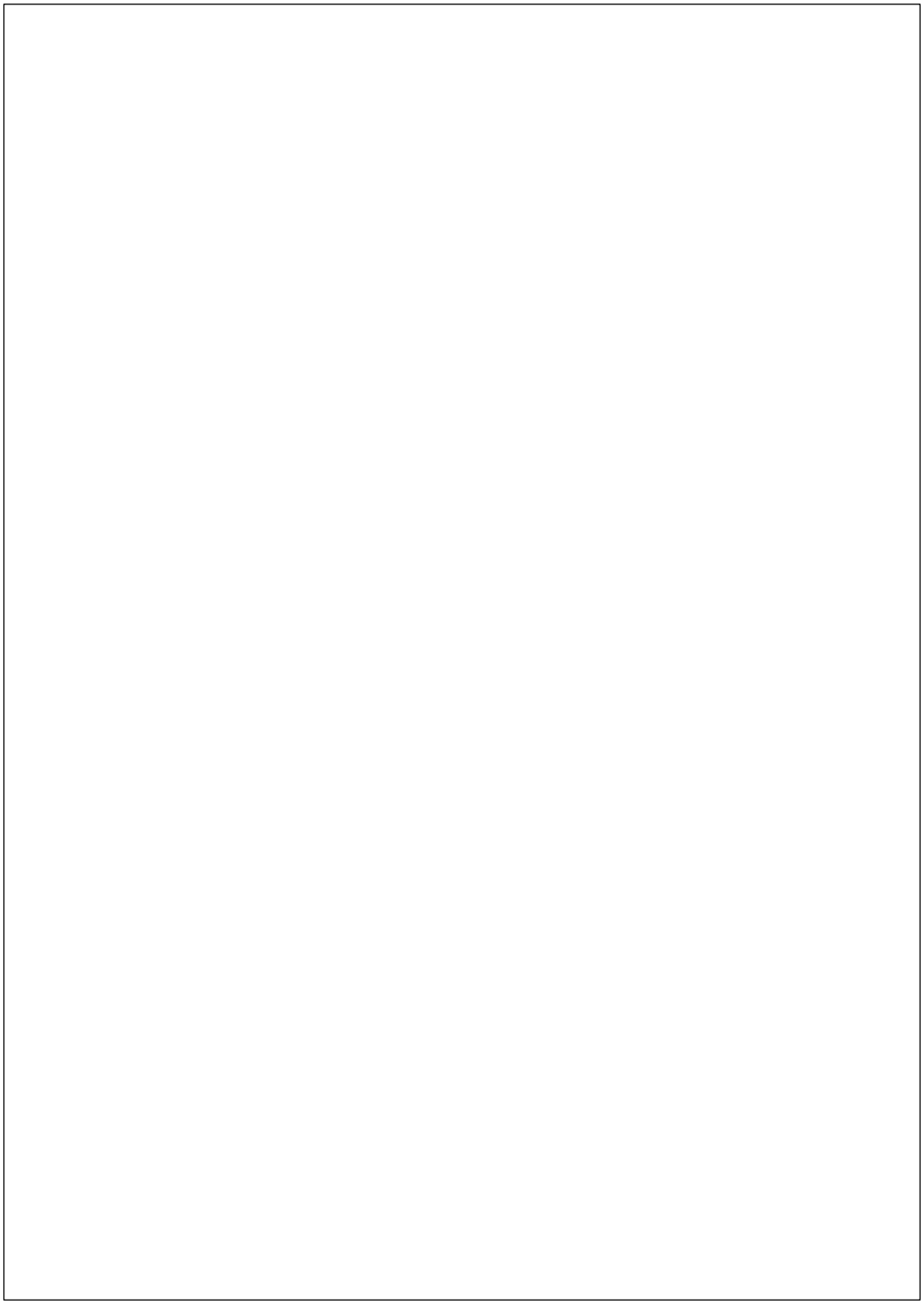

Table of contents

Abstract i

Kurzfassung iii

Acknowledgements v

---

1 Introduction 1
- 1.1 Background 1
- 1.2 Problem statement 4
- 1.3 Research objectives and methodology 5
- 1.4 Delimitations 6
- 1.5 Structure of the thesis 6
- 1.6 List of publications 8
  - 1.6.1 Journal publications 8
  - 1.6.2 Conference publications 8
- References 9

Part 1: Passive confinement 11

2 State of the art and new model approach 13
- 2.1 Introduction 14
- 2.2 State of the art of passive confinement 15
  - 2.2.1 Determination of passive confinement properties 16
- 2.3 A new model approach for passive confinement 20
  - 2.3.1 Geometrical definition of paraboloids for rectangular cross-sections 21
  - 2.3.2 Force flow 22
  - 2.3.3 Governing confined concrete area 25
  - 2.3.4 Adjustment of model for circular cross-sections 26
- 2.4 Comparison of the governing confined concrete areas 27
- 2.5 Model validation with experimental data 28
- 2.6 Conclusions 30
- Appendix 2.A Experimental data used for validation 32
- Appendix 2.B Comparison of model predictions with experimental data 38
- Notation 43
- References 45
- Corrections 47

3 Experimental investigation of welded reinforcement grids 49
- 3.1 Introduction 50
- 3.2 Experimental test 51

Table of contents

3.2.1 Reinforcement ... 51
3.2.2 Fibre optical (FO) sensing ... 53
3.3 Test results and discussion ... 53
3.3.1 Transverse reinforcement ... 54
3.3.2 Longitudinal reinforcement ... 55
3.4 Recommendations for practical design and outlook ... 57
3.5 Conclusions ... 58
References ... 60
Corrections ... 61

Part 2: Strip loading in reinforced concrete 63

4 Mechanical modelling and experimental validation of RC blocks 65
4.1 Introduction ... 67
4.2 Design of strip-loaded RC members ... 68
4.2.1 Dual-Wedge stress field ... 68
4.2.2 Square-root equation DAUB ... 76
4.2.3 GPC model ... 77
4.3 Experimental campaign ... 78
4.3.1 Specimens, materials, and casting ... 78
4.3.2 Test setup ... 82
4.3.3 Measurement systems ... 83
4.4 Results of the experimental campaign ... 83
4.4.1 Load bearing and failure behaviour ... 84
4.4.2 Crack development ... 85
4.5 Comparison of design approaches with experimental data ... 87
4.6 Conclusion ... 90
Appendix 4.A Dual-Wedge stress field ... 92
Appendix 4.B Mechanical properties of concretes and reinforcing steels ... 93
Appendix 4.C Load-penetration and load-crack width diagrams ... 94
Appendix 4.D Used test parameters and results of calculation with different model approaches ... 96
Notation ... 99
References ... 101
Corrections ... 103

5 Experimental and theoretical investigation of longitudinal tunnel lining joints 105
5.1 Introduction ... 107
5.2 Experimental campaign ... 108
5.2.1 Specimens, casting, and materials ... 109
5.2.2 Test setup and loading procedure ... 112
5.2.3 Measurement systems ... 113
5.3 Results and analysis of experimental campaign ... 113
5.3.1 Results ... 114
5.3.2 Load-bearing and failure behaviour ... 114
5.3.3 Crack development ... 120
5.3.4 Joint closing ... 121

5.4 Modelling ... 122
5.4.1 Unconfined zone ... 122
5.4.2 Confined zone ... 122
5.4.3 Guiding rod ... 126
5.4.4 Comparison with experimental data ... 127
5.5 Conclusion ... 129
Appendix 5.A. Definition of confinement properties ... 132
Appendix 5.B. Mechanical properties of concretes and reinforcing steels ... 133
Appendix 5.C. Machine control data ... 134
Appendix 5.D. Creep behaviour ... 135
Appendix 5.E. Equations of Multi-Wedge stress field ... 135
Appendix 5.F. Equations of Dual-Wedge stress field in longitudinal *z*-direction ... 136
Appendix 5.G. Test parameters and results of calculation with different model approaches ... 137
Notation ... 139
References ... 142

Part 3: Strip loading in steel fibre reinforced concrete 145

6 Experimental and theoretical investigation of strip-loaded SFRC 147
6.1 Introduction ... 148
6.2 Experimental campaign ... 149
6.2.1 Specimens, casting, and materials ... 149
6.2.2 Test setup and loading procedure ... 152
6.2.3 Measurement systems ... 152
6.3 Results and analysis of experimental campaign ... 153
6.3.1 Results ... 153
6.3.2 Load-bearing and failure behaviour ... 154
6.3.3 Comparison SFRC vs. RC ... 157
6.4 Modelling ... 159
6.4.1 Hybrid reinforcement ... 159
6.4.2 SFRC without additional reinforcement ... 162
6.5 Conclusion ... 164
Appendix 6.A. Mechanical properties of SFRC ... 166
Notation ... 169
References ... 171

7 Concluding remarks 173
7.1 Summary ... 173
7.2 Conclusion ... 176
7.2.1 Passive confinement ... 177
7.2.2 Strip loading in reinforced concrete ... 177
7.2.3 Strip loading in steel fibre reinforced concrete ... 178
7.3 Recommendations for future research ... 179
References ... 182

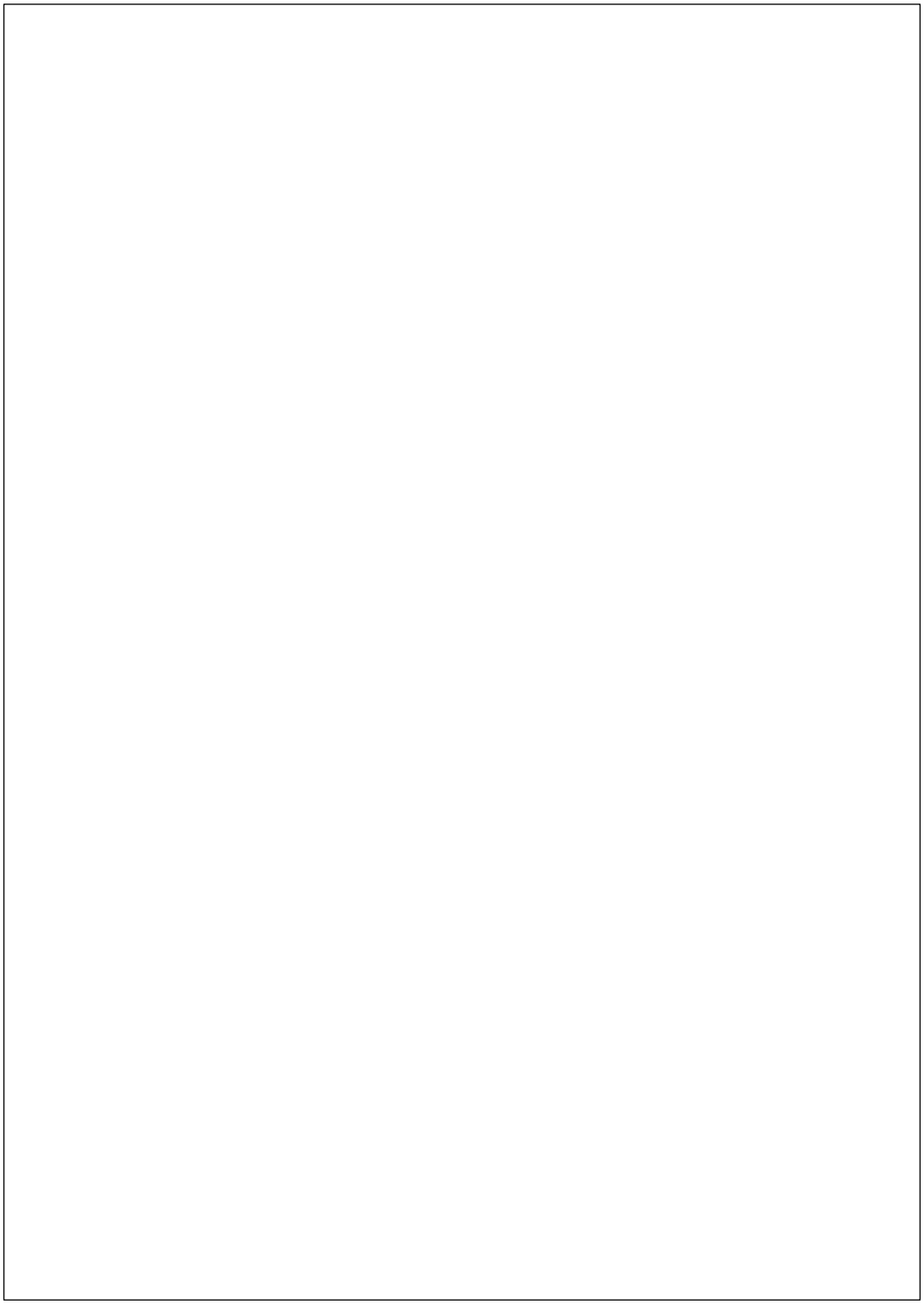

1 Introduction

This chapter sets out the framework of the research and places the work in its broader context. Following the problem statement and an overview of the research gaps, the research objectives are defined and the approach taken to address them is described. Finally, the structure and content of the thesis are outlined.

1.1 Background

Excavating long and deep tunnels with tunnel boring machines (TBMs) is a popular underground construction method due to its time and cost efficiency. TBM-built tunnels often use precast reinforced concrete (RC) lining segments installed almost immediately after excavation (see Fig. 1.1). These segments carry the loads throughout construction and, in case of so-called one-pass lining systems, during the entire tunnel service life, which can reach up to 200 years (e.g. Brenner Base Tunnel [1]). Commonly, several lining segments form a ring, resulting in longitudinal and ring joints. The longitudinal joints run approximately parallel to the tunnel axis, separating the segments of a ring, while the ring joints between adjacent segment rings are oriented perpendicular to the tunnel axis (see Fig. 1.2). The joints play a significant role in the design of the tunnel lining segments.

The longitudinal joints typically have a reduced contact area compared to the full cross-section, and are commonly designed as flat joints (see Fig. 1.1). The reduced contact area facilitates erection, reduces the risk of concrete spalling and allows to place gaskets to seal the tunnel. Furthermore, the longitudinal joints are often provided with a groove to insert a polymeric guiding rod to keep adjoining segments aligned during ring construction (see Fig. 1.1 left and Fig. 1.2). In one-pass linings, the longitudinal joints transfer normal forces, bending moments and shear forces between segments throughout the service life of the tunnel. These forces primarily result from rock and water pressure, the dead load of the

Fig. 1.1 - Stored segmental tunnel linings and installation of segments with TBM (author's own photographs).

lining and actions from tunnel installations. The ring joints on the other hand, are mainly subjected to the jacking forces of the TBM in construction.

The high degree of repetition in tunnelling projects offers a significant potential for optimisation of the segmental linings. A thinner lining would not only use less concrete but – more importantly – also reduce the required excavation volume, which can significantly impact cost and environmental impact for long tunnels. Consequently, an efficient design of the RC segments is required.

In tunnels under high hydrostatic pressure or crossing squeezing or swelling ground – such as the Brenner Base Tunnel [2] currently under construction or the planned Strait of Gibraltar tunnel [3], [4] – the lining is primarily subjected to high circumferential compressive forces, which are accompanied by relatively small bending moments. This loading configuration often leads to the longitudinal joints governing the design and determining the segment thickness due to the high normal compressive stresses along the contact area.

The stresses applied on the contact surface of the longitudinal joints spread within the segments until they eventually reach a uniform distribution over the full cross-section. Due to the geometry, the load dispersion is predominant in transverse (thickness) direction – corresponding to strip loading, a special case of partial area loading. By general definition, strip loading is applied over the entire length of a member, and the loaded area is much longer than wide. However, cases where the load is not applied on the whole length can still be considered as strip loading as long as the unloaded part of the length is small [5], which is generally the case for longitudinal tunnel lining joints.

It is well known that the load-bearing capacity of partially loaded RC can be several times higher than the uniaxial concrete compressive strength as long as the bursting stresses (resulting from load dispersion) are resisted (e.g. by reinforcement). First investigations of partial area loading date back nearly 150 years, when Bauschinger [6] investigated its effect on stone blocks. The strength increase of partially loaded RC, including strip loading, can be attributed to lateral confining stresses resulting either from load dispersion (geometrical confinement) or reinforcement (passive confinement). Confining stresses in both lateral directions cause a triaxial compressive stress state, increasing the axial concrete compressive strength by roughly four times the smallest lateral compressive stress, as already observed by Richart et al. [7], [8] nearly 100 years ago. In 1961, Spieth [9] introduced the so-called square root

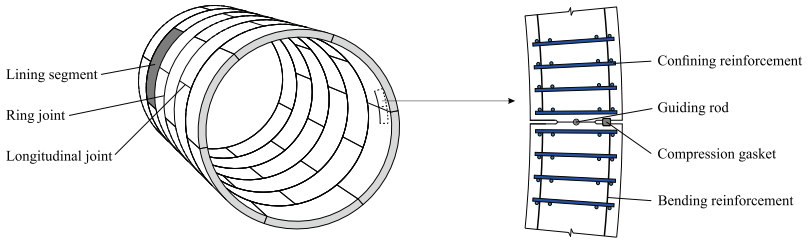

Fig. 1.2 - Definition of parameters of segmental tunnel linings and longitudianl joints.

equation to empirically determine the bearing capacity of partially loaded RC. Based on tests on centrically loaded plain concrete cylinders, he postulated that the resistance is proportional to the square-root of the ratio of the loaded area to the area available for load dispersion, multiplied by the uniaxial concrete compressive strength. Despite being restricted by several conditions due to its empirical nature, this approach is still included in current standards (EN 1992-1-1:2023 [10], *fib* Model Code 2020 [11], SIA 262:2013 [12]). While the required bursting reinforcement can readily be designed with a strut-and-tie model as already proposed by Mörsch [13], geometrical restrictions enforcing load dispersion in both directions drastically hinders its application to strip loading and thereby longitudinal joints. On the other hand, ignoring these restrictions (as proposed by the most recent recommendations of DAUB [14]) without any mechanical justification is unsatisfactory and, due to the empirical nature of the square-root equation, potentially unsafe.

Furthermore, the square-root equation does not account for any beneficial effect of confining reinforcement such that it is overly conservative if confinement is provided. In this context, several researchers [15]-[17] proposed semi-empirical models combining the square-root equation with confining effects. However, these approaches are not covered by current standards; only EN 1992-1-1:2023 [10] allows the combination of load dispersion and passive confinement if three-dimensional stress fields are considered. While EN 1992-1-1:2023 does not provide further guidance, Markić et al. [18] introduced a mechanically consistent stress field to determine the load-bearing capacity of strip-loaded RC with very narrow load application widths, as is typical for one-way concrete hinges. The model was successfully validated against experimental data [19] and showed that the load concentration ratio and the amount of confining reinforcement both influence the load-bearing capacity.

To effectively consider passive confinement for strip loading, its mechanical behaviour must first be understood. Load dispersion is also of importance for passive confinement: the confining reinforcement is activated by the lateral expansion of a RC member upon approaching the uniaxial compressive strength. This activation results in discrete confining forces being applied to the concrete by the reinforcing bars. For the concrete to be uniformly confined, a three-dimensional dispersion of these confining forces is necessary, which is the basis for determining (i) the confining stresses and (ii) the confined concrete, i.e., defining where and to what extent a triaxial stress state – increasing the concrete compressive strength – can be activated. The parameters (i) and (ii) depend on the reinforcement spacing and the material properties. In current standards, the modelling approaches by Mander et al. [20] and Sigrist [21] are typically adopted to determine the confining parameters by simplifying the three-dimensional load dispersion.

Steel fibre reinforced concrete (SFRC) provides a further option to increase the efficiency of tunnel lining segments. It is becoming more popular in tunnelling as an alternative option to conventional reinforcement due to its higher robustness, improved post-cracking behaviour and crack control [22] that e.g. facilitates handling in the construction phase and may be beneficial regarding watertightness. Incorporating the post-cracking behaviour of SFRC into the design of longitudinal joints may thus provide further optimisation potential for tunnel lining segments.

1.2 Problem statement

Accounting for load dispersion and passive confinement is a viable option for designing longitudinal joints of tunnel lining segments to resist high compressive forces. However, it has not yet been widely used in tunnelling practice, mainly because most current codes do not allow the beneficial effects of load dispersion and passive confinement to be combined. Although several recently proposed semi-empirical design approaches are available, assessing their suitability for the tunnelling industry is not straight forward since they lack mechanical consistency, and experimental data on longitudinal joints of tunnel lining segments with pronounced confining reinforcement are scarce.

The lack of experimental investigations on RC members subjected to strip loading with wide loaded areas and pronounced passive confinement not only impedes the validation of models, but also limits the general understanding of their load-bearing behaviour. Questions arise whether (i) confining reinforcement can be fully activated, and whether (ii) it is impacted by reinforcement type and ratio. Additional experimental tests could also provide insight into the behaviour under serviceability loads in particular regarding the occurrence of cracks due to the activation of the confining reinforcement and the potential risk of spalling of the concrete cover. Should significant cracking occur at relatively low loads, high amounts of confining reinforcement would not be a viable option in practice, even if high ultimate loads were theoretically achievable.

In order to determine the combined effect of load dispersion and passive confinement, mechanically sound modelling is required, such that the uncertainty in combining the two effects can be controlled. Stress fields provide a powerful method to describe the load-bearing behaviour as they follow mechanically consistent principles and allow tracing the entire load path, enabling reinforcement to be placed where required.

For tunnel lining segments, further specific uncertainties exist. It is generally not efficient to provide confining reinforcement within the entire element, hence only the zone close to the longitudinal joints is fully reinforced. Consequently, the load transfer between the two adjacent zones – confined and unconfined – must be ensured. In this regard, no modelling approaches nor published experimental data are known to the author. Furthermore, the impact of guiding rods at the load introduction zone further complicates the mechanical modelling.

Lastly, due to the increased use of SFRC in tunnelling and accounting for it in the design of longitudinal joints, the research gaps outlined above are complemented by additional questions concerning (i) consideration of the post-cracking behaviour of SFRC in strip loading, (ii) whether combining SFRC with conventional confining reinforcement is expedient or (iii) if the latter could even be omitted entirely in SFRC lining segments.

In conclusion, a remarkable knowledge gap currently exists concerning the analytical modelling and experimental validation of longitudinal tunnel lining joints.

1.3 Research objectives and methodology

This thesis aims to propose efficient design approaches for longitudinal joints of tunnel lining segments. This is accomplished through a fundamental investigation of the mechanical behaviour of strip-loaded RC and SFRC with substantial passive confinement, combining theoretical and experimental analyses and serving as a basis for the development of mechanically substantiated and experimentally validated modelling approaches. The investigations are divided in three parts.

The first part of the investigations is dedicated to the underlying mechanical behaviour of passive confinement provided by reinforcement. The main objectives of this part are:

- Provide a review of the current knowledge and the state of the art of confining reinforcement.
- Develop a mechanically consistent model describing the three-dimensional load dispersion of activated confining reinforcement.
- Validate the confinement model with experimental data from literature.
- Provide recommendations for determining the confining stresses and the confined concrete area.
- Experimentally investigate the load-bearing behaviour of welded grid reinforcement employed as confining reinforcement.
- Define practical recommendations for applying welded grid reinforcement as passive confinement.

After establishing the load-bearing behaviour of confining reinforcement, this knowledge is applied to strip-loaded RC focusing on longitudinal tunnel lining joints. The main objectives of this second part of the investigations are:

- Experimentally investigate the structural behaviour of strip-loaded and confined RC blocks focusing on the effects of reinforcement ratio and type, the width and position of the loaded area and the concrete compressive strength.
- Develop a mechanically consistent model for the load-bearing capacity of strip-loaded reinforced concrete blocks with wide load application widths and pronounced confining reinforcement by further developing an existing stress field solution, representing a lower bound solution according to plasticity theory and accounting for the multiaxial stress state caused by both load dispersion as well as passive confinement.
- Provide a simplification of the stress field solution to facilitate its application in engineering practice.
- Validate the predicted load-bearing capacity of the stress field with the obtained experimental data.
- Experimentally investigate the load-bearing behaviour of longitudinal joints of tunnel lining segments by conducting large-scale tests.

- Extend the stress field model to (i) account for an unconfined zone following the confined zone and (ii) cover the impact of a guiding rod groove, and (iii) validate the models against the experimental data.
- Relate the load-bearing capacity to the occurring crack widths and joint closings relevant for serviceability limit states.
- Define practical recommendations for a safe and efficient design of longitudinal tunnel lining joints.

Additionally, the load-bearing behaviour of strip-loaded SFRC is investigated. The main objectives of this third part of the investigations are:

- Experimentally investigate the influence of SFRC on strip loaded specimens with and without additional conventional confining reinforcement.
- Compare the behaviour of strip-loaded SFRC to RC.
- Account for the effect of SFRC in the proposed models and validate them against the experimental data.

1.4 Delimitations

The thesis focuses on the structural behaviour of strip loading, and specifically on longitudinal joints of tunnel lining segments with pronounced passive confinement for RC and SFRC. Only flat joints without connecting elements, such as e.g. bolts, are investigated. Furthermore, centric and slightly eccentric normal compressive loading is considered, excluding shear forces or predominant bending moments with associated joint rotations. Determination of the loads acting on the segments as well as interaction between segments of different rings or the adjacent soil are beyond the scope of the thesis.

The experimental investigation focuses on the short-term behaviour at ultimate load. Long-term effects due to creep are only marginally examined experimentally, while fatigue loading is completely disregarded. The experimental tests on the longitudinal tunnel lining joints are conducted on block specimens without curvature.

The theoretical modelling focuses on the prediction of the load-bearing capacity. The behaviour under serviceability loads is examined experimentally, focusing on surface crack widths and joint closing. Furthermore, the theoretical analyses use mean material properties and do not account for safety factors or the statistical variation in material characteristics. Further limitations are provided in the respective chapters where required.

1.5 Structure of the thesis

This cumulative thesis is divided into three main parts – corresponding to the three parts of the investigations outlined in Section 1.3 – whose content consists of four scientific journal publications and one

conference publication, all with first authorship of the author. These publications are presented as Chapters 2 to 6, with each chapter corresponding to one publication. These main parts of the thesis are framed by an introductory chapter (Chapter 1) and the conclusions with the main findings (Chapter 7).

The respective scientific publications of the thesis have been published in scientific journals and a conference proceeding. As the publications were published independently, each chapter contains its own introduction, conclusions, and references, leading to a certain amount of redundant information within this thesis when considered as one document.

Minor adjustments to the original content of the published publications were made with regards to the layout, formatting, section numbering, and style of references and language (American vs. British English), as well as minor linguistic improvements and figure enhancements for better legibility. Furthermore, the term *load-bearing capacity* was aligned throughout the thesis replacing *bearing capacity* where needed. More substantial adjustments to the content are noted at the end of each chapter in the corrections section, if provided.

The first main part, consisting of Chapters 2 and 3, focuses on passive confinement and investigates the confining behaviour of welded reinforcement grids. The second main part, consisting of Chapters 4 and 5, is dedicated to strip loading of RC. Thereby, Chapter 4 focuses theoretically and experimentally on confined concrete blocks, whereas Chapter 5 investigates the load-bearing behaviour of longitudinal tunnel lining joints. In the third main part, corresponding to Chapter 6, the investigations of the second part are extended to SFRC.

The present **Chapter 1** introduces the context of the research, states the research objectives and methodology, and gives an overview of the structure and content of the thesis.

Chapter 2 provides a thorough state of the art review of the theoretical knowledge of passive confinement in reinforced concrete, proposes a mechanical model considering the three-dimensional load dispersion of activated confining reinforcement and validates it against experimental data from literature.

Chapter 3 experimentally investigates the load-bearing behaviour of welded grid reinforcement acting as passive confinement using fibre optical strain measurements.

Chapter 4 presents and extends several models for strip loading, including the Dual Wedge stress field, and investigates a wide range of parameters with an experimental campaign on strip-loaded RC blocks with substantial confining reinforcement. The obtained load-bearing capacities are compared to the predictions of the models.

Chapter 5 presents and discusses the results of an extensive large-scale tests series on longitudinal tunnel lining joints with confining reinforcement. An optimised stress field solution is formulated and extended to account for guiding rod grooves. The performance of the models is validated against the obtained experimental data.

Chapter 6 presents and discusses the experimental results of strip-loaded blocks and longitudinal tunnel lining joints made of SFRC with and without conventional bar reinforcement. The analytical modelling is revisited and extended for the effect of SFRC. Validation of the models against the obtained experimental data is conducted.

Chapter 7 concludes the thesis with a summary of the main findings and provides an outlook for future research.

1.6 List of publications

In the course of the research, the doctoral student contributed to further scientific publications that are not part of this thesis. All publications with the doctoral student's contribution are listed below.

1.6.1 Journal publications

F. Morger, A. Kenel, W. Kaufmann, 'Passive confinement of reinforced concrete members revisited', *Structural Concrete*, vol. 25, no. 6, pp. 4283–4299, 2024, doi: 10.1002/suco.202400209. (**Chapter 2**)

F. Morger, A. Kenel, W. Kaufmann, 'Strip loading in reinforced concrete: Mechanical modeling and experimental validation', *Structural Concrete*, vol 27, no. 1, pp. 163-192, 2026, doi: 10.1002/suco.70154. (**Chapter 4**)

F. Morger, A. Kenel, W. Kaufmann, 'Experimental and theoretical investigation of longitudinal tunnel lining joints with confining reinforcement', *Structural Concrete*, 2026, doi: 10.1002/suco.70453. (**Chapter 5**)

F. Morger, A. Kenel, W. Kaufmann, 'Strip loading in steel fibre reinforced concrete: experimental and theoretical investigation', *Structural Concrete*, 2025, doi: 10.1002/suco.70339. (**Chapter 6**)

T. Markić, **F. Morger**, W. Kaufmann, 'Partially loaded areas in reinforced concrete: Mechanical modelling', *Engineering Structures*, vol. 271, p. 114938, 2022, doi: 10.1016/j.engstruct.2022.114938.

T. Markić, **F. Morger**, W. Kaufmann, 'Partially loaded areas in reinforced concrete: Experimental campaign and model validation', *Engineering. Structures*, vol. 273, p. 114905, 2022, doi: 10.1016/j.engstruct.2022.114905.

1.6.2 Conference publications

F. Morger, W. Kaufmann, 'Experimental investigation of welded reinforcement grids for partial area loading', in *Proceedings of the 15th fib PhD Symposium in Civil Engineering*, Féderation internationale du Béton (*fib*), vol. 66, pp. 181-188, 2024. doi: 10.3929/ethz-b-000711139. (**Chapter 3**)

F. Morger, W. Kaufmann, 'Design of longitudinal tunnel lining joints – experimental investigation on partially loaded reinforced concrete blocks', in *Proceedings of the 14th fib PhD Symposium in Civil Engineering*, Féderation internationale du Béton (*fib*), vol. 58, pp. 467-474, 2022. doi: 10.3929/ethz-b-000572924.

References

[1] K. Bergmeister, 'The Brenner Base Tunnel – geological, construction and logistical challenges and innovations at half time', *Geomechanics and Tunnelling*, vol. 12, no. 5, pp. 555–563, 2019, doi: 10.1002/geot.201900038.

[2] Brenner Basistunnel BBT SE, 'Brenner Basistunnel Ausschreibungsplanung', Technical Report, 2018.

[3] G. Lombardi, M. Neuenschwander, and A. Panciera, 'Gibraltar Tunnel Project update – the geomechanical challenges', *Geomechanics and Tunnelling*, vol. 2, no. 5, pp. 578–590, 2009, doi: 10.1002/geot.200900046.

[4] G. Anagnostou, 'Some critical aspects of subaqueous tunneling', presented at the World Tunnel Congress, ITA Secretariat c/o EPFL, 2014.

[5] T. Markić, 'Concrete hinges', Master's Thesis, Institute of Structural Engineering, ETH Zurich, Zurich, Switzerland, 2015.

[6] J. Bauschinger, 'Experimentelle Untersuchungen über die Gesetze der Druckfestigkeit', *Mitteilungen aus dem Mech. -Tech. Laboratorium der K. Polytechnischen Schule München*, vol. 6, 1876.

[7] F. E. Richart, A. Brandtzaeg, and R. L. Brown, 'A Study of the Failure of Concrete under Combined Compressive Stresses', University of Illinois Engineering Experimental Station, Bulletin 185, 1928.

[8] F. E. Richart, A. Brandtzaeg, and R. L. Brown, 'The failure of plain and spirally reinforced concrete in compression', University of Illinois Engineering Experimental Station, 1929.

[9] H. P. Spieth, 'Das Verhalten von Beton unter hoher örtlicher Pressung', *Beton- und Stahlbetonbau*, vol. 56, no. 11, pp. 257–263, 1961.

[10] EN 1992-1-1:2023, 'Eurocode 2 - Design of concrete structures - Part 1-1: General rules and rules for buildings, bridges and civil engineering structures', Brussels, 2023.

[11] International Federation for Structural Concrete (fib), *Model Code for Concrete Structures 2020*, Lausanne, 2024.

[12] SIA, *Swisscode SIA 262: Concrete Structures*, Zurich, Switzerland, 2013.

[13] E. Mörsch, 'Über die Berechnung der Gelenkquader', *Beton Eisen*, vol. 23, no. 12, pp. 156–161, 1924.

[14] German Tunnelling Committee (ITA-AITES), *Empfehlungen für den Entwurf, die Herstellung und den Einbau von Tübbingringen*. Deutscher Ausschuss für unterirdisches Bauen e. V. (DAUB), 2024.

[15] P. Wurm and F. Daschner, 'Teilflächenbelastung von Normalbeton: Versuche an bewehrten Scheiben', DAfStb, no. 344, 1983.

[16] M. Wichers, 'Bemessung von bewehrten Betonbauteilen bei Teilflächenbelastung unter Berücksichtigung der Rissbildung', Doctoral Thesis, Technische Universität Braunschweig, 2013.

[17] C. Proksch-Weilguni, M. Decker, and J. Kollegger, 'Load distribution and passive confinement in reinforced concrete: Development of a mechanical model', *Engineering Structures*, vol. 304, p. 117562, Apr. 2024, doi: 10.1016/j.engstruct.2024.117562.

[18] T. Markić, F. Morger, and W. Kaufmann, 'Partially loaded areas in reinforced concrete: Mechanical modelling', *Engineering Structures*, vol. 271, p. 114938, Nov. 2022, doi: 10.1016/j.engstruct.2022.114938.

[19] T. Markić, F. Morger, and W. Kaufmann, 'Partially loaded areas in reinforced concrete: experimental campaign and model validation', *Engineering Structures*, vol. 273, p. 114905, Dec. 2022, doi: 10.1016/j.engstruct.2022.114905.

[20] J. B. Mander, M. J. N. Priestley, and R. Park, 'Observed Stress-Strain Behavior of Confined Concrete', *Journal of Structural Engineering*, vol. 114, no. 8, pp. 1827–1849, Sep. 1988, doi: 10.1061/(ASCE)0733-9445(1988)114:8(1827).

[21] V. Sigrist, 'Zum Verformungsvermögen von Stahlbetonträgern', Doctoral thesis, ETH Zurich, Zurich, Switzerland, 1995. doi: 10.3929/ethz-a-001492371.
[22] ACI Committee 533, *Guide for Precast Concrete Tunnel Segments (ACI 533.5R-20)*. Farmington Hills, MI: American Concrete Institute, 2020.

Part 1

Passive confinement

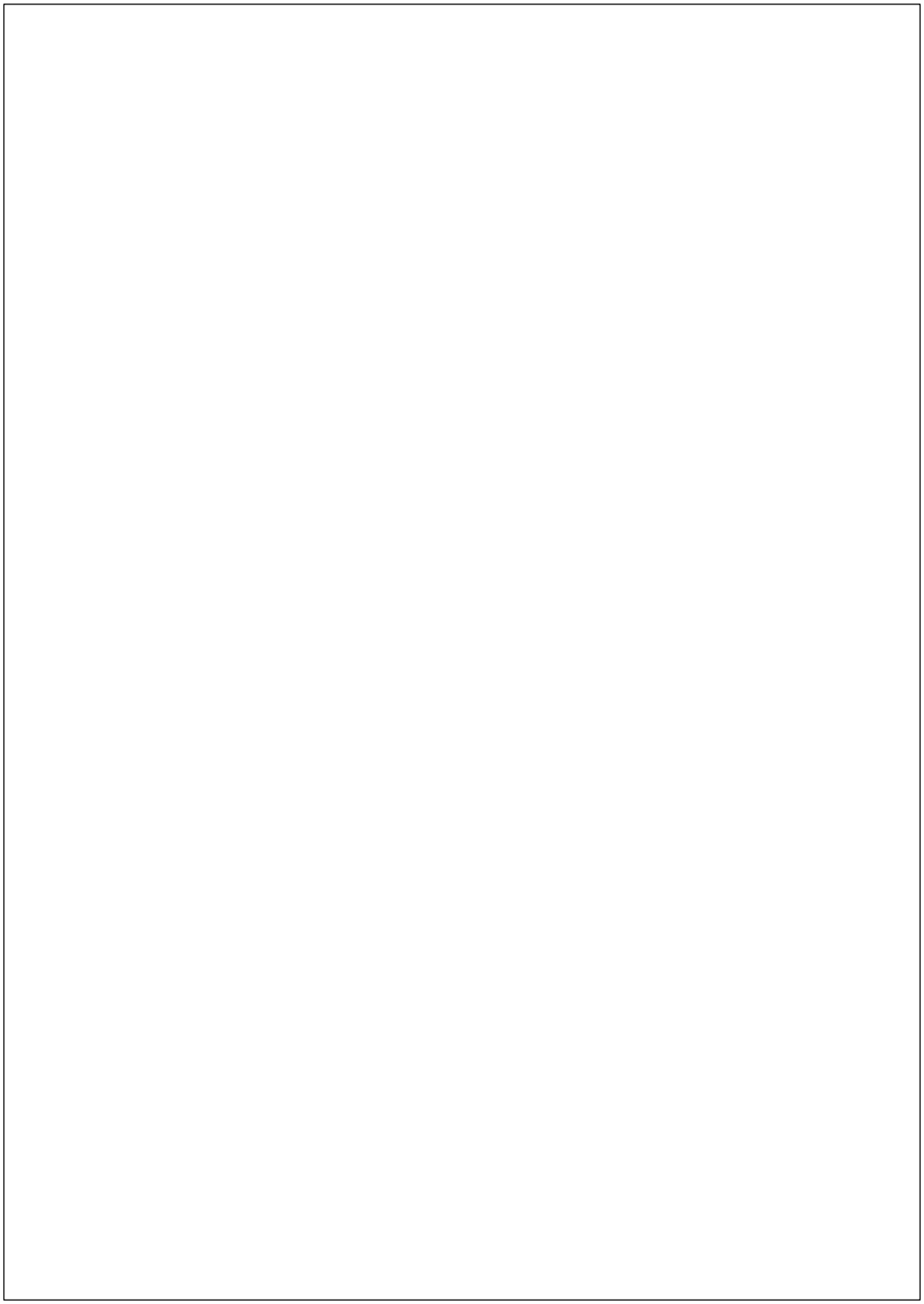

2 State of the art and new model approach

The content of this chapter corresponds to the postprint of the following published article:

> **F. Morger**, A. Kenel, W. Kaufmann, 'Passive confinement of reinforced concrete members revisited', *Structural Concrete*, vol. 25, no. 6, pp. 4283–4299, 2024, doi: 10.1002/suco.202400209.

This postprint includes some adjustments to the published version. For details see Section 1.5 and the corrections section at the end of this chapter.

As the lead author, Fabian Morger conducted the literature review and developed the concept of the proposed confinement model. He also formulated and implemented the model, validated it, and wrote the entire draft of the manuscript. The second author, Albin Kenel, contributed to the development of the confinement model, verified the mathematical formulation and was particularly involved in the validation of the model. The third author, Walter Kaufmann, supervised the conducted research and carefully reviewed the manuscript.

Abstract

Passive confinement provided by transverse reinforcement is taken into account in the design of reinforced concrete structures subjected to high compressive loading such as columns, piers or tunnel lining segments. In current guidelines, several models exist to account for this beneficial effect. However, these approaches lack mechanical consistency regarding the three-dimensional load dispersion of the confining forces. The article addresses this knowledge gap by introducing a new model based on a lower-bound solution according to the theory of plasticity, along with a simplification regarding the governing confined concrete area. The proposed model and its simplified version are compared to the design approaches proposed by current guidelines, and both are successfully validated against experimental data. The simplified new model is a valuable alternative to existing models in current guidelines, as (i) it is mechanically more consistent, (ii) its application is more straightforward and (iii) it allows the comprehensive treatment of rectangular and circular cross-sections using the same equations.

Keywords: Concrete compressive strength; Passive confinement; Confining reinforcement; Confined concrete area; Confining stresses; Concrete normal load-bearing resistance.

2. State of the art and new model approach

2.1 Introduction

The compressive strength of concrete is significantly enhanced by lateral compressive stresses, commonly referred to as *confining stresses* or simply *confinement*. The beneficial effect of triaxial compression on concrete has been thoroughly investigated for over a century. As early as 1902, Considère [1], [2] published an experimental study on concrete prisms incorporating confinement reinforcement and an approach to quantify its effect. Bach [3] studied the effect of confining reinforcement on the behaviour of concrete columns only few years later. In 1928, Richart et al. [4], [5] published their seminal contribution to this field, postulating a linear relationship between the triaxial compressive strength and the confining stresses based on extensive experimental campaigns on triaxially loaded concrete as well as uniaxially loaded specimens provided with closely spaced confining reinforcement. Accordingly, regardless of whether the stresses were actively applied or generated by reinforcement, the compressive strength is increased by 4.1 times the confining stresses. Besides the increase in compressive strength, they found that confinement of the concrete leads to an even more pronounced increase in ductility. These findings have been confirmed by many subsequent experimental campaigns and remain the basis of today's design approaches, though typically considering a slightly less pronounced strength increase (factor 4 instead of 4.1, further reduced at high stress levels).

In civil engineering practice, confining stresses are mainly generated in three different ways: (i) externally by prestressing, (ii) internally by providing closely spaced confining reinforcement or (iii) by geometry, i.e., curved principal compressive stress trajectories generating lateral compression. These are commonly referred to as (i) active, (ii) passive and (iii) geometrical confinement. This article focuses on the effect of passive confinement on the compressive load-bearing capacity of reinforced concrete (RC) members subjected to centrical loading over the entire cross-section. The reader is referred to Markić et al. [6] for partial area loading problems. Passive confinement is mainly accounted for in the design of structural elements subjected to predominant, high compressive loading such as columns, piers, compression struts or lining segments of tunnels with high overburden or in squeezing grounds.

Bach [3] had already observed that the longitudinal spacing of the transverse reinforcement affects the longitudinal compressive strength of a member. However, it was not until the 1970's and later that the related effects – attributed to the influence of the reinforcement spacing on the size of the concrete volume benefitting from passive confinement – were explicitly included in design approaches [7]-[10]. Several of these approaches form the basis of the design clauses for confining reinforcement in current standards such as *fib* Model Code for Concrete Structures 2010 (MC 2010) [11], SIA 262:2013 Concrete Structures (SIA 262) [12] or Eurocode 2 - Design of concrete structures EN 1992-1-1:2023 (EC 2) [13]. For a broader overview of the historical context of passive confinement, the reader is referred to Seelhofer-Schilling [14].

The passively confined concrete volume, i.e., the concrete volume subjected to triaxial compression, results from the dispersion of discrete lateral forces generated by confining reinforcement, which is activated by lateral expansion of the RC member upon approaching the uniaxial compressive strength. For circular cross-sections, load distribution only occurs longitudinally, whereas a three-dimensional load dispersion is required in rectangular cross-sections. While the design approaches underlying

current standards adequately cover the lateral load distribution in circular compression members, none of these effectively capture the three-dimensional load dispersion in compression members with rectangular cross-sections. Additionally, some of these design approaches are fairly complicated.

This article presents a mechanical model for the three-dimensional dispersion of the confining forces based on a lower-bound solution according to the theory of plasticity, thereby determining the volume of the passively confined concrete volume as well as the corresponding confining stresses on a sound mechanical basis. In addition, a simplified version of the model is presented. The model is developed for rectangular cross-sections, but can readily be adjusted for circular cross-sections.

In the following, the state of the art of confining reinforcement of rectangular cross-sections and its implementation in current design standards is presented (Section 2.2), the new model and its simplification are introduced (Section 2.3), and the governing confined concrete areas according to the new model and its simplification are compared to existing design approaches (Section 2.4). Subsequently, the respective model predictions are compared to those obtained from currently used design approaches and validated against experimental data (Section 2.5), pointing out that the new model as well as its simplification both capture the effect of confining reinforcement well, while the simplification can be applied easily in civil engineering practice. The article concludes with a summary of the main findings (Section 2.6).

2.2 State of the art of passive confinement

The load-bearing resistance of a RC member in compression can be obtained by summing up three individual components with their associated cross-sectional areas: (i) the uniaxial concrete compressive strength of the entire concrete cross-section, (ii) the compressive strength of the longitudinal reinforcement and (iii) the increase in concrete compressive strength due to a triaxial stress state provided by confining reinforcement:

$$N_R = \underbrace{\eta_{cc} \cdot f_{c0} \cdot A_{cs}}_{\text{(i)}} + \underbrace{\left(f_{sy,l} - f_{c0}\right) \cdot A_{s,l}}_{\text{(ii)}} + \underbrace{\Delta f_{conf} \cdot A_{conf}}_{\text{(iii)}} \qquad \text{with } \eta_{cc} = \left(\frac{30}{f_{c0}}\right)^{1/3} \leq 1.0 \tag{2.1}$$

where f_{c0} = uniaxial concrete compressive strength, η_{cc} = coefficient accounting for the brittleness of higher-strength concrete, A_{cs} = concrete cross-section within the confining reinforcement, $f_{sy,l}$ and $A_{s,l}$ = yield strength and total cross-sectional area of longitudinal reinforcement, respectively, Δf_{conf} = concrete compressive strength increase due to confinement, and A_{conf} = governing confined concrete area. Note that the definition of the brittleness factor η_{cc} in Eq. (2.1) is in line with that used in the calibration of safety factors for EC 2 [13] by Moccia et al. [15], who assumed that a brittleness factor is required for $f_{c0} > 30$ MPa but proposed to adopt a higher reference strength in EC 2 (i.e., $\eta_{cc} = (40/f_{c0})^{(1/3)} \leq 1$) to enable the use of a uniform partial safety factor of concrete $\gamma_c = 1.5$. Furthermore, Eq. (2.1) neglects the concrete area outside the confining reinforcement, as assumed in SIA 262 and MC 2010. To account for the cover concrete, as proposed by EC 2, A_{cs} in Eq. (2.1) can simply be replaced by the full cross-section of the compression member, i.e., A_c, such that the cover concrete contributes to the load-bearing

capacity with its uniaxial concrete compressive strength. Whether this makes sense is discussed further in Section 2.5. The following section (2.2.1) outlines how the contribution of the passive confinement (iii), focusing on the increase of concrete compressive strength (Δf_{conf}) and the governing confined concrete area (A_{conf}), is determined according to current guidelines (EC 2, SIA 262 and MC 2010).

In this article, the coordinate system of an RC member in compression is chosen such that the loading direction coincides with the *x*-axis, which is referred to as the longitudinal direction. The *y* and *z*-directions are thus referred to as lateral directions. The confining reinforcement is placed in the plane spanned by the lateral directions. Fig. 2.1 shows an RC compression member with confining reinforcement and illustrates the most important geometrical parameters used in this article.

2.2.1 Determination of passive confinement properties

As outlined in the introduction, experimental tests have shown that the increase of the concrete compressive strength (Δf_{conf}) due to confinement is approximately four times the lateral compressive stress, corresponding to the ratio (1+sin(φ))/(1-sin(φ)) obtained using a Coulomb failure criterion [16] with the common assumption of tan(φ) = 0.75. For RC compression members, the lateral compressive stresses result from confining reinforcement, activated by the lateral expansion of concrete when approaching the uniaxial compressive strength (dilatancy) under longitudinal loading. In rectangular RC cross-sections, the confining stresses must be considered in both lateral directions. Based on the Coulomb failure criterion, the minimum confining stress (compression positive, either σ_{confy} or σ_{confz}) governs for determination of Δf_{conf}:

$$\Delta f_{conf} = 4 \cdot \min\left(\sigma_{confy}, \sigma_{confz}\right) \tag{2.2}$$

This linear relationship is valid for a mechanical confinement reinforcement ratio up to about 0.6 [13]. As this applies to most cases in engineering practice, no other relationship is considered in this article. The confining stresses are assumed to be uniformly distributed over the confined concrete volume. The magnitude of the confining stresses depends, according to current guidelines (EC 2, SIA 262, MC 2010), on the cross-sectional areas ($A_{s,confy}$ and $A_{s,confz}$ per leg), the yield strength ($f_{sy,conf}$) and the longitudinal spacing (s_x) of the confining reinforcement, as well as the lateral dimensions b_{csy} and b_{csz} of the cross-sectional area within the confining reinforcement (see Fig. 2.1). Assuming yielding of the confining reinforcement and full dispersion of the confining forces, the confining stresses follow by equilibrium as:

$$\sigma_{confy} = \frac{\sum A_{s,confy} \cdot f_{sy,conf}}{s_x \cdot b_{csz}} \tag{2.3}$$

$$\sigma_{confz} = \frac{\sum A_{s,confz} \cdot f_{sy,conf}}{s_x \cdot b_{csy}} \tag{2.4}$$

Once activated, the confining reinforcement transfers forces to the concrete primarily at its bends or end plates [7], [17]. These locally applied forces must spread to reach a uniform confining stress distribution. Consequently, the governing confined concrete area (A_{conf}), corresponding to the smallest triaxially stressed cross-sectional area of the compression member, is smaller than the area within the confinement reinforcement (A_{cs}). Considering the required load distribution, the size of A_{conf} evidently

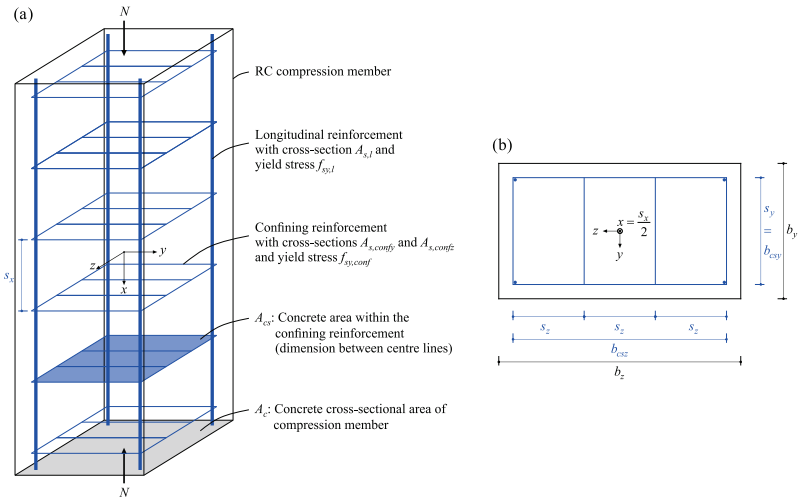

Fig. 2.1 - Definition of most important geometrical parameters used to account for passive confinement: (a) RC compression member (s_x:s_z:s_y = 1:1:1.5) and (b) section at the level of confining reinforcement (e.g. $x = s_x/2$).

depends on the spacing of the load introduction points: the denser the confining reinforcement is placed, the larger is the governing confined concrete area. The ratio between the governing confined concrete area A_{conf} and the area within the confining reinforcement A_{cs} is referred to as effectiveness factor k of the confining reinforcement:

$$k = \frac{A_{conf}}{A_{cs}} \tag{2.5}$$

Using this factor, Eq. (2.1) can be rewritten as:

$$N_R = \left(\eta_{cc} \cdot f_{c0} + k \cdot \Delta f_{conf}\right) \cdot A_{cs} + \left(f_{sy,l} - f_{c0}\right) \cdot A_{s,l} \tag{2.6}$$

The following sections present and discuss the different existing approaches to determine the governing confined concrete area A_{conf} (and the corresponding effectiveness factor k) according to current design guidelines (EC 2, SIA 262 and MC 2010), focusing on rectangular cross-sections. All models assume that the confining reinforcement is fully activated and that the confining stresses can be determined based on Eqs. (2.3) and (2.4).

2.2.1.1 EC 2

EC 2 determines the governing confined concrete area $A_{conf,EC2}$ based on arching action between the discretely distributed load introduction points of the confining reinforcement, as discussed by several authors [7], [8], [17]:

$$A_{conf,\mathrm{EC2}} = \underbrace{\left(b_{csy}\cdot b_{csz} - \frac{\sum s_i^2}{6}\right)}_{A} \cdot \underbrace{\frac{\left(b_{csy}-s_x/2\right)\cdot\left(b_{csz}-s_x/2\right)}{b_{csy}\cdot b_{csz}}}_{B} = \left(b_{csy}\cdot b_{csz} - \frac{\sum s_i^2}{6}\right)\cdot\left(1-\frac{s_x}{2\cdot b_{csy}}\right)\cdot\left(1-\frac{s_x}{2\cdot b_{csz}}\right) \tag{2.7}$$

$$k_{\mathrm{EC2}} = \left(1-\frac{\sum s_i^2}{6\cdot b_{csy}\cdot b_{csz}}\right)\cdot\left(1-\frac{s_x}{2\cdot b_{csy}}\right)\cdot\left(1-\frac{s_x}{2\cdot b_{csz}}\right) \tag{2.8}$$

This equation, applicable to rectangular cross-sections, is based on the work of Mander [10]. Its first part (labelled *A*) considers the lateral load dispersion by assuming second-order parabolic arches spanning between the load introduction points of the confining reinforcement with an initial inclination of π/4, defining a prismatic body whose cross-section corresponds to the confined concrete area at the level of the introduction points of the confining forces (e.g. $x = s_x/2$), see Fig. 2.2a. However, as pointed out by Mander, the governing section – i.e., the smallest confined concrete cross-sectional area – is located at the centre between two confining reinforcement layers in the longitudinal direction (e.g. $x = 0$). Consequently, load dispersion in the longitudinal direction, over the reinforcement spacing s_x, must also be considered. To this end, the confined concrete area at the section of the confining reinforcement (defined by Part *A* in Eq. (2.7)) is scaled by the ratio of the rectangle enclosed by arches spanning in the longitudinal direction – again with an initial inclination of π/4 – between the sections of the confining reinforcement Fig. 2.2b and c) to the area within the confining reinforcement (A_{cs}) (Part *B*). While this approach to determine the governing confined concrete area $A_{conf,\mathrm{EC2}}$ considers the reinforcement spacing in the lateral and longitudinal directions, these directions are considered independently and the three-dimensional load dispersion of the discretely introduced confining forces remains unclear. Fig. 2.2d illustrates the resulting governing confined concrete area $A_{conf,\mathrm{EC2}}$, whose shape clearly indicates its missing mechanical basis.

2.2.1.2 SIA 262

SIA 262 defines the governing confined concrete area $A_{conf,\mathrm{SIA262}}$ based on the stress field illustrated in Fig. 2.3, proposed by Sigrist [18]:

$$A_{conf,\mathrm{SIA262}} = \left(b_{csy}-s_x\right)\cdot\left(b_{csz}-s_x\right) \tag{2.9}$$

$$k_{\mathrm{SIA262}} = \left(1-\frac{s_x}{b_{csy}}\right)\cdot\left(1-\frac{s_x}{b_{csz}}\right) \tag{2.10}$$

The stress field is defined in a longitudinal section (Fig. 2.3a) through the compression member, where the confining forces are introduced as uniform line loads around the circumference (along the stirrups) in the lateral direction (Fig. 2.3b). The stress field thus spreads the confining forces longitudinally with semi-circular fans, whose diameter equals the spacing s_x of the confining reinforcement in the longitudinal direction. This implies that no dispersion of the discretely introduced confining forces is required in the lateral directions. Sigrist stated that this assumption is only justified for regularly distributed and stiff confining reinforcement, and that the stress field represents a simplification of the complex triaxial stress state. Compared to Mander's approach, the governing confined concrete area $A_{conf,\mathrm{SIA262}}$, enclosed

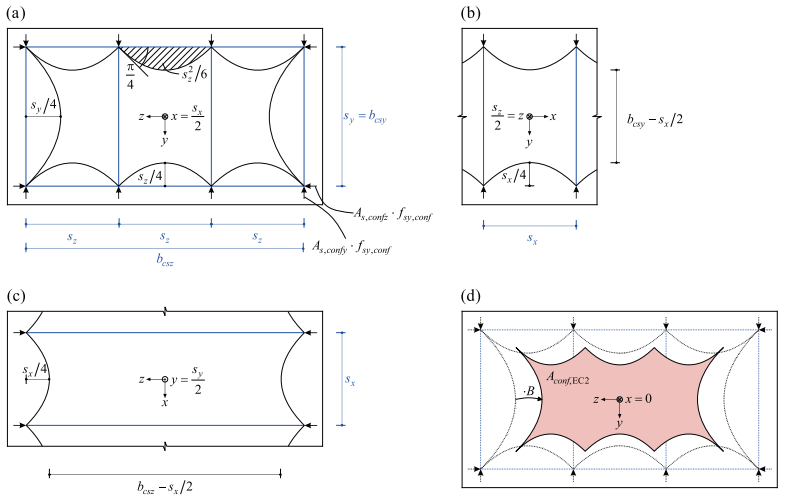

Fig. 2.2 - Definition of confined concrete area according to EC 2: (a) confined concrete area at the section of a confining reinforcement layer (e.g. $x = s_x/2$), (b) and (c) longitudinal dispersion of confining forces, and (d) governing confined concrete area at the centre between two confining reinforcement layers (e.g. $x = 0$, dotted lines indicating section from (a) as reference).

by the semi-circular fans, is located at the level of the introduction points of the confining forces (e.g. $x = s_x/2$, Fig. 2.3a), rather than in-between, and the reduction of the confined concrete area in the longitudinal direction is twice as big.

This approach to determine the governing confined concrete area $A_{conf,\mathrm{SIA262}}$ only considers the reinforcement spacing in the longitudinal direction and neglects the reinforcement spacing in the lateral directions. While the stress field represents a lower-bound solution of the theory of plasticity and allows partly to follow the flow of forces, the underlying assumption of a flexurally rigid transverse reinforcement – which is supposed to yield in tension when determining the confining stresses – is inconsistent. Furthermore, assuming the governing confined concrete area at the level of the confining reinforcement and full confinement in between contradicts experimental observations, where both the cover concrete and, more importantly, concrete between the load introduction points commonly spall [19]. Nonetheless, the load-bearing capacities predicted by SIA 262 correlate well with experimental results (since for common detailing, the lacking consideration of lateral load dispersion is compensated by the conservative longitudinal semi-circular fans), and $A_{conf,\mathrm{SIA262}}$ is the most straightforward formulation of the guidelines compared in this article.

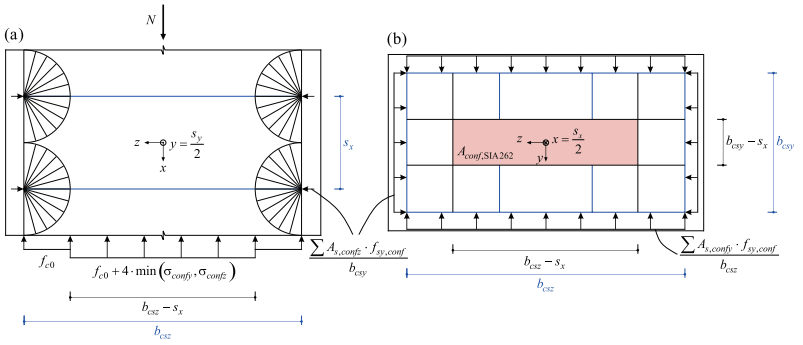

Fig. 2.3 - Definition of confined concrete area according to SIA 262: (a) stress field and (b) lateral section at the level of the confining reinforcement (e.g. $x = s_x/2$). Adapted and adjusted from Sigrist [18].

2.2.1.3 MC 2010

MC 2010 defines the governing confined concrete area as a combination of the two models forming the basis of the EC 2 and the SIA 262 formulation:

$$A_{conf,\mathrm{MC2010}} = \left(b_{csy}\cdot b_{csz} - \frac{\sum s_i^2}{6}\right)\cdot\frac{\left(b_{csy}-s_x\right)\cdot\left(b_{csz}-s_x\right)}{b_{csy}\cdot b_{csz}} = \left(b_{csy}\cdot b_{csz} - \frac{\sum s_i^2}{6}\right)\cdot\left(1-\frac{s_x}{b_{csy}}\right)\cdot\left(1-\frac{s_x}{b_{csz}}\right) \tag{2.11}$$

$$k_{\mathrm{MC2010}} = \left(1-\frac{\sum s_i^2}{6\cdot b_{csy}\cdot b_{csz}}\right)\cdot\left(1-\frac{s_x}{b_{csy}}\right)\cdot\left(1-\frac{s_x}{b_{csz}}\right) \tag{2.12}$$

In the lateral directions, the confined concrete area at the level of the confining reinforcement is determined as in EC 2 (Part *A* of Eq. (2.7)). This area is then scaled by a factor corresponding to the ratio of the rectangle enclosed by semi-circular fans in the longitudinal direction – as in the stress field underlying SIA 262 – and the area within the reinforcement (A_{cs}). Just like Mander's proposal underlying EC 2, this approach to determine the governing confined concrete area $A_{conf,\mathrm{MC2010}}$ considers the reinforcement spacing in longitudinal and lateral directions independently, such that the three-dimensional load dispersion remains unclear. Furthermore, the combination of two models with fundamentally different assumptions is inconsistent. Of the three models presented, $A_{conf,\mathrm{MC2010}}$ always results in the most conservative governing confined concrete area.

2.3 A new model approach for passive confinement

The three passive confinement models outlined in Section 2.2.1 do not consistently account for the three-dimensional load dispersion in rectangular RC compression members, nor is the force flow

comprehensible. This section presents a new model that closes this research gap, describing the three-dimensional load dispersion through paraboloids. These paraboloids span between the load introduction points as vaults, i.e., point-supported compression-only shells. The deviation forces caused by the shell curvature correspond to the confining stresses, whereas the shape of the paraboloids defines the confined concrete volume. The model relates the confined concrete volume to the confining stresses and allows the load path to be followed similar to the strip method known from slab design. In its presented formulation, the model assumes equal confining forces at all supports of the paraboloids and a uniform reinforcement spacing. While these conditions are common in engineering practice, it is worth noting that the model can be adapted to suit more general scenarios. However, such adaptations are beyond the scope of this article. Furthermore, the model can be easily adjusted for circular cross-sections, for which the load dispersion of confining forces only occurs in the longitudinal direction.

In the following, the new model is presented in more detail. First, the geometry of the paraboloids is defined (Section 2.3.1), followed by the description of the load path of the confining forces (Section 2.3.2) and the determination of the governing confined concrete area (Section 2.3.3). Lastly, the adaptation of the model to circular cross-sections is presented (Section 2.3.4).

2.3.1 Geometrical definition of paraboloids for rectangular cross-sections

For a compression member with a rectangular cross-section, two paraboloids I and II (Fig. 2.4a and b) are defined:

$$\text{I:} \qquad z_{\mathrm{I}} = \left(\frac{4 \cdot h_{zx}}{s_x^2} \cdot {x_{\mathrm{I}}}^2 + \frac{4 \cdot h_{zy}}{s_y^2} \cdot {y_{\mathrm{I}}}^2 \right) - h_z \qquad (2.13)$$

$$\text{with } h_z = h_{zx} + h_{zy}$$

$$\text{II:} \qquad y_{\mathrm{II}} = \left(\frac{4 \cdot h_{yx}}{s_x^2} \cdot {x_{\mathrm{II}}}^2 + \frac{4 \cdot h_{yz}}{s_z^2} \cdot {z_{\mathrm{II}}}^2 \right) - h_y \qquad (2.14)$$

$$\text{with } h_y = h_{yx} + h_{yz}$$

The geometry of the paraboloids depends on the spacing of the confining reinforcement (s_x, s_y, and s_z) and the rises of the parabolas (h_{zx}, h_{zy} and h_{yx}, h_{yz}). While the reinforcement layout determines the spacing, the rise of the parabolas can be chosen freely, noting that this choice affects the volume of confined concrete as well as the confining stresses (see Section 2.3.2).

In this article, the paraboloids are defined such that the lateral parabolas with rise h_{zy} and h_{yz} have an initial inclination of π/4, corresponding to a rise of a fourth of the confining reinforcement spacing in the corresponding direction:

$$\text{I:} \qquad h_{zy} = \frac{s_y}{4} \qquad (2.15)$$

$$\text{II:} \qquad h_{yz} = \frac{s_z}{4} \qquad (2.16)$$

The reason for this choice is further elaborated in Section 2.3.2. The initial inclination of the parabolas along the diagonal of each paraboloid with rise h_z and h_y is also set to π/4:

$$\text{I:} \qquad h_z = \frac{\sqrt{s_x^2 + s_y^2}}{4} \tag{2.17}$$

$$\text{II:} \qquad h_y = \frac{\sqrt{s_x^2 + s_z^2}}{4} \tag{2.18}$$

This choice allows the model to be applicable to circular cross-sections (see Section 2.3.4). Eqs. (2.15)-(2.18) define the geometry of the paraboloids, including the rise of the parabolas in longitudinal direction:

$$\text{I:} \qquad h_{zx} = h_z - h_{zy} = \frac{\sqrt{s_x^2 + s_y^2} - s_y}{4} \tag{2.19}$$

$$\text{II:} \qquad h_{yx} = h_y - h_{yz} = \frac{\sqrt{s_x^2 + s_z^2} - s_z}{4} \tag{2.20}$$

Fig. 2.4c illustrates the triaxially confined concrete volume for an RC compression member with a rectangular cross-section, four reinforcing bars per layer in y-direction and two per layer in z-direction based on the presented model, assuming s_x:s_z:s_y = 1:1:1.5. Note that the longitudinal reinforcement is omitted in the figures in this section, as it does not affect the passive confinement assumed in the model.

2.3.2 Force flow

Lateral expansion of an RC member subjected to compressive loading activates the confining reinforcement, resulting in discretely introduced confining forces F_y and F_z, respectively (Fig. 2.4d). The model assumes compression-only shells – whose geometry is defined by the paraboloids outlined in Section 2.3.1 – which disperse the confining forces. The chosen parabolic form ensures uniformly distributed deviation forces, hence uniform compressive stresses confining the concrete. The flow of forces assumed by the model, outlined in detail below, represents one of numerous possible stress fields satisfying equilibrium and thus corresponds to a lower-bound solution according to the theory of plasticity as long as the yield conditions of the materials are not infringed.

The confining forces F_y and F_z initially spread along infinitesimally narrow parabolas in the lateral directions (indicated in dark green in Fig. 2.4d). The associated deviation forces are equilibrated by parabolas spanning in the longitudinal direction (indicated in light green in Fig. 2.4d) along the circumference of the compression member. The deviation forces of these longitudinal parabolas correspond to the uniform confining stresses $\sigma_{confy,mod}$ and $\sigma_{confz,mod}$. The assumed orthogonal force flow in lateral and longitudinal directions, with the (distributed) longitudinal parabolas transferring the confining stresses to the (concentrated) lateral parabolas, which carry them to the point supports, is similar to the strip method known from slab design (confining stresses ≙ applied load, longitudinal parabolas ≙ slab strips, lateral parabolas ≙ strong bands).

To ensure a lower-bound solution, the thrust forces of the parabolas must be resisted without infringing the yield conditions. In the longitudinal direction, they are equilibrated by either the thrust force of the adjacent paraboloids or the applied longitudinal load at the top and bottom of the compression member. Consequently, the rises h_{yx} and h_{zx}, determining the magnitude of the longitudinal thrust force, can

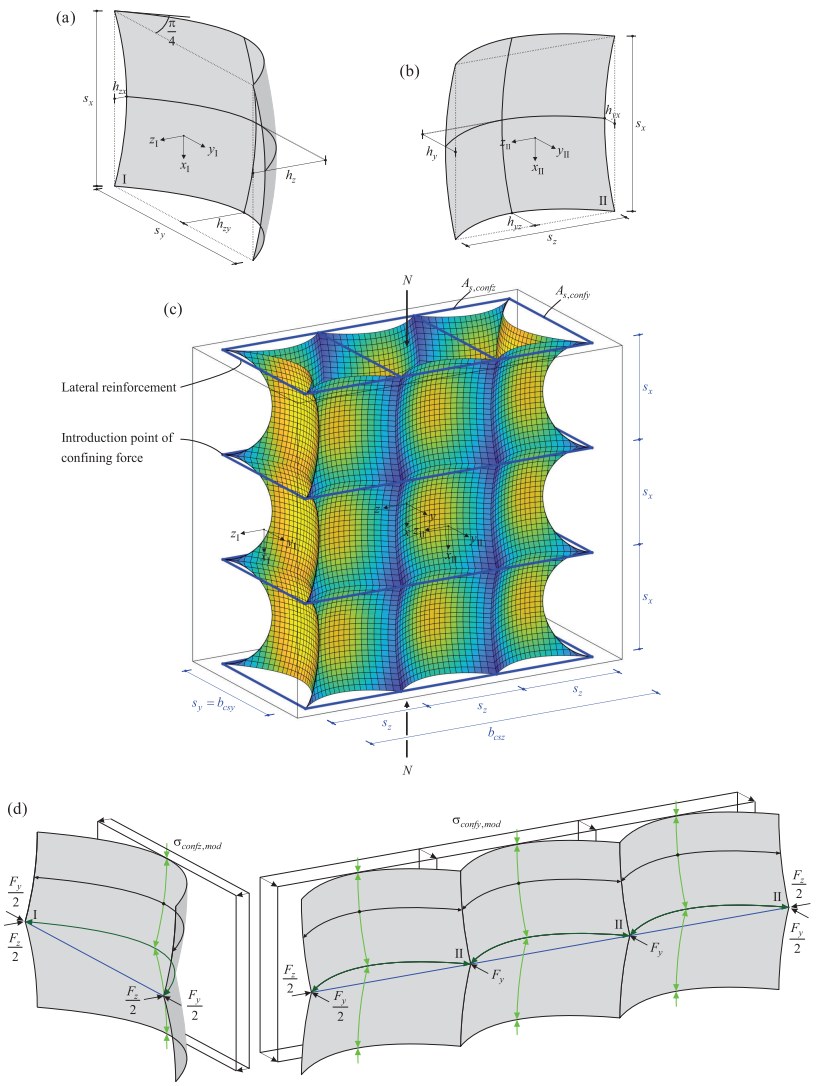

Fig. 2.4 - Definition of confined concrete volume in a rectangular compression member assuming s_x:s_z:s_y = 1:1:1.5: (a) definition of paraboloid I, (b) definition of paraboloid II, (c) triaxially confined concrete volume, and (d) force flow.

be assigned any value; this is the reason underlying the choice to define h_{yx} and h_{zx} as functions of the total heights of the paraboloids h_y and h_z, and the lateral parabola rises h_{yz} and h_{zy} (see Eqs. (2.19) and (2.20)). On the other hand, while the thrust of adjacent lateral parabolas is in equilibrium (under the assumptions made), similar to that in the longitudinal direction, the introduction of the confining forces at the edges of the compression member requires reinforcement to equilibrate the thrust force of the lateral parabolas. This situation is illustrated in Fig. 2.4d: Confining reinforcement in the z-direction generates confining stresses $\sigma_{confz,mod}$, and to equilibrate the thrust of the lateral parabola transferring these stresses to the edges, reinforcement in the y-direction is required. However, the same reinforcement in the y-direction generates the confining stresses $\sigma_{confy,mod}$. Accordingly, the outermost confining reinforcement legs in both directions cannot be fully utilised to generate confining stresses, as they must also resist the lateral thrust forces. Since the latter depend on the parabola rises h_{yz} and h_{zy}, these parameters affect both the confined concrete volume as well as the confining stresses: decreasing the rises results in a larger confined concrete volume, but reduces the confining stresses as more confining reinforcement is required to equilibrate the thrust force and vice versa. Theoretically, the optimum rises (h_{yz}, h_{zy}) in both lateral directions – maximising the product of confined area and confined concrete compressive strength, hence the load-bearing capacity of the compression member – could thus be sought, which could be interesting, e.g. in cases with different reinforcement spacings in the lateral directions. However, this is beyond the scope of this article, the initial inclination of the lateral parabolas is maintained at $\pi/4$. With these initial inclinations and equal reinforcement in both directions ($A_{s,confy} \cdot f_{sy,conf} = A_{s,confz} \cdot f_{sy,conf}$) – which applies e.g. in the common case of bent stirrups – equilibrium is fulfilled with the lateral thrust forces absorbing half of the confining force of the outermost stirrup leg in each lateral direction, leading to the following definition of the confining stresses:

$$\sigma_{confy,mod} = \frac{A_{s,confy} \cdot f_{sy,conf}}{s_x \cdot s_z} = \frac{F_y}{s_x \cdot s_z} \tag{2.21}$$

$$\sigma_{confz,mod} = \frac{A_{s,confz} \cdot f_{sy,conf}}{s_x \cdot s_y} = \frac{F_z}{s_x \cdot s_y} \tag{2.22}$$

In comparison to Eqs. (2.3) and (2.4), the confining stresses are thus reduced, since $b_{csy} = (n_{s,confy} - 1) \cdot s_y < n_{s,confy} \cdot s_y$ and $b_{csz} = (n_{s,confz} - 1) \cdot s_z < n_{s,confz} \cdot s_z$, where $n_{s,conf}$ = number of confining reinforcement legs per direction. For a compression member with rectangular cross-section and only one stirrup (two reinforcement legs), the reduction amounts to 50%. With increasing number of confining reinforcement legs the difference decreases (see Fig. 2.5).

Finally, to ensure a lower-bound solution according to the theory of plasticity, the concrete shells must be able to disperse the confining forces without infringing the yield condition, i.e., complying with the concrete compressive strength. As the paraboloids have been defined assuming an infinitesimally small thickness, this condition cannot be met strictly. However, it can be verified by checking that the required concrete shell dimensions are reasonably small, considering the distribution of the confining loads provided by the confining reinforcement's diameter and bends, as well as the longitudinal reinforcing bars. The lateral parabolas are subjected to the highest stresses and thus governing. Their required concrete cross-sectional area can be determined based on the uniaxial concrete compressive strength f_{c0} and the arch force required to transfer the confining forces. Assuming f_{c0} = 50 MPa and confining reinforcement with a diameter of 10 mm and a yield strength $f_{sy,conf}$ = 500 MPa, a cross-sectional area as small as

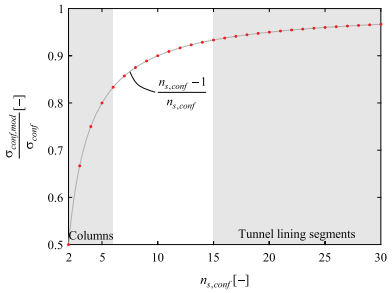

Fig. 2.5 - Comparison of the confining stresses resulting from determination with current guidelines (σ_{conf}) and the new model proposal ($\sigma_{conf,mod}$) depending on the number of confining reinforcement legs ($n_{s,conf}$).

approximately 20·20 mm² is sufficient. Hence, the assumption of an infinitesimally small thickness of the concrete shells appears appropriate. It can be further justified by observing that alternatively to the assumed force flow, it would be possible to directly disperse the confining forces both laterally as well as longitudinally (instead of prioritising the lateral direction), which would significantly decrease the thrust force of the lateral parabolas and thus the required cross-sectional area. Hence, the model can be classified as a mechanically consistent solution based on the lower-bound theorem of the theory of plasticity.

2.3.3 Governing confined concrete area

The triaxially confined concrete volume is illustrated in Fig. 2.4c. Accordingly, the confined concrete area is largest at the levels of the confining reinforcement and smallest in the cross-section at the centre between the confining reinforcement layers, which is thus governing. Fig. 2.6a and b illustrates these two sections with their dimensions. Fig. 2.6c indicates the different stress states in the governing section with patterns: plain = unconfined (uniaxial compression), lined = uniaxially confined (biaxial compression) and chequered = biaxially confined (triaxial compression). The compressive strength of biaxially loaded concrete is determined according to Vecchio [20] depending on the magnitude of the second non-zero compressive principal stress σ_2 (corresponding to the confining stresses $\sigma_{confy,mod}$ or $\sigma_{confz,mod}$):

$$f_{c,biax} = \left(1 + 0.92 \cdot \left(\frac{\sigma_2}{f_{c0}}\right) - 0.76 \cdot \left(\frac{\sigma_2}{f_{c0}}\right)^2\right) \cdot f_{c0} \tag{2.23}$$

Eq. (2.23) is based on the findings of Kupfer [21]. Determining the areas of the different regions shown in Fig. 2.6c is a straightforward but time-consuming task, involving the geometric parameters shown in Fig. 2.6b: first, the intersection points must be determined, followed by integration. This procedure has been implemented for the model validation, but is not elaborated further here as it is not suitable for engineering practice and guidelines. Instead, for the sake of simplicity, it is suggested to approximate the area of the governing confined concrete by the largest rectangle inscribed to $A_{conf,mod}$, which can

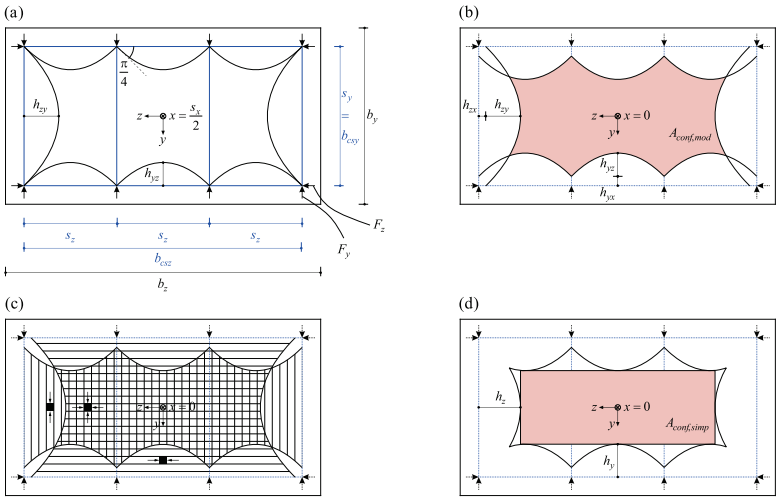

Fig. 2.6 - Different cross-sections of the compression member (Fig. 2.4) illustrating the confined concrete area according to the new model: (a) section at the level of the confining reinforcement (e.g. $x = s_x/2$), (b-d) sections at the centre between the confining reinforcement layers (e.g. $x = 0$), with (b,c) governing confined concrete area indicating (b) dimensions and (c) different stress states, and (d) simplified governing confined concrete area.

readily be defined as a function of the confining reinforcement geometry and spacing (Fig. 2.6d). The simplified confined concrete area $A_{conf,simp}$ and the effectiveness factor k_{simp} are thus:

$$A_{conf,simp} = \left(b_{csy} - 2 \cdot h_y\right) \cdot \left(b_{csz} - 2 \cdot h_z\right) = \left(b_{csy} - \frac{\sqrt{s_x^2 + s_z^2}}{2}\right) \cdot \left(b_{csz} - \frac{\sqrt{s_x^2 + s_y^2}}{2}\right) \tag{2.24}$$

$$k_{simp} = \frac{A_{conf,simp}}{A_{cs}} = \left(1 - \frac{\sqrt{s_x^2 + s_z^2}}{2 \cdot b_{csy}}\right) \cdot \left(1 - \frac{\sqrt{s_x^2 + s_y^2}}{2 \cdot b_{csz}}\right) \tag{2.25}$$

Eq. (2.24) is as simple to use as the expression of SIA 262 while accounting for both lateral as well as longitudinal confinement spacings more consistently than the approaches of EC 2 and MC 2010, which are more complicated to use.

2.3.4 Adjustment of model for circular cross-sections

Circular cross-sections with a diameter d_{cs} (instead of b_{csy} and b_{csz}) only require load dispersion of the confining forces in the longitudinal direction. Consequently, the governing confined concrete area ($A_{conf,mod,c}$) is obtained by setting the lateral reinforcement spacings s_y and s_z in Eq. (2.24) equal to zero:

$$A_{conf,mod,c} = \left(d_{cs} - \frac{s_x}{2} \right)^2 \cdot \frac{\pi}{4} \tag{2.26}$$

This formulation coincides with the formulation of EC 2 for circular cross-sections, representing longitudinal load dispersion by second-degree parabolic arches with an initial inclination of π/4. The thrust forces in the longitudinal direction can be equilibrated without any reinforcement, as pointed out in Section 2.3.2. Hence, the confining stresses for circular cross-sections can be determined by lateral equilibrium:

$$\sigma_{conf,c} = \frac{2 \cdot A_{s,conf} \cdot f_{sy,conf}}{s_x \cdot d_{cs}} \tag{2.27}$$

2.4 Comparison of the governing confined concrete areas

Fig. 2.7 compares the governing confined concrete area A_{conf} of rectangular cross-sections according to the new model (k_{mod}) and its simplification (k_{simp}) to those obtained from the EC 2 (k_{EC2}) and SIA 262 (k_{SIA262}) design approaches. The effectiveness factor k is used instead of A_{conf}, as this allows for a normalised comparison. To enhance the clarity of the plots, k_{MC2010} is omitted; note that it is always below k_{EC2} and k_{SIA262}, respectively.

The comparison is based on compression members with a square cross-section, plotting the effectiveness factors k against the longitudinal spacing s_x of the confining reinforcement. In Fig. 2.7a, the cross-section of the compression member varies, with the confining reinforcement comprising a single stirrup per layer in all cases. Conversely, in Fig. 2.7b, the cross-section of the compression member is constant, whereas the lateral spacings s_y and s_z of the confining reinforcement, hence also the number of confining reinforcement legs, vary.

Both plots show that the new model, its simplification and the design approach of EC 2 exhibit a similar behaviour in general. In most configurations, the new model yields the largest governing confined concrete area among these three approaches, with maximum differences of 25% and 30% compared to the simplified model and the EC 2 approach. The latter results in marginally larger areas only for small compression members with one stirrup per layer and a longitudinal spacing s_x >175 mm. A comparison of the simplified model to the EC 2 approach reveals that they match closely; for small longitudinal spacings s_x, the EC 2 approach yields somewhat larger areas, but this effect is reduced and even reversed with decreasing lateral spacings $s_y = s_z$: For lateral spacings < 150 mm, the simplified model always results in slightly larger areas than EC 2. The SIA 262 approach differs pronouncedly from the other three approaches since it only considers the longitudinal reinforcement spacing s_x. Significant differences thus occur for (i) small longitudinal spacings s_x in combination with large lateral spacings, where SIA 262 is unsafe, and (ii) for large longitudinal spacings s_x and small lateral spacings, where it is overly conservative.

For circular cross-sections, the approaches of EC 2, the new model and the simplification result in the same governing confined concrete area, while the SIA 262 approach always yields a smaller governing confined concrete area.

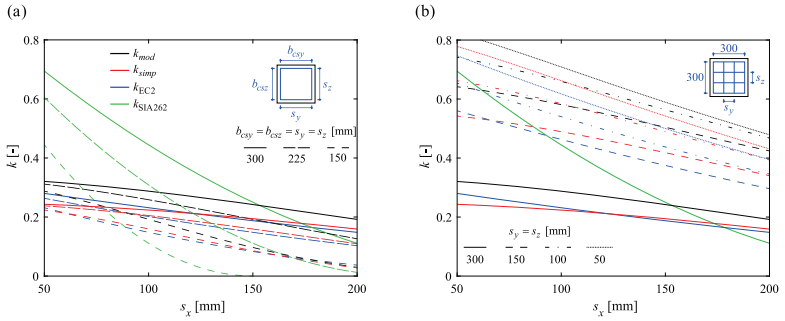

Fig. 2.7 - Comparison of the effectiveness factor k of the different model approaches: (a) RC member with one stirrup and varying cross-section and (b) RC member with fixed cross-section but varying reinforcement spacings.

2.5 Model validation with experimental data

This section validates the proposed model and its simplification against experimental data. The validation includes a further variation of the new model, referred to as *mixed model*. This model combines the confined concrete area A_{conf} according to the simplified model ($A_{conf,simp}$) with the confining stresses based on the approach of the current standards (Eqs. (2.3) and (2.4)), as this formulation is established in practice and could further enhance the ease of use of the new model (although sacrificing mechanical consistency).

Moccia et al. [15] compiled a database consisting of 264 RC specimens with confining reinforcement subjected to concentric compressive loading. The new model and its simplification differ from the approaches currently used in design practice mainly in the way that the confinement of rectangular cross-sections is considered. For this reason, only compression members with rectangular cross-section are used for the validation, reducing the data set to 193 specimens from 15 different authors [15], [22]-[35]; the details of all these specimens can be found in Appendix 2.A. The expected load-bearing capacity of a compression member is determined with Eq. (2.1). To meaningfully validate the confinement models, i.e., assess their prediction accuracy, it is essential that only experiments are considered for which no effects beyond those accounted for by Eq. (2.1) occur. One such effect is related to the treatment of the cover concrete: Eq. (2.1) considers only the concrete within the reinforcement but neglects the cover concrete (A_{cs} instead of A_c), but the tests in the data set had varying concrete cover thicknesses. In fact, current guidelines treat this aspect differently: While SIA 262 and MC 2010 neglect the cover concrete, EC 2 allocates the uniaxial concrete compressive strength to the concrete outside the confining reinforcement. The main debate in this context concerns the point at which the concrete cover begins to spall and no longer contributes to the load-bearing capacity. Fig. 2.8 investigates this matter by plotting the ratio of the experimentally observed load-bearing capacity ($N_{R,exp}$) to that predicted by current standards (N_R) against the ratio of the cover concrete area A_{cover} to the entire RC area A_c. In Fig. 2.8a, N_R was

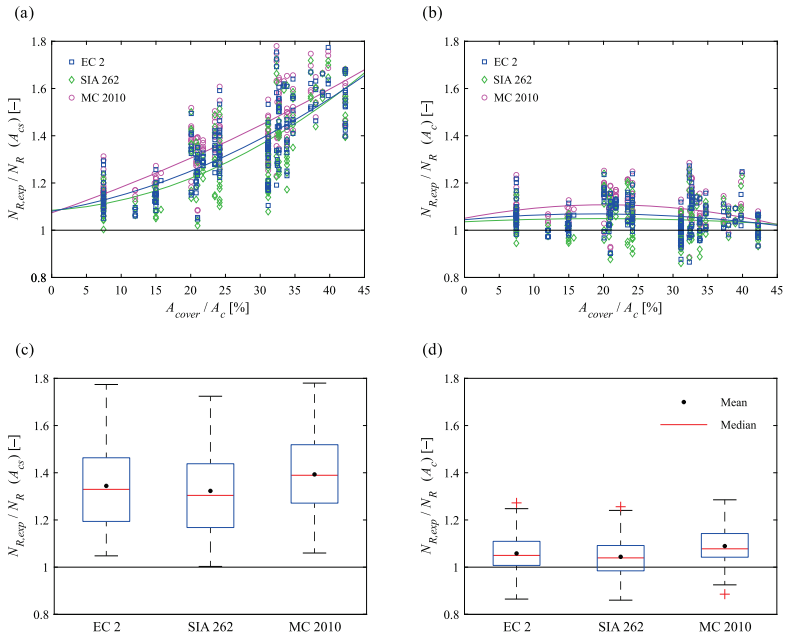

Fig. 2.8 - Impact of the cover concrete on the load-bearing capacity prediction N_R of current standards (EC 2, SIA 262 and MC 2010) and comparison with experimental results (193 specimens): (a) cover concrete neglected, (b) cover concrete considered with uniaxial concrete compressive strength, (c) box plot associated with (a), and (d) box plot associated with (b).

determined according to Eq. (2.1) (as in all approaches neglecting the cover concrete) while in Fig. 2.8b A_c instead of A_{cs} was inserted into Eq. (2.1) (following the EC 2 approach). Fig. 2.8a indicates that the cover concrete indeed contributes to the ultimate load: with increasing cover concrete the model predictions become more conservative considering only A_{cs}. However, Fig. 2.8b illustrates that fully considering the cover concrete overestimates the load-bearing capacity for several experimental results and may thus be unsafe. Fig. 2.8c and d shows the box plots associated with Fig. 2.8a and b, confirming these observations. Note that the ratios of the experimental results to the model predictions would be reduced if η_{cc} in Eq. (2.1) was defined as $(40/f_{c0})^{(1/3)} \leq 1$, (i.e., assuming that a brittleness factor is required for $f_{c0} > 40$ MPa instead of 30 MPa).

A further discussion of the treatment of the cover concrete is beyond the scope of this article. However, based on the findings the data set for the model validation is significantly reduced in order to minimise the effect of varying concrete cover thickness: only specimens where the cover concrete accounts for a maximum of 15% of the total cross-sectional area (A_c) are considered. This still ensures a representative data set with 40 specimens of the initial database (marked in the list of all 193 tests in Appendix 2.A), allowing for a meaningful validation of the confinement models. Consequently, the load-bearing

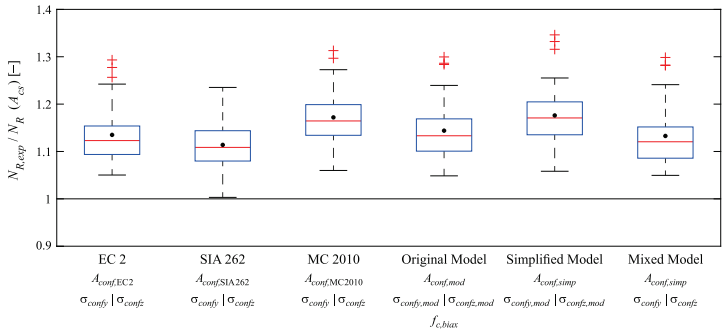

Fig. 2.9 - Comparison of the different models with the experimental data (40 specimens).

capacity of the different models is determined according to Eq. (2.1) accounting only for the concrete within the reinforcement (A_{cs}).

Fig. 2.9 summarises the comparison of the different model predictions to the experimental data by means of box plots. Besides the three approaches from current standards (EC 2, SIA 262, MC 2010), the new model and its two variants (Original Model, Simplified Model and the Mixed Model) are validated. Below each box plot, Fig. 2.9 indicates how the confined concrete area A_{conf} and the confining stresses (σ_{conf}) were determined; note that the impact of the biaxially stressed areas was considered in the original model. However, the effect of considering biaxially stressed areas is less than 3% of the predicted load-bearing capacity.

Fig. 2.9 indicates that all models provide a similarly good agreement between experimentally determined and predicted load-bearing capacities (mean values $N_{R,exp}/N_R(A_{cs})$ between 1.11 and 1.18). Consequently, the new model and its variations are successfully validated against experimental data.

MC 2010 proves to be the most conservative, and SIA 262 the least conservative of the three current guidelines. Of the new models, the simplified model shows, as expected, the most conservative predictions, but it is still within a satisfactory range. The original and mixed models exhibit hardly any differences and are similar to EC 2, with the mixed model standing out by its ease of use. Appendix 2.B lists the comparison of the experimental data with the model predictions for all models, both with and without consideration of the cover concrete and the most important statistical parameters.

2.6 Conclusions

Several models exist to consider the beneficial effect of confining reinforcement for RC members subjected to compressive loading. However, the current approaches do not consider the three-dimensional load dispersion of the confining forces in a mechanically consistent way. By introducing a new model, this article contributes to bridging this gap. The new model accounts for the three-dimensional force

flow and considers equilibrium and the yield conditions, thereby corresponding to a lower-bound solution according to the theory of plasticity.

The new model is compared to current design approaches for the confinement of RC structures and is successfully validated against experimental data. Compared to existing design approaches (EC 2, SIA 262, and MC 2010), the new model has several key advantages: (i) the confining reinforcement spacings in lateral and longitudinal directions are considered coherently, (ii) the model builds on a mechanical basis, (iii) it provides a solution that allows following the force flow, and (iv) the model can consistently explain the confining behaviour of rectangular and circular cross-sections. While the new model is mechanically consistent and improves the understanding of the behaviour of confined concrete, it is of limited use for engineering practice due to the complexity of determining the governing confined concrete area. By simplifying the determination of the governing confined concrete area, it was possible to present a model adaptation that can be successfully validated against experimental data and is even easier to apply than the existing models in current guidelines, proving to be a valuable alternative for design practice.

Acknowledgements

This study was partially funded by the Swiss Federal Roads Office and the Swiss Federal Office of Transport (Project AGT 2019/001).

Appendix 2.A Experimental data used for validation

Table 2.A.1 - Experimental data used for validation. See Fig. 2.A.1 for definition of stirrup type.

Authors	Specimen	f_{c0}	b_y=b_z	c_{nom}	b_{csy} = b_{csz}	$f_{sy,l}$	$A_{s,l}$	Stirrup type	$f_{sy,conf}$	$Ø_{conf}$	$\sum A_{s,conf}$	s_x	s_y=s_z	$N_{R,exp}$
		[MPa]	[mm]	[mm]	[mm]	[MPa]	[mm²]	[-]	[MPa]	[mm]	[mm²]	[mm]	[mm]	[kN]
Shin, Yoon, Cook, Mitchell 2016	C-NT-6.1	200	220	15	181	498	1588	diamond	549.5	9.5	242	40	90	7610
	D-NT-6.1	200	220	15	181	480	1520	multiple	549.5	9.5	284	47	60	7720
	C-HT-6.1	185	220	15	179	498	1588	diamond	806	11	324	50	90	7544
	D-HT-6.1	185	220	15	181	480	1520	multiple	786.9	9.2	266	42	60	7590
	C-HT-4.4	200	220	15	181	498	1588	diamond	786.9	9.2	227	50	90	7637
	D-HT-4.4	200	220	15	181	480	1520	multiple	786.9	9.2	266	58	60	6924
	C-NT-6.1-HL	200	220	15	181	642	1588	diamond	549.5	9.5	242	40	90	8049
	C-HT-4.4-HL	200	220	15	181	642	1588	diamond	786.9	9.2	227	50	90	7198
Shin, Yoon, Cook, Mitchell 2015	200-A1	200	220	15	181	498	1588	square	549.5	9.5	142	40	181	6898
	200-B1	200	220	15	181	498	1588	multiple	549.5	9.5	213	40	90	8009
	200-C1	200	220	15	181	498	1588	diamond	549.5	9.5	242	35	90	7301
	200-D1	200	220	15	181	480	1520	multiple	549.5	9.5	284	35	60	7503
	200-A2	200	220	15	181	498	1588	square	549.5	9.5	142	23	181	7231
	200-B2	200	220	15	181	498	1588	multiple	549.5	9.5	213	35	90	8002
	50-B1	70	220	15	181	498	1588	multiple	549.5	9.5	213	100	90	3634
	100-B1	111	220	15	181	498	1588	multiple	549.5	9.5	213	60	90	5531
	50-A1	70	220	15	181	498	1588	square	549.5	9.5	142	40	181	4182
	100-A1	111	220	15	181	498	1588	square	549.5	9.5	142	40	181	5402
Saatcioglu, Razvi 1998	CS-1	124	250	10	219	450	804	square	400	11.3	201	55	219	6040
	CS-2	124	250	10	224	450	1608	multiple	570	6.5	100	55	112	6597
	CS-3	124	250	10	224	450	2413	multiple	570	6.5	133	55	75	7402
	CS-4	124	250	10	223	450	1608	multiple	1000	7.5	133	55	111	6631
	CS-5	124	250	10	223	450	2413	multiple	1000	7.5	177	120	74	6849
	CS-6	124	250	10	224	450	1608	multiple	400	6.5	100	85	112	6927
	CS-7	124	250	10	224	450	2413	multiple	400	6.5	133	120	75	6910
	CS-8	124	250	10	219	450	1608	multiple	400	11.3	301	85	109	6165
	CS-9	124	250	10	219	450	2413	multiple	400	11.3	401	120	73	7177
	CS-11	81	250	10	219	450	804	square	400	11.3	201	40	219	4856
	CS-12	81	250	10	219	450	804	square	400	11.3	201	55	219	4366
	CS-13	92	250	10	224	450	1608	multiple	570	6.5	100	55	112	4874
	CS-14	92	250	10	224	450	2413	multiple	570	6.5	133	55	75	5561
	CS-15	81	250	10	223	450	1608	multiple	1000	7.5	133	55	111	5296
	CS-16	81	250	10	223	450	2413	multiple	1000	7.5	177	85	74	5578
	CS-17	81	250	10	224	450	1608	multiple	400	6.5	100	85	112	5242
	CS-18	81	250	10	224	450	2413	multiple	400	6.5	133	85	75	5536
	CS-19	92	250	10	219	450	1608	multiple	400	11.3	301	85	109	5536
	CS-20	92	250	10	219	450	2413	multiple	400	11.3	401	85	73	5911
	CS-22	60	250	10	223	450	1608	multiple	1000	7.5	133	85	111	4322
	CS-23	60	250	10	223	450	2413	multiple	1000	7.5	177	120	74	4790
	CS-24	60	250	10	219	450	1608	multiple	400	11.3	301	85	109	4763
	CS-25	60	250	10	219	450	2413	multiple	400	11.3	401	120	73	4996
	CS-26	60	250	10	224	450	2413	multiple	570	6.5	133	55	75	5365

Only **bold values** are considered for model validation.

Table 2.A.1 - Continued.

Authors	Specimen	f_{c0}	b_y=b_z	c_{nom}	b_{csy} = b_{csz}	$f_{sy,l}$	$A_{s,l}$	Stirrup type	$f_{sy,conf}$	$Ø_{conf}$	$\sum A_{s,conf}$	s_x	s_y=s_z	$N_{R,exp}$
		[MPa]	[mm]	[mm]	[mm]	[MPa]	[mm²]	[-]	[MPa]	[mm]	[mm²]	[mm]	[mm]	[kN]
Li 1994	1A	60	240	12.5	209	443	452	square	445	6	57	20	209	3475
	2A	60	240	12.5	209	443	905	diamond	445	6	97	20	105	4375
	4A	60	240	12.5	209	443	452	square	445	6	57	35	209	3225
	5A	60	240	12.5	209	443	905	diamond	445	6	97	35	105	3725
	7A	60	240	12.5	209	443	452	square	445	6	57	50	209	3350
	8A	60	240	12.5	209	443	905	diamond	445	6	97	50	105	3575
	10A	60	240	12.5	209	443	452	square	445	6	57	65	209	3325
	11A	60	240	12.5	209	443	905	diamond	445	6	97	65	105	3550
	1B	72	240	12.5	209	443	452	square	445	6	57	20	209	3725
	2B	72	240	12.5	209	443	905	diamond	445	6	97	20	105	5100
	4B	72	240	12.5	209	443	452	square	445	6	57	35	209	3950
	5B	72	240	12.5	209	443	905	diamond	445	6	97	35	105	4000
	7B	72	240	12.5	209	443	452	square	445	6	57	50	209	4200
	8B	72	240	12.5	209	443	905	diamond	445	6	97	50	105	4000
	10B	72	240	12.5	209	443	452	square	445	6	57	65	209	4000
	11B	72	240	12.5	209	443	905	diamond	445	6	97	65	105	4150
Cusson, Paultre 1994	1A	95	235	15.3	195	406	1195	square	410	9.5	142	50	195	4244
	1B	95	235	16.1	195	450	1205	diamond	392	7.9	167	50	98	4679
	1C	95	235	16.1	195	450	1203	octagon	392	7.9(2)	167	50	65	4716
	1D	100	235	16.1	195	450	1203	multiple	392	7.9	196	50	65	5001
	2A	96	235	16.1	195	406	1195	square	392	7.9	98	50	195	4657
	2B	96	235	16.8	195	450	1205	diamond	414	6.4	110	50	98	4388
	2C	96	235	16.8	195	450	1203	octagon	414	6.4(2)	110	50	65	4525
	2D	96	235	16.8	195	450	1203	multiple	414	6.4	129	50	65	4635
	3A	98	235	15.3	195	406	1195	square	410	9.5	142	100	195	4371
	3B	98	235	15.3	195	450	1205	diamond	410	9.5	242	100	98	4410
	3C	98	235	15.3	195	450	1203	octagon	410	9.5(2)	242	100	65	4499
	3D	98	235	15.3	195	450	1203	multiple	410	9.5	284	100	65	4661
	4A	93	235	15.3	195	420	1995	square	410	9.5	142	50	195	4606
	4B	93	235	16.1	195	424(1)	1999	diamond	392	7.9	167	50	98	4882
	4C	93	235	16.1	195	424(1)	1997	octagon	392	7.9(2)	167	50	65	4864
	4D	93	235	16.1	195	424(1)	1997	multiple	392	7.9	196	50	65	4863
	5A	100	235	15.3	195	420	1995	square	705	9.5	142	50	195	4728
	5B	100	235	16.1	195	424(1)	1999	diamond	770	7.9	167	50	98	5037
	5C	100	235	16.1	195	424(1)	1997	octagon	770	7.9(2)	167	50	65	5214
	5D	100	235	16.1	195	424(1)	1997	multiple	770	7.9	196	50	65	5457
	6B	116	235	15.3	195	463(1)	1999	diamond	715	9.5	242	50	98	5395
	6D	114	235	16.1	195	476(1)	1997	multiple	680	7.9	196	50	65	5545
	7B	76	235	15.3	195	463(1)	1999	diamond	715	9.5	242	50	98	4954
	7D	68	235	16.1	195	476(1)	1997	multiple	680	7.9	196	50	65	4701
	8B	53	235	15.3	195	463(1)	1999	diamond	715	9.5	242	50	98	4530
	8D	56	235	16.1	195	476(1)	1997	multiple	680	7.9	196	50	65	4532

(1) Weighted average of yield stress due to two different reinforcement types (cross-section and yield stress vary).
(2) To compute the confining stresses $\sigma_{conf,mod}$, $Ø_{conf}$ has to be multiplied by $\sqrt{2}/2$ to ensure introducing equal confining forces.
Only **bold values** are considered for model validation.

Table 2.A.1 - Continued.

Authors	Specimen	f_{c0}	b_y=b_z	c_{nom}	b_{csy} = b_{csz}	$f_{sy,l}$	$A_{s,l}$	Stirrup type	$f_{sy,conf}$	$Ø_{conf}$	$\sum A_{s,conf}$	s_x	s_y=s_z	$N_{R,exp}$
		[MPa]	[mm]	[mm]	[mm]	[MPa]	[mm²]	[-]	[MPa]	[mm]	[mm²]	[mm]	[mm]	[kN]
Sharma, Bhargava, Kaushik 2005	SA	62	150	10	122	395	452	square	412	8	101	50	122	1334
	SB	63	150	10	122	395	452	square	412	8	101	75	122	1364
	SC	62	150	10	122	395	452	square	520	8	101	50	122	1308
	SD	63	150	10	122	395	905	diamond	412	8	172	50	61	1626
	SE	83	150	10	122	395	452	square	412	8	101	30	122	1641
	SF	82	150	10	122	395	452	square	412	8	101	50	122	1604
	SG	83	150	10	122	395	452	square	412	8	101	75	122	1730
	SH	82	150	10	122	395	452	square	520	8	101	50	122	1621
	SI	83	150	10	122	395	905	diamond	412	8	172	50	61	1819
Scott, Park, Priestley 1982	2	25	450	20	400	434	3770	octagon	309	10(2)	268	72	133	7070
	3	25	450	20	400	434	3770	octagon	309	10(2)	268	72	133	8410
	6	25	450	20	400	394	3619	diamond	309	10	268	72	200	6720
	7	25	450	20	400	394	3619	diamond	309	10	268	72	200	7850
	12	25	450	20	400	434	3770	octagon	309	10(2)	268	98	133	8500
	13	25	450	20	400	434	3770	octagon	309	10(2)	268	72	133	8650
	14	25	450	20	398	434	3770	octagon	296	12(2)	386	88	133	8800
	15	25	450	20	398	434	3770	octagon	296	12(2)	386	64	133	9400
	17	25	450	20	400	394	3619	diamond	309	10	268	98	200	7900
	18	25	450	20	400	394	3619	diamond	309	10	268	72	200	8500
	19	25	450	20	398	394	3619	diamond	296	12	386	88	199	8400
	20	25	450	20	398	394	3619	diamond	296	12	386	64	199	8800
	22	24	450	20	400	272	3770	octagon	309	10(2)	268	98	133	7300
	23	24	450	20	400	272	3770	octagon	309	10(2)	268	72	133	7450
	24	24	450	20	398	272	3770	octagon	309	12(2)	386	88	133	7800
	25	24	450	20	398	272	3770	octagon	309	12(2)	386	64	133	8500
Sun, Oba, Tian, Ikeda 1996	**NA6-20**	**53**	**200**	**4.6**	**184**	**362**	**1062**	**square**	**342**	**6.4**	**64**	**20**	**184**	**2590**
	NA6-30	**53**	**200**	**4.6**	**184**	**362**	**1062**	**square**	**342**	**6.4**	**64**	**30**	**184**	**2372**
	NA10-47	53	200	3.4	184	362	1062	square	344	9.6	145	47	184	2426
	NB6-35	**53**	**200**	**4.6**	**184**	**362**	**1062**	**diamond**	**342**	**6.4**	**110**	**35**	**92**	**2519**
	NB6-50	**53**	**200**	**4.6**	**184**	**362**	**1062**	**diamond**	**342**	**6.4**	**110**	**50**	**92**	**2430**
	NB10-75	**53**	**200**	**2.9**	**185**	**362**	**1062**	**diamond**	**344**	**9.6**	**247**	**75**	**92**	**2514**
	NC6-30	**53**	**200**	**4.6**	**184**	**362**	**1062**	**multiple**	**342**	**6.4**	**97**	**30**	**92**	**2489**
	NC6-43	**53**	**200**	**4.6**	**184**	**362**	**1062**	**multiple**	**342**	**6.4**	**97**	**43**	**92**	**2421**
	NC10-70	**53**	**200**	**2.9**	**185**	**362**	**1062**	**multiple**	**344**	**9.6**	**217**	**70**	**92**	**2421**
	ND6-47	**53**	**200**	**4.6**	**184**	**362**	**1593**	**multiple**	**342**	**6.4**	**129**	**47**	**61**	**2671**
	ND6-70	**53**	**200**	**4.6**	**184**	**362**	**1593**	**multiple**	**342**	**6.4**	**129**	**70**	**61**	**2543**
	NE6-40	**53**	**200**	**4.6**	**184**	**362**	**1593**	**multiple**	**342**	**6.4**	**129**	**40**	**61**	**2680**
	NE6-60	**53**	**200**	**4.6**	**184**	**362**	**1593**	**multiple**	**342**	**6.4**	**129**	**60**	**61**	**2666**
	NBM-60	**53**	**200**	**1.4**	**188**	**362**	**1062**	**diamond**	**344**	**9.6**	**247**	**60**	**94**	**2571**
	NBM-75	**53**	**200**	**1.4**	**188**	**362**	**1062**	**diamond**	**344**	**9.6**	**247**	**75**	**94**	**2377**
	NCM-60	**53**	**200**	**1.4**	**188**	**362**	**1062**	**multiple**	**344**	**9.6**	**217**	**60**	**94**	**2435**
	NCM-75	**53**	**200**	**1.4**	**188**	**362**	**1062**	**multiple**	**344**	**9.6**	**217**	**75**	**94**	**2391**

(2) To compute the confining stresses $\sigma_{conf,mod}$, $Ø_{conf}$ has to be multiplied by √2/2 to ensure introducing equal confining forces.
Only **bold values** are considered for model validation.

Table 2.A.1 - Continued.

Authors	Specimen	f_{c0}	b_y=b_z	c_{nom}	b_{csy} = b_{csz}	$f_{sy,l}$	$A_{s,l}$	Stirrup type	$f_{sy,conf}$	$Ø_{conf}$	$\sum A_{s,conf}$	s_x	s_y=s_z	$N_{R,exp}$
		[MPa]	[mm]	[mm]	[mm]	[MPa]	[mm²]	[-]	[MPa]	[mm]	[mm²]	[mm]	[mm]	[kN]
Hwee, Rangan 1990	1	59	150	15	114	430	452	square	355	6	57	50	114	1250
	2	61	150	15	114	430	452	square	355	6	57	100	114	1253
	3	61	150	15	114	430	452	square	355	6	57	150	114	1340
	4	61	150	15	114	440	804	square	355	6	57	50	114	1389
	5	62	150	15	114	440	804	square	355	6	57	100	114	1389
	6	62	150	15	114	440	804	square	355	6	57	150	114	1370
	7	68	150	15	114	430	452	square	355	6	57	50	114	1400
	8	68	150	15	114	430	452	square	355	6	57	100	114	1420
	9	68	150	15	114	430	452	square	355	6	57	150	114	1422
	10	68	150	15	114	440	804	square	355	6	57	50	114	1615
	11	68	150	15	114	440	804	square	355	6	57	100	114	1518
	12	68	150	15	114	440	804	square	355	6	57	150	114	1381
Rangan, Saunders, Seng 1991	RC-1	65	160	15	126	430	452	square	450	4	25	100	126	1557
	RC-2	65	160	15	126	430	452	square	450	4	25	100	126	1495
	RC-4	65	160	15	125	430	452	square	450	5	39	200	125	1515
	RC-5	65	160	15	126	430	452	square	450	4	25	50	126	1453
	RC-7	65	160	15	124	430	452	square	450	6	57	200	124	1820
	RC-8	65	160	15	126	430	452	square	450	4	25	50	126	1620
	RC-9	65	160	15	125	430	452	square	450	5	39	100	125	1520
	RC-10	65	160	15	125	430	452	square	450	5	39	150	125	1595
Parvez, Foster, Valipour, McGregor 2017	2H0-70S-NS-1	105	200	15	165	520	905	square	810	5.5	48	70	165	3144
	2H0-70S-NS-2	115	200	15	165	520	905	square	810	5.5	48	70	165	4171
	2H0-120D-NS-1	105	200	15	165	520	905	diamond	810	5.5	81	120	82	2826
	2H0-120D-NS-2	115	200	15	165	520	905	diamond	810	5.5	81	120	82	3934
	2H0-70S-HS	115	200	15	165	650	719	square	810	5.5	48	70	165	4271
Khalajestani, Parvez, Foster, Valipour, McGregor 2018	1.8H0-70S-HS	110	200	15	165	670	719	square	810	5.5	48	70	165	4271
Moccia, Kubski, Fernandez, Muttoni 2020	CM1A0	35	250	20	202	531	314	square	496	8	101	150	202	2282
	CM1A2	35	250	20	202	531	314	square	496	8	101	150	202	2436
	CM1B0	35	250	20	198	531	314	square	531	12	226	150	198	2353
	CM1B1	35	250	20	198	531	314	square	531	12	226	150	198	2340
	CM1B2	35	250	20	198	531	314	square	531	12	226	150	198	2581
	CM1B3	35	250	20	198	531	314	square	531	12	226	150	198	2506
	CM1C0	35	250	20	194	531	314	square	474	16	402	150	194	2410
	CM1C1	35	250	20	194	531	314	square	474	16	402	150	194	2511
	CM1C2	35	250	20	194	531	314	square	474	16	402	150	194	2723
	CM1C3	35	250	20	194	531	314	square	474	16	402	150	194	2486

Only **bold values** are considered for model validation.

Table 2.A.1 - Continued.

Authors	Specimen	f_{c0}	$b_y=b_z$	c_{nom}	b_{csy} = b_{csz}	$f_{sy,l}$	$A_{s,l}$	Stirrup type	$f_{sy,conf}$	$Ø_{conf}$	$\sum A_{s,conf}$	s_x	$s_y=s_z$	$N_{R,exp}$
		[MPa]	[mm]	[mm]	[mm]	[MPa]	[mm²]	[-]	[MPa]	[mm]	[mm²]	[mm]	[mm]	[kN]
Al-Hussaini, Regan, Xue, Ramdane 1993	C12	101	250	20	204	549	1257	square	353	6	57	200	204	5500
	C13	100	250	20	202	472	1963	square	318	8	101	250	202	5500
	C14	106	250	20	202	472	3927	square	318	8	101	50	202	6616
	C21	89	250	20	204	559	452	square	353	6	57	70	204	4625
	C22	98	250	20	202	549	1257	square	318	8	101	50	202	5625
	C23	104	250	20	202	514	1608	square	318	8	101	50	202	5500
	C24	89	250	20	202	472	1963	square	318	8	101	50	202	4875
Fang, Hong, Wu 1994	**HA1-1**	**73**	**250**	**0**	**241**	**489**	**1140**	**square**	**310**	**9.5**	**142**	**50**	**241**	**4415**
	HA1-2	**79**	**250**	**0**	**241**	**489**	**1140**	**square**	**310**	**9.5**	**142**	**50**	**241**	**4326**
	HA2-1	**76**	**250**	**0**	**241**	**489**	**1140**	**square**	**310**	**9.5**	**142**	**62.5**	**241**	**4493**
	HA2-2	**76**	**250**	**0**	**241**	**489**	**1140**	**square**	**310**	**9.5**	**142**	**62.5**	**241**	**4331**
	HA3-1	**73**	**250**	**0**	**241**	**489**	**1140**	**square**	**310**	**9.5**	**142**	**125**	**241**	**4150**
	HA3-2	**79**	**250**	**0**	**241**	**489**	**1140**	**square**	**310**	**9.5**	**142**	**125**	**241**	**4047**
	MA1-1	**44**	**250**	**0**	**241**	**489**	**1140**	**square**	**310**	**9.5**	**142**	**50**	**241**	**3567**
	MA1-2	**57**	**250**	**0**	**241**	**489**	**1140**	**square**	**310**	**9.5**	**142**	**50**	**241**	**3836**
	MA2-1	**49**	**250**	**0**	**241**	**489**	**1140**	**square**	**310**	**9.5**	**142**	**62.5**	**241**	**3983**
	MA2-2	**49**	**250**	**0**	**241**	**489**	**1140**	**square**	**310**	**9.5**	**142**	**62.5**	**241**	**3934**
	MA3-1	**44**	**250**	**0**	**241**	**489**	**1140**	**square**	**310**	**9.5**	**142**	**125**	**241**	**3488**
	MA3-2	**57**	**250**	**0**	**241**	**489**	**1140**	**square**	**310**	**9.5**	**142**	**125**	**241**	**3782**
	HB1-3	**67**	**250**	**0**	**241**	**476**	**1588**	**multiple**	**310**	**9.5**	**213**	**62.5**	**120**	**4694**
	HB1-4	**63**	**250**	**0**	**241**	**476**	**1588**	**multiple**	**310**	**9.5**	**213**	**62.5**	**120**	**4522**
	HB2-3	**67**	**250**	**0**	**241**	**476**	**1588**	**multiple**	**310**	**9.5**	**213**	**90**	**120**	**4493**
	HB2-4	**63**	**250**	**0**	**241**	**476**	**1588**	**multiple**	**310**	**9.5**	**213**	**90**	**120**	**4209**
	HB3-1	**80**	**250**	**0**	**241**	**489**	**2280**	**multiple**	**310**	**9.5**	**213**	**125**	**120**	**4797**
	HB3-2	**67**	**250**	**0**	**241**	**489**	**2280**	**multiple**	**310**	**9.5**	**213**	**125**	**120**	**4655**
	MB1-3	**53**	**250**	**0**	**241**	**476**	**1588**	**multiple**	**310**	**9.5**	**213**	**62.5**	**120**	**4287**
	MB1-4	**53**	**250**	**0**	**241**	**476**	**1588**	**multiple**	**310**	**9.5**	**213**	**62.5**	**120**	**4052**
	MB2-3	**53**	**250**	**0**	**241**	**476**	**1588**	**multiple**	**310**	**9.5**	**213**	**90**	**120**	**3944**
	BM2-4	**53**	**250**	**0**	**241**	**476**	**1588**	**multiple**	**310**	**9.5**	**213**	**90**	**120**	**3934**
	MB3-1	**68**	**250**	**0**	**241**	**489**	**2280**	**multiple**	**310**	**9.5**	**213**	**125**	**120**	**4513**
	MB3-2	**70**	**250**	**0**	**241**	**489**	**2280**	**multiple**	**310**	**9.5**	**213**	**125**	**120**	**4542**

Only **bold values** are considered for model validation.

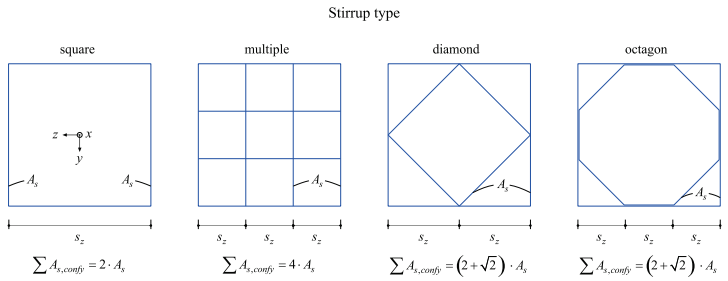

Fig. 2.A.1 - Definition of stirrup types.

Appendix 2.B Comparison of model predictions with experimental data

Table 2.B.1 - Comparison of model predictions with experimental data.

Authors	Specimen	$N_{R,exp}/N_R(A_{cs})$						$N_{R,exp}/N_R(A_c)$					
		EC 2	SIA 262	MC 2010	Original	Simp	Mixed	EC 2	SIA 262	MC 2010	Original	Simp	Mixed
Shin, Yoon, Cook, Mitchell 2016	C-NT-6.1	1.44	1.39	1.52	1.51	1.59	1.44	1.09	1.07	1.14	1.13	1.18	1.09
	D-NT-6.1	1.44	1.46	1.54	1.45	1.52	1.42	1.10	1.11	1.16	1.10	1.14	1.08
	C-HT-6.1	1.34	1.32	1.48	1.43	1.53	1.33	1.04	1.03	1.12	1.09	1.15	1.03
	D-HT-6.1	1.27	1.29	1.39	1.30	1.38	1.25	1.01	1.01	1.08	1.02	1.07	0.99
	C-HT-4.4	1.44	1.42	1.54	1.50	1.58	1.43	1.09	1.08	1.15	1.13	1.18	1.09
	D-HT-4.4	1.28	1.33	1.40	1.28	1.35	1.26	0.98	1.01	1.05	0.98	1.02	0.96
	C-NT-6.1-HL	1.46	1.41	1.54	1.53	1.60	1.46	1.12	1.09	1.16	1.16	1.20	1.12
	C-HT-4.4-HL	1.30	1.28	1.39	1.35	1.42	1.29	1.00	0.99	1.05	1.03	1.07	0.99
Shin, Yoon, Cook, Mitchell 2015	200-A1	1.56	1.41	1.59	1.57	1.63	1.57	1.13	1.05	1.14	1.14	1.17	1.13
	200-B1	1.56	1.51	1.64	1.59	1.67	1.56	1.17	1.15	1.22	1.19	1.24	1.17
	200-C1	1.33	1.26	1.40	1.41	1.49	1.33	1.02	0.98	1.06	1.07	1.11	1.02
	200-D1	1.26	1.25	1.35	1.29	1.36	1.25	0.98	0.97	1.03	1.00	1.04	0.97
	200-A2	1.52	1.24	1.55	1.56	1.66	1.55	1.12	0.96	1.14	1.15	1.20	1.14
	200-B2	1.50	1.44	1.58	1.55	1.63	1.51	1.14	1.10	1.18	1.17	1.22	1.14
	50-B1	1.34	1.40	1.43	1.33	1.38	1.32	1.02	1.06	1.08	1.02	1.04	1.01
	100-B1	1.52	1.53	1.62	1.53	1.60	1.51	1.16	1.17	1.22	1.17	1.21	1.15
	50-A1	1.50	1.29	1.55	1.53	1.61	1.52	1.15	1.02	1.18	1.17	1.22	1.17
	100-A1	1.61	1.41	1.65	1.63	1.70	1.62	1.20	1.09	1.22	1.21	1.25	1.21
Saatcioglu, Razvi 1998	CS-1	1.40	1.29	1.43	1.41	1.46	1.41	1.11	1.04	1.13	1.11	1.14	1.11
	CS-2	1.34	1.33	1.38	1.35	1.38	1.34	1.12	1.11	1.14	1.13	1.15	1.12
	CS-3	1.36	1.36	1.40	1.36	1.39	1.35	1.15	1.16	1.19	1.16	1.18	1.15
	CS-4	1.21	1.18	1.27	1.23	1.29	1.20	1.02	1.00	1.07	1.04	1.08	1.02
	CS-5	1.31	1.37	1.39	1.29	1.33	1.29	1.10	1.14	1.15	1.08	1.11	1.09
	CS-6	1.49	1.50	1.52	1.49	1.51	1.49	1.24	1.24	1.25	1.24	1.25	1.23
	CS-7	1.41	1.43	1.43	1.40	1.41	1.40	1.17	1.19	1.19	1.17	1.18	1.17
	CS-8	1.28	1.30	1.34	1.28	1.32	1.27	1.04	1.05	1.08	1.04	1.06	1.03
	CS-9	1.42	1.49	1.50	1.40	1.44	1.41	1.16	1.21	1.22	1.15	1.17	1.15
	CS-11	1.36	1.14	1.39	1.39	1.47	1.38	1.10	0.95	1.12	1.12	1.17	1.11
	CS-12	1.28	1.15	1.31	1.29	1.35	1.29	1.02	0.94	1.04	1.03	1.07	1.03
	CS-13	1.15	1.14	1.18	1.16	1.19	1.15	0.97	0.96	0.99	0.98	1.00	0.97
	CS-14	1.16	1.17	1.21	1.17	1.20	1.15	0.99	1.00	1.03	1.00	1.02	0.99
	CS-15	1.16	1.13	1.23	1.18	1.25	1.15	0.99	0.97	1.05	1.01	1.06	0.99
	CS-16	1.18	1.24	1.28	1.17	1.22	1.16	1.02	1.06	1.09	1.01	1.05	1.00
	CS-17	1.41	1.42	1.44	1.41	1.43	1.41	1.18	1.19	1.20	1.18	1.19	1.18
	CS-18	1.34	1.37	1.38	1.34	1.36	1.33	1.14	1.16	1.17	1.14	1.15	1.13
	CS-19	1.33	1.35	1.40	1.33	1.38	1.32	1.09	1.10	1.13	1.09	1.12	1.08
	CS-20	1.24	1.30	1.34	1.23	1.28	1.22	1.04	1.08	1.11	1.03	1.07	1.03
	CS-22	1.20	1.23	1.29	1.21	1.26	1.19	1.03	1.04	1.09	1.03	1.07	1.02
	CS-23	1.25	1.33	1.36	1.22	1.27	1.23	1.07	1.14	1.15	1.06	1.09	1.06
	CS-24	1.38	1.41	1.48	1.38	1.44	1.37	1.15	1.17	1.21	1.15	1.19	1.14
	CS-25	1.35	1.44	1.46	1.33	1.38	1.33	1.13	1.20	1.21	1.12	1.15	1.12
	CS-26	1.32	1.34	1.39	1.33	1.38	1.31	1.15	1.16	1.20	1.16	1.19	1.15

Only **bold values** are considered for model validation.

Table 2.B.1 - Continued.

Authors	Specimen	$N_{R,exp}/N_R(A_{cs})$						$N_{R,exp}/N_R(A_c)$					
		EC 2	SIA 262	MC 2010	Original	Simp	Mixed	EC 2	SIA 262	MC 2010	Original	Simp	Mixed
Li 1994	1A	1.35	1.12	1.37	1.39	1.46	1.38	1.07	0.92	1.08	1.10	1.14	1.09
	2A	1.25	1.13	1.29	1.37	1.45	1.28	1.05	0.96	1.08	1.14	1.19	1.07
	4A	1.33	1.21	1.35	1.34	1.38	1.34	1.04	0.97	1.05	1.05	1.08	1.05
	5A	1.24	1.19	1.28	1.30	1.35	1.25	1.02	0.98	1.04	1.06	1.09	1.02
	7A	1.42	1.34	1.43	1.42	1.45	1.42	1.11	1.06	1.12	1.11	1.13	1.11
	8A	1.28	1.26	1.32	1.31	1.35	1.27	1.03	1.02	1.06	1.05	1.08	1.03
	10A	1.42	1.38	1.44	1.43	1.45	1.43	1.11	1.08	1.12	1.11	1.12	1.11
	11A	1.32	1.32	1.36	1.34	1.37	1.31	1.06	1.06	1.08	1.07	1.09	1.05
	1B	1.31	1.10	1.32	1.34	1.40	1.34	1.04	0.90	1.04	1.05	1.09	1.05
	2B	1.35	1.23	1.39	1.47	1.55	1.38	1.13	1.04	1.15	1.21	1.27	1.15
	4B	1.46	1.34	1.48	1.48	1.52	1.48	1.15	1.07	1.16	1.15	1.18	1.15
	5B	1.22	1.18	1.26	1.28	1.32	1.23	0.99	0.96	1.02	1.03	1.06	1.00
	7B	1.59	1.51	1.61	1.60	1.63	1.60	1.24	1.19	1.25	1.24	1.26	1.24
	8B	1.30	1.28	1.34	1.33	1.37	1.30	1.05	1.03	1.07	1.07	1.09	1.05
	10B	1.53	1.49	1.55	1.54	1.56	1.54	1.19	1.16	1.20	1.19	1.21	1.19
	11B	1.40	1.40	1.44	1.42	1.45	1.39	1.12	1.12	1.14	1.13	1.15	1.11
Cusson, Paultre 1994	1A	1.37	1.26	1.40	1.38	1.43	1.38	1.01	0.95	1.02	1.01	1.04	1.01
	1B	1.36	1.34	1.42	1.40	1.45	1.36	1.03	1.02	1.06	1.05	1.08	1.03
	1C	1.34	1.36	1.41	1.45	1.47	1.33	1.02	1.03	1.05	1.08	1.09	1.01
	1D	1.35	1.37	1.42	1.36	1.41	1.34	1.03	1.04	1.07	1.03	1.06	1.02
	2A	1.53	1.45	1.55	1.54	1.57	1.54	1.12	1.07	1.13	1.12	1.14	1.12
	2B	1.33	1.32	1.37	1.36	1.39	1.33	0.99	0.99	1.01	1.01	1.03	0.99
	2C	1.35	1.36	1.40	1.42	1.44	1.34	1.01	1.02	1.04	1.05	1.06	1.01
	2D	1.35	1.37	1.41	1.36	1.39	1.34	1.02	1.03	1.05	1.02	1.04	1.01
	3A	1.46	1.45	1.48	1.45	1.48	1.46	1.06	1.05	1.07	1.05	1.07	1.06
	3B	1.36	1.40	1.43	1.36	1.40	1.34	1.00	1.03	1.04	1.01	1.03	1.00
	3C	1.36	1.43	1.44	1.41	1.44	1.35	1.01	1.05	1.06	1.04	1.05	1.01
	3D	1.39	1.46	1.49	1.37	1.42	1.37	1.04	1.08	1.09	1.03	1.05	1.03
	4A	1.37	1.27	1.40	1.38	1.42	1.38	1.03	0.98	1.05	1.04	1.06	1.04
	4B	1.34	1.33	1.39	1.38	1.42	1.34	1.03	1.02	1.06	1.05	1.08	1.03
	4C	1.31	1.32	1.37	1.40	1.43	1.30	1.01	1.02	1.04	1.06	1.08	1.00
	4D	1.27	1.29	1.34	1.28	1.32	1.26	0.99	1.00	1.03	0.99	1.02	0.98
	5A	1.31	1.16	1.34	1.32	1.38	1.32	0.99	0.91	1.01	1.00	1.03	1.00
	5B	1.19	1.17	1.27	1.25	1.31	1.19	0.94	0.92	0.99	0.97	1.01	0.93
	5C	1.19	1.21	1.28	1.34	1.38	1.17	0.94	0.95	1.00	1.03	1.06	0.93
	5D	1.19	1.22	1.29	1.20	1.27	1.17	0.95	0.97	1.02	0.96	1.00	0.94
	6B	1.10	1.08	1.19	1.17	1.24	1.10	0.88	0.86	0.93	0.92	0.96	0.87
	6D	1.17	1.19	1.25	1.18	1.23	1.15	0.92	0.94	0.98	0.93	0.96	0.92
	7B	1.17	1.14	1.28	1.25	1.34	1.16	0.96	0.93	1.02	1.01	1.06	0.95
	7D	1.18	1.20	1.28	1.19	1.26	1.16	0.97	0.98	1.03	0.97	1.02	0.95
	8B	1.19	1.16	1.32	1.29	1.38	1.19	1.00	0.97	1.08	1.06	1.13	0.99
	8D	1.21	1.23	1.32	1.22	1.29	1.19	1.00	1.02	1.08	1.01	1.06	0.99

Only **bold values** are considered for model validation.

Table 2.B.1 - Continued.

Authors	Specimen	$N_{R,exp}/N_R(A_{cs})$						$N_{R,exp}/N_R(A_c)$					
		EC 2	SIA 262	MC 2010	Original	Simp	Mixed	EC 2	SIA 262	MC 2010	Original	Simp	Mixed
Sharma, Bhargava, Kaushik 2005	SA	1.38	1.31	1.44	1.38	1.44	1.38	1.00	0.96	1.03	1.00	1.03	1.00
	SB	1.47	1.47	1.52	1.46	1.50	1.46	1.05	1.05	1.07	1.04	1.06	1.04
	SC	1.33	1.24	1.39	1.33	1.40	1.33	0.97	0.92	1.00	0.97	1.00	0.97
	SD	1.23	1.28	1.36	1.26	1.33	1.21	0.96	0.99	1.03	0.98	1.02	0.94
	SE	1.37	1.17	1.42	1.39	1.48	1.39	1.00	0.89	1.03	1.01	1.06	1.01
	SF	1.45	1.38	1.50	1.45	1.51	1.45	1.03	1.00	1.06	1.03	1.06	1.03
	SG	1.61	1.61	1.65	1.60	1.64	1.60	1.13	1.14	1.16	1.13	1.15	1.13
	SH	1.44	1.36	1.50	1.44	1.51	1.44	1.03	0.99	1.06	1.03	1.07	1.03
	SI	1.25	1.29	1.37	1.28	1.34	1.23	0.96	0.98	1.02	0.97	1.01	0.94
Scott, Park, Priestley 1982	2	1.05	1.04	1.08	1.14	1.16	1.04	0.90	0.90	0.93	0.97	0.98	0.90
	3	1.25	1.24	1.29	1.35	1.38	1.24	1.08	1.07	1.11	1.15	1.17	1.07
	6	1.05	1.02	1.09	1.09	1.13	1.06	0.90	0.88	0.93	0.93	0.96	0.90
	7	1.23	1.19	1.27	1.28	1.32	1.24	1.05	1.02	1.08	1.09	1.12	1.06
	12	1.35	1.36	1.39	1.43	1.45	1.34	1.16	1.16	1.19	1.21	1.23	1.15
	13	1.30	1.29	1.34	1.41	1.43	1.29	1.12	1.11	1.15	1.20	1.22	1.12
	14	1.31	1.31	1.37	1.43	1.46	1.30	1.13	1.13	1.17	1.21	1.23	1.12
	15	1.29	1.27	1.34	1.46	1.50	1.29	1.12	1.10	1.16	1.25	1.27	1.12
	17	1.32	1.30	1.36	1.35	1.38	1.32	1.12	1.11	1.15	1.14	1.17	1.12
	18	1.35	1.30	1.39	1.40	1.45	1.35	1.16	1.12	1.19	1.20	1.23	1.16
	19	1.33	1.29	1.38	1.38	1.43	1.33	1.13	1.11	1.17	1.17	1.20	1.13
	20	1.29	1.22	1.34	1.37	1.43	1.30	1.11	1.06	1.15	1.17	1.21	1.12
	22	1.30	1.31	1.35	1.39	1.41	1.29	1.10	1.11	1.14	1.16	1.18	1.10
	23	1.25	1.24	1.30	1.37	1.40	1.24	1.07	1.06	1.10	1.15	1.17	1.06
	24	1.29	1.29	1.35	1.42	1.46	1.28	1.09	1.10	1.14	1.19	1.21	1.09
	25	1.27	1.25	1.34	1.47	1.51	1.27	1.10	1.08	1.15	1.24	1.27	1.10
Sun, Oba, Tian, Ikeda 1996	**NA6-20**	**1.26**	**1.06**	**1.27**	**1.29**	**1.35**	**1.28**	**1.11**	**0.95**	**1.13**	**1.14**	**1.18**	**1.13**
	NA6-30	**1.20**	**1.08**	**1.22**	**1.22**	**1.25**	**1.21**	**1.06**	**0.97**	**1.07**	**1.07**	**1.10**	**1.07**
	NA10-47	1.21	1.09	1.24	1.22	1.28	1.22	1.06	0.97	1.09	1.07	1.11	1.07
	NB6-35	**1.12**	**1.08**	**1.16**	**1.17**	**1.21**	**1.12**	**1.00**	**0.97**	**1.03**	**1.04**	**1.08**	**1.00**
	NB6-50	**1.16**	**1.15**	**1.20**	**1.18**	**1.22**	**1.15**	**1.03**	**1.02**	**1.06**	**1.05**	**1.07**	**1.02**
	NB10-75	**1.15**	**1.18**	**1.24**	**1.17**	**1.22**	**1.14**	**1.03**	**1.05**	**1.10**	**1.05**	**1.08**	**1.02**
	NC6-30	**1.10**	**1.05**	**1.14**	**1.13**	**1.18**	**1.11**	**0.99**	**0.95**	**1.02**	**1.01**	**1.05**	**0.99**
	NC6-43	**1.15**	**1.13**	**1.19**	**1.17**	**1.20**	**1.15**	**1.02**	**1.01**	**1.05**	**1.04**	**1.07**	**1.02**
	NC10-70	**1.12**	**1.14**	**1.20**	**1.12**	**1.17**	**1.11**	**1.00**	**1.02**	**1.06**	**1.00**	**1.04**	**0.99**
	ND6-47	**1.12**	**1.13**	**1.17**	**1.13**	**1.16**	**1.11**	**1.01**	**1.02**	**1.05**	**1.01**	**1.04**	**1.00**
	ND6-70	**1.14**	**1.17**	**1.19**	**1.14**	**1.17**	**1.13**	**1.02**	**1.05**	**1.06**	**1.02**	**1.04**	**1.02**
	NE6-40	**1.08**	**1.08**	**1.13**	**1.10**	**1.13**	**1.08**	**0.98**	**0.98**	**1.02**	**0.99**	**1.02**	**0.97**
	NE6-60	**1.17**	**1.20**	**1.22**	**1.17**	**1.20**	**1.16**	**1.05**	**1.07**	**1.09**	**1.05**	**1.07**	**1.04**
	NBM-60	**1.09**	**1.09**	**1.17**	**1.13**	**1.18**	**1.08**	**1.00**	**1.00**	**1.07**	**1.03**	**1.08**	**0.99**
	NBM-75	**1.07**	**1.09**	**1.14**	**1.09**	**1.13**	**1.05**	**0.97**	**1.00**	**1.04**	**0.99**	**1.03**	**0.96**
	NCM-60	**1.06**	**1.06**	**1.13**	**1.07**	**1.12**	**1.05**	**0.97**	**0.97**	**1.03**	**0.98**	**1.02**	**0.96**
	NCM-75	**1.10**	**1.12**	**1.17**	**1.10**	**1.14**	**1.08**	**1.00**	**1.02**	**1.06**	**1.00**	**1.04**	**0.99**

Only **bold values** are considered for model validation.

Table 2.B.1 - Continued.

Authors	Specimen	$N_{R,exp}/N_R(A_{cs})$						$N_{R,exp}/N_R(A_c)$					
		EC 2	SIA 262	MC 2010	Original	Simp	Mixed	EC 2	SIA 262	MC 2010	Original	Simp	Mixed
Hwee, Rangan 1990	1	1.52	1.49	1.56	1.52	1.56	1.52	0.99	0.97	1.00	0.98	1.00	0.98
	2	1.55	1.57	1.57	1.54	1.56	1.55	0.99	1.00	1.00	0.99	0.99	0.99
	3	1.67	1.67	1.67	1.67	1.68	1.67	1.06	1.06	1.07	1.06	1.07	1.07
	4	1.42	1.40	1.45	1.42	1.45	1.42	0.97	0.96	0.98	0.97	0.98	0.97
	5	1.45	1.46	1.47	1.45	1.46	1.45	0.98	0.98	0.98	0.98	0.98	0.98
	6	1.44	1.44	1.44	1.44	1.44	1.44	0.97	0.97	0.97	0.97	0.97	0.97
	7	1.59	1.56	1.62	1.59	1.62	1.59	1.02	1.01	1.03	1.02	1.03	1.02
	8	1.66	1.68	1.68	1.66	1.67	1.66	1.06	1.06	1.06	1.05	1.06	1.06
	9	1.68	1.67	1.68	1.68	1.68	1.68	1.06	1.06	1.06	1.06	1.06	1.06
	10	1.58	1.55	1.61	1.58	1.61	1.58	1.07	1.05	1.08	1.07	1.08	1.07
	11	1.53	1.54	1.54	1.52	1.53	1.53	1.02	1.03	1.03	1.02	1.02	1.02
	12	1.40	1.39	1.40	1.40	1.40	1.40	0.93	0.93	0.93	0.93	0.93	0.93
Rangan, Saunders, Seng 1991	RC-1	1.60	1.60	1.61	1.59	1.60	1.59	1.06	1.07	1.07	1.06	1.07	1.06
	RC-2	1.53	1.54	1.54	1.53	1.54	1.53	1.02	1.02	1.03	1.02	1.02	1.02
	RC-4	1.58	1.56	1.58	1.58	1.58	1.58	1.04	1.03	1.04	1.04	1.04	1.04
	RC-5	1.46	1.44	1.48	1.46	1.48	1.46	0.98	0.97	0.99	0.98	0.99	0.98
	RC-7	1.93	1.88	1.91	1.92	1.93	1.93	1.25	1.23	1.24	1.25	1.25	1.25
	RC-8	1.63	1.60	1.65	1.63	1.65	1.63	1.09	1.08	1.10	1.09	1.10	1.09
	RC-9	1.57	1.58	1.59	1.57	1.58	1.57	1.04	1.04	1.04	1.03	1.04	1.03
	RC-10	1.66	1.66	1.67	1.66	1.66	1.66	1.09	1.09	1.09	1.09	1.09	1.09
Parvez, Foster, Valipour, McGregor 2017	2H0-70S-NS-1	1.34	1.31	1.36	1.34	1.36	1.34	0.97	0.96	0.98	0.97	0.98	0.97
	2H0-70S-NS-2	1.69	1.66	1.72	1.69	1.72	1.69	1.22	1.21	1.23	1.22	1.23	1.22
	2H0-120D-NS-1	1.19	1.23	1.23	1.19	1.21	1.18	0.86	0.88	0.89	0.86	0.87	0.86
	2H0-120D-NS-2	1.58	1.63	1.63	1.58	1.60	1.57	1.14	1.17	1.17	1.14	1.15	1.14
	2H0-70S-HS	1.73	1.70	1.75	1.72	1.75	1.72	1.25	1.23	1.26	1.25	1.26	1.25
Khalajestani, Parvez, Foster, Valipour, McGregor 2018	1.8H0-70S-HS	1.75	1.72	1.78	1.75	1.78	1.75	1.27	1.26	1.29	1.27	1.29	1.27
Moccia, Kubski, Fernandez, Muttoni 2020	CM1A0	1.47	1.49	1.50	1.46	1.48	1.47	1.00	1.01	1.02	1.00	1.01	1.00
	CM1A2	1.57	1.59	1.60	1.56	1.58	1.57	1.07	1.08	1.08	1.07	1.08	1.07
	CM1B0	1.52	1.57	1.59	1.50	1.56	1.52	1.01	1.03	1.04	1.00	1.03	1.01
	CM1B1	1.51	1.56	1.58	1.49	1.55	1.51	1.01	1.03	1.04	1.00	1.02	1.00
	CM1B2	1.67	1.72	1.75	1.65	1.71	1.66	1.11	1.13	1.14	1.10	1.13	1.11
	CM1B3	1.62	1.67	1.70	1.60	1.66	1.61	1.08	1.10	1.11	1.07	1.10	1.08
	CM1C0	1.57	1.65	1.69	1.54	1.63	1.56	1.02	1.05	1.07	1.00	1.04	1.01
	CM1C1	1.64	1.72	1.76	1.60	1.70	1.63	1.06	1.10	1.11	1.05	1.09	1.06
	CM1C2	1.77	1.86	1.91	1.74	1.84	1.76	1.15	1.19	1.21	1.14	1.18	1.15
	CM1C3	1.62	1.70	1.74	1.59	1.68	1.61	1.05	1.08	1.10	1.04	1.08	1.05

Only **bold values** are considered for model validation.

Table 2.B.1 - Continued.

Authors	Specimen	$N_{R,exp}/N_R(A_{cs})$						$N_{R,exp}/N_R(A_c)$					
		EC 2	SIA 262	MC 2010	Original	Simp	Mixed	EC 2	SIA 262	MC 2010	Original	Simp	Mixed
Al-Hussaini, Regan, Xue, Ramdane 1993	C12	1.61	1.61	1.61	1.61	1.61	1.61	1.14	1.14	1.14	1.14	1.14	1.14
	C13	1.56	1.56	1.56	1.56	1.56	1.56	1.10	1.10	1.10	1.10	1.10	1.10
	C14	1.46	1.41	1.47	1.46	1.48	1.46	1.09	1.07	1.10	1.10	1.11	1.10
	C21	1.62	1.59	1.63	1.62	1.64	1.62	1.11	1.10	1.12	1.12	1.12	1.12
	C22	1.64	1.57	1.66	1.65	1.67	1.64	1.16	1.12	1.16	1.16	1.17	1.16
	C23	1.51	1.45	1.52	1.51	1.54	1.51	1.07	1.04	1.08	1.07	1.08	1.07
	C24	1.41	1.35	1.42	1.41	1.44	1.41	1.02	0.98	1.02	1.02	1.03	1.02
Fang, Hong, Wu 1994	**HA1-1**	**1.15**	**1.06**	**1.16**	**1.15**	**1.18**	**1.15**	**1.07**	**1.00**	**1.09**	**1.08**	**1.11**	**1.08**
	HA1-2	**1.08**	**1.00**	**1.09**	**1.09**	**1.11**	**1.08**	**1.01**	**0.94**	**1.02**	**1.02**	**1.04**	**1.02**
	HA2-1	**1.15**	**1.10**	**1.17**	**1.16**	**1.18**	**1.16**	**1.08**	**1.03**	**1.09**	**1.08**	**1.10**	**1.08**
	HA2-2	**1.11**	**1.06**	**1.13**	**1.12**	**1.14**	**1.12**	**1.04**	**1.00**	**1.05**	**1.05**	**1.07**	**1.05**
	HA3-1	**1.12**	**1.12**	**1.13**	**1.12**	**1.13**	**1.12**	**1.05**	**1.05**	**1.06**	**1.05**	**1.06**	**1.05**
	HA3-2	**1.05**	**1.05**	**1.06**	**1.05**	**1.06**	**1.05**	**0.98**	**0.98**	**0.99**	**0.98**	**0.99**	**0.98**
	MA1-1	**1.20**	**1.09**	**1.22**	**1.21**	**1.25**	**1.21**	**1.13**	**1.03**	**1.15**	**1.14**	**1.18**	**1.14**
	MA1-2	**1.13**	**1.04**	**1.15**	**1.14**	**1.18**	**1.14**	**1.07**	**0.98**	**1.08**	**1.07**	**1.10**	**1.07**
	MA2-1	**1.29**	**1.22**	**1.31**	**1.30**	**1.33**	**1.30**	**1.22**	**1.15**	**1.23**	**1.22**	**1.25**	**1.22**
	MA2-2	**1.28**	**1.20**	**1.30**	**1.28**	**1.32**	**1.28**	**1.20**	**1.13**	**1.22**	**1.21**	**1.24**	**1.21**
	MA3-1	**1.24**	**1.24**	**1.26**	**1.24**	**1.26**	**1.24**	**1.17**	**1.16**	**1.18**	**1.16**	**1.18**	**1.17**
	MA3-2	**1.17**	**1.17**	**1.19**	**1.17**	**1.18**	**1.17**	**1.10**	**1.10**	**1.11**	**1.10**	**1.11**	**1.10**
	HB1-3	**1.14**	**1.12**	**1.17**	**1.15**	**1.18**	**1.13**	**1.07**	**1.06**	**1.11**	**1.08**	**1.11**	**1.07**
	HB1-4	**1.12**	**1.11**	**1.16**	**1.13**	**1.17**	**1.12**	**1.06**	**1.05**	**1.10**	**1.07**	**1.10**	**1.06**
	HB2-3	**1.14**	**1.15**	**1.18**	**1.14**	**1.17**	**1.13**	**1.08**	**1.08**	**1.11**	**1.08**	**1.10**	**1.07**
	HB2-4	**1.10**	**1.11**	**1.13**	**1.10**	**1.12**	**1.09**	**1.04**	**1.04**	**1.07**	**1.04**	**1.06**	**1.03**
	HB3-1	**1.07**	**1.08**	**1.09**	**1.06**	**1.08**	**1.06**	**1.01**	**1.02**	**1.03**	**1.00**	**1.02**	**1.00**
	HB3-2	**1.13**	**1.14**	**1.15**	**1.12**	**1.14**	**1.12**	**1.06**	**1.08**	**1.09**	**1.06**	**1.08**	**1.06**
	MB1-3	**1.15**	**1.14**	**1.20**	**1.17**	**1.21**	**1.15**	**1.09**	**1.08**	**1.13**	**1.11**	**1.14**	**1.09**
	MB1-4	**1.09**	**1.08**	**1.13**	**1.10**	**1.14**	**1.09**	**1.03**	**1.02**	**1.07**	**1.05**	**1.08**	**1.03**
	MB2-3	**1.12**	**1.13**	**1.16**	**1.12**	**1.15**	**1.11**	**1.06**	**1.07**	**1.10**	**1.06**	**1.08**	**1.05**
	BM2-4	**1.12**	**1.13**	**1.16**	**1.12**	**1.15**	**1.11**	**1.06**	**1.07**	**1.09**	**1.06**	**1.08**	**1.05**
	MB3-1	**1.08**	**1.10**	**1.11**	**1.08**	**1.09**	**1.08**	**1.02**	**1.04**	**1.05**	**1.02**	**1.03**	**1.02**
	MB3-2	**1.08**	**1.10**	**1.10**	**1.07**	**1.09**	**1.07**	**1.02**	**1.03**	**1.04**	**1.02**	**1.03**	**1.01**

Only **bold values** are considered for model validation.

Table 2.B.2 - Statistical evaluation.

		$N_{R,exp}/N_R(A_{cs})$						$N_{R,exp}/N_R(A_c)$					
		EC 2	SIA 262	MC 2010	Original	Simp	Mixed	EC 2	SIA 262	MC 2010	Original	Simp	Mixed
Whole Data Set n=193	μ	1.34	1.32	1.39	1.36	1.41	1.34	1.06	1.04	1.09	1.07	1.10	1.06
	σ	0.18	0.19	0.18	0.17	0.18	0.18	0.07	0.08	0.07	0.08	0.08	0.08
	COV	13%	14%	13%	13%	12%	14%	7%	7%	7%	7%	7%	7%
Data Set Validation n=40	**μ**	**1.14**	**1.11**	**1.17**	**1.14**	**1.18**	**1.13**	**1.05**	**1.03**	**1.08**	**1.06**	**1.08**	**1.05**
	σ	**0.06**	**0.05**	**0.05**	**0.06**	**0.06**	**0.06**	**0.06**	**0.05**	**0.05**	**0.06**	**0.06**	**0.06**
	COV	**5%**	**5%**	**5%**	**5%**	**5%**	**5%**	**5%**	**5%**	**5%**	**5%**	**5%**	**6%**

Notation

Latin letters

$A_c = b_y \cdot b_z$	Cross-sectional area of concrete
A_{conf}	Governing confined concrete area
$A_{conf,\mathrm{EC2}}$	Governing confined concrete area according to EC 2 [13]
$A_{conf,\mathrm{MC2010}}$	Governing confined concrete area according to MC 2010 [11]
$A_{conf,mod}$	Governing confined concrete area according to new model
$A_{conf,mod,c}$	Governing confined concrete area according to new model for circular cross-sections
$A_{conf,\mathrm{SIA262}}$	Governing confined concrete area according to SIA 262 [12]
$A_{conf,simp}$	Governing confined concrete area according to simplification
$A_{cover} = A_c - A_{cs}$	Cross-sectional area of cover concrete
$A_{cs} = b_{csy} \cdot b_{csz}$	Concrete area within the confining reinforcement
$A_{s,confy}$, $A_{s,confz}$	Cross-sectional area of confining reinforcement in *y* and *z*-direction (per leg)
$A_{s,l}$	Cross-sectional area of longitudinal reinforcement (total)
$b_{csy} = b_y - 2 \cdot c_{nom} - Ø_{conf}$ $b_{csz} = b_z - 2 \cdot c_{nom} - Ø_{conf}$	Maximum width of confining reinforcement in *y* and *z*-direction, respectively (dimension between centre lines)
b_y, b_z	Width of RC compression member
c_{nom}	Concrete cover
d_{cs}	Diameter of confining reinforcement (dimension between centre lines)
f_{c0}	Uniaxial concrete compressive strength
$f_{c,biax}$	Biaxial concrete compressive strength
$f_{sy,conf}$	Yield strength of confining reinforcement
$f_{sy,l}$	Yield strength of longitudinal reinforcement
$F_y = A_{s,confy} \cdot f_{sy,conf}$ $F_z = A_{s,confz} \cdot f_{sy,conf}$	Confining force in *y* and *z*-direction, respectively
h_{yx}	Rise of longitudinal parabola of paraboloid II
h_{yz}	Rise of lateral parabola of paraboloid II
h_{zx}	Rise of longitudinal parabola of paraboloid I
h_{zy}	Rise of lateral parabola of paraboloid I
h_y	Height of paraboloid II
h_z	Height of paraboloid I
$k = \frac{A_{conf}}{A_{cs}}$	Effectiveness factor of confining reinforcement
k_{EC2}	Effectiveness factor of confining reinforcement according to EC 2 [13]
k_{MC2010}	Effectiveness factor of confining reinforcement according to MC 2010 [11]
k_{mod}	Effectiveness factor of confining reinforcement according to new model
k_{SIA262}	Effectiveness factor of confining reinforcement according to SIA 262 [12]
k_{simp}	Effectiveness factor of confining reinforcement according to simplification of new model

N	Longitudinal normal force applied to compression member (defined positive in compression)
$n_{s,conf}$	Number of confining reinforcement legs
N_R	Normal force resistance of RC compression member (compression positive)
$N_{R,exp}$	Experimentally determined normal load-bearing capacity of RC compression member
s	Spacing of confining reinforcement in lateral direction
s_x	Longitudinal spacing of confining reinforcement (x-direction)
s_y	Lateral spacing of confining reinforcement (y-direction)
s_z	Lateral spacing of confining reinforcement (z-direction)
x	Longitudinal direction
y, z	Lateral directions
$x_\mathrm{I}, y_\mathrm{I}, z_\mathrm{I}$	Local coordinates of paraboloid I
$x_\mathrm{II}, y_\mathrm{II}, z_\mathrm{II}$	Local coordinates of paraboloid II

Greek letters

$\sum A_{s,confy}, \sum A_{s,confz}$	Sum of cross-sectional areas of confining reinforcement in one layer in y and z-direction
γ_c	Partial safety factor of concrete
Δf_{conf}	Increase of concrete strength due to confinement
η_{cc}	Strength reduction factor to account for higher-strength concrete brittleness
σ_{conf}	Confining stress generated by confinement (compression positive)
$\sigma_{conf,c}$	Confining stress generated by circular confinement (compression positive)
$\sigma_{confy}, \sigma_{confz}$	Confining stress generated by confinement according to current guidelines in the y and z-direction, respectively (compression positive)
$\sigma_{confy,mod}, \sigma_{confz,mod}$	Confining stress generated by confinement according to the presented model in the y and z-direction, respectively (compression positive)
σ_2	Second non-zero compressive principal stress (compression positive)

Special characters

$Ø_{conf}$	Diameter of confining reinforcement bar or stirrup

References

[1] A. Considère, "Étude expérimentale de la résistance à la compression du béton fretté," in *Comptes rendus des séances de l'académie des sciences*, Paris, 1902, pp. 415–419.

[2] A. Considère, "Étude théorique de la résistance à la compression du béton fretté," in *Comptes rendus des séances de l'académie des sciences*, Paris, 1902, pp. 365–368.

[3] C. Bach, "Versuche zur Klarstellung der Wirkungsweise der Umschnürung bei Eisenbetonsäulen," *Zeitschrift des Vereins deutscher Ingenieure*, vol. 59, no. 44, pp. 898–901, Oct. 1915.

[4] F. E. Richart, A. Brandtzaeg, and R. L. Brown, "A Study of the Failure of Concrete under Combined Compressive Stresses," University of Illinois Engineering Experimental Station, Bulletin 185, 1928.

[5] F. E. Richart, A. Brandtzaeg, and R. L. Brown, "The failure of plain and spirally reinforced concrete in compression," University of Illinois Engineering Experimental Station, 1929.

[6] T. Markić, F. Morger, and W. Kaufmann, "Partially loaded areas in reinforced concrete: Mechanical modelling," *Engineering Structures*, vol. 271, Nov. 2022, doi: 10.1016/j.engstruct.2022.114938.

[7] M. A. M. Badawi, "Einfluss der Längs- und Querarmierung auf die Tragfähigkeit und Verformbarkeit von gedrungenen Stahlbetonstützen," Eidgenössische Materialprüfungs- und Versuchsanstalt für Industrie, Bauwesen und Gewerbe (EMPA), Dübendorf, 199, 1973.

[8] B. Menne, "Zur Traglast der ausmittig gedrückten Stahlbetonstütze mit Umschnürungsbewehrung," *Deutscher Ausschuss für Stahlbeton*, Heft 285, p. 56, 1977.

[9] A. Kanellopoulos, "Zum unelastischen Verhalten und Bruch von Stahlbeton," ETH Zurich, 1986. doi: 10.3929/ethz-a-000391503.

[10] J. B. Mander, M. J. N. Priestley, and R. Park, "Observed Stress-Strain Behavior of Confined Concrete," *Journal of Structural Engineering*, vol. 114, no. 8, pp. 1827–1849, Sep. 1988, doi: 10.1061/(ASCE)0733-9445(1988)114:8(1827).

[11] International Federation for Structural Concrete (fib), *Model Code for Concrete Structures 2010*, Berlin, Germany, 2013.

[12] SIA, *Swisscode SIA 262: Concrete Structures*, Zurich, Switzerland, 2013.

[13] EN 1992-1-1:2023, "Eurocode 2 - Design of concrete structures - Part 1-1: General rules and rules for buildings, bridges and civil engineering structures," Brussels, 2023.

[14] B. Seelhofer-Schilling, "Umschnürte Stahlbetonstützen: geschichtliche Entwicklung," Doctoral Thesis, ETH Zurich, 2008. doi: 10.3929/ethz-a-005682151.

[15] F. Moccia, Q. Yu, M. Fernández Ruiz, and A. Muttoni, "Concrete compressive strength: From material characterization to a structural value," *Structural Concrete*, vol. 22, no. S1, pp. E634–E654, Jan. 2021, doi: 10.1002/suco.202000211.

[16] M. P. Nielsen and L. C. Hoang, *Limit Analysis and Concrete Plasticity, Third Edition*. Boca Raton: CRC Press, 2011. doi: 10.1201/b10432.

[17] S. A. Sheikh and S. M. Uzumeri, "Strength and Ductility of Tied Concrete Columns," *Journal of the Structural Division*, vol. 106, no. 5, pp. 1079–1102, May 1980, doi: 10.1061/JSDEAG.0005416.

[18] V. Sigrist, "Zum Verformungsvermögen von Stahlbetonträgern," Doctoral thesis, ETH Zurich, Zurich, Switzerland, 1995. doi: 10.3929/ethz-a-001492371.

[19] C. Proksch-Weilguni, M. Decker, and J. Kollegger, "Hochbelastete Lastübertragungszonen mit stumpf gestoßener Bewehrung: Experimentelle Untersuchungen und numerische Simulationen," *Beton- und Stahlbetonbau*, vol. 117, no. 11, pp. 913–927, 2022, doi: 10.1002/best.202200075.

[20] F. J. Vecchio, "Finite element modeling of concrete expansion and confinement," *Journal of Structural Engineering*, vol. 118, no. 9, pp. 2390–2406, 1992, doi: 10.1061/(ASCE)0733-9445(1992)118:9(2390).

[21] Kupfer, H. K. Hilsdorf, and H. Rusch, "Behavior of Concrete Under Biaxial Stresses," *ACI Journal Proceedings*, vol. 66, no. 8, Aug. 1969, doi: 10.14359/7388.

[22] H. O. Shin, Y. S. Yoon, W. D. Cook, and D. Mitchell, "Axial Load Response of Ultra-High-Strength Concrete Columns and High-Strength Reinforcement," *ACI Structural Journal*, vol. 113, no. 2, Mar. 2016, doi: 10.14359/51688063.

[23] H. O. Shin, Y. S. Yoon, W. D. Cook, and D. Mitchell, "Effect of Confinement on the Axial Load Response of Ultrahigh-Strength Concrete Columns," *Journal of Structural Engineering*, vol. 141, no. 6, p. 04014151, Jun. 2015, doi: 10.1061/(ASCE)ST.1943-541X.0001106.
[24] M. Saatcioglu and S. R. Razvi, "High-Strength Concrete Columns with Square Sections under Concentric Compression," *Journal of Structural Engineering*, vol. 124, no. 12, pp. 1438–1447, Dec. 1998, doi: 10.1061/(ASCE)0733-9445(1998)124:12(1438).
[25] B. Li, *Strength and ductility of reinforced concrete members and frames constructed using high strength concrete*. in Research report (University of Canterbury. Department of Civil Engineering). New Zealand: Christchurch, 1994.
[26] D. Cusson and P. Paultre, "High-Strength Concrete Columns Confined by Rectangular Ties," *Journal of Structural Engineering*, vol. 120, no. 3, pp. 783–804, Mar. 1994, doi: 10.1061/(ASCE)0733-9445(1994)120:3(783).
[27] U. K. Sharma, P. Bhargava, and S. K. Kaushik, "Behavior of Confined High Strength Concrete Columns under Axial Compression," *Journal of Advanced Concrete Technology*, vol. 3, no. 2, pp. 267–281, 2005, doi: 10.3151/jact.3.267.
[28] B. D. Scott, R. Park, and M. J. N. Priestley, "Stress-Strain Behavior of Concrete Confined by Overlapping Hoops at Low and High Strain Rates," *ACI Journal Proceedings*, vol. 79, no. 1, pp. 13–27, Jan. 1982, doi: 10.14359/10875.
[29] Y. P. Sun, T. Oba, F. S. Tian, and T. Ikeda, "Confinement effects of transverse hoops in high-strength concrete," in *Proceedings of the 11th world conference on earthquake engineering.*, Amsterdam: Elsevier Science, 1996, p. 8.
[30] Y. S. Hwee and B. V. Rangan, "Studies on Commercial High-Strength Concretes," *ACI Materials Journal*, vol. 87, no. 5, pp. 440–445, Sep. 1990, doi: 10.14359/1811.
[31] B. V. Rangan, P. Saunders, and E. J. Seng, "Design of High-Strength Concrete Columns," *ACI Special Publication*, vol. 128, pp. 851–862, Nov. 1991, doi: 10.14359/3206.
[32] A. Parvez, S. J. Foster, H. Valipour, and G. McGregor, "Strength and ductility of high-strength concrete columns confined with high-strength steel ties," in *28th Biennial National Conference of the Concrete Institute of Australia*, Adelaide, Australia: North Sydney: The concrete institute of Australia, 2017.
[33] M. K. Khalajestani, A. Parvez, S. J. Foster, H. Valipour, and G. McGregor, "Strength and Ductility of High-Strength Concrete Columns Reinforced with High-Strength Steel," presented at the The International Federation for Structural Concrete, 5th International fib Congres, Melbourne, Australia: fib Structural Concrete Federation, 2018.
[34] A. Al-Hussaini, P. Regan, H.-Y. Xue, and K.-E. Ramdane, "The behaviour of HSC columns under axial load," in *High Strength Concrete Proceedings*, 1993, pp. 83–89.
[35] I. Fang, K. Hong, and J. WU, "Strength and Ductility of High Strength Tied Columns," in *Proceedings of the National Science Council, Republic of China*, 1994, pp. 63–74.

Corrections

Corrections to the original content of the published article are listed below:

	Published	Adjusted
Section 2.2	$\eta_{cc} = (40/f_{c0})^{(1/3)}) \leq 1$	$\eta_{cc} = (40/f_{c0})^{(1/3)} \leq 1$
Section 2.2.1	$A_{s,confy}$ and $A_{s,confy}$ per leg	$A_{s,confy}$ and $A_{s,confz}$ per leg
Fig. 2.3	$f_{c0} + 4 \cdot \min(\sigma_{conf,y,} \sigma_{conf,z})$	$f_{c0} + 4 \cdot \min(\sigma_{confy,} \sigma_{confz})$
Section 2.3.2	$b_{csz} = (n_{s,confz} - 1)\, s_z < n_{s,confz} \cdot s_z$	$b_{csz} = (n_{s,confz} - 1) \cdot s_z < n_{s,confz} \cdot s_z$
Fig 2.5	σ_{confz}	σ_{conf}
Fig 2.5	$\sigma_{confz,mod}$	$\sigma_{conf,mod}$
Notation	$\sum A_{s,conf,y}$, $\sum A_{s,conf,z}$	$\sum A_{s,confy}$, $\sum A_{s,confz}$
Table 2.A.1	[no label]	[label added]
Fig. 2.A.1	[no label]	[label added]
Fig. 2.A.1	$\sum A_{s,conf,y}$	$\sum A_{s,confy}$
Table 2.B.1	[no label]	[label added]
Table 2.B.2	[no label]	[label added]

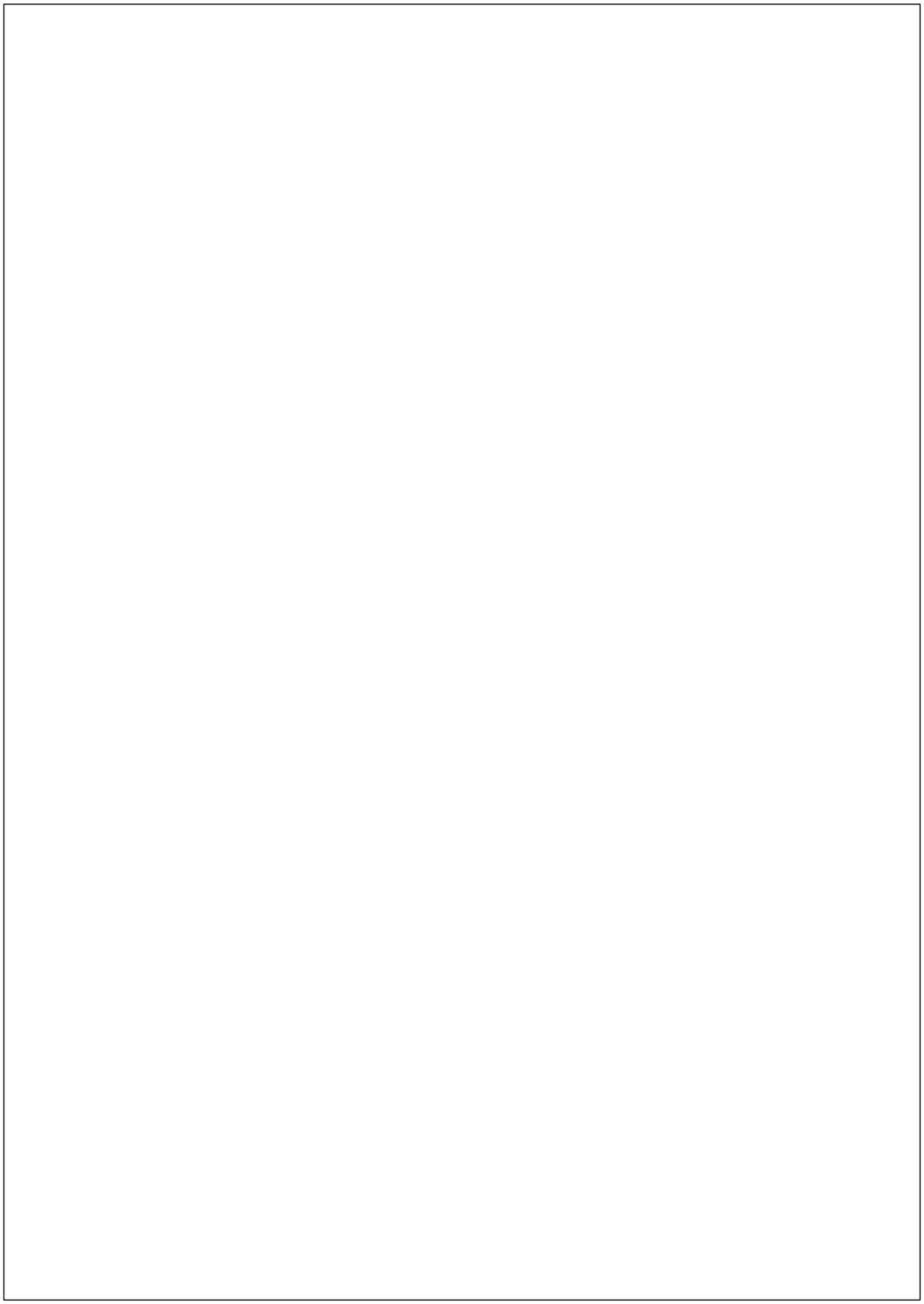

3 Experimental investigation of welded reinforcement grids

The content of this chapter corresponds to the postprint of the following published article:

> **F. Morger**, W. Kaufmann, 'Experimental investigation of welded reinforcement grids for partial area loading', in *Proceedings of the 15th fib PhD Symposium in Civil Engineering*, Féderation internationale du Béton (fib), vol. 66, pp. 181-188, 2024. doi: 10.3929/ethz-b-000711139.

This postprint includes some adjustments to the published version. For details see Section 1.5 and the corrections section at the end of this chapter.

As the lead author, Fabian Morger planned, prepared and carried out the experiment, analysed and post-processed the obtained data, and wrote the entire draft of the manuscript. The second author, Walter Kaufmann, supervised the conducted research and carefully reviewed the manuscript.

Abstract

Welded reinforcement grids are increasingly used in the production of reinforced concrete tunnel lining segments. The welded grids simplify the reinforcement assembly, reduce time and cost in the prefabrication process, are resource-efficient and facilitate casting by avoiding congestion. While their advantages are known, their load-bearing behaviour is not yet fully understood. To close this research gap, fibre optical measurements of several reinforcing bars of the welded reinforcement grid of a partially loaded reinforced concrete specimen were conducted. The experimental data obtained from these measurements are presented in this article. Based on the fibre optical strain measurements and the characteristics of the bare reinforcing bars, the normal stresses and the curvature of the reinforcing bars could be inferred. Thereby, it could be shown that the transverse reinforcing bars can be fully activated. Furthermore, the measurements yielded insight into the load transfer between reinforcement and the surrounding concrete, which is required to determine the effect of the welded grids acting as passive confinement. Additionally, the measurements showed that the longitudinal reinforcing bars (i) contribute to the anchoring of the transverse reinforcing bars as well as (ii) provide passive confinement in the longitudinal direction.

3.1 Introduction

With the introduction of welding robots, welded load-bearing reinforcement has become increasingly popular in the construction industry. The robots guarantee a consistent welding quality and reduce expensive human labour, as they can be programmed to work autonomously. Welded reinforcement grids are particularly suited to the production of tunnel lining segments with their typically high level of repetition. Compared to conventional stirrup reinforcement, prefabricated welded grids greatly simplify the reinforcement assembly, reducing time and costs in the prefabrication process. Furthermore, the amount of reinforcement can be reduced, saving resources and facilitating casting by avoiding congestion.

In longitudinal joints of reinforced concrete (RC) segmental linings, welded reinforcement grids must resist bursting stresses or provide confinement. Understanding their load-bearing behaviour is thus essential for a safe design of the lining joints. Experiments on partially loaded RC concrete blocks conducted by the authors have shown equivalent or even superior performance of specimens with welded reinforcement grids compared to companion specimens with conventional stirrup or double-headed bar reinforcement [1]. However, for all but one of the specimens with welded grids, the reinforcement content in the longitudinal direction was higher than in the conventionally reinforced specimen with equal transverse reinforcement content, making it difficult to draw final conclusions regarding the efficiency of the welded grids based on this comparison. Furthermore, current guidelines do not provide design approaches suitable for welded reinforcement in segmental tunnel linings: due to their small thickness (usually 200-500 mm), anchorage has to be guaranteed over a very short length. For example, Eurocode 2 [2] allows the reduction of the anchorage length by 15 times the diameter (Ø) for bars with additional welded transverse reinforcement. Accordingly, a reinforcing bar with Ø12 mm and concrete class C50/60 still requires an anchorage length of 15Ø = 180 mm to be fully anchored. Additionally, specific experimental investigations of the load-bearing behaviour of welded grids are scarce. Schmidt-Thrö [3] conducted pull-out tests on reinforcing bars with welded transverse reinforcement. However, the test setup varied substantially from welded reinforcement grids in tunnel lining segments, particularly regarding the load distribution among two welding connections (see Section 3.3.2).

To address the knowledge gap regarding the load-bearing behaviour of welded reinforcement grids, several reinforcing bars of one specimen (see Fig. 3.1) presented in Morger and Kaufmann [1] were equipped with fibre optical sensors to measure the steel strains. Thereby, it could be investigated (i) whether the welded cross joints and the longitudinal reinforcement are capable of providing sufficient anchorage to fully activate (reaching yielding) the welded transverse bars, and (ii) to what extent the grids – regarding both the transverse as well as the longitudinal bars – can provide passive confinement.

Passive confinement is a viable option to increase the load-bearing capacity of the longitudinal joints of tunnel lining segments. To account for confinement, the governing confined concrete area, i.e., the smallest triaxially stressed cross-section resulting from the dispersion of the discretely introduced confining forces, must be determined. According to current design approaches, the confined concrete area directly depends on the location of the load introduction of the confining forces (see [4] for further details on passive confinement). Consequently, the location of the load transfer from the activated welded grids to the surrounding concrete needs to be identified, which is intricate due to the complex

interaction of several rebars. Here, fibre optical (FO) strain measurements provide highly valuable insight into the behaviour, as they allow inferring the force variation along the reinforcing bars.

3.2 Experimental test

The analysed partially loaded concrete block measured 350·550 mm^2 in transverse (y-) and longitudinal (z-) directions, and 525 mm in axial (x-) direction (Fig. 3.2). The loaded area was 140·450 mm^2, which corresponds to 33% of the block area. The specimen was made of normal strength concrete with a maximum aggregate size of D_{max} = 16 mm. The compressive strength was f_{c0} = 46.5 MPa, and the tensile strength was f_{ct} = 3.7 MPa.

The test was carried out on a 20 MN compression machine at Empa in Dübendorf, Switzerland, introducing the load to the specimen by small steel bricks (Fig. 3.1a). The load was increased monotonically in deformation control at a rate between 0.2 mm/min and 0.3 mm/min, pausing three times to generate a new measurement key for the fibre optical measurements (which caused slight load drops by relaxation). The load-displacement diagram shows four measurement points considered in the analysis of the fibre optical measurements (Fig. 3.1b). The specimen exhibited a ductile behaviour with an almost horizontal plateau at the peak load, indicating a concrete compressive failure while the horizontal confining reinforcement yielded. For a detailed description of the specimen and the test setup as part of a larger experimental campaign, where the specimen presented here corresponds to WG-NC-1, see Morger and Kaufmann [1].

3.2.1 Reinforcement

Fig. 3.2 illustrates the welded reinforcement grids, which consisted of cold-worked B500B reinforcing bars with a diameter of Ø12 mm. The cross joints, which were welded by machine, had a nominal shear strength factor of at least 0.5, i.e. SF50, according to DIN EN ISO 17660 [5]. Consequently, two longitudinal reinforcing bars were positioned on each side to fully anchor a transverse bar. The longitudinal reinforcing bars were placed as far as possible to the outside of the transverse reinforcing bars, taking

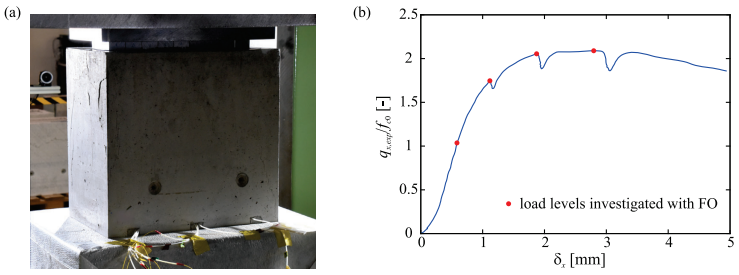

Fig. 3.1 - Experimental test: (a) partially loaded concrete specimen and (b) load-displacement diagram of test with indicated load levels used for the presentation of fibre optical measurements.

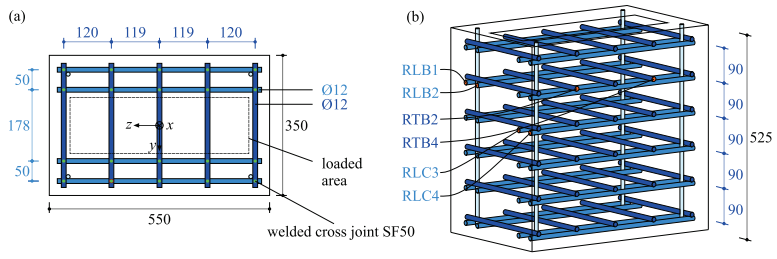

Fig. 3.2 - Reinforcement of welded grids: (a) grid with positions of welded cross joints and dimensions and (b) reinforcement layout of the specimen [mm].

into account the minimum centre line between two reinforcing bars of 50 mm, which was given through the use of the welding machine. The exact dimensions of the welded grids can be seen in Fig. 3.2a.

The specimen was reinforced with six grids equally spaced over its height, while four subsidiary bars (Ø10 mm), placed outside the loaded area, ensured the vertical spacing of 90 mm. The reinforcement layout is illustrated in Fig. 3.2b, indicating which reinforcing bars were instrumented with fibre optical sensors. The reinforcing bar (R) designation consists of the bar direction (L = longitudinal, T = transverse), the layer position (letters A-F starting from the top) and a number (starting with 1 at the most negative *y* or *z* coordinate, respectively).

The mechanical properties of the bare reinforcing bars were determined with deformation-controlled tensile tests on six specimens with a length of 1.2 m of the same batch as used for the welded grids. Up to a strain of 5.5‰, the loading rate was 0.04 mm/s (similar to strain rate of grids), followed by a stop of 2 min and subsequent loading with a rate of 0.4 mm/s up to failure. Fig. 3.3 shows the stress-strain diagrams of the material tests and the mechanical parameters, as well as an idealised stress-strain curve (see [6] based on [7], for cold-worked bars). This idealised stress-strain curve is used to infer the steel stresses from the FO strain measurements. Note that Fig. 3.3 only shows the strain measurements of a linear variable differential transformer (LVDT) of 300 mm gauge length, which was removed at approximately 25‰.

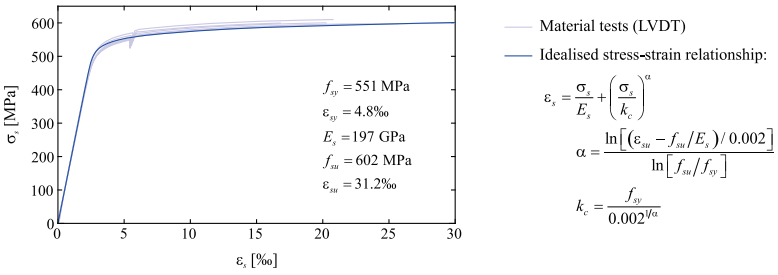

Fig. 3.3 - Material property of reinforcing bars used for welded grid reinforcement, showing material tests and idealised stress-strain relationship.

3.2.2 Fibre optical (FO) sensing

Six reinforcing bars (two transverse bars in reinforcement layer B, two longitudinal bars in layer B and two longitudinal bars in layer C, see Fig. 3.2b) were instrumented with optical fibre sensors (single-mode polyimide-coated bend-insensitive glass fibres). The fibres were connected to an optical reflector device (ODiSI-6104 from Luna Innovations Inc.), allowing for quasi-continuous strain measurements.

Two optical fibres were placed on opposite sides of each instrumented bar at the same vertical position, in grooves of approximately 1·1mm^2, filled with a two-component epoxy resin (Sikadur 52) (see Fig. 3.4). The two fibres are distinguished regarding their lateral position: For the transverse bars, "z^+" and "z^-" designate the fibre located on the side oriented in the positive and negative z-direction of the bar, respectively (same concept for y^+ and y^-). This optical fibre configuration allows determining the mean strain of the reinforcing bar as the average of the two measurements, as well as detecting any lateral bending effect. As the fibres had to be applied to the already welded reinforcement grids, it was not always possible to place the grooves in a position that did not cross the ribs. Otherwise, best practice as described in Galkovski et al. [8] was followed to instrument the reinforcing bars and collect the data.

The fibre optical data was recorded with a frequency of 1.56 Hz and an initial spacing between measurement points of 0.65 mm. It is anticipated that a maximum error of ±50 microstrains occurred at the point of steel yielding with the aforementioned FO configuration [9].

3.3 Test results and discussion

This section presents the results of the FO measurements of the six reinforcing bars indicated in Fig. 3.2b for the four load levels indicated by red dots in Fig. 3.1b (higher absolute FO measurements correspond to higher load levels). For each bar, the measured strains of both fibre optical sensors are reported separately. These measurements were filtered with a moving average over a time span of 1.92 seconds, which corresponds to three data points. Furthermore, the mean normal stresses in each reinforcing bar, inferred from the average of the two strain measurements using the idealised stress-strain relationship of the bare bar (Fig. 3.3), are documented. Finally, the curvatures of the longitudinal reinforcing bars, determined from the diametrically opposed strain measurements with a lever arm of

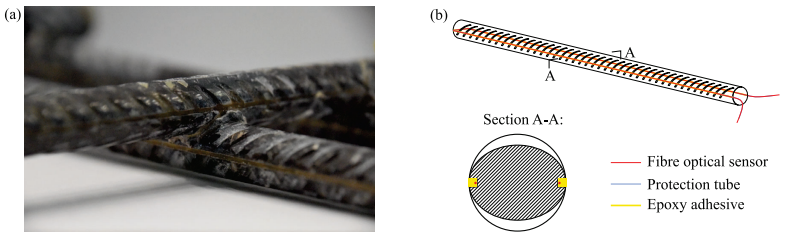

Fig. 3.4 - Instrumentation of welded reinforcement grid with FO: (a) welded cross joint with fibre optical sensors placed in the grooves and glued with epoxy resin and (b) schematic drawing of placing of fibre optical sensors on reinforcing bars (not to scale).

9.5 mm (measured distance between the fibres after testing) and assuming plane sections, are reported. Note that the results of the normal stresses and the curvatures were additionally filtered with a moving average over the reinforcing bar length with a filter window corresponding to the diameter of the reinforcing bar, i.e. 12 mm. In all figures, the positions of the bars welded perpendicularly to the reinforcing bar of interest are indicated by dashed blue lines.

3.3.1 Transverse reinforcement

Fig. 3.5 presents the results of the transverse reinforcing bars RTB2 and RTB4. In the strain profiles, the position of the inner longitudinal reinforcing bars is clearly reflected by local peaks. Furthermore, for both bars, the two measurements (z^+ and z^-) are similar, indicating that no relevant bending in the lateral direction of the transverse bars occurred. Additionally, the rib spacing of the bars (7 mm) is clearly visible, particularly for the sensors located on the z^+ side. There is no clear explanation for why the sensors on the z^- side did not show the rib spacing.

The normal stresses in the reinforcing bars increased with the load applied to the specimen. The reinforcement was barely activated at the first load level (corresponding to approximately half the peak load). At the peak load of the specimen (last presented load level), the normal stresses of both transverse reinforcing bars indicate three zones: the two anchorage zones at the ends ($y \in$ [-139 mm,-89 mm] and $y \in$ [89 mm,139 mm]) and the middle zone between the longitudinal bars ($y \in$ [-89 mm,89 mm]). While in the middle zone, the reinforcing bar yielded (with a slight stress reduction only near the inner longitudinal reinforcing bars), the stresses gradually decreased in the anchorage zones. This decrease is likely attributed to bond: the stress profile obtained using nominal bond shear stresses of $\tau_{b0} = 2\,f_{ct}$ (according to the Tension Chord Model [10]), shown in green, follows the same trend as the observed stress distribution in the anchorage zone. Even though the fibre optical sensors did not extend all the way to the outer longitudinal reinforcing bars, it can be approximated that a stress level of around 300 MPa,

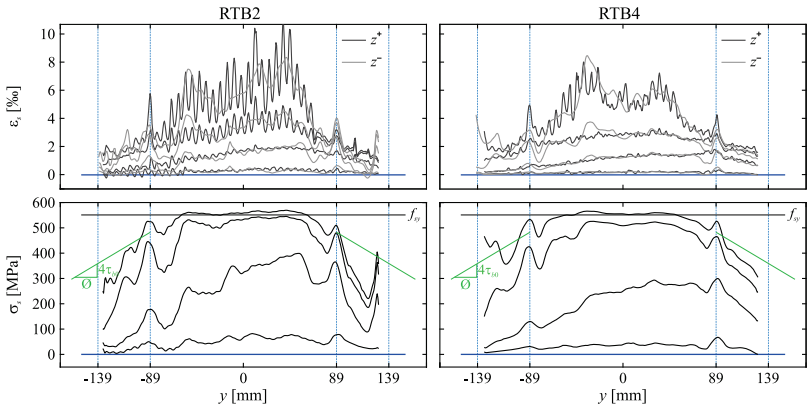

Fig. 3.5 - Results of FO measurements of the transverse reinforcing bars RTB2 and RTB4 showing the individual measured strains and the mean normal stresses for different load levels.

corresponding to a normal force of 34 kN, must have been anchored through these reinforcing bars. It is worth noting that except at the second load level, the normal stresses were fairly symmetrical. The strain measurements highlight that the transverse reinforcing bars of the welded reinforcement grid reached the yield stress. They were thus fully activated, indicating that the anchorage, including the welding connection, was sufficient. The chosen system, with two longitudinal reinforcing bars welded to the transverse bars as far as possible to the outside and a shear strength factor of 0.5, proves to be a functioning system.

The normal stress profiles of the transverse reinforcing bars show that forces are transferred to the concrete in the previously defined anchorage zones by a combination of bond and local anchorage through the two longitudinal reinforcing bars. While the exact force transferred to the concrete at the inner cross joint is difficult to determine, the normal stress profiles reveal that around 50% of the transverse reinforcing bar yield force was introduced to the concrete at the outer cross joint. Based on this finding and the fact that some load is also transferred by bond, it can be concluded that the load transfer at the inner joint is smaller than 50% of the yield force. All these forces cause horizontal compression of the concrete and can be accounted for as confinement.

3.3.2 Longitudinal reinforcement

The results of the FO measurements of the longitudinal reinforcing bars are shown in Fig. 3.6 (RLB1 and RLB2) and Fig. 3.7 (RLC3 and RLC4). The strain measurements clearly indicate the position of the transverse reinforcing bars by peak values. Furthermore, they reveal that the longitudinal bars were subjected to substantial lateral bending, with strains in a range between 1‰ in compression and 4.5‰ in tension, slightly below the yield strain of 4.8‰.

The curvature (determined as described in Section 3.3) of the longitudinal reinforcing bars increased with the load applied to the specimen. While the longitudinal reinforcing bars in layer B showed noticeable curvatures from the second load level on, those in layer C exhibited pronounced curvatures only for the last two load levels. Furthermore, it is noticeable that the outer longitudinal reinforcing bars (RLB1 and RLC4, respectively) experienced higher curvatures compared to the adjacent inner longitudinal reinforcing bars (RLB2 and RLC3, respectively). The curvature distribution, apart from reinforcing bar RLB1, was similar to that of a continuous beam with uniform loading and constant bending stiffness. Note that the different signs of curvatures between the bars in layers B and C result from the coordinate system (instrumented bars had different sign of y-coordinate).

The normal stresses in the longitudinal reinforcing bars did not reach the yield stress. At the location of the transverse reinforcing bars, the normal stress distribution experienced abrupt changes in all cases. reinforcing bar RLB1 also experienced such changes in between the transverse bars. The average of the normal stresses of the load level at the peak load is shown in the figures (Fig. 3.6, Fig. 3.7), revealing that the longitudinal reinforcing bars in layer C carried roughly 20% more load than those in layer B.

While it is commonly assumed that a considerable portion of the force in the transverse reinforcing bars is transferred directly to the concrete at the stiff welding connection between the transverse and longitudinal bars, the curvature of the longitudinal bars highlights that a relevant part of the force is transferred to the concrete via bending of the longitudinal bars. This means that the confining forces are

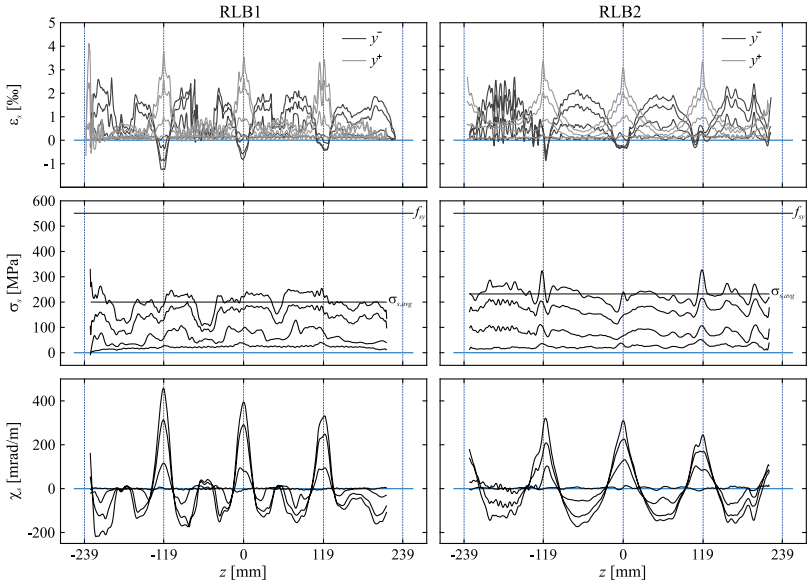

Fig. 3.6 - Results of FO measurements of the longitudinal reinforcing bars RLB1 and RLB2 showing the individual measured strains, the mean normal stresses and the curvatures.

not only introduced at discrete load introduction points but are partially distributed over the circumference of the concrete by the longitudinal reinforcement.

Quantitative assessments of the corresponding force flow, i.e., the partial load introduction through the bending stiffness of the longitudinal reinforcing bars (rather than the commonly assumed distribution of locally acting confining forces), are difficult due to the complex stress state of the longitudinal reinforcing bars, and are beyond the scope of this article. Qualitatively, however, the outer longitudinal reinforcing bars clearly exhibited higher curvatures than the inner ones, which is in line with the observation in Section 3.3.1 that more load was transferred at the outer welded connection than at the inner one. To mechanically explain this finding, the deformation of the RC specimen has to be considered: At high vertical loading (close to the uniaxial compressive strength), the concrete expands laterally (dilatancy), resulting in horizontal displacements that increase with the distance from the member axis. Consequently, the concrete displacement, and hence the load transfer to the confining reinforcement, is higher at the outer welded connection between transverse and longitudinal reinforcing bars than at the inner one. Note that this is the reason why pull-out tests on reinforcing bars with more than one welded transverse reinforcement are not representative of welded grids subjected to partial area loading: in a pull-out test, the connection close to the load application experiences higher displacements than the one towards the unloaded concrete side and thus transfers more load, which contradicts the findings of the FO measurements of the welded grids.

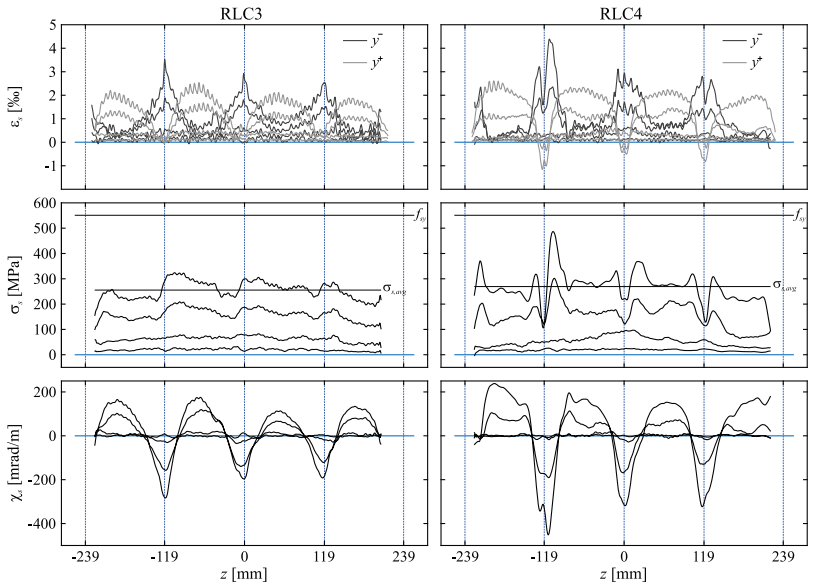

Fig. 3.7 - Results of FO measurements of the longitudinal reinforcing bars RLC3 and RLC4 showing the individual measured strains, the mean normal stresses and the curvatures.

In addition to the anchorage of the transverse reinforcing bars, the longitudinal reinforcing bars are also responsible for providing confinement in the longitudinal z-direction. The FO measurements show that average normal stresses ($\sigma_{s,avg}$) along the reinforcing bars up to 270 MPa occurred at the peak load while the outmost fibres had not reached the yield stress (maximum measured strains < ε_{sy} = 4.8‰). This indicates that for the given loading configuration of the RC specimen, the longitudinal reinforcement was able to provide sufficient confinement as well as anchorage of the transverse reinforcing bars. According to the Dual-Wedge stress field [11], two longitudinal reinforcing bars (not additionally loaded in bending due to anchorage) would be sufficient per layer to provide sufficient confinement, which is in line with the measurements (layer C: $4 \cdot A_s \cdot (270 \text{ MPa} + 255 \text{ MPa})/2 \simeq 2 \cdot A_s \cdot f_{sy}$).

In order to determine the required longitudinal reinforcement content for any configuration, the quantitative loading of the longitudinal bars due to the anchorage of the transverse bars must be known so that it can be superimposed with the loading due to confinement. Given the superimposed loading, the longitudinal reinforcement could be determined, e.g. with the von Mises yield criterion.

3.4 Recommendations for practical design and outlook

In order to fully anchor transverse reinforcing bars for RC specimens subjected to partial area loading, two longitudinal reinforcing bars connected with welded cross joints SF50 are sufficient for the layout

of the welded reinforcement grid, concrete properties and loading situation presented in this article. This statement is supported by another specimen of the experimental campaign [1], reinforced with welded grids (WG-NC-2), which performed equally well as an otherwise identical specimen reinforced with conventional stirrup reinforcement (BT-NC-3).

Furthermore, it is proposed to assume the position of the outer welded cross joints between the transverse and longitudinal reinforcing bars as the location of the discrete load introduction points to determine the governing confined concrete area according to current design approaches. This represents a reasonable simplification of the effective load-bearing behaviour: according to the FO measurements, roughly 50% of the confining force is introduced to the transverse bars at that location, with a beneficial effect of the load distribution through the longitudinal bars on the governing confined concrete area that is neglected in the current design approaches. Defining the inner welded cross joints as load introduction points would be highly conservative.

It should be kept in mind, however, that these findings are essentially based on merely one specimen. For future research on the load-bearing behaviour of welded reinforcement grids, obtaining FO measurement data of specimens subjected to partial area loading with denser reinforcement layouts (affecting the interaction of transverse and longitudinal reinforcement) and larger reinforcement diameters (with the local load-bearing capacity of the concrete governing at large diameters) would be of particular interest. Furthermore, varying the size of the partially loaded area may also impact the behaviour and could reveal if welded grids are also applicable to heavily reinforced RC structures loaded over the entire cross-section, such as piers or columns, at least where the welded joints do not provide fatigue issues. With more data, it may be possible to reliably determine the force flow in the longitudinal reinforcing bars resulting from the anchorage of the transverse reinforcing bars. Based on this, design recommendations that consider anchorage, as well as confinement, could be proposed.

3.5 Conclusions

This article presents the results of FO strain measurements along reinforcing bars that are part of the welded grid reinforcement (SF50) of a partially loaded RC specimen. Two transverse and four longitudinal reinforcing bars were instrumented with fibre optical sensors.

The results show that two longitudinal reinforcing bars are sufficient to fully activate (reaching yielding) the transverse reinforcing bars over the length between the inner welded cross joints. Besides direct load introduction at the cross joints, the longitudinal reinforcing bars are activated in bending, as highlighted by the observed transverse curvatures. Nonetheless, they are able to provide confinement in the longitudinal direction.

Further research would be needed to validate if the results also apply to varying reinforcement layouts or loading configurations. Nevertheless, the study increases the understanding of the load-bearing behaviour of welded reinforcement grids and proves that they are a promising alternative to conventional stirrup reinforcement for the production of tunnel lining segments.

Acknowledgements

This study was partially funded by the Swiss Federal Roads Office and the Swiss Federal Office of Transport (Project AGT 2019/001). The authors acknowledge the support of SABAG Biel AG for providing the welded grids and Christoph Gisler (IBK) for preparing the grooves of the reinforcing bars.

References

[1] F. Morger and W. Kaufmann, 'Design of longitudinal tunnel lining joints - experimental investigation on partially loaded reinforced concrete blocks', in *Proceedings of the 14th fib PhD Symposium in Civil Engineering*, Fédération Internationale du Béton (fib), 2022, pp. 467–474. doi: 10.3929/ethz-b-000572924.

[2] EN 1992-1-1:2023, 'Eurocode 2 - Design of concrete structures - Part 1-1: General rules and rules for buildings, bridges and civil engineering structures', Brussels, 2023.

[3] G. Schmidt-Thrö, 'Zum Tragverhalten der Tübbinglängsfuge', Doctoral Thesis, Technische Universität München, 2019.

[4] F. Morger, A. Kenel, and W. Kaufmann, 'Passive confinement of reinforced concrete members revisited', *Structural Concrete*, vol. 25, no. 6, pp. 4283–4299, 2024, doi: 10.1002/suco.202400209.

[5] DIN EN ISO 17660-1:2006-12, 'Schweißen - Schweißen von Betonstahl - Teil 1: Tragende Schweißverbindungen (ISO 17660-1:2006)', Brussels, 2006.

[6] M. Alvarez, 'Einfluss des Verbundverhaltens auf das Verformungsvermögen von Stahlbeton', Doctoral thesis, ETH Zurich, Zurich, Switzerland, 1998. doi: 10.3929/ETHZ-A-002000033.

[7] W. Ramberg and W. R. Osgood, 'Description of stress–strain curves by three parameters', National Advisory Committee For Aeronautics, Washington DC, Technical Note No. 902, 1943.

[8] T. Galkovski, Y. Lemcherreq, J. Mata-Falcón, and W. Kaufmann, 'Fundamental Studies on the Use of Distributed Fibre Optical Sensing on Concrete and Reinforcing Bars', *Sensors*, vol. 21, no. 22, p. 7643, 2021, doi: 10.3390/s21227643.

[9] J. Mata-Falcón, S. Häfliger, M. Lee, T. Galkovski, and N. Gehri, 'Combined application of distributed fibre optical and digital image correlation measurements to structural concrete experiments', *Engineering Structures*, vol. 225, p. 111309, 2020, doi: 10.1016/j.engstruct.2020.111309.

[10] P. Marti, M. Alvarez, W. Kaufmann, and V. Sigrist, 'Tension Chord Model for Structural Concrete', *Structural Engineering International*, vol. 8, no. 4, pp. 287–298, 1998, doi: 10.2749/101686698780488875.

[11] T. Markić, F. Morger, and W. Kaufmann, 'Partially loaded areas in reinforced concrete: Mechanical modelling', *Engineering Structures*, vol. 271, p. 114938, Nov. 2022, doi: 10.1016/j.engstruct.2022.114938.

Corrections

Corrections to the original content of the published article are listed below:

	Published	Adjusted
Section 3.1	headed bar reinforcement	double-headed bar reinforcement
Section 3.3.2	longitudinal *y*-direction	longitudinal *z*-direction

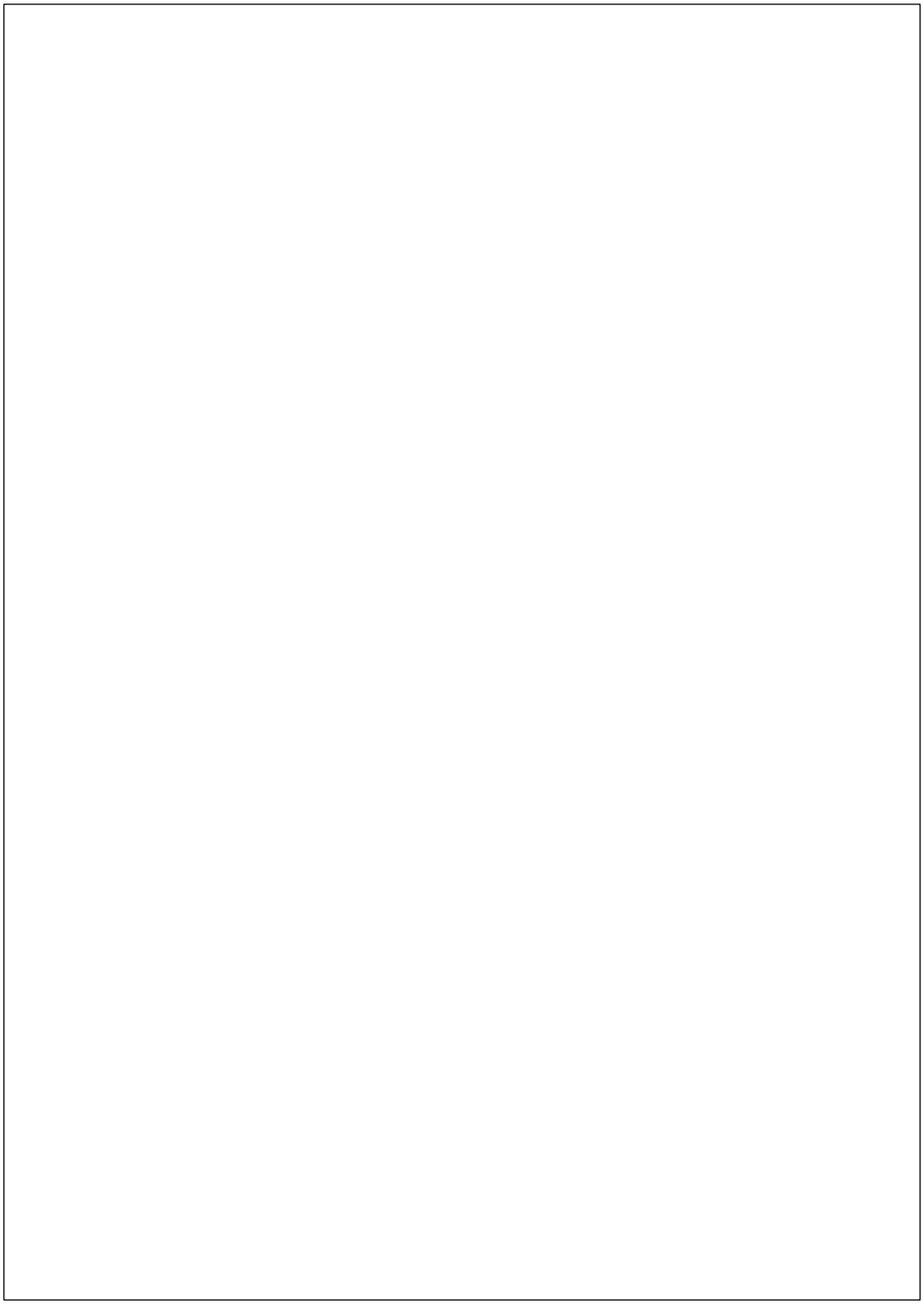

Part 2

Strip loading in reinforced concrete

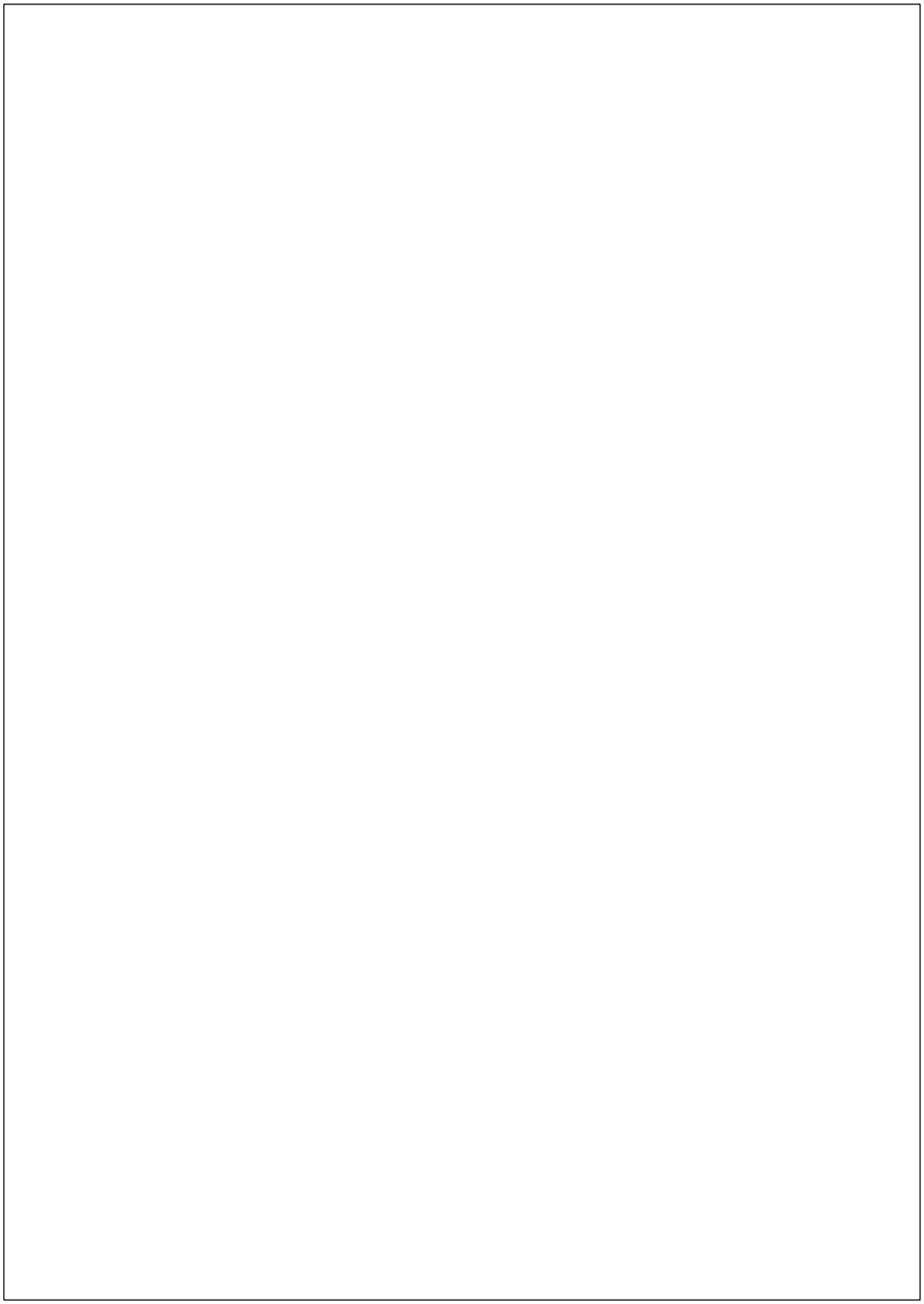

4 Mechanical modelling and experimental validation of RC blocks

The content of this chapter corresponds to the postprint of the following published article:

> **F. Morger**, A. Kenel, W. Kaufmann, 'Strip loading in reinforced concrete: Mechanical modeling and experimental validation', *Structural Concrete*, vol. 27, no. 1, pp. 163-192, 2026, doi: 10.1002/suco.70154.

This postprint includes some adjustments to the published version. For details see Section 1.5 and the corrections section at the end of this chapter.

As the lead author, Fabian Morger planned, prepared and carried out the experiments, analysed and post-processed the obtained data, extended the strip loading models, conducted the parametric study and compared the model predictions with the experimental data, and wrote the entire draft of the manuscript. The last two authors both supervised the conducted research by giving constant and valuable inputs. The second author, Albin Kenel, was particularly involved in the validation of the models. The third author, Walter Kaufmann, initially designed the experimental campaign, and carefully reviewed the manuscript.

Abstract

Strip loading of reinforced concrete is a common problem in engineering practice. The concrete compressive strength at the load introduction can be several times higher than the uniaxial concrete compressive strength, which can be attributed to geometrical and passive confining stresses caused by load dispersion and reinforcement, respectively. However, current design provisions do not allow combining these two confining effects, leading to overly conservative designs. Furthermore, experimental data on strip-loaded concrete members with pronounced passive confinement and moderate load concentration ratios, common e.g. in longitudinal joints of segmental tunnel linings, are scarce. This article presents different models for strip loading as well as an experimental campaign of 15 concrete blocks subjected to strip loading. The test parameters included (i) the reinforcement ratio and type, (ii) the width and position of the loaded area, and (iii) the concrete strength. Digital image correlation was applied to determine the crack widths. The experimental results give insight into the mechanical behaviour and were used to compare the different model approaches for strip loading, including the recently published Dual-Wedge stress field and a simplification of the same. The models are presented in detail and adjusted for strip loading with moderate load concentration ratios where required. Furthermore, it is discussed how passive confinement can be accounted for with regular and irregular reinforcement spacings. The load-bearing capacity predictions of models accounting for the combined effect of load

dispersion and passive confinement are in good agreement with the tests and allow for an efficient and safe design, whereas the simplification stands out for its ease of use and lowest coefficient of variation.

Keywords: Reinforced concrete; Strip loading; Load-bearing capacity; Confinement; Multiaxial compressive strength; Stress field; Partial area loading; Plasticity; Digital image correlation.

4.1 Introduction

Strip loading is a type of partial area loading, where a concentrated load is applied to a reinforced concrete (RC) member on an area smaller than its full cross-section and thus spreads inside the member. For strip loading, the load is strictly speaking applied over the entire length of the member, resulting in a unidirectional load dispersion, and the loaded area is much longer than wide ($b_{lz} > 2 \cdot b_{ly}$ [1], see Fig. 4.1). Cases where the load is not applied on the whole length can still be considered as strip loading as long as the unloaded part of the length is small ($b_z - b_{lz} << b_z$) [2]. Typical examples of strip loading in structural concrete are longitudinal joints of tunnel lining segments, one-way concrete hinges and narrow bridge bearings on abutment walls. Especially for tunnel lining segments with a high degree of repetition, understanding the load-bearing behaviour of the longitudinal joints is crucial to providing a safe and efficient design.

Experimental campaigns (e.g. [3] and [4]) show that the concrete compressive strength at the load introduction of strip-loaded RC members can be several times higher than the uniaxial concrete compressive strength f_{c0}. The strength increase can be attributed to lateral confining stresses, resulting either from load dispersion (geometrical confinement) or reinforcement (passive confinement). Confining stresses in both lateral directions (y and z in Fig. 4.1) cause a triaxial compressive stress state, increasing the axial concrete compressive strength (in x-direction) by four times the minimum lateral compressive stress, as already observed by Richart et al. [5], [6] nearly 100 years ago. As load dispersion occurs only in one direction for strip loading, confinement in the lateral longitudinal z-direction is only achieved by passive confining reinforcement. In the other direction (lateral transverse y-direction), load dispersion causes confining stresses near the load introduction but bursting stresses further away from it, requiring adequate transverse reinforcement to avoid a brittle concrete tensile failure. To provide additional passive confinement, the reinforcement in the latter region must exceed the amount required for the bursting stresses. For a more detailed discussion of the underlying phenomena and previous works, see for example Markić et al. [1], [4], [7].

The longitudinal joints of lining segments of tunnels with high overburden or in squeezing ground are subjected to high normal compressive forces and often govern the design of the entire segment. For such joints, the load concentration ratio b_{ly}/b_y is usually around 40%-60%. While other solutions such

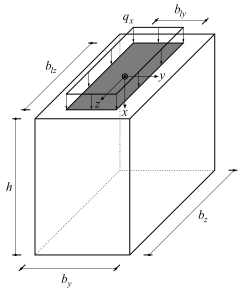

Fig. 4.1 - Definition of strip loading parameters.

as directly reinforcing the joint with steel dowels in direct contact [8] are possible, providing higher amounts of passive confinement is the most straightforward option to increase the load-bearing capacity of the joints and thereby enable thinner segments; note that reducing the contact width b_{ly} to increase geometrical confinement would lead to higher possible concrete stresses, but the load-bearing capacity of the joint would decrease due to the smaller contact area. However, experimental data on strip-loaded RC members with pronounced passive confinement and moderate load concentration ratios are scarce, making it especially difficult to assess newly developed design approaches that, in comparison to design approaches in codes (e.g. *fib* Model Code 2020 [9] or SIA 262 [10]) allow for combining the beneficial effects of load dispersion and passive confinement. This article thus aims to reduce this knowledge gap by presenting an extensive experimental campaign and investigating the suitability of different model approaches regarding strip loading. The scope is limited to the effect of passive confinement on strip loading with continuously placed reinforcement (with regular or irregular spacing) in the axial direction.

In the following, recently developed design approaches for strip-loaded RC members are presented first (Section 4.2). Subsequently, the experimental campaign, consisting of 15 RC blocks subjected to strip loading, is presented in Section 4.3, followed by the discussion of the experimental results (Section 4.4). The experimental data is finally compared to the different modelling approaches, proving that models incorporating geometrical and passive confinement provide reliable predictions of the load-bearing capacity of strip-loaded RC members (Section 4.5). The article concludes with a summary of the main findings and design recommendations for engineering practice (Section 4.6).

4.2 Design of strip-loaded RC members

This section describes four models to design strip-loaded RC members: (i) the Dual-Wedge stress field [7], (ii) a newly proposed simplification of the same, (iii) the square-root equation recommended for the design of longitudinal tunnel lining joints by the guideline of Deutscher Ausschuss für unterirdisches Bauen e. V. (DAUB) [11] and (iv) the so-called geometric and passive confinement (GPC) model [12]. All four models account for the effect of load dispersion, but only the DAUB and the GPC models consider load dispersion in both lateral directions. Furthermore, all models except DAUB consider the beneficial effect of passive confinement provided by the reinforcement. The determination of the confinement properties is described in detail for the Dual-Wedge stress field but can be applied in the same way to the other two models accounting for passive confinement. Additionally, this article considers RC members loaded eccentrically in the transverse direction, i.e., cases where the centroid of the loaded area does not coincide with that of the specimen but exhibits an eccentricity e_y. Leonhardt and Mönning [13] proposed, based on Guyon [14], to account for eccentric strip loading by reducing the width b_y of the specimen by $2 \cdot e_y$, such that a prism with centric loading remains. This approach is adopted in this article and applied to the different models, assuming a uniform stress on the loaded area ($b_{ly} \cdot b_{lz}$) with eccentricity e_y.

4.2.1 Dual-Wedge stress field

The Dual-Wedge stress field, developed by Markić et al. [7], is illustrated in Fig. 4.2. It describes the dispersion of a normal stress σ_{x0} loaded on a partial width d_1 of an RC member until a homogeneous

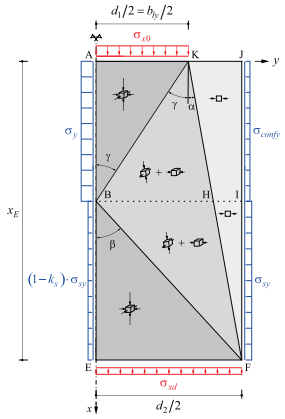

Fig. 4.2 - Dual-Wedge stress field (only one symmetrical half is shown). Transverse stresses are exaggerated compared to vertical stresses.

loading over the width $d_2 > d_1$ is reached. The stress field allows for determining the maximum load-bearing capacity σ_{x0} of strip-loaded RC members, combining the beneficial effects of the load dispersion and the passive confinement provided by transverse reinforcement on the concrete compressive strength.

The stress field represents a slice of unit length in the longitudinal z-direction and consists of several sub-fields, which are separated by discontinuity lines: The load σ_{x0} is applied on the wedge ABK, from where it spreads by the strut BFK (inclined at an angle α) until it is continuously deviated by the horizontal stresses $k_s \cdot \sigma_{sy}$ along BF to reach a uniform vertical stress σ_{xd} in the wedge BEF. While ABK and BFK are fully confined by the stresses σ_{confy} and σ_{sy}, respectively, BEF is only confined by the fraction $(1-k_s)$ of σ_{sy}, corresponding to the confining stresses below the discontinuity line BF, which is also required beyond the load introduction zone if the vertical stress over d_2 exceeds the uniaxial load-bearing capacity f_{c0}. Note that the confinement stress σ_{sy} must be greater than zero to fulfil equilibrium, while σ_{confy} could be equal to zero. The previously described sub-fields are all subjected to a triaxial stress state (assuming $\sigma_z \neq 0$, see below) whereas the sub-fields IJKH and FIH are only subjected to uniaxial compressive stresses σ_{confy} and σ_{sy}, respectively.

The input parameters for the Dual-Wedge stress field are the uniaxial concrete compressive strength f_{c0}, the width of the loaded area d_1, the width available for load dispersion d_2 and the confining stresses σ_{confy} and σ_{sy}. While f_{c0} and d_1 are mostly fixed, the other parameters depend on the reinforcement (see Section 4.2.1.1 for determination). With the input parameters defined, the geometry of the stress field and the load-bearing capacity can be determined such that equilibrium is fulfilled and the failure criteria are not infringed in any of the sub-fields, ensuring that the stress field corresponds to a lower bound solution according to plasticity theory. For concrete, the modified Coulomb failure criterion [15] with a tension cut-off is adopted (compression positive):

$$Y = \sigma_1 \cdot (1 - \sin\varphi) - \sigma_3 \cdot (1 + \sin\varphi) - 2 \cdot c \cdot \cos\varphi \leq 0 \quad \text{with } \sigma_1 \geq \sigma_2 \geq \sigma_3 \geq 0 \tag{4.1}$$

Eq. (4.1) can be simplified by the common assumption tanφ = 0.75 and $c = f_{c0}/4$ for concrete with uniaxial concrete compressive strength f_{c0}:

$$Y = \sigma_1 - 4 \cdot \sigma_3 - f_{c0} \leq 0 \tag{4.2}$$

As seen from Eqs. (4.1) and (4.2), the stress σ_z in the longitudinal z-direction does not govern failure if it is the intermediate principal stress ($\sigma_1 \geq \sigma_2 = \sigma_z \geq \sigma_3$ with σ_1, σ_3 in the x,y-plane). For the sub-fields with a triaxial stress state, this is achieved by providing sufficient confining reinforcement in the longitudinal direction; this is not required in the uniaxially stressed sub-fields. The reinforcement is assumed to only carry tension in the reinforcing bar direction, up to the yield stress f_{sy}.

For a more detailed overview of the Dual-Wedge stress field and the iterative procedure to determine the load-bearing capacity σ_{x0}, the reader is referred to Markić et al. [7].

4.2.1.1 Consideration of passive confinement

Passive confinement can substantially increase the load-bearing capacity of RC members subjected to strip loading. Its influence is particularly relevant for high load concentration ratios b_{ly}/b_y due to the reduced contribution of the geometrical confinement. According to the Dual-Wedge stress field, passive confining stresses (σ_{confy} and σ_{sy}) act uniformly distributed over the entire height x_E of the stress field. From research on passive confinement in RC it is well known that confining reinforcement is activated by the lateral expansion of concrete when approaching the uniaxial compressive strength (dilatancy), which results in discrete confining forces primarily introduced to the concrete at bends, end plates or cross joints of welded grid reinforcement [16]-[18], from where they must be spread to reach a uniform distribution. Hence, the confined concrete area inside which uniform confining stresses occur is smaller than the area inside the confining reinforcement. Furthermore, the spreading of the confining forces affects the confining stresses, as pointed out by Morger et al. [19]; the reader is referred to [19] for more details on passive confinement regarding confined concrete areas and confining stresses. Nonetheless, Markić et al. [7] assumed that the confined concrete area coincides with the area inside the confining reinforcement and determined the confining stresses according to global equilibrium for the application of the Dual-Wedge stress field. While these assumptions were successfully validated with tests on RC blocks subjected to strip loading with very narrow loaded areas as common in concrete hinges and correspondingly small load concentration ratios ($b_{ly}/b_y \leq 0.2$) [4], the comparison with the experimental data presented in this article (Section 4.5) highlights that for wider loaded areas as common in tunnel lining segment joints and correspondingly higher load concentration ratios, this approach (referenced in the following as DW-cs) is not conservative. Consequently, this article proposes to consider the effect of the spreading of the confining forces on both the confined concrete area as well as the confining stresses in the Dual-Wedge stress field (referenced as DW-cc). The following sections present how to determine the confinement parameters in the transverse (Section 4.2.1.1.1) and longitudinal direction (Section 4.2.1.1.2) for regular reinforcement spacings (see Fig. 4.3) and extend the approach to irregular reinforcement spacings (Section 4.2.1.1.3, Fig. 4.4). For simplicity, only the confining stresses σ_{conf} are used below (assuming $\sigma_{conf} = \sigma_s$); however, all presented aspects analogously apply to σ_s. Appendix 4.A.1 compiles the definition of all input parameters of DW-cs.

4.2.1.1.1 Transverse direction

The confining stresses depend on the cross-sectional area of the reinforcing bars ($Ø_s$), their spacings (s_x, s_y, and s_z) and the yield stress f_{sy}. Assuming a three-dimensional dispersion of the activated confining forces by paraboloids and respecting equilibrium, the confining stresses in the transverse direction can be determined for regular reinforcing spacings as follows [19]:

$$\sigma_{confy} = \frac{\pi \cdot Ø_s^2}{4} \cdot \frac{f_{sy}}{s_x \cdot s_z} \tag{4.3}$$

As described previously, the confined concrete area corresponds to the area with uniform confining stresses. Since the DW-cc stress field requires uniform confining stresses over its height x_E, the width d_2 available for load dispersion can be chosen equal (or smaller) to the confined concrete width b_{ccy}, which, as outlined in Morger et al. [19], corresponds to the largest uniformly confined width over the entire length of the RC member (indicated as $A_{conf,simp}$ in Fig. 4.3c, note the difference to the effective confined concrete area $A_{conf,mod}$ according to the confinement model):

$$d_2 = b_{ccy} = b_{csy} - 2 \cdot e_y - \frac{\sqrt{s_x^2 + s_z^2}}{2} \tag{4.4}$$

4.2.1.1.2 Longitudinal direction

In the longitudinal direction, the confining stresses can be determined analogously as in the transverse direction:

$$\sigma_{confz} = \frac{\pi \cdot Ø_s^2}{4} \cdot \frac{f_{sy}}{s_x \cdot s_y} \tag{4.5}$$

The longitudinal confining stresses are no input parameter of the DW-cc stress field since the longitudinal direction is assumed to be not governing. This assumption must be verified, i.e., it must be shown that the longitudinal stress σ_z provided by the longitudinal confining reinforcement ($\sigma_z = \sigma_{confz}$) indeed corresponds to the intermediate principal stress σ_2. Accordingly, assuming that the longitudinal confinement reinforcement can be activated (and averaged) over $b_{csy} - 2 \cdot e_y$, its required magnitude can be determined based on the (maximum) principal stresses ($\sigma_{1,i}$) in the triaxially stressed sub-fields as outlined in Markić et al. [7]:

$$\begin{aligned} \sigma_{confz,req,\text{DW-cc}} &= \frac{Z_{z,conf}}{\left(b_{csy} - 2 \cdot e_y\right) \cdot x_E} \\ Z_{z,conf} &= 2 \cdot \sum \sigma_{z,i} \cdot A_i \text{ with } i = \{ABK, BHK, BFH, BEF\} \\ \sigma_{z,i} &= \frac{1}{4}\left(\sigma_{1,i} - f_{c0}\right) \geq 0 \end{aligned} \tag{4.6}$$

where $Z_{z,conf}$ = integral of the required longitudinal confining stresses. For $\sigma_{confz} \geq \sigma_{confz,req,\text{DW-cc}}$ the load-bearing capacity σ_{x0} determined with the DW-cc stress field does not infringe the failure criterion. Otherwise, the longitudinal direction is governing and the calculation of σ_{x0} by the DW-cc stress field needs to be adjusted by reducing the transverse confining stress σ_{confy} until $\sigma_{confz} \geq \sigma_{confz,req,\text{DW-cc}}$, i.e., the transverse confining reinforcement cannot be fully activated due to limited longitudinal confining reinforcement.

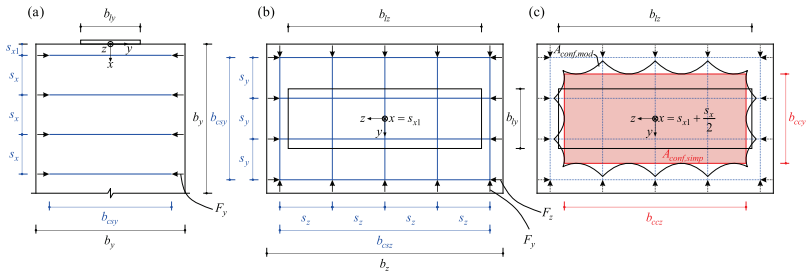

Fig. 4.3 - Confinement properties for regular reinforcement spacings: (a) vertical section, (b) horizontal section at the height of a reinforcement layer, and (c) horizontal section at the centre between two reinforcement layers.

Besides the amount of longitudinal confining stresses, the confined concrete length b_{ccz} ($b_{ccz} < b_{lz}$) impacts the load-bearing capacity of a strip-loaded RC member; its value can be determined as follows [19]:

$$b_{ccz} = b_{csz} - \frac{\sqrt{s_x^2 + s_y^2}}{2} \tag{4.7}$$

The loaded concrete area inside b_{ccz} can sustain the vertical loading σ_{x0} determined by the DW-cc stress field, while areas outside can only contribute to the load-bearing capacity with the uniaxial concrete compressive strength f_{c0}. Consequently, the ultimate load-bearing capacity $q_{x,u,\text{DW-cc}}$ of a strip-loaded RC member is:

$$q_{x,u,\text{DW-cc}} = \frac{\sigma_{x0,\text{DW-cc}} \cdot b_{ccz} + f_{c0} \cdot (b_{lz} - b_{ccz})}{b_{lz}} = f_{c0} \cdot \left(1 + \frac{b_{ccz}}{b_{lz}} \cdot \left(\frac{\sigma_{x0,\text{DW-cc}}}{f_{c0}} - 1\right)\right) \tag{4.8}$$

Note that the cover concrete (concrete outside the centre line of the outermost reinforcement) is disregarded, as it is prone to spalling due to (i) the activation of the confinement reinforcement, (ii) the high axial strains required to activate the confined strength and (iii) the pronounced lateral expansion.

4.2.1.1.3 Irregular reinforcement spacings

In the previous sections, the confining stresses (σ_{conf}) and the confined concrete area ($b_{ccy} \cdot b_{ccz}$) were determined presuming regular reinforcement spacings, which are not always practical or possible in engineering practice. Therefore, irregular confining reinforcement spacings are discussed in the following.

In the vertical direction, the largest reinforcement spacing $s_{x,max}$ determines the governing confined concrete cross-section. Consequently, the confining stresses and the confined concrete area must be determined based on $s_{x,max}$. Hence, locally smaller vertical spacings are of no use, i.e., a uniform vertical spacing of the confining reinforcement ($s_x = s_{x,max}$) should always be chosen. Besides the vertical spacing in general, the distance of the first reinforcement layer from the load application (s_{x1}, Fig. 4.3a) requires special attention, as it is governing if $s_{x1} > s_x/2$. Based on the confinement model [19], uniform confining stresses are possible by increasing the rise of the vertical (half) parabola adjacent to the load

introduction, whereby the confining stresses become a function of both s_{x1} as well as s_x. Specifically, s_x in Eq. (4.3) has to be replaced by $\max(s_x,(s_x+2\cdot s_{x1})/2)$. Note that in such cases, according to the confinement model, only the first reinforcement layer is fully activated, which has been confirmed by experimental results [4]. Accordingly, such reinforcement layouts lack efficiency. On the other hand, for strip loading – as in general for partial area loading – the spacing s_{x1} does not impact the width available for load dispersion d_2 and has no impact on d_1 only if:

$$b_{ly} < b_{csy} - 2\cdot\left(\left(\frac{s_{x1}}{s_x}\right)^2\cdot\left(\sqrt{s_x^2+s_z^2}-s_z\right)+\frac{s_z}{4}\right) \tag{4.9}$$

where the squared term on the right-hand side reflects the larger rise of the vertical (half) parabola adjacent to the load introduction to ensure vertical equilibrium. Otherwise, b_{ly} is wider than the confined concrete width at the load introduction area, which should be avoided; such cases are not covered in this article. However, even if the condition (4.9) is complied with, s_{x1} has an influence on the confined concrete length b_{ccz} in the longitudinal direction as further outlined below. On a side note, the paraboloids spreading the confinement stresses according to the confinement model [19] lack vertical support at the height of the load introduction, i.e., they do not strictly satisfy equilibrium, in the case of strip loading since in comparison to loading on the full cross-section, as occurring for columns, equilibrium cannot be ensured through the applied load.

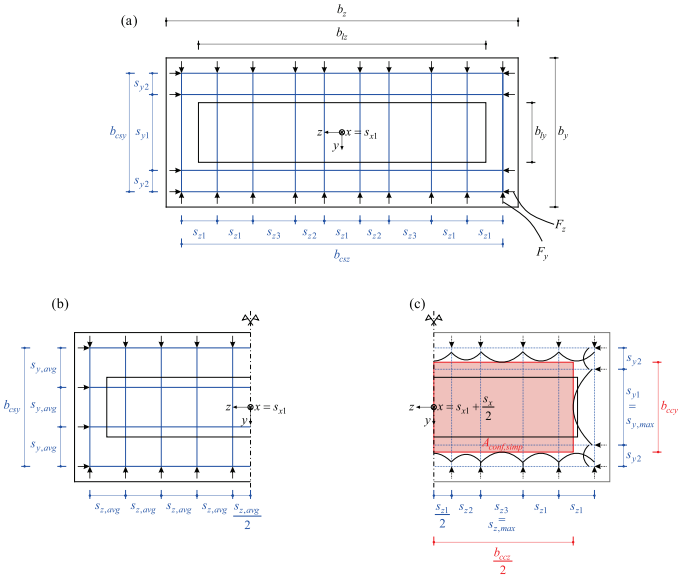

Fig. 4.4 - Confinement properties for irregular reinforcement spacings: (a) horizontal section at the level of the confining reinforcement with irregular reinforcement spacings in the transverse and longitudinal directions, (b) assumed average reinforcement spacings to compute confining stresses, and (c) confined concrete area determined based on maximum spacings in the respective directions.

Fig. 4.4 shows a reinforcement layout with irregular spacings in the lateral directions. It is assumed that the confining reinforcement layout is the same over the entire height. In contrast to the vertical direction, different reinforcement spacings in the lateral directions have a local effect on the confining stresses and the confined concrete area, resulting in several regions (in the cross-section) with different confinement properties. Essentially, the load-bearing capacity could be computed with the DW-cc stress field for all regions, followed by the determination of the total load-bearing capacity of the member. However, this process is tedious, particularly since equilibrium of the dispersion of the confining forces should be satisfied. Hence, the following simplifications are adopted: (i) the confining stresses σ_{conf} are determined using the average of the different reinforcement spacings $s_{y,avg}$ and $s_{z,avg}$ (see Fig. 4.4b), whereas (ii) the confined concrete area ($b_{ccy} \cdot b_{ccz}$) is defined based on the maximum spacings $s_{y,max}$ and $s_{z,max}$ in the respective directions (Fig. 4.4c).

Based on the above considerations, Eqs. (4.3)-(4.5) and (4.7) are adjusted in the case of irregular spacings of the confining reinforcement in the vertical or lateral directions as follows:

$$\sigma_{confy} = \frac{\pi \cdot Ø_s^2 \cdot f_{sy}}{4 \cdot \max\left(s_x, \frac{s_x + 2 \cdot s_{x1}}{2}\right) \cdot s_{z,avg}} \tag{4.10}$$

$$d_2 = b_{ccy} = b_{csy} - 2 \cdot e_y - \frac{\sqrt{s_x^2 + s_{z,\max}^2}}{2} \tag{4.11}$$

$$\sigma_{confz} = \frac{\pi \cdot Ø_s^2 \cdot f_{sy}}{4 \cdot \max\left(s_x, \frac{s_x + 2 \cdot s_{x1}}{2}\right) \cdot s_{y,avg}} \tag{4.12}$$

$$b_{ccz} = b_{csz} - 2 \cdot \left(\frac{s_{x1}}{s_x}\right)^2 \cdot \left(\sqrt{s_x^2 + s_{y,\max}^2} - s_{y,\max}\right) - \frac{s_{y,\max}}{2} \quad \text{with } s_{x1} \geq \frac{s_x}{2} \tag{4.13}$$

4.2.1.2 Simplified Dual-Wedge stress field

The Dual-Wedge stress field allows for a detailed computation of the load-bearing capacity but requires an iterative solution, which is less straightforward than analytical equations. For practical application, a simplification (DW-s) considering the effects of load dispersion and passive confinement is thus proposed:

$$\sigma_{x0,\text{DW-s}} = \left(\frac{d_2}{d_1}\right)^{\frac{2}{5}} \cdot \left(f_{c0} + 4 \cdot \sigma_{confy}\right) \leq \frac{5}{2} \cdot \left(f_{c0} + 4 \cdot \sigma_{confy}\right) \quad \text{with } d_2 \geq d_1 \tag{4.14}$$

Eq. (4.14) results from a best fit of a parametric investigation of the Dual-Wedge stress field and yields similar load-bearing capacities as the Dual-Wedge stress field; its formulation is inspired by a student project thesis supervised by the first and last authors [20]. Its comparison to the Dual-Wedge stress field in Appendix 4.A.2 shows the simplification yields lower load-bearing capacities for load concentration ratios (d_1/d_2) of approximately 0.2...0.6, but is less conservative for $d_1/d_2 < 0.2$. However, the

comparison with the experimental data in Section 4.5 indicates that the predictions of the DW-s are still on the safe side even for these low concentration ratios. All input parameters of the simplified Dual-Wedge model (DW-s) follow the same definition as for the DW-cc, and the load-bearing capacity of a strip-loaded RC member according to the DW-s is determined analogously to Eq. (4.8):

$$q_{x,u,\text{DW-s}} = \frac{\sigma_{x0,\text{DW-s}} \cdot b_{ccz} + f_{c0} \cdot (b_{lz} - b_{ccz})}{b_{lz}} = f_{c0} \cdot \left(1 + \frac{b_{ccz}}{b_{lz}} \cdot \left(\frac{\sigma_{x0,\text{DW-s}}}{f_{c0}} - 1\right)\right) \tag{4.15}$$

Due to the semi-empirical nature of Eq. (4.14), the required longitudinal confining stress $\sigma_{confz,req,\text{DW-s}}$ and the height of the load introduction zone x_E requiring confining reinforcement cannot be mechanically determined. Instead, the following semi-empirical expressions obtained from the parametric study of the Dual-Wedge stress field (see Fig. 4.A.1) are adopted:

$$\sigma_{confz,req,\text{DW-s}} = \frac{d_1}{(b_{csy} - 2 \cdot e_y)} \cdot \left(1.75 - 0.75 \cdot \frac{d_1}{d_2}\right) \cdot \sigma_{confy} \tag{4.16}$$

$$x_E = d_1 + d_2 \leq 1.5 \cdot d_2 \tag{4.17}$$

Note that just as in the Dual-Wedge stress field, (i) confining reinforcement is required beyond the load dispersion zone if the vertical stress exceeds the uniaxial load-bearing capacity f_{c0}, and (ii) the confinement in the transverse direction cannot be fully activated if the longitudinal reinforcement governs, i.e., in such cases, the transverse confining stresses need to be reduced. To achieve the latter, Eq. (4.16) can be rearranged and solved for σ_{confy} with $\sigma_{confz,req,\text{DW-s}}$ = longitudinal confining stress σ_{confz} provided by the given longitudinal reinforcement.

In comparison to the other design approaches presented in this article considering geometrical as well as passive confinement, the DW-s is the most straightforward and simplest model to apply.

4.2.1.3 Cases $b_{csy} \geq b_{ly} \geq b_{ccy}$

If the width of the loaded area b_{ly} exceeds the confined concrete width b_{ccy}, neither DW-cc nor DW-s can be applied as no load dispersion is possible. Hence, the load-bearing capacity can be determined as in the standard case of confinement by accounting for (i) the uniaxial compressive strength f_{c0} over the entire loaded area and (ii) the strength increase due to confinement ($4 \cdot \min(\sigma_{confy}, \sigma_{confz})$) inside the confined concrete area:

$$\begin{aligned} q_{x,u} &= \frac{f_{c0} \cdot b_{ly} \cdot b_{lz} + 4 \cdot \min\left(\sigma_{confy}, \sigma_{confz}\right) \cdot b_{ccy} \cdot b_{ccz}}{b_{ly} \cdot b_{lz}} \\ &= f_{c0} \cdot \left(1 + 4 \cdot \frac{\min\left(\sigma_{confy}, \sigma_{confz}\right)}{f_{c0}} \cdot \frac{b_{ccy} \cdot b_{ccz}}{b_{ly} \cdot b_{lz}}\right) \end{aligned} \tag{4.18}$$

In case of eccentric loading fulfilling the condition $b_{ly}/2 < b_{ccy}/2 + 2 \cdot e_y$, the load-bearing capacity can be computed as follows:

$$q_{x,u} = \frac{f_{c0} \cdot b_{ly} \cdot b_{lz} + 4 \cdot \min\left(\sigma_{confy}, \sigma_{confz}\right) \cdot \left(\frac{b_{ly} + b_{ccy}}{2}\right) \cdot b_{ccz}}{b_{ly} \cdot b_{lz}}$$
$$= f_{c0} \cdot \left(1 + 4 \cdot \frac{\min\left(\sigma_{confy}, \sigma_{confz}\right)}{f_{c0}} \cdot \frac{\left(\frac{b_{ly} + b_{ccy}}{2}\right) \cdot b_{ccz}}{b_{ly} \cdot b_{lz}} \right) \tag{4.19}$$

4.2.2 Square-root equation DAUB

According to the latest recommendations for the design of tunnel lining segments by DAUB [11], the load-bearing capacity of the longitudinal joints, which correspond to strip loading situations, can be determined based on the well-known square-root equation (from here on referenced as DAUB only):

$$q_{x,u,\mathrm{DAUB}} = \sqrt{\frac{A_c}{A_{c0}}} \cdot f_{c0} \le 3 \cdot f_{c0}$$
$$A_c = \left(b_y - 2 \cdot e_y\right) \cdot b_z \tag{4.20}$$
$$A_{c0} = b_{ly} \cdot b_{lz}$$

The purely empirical Eq. (4.20) merely accounts for the load dispersion (ratio of area available for load dispersion A_c to loaded area A_{c0}, see Fig. 4.5c), neglecting any effect of confining reinforcement. The load is assumed to spread over the entire concrete cross-section A_c, including the cover concrete. To prevent splitting failure in the predominant load dispersion direction, transverse reinforcement capable of resisting the bursting force F_{ty} (= integral of bursting stresses) must be provided at a distance $0.4 \cdot (b_y - 2 \cdot e_y)$ from the load application area:

$$F_{ty,\mathrm{DAUB}} = \frac{q_{x,u,\mathrm{DAUB}} \cdot b_{ly} \cdot b_{lz}}{4} \cdot \left(1 - \frac{b_{ly}}{b_y - 2 \cdot e_y}\right) \tag{4.21}$$

The square-root equation was proposed by Spieth [21] in 1961 for partial area loading problems based on tests on centrically loaded plain concrete cylinders. Due to the empirical nature of Eq. (4.20), previous DAUB editions [22] required geometrical similarity between the loaded area and the area available for load dispersion, which is highly restrictive and typically conservative for strip loading. In contrast, the latest edition only (i) requires sufficient height to enable a load dispersion with an inclination of 2:1 and (ii) limits the width of the area available for load dispersion in the transverse direction to three times the loaded width b_{ly} for mean concrete compressive strengths $f_{c0} > 58$ MPa (C50/60). However, these conditions are not governing for any specimen presented in this article and used for the comparison of the different models in Section 4.5.

Note that the EN 1992-1-1:2023 [23] also determines the load-bearing capacity of partially loaded RC members with the square-root equation, but is more restrictive than the latest DAUB regarding the area available for load dispersion, resulting in lower load-bearing capacities. Hence, it is not considered further in this article.

4.2.3 GPC model

The GPC model proposed by Proksch-Weilguni et al. [12] incorporates the effects of geometrical confinement (load dispersion) as well as passive confinement on the load-bearing capacity of partially loaded axisymmetric RC members such as partially loaded cylinders. For this article, it has been adjusted for strip loading, accounting for a three-dimensional load dispersion with a predominant direction.

The GPC model assumes that the load is dispersed to the area inside the reinforcement ($A_{cs} = b_{csy} \cdot b_{csz}$) over a height $b_y - 2 \cdot e_y$ and determines the load-bearing capacity as the lower of the resistances in two control sections, which are located at both ends of this height. At the load introduction (control section 0-0), the strength increase by geometrical confinement is determined with the square-root equation, and passive confinement is accounted for by increasing the concrete compressive strength f_{c0} by four times the minimum lateral confining stress (σ_{confy} or σ_{confz}) inside the confined concrete area A_{cc}, which may not exceed the loaded area A_{c0}. The contributions of load dispersion and confinement are simply added up, resulting in the upper bound of the load-bearing capacity F_{GPC0}:

$$\begin{aligned} F_{\mathrm{GPC0}} &= f_{c0} \cdot \min\left(\sqrt{\frac{A_{cs}}{A_{c0}}}, 1\right) \cdot A_{c0} + 4 \cdot \min\left(\sigma_{confy}, \sigma_{confz}\right) \cdot \min\left(A_{c0}, A_{cc}\right) \\ A_{cs} &= \left(b_{csy} - 2 \cdot e_y\right) \cdot b_{csz} \\ A_{cc} &= b_{ccy} \cdot b_{ccz} \end{aligned} \tag{4.22}$$

In the control section 1-1, the load is assumed to be distributed over the partially confined area inside the reinforcement ($A_{cs} = b_{csy} \cdot b_{csz}$). The upper bound of the load-bearing resistance F_{GPC1} thus comprises the contribution of the uniaxial concrete compressive strength f_{c0} inside A_{cs} and the increased concrete compressive strength due to confinement inside the confined area A_{cc}:

$$\begin{aligned} F_{\mathrm{GPC1}} &= f_{c0} \cdot A_{cs} + 4 \cdot \min\left(\sigma_{confy} - \frac{F_{ty,\mathrm{GPC}}}{n_{sp} \cdot s_x \cdot b_{csz}}, \sigma_{confz} - \frac{F_{tz,\mathrm{GPC}}}{n_{sp} \cdot s_x \cdot \left(b_{csy} - 2 \cdot e_y\right)}\right) \cdot A_{cc} \\ \text{with } F_{ty,\mathrm{GPC}} &= \xi_y \cdot F_{\mathrm{GPC}} \cdot \frac{b_{csy} - 2 \cdot e_y - b_{ly}}{8 \cdot x_{sp}} \\ \text{with } \xi_y &= \frac{\left(b_{csz} + b_{lz}\right) \cdot \left(b_{csy} - 2 \cdot e_y - b_{ly}\right)}{2 \cdot \left(A_{cs} - A_{c0}\right)} \\ \text{with } F_{tz,\mathrm{GPC}} &= \xi_z \cdot F_{\mathrm{GPC}} \cdot \frac{b_{csz} - b_{lz}}{8 \cdot x_{sp}} \\ \text{with } \xi_z &= 1 - \xi_y \end{aligned} \tag{4.23}$$

where x_{sp} (defined by the parameters R_0, R_1, see Fig. 4.5b) is determined by the predominant load dispersion direction y and the confining stresses in both lateral directions are reduced by the amount required to equilibrate the bursting stresses due to load dispersion (see $F_{ty,\mathrm{GPC}}$ and $F_{tz,\mathrm{GPC}}$ in Eq. (4.23)). While the GPC model [12] is limited to axisymmetric cases, it is assumed here that F_{GPC} is spread into the two directions in proportion to the parts of the load-spreading area inside the reinforcement ($A_{cs} = b_{csy} \cdot b_{csz}$) available for load dispersion per direction (allocated according to the shortest distance to the respective edge of the loaded area, see Fig. 4.5c), indicated by the parameters ξ_y and ξ_z in

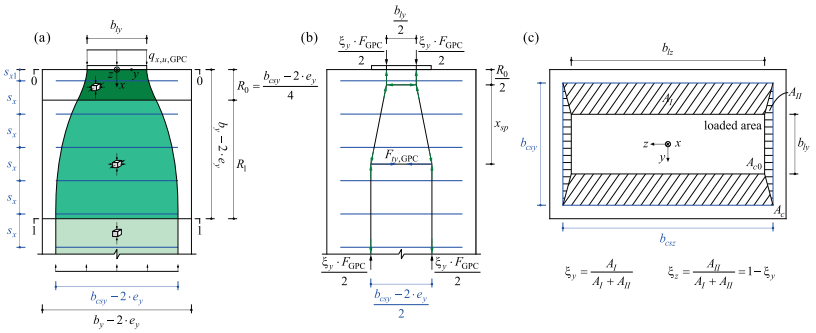

Fig. 4.5 - Geometric and passive confinement model: (a) definition of the two control sections, (b) determination of bursting force F_{ty} with strut-and-tie model, and (c) definition of ξ_y and ξ_z determining the load spreading in the two lateral directions.

Eq. (4.23). The minimum resistance of the two control sections investigated determines the load-bearing capacity:

$$q_{x,u,\mathrm{GPC}} = \frac{F_{\mathrm{GPC}}}{A_{c0}} \qquad \text{with } F_{\mathrm{GPC}} = \min\left(F_{\mathrm{GPC0}}, F_{\mathrm{GPC1}}\right) \tag{4.24}$$

Note that the GPC model requires an iterative solution procedure since the ultimate load-bearing capacity F_{GPC} is required to determine the bursting forces $F_{ty,\mathrm{GPC}}$ and $F_{tz,\mathrm{GPC}}$ in section 1-1, and does not check the concrete stresses between the two control sections. In the lower part of this region, bursting stresses occur as in the control section 1-1, but the loaded area is smaller; accordingly, lower load-bearing capacities than predicted by Eq. (4.23) could result.

4.3 Experimental campaign

This section presents 15 RC specimens subjected to strip loading. They were part of a wider experimental campaign consisting of 21 specimens in total; the remaining six specimens were cast with steel fibre reinforced concrete (SFRC) and will be described in an upcoming article focusing on strip loading with SFRC. The following sections compile the specimen geometry and production, the material properties, the test setup and the measurement systems.

4.3.1 Specimens, materials, and casting

An overview of the 15 specimens is given in Table 4.1. They consisted of geometrically identical concrete blocks with dimensions $b_y \cdot b_z$ = 350·550 mm² in transverse (y-) and longitudinal (z-) directions and h = 525 mm in axial (x-) direction. The width of the loaded area (b_{ly}) varied between 140 and 210 mm, corresponding to 40% and 60% of the block width, respectively. The length of the loaded area was

Table 4.1 - Overview of experimental campaign.

Specimen	b_{ly} [mm]	e_y [mm]	f_{c0} [MPa]	Reinf. layout [-]	f_{sy} [MPa]	s_x [mm]	$s_{z,avg}$ = $s_{z,max}$ [mm]	$s_{y,avg}$ [mm]	$s_{y,max}$ [mm]	ω_y(1) [-]	ω_z(2) [-]	$N_{x,u,exp}$ [MN]	$q_{x,u,exp}/f_{c0}$ [-]
BT-NC-1	140	0	46.5	BT1	545	90	120	278	238	0.12	0.05	5.37	1.83
BT-NC-2	140	0	50.8	BT2	545	85	68	278	238	0.21	0.05	6.61	2.07
BT-NC-3	140	0	50.8	BT3	545	85	68	93	108	0.21	0.15	7.44	2.32
BT-NC-3e	140	58	50.8	BT3	545	85	68	93	108	0.21	0.15	5.34	1.67
BT-NC-4	140	0	50.8	BT4	545	85	68	70	108	0.21	0.21	7.72	2.41
BT-NC-5	210	0	46.5	BT3	545	85	68	93	108	0.23	0.17	7.84	1.78
BT-HC-1	140	0	76.6	BT1	545	90	120	278	238	0.07	0.03	7.59	1.57
BT-HC-2	140	0	76.6	BT3	545	85	68	93	108	0.14	0.10	8.33	1.73
BT-HC-2e	140	29	76.6	BT3	545	85	68	93	108	0.14	0.10	7.43	1.54
WG-NC-1	140	0	46.5	WG1	551	90	120	93	178	0.12	0.16	6.12	2.09
WG-NC-2	140	0	50.8	WG2	551	85	68	93	178	0.21	0.16	7.57	2.36
WG-NC-3	140	0	50.8	WG3	551	85	68	56	60	0.21	0.26	8.59	2.68
WG-NC-4	140	0	46.5	WG4	551	50	60	56	60	0.37	0.40	11.03	3.76
WG-NC-5	210	0	46.5	WG3	551	85	68	56	60	0.23	0.28	9.66	2.20
HB-NC-1	140	0	46.5	HB1	552	50	60	93	80	0.37	0.24	10.53	3.60

All specimens with b_y = 350 mm, b_z = 550 mm and h = 525 mm, b_{lz} = 450 mm, $Ø_s$ = 450 mm, c_{nom} = 30 mm, b_{csy} = 270 mm, b_{csz} = 450 mm, and s_{x1} = 36 mm.

(1): $\omega_y = \sigma_{confs}$(Eq. (4.10))/$f_{c0}$

(2): $\omega_z = \sigma_{confs}$(Eq. (4.12))/$f_{c0}$

b_{lz} = 450 mm (i.e. 82% of the block length) and was kept constant for all tests. For two specimens the loaded area was eccentrical in the transverse direction, with eccentricities e_y of 29 and 58 mm. The block geometry with the loaded area is illustrated in Fig. 4.6a.

All specimens were cast in lubricated formwork on a vibrating table. In order to obtain a smooth concrete surface for the load introduction, the specimens were cast upside down with a mechanically polished steel plate as the bottom formwork. After curing, the casting surface was mechanically ground to ensure coplanar surfaces and avoid unintended eccentricities. Due to limited formwork availability, the specimens were cast in three different batches. Two batches were made of normal strength concrete (NC) and the third batch was of high strength concrete (HC). The maximum aggregate size was D_{max} = 16 mm for all specimens, and the clear concrete cover (c_{nom}) of the load-bearing reinforcement measured 30 mm. A sufficient number of standard cylinders were cast simultaneously with the specimens. All specimens and cylinders from the same batch were tested at an age greater than 28 days and within as short a period as possible to minimise the influence of concrete ageing. The measured average uniaxial cylinder compressive strengths are reported in Table 4.1. Additional mechanical concrete properties can be found in Appendix 4.B.

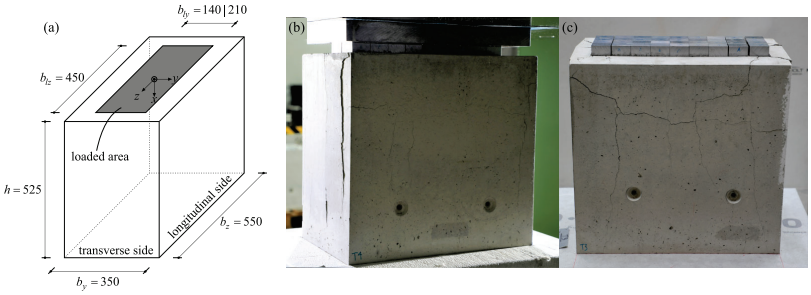

Fig. 4.6 - (a) Specimen geometry [mm], (b) test setup, and (c) tested specimen with steel bricks used for load introduction. Adapted from Morger and Kaufmann [24].

The specimens were reinforced with bent ties (designation BT), welded grids (WG), and double-headed bars (HB), which were continuously placed in the transverse and longitudinal direction over the full height. Bent ties and double-headed bars are state of the art reinforcement today, while welded grids are less common in load-bearing structures. However, compared to bent ties, prefabricated welded grids greatly simplify the reinforcement assembly, reducing time and costs in the prefabrication process, making them particularly suitable for bulk production as common in tunnel lining segments. The diameter ($Ø_s$) of the confining reinforcement measured 12 mm for all three reinforcement types. The reinforcement spacing in the vertical direction was ensured by four subsidiary bars ($Ø_s$ = 10 mm) placed outside the loaded area. The connections between the transverse and longitudinal reinforcing bars of the welded grids were produced by machine welding, with a nominal shear strength factor of at least 0.5, i.e., SF50, according to ISO 17660-1:2006 [25]. Hence, two longitudinal bars were required on each side to fully anchor a transverse bar. Due to the welding machine, the minimum centreline distance of two bars was 50 mm. In order to generate the largest possible confined concrete area, the two longitudinal bars were placed as far to the outside of the transverse bars as possible. The double-headed bars were of the type *ancoPLUS*, produced by the company *Ancotech*, with a head diameter of approximately

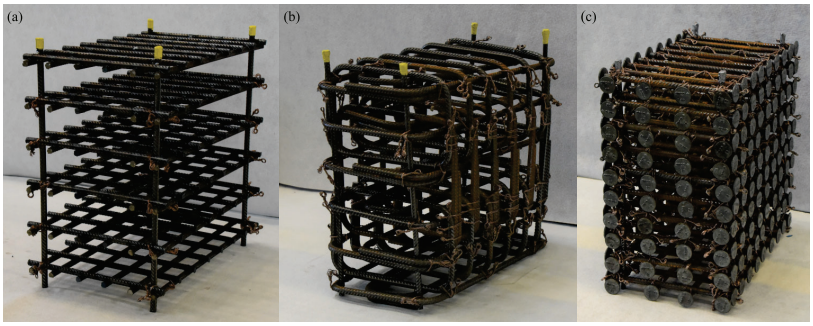

Fig. 4.7 - Reinforcement configurations: (a) welded grids (WG3), (b) bent ties (BT3) and (c) double-headed bars (HB1) [24].

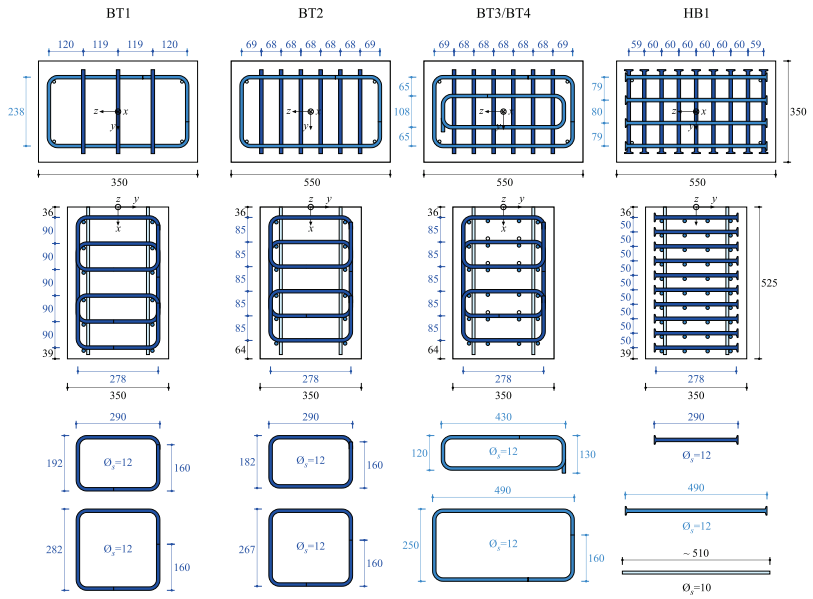

Fig. 4.8 - Reinforcement configurations of bent ties and double-headed bars (dimensions in mm). Top two rows show reinforcement spacings between centre lines, bottom two rows external dimensions. Three pairs of the inner longitudinal ties (shown without filling) were placed in BT4 but not in BT3.

2.5 times the nominal bar diameter. Fig. 4.7 shows a reinforcement configuration of each type. The reinforcing steel of all three reinforcement types was of class B500B, with only the double-headed bars exhibiting a distinct yield plateau. The yield stresses of the reinforcement are summarised in Table 4.1; Appendix 4.B compiles further information on its mechanical properties. Besides the different reinforcement types, the reinforcement ratio of the specimens varied in the transverse and longitudinal directions. Four distinct reinforcement configurations were employed for the bent ties (BT1-BT4) and welded grids (WG1-WG4), along with one of the double-headed bars (HB-1). Fig. 4.8 (BT and HB) and Fig. 4.9 (WG) illustrate the reinforcement arrangements in detail, with Table 4.1 summarising the reinforcement spacings required to compute the confining stresses and the confined concrete area for each specimen according to Section 4.2.1.1. Based on the confining stresses (σ_{confy} and σ_{confz}) and the uniaxial concrete compressive strength f_{c0}, mechanical reinforcement ratios (determined according to the confinement model [19]) of $\omega_y = 0.07...0.37$ and $\omega_z = 0.03...0.40$ were achieved in the transverse and longitudinal direction, respectively. The longitudinal bars of the welded grids were, besides providing confinement in the longitudinal direction, subjected to lateral bending due to activation of the transverse bars. Due to the complexity of the interaction (see [18]), a higher longitudinal reinforcement ratio was generally chosen for the welded grids than for the bent ties and double-headed bars to avoid premature failure due to limited longitudinal reinforcement.

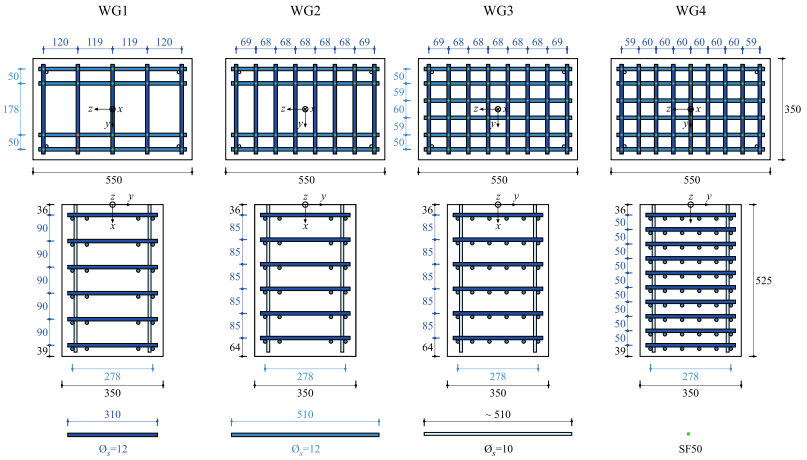

Fig. 4.9 - Reinforcement configurations of welded grids (dimensions in mm). Top two rows show reinforcement spacings between centre lines, bottom row external dimensions.

4.3.2 Test setup

All tests were conducted with a 20 MN compression testing machine at Empa in Dübendorf, Switzerland. The specimens were loaded quasi-statically in compression by controlling the machine displacement, which was monotonically increased at a rate between 0.2 and 0.3 mm/min until the peak load. The specimens were unloaded past the peak load after a significant load decrease was observed. Specimen WG-NC-5 was loaded in four steps, keeping the load constant for 2...4 hours between the steps to investigate the short-term creep behaviour. For two specimens (WG-NC-1 and WG-NC-3), the testing machine displacement was several times kept constant (3…6 minutes) to facilitate fibre optical strain measurements, which caused slight load drops by relaxation. The specimens were loaded at the partial load introduction via small steel bricks (17.5·45·30 mm^3) whose interface with the load introduction plate was adequately lubricated to ensure that they could follow any lateral displacement of the loaded concrete surface with little restraint. In contrast to a conventional steel loading plate, which would restrain the lateral expansion of the concrete by its stiffness, this load introduction system minimises the additional confinement of the concrete, ensuring that the load-bearing capacity obtained in the tests is representative of situations with a concrete-concrete interface, such as in longitudinal joints of tunnel lining segments. On the opposite side of the partial load introduction, the specimens were placed on a steel block with a narrow floor liner in between. Friction may thus have generated additional confinement near this end. However, as (i) the stresses at this end are much lower than at the load introduction and hence, (ii) the governing sections are outside this region, since continuous confining reinforcement is provided over the full specimen height, the additional confinement did not affect the load-bearing capacity. For a more in-depth discussion about the effect of the load introduction system see Markić et al. [4].

4.3.3 Measurement systems

The testing machine measured the applied normal force N_x and displacements. In addition, digital image correlation (DIC) was applied to measure the displacement fields on the specimen surfaces and the displacement of the load introduction plate. The DIC data was processed with the commercial software VIC-3D [26]. The resulting strain fields were further processed with the open-source software ACDM [27], [28] to determine the crack patterns and crack widths. Furthermore, fibre optical measurements were conducted to gain insight into the activation of the reinforcement. The latter results are presented in Morger and Kaufmann [18] and are not discussed further in this article.

4.3.3.1 DIC setup

For every test, two neighbouring lateral sides (transverse and longitudinal direction) of the RC specimens were investigated with DIC systems. Except for the specimen BT-NC-1, whose transverse side was monitored with a 2D DIC system, only 3D DIC systems were used. FLIR Grasshopper3 cameras (4096·3000 px) with lenses with focal lengths of 25 or 24 mm, respectively, measured the transverse sides of all specimens and the longitudinal sides of BT-NC-1 and WG-NC-1. For the longitudinal sides of the remaining specimens PointGrey cameras (1920·1200 px) with lenses with a focal length of 28 mm were used. The resolution was always above 5 px/mm and 2 px/mm for the transverse and longitudinal sides, respectively. The stereo angles varied between 19 and 31 degrees. The speckle pattern consisted of randomly placed black dots of diameter 0.66 mm (FLIR) or 2.54 mm (PointGrey), applied on the white-painted and well-lit specimen surfaces. Average noise levels with standard deviations $\sigma(U,V)$ below 3 µm resulted from zero displacement tests performed according to Mata-Falcón et al. [29] with the following correlation parameters: subset size = 17 px and step size = 4 px for the transverse sides and subset size = 23 px and step size = 6 px for the longitudinal sides with a strain filter size = 5 for both sides.

4.4 Results of the experimental campaign

This section presents the results of the 15 RC specimens subjected to strip loading. The peak loads $N_{x,u,exp}$ and corresponding average peak stresses $q_{x,u,exp}$ applied on the loaded area, normalised by the concrete compressive strength f_{c0}, are shown in Table 4.1. Fig. 4.10 illustrates the load-deformation behaviour by plotting the average axial stress $q_{x,exp}$ (normalised by the concrete strength f_{c0}) against the penetration δ_x, and Fig. 4.11 shows the development of a typical crack pattern by additionally plotting $q_{x,exp}/f_{c0}$ against the crack width $w_{r,max}$. These plots are discussed in the following. For further reference, Appendix 4.C compiles the corresponding diagrams for all normal strength (Fig. 4.C.1) and high strength (Fig. 4.C.2) concrete specimens. In all these plots, the penetration δ_x refers to the axial deformation between the bottom of the specimen and the load introduction plate obtained by DIC, thus eliminating any influence of the machine deformation.

4.4.1 Load-bearing and failure behaviour

Fig. 4.10 compares the load-deformation curves of all specimens, grouped to study the influence of different parameters: Except for Specimen BT-HC-1, the load-penetration diagrams highlight a ductile failure behaviour with a pronounced increase in deformation (= vertical penetration δ_z) with only a small increase in load. The failure can be described as crushing failure due to limited passive confinement. Specimen BT-HC-1 (see Fig. 4.10d) exhibited an almost linear load-penetration behaviour up to the peak load and a brittle failure, which can be attributed to the low mechanical transverse reinforcement ratio of 0.07, which is below the recommended minimum reinforcement ratio of 0.1 [4] in this direction.

The influence of the load concentration ratio $b_{ly}/(b_y - 2{\cdot}e_y)$ is illustrated in Fig. 4.10a. As the load concentration ratio increases (wider load), the geometrical confinement and hence the load-bearing capacity ($q_{x,u,exp}/f_{c0}$) of otherwise identical specimens (f_{c0} of 46.5 MPa or 50.8 MPa, respectively) decreases. This observation applies to specimens with reinforcement configurations WG and BT, normal and high strength concrete and centric loading. For example, Specimens WG-NC-3 and BT-NC-3 with a load concentration ratio of 0.40 experienced a peak stress corresponding to $2.68{\cdot}f_{c0}$ and $2.32{\cdot}f_{c0}$, respectively, whereas Specimens WG-NC-5 and BT-NC-5 with a load concentration ratio of 0.60 achieved a peak stress of only $2.20{\cdot}f_{c0}$ and $1.78{\cdot}f_{c0}$, respectively. Note that a higher load concentration ratio due to a wider loaded width b_{ly} results in lower peak stresses $q_{x,u}$; however, the peak normal force $N_{x,u}$ increases due to the larger loaded area. The specimens loaded eccentrically sustained lower load-bearing capacities in comparison to centrically loaded but otherwise equal specimens (BT-NC-3e vs. BT-NC-3 and BT-HC-2e vs. BT-HC-2). Even compared to a specimen with the same load concentration ratio (BT-NC-3e vs. BT-NC-5), the eccentrically loaded specimen exhibited a lower load-bearing capacity. These experimental observations would be in accordance with the test results if the load concentration ratios were determined based on the width inside the reinforcement b_{csy} instead of the block width b_y (BT-NC-3e: 0.86; BT-NC-5: 0.76); note that this change would not affect the interpretation of the test results in

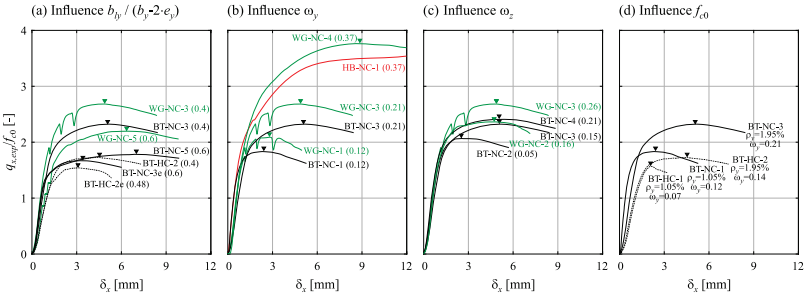

Fig. 4.10 - Load-penetration diagrams for all specimens investigating different influences: (a) load concentration ratio $b_{ly}/(b_y - 2{\cdot}e_y)$, (b) mechanical transverse reinforcement ratio ω_y, and (c) mechanical longitudinal reinforcement ratio ω_z and (d) concrete compressive strength f_{c0}. The value of the respective influence parameter is indicated in brackets where applicable. For more detailed information on the specimens, see Table 4.1.

the centrically loaded specimens. However, based on one comparison alone, no final conclusion can be drawn.

Fig. 4.10b presents the results of specimens differing in the mechanical reinforcement ratio ω_y (ω_z varying simultaneously) and the reinforcement configuration. All specimens were loaded over a width b_{ly} = 140 mm, and the concrete compressive strengths were similar (46.5 or 50.8 MPa). It is evident that a higher reinforcement ratio results in higher load-bearing capacities as the passive confinement increases. While the reinforcement ratio did not affect the initial stiffness, the penetration δ_x at peak load increased with higher reinforcement ratios. It should be noted that the specimens with welded grids had a higher longitudinal reinforcement ratio than otherwise identical specimens reinforced with bent ties or double-headed bars.

Fig. 4.10c illustrates the effect of varying the longitudinal reinforcement ratio ω_z for different reinforcement configurations but otherwise identical properties (ω_y = 0.21, f_{c0} = 50.8 MPa, b_{ly} = 140 mm). It can be seen that the longitudinal reinforcement ratio affects the load-bearing capacity despite the predominant two-dimensional load dispersion, with higher ratios ω_z resulting in higher load-bearing capacities. While Specimen BT-NC-2 was designed such that ω_z was governing, the other specimens contained sufficient reinforcement in the longitudinal direction according to DW-cc. As a result, BT-NC-2 sustained the lowest load and a reduced penetration at the peak load. The difference in the peak load of the other specimens can be attributed to the different longitudinal reinforcement ratios, including the correspondingly different confined concrete areas in the longitudinal direction. The comparison of Specimens WG-NC-2 and BT-NC-3 – the only direct comparison between bent ties and welded grids with the same properties (the others always varied in the longitudinal reinforcement ratio) – indicates that welded grids perform at least as well as bent ties.

Fig. 4.10d compares NC and HC specimens with bent ties, loaded over a width b_{ly} = 140 mm and with two different geometrical reinforcement ratios (BT-NC-1 and BT-HC-1: ρ_y = 1.05%, ρ_z = 0.45%; BT-NC-3 and BT-HC-2: ρ_y = 1.95%, ρ_z = 1.44%). The figure highlights that the normalised load-bearing capacity is significantly lower for HC specimens than for NC specimens with the same geometrical reinforcement content. However, the difference is much less pronounced when comparing test specimens with similar mechanical reinforcement ratios (BT-NC-1 vs. BT-HC-2). This comparison indicates that the load-bearing capacity normalised by the concrete strength is slightly lower for high-strength specimens compared to normal-strength specimens with the same mechanical reinforcement ratio. However, this observation is based on a comparison of merely two specimens; hence, further tests are essential to validate it effectively.

4.4.2 Crack development

The crack widths are of primary interest in the serviceability limit state (SLS), where crack width limitations – typically in the range of 0.2...0.3 mm – are defined to prevent durability issues of RC structures. For example, issues can occur in tunnel lining segments due to increased permeability, excessive water leaks, or reinforcement corrosion [30]. In the context of normal force on longitudinal lining joints, cracks can initiate on the load introduction side due to compatibility of the loaded and unloaded areas, or on the lateral sides due to concrete expansion related to passive confinement activation or tensile stresses resulting from load dispersion.

Fig. 4.11a illustrates the development of the crack width $w_{r,max}$, using Specimen WG-NC-3 as an example; corresponding plots of all specimens can be found in Appendix 4.C. The crack width $w_{r,max}$, representing the maximum measured crack width (averaged over a crack length of 10 mm) obtained by ACDM, is plotted in orange for the transverse (dashed line) and longitudinal (solid line) sides with respect to the average axial stress $q_{x,exp}$ (normalised by the concrete strength f_{c0}). In addition, the load levels at which a crack width of 0.2, 0.3 and 0.5 mm occurs for the first time are indicated by black dots on the load-penetration curve, and a triangle indicates the peak load. Commonly, cracks on the transverse side were wider than on the longitudinal side. The longitudinal side was only governing in Specimen BT-HC-2e for a crack width of 0.2 mm; for 0.3 mm, all specimens were governed by the transverse side. In most tests, the crack widths initially grew slowly with increasing load, until they started to open more pronouncedly, in many cases suddenly. This sudden crack width increase is related to spalling of the cover concrete, which was in turn caused by the activation of the confining reinforcement and associated lateral concrete expansion. Concrete cover spalling depends on the tensile strength of the concrete, which makes it difficult to predict and explains the scatter in the test results, which could further be influenced by self-equilibrated initial stresses.

Fig. 4.11b, c and d show the crack patterns on the transverse and longitudinal side of Specimen WG-NC-3 at crack widths = $w_{r,max}$ = 0.2, 0.3 and 0.5 mm, respectively. The development of the crack pattern in this specimen was similar to that observed in several other tests. On the transverse side, a crack formed first in the centre in the axial direction, indicating transverse load propagation and bursting stresses. Further cracks appeared as the load increased and spalling became dominant. In the

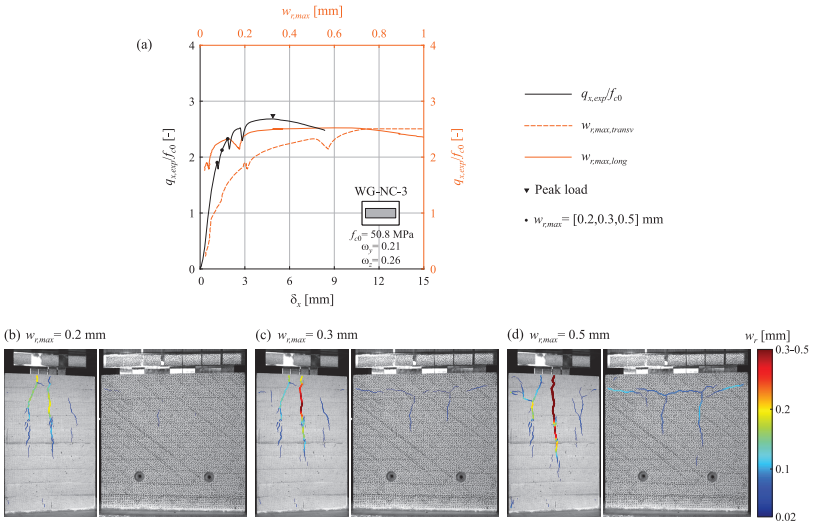

Fig. 4.11 - Crack development in Specimen WG-NC-3: (a) normalised applied average stresses $q_{x,exp}/f_{c0}$ versus penetration δ_x and maximum crack width $w_{r,max}$, (b)-(d) crack patterns of two neighbouring lateral sides for load stages with (b) $w_{r,max}$ = 0.2 mm, (c) $w_{r,max}$ = 0.3 mm and (d) $w_{r,max}$ = 0.5 mm.

Table 4.2 - Ratio between the stress at a maximum crack width $w_{r,max}$ of 0.2, and 0.3 mm and the peak stress, expressed in percentage [%] (bold values indicate that the crack width governs the design).

Specimen	BT-NC-1	BT-NC-2	BT-NC-3	BT-NC-3e	BT-NC-4	BT-NC-5	BT-HC-1	BT-HC-2	BT-HC-2e	WG-NC-1	WG-NC-2	WG-NC-3	WG-NC-4	WG-NC-5	HB-NC-1	NC		HC	
																min	mean	min	mean
$\frac{q_{x,exp}(w_{r,max}=0.2\text{mm})}{q_{x,u,exp}}$	82	73	**49**	79	70	61	**47**	54	**35**	63	69	71	59	71	**52**	49	67	35	45
$\frac{q_{x,exp}(w_{r,max}=0.3\text{mm})}{q_{x,u,exp}}$	89	78	53	79	73	65	**49**	58	**44**	75	77	79	66	74	56	53	72	44	50

longitudinal direction, a horizontal crack frequently occurred near the upper edge of the specimen, with cracks emanating from it in the axial direction. Specimen WG-NC-5, which was loaded in four steps, keeping the load constant for 2...4 hours between the steps, reveals that the crack widths grow along with short-term creep deformations. This should be kept in mind when interpreting the test data and discussing the load levels at which a certain crack width is reached.

Table 4.2 compiles the ratios between the applied stress at crack widths $w_{r,max}$ of 0.2 and 0.3 mm, respectively, and the peak stress. Assuming a partial safety factor of 1.35 for the load (only permanent loads) and an average partial safety factor of 1.40 for the materials – noting that the load-bearing capacity depends on the compressive strength of the concrete as well as the tensile strength of the confining reinforcement, and that mean rather than characteristic material properties are relevant in SLS – the SLS load level corresponds to roughly 1/(1.35·1.40) = 53% of the experimentally obtained peak stress. Consequently, neglecting creep-related crack growth, the crack width would govern the design and reduce the admissible stress in comparison to the experimentally obtained structural load-bearing capacity for values below 53% in Table 4.2. Accordingly, the serviceability criterion would govern for two of the three high strength specimens, but only for two normal strength specimens, BT-NC-3 and HB-NC-1. In comparison with other similar specimens, the crack widths of BT-NC-3 are far off and can be considered an outlier though no specific causes for this behaviour were identified. In HB-NC-1, on the other hand, the end plates of the double-headed bars were extremely close to each other (see Fig. 4.7c), such that the cover concrete was barely connected to the core of the specimen, favouring spalling and explaining the large crack widths at moderate load. Note that the crack widths influenced by spalling are affected by the thickness of the concrete cover, such that the results presented here cannot be extrapolated to RC members with differing properties.

In conclusion, predicting the crack widths for strip-loaded RC members is highly challenging, and corresponding recommendations are beyond the scope of this article.

4.5 Comparison of design approaches with experimental data

In this section, the models for strip loading discussed in Section 4.2 are compared to the experimental results presented in Section 4.4 and additional data from literature. Several conditions need to be fulfilled for experiments to be valid for the comparison: (i) The specimen must be considered strip-loaded

($b_{le} > 2 \cdot b_{ly}$) and (ii) confining reinforcement needs to be provided over the entire height of the specimen with the required information on the reinforcement spacings given. Furthermore, (iii) only specimens for which the load is applied centrically on the loaded area are considered, excluding tests on longitudinal tunnel lining joints with applied joint rotations. Given these limitations, only selected data from Markić et al. [4] is used for the comparison. All specimens considered and their input parameters for the different models are summarised in Table 4.D.1 in Appendix 4.D.

Several publications [4], [18] provided insight into the reinforcement activation of strip-loaded RC members by fibre optical measurements, confirming that the confining reinforcement can be fully activated (i.e. reaches the yield strain). Consequently, the yield stress of the reinforcement is taken into account to determine the confining stresses σ_{conf}. The confining forces are assumed to be introduced to the concrete at the bends of stirrups or the end plates of double-headed bars. The load transfer is more complex for welded grids with several transverse bars anchoring a reinforcing bar. In this article, it is assumed that for the welded grid configurations presented in Section 4.3.1, the confining force is applied to the concrete at the outer welded cross joint, as proposed in Morger and Kaufmann [18], based on fibre optical measurements of welded grids.

Fig. 4.12 plots the ratios of the experimentally observed load-bearing capacity ($q_{x,u,exp}$) to the predictions of the different models ($q_{x,u,model}$) based on the Dual-Wedge stress field against (a) the load concentration ratio, (b) the mechanical reinforcement ratio in the transverse direction and (c) the concrete compressive strength. Additionally, the plots contain a linear regression curve for each model. As already pointed out in Section 4.2.1.1, the application of the Dual-Wedge stress field assuming load dispersion until the outermost confining reinforcement and confining stresses according to global equilibrium (DW-cs, see Appendix 4.A.1), overestimates the load-bearing capacity of specimens with increasing load concentration ratios (Fig. 4.12a). Only for very narrow load application widths ($b_{ly}/(b_y - 2 \cdot e_y) < 0.2$), the predictions of DW-cs are on the safe side. The predictions of the models defined in this paper, DW-cc and DW-s, assume load dispersion only within the confined concrete width b_{ccy} and the confining stresses σ_{conf} determined according to the confinement model [19]. They provide similar predictions, with DW-s being more conservative than DW-cc for moderate load concentration ratios and vice versa

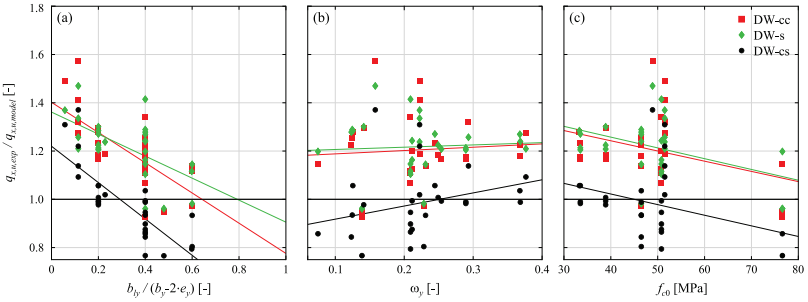

Fig. 4.12 - Comparison of experimental data with different model approaches based on the Dual-Wedge stress field plotted against (a) load concentration ratio $b_{ly}/(b_y - 2 \cdot e_y)$, (b) transverse mechanical reinforcement ratio ω_y, and (c) uniaxial concrete compressive strength f_{c0}.

Table 4.3 - Statistical parameters of different models compared to experimental tests.

$\frac{q_{x,u,\exp}}{q_{x,u,model}}$	DW-cc	DW-cc(η_{cc})	DW-s	DW-cs	GPC	DAUB
Mean	1.20	1.32	1.22	0.98	1.23	1.48
COV	12%	12%	10%	15%	15%	24%
Min	0.93	1.05	0.96	0.77	0.91	0.90
Max	1.57	1.72	1.47	1.37	1.54	2.15

for narrow load concentration ratios (<0.2); which is to be expected according to the comparison of these two models in Appendix 4.A.2. Both models show the same tendency as DW-cs to be more conservative for narrow load application widths b_{ly} than for wider ones, for which some predictions are even slightly unsafe. The high conservatism for narrow load application widths can be explained by the fact that for these situations, the impact of confinement is limited, and load dispersion can occur beyond the confined concrete area or even, supported by the concrete tensile strength, extend into the cover concrete. This increases the load-bearing capacity due to an increase of the geometrical confinement. However, such a load transfer cannot be explained mechanically consistent with the Dual-Wedge stress field, and should not be benefited from in design due to the dependency on the unreliable tensile concrete strength and potentially brittle failure modes. Fig. 4.12b reveals no trend of the load-bearing capacity predictions of DW-cc and DW-s with the transverse mechanical reinforcement ratio ω_y. This indicates that the impact of confinement is reliably covered, including the effect of the factor k_s (see Fig. 4.2 and Table 4.D.1 in the appendix), which determines the fraction of the confining stresses that is required for equilibrating the load dispersion. Furthermore, the comparison in Fig. 4.12c indicates that for high-strength concrete, the model predictions are slightly unsafe. However, applying the concrete brittleness factor $\eta_{cc} = (30/f_{c0})^{(1/3)} \leq 1$ and accordingly reducing the concrete compressive strength, as often used in current codes (e.g. SIA 262 [10]) would result in more conservative predictions for the normal-strength specimens (for illustration see comparison of experimental data with predictions of DW-cc considering η_{cc} in Table 4.D.1). Table 4.3 compiles the statistical evaluation of comparing the different models with the experimental data.

Fig. 4.13 presents the comparison of the DW-s and GPC models, as well as the DAUB approach, with the experimental data. Generally, it can be seen that DW-s and GPC provide similar results, while DAUB is highly conservative. GPC and DAUB are most conservative for narrow load application widths but the least conservative for wide load application widths, just as the models based on the Dual-Wedge stress field. However, in comparison to DW-s the predictions of GPC and DAUB indicate a linear dependency on the mechanical reinforcement ratio in the transverse direction (Fig. 4.13b): On the one side, for low reinforcement ratios, the predictions of the load-bearing capacity match the experimental data well and are less conservative than DW-s. Conversely, for highly reinforced specimens, the load-bearing capacity is significantly underestimated particularly by DAUB but also GPC, corresponding to more conservative predictions than DW-s. Primarily due to these observations, the coefficient of variation (COV) of the GPC and DAUB is higher than that of DW-s (see Table 4.3). Note that since DAUB does not account for confining reinforcement at all, the difference in the predictions to GPC must increase with increasing reinforcement ratio. Fig. 4.13c highlights that GPC and DAUB follow the same trend as DW-s regarding the influence of the concrete compressive strength, becoming

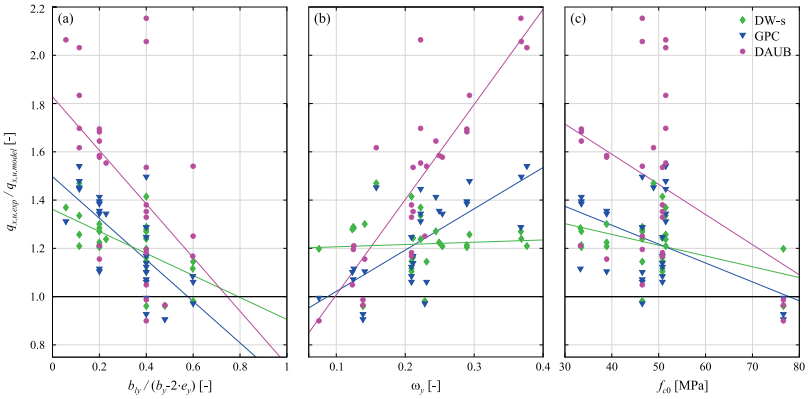

Fig. 4.13 - Comparison of experimental data with model predictions plotted against (a) load concentration ratio $b_{ly}/(b_y - 2{\cdot}e_y)$, (b) transverse mechanical reinforcement ratio ω_y, and (c) uniaxial concrete compressive strength f_{c0}.

slightly unconservative for high strength concrete. Furthermore, it is worth noting that in the GPC, the loaded cross-section 0-0 governs for all specimens except WG-NC-5.

The comparison of the different model approaches with the experimental data indicates that for strip-loaded RC members with pronounced confining reinforcement, models combining the effects of load dispersion and passive confinement (DW-cc, DW-s and GPC) predict the load-bearing capacity more reliably than approaches only accounting for load dispersion (DAUB). In this context, the simplification of the Dual-Wedge stress field (DW-s) stands out due to its simplicity and the lowest coefficient of variation. The comparison successfully validates the DW-cc and DW-s models and the adjustment of the GPC model for strip loading. Furthermore, it confirms that the proposed procedures to determine the confinement parameters (Section 4.2.1.1) are reasonable, and it indicates that the proposal to consider the effect of eccentric loading (Section 4.2) is plausible. However, with only two eccentrically loaded specimens in the data set, the latter conclusion lacks rigorous validation. Lastly, none of the models indicates that the quality of the prediction depends on the reinforcement type.

4.6 Conclusion

This article presents different models for strip loading as well as an experimental campaign on 15 strip-loaded concrete blocks with pronounced passive confinement and moderate load concentration ratios tested to failure. The investigated parameters were (i) the reinforcement ratio and type, (ii) the width and position of the loaded area and (iii) the concrete strength. The results show that specimens with a mechanical reinforcement ratio above the minimum of 0.1 in the transverse direction experience a ductile behaviour and that the load-bearing capacity can be substantially increased with higher amounts of confining reinforcement, which was shown for different reinforcement types (bent ties, welded grids, and double-headed bars). The performance of the different reinforcement types did not vary

substantially, indicating that welded grids can be a viable alternative to bent ties. Furthermore, the tests confirm that the geometrical confinement decreases with a larger loaded width or eccentric loading, thereby reducing the maximum contact stress at the load introduction. Finally, the results reveal that compared to normal strength specimens, high strength specimens tend to have lower normalised load-bearing capacities, which in addition may not be fully utilised as the crack width governs the design. However, only three specimens were made of high strength concrete, and more experimental data is required to substantiate these preliminary conclusions.

Besides the experimental campaign, the article presents four different models (DW-cc, DW-s, GPC, DAUB) to design RC members subjected to strip loading and introduces how to determine the confining stresses and confined concrete area for regular and irregular reinforcement spacings. The different models are compared to experimental data. It is shown that the models combining the effects of load dispersion and passive confinement (DW-cc, DW-s and GPC) predict the load-bearing capacity similarly on average and all with good accuracy, comparable levels of scatter and generally on the safe side. The DAUB approach, which considers load dispersion only, is found to be highly conservative in the majority of cases. The successful validation of the three models incorporating passive confinement indirectly confirms that the proposed approaches to determine the confining stresses and the confined concrete area are reasonable. Among these models, the GPC model only investigates two sections to determine the load-bearing capacity of strip-loaded RC members: one at the load introduction and one at the position where the load is fully spread. In contrast, the Dual-Wedge stress field captures the entire load path, allowing for the analyse of the load-bearing capacity of every horizontal section of the load dispersion area and to consistently determine the reinforcement position. Furthermore, it complies with EN 1992-1-1:2023 [23], which allows the combination of passive and geometrical confinement for the design of partially loaded areas if three-dimensional stress fields are applied. On the other hand, while the application of the DW-cc in design is rather cumbersome, the simplified DW-s, obtained from a parametric study of the Dual-Wedge stress field, stands out because of its straightforward formulation and the lowest coefficient of variation, which indicates that it is best able to cover the different influences on the load-bearing capacity despite its simplicity.

The authors propose to design strip-loaded RC members according to the simplification of the Dual-Wedge stress field (DW-s) with the input parameters determined as presented in Section 4.2.1.1 based on the passive confinement model [19]. The mechanically consistent DW-cc model can provide further insight regarding the reinforcement layout and is the only model that is capable of accounting for varying confining stresses in the confining and bursting regions ($\sigma_{confy} \neq \sigma_{sy}$). Consequently, the DW-cc is proposed for detailed evaluations and is particularly useful for the evaluation of existing structures.

Acknowledgements

The authors gratefully acknowledge the support by: The Swiss Federal Roads Office and the Swiss Federal Office of Transport for partially funding this work (Project AGT 2019/001). The SABAG Biel AG for providing the welded grids. The *Ancotech* company for sponsoring the double-headed bars *ancoPLUS*. The staff of the IBK structures lab at ETH Zurich for their support during the preparation of the experiments. Robert Widmann for his support at testing at Empa testing hall. The staff of the Empa testing hall for their support during the conduction of the experiments. The Master's student Nino Hasler for his support in finding a simplification for the Dual-Wedge stress field.

Appendix 4.A Dual-Wedge stress field

4.A.1 DW-cs

$$\sigma_{confy} = \frac{n_{sy} \cdot \pi \cdot \varnothing_s^2 \cdot f_{sy}}{4 \cdot \max\left(s_x, \frac{s_x + 2 \cdot s_{x1}}{2}\right) \cdot b_{csz}} \tag{4.A.1}$$

$$\sigma_{confz} = \frac{n_{sz} \cdot \pi \cdot \varnothing_s^2 \cdot f_{sy}}{4 \cdot \max\left(s_x, \frac{s_x + 2 \cdot s_{x1}}{2}\right) \cdot b_{csy}} \tag{4.A.2}$$

$$d_2 = b_{csy} - 2 \cdot e_y \tag{4.A.3}$$

$$b_{ccz} = b_{csz} \tag{4.A.4}$$

Eqs. (4.A.1)-(4.A.4) determine the parameters to apply the Dual-Wedge stress field as proposed by Markić et al. [4], denoted as DW-cs in this article.

4.A.2 Comparison of Dual-Wedge stress field and simplification

Fig. 4.A.1 compares the Dual-Wedge stress field (DW) and the simplification (DW-s) for three different mechanical reinforcement ratios (0.1, 0.25 and 0.4). For the discussion, see Section 4.2.1.2.

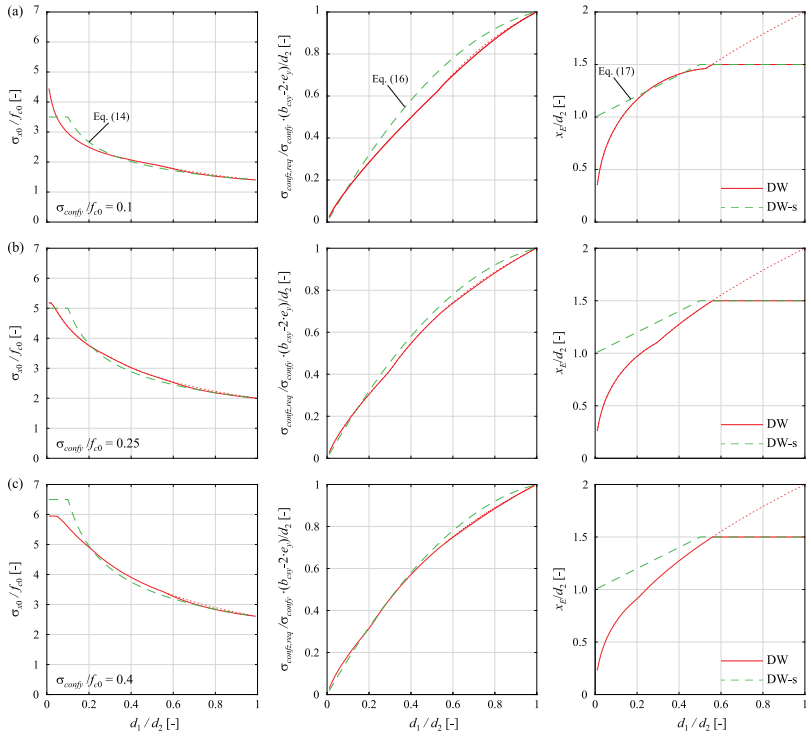

Fig. 4.A.1 - Comparison of Dual-Wedge stress field and the simplification for different mechanical confining reinforcement ratios.

Appendix 4.B Mechanical properties of concretes and reinforcing steels

4.B.1 Concrete

Table 4.B.1 compiles the mean values, the number of tested samples and the coefficients of variation of the mechanical properties of the different concrete batches. Standard cylinders with a diameter of 150 mm and a height of 300 mm were used to determine the cylinder compressive strength f_{c0} and the Young's modulus E_c (secant modulus at a stress of roughly $0.3 \cdot f_{c0}$). The cube compressive strength $f_{c,cube}$

was determined from standard cubes of 150 mm side length. The tensile strength f_{ct} was determined indirectly using double punch tests on half standard cylinders with 37.5 mm diameter steel punches [31], [32].

Table 4.B.1 - Mechanical properties of the concretes used (mean values with numbers of samples tested and coefficient of variation in brackets).

Specimens	f_{c0} [MPa]	$f_{c,cube}$ [MPa]	f_{ct} [MPa]	E_c [GPa]
BT-NC-1, BT-NC-5, WG-NC-1, WG-NC-4,WG-NC5, HB-NC-1	46.5 (6, 2%)	50.2 (4, 2%)	3.7 (4, 8%)	34.7 (5, 6%)
BT-NC-2, BT-NC-3, BT-NC-3e, BT-NC-4,WG-NC-2, WG-NC-3	50.8 (9, 3%)	55.7 (4, 5%)	-	38.1 (4, 11%)
BT-HC-1, BT-HC-2, BT-HC-2e	76.6 (5, 2%)	80.9 (4, 2%)	-	30.0 (5, 7%)

4.B.2 Reinforcing steel

Table 4.B.2 summarises the mean values and the coefficients of variation of the mechanical properties of the reinforcing steel. All reinforcement was of Class B500B. The mechanical properties of the different reinforcement types were determined by testing 1.2 m long bars (free length approximately 965 mm), which were ordered from the same batch as the reinforcement used for the specimens, in tension up to failure. No tests were performed on the subsidiary bars. To determine the static yield and ultimate stresses $f_{sy,stat}$ and $f_{su,stat}$, the tensile tests were halted twice near the yield and ultimate stresses, keeping the stroke of the testing machine constant for approximately two minutes. However, only the dynamic values ($f_{sy,dyn}$ and $f_{su,dyn}$) are used for the analysis and comparison of the test data, since they better approximate the effective steel behaviour during the tests [33].

Table 4.B.2 - Mechanical properties of the reinforcing steels used (mean values with coefficients of variation in brackets).

Reinforcement type	Yield plateau	$Ø_s$ [mm]	$f_{sy,dyn}$ [MPa]	$f_{sy,stat}$ [MPa]	$f_{su,dyn}$ [MPa]	$f_{su,stat}$ [MPa]	E_s [GPa]	ε_{sh} [‰]	ε_{su} [‰]	n_{sample} [-]
Bent ties (BT)	No	12	545 (1%)	520 (1%)	610 (1%)	567 (1%)	200 (1%)	-	45 (14%)	6
Welded grids (WG)	No	12	551 (2%)	527 (2%)	602 (1%)	563 (2%)	197 (1%)	-	43 (15%)	6
Double-headed bars (HB)	Yes	12	552 (0%)	525 (0%)	626 (0%)	586 (0%)	207 (2%)	31 (3%)	132 (7%)	5

Appendix 4.C Load-penetration and load-crack width diagrams

Fig. 4.C.1 (normal strength concrete specimens) and Fig. 4.C.2 (high strength concrete specimens) plot the average axial stress q_x across the loaded area (normalised by the concrete strength f_{c0}) (i) in black against the axial penetration δ_x and (ii) in orange against the maximum crack width $w_{r,max}$ on the transverse and longitudinal side. It is referred to Section 4.4 for the definition of δ_x and $w_{r,max}$ and the discussion.

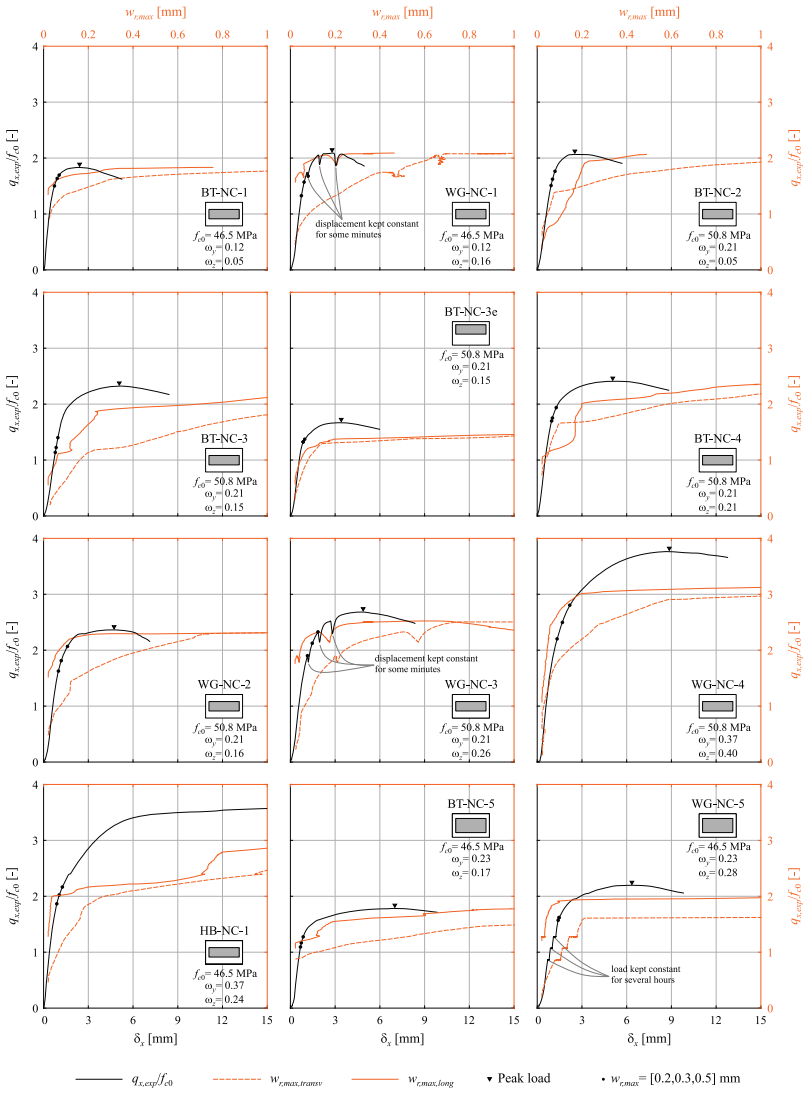

Fig. 4.C.1 - Load-penetration and load-crack width diagrams for normal strength concrete specimens.

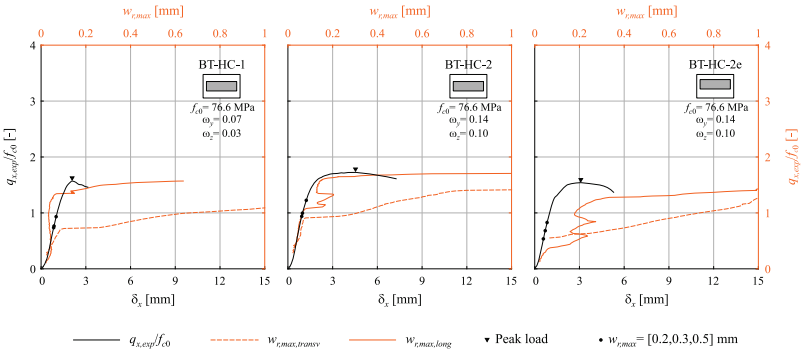

Fig. 4.C.2 - Load-penetration and load-crack width diagrams for high strength concrete specimens.

Appendix 4.D Used test parameters and results of calculation with different model approaches

Table 4.D.1 summarises the experimental data used for the model comparison and presents the results.

Table 4.D.1 - Tests used to compare the different model approaches and respective parameters.

Source	Specimen	b_{ly} = d_l	b_{ccy}	b_{ccz}	e_y	f_{c0}	b_{ccy} = $d_{2,DW-cc}$ = $d_{2,DW-s}$	$d_{2,DW-cs}$	b_{ccz}	σ_{confy}			σ_{confz}	$q_{2,u,Test}/q_{2,u,Model}$							k_s	x_E
										DW-cc	DW-s	DW-s GPC	DW-cs	DW-cc DW-s GPC	DW-cc	DW-cc (η_{bc})	DW-s	DW-cs	GPC	DAUB	DW-cc	DW-cc
		[mm]	[mm]	[mm]	[mm]	[MPa]	[mm]	[mm]	[mm]	[MPa]	[MPa]	[MPa]	[MPa]	[MPa]	[-]	[-]	[-]	[-]	[-]	[-]	[-]	[mm]
Present article	BT-NC-1	140	278	478	0	46.5	203.2	278	350.8	4.3	4.0	5.7	6.7	2.5	1.22[1]	1.37[1]	1.28[1]	0.84	1.10	1.05	0.65	338
	BT-NC-2	140	278	478	0	50.8	223.5	278	351.6	4.5	4.0	10.6	7.4	2.6	1.34[1]	1.54[1]	1.41[1]	0.95[1]	1.25	1.18	0.83	355
	BT-NC-3	140	278	478	0	50.8	223.5	278	409.3	10.6	10.6	10.6	12.1	7.8	1.07	1.17	1.10	0.86	1.12	1.33	0.48	355
	BT-NC-3e	140	278	478	58	50.8	107.5	162	409.3	10.6	10.6	10.6	12.1	7.8	1.12[2]	1.25[2]	1.12[2]	0.79	1.08	1.17	-	-
	BT-NC-4	140	278	478	0	50.8	223.5	278	409.3	10.6	10.6	10.6	12.1	10.4	1.11	1.22	1.15	0.90	1.06	1.38	0.48	355
	BT-NC-5	210	278	478	0	46.5	223.5	278	409.3	10.0	9.9	10.6	10.9	7.8	0.97[1]	1.05[1]	0.98[1]	0.80	0.97	1.25	0.07	433
	BT-HC-1	140	278	478	0	76.6	203.2	278	350.8	4.4	4.0	5.7	6.7	2.5	1.15[1]	1.49[1]	1.20[1]	0.86	0.99	0.90	0.93	338
	BT-HC-2	140	278	478	0	76.6	223.5	278	409.3	10.6	10.6	10.6	12.1	7.8	0.93	1.13	0.96	0.77	0.93	0.99	0.61	355
	BT-HC-2e	140	278	478	29	76.6	165.5	220	409.3	10.6	10.6	10.6	11.9	7.8	0.95	1.15	0.96	0.77	0.91	0.96	0.23	305
	WG-NC-1	140	278	478	0	46.5	203.2	278	378.3	5.8	5.8	5.8	7.2	7.5	1.25	1.39	1.29	0.93	1.07	1.20	0.53	338
	WG-NC-2	140	278	478	0	50.8	223.5	278	379.4	10.7	10.7	10.7	12.3	7.9	1.13	1.24	1.16	0.88	1.14	1.35	0.47	355
	WG-NC-3	140	278	478	0	50.8	223.5	278	426.0	10.7	10.7	10.7	12.3	13.2	1.20	1.32	1.24	0.99	1.17	1.54	0.47	355
	WG-NC-4	140	278	478	0	46.5	239.0	278	429.2	17.1	17.1	17.1	19.2	18.4	1.22	1.30	1.27	1.04	1.29	2.15	0.42	367
	WG-NC-5	210	278	478	0	46.5	223.5	278	426.0	10.7	10.7	10.7	12.3	13.2	1.14	1.23	1.14	0.93	1.06	1.54	0.06	433
	HB-NC-1	140	278	478	0	46.5	239.0	278	423.1	17.1	17.1	17.1	19.3	11.0	1.18	1.25	1.24	0.99	1.50	2.06	0.42	367

All specimens with b_y = 350 mm, b_z = 550 mm, h = 525 mm, and b_E = 450 mm.
(1): Longitudinal direction governing, σ_{confy} reduced.
(2): No load dispersion possible. Model cannot be applied. Eq. (4.19) used to determine load-bearing capacity.

Table 4.D.1 - Continued.

Source	Specimen	b_{fy} = d_1	b_{cy}	b_{cz}	e_y	f_{c0}	b_{cy} = $d_{2,DW-cc}$ = $d_{2,DW-s}$	$d_{2,DW-cs}$	b_{ccz}	σ_{confy}			σ_{confz}	$q_{c,u,Test}/q_{c,u,Model}$						k_s	x_E
										DW-cc	DW-s	DW-s GPC	DW-cs	DW-cc DW-s GPC	DW-cc	DW-cc (η_{sc})	DW-s	DW-cs	GPC	DAUB	DW-cc	DW-cc
		[mm]	[mm]	[mm]	[mm]	[MPa]	[mm]	[mm]	[mm]	[MPa]	[MPa]	[MPa]	[MPa]	[MPa]	[-]	[-]	[-]	[-]	[-]	[-]	[-]	[mm]
[4]	C1	70	303	498	0	33.5	247.6	303	428.5	9.7	9.7	9.7	11.1	6.8	1.17	1.19	1.20	0.98	1.38	1.68	0.96	267
	C2	70	303	498	0	33.5	247.6	303	428.5	9.7	9.7	9.7	11.1	6.8	1.17	1.19	1.21	0.99	1.39	1.69	0.96	267
	C3	70	303	498	0	38.9	247.6	303	428.5	9.7	9.7	9.7	11.1	6.8	1.18	1.23	1.22	1.01	1.36	1.58	1.00	269
	C4	70	303	498	0	33.5	256.5	303	425.8	8.2	8.2	8.2	9.4	5.8	1.23	1.26	1.27	1.06	1.41	1.64	1.00	277
	C5	70	303	498	0	38.9	247.6	303	428.5	9.9	9.9	9.9	11.3	7.0	1.17	1.22	1.21	0.99	1.34	1.58	1.00	269
	C7	70	303	498	0	38.9	253.1	303	333.0	5.5	5.5	5.5	6.3	3.9	1.30	1.37	1.30	0.98	1.10	1.16	1.00	302
	C12	70	303	498	0	33.3	230.6	303	422.0	4.2	4.2	4.2	5.0	4.1	1.28	1.30	1.28	1.06	1.12	1.21	1.00	290
	C13	40	303	498	0	48.9	256.5	303	425.8	7.7	7.7	7.7	8.8	5.4	1.57	1.72	1.47	1.37	1.45	1.62	1.00	248
	C14	40	303	498	0	51.5	256.5	303	425.8	15.1	15.1	15.1	17.3	10.6	1.32	1.43	1.26	1.14	1.48	1.83	1.00	222
	C15	40	303	498	0	51.5	256.5	303	425.8	19.4	19.4	19.4	22.2	13.7	1.27	1.37	1.21	1.09	1.54	2.03	1.00	215
	C16	20	303	498	0	51.5	256.5	303	425.8	11.4	11.4	11.4	13.1	8.1	1.49	1.64	1.37	1.31	1.31	2.06	1.00	177
	C17	40	303	498	0	51.5	256.5	303	425.8	11.4	11.4	11.4	13.1	8.1	1.41	1.54	1.34	1.22	1.45	1.70	1.00	232
	C18	80	303	498	0	51.5	256.5	303	425.8	11.4	11.4	11.4	13.1	8.1	1.19	1.31	1.24	1.02	1.34	1.55	1.00	292

All specimens with b_y = 350 mm, b_z = 550 mm, h = 525 mm, and b_b = 450 mm.

Notation

Latin letters

$A_{\mathrm{I}}, A_{\mathrm{II}}$	Areas defined according to Fig. 4.5c
$A_c = b_y \cdot b_z$	Cross-sectional area of concrete block
$A_{c0} = b_{ly} \cdot b_{lz}$	Partially loaded area
$A_{cc} = A_{conf,simp} = b_{ccy} \cdot b_{ccz}$	Confined concrete area according to simplification of confinement model [19]
$A_{conf,mod}$	Confined concrete area according to confinement model [19]
$A_{cs} = b_{csy} \cdot b_{csz}$	Concrete area inside the confining reinforcement
A_i	Area in the (x,y)-plane of the Dual-Wedge stress field region i
b_{ccy}, b_{ccz}	Confined concrete width and length
$b_{csy} = b_y - 2 \cdot c_{nom} - Ø_{conf}$ $b_{csz} = b_z - 2 \cdot c_{nom} - Ø_{conf}$	Maximum width and length of confining reinforcement (dimension between centre lines)
b_{ly}, b_{lz}	Width and length of loaded area
b_y, b_z	Width and length of concrete block
c	Cohesion
c_{nom}	Concrete cover
d_1	Width of loaded area of Dual-Wedge stress field
d_2	Width available for load dispersion of Dual-Wedge stress field
D_{max}	Maximum aggregate size
E_c	Modulus of elasticity of concrete in compression
E_s	Modulus of elasticity of reinforcing steel
e_y	Eccentricity of loaded area in transverse direction
f_{c0}	Uniaxial concrete cylinder compressive strength
$f_{c,cube}$	Uniaxial concrete cube compressive strength
f_{ct}	Concrete tensile strength
$F_{\mathrm{GPC}} = \min\left(F_{\mathrm{GPC0}}, F_{\mathrm{GPC1}}\right)$	Load-bearing capacity according to GPC model depending on capacity of sections 0-0 and 1-1
f_{sy}	Yield stress of reinforcing steel
$f_{sy,dyn}, f_{su,dyn}$	Dynamic yield and ultimate stress of reinforcing steel
$f_{sy,stat}, f_{su,stat}$	Static yield and ultimate stress of reinforcing steel
F_{ty}, F_{tz}	Tensile force in transverse and longitudinal direction due to load dispersion
h	Block height (in x-direction)
$k_s \in [0,1]$	Parameter of Dual-Wedge stress field indicating the part of σ_{sy} available to equilibrate the bursting stresses
n_{sample}	Sample size
n_{sp}	Number of transverse reinforcement layers considered to account for transverse tensile force
n_{sy}, n_{sz}	Number of reinforcing bars per layer in transverse and longitudinal direction
$N_{x,u}$	Peak axial force

q_x	Average axial stress across loaded area
$q_{x,u}$	Load-bearing capacity, average axial stress across loaded area at peak load
R_0	Region with transverse confining stresses due to load dispersion (GPC)
R_1	Region with transverse bursting stresses due to load dispersion (GPC)
s_x, s_y, s_z	Spacing of confining reinforcement in respective directions
s_{x1}	Spacing in x-direction between load introduction and first reinforcement layer
$s_{y,avg}, s_{z,avg}$	Average confining reinforcement spacing in lateral y- and z-direction
$s_{x,max}, s_{y,max}, s_{z,max}$	Maximum confining reinforcement spacing in respective directions
$w_{r,max}, w_{r,max,long}, w_{r,max,transv}$	Maximum crack width generally, on a longitudinal and transverse side
x	Loading direction (axial, vertical)
x_E	Height of Dual-Wedge stress field
x_{sp}	Distance between resultants of confining force and tensile force depending on reinforcement layout in transverse direction (GPC)
y	Lateral transverse direction
z	Lateral longitudinal direction
$Z_{z,conf}$	Total confining force in longitudinal direction

Greek letters

α	Inclination angle of diagonal compressive strut of Dual-Wedge stress field
δ_x	Penetration in axial direction
ε_{sh}	Strain at beginning of hardening branch of reinforcing steel
ε_{su}	Ultimate strain of reinforcing steel
φ	Angle of internal friction
η_{cc}	Strength reduction factor to account for higher-strength concrete brittleness
$\sigma(U,V)$	Standard deviation of displacements in lateral and vertical direction
$\sigma_1, \sigma_2, \sigma_3$	Maximum, intermediate, and minimum principal stress (defined positive in compression)
σ_{conf}, σ_s	Confining stress in the confined and bursting region
$\sigma_{confy}, \sigma_{confz}$	Confining stress in the transverse and longitudinal direction
$\sigma_{confz,req}$	Required confining stress in longitudinal direction
σ_{sy}	Confining stress in the bursting region of the Dual-Wedge stress field
σ_{x0}	Axial stress on the loaded area
σ_{xd}	Axial stress after load dispersion
σ_z	Stress in longitudinal direction
ρ_y, ρ_z	Transverse and longitudinal geometrical reinforcement ratio (computed according to confinement model [19])
ω_y, ω_z	Transverse and longitudinal mechanical reinforcement ratio (computed according to confinement model [19])
ξ_y, ξ_z	Parameters determining the amount of load transferred in transverse and longitudinal direction

Special characters

$Ø_s$	Diameter of reinforcing steel

References

[1] T. Markić, W. Kaufmann, and A. Amin, 'Stress field solution for strip loaded reinforced concrete blocks', *Engineering Structures*, vol. 171, pp. 911–920, 2018, doi: 10.1016/j.engstruct.2018.03.027.

[2] T. Markić, 'Concrete hinges', Master's Thesis, Institute of Structural Engineering, ETH Zurich, Zurich, Switzerland, 2015.

[3] G. Schmidt-Thrö, M. Smarslik, B. Tabka, W. Scheufler, O. Fischer, and P. Mark, 'Experimental analysis of concrete elements under partial area strip loading', *Civil Engineering Design*, vol. 1, no. 1, pp. 28–38, 2019, doi: 10.1002/cend.201900001.

[4] T. Markić, F. Morger, and W. Kaufmann, 'Partially loaded areas in reinforced concrete: experimental campaign and model validation', *Engineering Structures*, vol. 273, p. 114905, Dec. 2022, doi: 10.1016/j.engstruct.2022.114905.

[5] F. E. Richart, A. Brandtzaeg, and R. L. Brown, 'A Study of the Failure of Concrete under Combined Compressive Stresses', University of Illinois Engineering Experimental Station, Bulletin 185, 1928.

[6] F. E. Richart, A. Brandtzaeg, and R. L. Brown, 'The failure of plain and spirally reinforced concrete in compression', University of Illinois Engineering Experimental Station, 1929.

[7] T. Markić, F. Morger, and W. Kaufmann, 'Partially loaded areas in reinforced concrete: Mechanical modelling', *Engineering Structures*, vol. 271, p. 114938, Nov. 2022, doi: 10.1016/j.engstruct.2022.114938.

[8] C. Proksch-Weilguni, M. Decker, and J. Kollegger, 'Hochbelastete Lastübertragungszonen mit stumpf gestoßener Bewehrung: Experimentelle Untersuchungen und numerische Simulationen', *Beton- und Stahlbetonbau*, vol. 117, no. 11, pp. 913–927, 2022, doi: 10.1002/best.202200075.

[9] International Federation for Structural Concrete (fib), *Model Code for Concrete Structures 2020*, Lausanne, 2024.

[10] SIA, *Swisscode SIA 262: Concrete Structures*, Zurich, Switzerland, 2013.

[11] German Tunnelling Committee (ITA-AITES), *Empfehlungen für den Entwurf, die Herstellung und den Einbau von Tübbingringen*. Deutscher Ausschuss für unterirdisches Bauen e. V. (DAUB), 2024.

[12] C. Proksch-Weilguni, M. Decker, and J. Kollegger, 'Load distribution and passive confinement in reinforced concrete: Development of a mechanical model', *Engineering Structures*, vol. 304, p. 117562, Apr. 2024, doi: 10.1016/j.engstruct.2024.117562.

[13] F. Leonhardt and E. Mönnig, *Vorlesungen über Massivbau - Teil 2: Sonderfälle der Bemessung im Stahlbetonbau*, Dritte Auflage. Springer Berlin Heidelberg, 1986.

[14] Y. Guyon, 'Contraintes dans les pièces prismatiques soumises à des forces appliquées sur leurs bases, au voisinage de ces bases', *IABSE publications*, vol. 11, pp. 165–226, 1951.

[15] M. P. Nielsen and L. C. Hoang, *Limit Analysis and Concrete Plasticity, Third Edition*. Boca Raton: CRC Press, 2011. doi: 10.1201/b10432.

[16] M. A. M. Badawi, 'Einfluss der Längs- und Querarmierung auf die Tragfähigkeit und Verformbarkeit von gedrungenen Stahlbetonstützen', Eidgenössische Materialprüfungs- und Versuchsanstalt für Industrie, Bauwesen und Gewerbe (EMPA), Dübendorf, 199, 1973.

[17] S. A. Sheikh and S. M. Uzumeri, 'Strength and Ductility of Tied Concrete Columns', *Journal of the Structural Division*, vol. 106, no. 5, pp. 1079–1102, May 1980, doi: 10.1061/JSDEAG.0005416.

[18] F. Morger and W. Kaufmann, 'Experimental investigation of welded reinforcement grids for partial area loading', in *Proceedings of the 15th fib PhD Symposium in Civil Engineering*, Fédération Internationale du Béton (fib), 2024. doi: https://doi.org/10.3929/ethz-b-000711139.

[19] F. Morger, A. Kenel, and W. Kaufmann, 'Passive confinement of reinforced concrete members revisited', *Structural Concrete*, vol. 25, no. 6, pp. 4283–4299, 2024, doi: 10.1002/suco.202400209.

[20] N. Hasler, 'Bemessung von Tübbinglängsfugen', Master Projektarbeit, ETH Zürich, 2022.

[21] H. P. Spieth, 'Das Verhalten von Beton unter hoher örtlicher Pressung', *Beton- und Stahlbetonbau*, vol. 56, no. 11, pp. 257–263, 1961.

[22] German Tunnelling Committee (ITA-AITES), *Empfehlungen für den Entwurf, die Herstellung und den Einbau von Tübbingringen*. Deutscher Ausschuss für unterirdisches Bauen e. V. (DAUB), 2013.
[23] EN 1992-1-1:2023, 'Eurocode 2 - Design of concrete structures - Part 1-1: General rules and rules for buildings, bridges and civil engineering structures', Brussels, 2023.
[24] F. Morger and W. Kaufmann, 'Design of longitudinal tunnel lining joints - experimental investigation on partially loaded reinforced concrete blocks', in *Proceedings of the 14th fib PhD Symposium in Civil Engineering*, Fédération Internationale du Béton (fib), 2022, pp. 467–474. doi: 10.3929/ethz-b-000572924.
[25] ISO 17660-1:2006, *Welding - Welding of reinforcing steel - Part 1: Load-bearing welded joints*, Geneva, 2006.
[26] Correlated Solutions Inc., 'Vic-3D software manual', Correlated Solutions, Irmo, 2019.
[27] N. Gehri, J. Mata-Falcón, and W. Kaufmann, 'Automated crack detection and measurement based on digital image correlation', *Construction and Building Materials*, vol. 256, p. 119383, 2020, doi: 10.1016/j.conbuildmat.2020.119383.
[28] N. Gehri, J. Mata-Falcón, and W. Kaufmann, 'Refined extraction of crack characteristics in Large-scale concrete experiments based on digital image correlation', *Engineering Structures*, vol. 251, p. 113486, 2022, doi: 10.1016/j.engstruct.2021.113486.
[29] J. Mata-Falcón, S. Häfliger, M. Lee, T. Galkovski, and N. Gehri, 'Combined application of distributed fibre optical and digital image correlation measurements to structural concrete experiments', *Engineering Structures*, vol. 225, p. 111309, 2020, doi: 10.1016/j.engstruct.2020.111309.
[30] ACI Committee 533, *Guide for Precast Concrete Tunnel Segments (ACI 533.5R-20)*. Farmington Hills, MI: American Concrete Institute, 2020.
[31] W. F. Chen, 'Double Punch Test for Tensile Strength of Concrete', *ACI Journal*, vol. 67, no. 12, pp. 993–995, 1970.
[32] P. Marti, 'Size Effect in Double-Punch Tests on Concrete Cylinders', *Materials Journal*, vol. 86, no. 6, pp. 597–601, 1989, doi: 10.14359/2261.
[33] S. Häfliger, S. Fomasi, and W. Kaufmann, 'Influence of quasi-static strain rate on the stress-strain characteristics of modern reinforcing bars', *Construction and Building Materials*, vol. 287, p. 7, 2021, doi: 10.1016/j.conbuildmat.2021.122967.

Corrections

Corrections to the original content of the published article are listed below:

	Published	Adjusted
Section 4.4.2	plain concrete blocks	plain concrete cylinders
Section 4.3	fibre-reinforced concrete (FRC)	steel fibre reinforced concrete (SFRC)
Section 4.4.1	As the load concentration ratio increases (wider load), the geometrical confinement and hence the load-bearing capacity ($q_{x,u,exp}/f_{c0}$) of otherwise identical specimens decreases.	As the load concentration ratio increases (wider load), the geometrical confinement and hence the load-bearing capacity ($q_{x,u,exp}/f_{c0}$) of otherwise identical specimens (f_{c0} of 46.5 MPa or 50.8 MPa, respectively) decreases.
Fig. 4.10 (a)	BT-HC-2-e	BT-HC-2e
Section 4.4.1	headed bars	double-headed bars
Section 4.4.2	headed bars	double-headed bars
Section 4.5	headed bars	double-headed bars
Section 4.5	The high conservatism for narrow load application widths can be explained by the fact that for these situations, the impact of confinement is limited, and load dispersion can, supported by the concrete tensile strength, occur beyond the confined concrete area or even extend into the cover concrete.	The high conservatism for narrow load application widths can be explained by the fact that for these situations, the impact of confinement is limited, and load dispersion can occur beyond the confined concrete area or even, supported by the concrete tensile strength, extend into the cover concrete.
Section 4.5	$\eta_{cc} = (30/f_{c0})^{(1/3)} < 1$	$\eta_{cc} = (30/f_{c0})^{(1/3)} \leq 1$

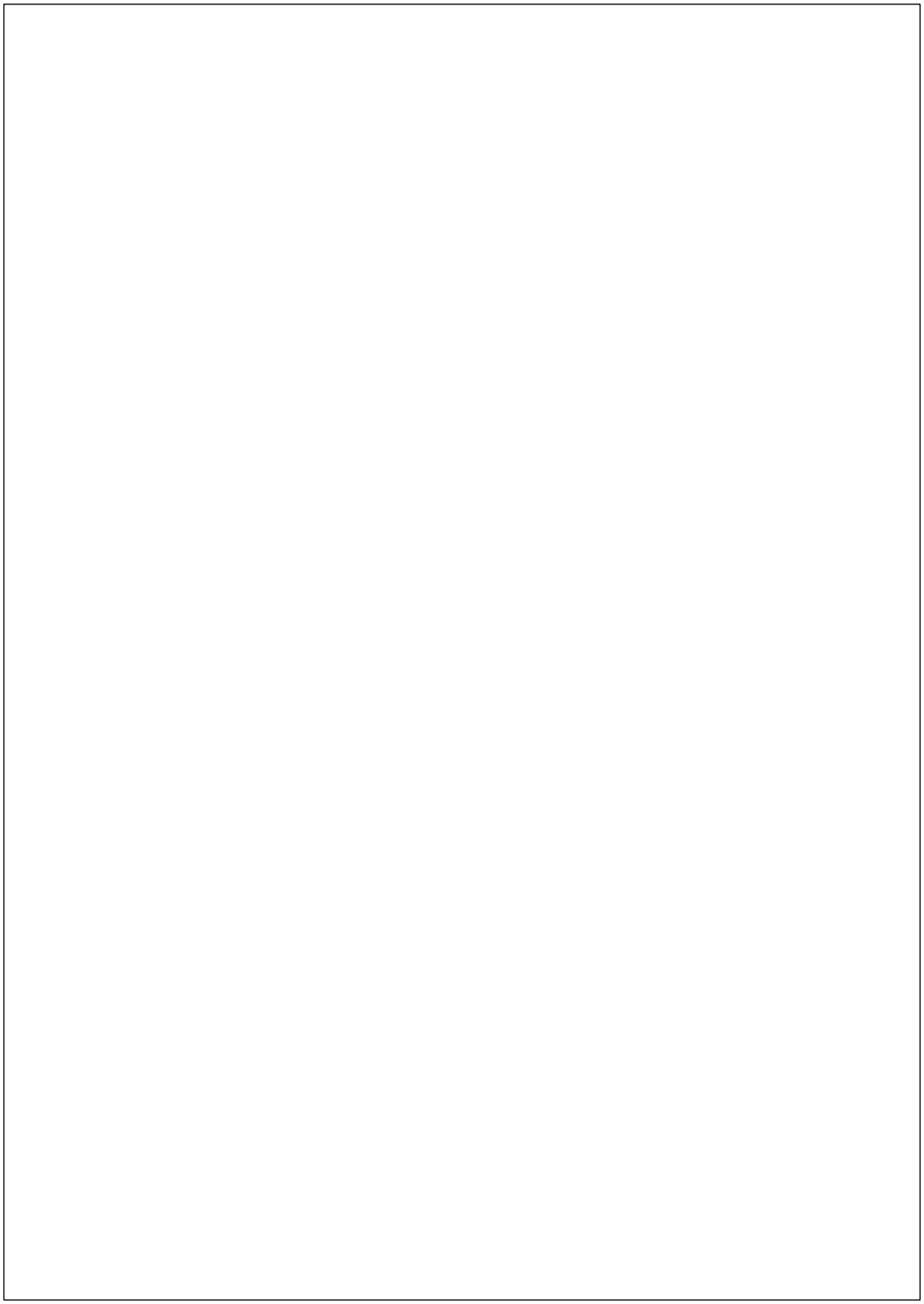

5 Experimental and theoretical investigation of longitudinal tunnel lining joints

The content of this chapter corresponds to the postprint of the following published article:

> **F. Morger**, A. Kenel, W. Kaufmann, 'Experimental and theoretical investigation of longitudinal tunnel lining joints with confining reinforcement', *Structural Concrete*, 2026, doi: 10.1002/suco.70453

This postprint includes some adjustments to the published version. For details see Section 1.5.

As the lead author, Fabian Morger planned, prepared and carried out the experiments, analysed and post-processed the obtained data, developed the Multi-Wedge stress field and extended it for guiding rod grooves, compared the model predictions with the experimental data, and wrote the entire draft of the manuscript. The last two authors both supervised the conducted research by giving constant and valuable inputs especially regarding the experimental campaign. The second author, Albin Kenel, was involved in the validation of the models. The third author, Walter Kaufmann, initially designed the experimental campaign, and carefully reviewed the manuscript.

Abstract

Precast reinforced concrete segmental linings are frequently used in modern tunnelling. In these linings, the longitudinal joints typically have a reduced contact cross-section and thus often govern the design, particularly in tunnels under high hydrostatic pressure or crossing squeezing or swelling ground with correspondingly high circumferential compressive forces. Reinforced concrete segments with substantial confining reinforcement in the load dispersion zone next to the joints are a viable option to resist such loads. However, this solution has not been widely used in tunnelling yet, mainly due to limited coverage by existing guidelines and lack of experimental validation. The present article addresses this knowledge gap. It (i) presents the results of an experimental campaign investigating the structural behaviour of tunnel lining segments with longitudinal joints in nine reinforced concrete specimens with pronounced passive confinement, (ii) proposes a modelling approach based on a bespoke stress field solution for the design of longitudinal joints allowing the entire load path to be followed and (iii) extends this stress field to cover the effect of guiding rod grooves. The results of the experimental campaign provide valuable insight into the structural behaviour of the longitudinal joints. They confirm that substantial passive confinement can be activated and can contribute to the load-bearing capacity, but also highlight that the unconfined zone of the segments can become governing for high compressive forces resulting from high confining stresses and wide longitudinal joints. The comparison of the experimental data and the proposed modelling approach shows very good agreement. Thus, it can be recommended as a valid basis for design.

5. Experimental and theoretical investigation of longitudinal tunnel lining joints

Keywords: Reinforced concrete; Tunnel lining segments; Longitudinal joints; Load-bearing capacity; Strip loading; Stress field; Passive confinement; Multiaxial compressive strength; Experimental campaign.

5.1 Introduction

The excavation of long and deep tunnels with the use of tunnel boring machines (TBMs) is a popular construction method due to its time- and cost-efficiency. TBM-built tunnels often use precast reinforced concrete (RC) lining segments, which are installed almost immediately after excavation. These segments carry the loads during construction and, in the case of so-called one-pass lining systems, during the entire tunnel service life. In tunnels under high hydrostatic pressure or crossing squeezing or swelling ground – as for example the Brenner Base Tunnel [1] currently under construction or the planned Strait of Gibraltar tunnel [2], [3] – the segments are primarily loaded by high circumferential compressive forces, which are accompanied by relatively small bending moments.

The longitudinal joints between segments generally have a reduced contact surface compared to the full cross-section in order to facilitate erection. The resulting load dispersion of the axial force is predominantly unidirectional and can be idealised as strip loading. Due to the reduced contact area, the longitudinal joints often govern the design. To sustain high axial forces, several options in the design of the segments for one-pass lining systems exist: (i) thick-walled linings, (ii) high concrete compressive strength, and (iii) confining reinforcement. This list is not conclusive and the options, which are briefly discussed in the following, can be combined; for an in-depth overview, the reader is referred to Mezger et al. [4]. Increasing the segment thickness (i) is the most straightforward approach, limited mainly by the allowable weight for transport and erection. However, a thinner lining would not only use less construction material but – more importantly – also reduce the required excavation volume, which can significantly impact cost and environmental impact for long tunnel lining projects. For high strength concrete (ii), current codes limit the design of structural elements to concrete compressive strength class C100/115 [5], [6] or C120/140 [7]. Furthermore, high strength concrete exhibits a brittle failure behaviour (failure through the aggregates instead of the cement matrix as for normal strength concrete) and is prone to explosive spalling under fire conditions [8]. The incorporation of passive confinement into the design of the segments (iii) is not widely used in tunnelling practice yet (e.g. confining reinforcement was incorporated partly into the segments at the Brenner Base Tunnel). This is mainly due to most current codes, for example, *fib* Model Code for Concrete Structures [7] or SIA 262: Concrete Structures [9], not allowing the beneficial effects of load dispersion and passive confinement to be combined, despite that several experimental campaigns on concrete blocks with pronounced confining reinforcement subjected to strip loading have shown that both confining effects contribute to the load-bearing capacity [10], [11]. Only the recent version of Eurocode 2 - Design of concrete structures EN 1992-1-1:2023 [6] allows the combination when three-dimensional stress fields are applied, albeit without providing further guidance. Meanwhile, several design approaches have recently been proposed [10], [12]. However, assessing their suitability for the tunnelling industry is not straightforward since experimental data on longitudinal joints of tunnel lining segments with pronounced confining reinforcement are scarce. To address this knowledge gap, the authors carried out an experimental campaign consisting of nine tests investigating the structural behaviour of RC specimens with pronounced passive confinement, representing tunnel lining segments with longitudinal joints. This article presents the results of these tests, as well as a stress field solution suitable for the design of longitudinal joints in segmental linings, which is extended to consider a guiding rod groove. Ultimately, this article aims at fostering designers' awareness of confined tunnel lining segments for projects with high axial loads, thus providing an alternative design option facilitating a more efficient design.

In the following sections, the experimental campaign is presented (Section 5.2) followed by a discussion of the experimental results (Section 5.3). Subsequently, modelling approaches for longitudinal joints are proposed and compared to the experimental results as well as current design approaches (Section 5.4). The article concludes with a summary of the main findings and design recommendations for tunnelling practice (Section 5.5).

The models proposed in this article build on previous work of the authors on the load-bearing behaviour of strip-loaded RC specimens. The reader is referred to Morger et al. [10] for a detailed discussion of the mechanical behaviour and background information on the previously established models.

5.2 Experimental campaign

Nine tests investigating the load-bearing behaviour of longitudinal joints of segmental tunnel linings were carried out. The tests were part of a broader experimental campaign consisting of 14 tests; the specimens of the remaining five tests were cast with steel fibre reinforced concrete (SFRC) and will be described in a separate article. The following sections provide a comprehensive overview of the specimen geometry and production, the material properties, the test setup and the measurement systems.

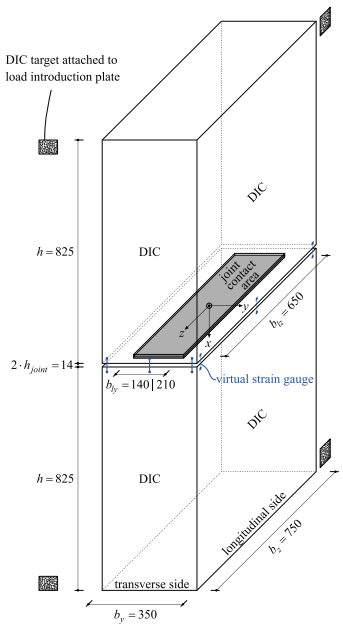

Fig. 5.1 - Geometry of the specimens (dimensions in mm).

5.2.1 Specimens, casting, and materials

An overview of the nine tests is given in Table 5.1; Fig. 5.1 illustrates the specimen geometry. Each specimen consisted of two identical RC blocks (half specimens) with dimensions $b_y \cdot b_z = 350 \cdot 750$ mm^2 in transverse y- and longitudinal z-directions and $h = 825$ mm in axial x-direction, placed on top of each other. Even though tunnel lining segments can be longer (b_z up to 2.25 m [13]) no substantial size effect is expected. The contact area of the two half specimens, corresponding to the longitudinal joint, was reduced with respect to the full cross-section. Three different flat joint geometries (designated as TLJ-40, TLJ-40g, and TLJ-60) were applied (see Fig. 5.2). The width of the joints (b_{ly}) varied between 140 mm (TLJ-40 and TLJ-40g) and 210 mm (TLJ-60), corresponding to 40% and 60% of the block width, respectively. The geometry of TLJ-40g contained a central opening of 40 mm, which simulated a guiding rod groove (as often used in tunnel lining segments, see Fig. 5.3b), effectively reducing the net loaded width to 29% of the block width. The length of all joints measured $b_{lz} = 650$ mm (i.e. 87% of the block length). The height of the joints (h_{joint}) on either side of the contact surface was set to 7 mm, based on the required vertical compression of the block tests presented in Morger et al. [10], to activate the confining reinforcement before joint closure, resulting in a total joint gap of 14 mm between the half specimens. The impact of this choice is discussed in Section 5.3.4. For test TLJ-40e-WG2p-B5, the two half specimens were placed on each other with an offset of 20 mm in the transverse direction, resulting in a loaded width b_{ly} of each specimen of 120 mm with an eccentricity e_y of the axial force (assuming uniform pressure) of 10 mm. All specimens were produced by Marti Tunnel AG in Klus-Balsthal, Switzerland. They were cast in lubricated formwork and compacted with a needle. Machined steel plates were used as joint formwork to obtain a precise joint geometry. The half specimens were cast such that the side opposite the joint was a moulded surface and could, therefore, be made as even and as parallel to the joint as possible. Due to limited formwork availability, the specimens were cast in five batches (designated as B1…B5), with the two half specimens of one test always cast simultaneously. The same concrete recipe with a maximum aggregate size of $D_{max} = 16$ mm was used for all batches. The concrete compressive strength f_{c0} of the specimens was determined from cores sampled after testing. The resulting cylinder concrete compressive strengths are reported in Table 5.1, and detailed information on the testing procedure can be found in Appendix 5.B.1.

The specimens were reinforced with prefabricated welded grids having a clear concrete cover c_{nom} of 30 mm, analogously to the specimens in Morger et al. [10], to allow direct comparability of the experimental campaigns. The yield stresses of the reinforcing steel (Class B500B, cold-worked without distinct yield plateau) are summarised in Table 5.1; Appendix 5.B.2 compiles further information on its mechanical properties. Welded grids are particularly suitable for bulk productions as common in tunnel

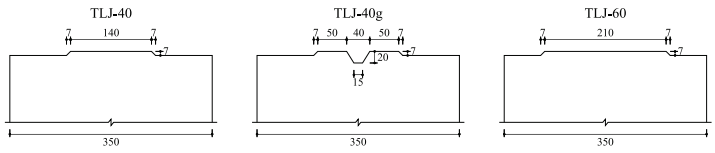

Fig. 5.2 - Joint geometries (dimensions in mm).

Table 5.1 - Overview of experimental campaign. See Fig. 5.1, Fig. 5.2, Fig. 5.4, and Fig. 5.A.1 for definition of variables.

Specimen	Concrete age at testing [days]	b_{fy} [mm]	b_{rod} [mm]	e_y [mm]	f_{c0} [MPa]	Welded grid type [-]	f_{sy} [MPa]	s_x [mm]	$s_{x,avg}$ = $s_{x,max}$ [mm]	$x_{E,max}$ [mm]	$\omega_y^{(1)}$ [-]	$\omega_E^{(2)}$ [-]	$N_{x,u,exp}$ [MN]	$q_{x,u,exp}/f_{c0}$ [-]	$\delta_{x,peak}$ [mm]	Failure zone[3] [-]
TLJ-40-WG2p-B1	85	140	0	0	46.0	WG2p	472.1	82	75	410	0.19	0.15	9.39	2.24	6.8	I/II
TLJ-40g-WG2p-B1	112	140	40	0	46.0	WG2p	472.1	82	75	410	0.19	0.15	8.48	2.84	5.1	III
TLJ-40-WG2p-B2	85	140	0	0	42.1	WG2p	472.1	82	75	410	0.21	0.17	8.91	2.33	8.5	I/II
TLJ-40-WG3p-B3	113	140	0	0	46.9	WG3p	472.1	72	57	365	0.26	0.16	9.60	2.25	6.0	II
TLJ-40-WG2f-B4	147	140	0	0	55.2	WG2f	472.1	82	75	820	0.16	0.13	10.79	2.15	7.6	I
TLJ-60-WG2f-B4	227	210	0	0	55.2	WG2f	478.0	82	75	820	0.16	0.13	13.32	1.77	7.6	I
TLJ-40e-WG2p-B5	168	120	0	10	47.9	WG2p	472.1	82	75	410	0.18	0.15	9.03	2.42	7.8	I
TLJ-60-WG1p-B3	93	210	0	0	46.9	WG1p	472.1	104	113	405	0.10	0.12	9.05	1.41	4.0	I
TLJ-60-WG2p-B5	161	210	0	0	47.9	WG2p	472.1	82	75	410	0.18	0.15	10.30	1.58	5.0	II

All specimens with b_y = 350 mm, b_z = 750 mm, h = 825+7 mm, h_{joint} = 7 mm, b_E = 650 mm, $\varnothing_s$ = 12 mm, $c_{x,com}$ = 30 mm, b_{zy} = 278 mm, b_{zz} = 678 mm, s_{y1} = 34 + 7 mm, $s_{y,avg}$ = 93 mm, and $s_{y,max}$ = 178 mm.
Specimen designation TLJ-{joint width [%] + guiding rod (g) or eccentricity (e) if present-welded grid type-concrete batch}, details see text.

(1): $\sigma_{conf}/(\text{Eq}(5.A.1))/f_{c0}$
(2): $\sigma_{conf}/(\text{Eq}(5.A.3))/f_{c0}$
(3): I: Confined zone, II: Unconfined zone, III: Local zone at joint.

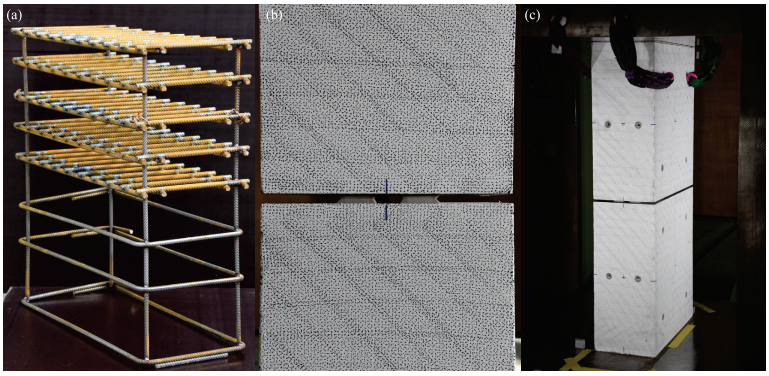

Fig. 5.3 - (a) Reinforcement configuration WG2p, (b) joint geometry TLJ-40g, and (c) test setup.

lining segments since, in comparison to bent ties, the reinforcement assembly and casting are simplified, reducing time and cost of the production process.

The transverse and longitudinal reinforcing bars were connected by machine welding with a nominal shear strength factor of at least 0.5, i.e., SF50 according to ISO 17660-1:2006 [14]. Hence, to fully anchor a transverse bar, two longitudinal bars were required on each side. In order to generate the largest possible confined concrete area, the two longitudinal bars were placed as far to the outside of the transverse bars as possible, exploiting the minimum bar centreline distance of 50 mm possible with the welding machine used. Three different grid configurations (designated as WG1-WG3) were employed, varying only in the number of transverse reinforcing bars, while the reinforcing bar diameter $Ø_s$ = 12 mm and the number (=4) and position of the longitudinal reinforcing bars were kept constant. The grids were point-welded to four assembly bars ($Ø_s$ = 10 mm) to ensure the vertical spacing s_x. In most half specimens, the welded grids were placed only over a reduced height adjacent to the joint (referred to as confined zone), as common in tunnel lining segments, with merely three additional stirrups ($Ø_s$ = 10 mm) in the remaining height (unconfined zone; these stirrups do not provide noticeable confinement due to the low confining stress and associated very small confined concrete area). These reinforcement configurations are designated with an additional "p" to indicate that they are reinforced over a partial height; Fig. 5.3a shows the reinforcement configuration of WG2p as an example. The specimens of two tests were reinforced with welded grids over the full height and are designated with an additional "f". Fig. 5.4 illustrates the reinforcement configuration in detail, and Table 1 summarises the reinforcement spacings and the height of the half specimen, where the welded grids can be activated, denoted as $x_{E,max}$. With the reinforcement spacings and considering the yield stress, based on experimental investigations of welded reinforcement grids with fibre optical sensors [15], the confining stresses σ_{conf} provided by the reinforcement can be determined based on the confinement model [16] (see Appendix 5.A); combined with the concrete compressive strength f_{c0}, mechanical reinforcement ratios of $\omega_y = \sigma_{conf}/f_{c0}$ = 0.10...0.26 and $\omega_z = \sigma_{conf,z}/f_{c0}$ = 0.12...0.17 result in the transverse and longitudinal direction, respectively.

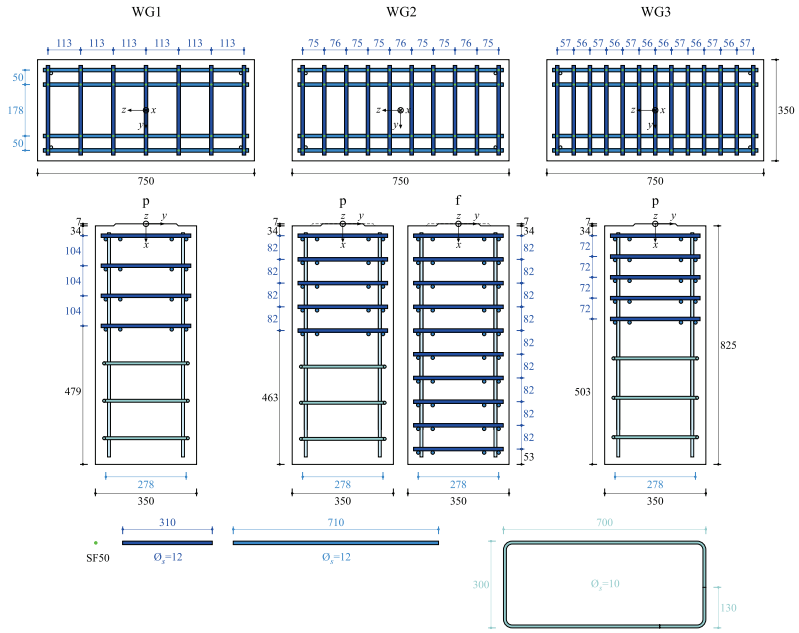

Fig. 5.4 - Configurations of welded grids (upper rows centre-line spacings, bottom row external dimensions, both in mm).

5.2.2 Test setup and loading procedure

All tests were carried out in a stiff 20 MN compression testing machine at Empa in Dübendorf, Switzerland. The lower load introduction plate of this machine is attached to the actuators and was kept horizontal (α_y and α_z = 0°, see Fig. 5.7) throughout the tests. The upper load introduction plate is connected to a crosshead via a spherical bearing, which was blocked after the specimens had been preloaded to 100 kN to account for inaccuracies in specimen height and to avoid uneven loading.

In all but one test, the load was applied in four steps, with the load held constant for 15 min in the three load stages in-between, which were selected at 40%, 55%, and 70% of the expected peak load. For the first loading step up to 300 kN, the machine displacement was controlled at a rate of 0.15 mm/min. After reaching 300 kN in the first loading step, the system was switched to force control, with the load monotonically increasing at a rate of 6 kN/s in the following two loading steps. For the final loading step, the machine displacement was again controlled at a rate of 0.15 mm/min until the peak load was reached. The tests were stopped after a significant load decrease was observed (further loading was prevented, so that cuts of the half specimens after testing (see Fig. 5.7) would still be representative of the peak load) or the introduced moment at the lower load introduction plate exceeded 350 kNm, which was a

boundary given by the safety requirements of the testing machine. The test protocol for TLJ-60-WG2f-B4 differed from the above: the load was held constant at only two stages, 50% and 70% of the expected peak load, and in the first load stage the force was held constant for almost 12 days to study the short-term creep behaviour at service loads.

To prevent the top half specimen from falling in the event of brittle failure of the bottom half specimen, it was loosely connected to the top load introduction plate by ropes, as can be seen in Fig. 5.3c. However, this safety measure was not used.

5.2.3 Measurement systems

The testing machine measured the applied axial force N_x, the bending moments M_y and M_z and rotations α_y and α_z (defined positive into positive coordinate direction, see sketch in Fig. 5.7) as well as the displacement u_x. All these measurements were with respect to the bottom load introduction plate – no measurements were available from the top load introduction plate. Additionally, digital image correlation (DIC) was applied to measure the displacement fields on the specimens' surfaces and the displacement of the load introduction plates (two DIC targets on each plate, one for each DIC system; see Fig. 5.1 and Fig. 5.3c). The DIC data was processed with the commercial software VIC-3D [17]. The resulting strain fields were further processed with the open-source software ACDM [18], [19] to determine the crack widths.

5.2.3.1 DIC setup

For every test, two neighbouring lateral sides (transverse and longitudinal direction) of the RC specimens were monitored with 3D DIC systems. Alvium Vimba cameras (5328·4608 px) measured the transverse side of all specimens, while for the longitudinal side FLIR Grasshopper3 cameras (4096·3000 px) were used. Both camera systems were equipped with lenses having a focal length of 25 mm. The resolution was always above 2.7 px/mm and 2.2 px/mm for the transverse and longitudinal sides, respectively. The stereo angles measured approximately 18° for the transverse and 25° for the longitudinal sides. The speckle pattern consisted of randomly placed black dots of diameter 1.27 mm, applied on the white-painted and well-lit specimen surfaces. Average noise levels with standard deviations $\sigma(U,V)$ below 10 µm resulted from zero displacement tests carried out according to Mata-Falcón et al. [20] with the following correlation parameters: subset size = 25 px, step size = 6 px with a strain filter size = 5 for both sides. The measuring frequency was 0.2 Hz for all tests apart from the creep behaviour investigation of the specimen TLJ-60-WG2f-B4 with a frequency of 1/300 Hz. The processed DIC measurements were filtered with a moving average filter over 7 data points over the time period, corresponding to a filter window of 30 s or 1800 s, respectively.

5.3 Results and analysis of experimental campaign

This section presents the results and analysis of the nine tests on longitudinal tunnel lining joints.

5.3.1 Results

The peak axial force $N_{x,u,exp}$ and the corresponding average peak stress $q_{x,u,exp}$ applied on the joint contact area, normalised by the concrete compressive strength f_{c0}, are shown in Table 5.1. Fig. 5.5 illustrates the load-deformation behaviour by plotting in black the average axial stress $q_{x,exp}$ at the joint (again normalised by f_{c0}) against the total compression δ_x of the two half specimens as well as the closing of the joint $\delta_{x,joint}$. Additionally, $q_{x,exp}/f_{c0}$ is plotted against the crack width $w_{r,max}$. Note that in this article the term *load* is used to describe the axial force or the average stress at the joint, respectively, unless specified in more detail, while the normalised average peak stress at the joint ($q_{x,u,exp}/f_{c0}$) is used to compare the load-bearing capacities of different specimens. Furthermore, the compression δ_x refers to the axial deformation between the lower and upper load introduction plate, determined by the DIC targets as the average value of the two DIC systems, thus eliminating any influence of the machine deformation. The joint closing was determined with DIC by investigating the vertical displacements of virtual strain gauges with a length of approximately 50 mm across the joint located at the centre and at the two edges in the longitudinal and transverse directions (see Fig. 5.1). The resulting six values determine the range of the joint closing shown in grey, while the average of the two values in the centre of each direction is plotted separately in blue. Note that the compression δ_x and the joint closing $\delta_{x,joint}$ were set to zero at an axial force of 300 kN, as the machine's crosshead was fully activated at this load. The crack width $w_{r,max}$ represents the maximum measured crack width (averaged over a crack length of 10 mm) obtained with ACDM and plotted in orange tones for the transverse (dashed line) and the longitudinal (solid line) sides for the bottom and top half specimens separately. The joint closing and crack widths are only plotted up to the peak load. In addition, the figure indicates the load levels at which a crack width of 0.2, 0.3, and 0.4 mm occurred for the first time (circular markers on the normalised stress-compression curve) as well as the peak load (triangular markers). These plots are discussed in the following.

Fig. 5.D.1 in Appendix 5.D presents the creep investigation of TLJ-60-WG2f-B4 by plotting the compression δ_x determined with both DIC-systems and their mean versus the time $t-t_0$ for a constant force of 6.07 MN, which corresponds to an average stress of $0.81 \cdot f_{c0}$ at the joint. Furthermore, the development of the moments M_y and M_z, respectively, as well as the temperature T in the laboratory, is shown. Due to length limitations, the results of the creep investigation are not discussed further in this article.

5.3.2 Load-bearing and failure behaviour

The normalised stress-compression curves shown in Fig. 5.5 are plotted again in groups in Fig. 5.6 to study the influence of different parameters. In order to gain further insight, some of the half specimens were cut vertically after testing, perpendicular to the longitudinal z-direction as close to the centre as possible, but avoiding the transverse reinforcement. Fig. 5.7 shows the cut surfaces of seven half specimens (top or bottom; for each test, the one with more visible damage from the outside was chosen).

All specimens exhibited a somewhat ductile failure behaviour, with a gradual stiffness decrease before reaching the peak load but varying degrees of ductility (which can be expressed e.g. by $\delta_{x,peak}$ = compression at peak load, see Fig. 5.6). The cuts (Fig. 5.7) clearly show different degrees of cover concrete spalling (discussed in more detail later). More importantly, no splitting cracks are visible, which implies that neither tensile failure of the concrete nor rupture of the reinforcement occurred. Consequently, the

specimens failed by concrete crushing either in the confined or, if present, in the unconfined zone. Additionally, for the specimen with an opening for a guiding rod, a localised crushing failure at the joint is possible. From literature, it is anticipated that the failure modes in the confined and unconfined zone can be distinguished by their ductility: confined concrete exhibits an increased ductility compared to concrete in uniaxial compression [21], which also sustains a more pronounced softening response after the peak load in displacement control [22]. Furthermore, the experimental campaign by Morger et al. [10] revealed that for strip-loaded concrete blocks containing confining reinforcement over the entire

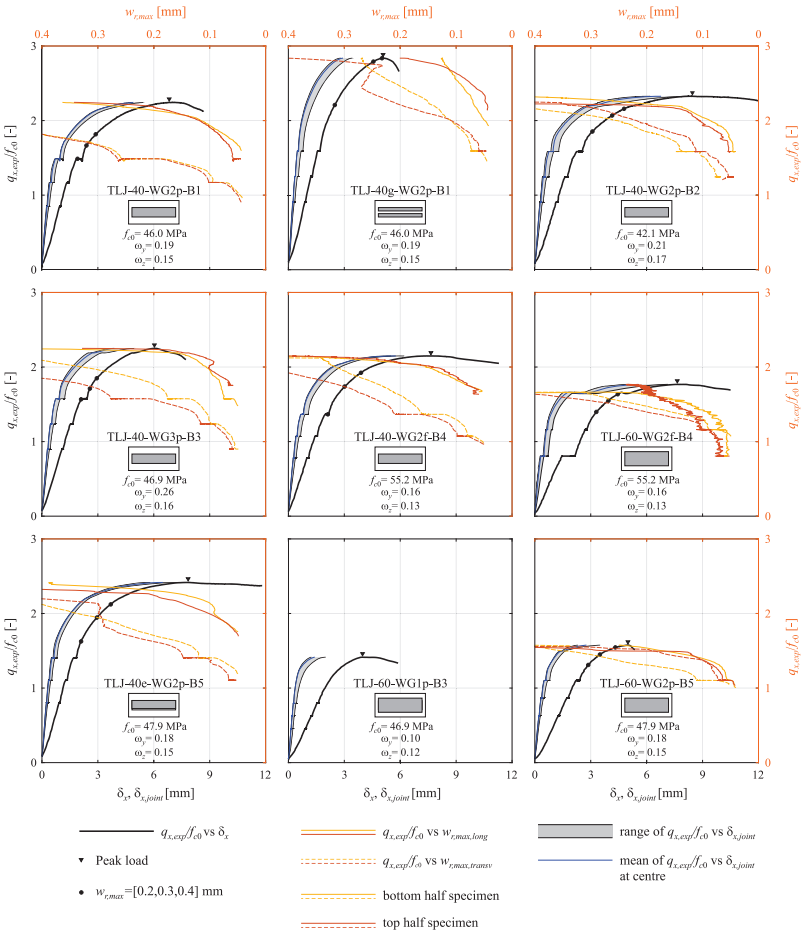

Fig. 5.5 - Load-bearing behaviour: Normalised stress-compression, normalised stress-joint closing, and normalised stress-crack width diagrams for tests on longitudinal joints of tunnel lining segments.

specimen height (no unconfined zone present) higher reinforcement ratios consistently lead to higher load-bearing capacities and increased axial compression at the peak load for otherwise nearly equal blocks. Based on this information and comparison between the different test specimens, the failure mode of the specimens is defined below. Table 5.1 indicates the identified governing failure zone of the specimens.

The influence of the mechanical transverse reinforcement ratio ω_y and the height of reinforcement placing $x_{E,max}$ for specimens with joint type TLJ-40 and concrete compressive strengths in the range of f_{c0} = 42.1…55.2 MPa is studied in Fig. 5.6a. The normalised stress-compression curves differ very little, and particularly the initial stiffness is almost identical. Comparing the specimens TLJ-40-WG2p-B1 and TLJ-40-WG3p-B3, with nearly equal f_{c0} (B1: 46.0 MPa, B3: 46.9 MPa), it is evident that a substantially higher ω_y (0.19 vs. 0.26) did not lead to a significantly higher normalised average peak stress at the joint ($q_{x,u,exp}/f_{c0}$: 2.24 vs. 2.25) nor increased compression δ_x at the peak load (6.8 mm vs. 6.0 mm). This outcome is not in accordance with the results of the experimental campaign on strip-loaded concrete blocks confined over the entire block height ($x_{E,max} = h$) presented in Morger et al. [10]. Specimen TLJ-40-WG3p-B3 experienced an immediate load drop after the peak load, whereas the other tests with joint geometry TLJ-40 exhibited a less pronounced softening response and some even showed a load plateau with increasing compression. One can thus conclude that in the specimen TLJ-40-WG3p-B3, the confining reinforcement was not fully activated due to the presence of the unconfined zone, which limited the load-bearing capacity by failing in uniaxial compression. Specimen TLJ-40-WG2f-B4, which was reinforced over the entire height, failed in a more ductile manner, due to the confinement governing failure. Furthermore, it sustained the lowest normalised peak stress at the joint which is in accordance with having the lowest mechanical reinforcement ratio. The specimens TLJ-40-WG2p-B1 and TLJ-40-WG2p-B2 only varied regarding f_{c0} (B1: 46.0 MPa, B2: 42.1 MPa). Surprisingly, TLJ-40-WG2p-B1 with higher f_{c0} hence lower ω_y exhibited a more pronounced softening response, indicating failure in the unconfined zone, whereas the ductile behaviour of TLJ-40-WG2p-B2 indicates a failure in the confined zone. If only one of these two specimens would fail in the unconfined zone one would expect it to be the specimen with higher ω_y since it contains higher capacity in the confined zone. This indicates that in these two specimens, the load-bearing capacities of the confined and unconfined zones were similar, such that failure was possible in both. It is worth pointing out that all specimens investigated in Fig. 5.6a contained substantial confining reinforcement (ω_y = 0.16…0.26) which, however, due to the presence of the unconfined zone allowed only for a small increase of the normalised average peak stress between these specimens e.g. TLJ-40-WG2f-B4 (ω_y = 0.16) vs. TLJ-40-WG2p-B1 (ω_y = 0.19, + 4%) or TLJ-40-WG2p-B2 (ω_y = 0.21, + 8%) or TLJ-40-WG3p-B3 (ω_y = 0.26, + 5%), respectively. Accordingly, the critical reinforcement ratio at which the unconfined zone governs failure lays approximately at ω_y = 0.20 (failure possible in both zones for TLJ-40-WG2p-B1 and TLJ-40-WG2p-B2). Hence it is expected that specimens with lower confining reinforcement ratios, but otherwise equal properties, would fail in the confined zone and consequently exhibit lower normalised average peak stresses – and thus lower load-bearing capacities – as also observed in the experimental campaign presented in Morger et al. [10]. Therefore, it can be concluded, that confining reinforcement can substantially increase the load-bearing capacity of longitudinal tunnel lining joints up to the point where an unconfined zone governs.

Fig. 5.6b illustrates the influence of the mechanical transverse reinforcement ratio ω_y and the height of the confined zone $x_{E,max}$ for the specimens with joint type TLJ-60, which had a wider joint contact area

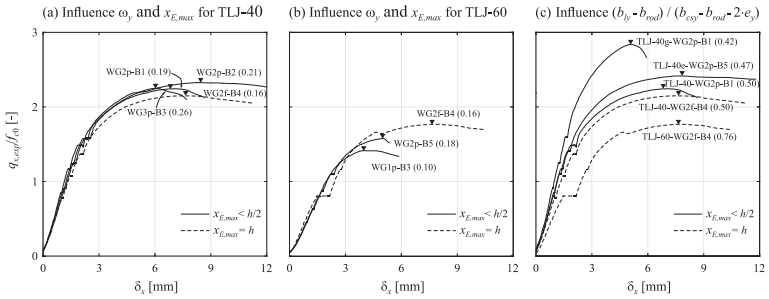

Fig. 5.6 - Normalised stress-compression diagrams for all tests investigating different influences: (a) mechanical transverse reinforcement ratio ω_y and confined height $x_{E,max}$ for tests with joint geometry TLJ-40, (b) mechanical transverse reinforcement ratio ω_y and confined height $x_{E,max}$ for specimens with joint geometry TLJ-60, and (c) load concentration ratio given by the joint type. The value of the respective influence parameter is indicated in brackets or by the legend. For more detailed information on the specimens, see Table 5.1.

compared to TLJ-40. The concrete compressive strength of the investigated test specimens varied between f_{c0} = 46.9…55.2 MPa, and only the specimen TLJ-60-WG2f-B4 was reinforced over the entire height. The initial stiffness of all specimens was almost identical, but the normalised average peak stress at the joint ($q_{x,u,exp}/f_{c0}$) and the compression at the peak load varied considerably. TLJ-60-WG1p-B3, with the lowest ω_y, experienced the lowest normalised average peak stress and smallest compression at the peak load, while TLJ-60-WG2f-B4, which was confined over its entire height, sustained the highest normalised average peak stress and experienced the largest compression. Even though TLJ-60-WG2p-B5 had the highest ω_y, it exhibited a lower normalised average peak stress (1.58 vs. 1.77) and significantly smaller compression at the peak load (5.0 mm vs. 7.6 mm) than TLJ-60-WG2f-B4. These results clearly indicate that the confining reinforcement could not be fully activated in the specimen TLJ-60-WG2p-B5. Furthermore, looking at the post-peak behaviour, TLJ-60-WG2f-B4 experienced a load plateau with increasing displacement, whereas TLJ-60-WG2p-B5 exhibited a sudden load drop. Accordingly, it can be concluded that TLJ-60-WG2p-B5 failed in the unconfined zone in uniaxial compression, while for TLJ-60-WG2f-B4 the confinement was governing. For the specimen TLJ-60-WG1p-B3, failure in the confined zone is anticipated due to the fact that in the otherwise nearly identical specimen with a higher reinforcement ratio (TLJ-60-WG2p-B5, only varying regarding f_{c0}: 46.7 MPa vs. 47.9 MPa), a higher normalised average peak stress was achieved (+ 12%), i.e., it is unlikely that the unconfined zone was governing. Furthermore, the load drop post peak was less pronounced compared to TLJ-60-WG2p-B5, which failed in the unconfined zone.

Note that in a normalised stress-compression diagram for specimens with the same joint geometry, failure in the unconfined zone would occur at the same normalised stress assuming that the load-bearing capacity of the unconfined zone is not affected by the reinforcement ratio of the confined zone, as proposed in the modelling of the unconfined zone in Section 5.4.1. This furthermore supports the identified failure modes of the specimens in Fig. 5.6a and b. Nevertheless, note that in specimens with similar

load-bearing capacity of the confined and unconfined zone the scatter of the concrete compressive strength may impact the governing zone.

Fig. 5.6c illustrates the influence of the joint width for fully confined specimens with equal reinforcement layout (WG2f) and concrete compressive strength (B4: f_{c0} = 55.2 MPa) as well as the influence of a guiding rod groove and eccentricity for specimens with equal reinforcement layout (WG2p) and very similar concrete compressive strengths (B1: f_{c0} = 46.0 MPa, B5: f_{c0} = 47.9 MPa). The specimen arrangement is described here by the load concentration ratio $(b_{ly} - b_{rod})/(b_{csy} - b_{rod} - 2 \cdot e_y)$; note that this formulation only considers the width within the reinforcement available for load dispersion, which, according to Markić et al. [11], solely contributes to the load-bearing capacity. The fully confined specimens (TLJ-40-WG2f-B4 vs. TLJ-60-WG2f-B4) varied regarding the normalised average peak stress ($q_{x,u,exp}/f_{c0}$). This observation is attributed to the load concentration ratio: with decreasing load concentration ratio, e.g. narrower joints, the geometrical confinement increases, resulting in a higher concrete compressive strength at the joint and consequently higher $q_{x,u,exp}/f_{c0}$ for otherwise equal properties. However, note that the peak axial force $N_{x,u,exp}$ decreases due to the smaller loaded area. Comparison of the specimens TLJ-40-WG2p-B1, TLJ-40g-WG2p-B1, and TLJ-40e-WG2p-B5 reveals that the normalised average peak stresses are in accordance with the load concentration ratio: a lower load concentration ratio led to higher normalised average peak stresses. Despite sustaining a higher normalised average peak stress, longitudinal joints of tunnel lining segments with guiding rod grooves (TLJ-40g-WG2p-B1) or misalignment (TLJ-40e-WG2p-B5) thus exhibit a reduced axial force bearing capacity compared to segments with the same joint geometry loaded over the entire joint width (TLJ-40-WG2p-B1). Furthermore, TLJ-40g-WG2p-B1 shows reduced ductility and an immediate load drop after the peak load, whereas the specimens TLJ-40-WG2p-B1 and TLJ-40e-WG2p-B5 experienced higher compression at the peak load and a less pronounced softening response. The failure mode of TLJ-40-WG2p-B1 (load-bearing capacity of confined and unconfined zone similar) has been discussed previously. For the eccentrically placed half specimens of TLJ-40e-WG2p-B5, which exhibited a very ductile response, confinement was likely governing failure. Specimen TLJ-40g-WG2p-B1 (simulating the guiding rod groove) sustained the highest normalised average peak stress, but due to the reduced joint contact area, the lowest axial force $N_{x,u,exp}$. Consequently, failure in the unconfined zone can be ruled out. Nonetheless, the normalised stress-compression curve indicates a brittle failure, potentially caused by a localised concrete failure at the joint due to the geometry. Note that the $q_{x,exp}/f_{c0}$-δ_x curves in Fig. 5.6c do not allow for a direct comparison of the axial normal force stiffnesses of the specimens due to the varying joint contact areas.

The investigation of the cut surfaces in Fig. 5.7 yields further insight into the load-bearing behaviour. Inside the half specimens, concrete cracks occurred at the edges of the joint and propagated towards the outside of the confining reinforcement, where they clearly separated the unloaded shoulders and the cover concrete from the concrete within the confining reinforcement. The separation of cover concrete, which did not occur symmetrically in most cases, can be described as spalling due to increasing lateral displacement and confinement activation. As clearly visible in several half specimens, the spalling cracks were not limited to the confined zone but extended into the unconfined zone, hence impairing the load-bearing capacity in the unconfined zone since the full concrete cross-section ($b_y \cdot b_z$) cannot be activated. Accordingly, the resistance of the unconfined zone can be governing particularly in specimens with high confining stresses or wide joint contact areas.

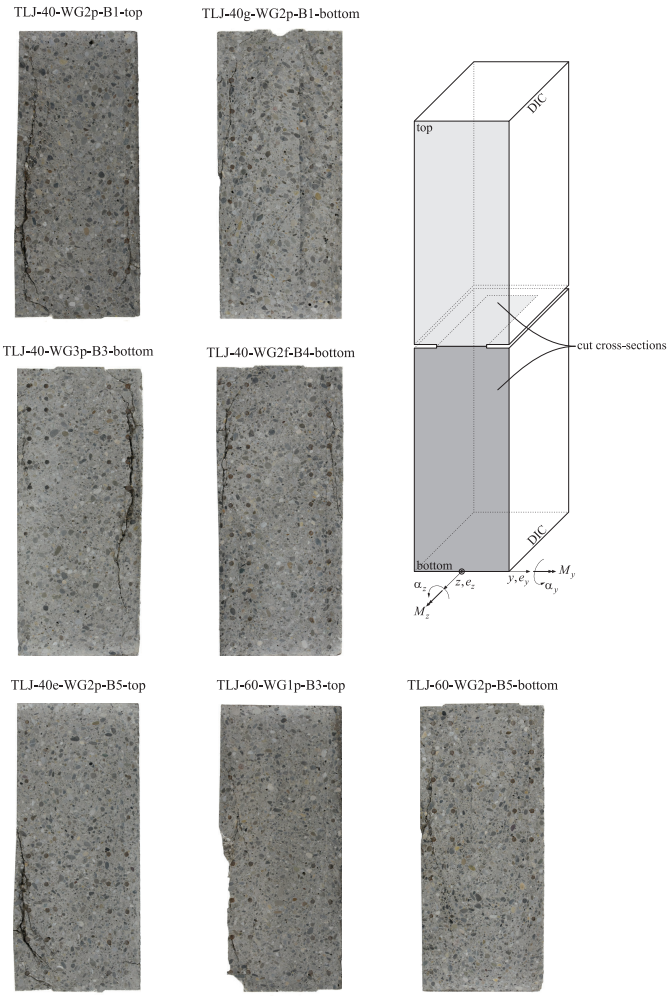

Fig. 5.7 - Vertical transverse cuts through half specimens (top or bottom) after testing. Orientation of half specimens as in the experiments. Longitudinal DIC surface to the positive *y* side.

The testing machine data in Fig. 5.C.1 (Appendix 5.C) shows that with increasing load, the measured bending moments at the lower load introduction plate (definition of positive direction see sketch in Fig. 5.7) either reduced or remained constant, resulting in a decrease of eccentric loading at the lower load introduction plate. At the peak load only marginal eccentricities ($e_y < 0.06 \cdot b_y$, $e_z < 0.02 \cdot b_z$) occurred, indicating that uniform loading of the joints can indeed be considered. In the post-peak range of

the applied load, the bending moments and thus also the eccentricities increased significantly in some tests. In the half specimens TLJ-40-WG3p-B3 and TLJ-60-WG2p-B5, which were placed at the bottom and hence, subjected to the measured bending moments at their ends, the increasing bending moments corresponded to an unloading on the sides where more pronounced spalling cracks were observed after cutting them (Fig. 5.7). This clearly indicates that the bending moments and eccentricities resulted due to the spalling cracks, and not vice versa.

5.3.3 Crack development

For tunnel lining segments, crack width limitations are required to prevent issues related to increased permeability, excessive water leaks or reinforcement corrosion [23]. In the serviceability limit state (SLS), the crack widths are typically limited to 0.2…0.3 mm [13], [23]. In tunnel lining segments subjected to predominant axial force, cracks can occur on the joint side due to compatibility of the heavily loaded joint contact area and the surrounding unloaded areas (where gaskets ensuring watertightness are often provided) or on the longitudinal and transverse sides due to concrete expansion related to passive confinement activation or tensile stresses caused by load dispersion.

The evolution of the crack widths on the lateral sides (determined with DIC and ACDM) in Fig. 5.5 shows that in all tests, a maximum crack opening of 0.2 and 0.3 mm was first reached in the transverse direction, with only marginal differences between the crack width developments in the top and bottom half specimens per test. In most specimens, the crack widths gradually increased until they opened suddenly due to the spalling of the cover concrete. Furthermore, in some tests the crack widths grew considerably in the load stages while the load was kept constant for 15 min. This increase of the crack width, which can be attributed to short-term creep deformations, should be kept in mind when interpreting the test data and discussing the load levels at which a certain crack width is reached. Note that while no cracks were detected in the specimen TLJ-60-WG1p-B3 until the peak load, cracks were visible by eye well before the peak on the opposite sides (not monitored by DIC). Accordingly, any conclusions related to crack widths based on the results presented in this article should be treated with caution, as experimental data is limited.

Table 5.2 - Ratio between the stress at a maximum crack width $w_{r,max}$ of 0.2, and 0.3 mm and the peak stress, expressed in percentage [%].

Specimen	TLJ-40-WG2p-B1	TLJ-40g-WG2p-B1	TLJ-40-WG2p-B2	TLJ-40-WG3p-B3	TLJ-40-WG2f-B4	TLJ-60-WG2f-B4	TLJ-40e-WG2p-B5	TLJ-60-WG1p-B3	TLJ-60-WG2p-B5	Min	Mean
$\frac{q_{x,exp}\left(w_{r,max}=0.2\,\mathrm{mm}\right)}{q_{x,u,exp}}$	66	78	80	70	64	79	67	-	83	64	73
$\frac{q_{x,exp}\left(w_{r,max}=0.3\,\mathrm{mm}\right)}{q_{x,u,exp}}$	74	98	89	76	81	88	80	-	92	74	85

Table 5.2 compiles the ratios between the applied stress at crack widths $w_{r,max}$ of 0.2 and 0.3 mm, respectively, and the peak stress. To assess whether the crack widths (SLS) or the load-bearing capacity (ultimate limit state, ULS) governs the design, the same approach as presented in Morger et al. [10] is applied: With a partial safety factor of 1.35 for the load (predominant permanent loads) and an average partial safety factor for the materials of 1.40 (accounting for the compressive strength of the concrete and the tensile strength of the reinforcement), the SLS load level roughly corresponds to 1/(1.35·1.40) = 53% of the experimentally obtained peak load. Consequently, the crack width would govern the design and reduce the admissible stress compared to the experimentally determined structural load-bearing capacity for ratios below 0.53. Table 5.2 thus indicates that the crack width would not govern the design of any of the tested specimens, with a reasonable margin for potential creep-related crack growth that has been neglected in the calculations. It can be concluded that for tunnel lining segments with confining reinforcement only in the zone next to the joint and joint geometries and material parameters as used in the present experimental campaign, the full potential of the confining reinforcement can be exploited without compromising serviceability. Crack widths should neither be critical for lower reinforcement ratios, as smaller axial compressions δ_x would be sufficient to fully activate the confining reinforcement. On the other hand, higher ratios would not be of any use, since the unconfined zone would become governing in ULS as discussed in Section 5.3.2. Note, however, that the specimens in this experimental campaign were made of normal strength concrete (f_{c0} = 42.1…55.2 MPa); high strength concrete specimens may experience less favourable crack growth as shown in Morger et al. [10]. The same applies to fully confined segments with high reinforcement ratios.

5.3.4 Joint closing

Knowledge of the joint deformation is relevant to designing the joint height and, if required, the segment gaskets, which ensure the watertightness of tunnels in one-pass lining systems. Fig. 5.5 shows the joint closing $\delta_{x,joint}$ in all tests up to the peak load. Note that $\delta_{x,joint}$ was determined by DIC on the specimen surfaces rather than directly at the joint contact area. Differences are thus possible, particularly at higher load levels, when the unloaded shoulders are separated from the specimen by spalling cracks; the DIC measurements should thus result in conservative (= higher) values of $\delta_{x,joint}$. The range of $\delta_{x,joint}$ varied within a few tenths of a millimetre (grey shaded areas in Fig. 5.5), increasing with higher loads and having higher values at the edges than at the centre.

The plots reveal that the initial joint height of h_{joint} = 7 mm (shoulder distance $2 \cdot h_{joint}$ = 14 mm) was sufficient to activate the full load-bearing capacity of the specimens without fully closing the joint. Based on the maximum joint closing of approximately $\delta_{x,joint}$ = 8.4 mm, a joint height of h_{joint} = 5 mm would have been sufficient. Note that a reduced (increased) joint height would have a beneficial (detrimental) effect on the confinement and potentially also the load-bearing capacity. Assuming the same ratio between SLS and the experimentally obtained load-bearing capacity (= 0.53) as outlined in Section 5.3.3, the gaskets would have to sustain an additional compression of 0.2...0.8 mm (on top of their initial compression corresponding to full contact of the joints upon segment installation).

5.4 Modelling

The experimental results presented in Section 5.3 revealed that the load-bearing capacity of longitudinal joints of tunnel lining segments with pronounced confining reinforcement is governed either by the confined zone at the joint or, if present, by the unconfined zone further away, determining the maximum stress at the joint $q_{x,u}$:

$$q_{x,u} = \min\left(q_{x,u,conf}, q_{x,u,unconf}\right) \tag{5.1}$$

This section presents modelling approaches for both zones. The modelling of the unconfined zone is relatively simple as it only requires the determination of the area subjected to compressive loading. For the confined zone, the stress field solution for strip loading presented in Morger et al. [10] and shown in Fig. 5.8b is enhanced: the transverse load dispersion is extended to the width within the reinforcement, and longitudinal load dispersion is considered. Additionally, it is illustrated how the effect of a guiding rod groove can be taken into account. Lastly, the modelling approaches are compared to the experimental data and other design proposals.

5.4.1 Unconfined zone

Load dispersion in the unconfined zone is not possible if the concrete tensile strength is neglected, as commonly assumed by current design codes. Consequently, this zone is subjected to uniaxial compression only. As shown in Section 5.3.2, spalling cracks caused by transverse concrete expansion and the activation of confining reinforcement extended into the unconfined zone of the experimentally tested specimens. Consequently, the concrete area between the cracks and the specimen surface (concrete cover) cannot carry any load. The same situation can occur in the longitudinal direction: in order to generate a triaxial stress state in the confined zone, activation of the confining reinforcement in this direction is required as well, which may initiate spalling with cracks extending into the unconfined zone. Therefore, it is proposed to restrict the load-bearing capacity of the unconfined zone by considering only the uniaxial compressive strength of the concrete f_{c0} within the area $A_{cs} = b_{csy} \cdot b_{csz}$, resulting in a maximum applicable stress at the joint $q_{x,u,unconf}$:

$$q_{x,u,unconf} = \frac{f_{c0} \cdot b_{csy} \cdot b_{csz}}{\left(b_{ly} - b_{rod}\right) \cdot b_{lz}} \tag{5.2}$$

5.4.2 Confined zone

The design of RC structures with stress fields corresponds to a lower bound solution according to plasticity theory: equilibrium is fulfilled and the yield criteria of the concrete and the reinforcing steel are not infringed. Besides being mechanically consistent, stress fields offer the opportunity to follow the load path and place reinforcement where required. In Morger et al. [10], based on Markić et al. [24], the authors presented the Dual-Wedge (DW) stress field for strip-loaded RC specimens with moderate load concentration ratios. This stress field (see Fig. 5.8b) accounts for confining reinforcement and load dispersion in the transverse direction. However, load dispersion is limited to the confined concrete width

b_{ccy}. While this is not a problem for specimens confined over the entire height or specimens for which stresses $\sigma_{xd} \leq f_{c0}$ result after load dispersion, the transition to an adjacent unconfined zone as proposed in Section 5.4.1, where the width within the reinforcement $b_{csy} > b_{ccy}$ carries the load with a maximum stress of f_{c0}, would involve statically inadmissible discontinuities of the axial stresses. To overcome this inconsistency, the Multi-Wedge (MW) stress field shown in Fig. 5.8a, was developed. It consists of two load paths: The majority of load ($\sigma_{x0,ccy}$) is transferred from the wedge ABK through the strut BFK (inclined at an angle α) to the wedge BEF, where the load has spread to the confined width b_{ccy}, resulting in the vertical principal stress $\sigma_{xd,ccy}$. This load path corresponds to the load path of the DW stress field. The second load path transfers the load $\sigma_{x0,csy}$ from the wedge ABK through the trapezoidal strut BFLK at an angle β to the wedge FML, where the vertical principal stress $\sigma_{xd,csy}$ is limited to f_{c0} as it is applied outside the confined concrete width b_{ccy}. Since the wedge FML lies inside the width b_{csy} of the reinforcement, the reinforcement can be activated as bursting reinforcement at the discontinuity line FL to equilibrate the transverse component of the force in strut BFLK. Due to the partial activation of the reinforcement in tension, the confining stresses in this area ($\sigma_{confy,red}$, $x \geq x_B$) are reduced compared to the region at load introduction (σ_{confy}, $x < x_B$). Superimposing the two load paths and the confining stresses provided by the reinforcement results in principal stresses in each sub-field which need to comply with the failure criterion for concrete (modified Coulomb failure criterion with a tension cut-off, assuming the longitudinal z-direction does not govern failure, see Morger et al. [10]) while the reinforcement is assumed to only carry tension in the reinforcing bar direction up to the yield stress f_{sy}. The

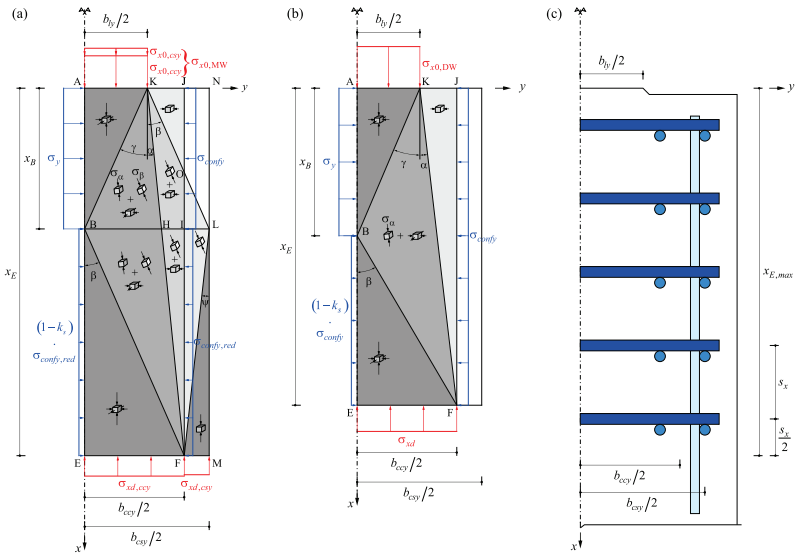

Fig. 5.8 - Modelling of longitudinal joints with stress fields: (a) Multi-Wedge stress field, (b) Dual-Wedge stress field, and (c) corresponding reinforcement layout for the half specimens of TLJ-40-WG2p-B1. Only one symmetrical half is shown. Transverse stresses are exaggerated compared to vertical stresses.

transverse stress $(1-k_s)\cdot\sigma_{confy,red}$ on the wedge BEF is required to correspond to be compressive; otherwise, transverse reinforcement is insufficient. For a given height x_E of the stress field (not larger than the confined height $x_{E,max}$, see Fig. 5.8c) and the values of b_{ly}, b_{ccy} (see Appendix 5.A) and b_{csy}, the geometry of the stress field is determined (β identical for strut BFLK and wedge BEF), and the load-bearing capacity $\sigma_{x0,MW} = \sigma_{x0,ccy} + \sigma_{x0,csy}$ can be determined for uniform confining stresses σ_{confy} by maximising $\sigma_{x0,ccy}$ without infringing the failure criteria. All equations to determine the geometrical parameters (x_B, α, β, γ, and ψ) and the stresses ($\sigma_{x0,csy}$, σ_α, σ_β, σ_y, and $\sigma_{confy,red}$) of the MW stress field for a given x_E are compiled in Appendix 5.E. Note that setting $x_E = x_{E,max}$ does not necessarily result in the maximum load-bearing capacity; reducing x_E can be beneficial. Furthermore, if the loaded width b_{ly} exceeds the confined width b_{ccy}, $\sigma_{x0,ccy}$ can only be applied within b_{ccy}, and no load dispersion occurs (α = 0). The calculation process outlined in Appendix 5.E, however, is not affected. Note that the loaded width b_{ly} should not exceed b_{csy} since the cover concrete is prone to spalling. To ensure that the longitudinal z-direction does not govern failure, confining reinforcement may be required in the sub-fields ABK, BHK, BFH and BEF. The required confining stresses of each sub-field in z-direction corresponds to its minimum principal stress σ_3 (compression positive) in the (x,y)-plane. If the corresponding confining reinforcement in the longitudinal direction cannot be provided, the load-bearing capacity prediction of the MW stress field needs to be reduced. For more details regarding the longitudinal reinforcement, the reader is referred to Morger et al. [10].

Fig. 5.8a and b show the MW and DW optimised stress fields for the half specimens of TLJ-40-WG2p-B1 (geometry and reinforcement layout in Fig. 5.8c drawn to scale of the stress fields), predicting the highest load-bearing capacity. Generally, the MW stress field requires a higher confined height x_E to reach the maximum load-bearing capacity prediction (see Fig. 5.8 and Table 5.G.1). The two models predict similar peak loads: for high ratios ($b_{ccy} - b_{ly}$) to ($b_{csy} - b_{ccy}$) the DW stress field predicts higher load-bearing capacities, but with decreasing ratio the difference reduces and can even result in the MW yielding higher capacities if sufficient confined height $x_{E,max}$ is available (see σ_{x0} Table 5.G.1). The stress fields also differ in the utilisation of the sub-fields. While all sub-fields affected by load dispersion are fully utilised in the DW stress field, this is not the case for the MW stress field, for which most often only sub-fields FML and ABK or BFH are fully utilised, while the others have reserve capacities.

For longitudinal joints of tunnel lining segments, the length of the joint contact area often exceeds the confined length ($b_{lz} > b_{ccz}$). In these cases, the stress σ_{x0} determined with either the MW or DW stress field can only be applied on the confined length b_{ccz}. In Morger et al. [10], it was proposed to apply the uniaxial concrete compressive strength f_{c0} on the loaded area outside the confined length ($b_{lz} - b_{ccz}$). However, as shown with the MW stress field, load dispersion is possible inside the length of the reinforcement (b_{csz}) by activating parts of the reinforcement in tension to account for bursting stresses. Load dispersion in the longitudinal direction can be modelled by the simplest version of the DW stress field [24], as illustrated in Fig. 5.9a (the definition of the geometry follows Fig. 5.8b): the stress $\sigma_{x0,csz}$ applied on the length $b_{lz} - b_{ccz}$ and spreading to the length $b_{csz} - b_{ccz}$ by activating the bursting stress σ_{sz} can be determined according to Appendix 5.F, resulting in $\sigma_{x0,csz} > f_{c0}$. Due to the activation of the longitudinal reinforcement in tension, a redistribution of confining stresses occurs: In the region with bursting stresses (only on the width b_{ly}), the longitudinal confining stresses σ_{confz} are reduced by σ_{sz}, while in the region above, the longitudinal confining stresses are increased by $\sigma_{confz,add}$. Based on a limited parametric study with the DW stress field, the authors propose to account for 20% redistribution of the confining

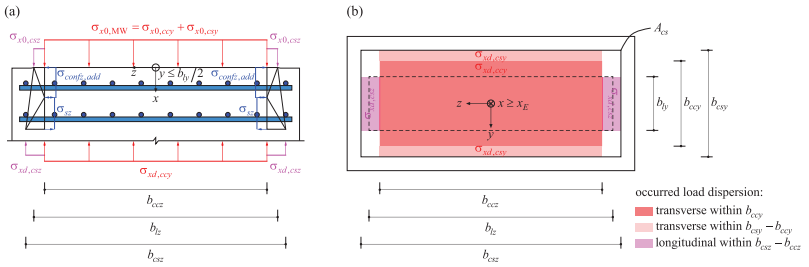

Fig. 5.9 - Load dispersion in longitudinal direction shown for the half specimens of TLJ-40-WG2p-B1: (a) vertical cut through centre with Dual-Wedge stress fields on the sides and (b) horizontal cut after load dispersion indicating the loaded areas. Transverse load dispersion considered according to the Multi-Wedge stress field.

stresses ($\sigma_{sz} \approx \sigma_{confz}/5$) for geometrical situations similar to these of the specimens presented in this article. A higher σ_{sz} does not increase $\sigma_{x0,csz}$ since the diagonal compressive strut becomes governing (limited to f_{c0}). Furthermore, for geometrical situations substantially varying from the specimens in this article, σ_{sz} needs to be computed with the DW stress field. Note that the triaxial compressive stresses required for the upper wedge can be provided by activating the transverse confining stress σ_{confy}.

Fig. 5.9b shows a horizontal cut of a strip-loaded RC segment at a height with completed load dispersion ($x \geq x_E$), indicating the distribution of vertical stresses determined with the MW stress field in the transverse direction and the DW stress field in the longitudinal direction. Evidently, the model cannot capture load dispersion to the entire area within the reinforcement ($A_{cs} = b_{csy} \cdot b_{csz}$): the corners of A_{cs} (white) are unstressed. The reason is the independent 2D load dispersion in the transverse and longitudinal directions. In order to be able to reach a load-bearing axial force corresponding to $f_{c0} \cdot A_{cs}$ (which is the limit of the unconfined zone, see Section 5.4.1) it is thus proposed to allow vertical stresses $\sigma_{xd,ccy}$ (determined with the MW stress field) slightly higher than f_{c0} for specimens with an unconfined zone. While this approach, strictly speaking, infringes the failure criterion of unconfined concrete, it can be justified by the fact that the beneficial load dispersion into the unstressed corners is otherwise neglected.

Accounting for the load dispersion in the transverse and longitudinal directions, the load-bearing capacity of the confined zone thus reads as follows:

$$q_{x,u,conf} = \frac{\sigma_{x0,MW} \cdot b_{ccz} + \sigma_{x0,csz} \cdot (b_{lz} - b_{ccz})}{b_{lz}} \tag{5.3}$$

For entirely confined segments, the required confining reinforcement in the transverse direction after load dispersion ($x > x_E$) is smaller than σ_{confy} and corresponds to $(1-k_s) \cdot \sigma_{confy,red}$ determined with the MW stress field. To avoid a change in the size of the confined area, equal reinforcement spacings are required, allowing only the reduction of the reinforcement diameter. The load-bearing capacity of the confined region after load dispersion can be determined as for pure passive confinement:

$$q_{x,u,conf,x>x_E} = \frac{f_{c0} \cdot b_{csy} \cdot b_{csz} + 4 \cdot \min\left(\sigma_{confy}, \sigma_{confz}\right) \cdot b_{ccy} \cdot b_{ccz}}{b_{ly} \cdot b_{lz}} \tag{5.4}$$

5.4.3 Guiding rod

Comparing the experimentally determined normalised average peak stresses of the specimens TLJ-40-WG2p-B1 and TLJ-40g-WG2p-B1 (2.24 vs. 2.84), it can be concluded that (i) a guiding rod groove impacts the load-bearing capacity, as (ii) the reduced joint contact area is only partly compensated by the associated higher geometrical confinement. Consequently, the impact of guiding rod grooves on the design of longitudinal tunnel lining joints should be studied in detail. Fig. 5.10 presents three different modelling approaches (Variants A-C) of the confined zone related to the MW stress field. The drawings represent the optimal stress fields for the half specimens of TLJ-40g-WG2p-B1. Note that in all models, the groove is only considered as a not loaded area b_{rod}, but the depth of it in the x-direction is neglected for simplification so that the transverse stresses σ_y or $\sigma_{y,i}$ are directly applied at the load introduction.

Variant A in Fig. 5.10a determines the load-bearing capacity with the MW stress field ($\sigma_{x0,MW}$) as presented in Fig. 5.8a, neglecting the absence of contact of the joints over b_{rod}, and – a posteriori accounting for the guiding rod groove – determines the axial force resistance of the joints with the stress $q_{x,u,conf}$ according to Eq. (5.3) applied over the effective contact width $b_{ly} - b_{rod}$. Note that this approach is not a mechanically consistent solution according to the theory of plasticity. Variant B applies the MW stress field on the two loaded widths $(b_{ly} - b_{rod})/2$ and complements them by the sub-fields AQRB and BRSE, which are subjected to uniaxial transverse compressive stresses σ_y and $(1-k_s)\cdot\sigma_{confy,red}$, respectively. This is a mechanically consistent stress field solution, accounting for the beneficial effect of the narrower loaded width on the load-bearing capacity; note that it must be verified that σ_y does not exceed the uniaxial concrete compressive strength f_{c0} (for $(1-k_s)\cdot\sigma_{confy,red}$, this is implicitly satisfied since σ_{confy} must be smaller than f_{c0} when applying the MW stress field). The load-bearing capacity $q_{x,u,conf,rod}$ according to Variant B can be determined analogously to Eq. (5.3). Unlike the previous two variants, Variant C allows for load dispersion towards the guiding rod groove on the inside over $b_i/2$ in combination with a MW stress field transferring $\sigma_{x0,MW}$ over $b_o/2$ to the outside. The stress $\sigma_{x0,ccy,i}$ applied on $b_i/2$ on the wedge APB is transferred at an angle α_i to the discontinuity line BR where it is continuously deviated by a transverse force such that only a vertical stress $\sigma_{xd,ccy,i}$ remains in the sub-field BRSE. The integration of the transverse forces along BR results in a concentrated compressive force R_y, which should only activate a small concrete area compared to the height of the stress field. The transverse confining stress $\sigma_{y,i}$, which is limited by f_{c0}, is determined by fulfilling transverse equilibrium at the discontinuity line AB while the transverse stress of the sub-field BRSE corresponds to the transverse stress $(1-k_s)\cdot\sigma_{confy,red}$ resulting from the outside load path of the MW stress field. The maximum load-bearing capacity is found iteratively by varying the ratio b_o to b_i. For a given ratio, the calculation process is as follows: Firstly, the MW stress field is computed for the load transfer towards the outside. The MW stress field directly defines the geometry of the inside load path as well as the third principal stress in the sub-fields APB and BRSE. $\sigma_{x0,ccy,i}$ can then be defined to not govern in these sub-fields. In the last step, for a given $\sigma_{x0,ccy,i}$, the failure criterion in sub-field BPR is investigated and $\sigma_{x0,ccy,i}$ is reduced if required. The resulting load-bearing capacity, also considering longitudinal load dispersion as proposed in Section 5.4.2, of Variant C is:

$$q_{x,u,rod,conf} = \frac{\frac{\sigma_{x0,MW}\cdot b_o + \sigma_{x0,ccy,i}\cdot b_i}{b_o + b_i}\cdot b_{ccz} + \sigma_{x0,csz}\cdot\left(b_{lz} - b_{ccz}\right)}{b_{lz}} \tag{5.5}$$

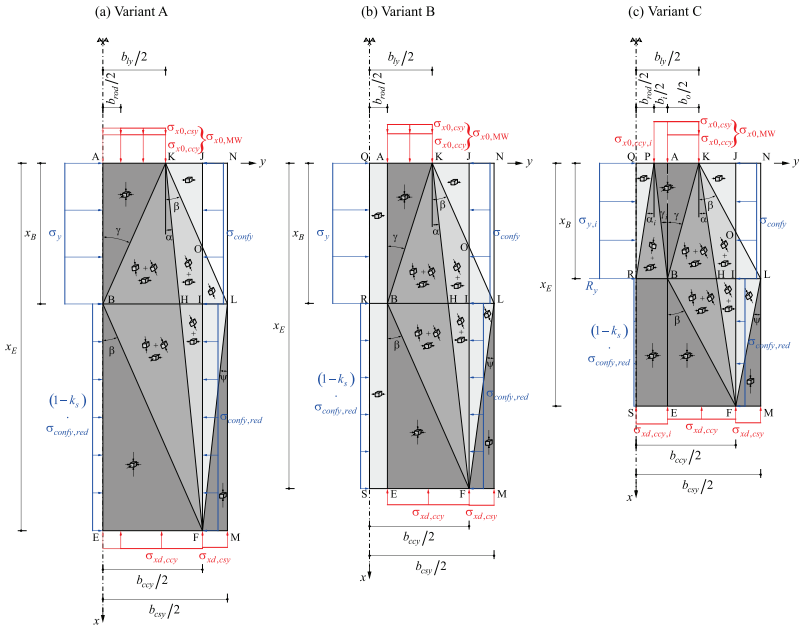

Fig. 5.10 - Stress fields to account for guiding rod groove shown for the half specimens of test TLJ-40g-WG2p-B1: (a) Multi-Wedge stress field from Fig. 5.8a with a posteriori reduced loaded width (mechanically inconsistent approach), (b) Multi-Wedge stress field accounting for guiding rod in model, and (c) stress field with bi-directional load dispersion including Multi-Wedge stress field. For all stress fields only one symmetrical half is shown. The plotted transverse stresses are exaggerated compared to the vertical stresses and scaled differently compared to Fig. 5.8 for better legibility.

Note that the equations in Appendix 5.E require adjustment for the impact of the guiding rod groove to determine $\sigma_{x0,MW}$ for Variants B and C.

5.4.4 Comparison with experimental data

Fig. 5.11 plots the ratios of the experimentally observed load-bearing capacity ($q_{x,u,exp}$) of the eight tests without guiding rod groove to the predictions of different models ($q_{x,u,model}$) against (a) the load concentration ratio, (b) the mechanical reinforcement ratio in the transverse direction, and (c) the concrete compressive strength. The comparison contains, besides the MW and DW stress fields, the geometric-passive confinement model (GPC, introduced in Proksch-Weilguni et al. [12] and extended in Morger et al. [10]) and the modelling approach according to the guideline of Deutscher Ausschuss für unterirdisches Bauen e.V. (DAUB) [13]. For the three models accounting for confining reinforcement (MW, DW and GPC), the minimum load-bearing capacity of the confined and unconfined zones is considered

(filled markers). The markers without filling represent the comparison of the observed load-bearing capacity with the predictions of the confined zone for specimens for which the unconfined zone is governing ($q_{x,u,unconf} < q_{x,u,conf}$). The DAUB approach does not differentiate between the two zones. The predictions of the different models were determined with the mean material properties summarised in Table 5.1 and the definition of the confinement properties outlined in Appendix 5.A. Furthermore, Table 5.G.1 in Appendix 5.G.1 summarises the parameters of the different models and compiles the statistical evaluation of comparing the different models with the experimental data.

The comparison reveals that for all models, the load-bearing capacity predictions are on the safe side (ratio > 1). The three models accounting for confining reinforcement (MW, DW, and GPC) show very similar predictions (mean 1.10…1.11, coefficient of variation (COV) 2.9%…3.9%), while the DAUB approach becomes more conservative with increasing mechanical transverse reinforcement ratio. Furthermore, it becomes evident that the load-bearing capacity prediction must consider the resistance of the confined and unconfined zones. Only considering the resistance of the confined zone can overestimate the load-bearing capacity, particularly for specimens with high mechanical confining ratios ω_y and wide load application widths $b_{ly,}$ since in these cases, high axial forces occur that exceed the capacity of the unconfined zone. The proposal to only consider the uniaxial concrete compressive strength f_{c0} within the area of the confining reinforcement (A_{cs}) for the unconfined zone (see Section 5.4.1) proves to be an appropriate approach. The predictions of the stress field models regarding the failure mode (governing zone) are in accordance with the observation of the tests (see Section 5.3.2). A direct comparison of the load-bearing predictions for the specimens of the campaign presented in this article – using the newly proposed MW stress field in combination with the modelling approach for the unconfined zone and the DAUB approach – is also provided in Table 5.G.1 in Appendix 5.G.1. The results of the specimens containing an unconfined zone, which is presumably the most relevant case for tunnelling practice, show that for narrow joint widths (TLJ-40) an increase of 16%…22% of the predicted load-bearing capacity

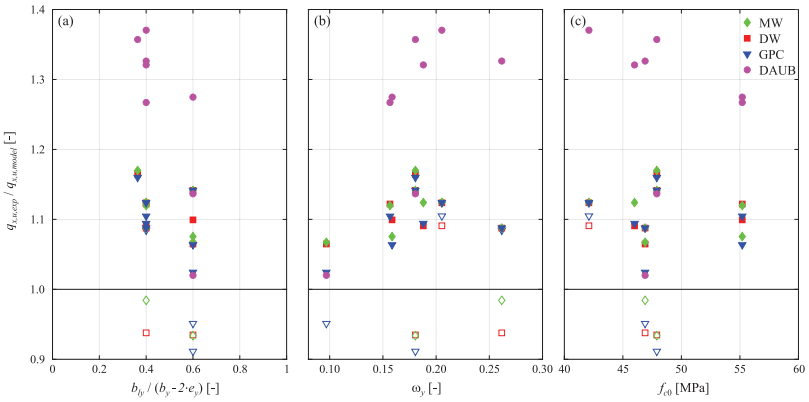

Fig. 5.11 - Comparison of experimental data with model predictions plotted against (a) load concentration ratio $b_{ly}/(b_y - 2 \cdot e_y)$, (b) transverse mechanical reinforcement ratio ω_y, and (c) uniaxial concrete compressive strength f_{c0}. Markers without filling indicate the comparison if only the confined zone is considered for specimens with a governing unconfined zone.

is possible by considering confining reinforcement. In contrast, for wide joint widths (TLJ-60) the benefit of confinement is much smaller due to the presence of the unconfined zone, with the DAUB approach even predicting slightly higher capacities (0%…4%). These findings highlight the impact of the unconfined zone but also emphasise the optimisation potential in the design of longitudinal joints accounting for confining reinforcement. Note that the comparison only applies to the specific properties of the specimens investigated and cannot be assumed a priori for other configurations. Moreover, the reinforcement used in the specimens exceeded the minimum reinforcement required to prevent splitting according to the DAUB guideline [13].

Table 5.G.2 in Appendix 5.G.2 compiles the comparison of the three stress fields considering a guiding rod groove with the experimental results of TLJ-40g-WG2p-B1. The DAUB guideline [13] also defines how the impact of a guiding rod groove can be considered: the empirical square-root equation without geometrical similarity is applied (as for joints without guiding rod groove), considering the two joint areas next to the groove as independently loaded areas with intersecting areas available for load dispersion (see Eq. (5.G.1) in Appendix 5.G.2). This approach is also considered in the comparison.

All approaches provide safe predictions. Of the three stress fields, Variant A is the most conservative one ($q_{x,u,exp}/q_{x,u,model}$ = 1.42). While being mechanically inconsistent, it could still be used in engineering practice to estimate the impact of adding a guiding rod to an already designed longitudinal joint. The additional load transfer towards the guiding rod groove of Variant C results in a better prediction compared to Variant B (1.21 vs. 1.29). Note that for both variants, the required confined height x_E according to the stress fields can be substantially smaller than the actual confined height of the half specimens (363 mm in Variant B and 271 mm in Variant C, respectively, vs. 410 mm). The empirical DAUB design approach is the least conservative one (1.16), which is surprising since for the comparison of the tests with similar reinforcement ratio and joint geometry but no guiding rod groove, the DAUB approach is far more conservative than the stress fields.

In conclusion, the comparison indicates that the stress fields are a useful tool to account for the impact of a guiding rod groove. However, with only one test available to compare, no reliable conclusion can be drawn on their applicability in engineering practice. To properly validate them, more tests are required, particularly with varying reinforcement ratios and joint geometries.

As a final remark, note that each test consisted of two identical half specimens, and the reported load-bearing capacity of the test is the lower one of the two. Consequently, the comparison is made with a lower bound of the experimental data. On the other hand, the calculations of the models were carried out without considering a concrete brittleness factor and accordingly reducing the concrete compressive strength, as often used in current codes, for example, $\eta_{cc} = (30/f_{c0})^{(1/3)} \leq 1$ according to SIA 262 [9].

5.5 Conclusion

This article presents an experimental campaign of nine tests investigating the load-bearing behaviour of longitudinal tunnel lining joints with pronounced confining reinforcement along with modelling approaches, including new stress field solutions for longitudinal joints with and without guiding rod grooves.

The investigated parameters of the experimental campaign were (i) the transverse reinforcement ratio, (ii) the reinforcement configuration, and (iii) the joint geometry of RC specimens reinforced with welded grids. The experimental results highlight that with a higher load concentration ratio (larger joint width), the contact stress at the joint decreases due to the limited geometrical confinement, but the axial force still increases because of the larger joint area. Confining reinforcement contributes to the load-bearing capacity of longitudinal joints. However, the possible load increase by providing confining reinforcement is limited if the segments contain – besides the confined zone at the joint – an unconfined zone. In the unconfined zone, only the uniaxial concrete compressive strength can be activated, and on an area smaller than the segment cross-section due to spalling cracks occurring in the confined zone propagating into the unconfined zone. Consequently, segments with high reinforcement ratios and wide joints that can sustain high axial forces are prone to fail in the unconfined zone. Specimens failing in the unconfined zone exhibited a less ductile behaviour than those failing in the confined zone. In order to increase the load-bearing capacity of segments with a governing unconfined zone, confining reinforcement can be placed in that zone with reduced reinforcement content compared to the confined zone at the joint. Fully confined segments can particularly be useful for tunnels with varying loading scenarios along their length, as they can be used to strengthen the segments locally and thereby maintain a constant, smaller thickness throughout the tunnel. Furthermore, the DIC measurements used to investigate the cracks on two lateral sides of each specimen indicate that crack widths do not govern the design; thus the full load-bearing capacity can be utilised.

The article also introduces the Multi-Wedge (MW) stress field, which disperses the load from the joint to the area within the reinforcement in the confined zone, thereby ensuring a consistent transition to an adjoining unconfined zone. Regarding the strength of the latter, it is proposed to consider the uniaxial concrete compressive strength only within the area of the confining reinforcement. With these two approaches, the load-bearing behaviour of longitudinal joints of tunnel lining segments can be investigated in a mechanically consistent manner while following the entire load path. In addition, the MW stress field is extended to account for the effect of a guiding rod groove. Three different variants are presented, whereas the variant that allows for load dispersion towards the inside (towards the guiding rod groove) results in the highest predicted load-bearing capacity.

The comparison of the experimental data with the MW stress field and three existing design approaches (DW, GPC, and DAUB) for the tests without guiding rod groove reveals that models combining the effect of load dispersion and passive confinement in the confined zone (MW, DW, and GPC) predict the load-bearing capacity similarly and with good accuracy as long as the unconfined zone is considered as well. Otherwise, unconservative predictions can result. The DAUB approach, which does not account for confining reinforcement, is the most conservative. The comparison of the MW stress field variant for guiding rod grooves with the highest load-bearing capacity prediction with the experimental results shows that the model is promising. However, having only one test to compare with is not sufficient to successfully validate it, and further tests are thus required.

In conclusion, (i) the presented experimental campaign confirms that substantial confining reinforcement can be activated thereby being a viable option to increase the axial force resistance of the longitudinal joints of tunnel lining segments and (ii) the MW stress field is the only design approach that can explain the force flow in a mechanically consistent manner. It shows good agreement with the experimental data, which successfully validates the model.

Acknowledgements

The authors gratefully acknowledge the support by: The Swiss Federal Roads Office and the Swiss Federal Office of Transport for partially funding this work (Project AGT 2019/001). Robert Widmann for his support at testing at Empa testing hall. The staff of the Empa testing hall for their support during the conduction of the experiments. Marti Tunnel AG for their contribution to the specimen production. Dr. Clemens Proksch-Weilguni and Marion Decker from TU Wien for discussing and exchanging ideas about experimental campaigns.

Appendix 5.A Definition of confinement properties

$$\sigma_{confy} = \frac{F_y}{\max\left(s_{x,}\frac{s_x + 2\cdot s_{x1}}{2}\right)\cdot s_{z,avg}} = \frac{\pi\cdot \varnothing_s^2\cdot f_{sy}}{4\cdot\max\left(s_{x,}\frac{s_x + 2\cdot s_{x1}}{2}\right)\cdot s_{z,avg}} \tag{5.A.1}$$

$$b_{ccy} = b_{csy} - 2\cdot e_y - \frac{\sqrt{s_x^2 + s_{z,\max}^2}}{2} \tag{5.A.2}$$

$$\sigma_{confz} = \frac{F_z}{\max\left(s_{x,}\frac{s_x + 2\cdot s_{x1}}{2}\right)\cdot s_{y,avg}} = \frac{\pi\cdot \varnothing_s^2\cdot f_{sy}}{4\cdot\max\left(s_{x,}\frac{s_x + 2\cdot s_{x1}}{2}\right)\cdot s_{y,avg}} \tag{5.A.3}$$

$$b_{ccz} = b_{csz} - 2\cdot\left(\frac{s_{x1}}{s_x}\right)^2\cdot\left(\sqrt{s_x^2 + s_{y,\max}^2} - s_{y,\max}\right) - \frac{s_{y,\max}}{2} \tag{5.A.4}$$

$$\text{with } s_{x1} \geq \frac{s_x}{2}$$

The confinement properties were determined with Eqs. (5.A.1)-(5.A.4). These equations are further elaborated in Morger et al. [10] and are based on the confinement model presented in Morger et al. [16]. For confining reinforcement consisting of welded grids, as applied in the experimental campaign and

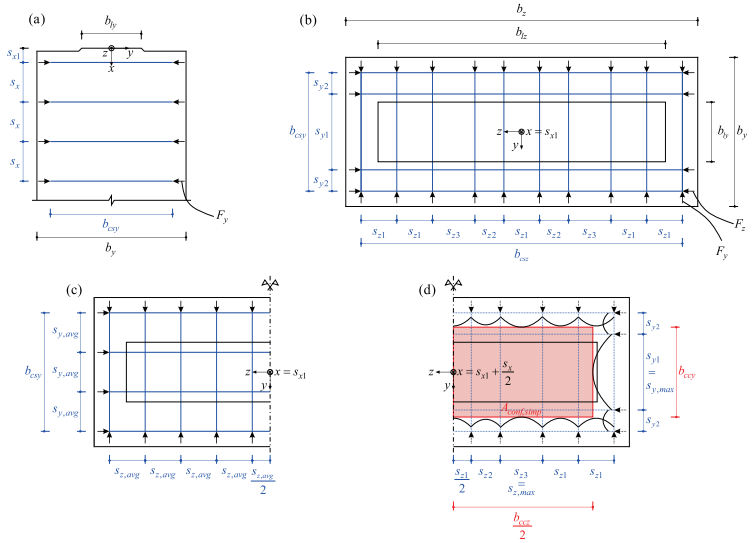

Fig. 5.A.1 - Definition of reinforcement spacings to determine the confinement properties: (a) vertical section, (b) horizontal section at the level of the confining reinforcement, (c) assumed average reinforcement spacings to compute confining stresses, and (d) confined concrete area determined based on maximum spacings in the respective directions. Adapted from Morger et al. [10].

presented in Section 5.2.1, it is assumed that the yield stress f_{sy} can be activated and that the confining forces F_y and F_z, respectively are introduced to the concrete at the outer welded cross joint as proposed in Morger and Kaufmann [15] based on fibre optical measurements of welded grids. Fig. 5.A.1 shows the definition of the input parameters depending on the reinforcement spacing.

Appendix 5.B Mechanical properties of concretes and reinforcing steels

5.B.1 Concrete

Table 5.B.1 compiles the information of the concrete cores sampled from the specimens. The cores were taken from the less damaged half specimen in transverse or longitudinal direction on the opposite side of the longitudinal joint. The $f_{c0,i}$ values were determined by multiplying the measured strength of the cores ($f_{c,core,i}$) by the core length factor *CLF* according to SN EN 13791:2019 [25]; their mean determines the cylinder compressive strength f_{c0} with standard deviation (s) and coefficient of variation (COV). No further reduction factors were applied.

Table 5.B.1 - Mechanical properties of the concretes used.

Batch	Investigated specimen	Age	$\rho_{c,core,i}$	$f_{c,core,i}$	$d_{core,i}$	$h_{core,i}$	*CLF*	$f_{c0,i}$	f_{c0}	$s(f_{c0})$	COV(f_{c0})
		[days]	[kg/m³]	[MPa]	[mm]	[mm]	[-]	[MPa]	[MPa]	[MPa]	[-]
B1	TLJ-40g-WG2p-B1	143	2374	59.1	80.3	79.8	0.82	48.3	46.0	2.5	5%
			2353	56.9	80.3	79.9		46.5			
			2358	53.0	80.3	79.9		43.3			
B2	TLJ-40-WG2p-B2	121	2347	51.8	80.0	80.0		42.4	42.1	2.7	6%
			2287	48.0	79.9	80.0		39.3			
			2360	54.5	80.0	80.0		44.6			
B3	TLJ-60-WG1p-B3	107	2374	59.3	80.2	79.6		48.4	46.9	3.2	7%
			2338	59.9	80.2	80.0		49.0			
			2336	52.8	80.2	80.3		43.2			
B4	TLJ-40-WG2f-B4	178	2413	68.5	60.0	60.1		56.1	55.2	2.9	5%
			2423	63.6	60.0	60.0		52.0			
			2432	70.4	60.0	60.1		57.6			
B5	TLJ-60-WG2p-B5	182	2349	59.1	80.3	79.6		48.2	47.9	1.6	3%
			2376	61.5	80.3	79.7		50.2			
			2354	57.6	80.3	79.8		47.0			
	TLJ-40e-WG2p-B5		2352	59.3	80.3	79.6		48.4			
			2360	56.1	80.3	79.7		45.8			

5.B.2 Reinforcing steel

Table 5.B.2 summarises the mean values and the coefficients of variation of the mechanical properties of the reinforcing steel. All reinforcement was of Class B500B. The mechanical properties of the welded grid reinforcement were determined by testing 1.2 m long bars (free length approximately 980 mm, nominal cross-section considered), which were ordered from the same batch as the reinforcement used for the specimens, in tension up to failure. No tests were performed on the assembly bars. To determine the static yield and ultimate stresses $f_{sy,stat}$ and $f_{su,stat}$, the tensile tests were halted twice near the yield

and ultimate stresses, keeping the stroke of the testing machine constant for approximately 2 min. However, only the dynamic values ($f_{sy,dyn}$ and $f_{su,dyn}$) are used for the analysis and comparison of the test data, since they better approximate the effective steel behaviour during the tests [26]. Due to the long duration of the experimental campaign, the reinforcement was tested in two series in order to account for potential material property changes due to strain ageing of the reinforcement. For test TLJ-60-WG2f-B4 the average of the two test series was taken; for the remaining tests, the values of the first series were adopted.

Table 5.B.2 - Mechanical properties of the reinforcing steels used (mean values with coefficient of variation in brackets).

Reinforcement type	Testing time [days after casting]	$Ø_s$ [mm]	$f_{sy,dyn}$ [MPa]	$f_{sy,stat}$ [MPa]	$f_{su,dyn}$ [MPa]	$f_{su,stat}$ [MPa]	E_s [GPa]	ε_{su} [‰]	n_{sample} [-]
Welded grids (WG) cold-worked	146 ± 11	12	472 (1%)	441 (1%)	590 (1%)	543 (1%)	194 (2%)	89 (7%)	5
	300 ± 11	12	484 (2%)	464 (2%)	600 (1%)	559 (1%)	191 (1%)	87 (6%)	4

Appendix 5.C Machine control data

Fig. 5.C.1 displays the raw machine data, plotting the bending moments M_{exp} versus the axial force $N_{x,exp}$ as well as the eccentricity e of the axial force, computed as $M_{exp}/N_{x,exp}$, plotted versus $N_{x,exp}$.

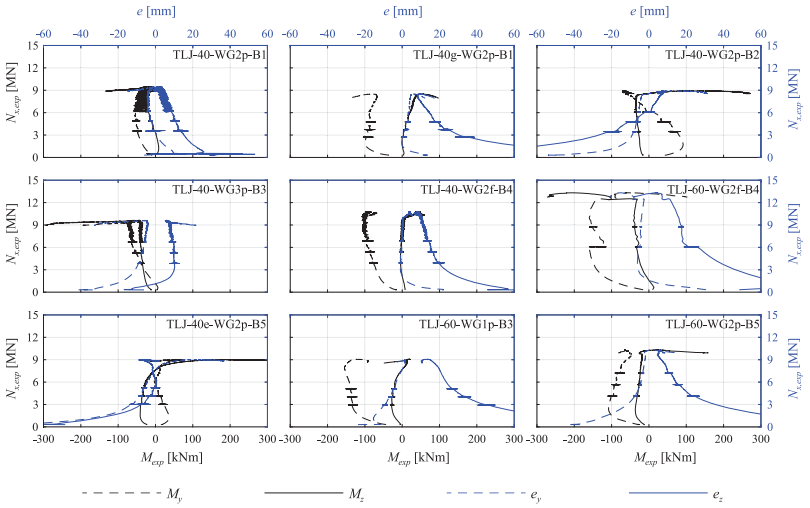

Fig. 5.C.1 - Measured bending moments and calculated load eccentricity at lower load introduction plate.

Appendix 5.D Creep behaviour

Fig. 5.D.1 presents the investigation of the creep behaviour of test TLJ-60-WG2f-B4 at an average stress at the joint of $0.81 \cdot f_{c0}$.

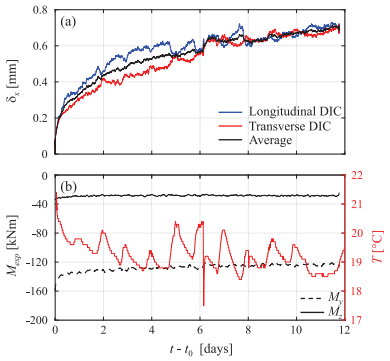

Fig. 5.D.1 - Creep investigation of TLJ-60-WG2f-B4: (a) Creep deformation determined with transverse and longitudinal DIC systems separately and average value and (b) bending moments M_y and M_z, respectively, and temperature T in the construction hall. All values plotted versus time $t–t_0$, with $t_0 = 215$ days.

Appendix 5.E Equations of Multi-Wedge stress field

Eqs. (5.E.1)-(5.E.14) determine the geometry and the stresses of the MW stress field.

$$x_B = x_E \cdot \frac{b_{csy} - b_{ly}}{b_{ccy} + b_{csy} - b_{ly}} \tag{5.E.1}$$

$$\alpha = \arctan\left(\frac{b_{ccy} - b_{ly}}{2 \cdot x_E}\right) \geq 0 \tag{5.E.2}$$

$$\beta = \arctan\left(\frac{b_{ccy}}{2 \cdot (x_E - x_B)}\right) > 0 \tag{5.E.3}$$

$$\gamma = \arctan\left(\frac{b_{ly}}{2 \cdot x_B}\right) > 0 \tag{5.E.4}$$

$$\psi = \arctan\left(\frac{b_{csy} - b_{ccy}}{2 \cdot (x_E - x_B)}\right) > 0 \tag{5.E.5}$$

$$\sigma_{confy} \leq f_{c0} \tag{5.E.6}$$

$$\sigma_{xd,csy} = f_{c0} \tag{5.E.7}$$

$$\sigma_{x0,csy} \leq \begin{cases} f_{c0} \cdot \dfrac{b_{csy} - b_{ccy}}{b_{ly}} \\ \dfrac{f_{c0} \cdot \sigma_{confy} - f_{c0}^2}{\dfrac{\sigma_{confy}}{2} \cdot \left(1 + \cos\left(2 \cdot \beta\right)\right) - f_{c0}} \cdot \dfrac{\cos\left(\beta\right) \cdot \sin\left(\beta + \gamma\right)}{\sin\left(\gamma\right)} \end{cases} \tag{5.E.8}$$

$$\sigma_{\alpha} = \sigma_{x0,ccy} \cdot \frac{\sin\left(\gamma\right)}{\cos\left(\alpha\right) \cdot \sin\left(\alpha + \gamma\right)} \tag{5.E.9}$$

$$\sigma_{\beta} = \sigma_{x0,csy} \cdot \frac{\sin\left(\gamma\right)}{\cos\left(\beta\right) \cdot \sin\left(\beta + \gamma\right)} \tag{5.E.10}$$

$$\sigma_{y} = \tan\left(\gamma\right) \cdot \left(\sigma_{x0,ccy} \cdot \tan\left(\alpha\right) + \sigma_{x0,csy} \cdot \tan\left(\beta\right)\right) + \sigma_{confy} \tag{5.E.11}$$

$$\sigma_{confy,red} = \sigma_{confy} - \frac{\sigma_{x0,csy} \cdot b_{ly}}{b_{csy} - b_{ccy}} \cdot \tan\left(\beta\right) \cdot \tan\left(\psi\right) \tag{5.E.12}$$

$$k_s = \frac{\sigma_{\alpha} \cdot \sin\left(\beta - \alpha\right) \cdot \sin\left(\alpha\right)}{\cos\left(\beta\right) \cdot \sigma_{confy,red}} \tag{5.E.13}$$

$$\sigma_{xd,ccy} = \sigma_{x0,ccy} \cdot \frac{b_{ly}}{b_{ccy}} \tag{5.E.14}$$

Appendix 5.F Equations of Dual-Wedge stress field in longitudinal *z*-direction

With Eqs. (5.F.1)-(5.F.4) the load-bearing capacity $\sigma_{x0,csz}$ of the loaded area outside the confined length b_{ccz}, accounting for longitudinal load dispersion, can be determined while Eqs. (5.F.5)-(5.F.9) allow to determine the geometry of the stress field and the occurring stresses. The equations are based on the simplest variant of the DW stress field [24].

$$d_1 = b_{lz} - b_{ccz} \tag{5.F.1}$$

$$d_2 = b_{csz} - b_{ccz} \tag{5.F.2}$$

$$\alpha = \arcsin\left(\sqrt{\frac{\sigma_{sz}}{f_{c0}} \cdot \frac{f_{c0} \cdot \left(1 - \dfrac{d_1}{d_2}\right) + \dfrac{\sigma_{sz}}{2} \cdot \left(\dfrac{d_2}{d_1} + 3\right) - \Delta}{f_{c0} \cdot \dfrac{d_1}{d_2} - 3 \cdot \sigma_{sz}}}\right) \geq \arctan\left(\frac{d_2 - d_1}{2 \cdot x_{E,\max}}\right) \tag{5.F.3}$$

$$\text{with } \Delta^2 = \frac{\sigma_{sz}^2}{4} \cdot \left(\frac{d_2}{d_1} + 3\right) + 4 \cdot f_{c0} \cdot \sigma_{sz} \cdot \left(\frac{d_2}{d_1} - 1\right)$$

$$\sigma_{x0,csz} = \frac{d_2}{d_1} \cdot \frac{\sigma_{sz} \cdot f_{c0} \cdot \cos\left(\alpha\right)^2}{\sigma_{sz} + f_{c0} \cdot \sin\left(\alpha\right)^2} \tag{5.F.4}$$

$$\sigma_{xd,csz} = \sigma_{x0,csz} \cdot \frac{d_1}{d_2} \tag{5.F.5}$$

$$\sigma_{confz,add} = \frac{\sigma_{sz} \cdot f_{c0} \cdot \sin(\alpha)^2}{\sigma_{sz} - \frac{d_1}{d_2} \cdot \left(\sigma_{sz} + f_{c0} \cdot \sin(\alpha)^2\right)} \tag{5.F.6}$$

$$x_E = \frac{d_2 - d_1}{2 \cdot \tan(\alpha)} \tag{5.F.7}$$

$$\gamma = \arctan\left(\frac{f_{c0} \cdot \sin(\alpha) \cdot \cos(\alpha)}{\sigma_{x0,csz} - f_{c0} \cdot \cos(\alpha)^2}\right) \tag{5.F.8}$$

$$x_B = \frac{d_1}{\tan(\gamma)} \tag{5.F.9}$$

Appendix 5.G Test parameters and results of calculation with different model approaches

5.G.1 Test specimens without guiding rod groove

Table 5.G.1 summarises the parameters of the different models and the comparison with the experimental data.

5.G.2 Test specimen with guiding rod groove

Table 5.G.2 summarises the parameters of the different models and the comparison with the experimental data.

$$q_{x,u,rod,DAUB} = \sqrt{\frac{\left(2 \cdot b_y - b_{ly} - b_{rod}\right) \cdot b_z}{\left(b_{ly} - b_{rod}\right) \cdot b_{lz}}} \cdot f_{c0} \tag{5.G.1}$$

Table 5.G.1 - Parameters of different model approaches and comparison with experimental data of specimens without guiding rod groove.

Specimen	MW,DW,GPC			MW					DW				GPC	DAUB	$q_{x,u,exp}/q_{x,u,model}$				$q_{x,u,MW}/q_{x,u,DAUB}$
	b_{ccy}	b_{ccz}	$q_{x,u,unconf}$	σ_{x0}	$\sigma_{x0,csz}$(2)	$\sigma_{xd,cc}$	x_E	$q_{x,u,conf}$	σ_{x0}	σ_{xd}	x_E	$q_{x,u,conf}$	$q_{x,u,conf}$	$q_{x,u}$	MW	DW	GPC	DAUB	
	[mm]	[mm]	[MPa]	[MPa]	[MPa]	[MPa]	[mm]	[MPa]	[MPa]	[MPa]	[mm]	[MPa]	[MPa]	[MPa]	[-]	[-]	[-]	[-]	[-]
TLJ-40-WG2p-B1 (I/II)(1)	222.3	580.0	95.3	96.6	53.5	49.3	410	92.0	100.5	63.3	354	94.6	94.3	78.1	1.12	1.09	1.09	1.32	1.18
TLJ-40-WG2p-B2 (I/II)(1)	222.3	580.0	87.2	91.9	49.2	47.4	410	87.3	95.6	60.2	354	89.8	88.7	71.5	1.12	1.12	1.12	1.37	1.22
TLJ-40-WG3p-B3 (II)(1)	232.2	579.9	97.1	113.9	54.7	59.4	365	107.5	120.6(4)	72.7(4)	362(4)	112.7(4)	97.4	79.7	1.09	1.09	1.09	1.33	1.22
TLJ-40-WG2f-B4 (I)(1)	222.3	580.0	154.2(3)	111.4	63.7	56.4	509	106.3	112.0	70.5	354	105.9	107.5	93.8	1.12	1.12	1.10	1.27	1.13
TLJ-60-WG2f-B4 (I)(1)	222.3	580.0	103.1(3)	94.2	63.7	75.2	820	91.0	92.8	87.7	432	88.8	91.8	76.5	1.07	1.10	1.06	1.27	1.19
TLJ-40e-WG2p-B5 (I)(1)	202.3	580.0	107.4	104.4	55.6	48.8	410	99.2	105.7	62.7	313	99.4	99.8	85.3	1.17	1.16	1.16	1.36	1.16
TLJ-60-WG1p-B3 (I)(1)	201.2	574.9	64.8	63.5	53.6	50.5	405	62.3	62.3(5)	62.3(5)	-(5)	62.3(5)	69.7	65.0	1.06	1.06	1.02	1.02	0.96
TLJ-60-WG2p-B5 (II)(1)	222.3	580.0	66.1	84.1	55.6	67.5	410	81.1	84.7	80.0	410	80.8	82.8	66.4	1.14	1.14	1.14	1.14	1.00
(1): Identified failure zone in test specimens: I: Confined zone, II: Unconfined zone, III: Local zone at the joint.														Mean	1.11	1.11	1.10	1.26	
(2): Computed with $\sigma_{xz} = \sigma_{conf,z}/5$.																			
(3): Resistance of confined section after load dispersion ($q_{x,u,conf,x>xE}$, Eq.(5.4)).																			
(4): Longitudinal direction governing. $\sigma_{conf,b}$ reduced from 12.3 MPa to 12.0 MPa.														COV [%]	3.16	2.90	3.94	9.63	
(5): No load dispersion possible since $b_{fy} > b_{ccy}$.																			

Table 5.G.2 - Parameters of different model approaches and comparison with experimental data of specimen with guiding rod groove.

Specimen TLJ-40g-WG2p-B1	b_{rod}	b_o	b_l	b_{ccy}	b_{ccz}	$\sigma_{x0,ccy}$	$\sigma_{x0,csy}$	$\sigma_{x0,MW}$	$\sigma_{x0,ccy,i}$	$\sigma_{xd,csy}$	$\sigma_{xd,ccy}$	$\sigma_{xd,csy,i}$	R_y	x_E	$\sigma_{x0,csz}$	$q_{x,u,conf}$	$q_{x,u,unconf}$	$q_{x,u,exp}/q_{x,u,model}$
	[mm]	[mm]	[mm]	[mm]	[mm]	[MPa]	[MPa]	[MPa]	[MPa]	[MPa]	[MPa]	[MPa]	[N/mm]	[mm]	[MPa]	[MPa]	[MPa]	[-]
Variant A	40	-	-	222.3	580.0	78.3	18.3	96.6	-	46.0	49.3	-	-	410	53.5	92.0	133.4	1.42
Variant B	40	100	0	222.3	580.0	81.3	25.6	106.9	-	46.0	44.6	-	-	363	53.5	101.2	133.4	1.29
Variant C	40	70.0	30.0	222.3	580.0	78.3	36.6	114.9	114.8	46.0	36.0	49.2	267(1)	271	53.5	108.3	133.4	1.21
DAUB	$q_{x,u}$ = 112.7 MPa																	1.16
(1): R_y/f_{c0} = 5.8 mm << x_E = 271 mm → stress field is applicable.																		

Notation

Latin letters

$A_{cs} = b_{csy} \cdot b_{csz}$	Concrete area inside the confining reinforcement
b_{ccy}, b_{ccz}	Confined concrete width and length
$b_{csy} = b_y - 2 \cdot c_{nom} - Ø_{conf}$ $b_{csz} = b_z - 2 \cdot c_{nom} - Ø_{conf}$	Maximum width and length of confining reinforcement (dimension between centre lines)
b_i, b_o	Part of the loaded width with guiding rod groove transferring load towards the inside or outside, respectively
b_{ly}, b_{lz}	Width and length of loaded area
b_{rod}	Width of guiding rod groove
b_y, b_z	Width and length of concrete block
CLF	Core length factor
c_{nom}	Concrete cover
d_1	Width of loaded area in Dual-Wedge stress field
d_2	Width available for load dispersion in Dual-Wedge stress field
d_{core}	Diameter of cored concrete sample
D_{max}	Maximum aggregate size
E_s	Modulus of elasticity of reinforcing steel
e_y, e_z	Eccentricity of loaded area in lateral y or z-direction
f_{c0}	Uniaxial concrete cylinder compressive strength
f_{sy}	Yield stress of reinforcing steel
$f_{sy,dyn}, f_{su,dyn}$	Dynamic yield and ultimate stress of reinforcing steel
$f_{sy,stat}, f_{su,stat}$	Static yield and ultimate stress of reinforcing steel
h	Half specimen height (in x-direction)
h_{core}	Height of cored concrete sample
h_{joint}	Joint height (half of shoulder distance)
$k_s \in [0,1]$	Parameter indicating the part of σ_{confy} resp. $\sigma_{confy,red}$ available to equilibrate the bursting stresses for Dual-Wedge or Multi-Wedge stress field
M_y, M_z	Moment around y or z-axis at lower load introduction plate
n_{sample}	Sample size
$N_{x,u}$	Peak axial force
q_x	Average axial stress across the joint contact area respectively the loaded area
$q_{x,u}$	Average axial stress across the joint contact area respectively the loaded area at peak load
$q_{x,u,conf}$	Load-bearing capacity of confined zone (referred to stress at the joint contact area respectively the loaded area)
$q_{x,u,unconf}$	Load-bearing capacity of unconfined zone (referred to stress at the joint contact area respectively the loaded area)
R_y	Concentrated transverse compressive force
s_x, s_y, s_z	Spacing of confining reinforcement in respective directions
s_{x1}	Distance in x-direction between load introduction and first reinforcement layer

$s_{y,avg}, s_{z,avg}$	Average confining reinforcement spacing in lateral *y*- and *z*-direction
$s_{y,max}, s_{z,max}$	Maximum confining reinforcement spacing in lateral *y*- and *z*-direction
T	Temperature
t	Time
t_0	Time of specimen casting
$w_{r,max}$	Maximum crack width
x	Loading direction (axial, vertical)
x_B	Height of top wedge of Multi-Wedge or Dual-Wedge stress field
x_E	Height of Multi-Wedge or Dual-Wedge stress field
$x_{E,max}$	Confined height of half specimen
y	Lateral transverse direction
z	Lateral longitudinal direction

Greek letters

α	Inclination angle of diagonal compressive strut of Multi-Wedge and Dual-Wedge stress field
α_i	Inclination angle of diagonal compressive strut towards inside of guiding rod groove
α_y, α_z	Inclination angle of lower load introduction plate around *y* or *z*-axis
β	Inclination angle of trapezoidal compressive strut of Multi-Wedge stress field
γ	Inclination angle of top wedge of Multi-Wedge and Dual-Wedge stress field
δ_x	Compression in axial *x*-direction
$\delta_{x,joint}$	Closing of joint in axial *x*-direction
ε_{su}	Ultimate strain of reinforcing steel
η_{cc}	Strength reduction factor to account for higher-strength concrete brittleness
$\sigma(U,V)$	Standard deviation of displacements in lateral and vertical direction
σ_1, σ_3	Maximum and minimum principal stresses (defined positive in compression)
σ_α	Compressive stress in diagonal strut with inclination α of Multi-Wedge and Dual-Wedge stress field
σ_β	Compressive stress in trapezoidal strut with inclination β of Multi-Wedge stress field
σ_{conf}	Confining stress provided by reinforcement
$\sigma_{confy}, \sigma_{confz}$	Confining stress in the transverse and longitudinal direction
$\sigma_{confy,red}$	Reduced transverse confining stress
$\sigma_{confz,add}$	Additional longitudinal confining stress
σ_{sz}	Bursting stress in longitudinal direction
σ_{x0}	Axial stress across the joint contact area respectively the loaded area
$\sigma_{x0,ccy}, \sigma_{x0,csy}$	Axial stress across the joint width respectively loaded width for load dispersion within b_{ccy} or $b_{csy} - b_{ccy}$ determined with Multi-Wedge stress field
$\sigma_{x0,ccy,i}$	Axial stress across b_i for load dispersion within $b_i + b_{rod}$ towards the inside of guiding rod groove
$\sigma_{x0,csz}$	Axial stress across the joint contact area respectively the loaded area outside b_{ccz} for load dispersion within $b_{csz} - b_{ccz}$

σ_{xd}	Axial stress after load dispersion within b_{ccy} determined with Dual-Wedge stress field
$\sigma_{xd,ccy}, \sigma_{xd,csy} = f_{c0}$	Axial stress after load dispersion within b_{ccy} or $b_{csy} - b_{ccy}$ determined with Multi-Wedge stress field
$\sigma_{xd,ccy,i}$	Axial stress after load dispersion within $b_i + b_{rod}$ determined with Multi-Wedge extension for guiding rod groove (Variant C)
σ_y	Transverse principal confining stress determined with Multi-Wedge or Dual-Wedge stress field
$\sigma_{y,i}$	Transverse principal confining stress determined with Multi-Wedge extension for guiding rod groove (Variant C)
$\rho_{c,core}$	Density of cored concrete sample
ω_y, ω_z	Transverse and longitudinal mechanical reinforcement ratio

Special characters

$Ø_s$	Diameter of reinforcing steel

References

[1] Brenner Basistunnel BBT SE, 'Brenner Basistunnel Ausschreibungsplanung', Technical Report, 2018.

[2] G. Lombardi, M. Neuenschwander, and A. Panciera, 'Gibraltar Tunnel Project update – the geomechanical challenges', *Geomechanics and Tunnelling*, vol. 2, no. 5, pp. 578–590, 2009, doi: 10.1002/geot.200900046.

[3] G. Anagnostou, 'Some critical aspects of subaqueous tunneling', presented at the World Tunnel Congress, ITA Secretariat c/o EPFL, 2014.

[4] F. Mezger, M. Ramoni, G. Anagnostou, A. Dimitrakopoulos, and N. Meystre, 'Evaluation of higher capacity segmental lining systems when tunnelling in squeezing rock', *Tunnelling and Underground Space Technology*, vol. 65, pp. 200–214, May 2017, doi: 10.1016/j.tust.2017.02.012.

[5] SIA, *SN EN 206:2013+A2:2021: Concrete - Specification, performance, production and conformity*, Zurich, Switzerland, 2022.

[6] EN 1992-1-1:2023, 'Eurocode 2 - Design of concrete structures - Part 1-1: General rules and rules for buildings, bridges and civil engineering structures', Brussels, 2023.

[7] International Federation for Structural Concrete (fib), *Model Code for Concrete Structures 2020*, Lausanne, 2024.

[8] EN 1992-1-2:2023, 'Eurocode 2: Design of concrete structures - Part 1-2: Structural fire design', Brussels, 2023.

[9] SIA, *Swisscode SIA 262: Concrete Structures*, Zurich, Switzerland, 2013.

[10] F. Morger, A. Kenel, and W. Kaufmann, 'Strip loading in reinforced concrete: Mechanical modeling and experimental validation', *Structural Concrete*, vol. 27, pp. 163–192, 2026, doi: 10.1002/suco.70154.

[11] T. Markić, F. Morger, and W. Kaufmann, 'Partially loaded areas in reinforced concrete: experimental campaign and model validation', *Engineering Structures*, vol. 273, p. 114905, Dec. 2022, doi: 10.1016/j.engstruct.2022.114905.

[12] C. Proksch-Weilguni, M. Decker, and J. Kollegger, 'Load distribution and passive confinement in reinforced concrete: Development of a mechanical model', *Engineering Structures*, vol. 304, p. 117562, Apr. 2024, doi: 10.1016/j.engstruct.2024.117562.

[13] German Tunnelling Committee (ITA-AITES), *Empfehlungen für den Entwurf, die Herstellung und den Einbau von Tübbingringen*, Deutscher Ausschuss für unterirdisches Bauen e. V. (DAUB), 2024.

[14] ISO 17660-1:2006, *Welding - Welding of reinforcing steel - Part 1: Load-bearing welded joints*, Geneva, 2006.

[15] F. Morger and W. Kaufmann, 'Experimental investigation of welded reinforcement grids for partial area loading', in *Proceedings of the 15th fib PhD Symposium in Civil Engineering*, Fédération Internationale du Béton (fib), 2024. doi: https://doi.org/10.3929/ethz-b-000711139.

[16] F. Morger, A. Kenel, and W. Kaufmann, 'Passive confinement of reinforced concrete members revisited', *Structural Concrete*, vol. 25, no. 6, pp. 4283–4299, 2024, doi: 10.1002/suco.202400209.

[17] Correlated Solutions Inc., 'Vic-3D software manual', Correlated Solutions, Irmo, 2019.

[18] N. Gehri, J. Mata-Falcón, and W. Kaufmann, 'Automated crack detection and measurement based on digital image correlation', *Construction and Building Materials*, vol. 256, p. 119383, 2020, doi: 10.1016/j.conbuildmat.2020.119383.

[19] N. Gehri, J. Mata-Falcón, and W. Kaufmann, 'Refined extraction of crack characteristics in Large-scale concrete experiments based on digital image correlation', *Engineering Structures*, vol. 251, p. 113486, 2022, doi: 10.1016/j.engstruct.2021.113486.

[20] J. Mata-Falcón, S. Häfliger, M. Lee, T. Galkovski, and N. Gehri, 'Combined application of distributed fibre optical and digital image correlation measurements to structural concrete experiments', *Engineering Structures*, vol. 225, p. 111309, 2020, doi: 10.1016/j.engstruct.2020.111309.

[21] F. E. Richart, A. Brandtzaeg, and R. L. Brown, 'A Study of the Failure of Concrete under Combined Compressive Stresses', University of Illinois Engineering Experimental Station, Bulletin 185, 1928.
[22] B. D. Scott, 'Stress - Strain relationship for confined concrete: Rectangular sections', University of Canterbury, Christchurch, New Zealand, 1980.
[23] ACI Committee 533, *Guide for Precast Concrete Tunnel Segments (ACI 533.5R-20)*. Farmington Hills, MI: American Concrete Institute, 2020.
[24] T. Markić, F. Morger, and W. Kaufmann, 'Partially loaded areas in reinforced concrete: Mechanical modelling', *Engineering Structures*, vol. 271, p. 114938, Nov. 2022, doi: 10.1016/j.engstruct.2022.114938.
[25] SIA, *SN EN 13791:2019: Assessment of in-situ compressive strength in structures and precast concrete components*, Zurich, 2021.
[26] S. Häfliger, S. Fomasi, and W. Kaufmann, 'Influence of quasi-static strain rate on the stress-strain characteristics of modern reinforcing bars', *Construction and Building Materials*, vol. 287, p. 7, 2021, doi: 10.1016/j.conbuildmat.2021.122967.

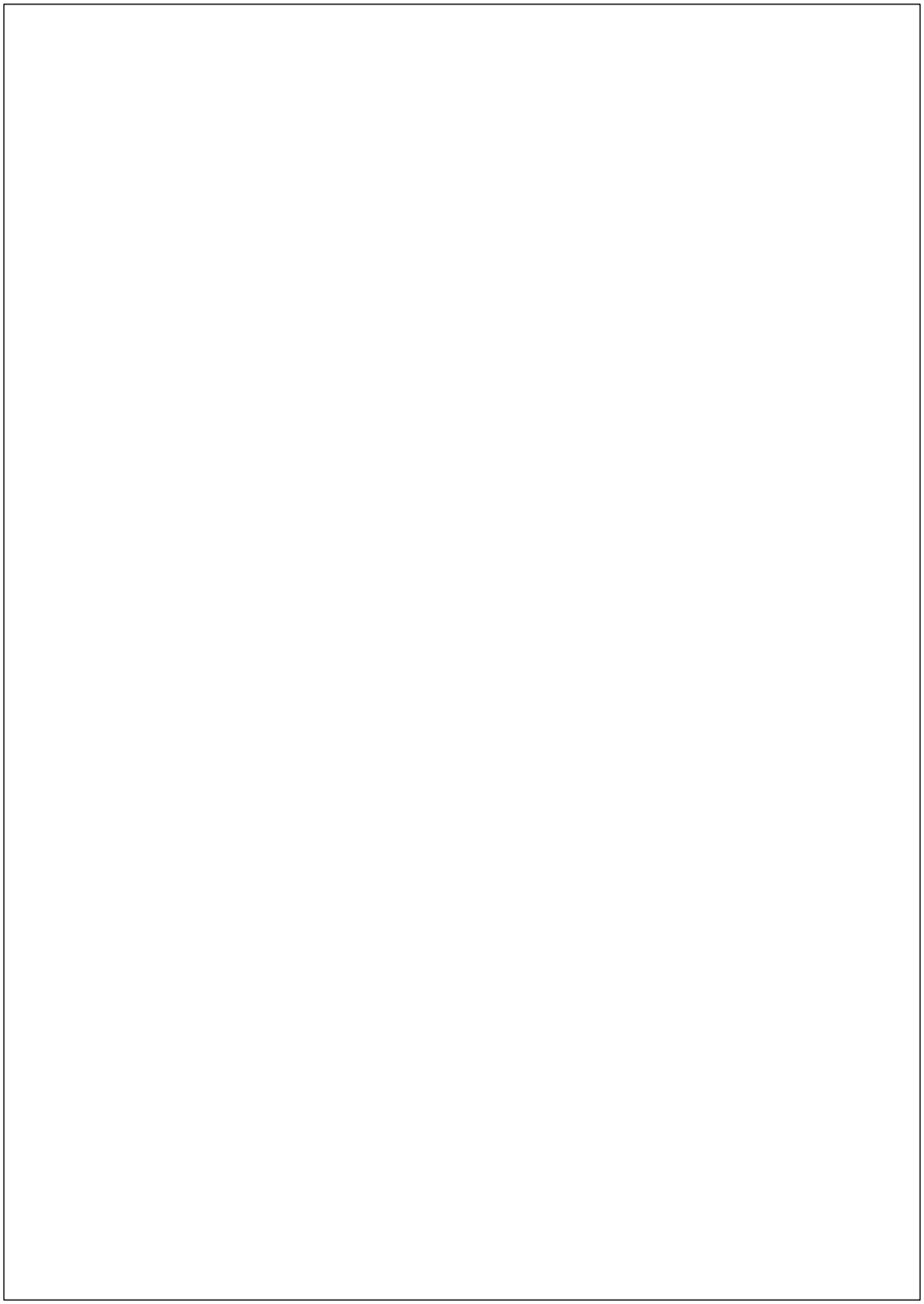

Part 3

Strip loading in steel fibre reinforced concrete

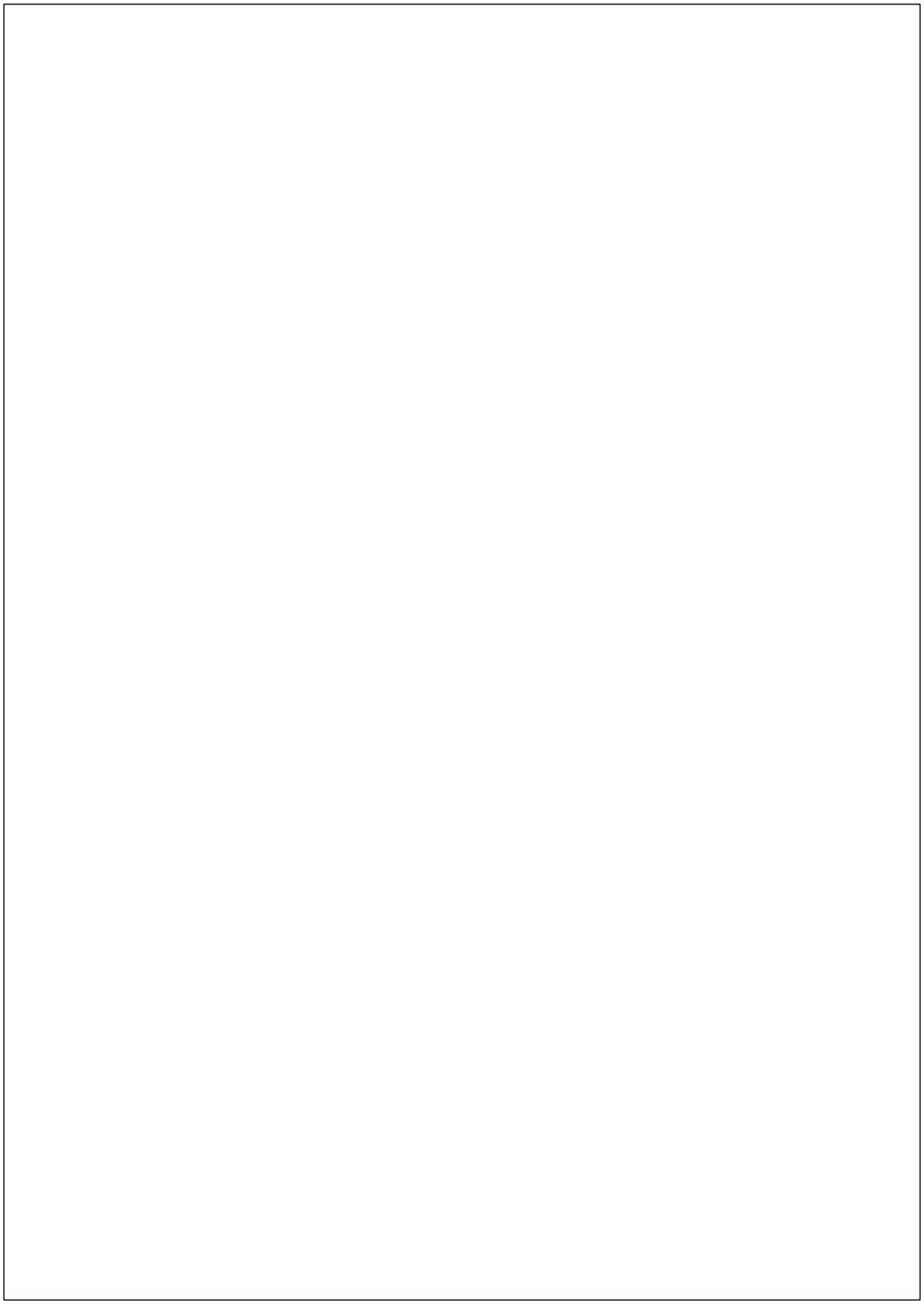

6 Experimental and theoretical investigation of strip-loaded SFRC

The content of this chapter corresponds to the postprint of the following published article:

> **F. Morger**, A. Kenel, W. Kaufmann, 'Strip loading in steel fibre reinforced concrete: Experimental and theoretical investigation', *Structural Concrete*, 2025, doi: 10.1002/suco.70339.

This postprint includes some adjustments to the published version. For details see Section 1.5.

As the lead author, Fabian Morger planned, prepared and carried out the experiments, analysed and post-processed the obtained data, extended the stress fields for the application in steel fibre reinforced concrete, compared the model predictions with the experimental data, and wrote the entire draft of the manuscript. The last two authors both supervised the conducted research by giving constant and valuable inputs. The second author, Albin Kenel, was involved in the validation of the models. The third author, Walter Kaufmann, initially designed the experimental campaign, and carefully reviewed the manuscript.

Abstract

Fibre reinforced concrete is becoming increasingly popular in engineering practice due to its high robustness, post-cracking behaviour and crack control. For strip loading, as common, for example, in longitudinal joints of tunnel lining segments, the use of fibre reinforced concrete has the potential to reduce conventional reinforcement. However, no existing design approaches combine the effects of load dispersion, confining reinforcement and fibre reinforcement, and experimental data is scarce. This article presents eleven tests on strip-loaded steel fibre reinforced concrete specimens. Four of the specimens were made of purely steel fibre reinforced concrete, while the remaining seven were hybrid-reinforced specimens containing additional confining bar reinforcement. The cracks on the specimen surfaces were measured with digital image correlation systems. Design approaches are proposed for both reinforcement cases. The results demonstrate that steel fibre reinforcement is able to enhance the load-bearing capacity of strip-loaded reinforced concrete and minimise crack widths. For hybrid-reinforced specimens, steel fibres are particularly effective when combined with low conventional reinforcement ratios and are thus a viable option to reduce conventional reinforcement. The proposed modelling approach, combining load dispersion, confining reinforcement and steel fibre reinforced concrete, is mechanically sound and shows good agreement with the experimental data, and is thus proposed for design. The purely steel fibre reinforced specimens sustained loads that exceeded those at which initial surface cracks occurred. However, their application requires further investigation, particularly regarding the consideration of the associated brittle failure mechanism.

Keywords: Steel fibre reinforced concrete; Strip loading; Experimental campaign; Load-bearing capacity; Longitudinal joints; Confinement; Stress field.

6.1 Introduction

Strip loading is a common problem in engineering practice. Typical examples in structural concrete are longitudinal joints of tunnel lining segments, one-way concrete hinges and narrow bridge bearings on abutment walls. The load-bearing capacity of strip-loaded reinforced concrete (RC) members was limited by empirical formulae [1] until recently. Over the past few years, however, the load-bearing behaviour of strip-loaded reinforced concrete has been revisited and intensively studied theoretically as well as experimentally [2]-[5], establishing mechanically sound models explaining why the applied load can be several times higher than the uniaxial concrete compressive strength f_{c0}. The strength increase of the concrete can be attributed to lateral confining stresses resulting from load dispersion (geometrical confinement) and reinforcement (passive confinement), causing a triaxial compressive stress state at the load introduction. The bursting stresses resulting from load dispersion need to be equilibrated by reinforcement, justifying this aspect of the formerly used design approaches. For a more detailed discussion of the underlying phenomena and previous works, see, for example, Markić et al. [2], [6] and Morger et al. [3].

Especially for tunnel lining segments with a high degree of repetition, an efficient design can greatly impact costs and material consumption. Fibre reinforced concrete (FRC) becomes more popular in tunnelling as an alternative option to conventional reinforcement due to its robustness, improved post-cracking behaviour and crack control [7] that, for example, facilitates handling in the construction phase and provides advantages regarding watertightness. As the strength of the longitudinal joints often governs the lining thickness, it is the aim to incorporate FRC into their design. FRC has two possible applications for designing tunnel lining segments: (i) purely fibre-reinforced segments, and (ii) hybrid-reinforced segments, which combine fibres with conventional bar reinforcement. For the former, extensive experimental investigations have been conducted [8]-[11] resulting in empirical and semi-empirical design approaches [11], [12]. For the latter, experimental investigations combining the effects of fibre reinforcement with confining bar reinforcement under wide strip loading (as is typical for longitudinal joints in lining segments) are scarce, and no specific design approaches are known. Aoude [13] investigated the effect of confining bar reinforcement in steel fibre reinforced concrete (SFRC) for columns, observing an increase in the compressive strength compared to RC columns, which he described by superimposing the confining stresses provided by the reinforcement with a contribution of the residual tensile strength provided by the SFRC. On the other hand, for SFRC without additional reinforcement, current codes assume that the concrete compressive strength is not affected by the presence of the steel fibres [14]. Furthermore, Markić et al. [4] showed that for very narrow loaded strips, as common in one-way concrete hinges, the load-bearing capacity of confined RC specimens can be increased by adding steel fibres. Note that while in concrete hinges the effect of load dispersion dominates over that of passive confinement, the latter is more relevant in tunnel lining segments due to the commonly much larger loaded width.

Seven experiments were conducted to address the knowledge gap related to the load-bearing behaviour of strip-loaded SFRC specimens with pronounced confining reinforcement (hybrid-reinforced specimens) and relatively wide loaded areas. Additionally, four tests on SFRC specimens without additional reinforcement were carried out. These tests were part of two broader experimental campaigns including RC specimens without fibres (see [3], [15]). The results of the SFRC specimens can thus be compared

to those of otherwise similar RC specimens to highlight the effect of the additional steel fibres. Furthermore, modelling approaches for the design of strip-loaded SFRC with and without additional reinforcement are presented.

This article presents the strip-loaded SFRC specimens (Section 6.2), followed by the discussion of the results, including the comparison with the tests on RC specimens (Section 6.3). The modelling approaches are presented and compared to the experimental data in Section 6.4. The article concludes with a summary of the main findings and design recommendations for engineering practice (Section 6.5).

6.2 Experimental campaign

This section presents eleven tests on SFRC specimens, with and without additional conventional confining reinforcement, subjected to strip loading. The tests presented here were part of two broader experimental campaigns on (i) strip-loaded concrete blocks (six SFRC specimens) and (ii) longitudinal joints of segmental tunnel linings (five SFRC specimens), referred to as *block tests* and *joint tests* in the following. The results of the RC specimens have been published previously (see [3] and [15], respectively). The following sections provide a detailed overview of the specimen geometry and production as well as the material properties of the SFRC specimens. For the conventional reinforcement configurations, as well as more detailed information on the test setup and the measurement systems, the reader is referred to Morger et al. [3], [15].

6.2.1 Specimens, casting, and materials

Table 6.1 and Table 6.2 provide an overview of the block and joint tests, respectively. The block test specimens were geometrically identical concrete cuboids with dimensions $b_y \cdot b_z = 350 \cdot 550$ mm^2 in the transverse y- and longitudinal z-directions and $h = 525$ mm in the axial x-direction. Each joint test specimen consisted of two cuboids (half specimens) with $b_y \cdot b_z \cdot h = 350 \cdot 750 \cdot 825$ mm^3 placed on top of each other. Fig. 6.1a and b illustrate the specimen geometries. The block tests were loaded on an area $b_{ly} \cdot b_{lz}$ of $140 \cdot 450$ mm^2 or $210 \cdot 450$ mm^2, respectively. Fig. 6.1c shows the different flat joint geometries used for the joint specimens. The joints measured 7 mm in height, resulting in a total joint gap between the specimens of 14 mm, and 650 mm in length with a width of 140 mm (TLJ-40) or 210 mm (TLJ-60), corresponding to 40% and 60% of the block width b_y.

All specimens were cast in lubricated formwork and compacted on a vibration table (block specimens) or with external vibrators (joint specimens). The specimens were cast upside down with a milled steel plate as bottom formwork. This formwork arrangement ensured a smooth planar surface of the load introduction (block tests) or the joints (joint tests), and even more importantly, allowed the steel fibres to orient perpendicularly to the load application direction in the y-z plane. The casting surface was mechanically ground after hardening to ensure parallel surfaces and avoid unintended eccentricities. While the specimens of the block tests were cast in one batch (designated as SFRC1), three different batches, following the same concrete recipe, were cast for the joint tests (designated as SFRC2, SFRC3, and SFRC4) due to limited formwork availability. The two half specimens of each joint test were always cast in the same batch. All SFRC concrete mixes contained a maximum aggregate size $D_{max} = 16$ mm

and 40 kg/m^3 Dramix 3D 80/30 BGP steel fibres with a length of 30 mm, a diameter of 0.38 mm, and a nominal tensile strength of 3070 MPa. Table 6.1 and Table 6.2 include the concrete compressive strength f_{c0}, determined on standard cylinders or cores sampled after testing; detailed information can be found in Appendices 6.A.1 and 6.A.2. Furthermore, both tables indicate the post-cracking residual fibre tensile strength $\sigma_{f,f}$ for a crack width w of 0.5 or 1.0 mm, respectively, obtained from three-point bending tests on notched SFRC prisms (150·150·550 mm^3) according to EN 14651 [16] and the linear model of *fib* Model Code 2020 [14]. The results of the three-point bending tests and the calculated linear $\sigma_{f,f}$-w relation can be found in Appendix 6.A.3.

Four tests (one block, three joint tests) were conducted on specimens that were reinforced exclusively with steel fibres (designated as FO = fibres only). The specimens of the hybrid-reinforced tests contained additional confining reinforcement consisting of bent ties (BT) or welded grids (WG) with a diameter ($Ø_s$) of 12 mm and a clear concrete cover c_{nom} of 30 mm. For the block tests, the reinforcement was continuously placed in the transverse and longitudinal directions over the full specimen height, whereas for the specimens of the joint tests, only the parts adjacent to the joint (approximately 50% of the total height) were reinforced, dividing each half specimen into a confined and an unconfined zone. The reinforcement layout, the yield stress (f_{sy}), the spacings (s_x, s_y, and s_z) and the height of the confined zone ($x_{E,max}$) are also included in Table 6.1 and Table 6.2, along with the confining stress σ_{conf} provided

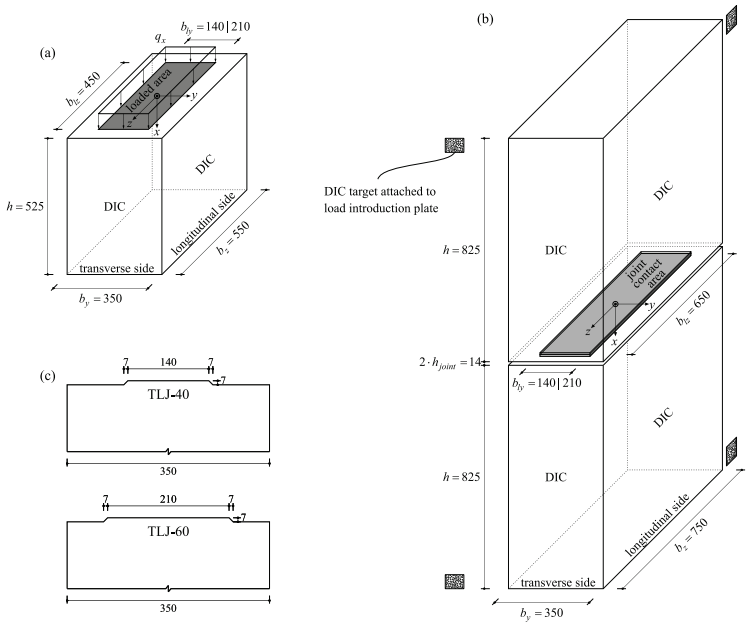

Fig. 6.1 - Geometry of the specimens (dimensions in mm): (a) block specimen, (b) longitudinal joint specimens, and, (c) joint geometry. Adapted from Morger et al. [3], [15].

Table 6.1 - Overview of SFRC block tests.

Specimen	Age at testing	b_{ly}	f_{c0}	Reinf. layout	f_{sy}	s_x	$s_{z,avg} = s_{z,max}$	$s_{y,avg}$	$s_{y,max}$	$x_{E,max}$	σ_{confy}	σ_{confz}	$\sigma_{t,f}$	$\widetilde{\omega}_{y,hyb}$	$\widetilde{\omega}_{z,hyb}$	$N_{x,u,exp}$	$q_{x,u,exp}/f_{c0}$
	[days]	[mm]	[MPa]	[-]	[MPa]	[mm]	[mm]	[mm]	[mm]	[mm]	[MPa]	[MPa]	[MPa]	[-]	[-]	[MN]	[-]
FO-SFRC1-1	47	140	50.1	-	-	-	-	-	-	-	-	-	2.30(1)	0.05(3)	0.05(3)	4.89	1.55
BT-SFRC1-1	48	140	50.1	BT1	545	90	120	278	238	525	5.73	2.46	2.19(2)	0.16	0.09	6.54	2.07
WG-SFRC1-1	48	140	50.1	WG1	551	90	120	93	178	525	5.79	7.47	2.19(2)	0.16	0.19	7.01	2.22
BT-SFRC1-2	49	210	50.1	BT3	545	85	68	93	108	525	10.62	7.83	2.19(2)	0.26	0.20	8.92	1.88
WG-SFRC1-2	49	210	50.1	WG3	551	85	68	56	60	525	10.73	13.19	2.19(2)	0.26	0.31	10.66	2.25
WG-SFRC1-3	51	140	50.1	WG4	551	50	60	56	60	525	17.08	18.37	2.19(2)	0.38	0.41	11.79	3.73

Note: Reinforcement layout BT = bent ties and WG = welded grids (see Morger et al. [3] for details), and FO = fibres only. All specimens with b_y = 350 mm, b_z = 550 mm, h = 525 mm, b_{li} = 450 mm, and $\varnothing_s$ = 12 mm, c_{nom} = 30 mm, b_{csy} = 278 mm, b_{csz} = 478 mm, s_{s1} = 36 mm when bar reinforcement was provided.
(1): w = 0.5 mm, see Fig. 6.A.1 in Appendix 6.A.3.
(2): w = 1 mm, see Fig. 6.A.1 in Appendix 6.A.3.
(3): $\widetilde{\omega}_{y,f}$ and $\widetilde{\omega}_{z,f}$ for reference only.

Table 6.2 - Overview of SFRC joint tests.

Specimen	Age at testing	b_{ly}	f_{c0}	Reinf. layout	f_{sy}	s_x	$s_{z,avg} = s_{z,max}$	$s_{y,avg}$	$s_{y,max}$	$x_{E,max}$	σ_{confy}	σ_{confz}	$\sigma_{t,f}$	$\widetilde{\omega}_{y,hyb}$	$\widetilde{\omega}_{z,hyb}$	$N_{x,u,exp}$	$q_{x,u,exp}/f_{c0}$
	[days]	[mm]	[MPa]	[-]	[MPa]	[mm]	[mm]	[mm]	[mm]	[mm]	[MPa]	[MPa]	[MPa]	[-]	[-]	[MN]	[-]
TLJ-40-FO-SFRC2	225	140	42.3	-	-	-	-	-	-	-	-	-	1.50(1)	0.04(3)	0.04(3)	6.61	1.72
TLJ-40-FO-SFRC3	337	140	46.7	-	-	-	-	-	-	-	-	-	2.22(1)	0.05(3)	0.05(3)	6.92	1.63
TLJ-60-FO-SFRC2	241	210	42.3	-	-	-	-	-	-	-	-	-	1.50(1)	0.04(3)	0.04(3)	9.19	1.59
TLJ-40-WG2p-SFRC4	277	140	47.6	WG2p	484	82	75	93	178	410	8.86	7.20	2.14(2)	0.23	0.20	10.11	2.33
TLJ-60-WG1p-SFRC4	263	210	47.6	WG1p	484	104	113	93	178	405	4.66	5.68	2.14(2)	0.14	0.16	10.82	1.67

Note: WG = welded grids (see Morger et al. [15] for details) and FO = fibres only. All specimens with b_y = 350 mm, b_z = 750 mm, h = 825 mm, h_{joint} = 7 mm, b_{li} = 650 mm, and $\varnothing_s$ = 12 mm, c_{nom} = 30 mm, b_{csy} = 278 mm, b_{csz} = 678 mm, s_{s1} = 34 + 7 mm when bar reinforcement was provided.
(1): w = 0.5 mm, see Fig. 6.A.1 in Appendix 6.A.3.
(2): w = 1 mm, see Fig. 6.A.1 in Appendix 6.A.3.
(3): $\widetilde{\omega}_{y,f}$ and $\widetilde{\omega}_{z,f}$ for reference only.

by the reinforcement (in transverse y- and longitudinal z-directions) computed according to the confinement model [17] using these values. By linear superposition of the confining stresses σ_{conf} with the residual tensile strength of the SFRC $\sigma_{t,f}$ (considered at w = 1 mm), as recommended by Aoude [13] for SFRC columns with additional confining reinforcement:

$$\sigma_{conf,hyb} = \sigma_{conf} + \sigma_{t,f} \tag{6.1}$$

and accounting for the concrete compressive strength $f_{c0,}$ mechanical reinforcement ratios of $\tilde{\omega}_{y,hyb} = \sigma_{confy,hyb}/f_{c0}$ = 0.14...0.38 and $\tilde{\omega}_{z,hyb} = \sigma_{confz,hyb}/f_{c0}$ = 0.09...0.41 in the transverse and longitudinal direction, respectively, result for the hybrid specimens. Note that the corresponding ratios of the purely fibre-reinforced specimens ($\tilde{\omega}_{y,f} = \tilde{\omega}_{z,f} = \sigma_{t,f}/f_{c0}$ = 0.04...0.05 with w = 0.5 mm) are included in the tables for reference, although they are not used in the model proposed for such cases (see Section 6.4.2). For further information on the confining reinforcement, the reader is referred to Morger et al. [3], [15].

6.2.2 Test setup and loading procedure

All tests were carried out in a stiff 20 MN compression testing machine at Empa in Dübendorf, Switzerland. The block tests were loaded quasi-statically to failure in compression by controlling the machine displacement (0.2-0.3 mm/min), using small lubricated steel bricks (17.5·45·30 mm^3) for the load introduction in order to minimise lateral restraint. The joint tests were loaded in four steps, keeping the load constant for 15 min in-between. The machine was force controlled (6 kN/s) in the first three loading steps, and displacement-controlled (0.15 mm/min) in the last step. TLJ-40-FO-SFRC3 was additionally subjected to joint rotations around the weak z-axis in both directions at load levels of 1 MN, 1.5 MN, 2 MN and 2.5 MN; note that the results of the joint rotations are not part of this article. All specimens reported here were loaded centrically and stopped when a significant load decrease or excessive load eccentricities were observed. For more details of the test setups, the reader is referred to Morger et al. [3], [15].

6.2.3 Measurement systems

For both campaigns, two neighbouring sides (transverse and longitudinal direction, see Fig. 6.1a and b) of the specimens were investigated with 3D digital image correlation (DIC). The DIC setups are described in detail in Morger et al. [3], [15]. Average noise levels with standard deviations $\sigma(U,V)$ below 3 µm for the block tests and below 16 µm for the joint tests resulted from zero displacement tests performed according to Mata-Falcón et al. [18] with the following correlation parameters: block tests with subset size = 17 px and step size = 4 px for the transverse sides and subset size = 23 px and step size = 6 px for the longitudinal sides; joint tests with subset size = 25 px and step size = 6 px for both sides. With the open source software ACDM [19], [20] the resulting DIC strain fields were analysed to determine the crack widths.

6.3 Results and analysis of experimental campaign

This section presents the results and analysis of the eleven tests on the block and joint specimens with SFRC and their comparison to RC specimens.

6.3.1 Results

The peak loads $N_{x,u,exp}$ and the corresponding average peak stresses $q_{x,u,exp}$ applied on the loaded area or the joint contact area – normalised by the concrete compressive strength f_{c0} – are shown in Table 6.1 and Table 6.2, respectively. Fig. 6.2 (block tests) and Fig. 6.3 (joint tests) illustrate the load-deformation behaviour by plotting the normalised average axial stress $q_{x,exp}/f_{c0}$ against the total compression δ_x. Additionally, $q_{x,exp}/f_{c0}$ is plotted against the crack width $w_{r,max}$. In all these plots, the compression δ_x refers to the axial deformation between the bottom of the specimen and the load introduction plate (block tests, $h = 525$ mm) or the lower and upper load introduction plate (joint tests, $h_{tot} = 2\cdot(h+h_{joint}) = 1664$ mm), determined by the DIC, thus eliminating any influence of the machine deformation. Note that for the joint tests, the compression δ_x was set to zero at an axial force of 300 kN, as the machine's crosshead was fully activated at this load. The crack width $w_{r,max}$, representing the maximum measured crack width (averaged over a crack length of 10 mm) obtained with ACDM, is plotted in orange for the transverse (dashed line) and the longitudinal (solid line) sides up to the peak load. In addition, the figures indicate the load levels at which a certain crack width (0.2, 0.3, and 0.5 mm for the block tests and

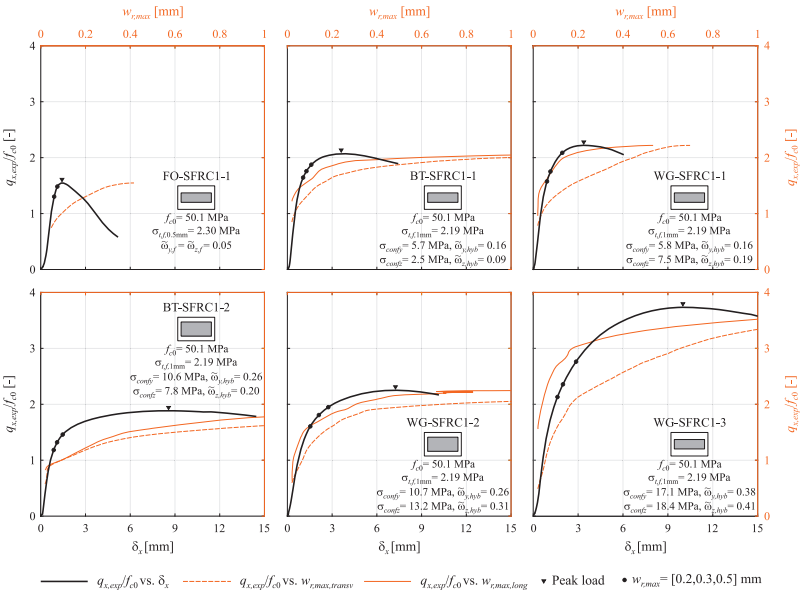

Fig. 6.2 - Load-compression and load-crack width diagrams for strip-loaded SFRC block specimens.

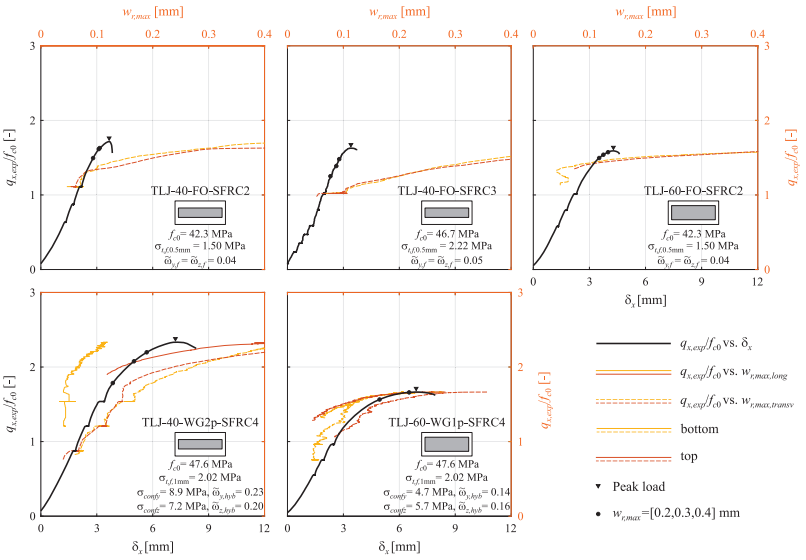

Fig. 6.3 - Load-compression and load-crack width diagrams for tests on longitudinal joints of tunnel lining segments.

0.2, 0.3, and 0.4 mm for the joint tests) occurred for the first time (circular markers on the load-compression curve) as well as the peak load (triangular markers). These plots are discussed in the following sections.

6.3.2 Load-bearing and failure behaviour

The load-compression curves of the block tests (Fig. 6.2) show that the hybrid-reinforced specimens (SFRC combined with conventional confining reinforcement) exhibited a ductile behaviour with a relatively large increase in deformation (= vertical compression δ_x) and a small increase in load until failure. The extent of ductility (as reflected by $\delta_{x,peak}$ = compression at peak load) varied strongly. Comparing the specimens WG-SFRC1-1 and WG-SFRC1-3 reveals that not only the load-bearing capacity increased with a higher mechanical reinforcement ratio but also the ductility. The same behaviour was observed for the RC specimens in Morger et al. [3]. The lower load-bearing capacity of the BT specimens compared to WG specimens with otherwise equal parameters can be attributed to the lower amount of conventional longitudinal reinforcement and the associated smaller confined concrete area [3]. The SFRC specimen without additional reinforcement (FO-SFRC1-1) exhibited a nearly linear elastic load-compression response, followed by pronounced softening. Such responses, also common in SFRC material tests, are often erroneously referred to as „ductile“. However, while the softening branch is observed in deformation-controlled experiments using sufficiently stiff testing machines, the

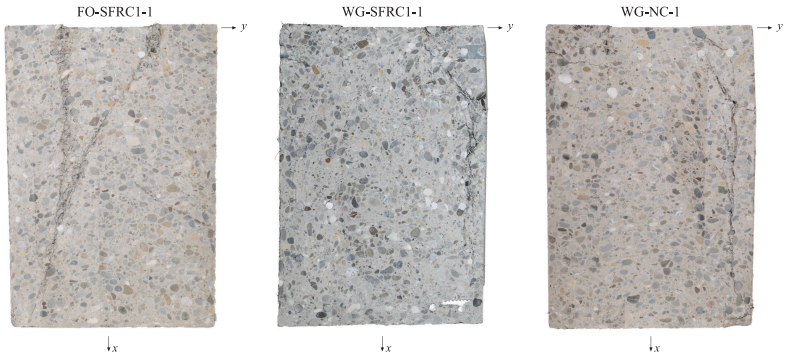

Fig. 6.4 - Vertical transverse cuts through three specimens after testing. Longitudinal DIC surface to the positive *y* side.

same specimen would exhibit a brittle failure in load control – which is more representative for most real structures. Comparing the vertical transverse cuts of the specimens FO-SFRC1-1, WG-SFRC1-1, and the RC specimen WG-NC-1 [3] after testing, shown in Fig. 6.4, indicates different failure modes: While the specimen FO-SFRC1-1 exhibited a classical tensile failure with a clear formation of a wedge, no continuous cracks within the reinforcement are visible and only cover concrete spalling can be observed for the hybrid-reinforced specimen WG-SFRC1-1, indicating a concrete compressive failure due to limited confinement, as in the RC specimen WG-NC-1. Accordingly, it can be concluded that the conventional reinforcement controlled cracking within the reinforced volume ($b_{csy} \cdot b_{csz} \cdot x_{E,max}$) of the hybrid-reinforced specimens.

The crack widths measured on the block specimen surfaces (see Fig. 6.2) grew continuously until the peak load, with the transverse side governing for all specimens; excessive spalling of the cover concrete – as observed in strip-loaded confined RC specimens [3] – was thus avoided due to the fibres bridging the cracks. The purely fibre-reinforced specimen FO-SFRC1-1 experienced a maximum crack opening of 0.4 mm in the transverse direction at the peak load, whereas the maximum crack widths in the hybrid-reinforced specimens exceeded 1 mm.

The load-compression curves of the joint tests (Fig. 6.3) show that the hybrid-reinforced specimens (bottom row) exhibited limited ductility, with a gradual stiffness decrease before reaching the peak load, but an immediate load drop thereafter. The latter may be attributed to the unconfined zone of these specimens. Cracks are visible in the cut surface (see Fig. 6.5) in the unconfined zone of the specimen TLJ-60-WG1p-SFRC4, besides cover spalling in the confined zone. For the SFRC specimens without additional reinforcement (top row in Fig. 6.4), a nearly linear elastic behaviour up to the peak load, followed by an immediate and pronounced load drop can be observed. The specimen TLJ-60-FO-SFRC2 experienced a sudden brittle failure despite the deformation-controlled loading in a stiff testing machine, separating the top half specimen into two parts (see Fig. 6.5 for the failure surface). For the other two purely fibre-reinforced specimens, the loading was supposedly stopped shortly before such failure. Note that Böhme et al. [21] described a very similar failure in large-scale tests of longitudinal

Fig. 6.5 - Vertical transverse cut through half specimen TLJ-60-WG1p-SFRC4 after testing and failure plane of half specimen TLJ-60-FO-SFRC2.

joints in purely fibre-reinforced specimens. A considerable difference in ductility ($\delta_{x,peak}$ = compression at peak load) between the purely fibre-reinforced and the hybrid-reinforced specimens can be observed. For the SFRC specimens without additional reinforcement, a tensile failure is identified, whereas for the hybrid-reinforced specimens, a compression failure either in the confined zone due to limited confinement or in the unconfined zone by reaching the concrete compressive strength is anticipated. The failure mode of the hybrid-reinforced joint specimens is further discussed in the comparison of SFRC and RC specimens in Section 6.3.3.

The crack widths grew continuously in all joint tests, with the SFRC specimens without additional reinforcement experiencing a nearly linear increase with higher loads, whereas the crack widths in the hybrid-reinforced specimens increased progressively with the load, similar to the axial deformations. The governing crack widths occurred in the transverse direction, amounting to around 0.3...0.7 mm at the peak load. Note that no crack measurements of the joints were possible with the given DIC setup.

Direct comparison of the hybrid-reinforced specimens between the block and joint tests is not possible as either the reinforcement type, the reinforcement ratio or the load application width varied. The SFRC specimens without additional reinforcement in the block and joint tests sustained failure loads higher than the load at which surface cracks were initially observed, as demonstrated by the obtained crack width measurements. This indicates that the steel fibres were successfully activated, likely hindering the growth of (micro-)cracks and is in line with other experimental campaigns investigating strip loading that observed increased load-bearing capacities of SFRC specimens without additional reinforcement compared to plain concrete [4], [11]. All SFRC specimens without additional reinforcement would have exhibited brittle failures in load control. In the displacement-controlled tests, however, the block specimen experienced a pronounced softening, while an immediate load drop with barely any additional vertical displacement δ_x occurred in the joint specimens. This indicates a potential dependency on the specimen size and, more importantly, a very unfavourable load-displacement behaviour for longitudinal joints of purely fibre-reinforced tunnel lining segments. However, being based on merely

three joint tests, further large-scale experiments on SFRC joint specimens are required to substantiate this hypothesis.

6.3.3 Comparison SFRC vs. RC

This section compares the results of the SFRC specimens described in this article with those of RC specimens published previously [3], [15] having equal geometries and, where applicable, reinforcement layouts.

Fig. 6.6 compares the SFRC specimens to the RC block tests presented in Morger et al. [3], differentiating between narrow (Fig. 6.6a) and wide (Fig. 6.6b) load application widths. It is visible that for most hybrid-reinforced specimens additional steel fibres increased the load-bearing capacity of otherwise similar specimens (differing only regarding f_{c0}: 50.1 MPa (SFRC) vs. 46.5 MPa (RC)). The effect is most pronounced for specimens with low conventional confining reinforcement content (e.g. BT-SFRC1-1 vs. BT-NC-1 and WG-SFRC1-1 vs. WG-NC-1). With increasing content of the conventional confining reinforcement, the impact of the steel fibres diminishes (WG-SFRC1-3 vs. WG-NC-4). This behaviour is to be expected, assuming a linear superposition of the confining stresses by the conventional reinforcement and the residual tensile strength of the SFRC (see Eq. (6.1)): for higher conventional confinement, the relative impact of the SFRC reduces. Nevertheless, the ductility ($\delta_{x,peak}$) increased for all specimens with SFRC. The purely fibre-reinforced specimen FO-SFRC1-1 exhibited the lowest load-bearing capacity and ductility – also compared to the RC specimens with low confining reinforcement. The cut surfaces of WG-SFRC1-1 and WG-NC-1 in Fig. 6.4 show no indications of a splitting failure, indicating that concrete failure due to limited confinement occurred in both specimens. Fig. 6.8 shows the load levels at which a certain crack width on the specimen surfaces was reached in the hybrid-reinforced SFRC and the RC specimens. In the block tests, the SFRC specimens sustained higher loads than the RC specimens until the same crack width was reached for all but the most confined specimens (WG-SFRC1-3 vs. WG-NC-4). This highlights that steel fibres can reduce crack widths due to their ability to bridge cracks. However, as for the load-bearing capacity, the effect diminishes for high conventional reinforcement ratios.

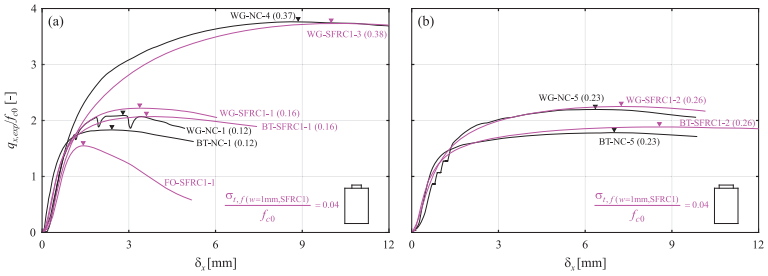

Fig. 6.6 - Comparison of SFRC (purple) and RC (black) block tests: (a) specimens with load concentration ratio b_{ly}/b_y = 0.40 and (b) specimens with load concentration ratio b_{ly}/b_y = 0.60. Transverse mechanical reinforcement ratio $\widetilde{\omega}_{y,hyb}$ for hybrid and ω_y for conventional reinforcement in brackets, where applicable.

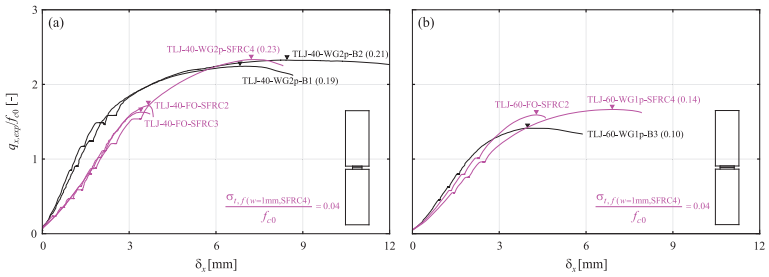

Fig. 6.7 - Comparison of joint tests made of SFRC (purple) and RC (black): (a) specimens with load concentration ratio b_{ly}/b_y = 0.40 and (b) specimens with load concentration ratio b_{ly}/b_y = 0.60. Transverse mechanical reinforcement ratio $\widetilde{\omega}_{y,hyb}$ for hybrid and ω_y for conventional reinforcement in brackets, where applicable.

Fig. 6.7 compares the SFRC joint tests to the RC joint tests presented in Morger et al. [15], separately for the different joint widths (Fig. 6.7a: 40%, Fig. 6.7b 60% of block width). The hybrid-reinforced specimen TLJ-40-WG2p-SFRC4 (Fig. 6.7a) experienced a very similar load-bearing capacity as the RC specimens, for which the failure load of the confined and unconfined zones was supposedly almost identical [15]. Consequently, failure of the hybrid-reinforced specimen likely occurred in its unconfined zone by reaching the uniaxial concrete compressive strength of the concrete, which was not affected by the additional steel fibres; its confined zone presumably had reserve capacity due to the additional confinement provided by the fibres. A comparison of the SFRC specimens without additional reinforcement to the specimens TLJ-40-WG1p-B1 and TLJ-40-WG1p-B2 regarding load-bearing capacity is not pertinent, as the RC specimens were provided with substantial confining reinforcement. However, the lack of ductility of the purely fibre-reinforced specimens is striking. On the other hand, the hybrid-reinforced specimen with a wider joint and low conventional reinforcement ratio (TLJ-60-WG1p-SFRC4, Fig. 6.7b) sustained a higher load and exhibited a more ductile response than the otherwise identical (except for f_{c0}: 47.6 MPa vs. 46.9 MPa) RC specimen TLJ-60-WG1p-B3. The different behaviour can only be explained by assuming that the confined zone governed TLJ-60-WG1p-B3 (in [15] the failure mode could not be clearly defined) and the fibres effectively increased the confinement in that zone, leading to a higher load-bearing capacity of TLJ-60-WG1p-SFRC4. The cracks in the unconfined zone of the cut surface of the specimen TLJ-60-WG1p-SFRC4 (see Fig. 6.5) indicate that this region governed failure, though this hypothesis cannot be further substantiated. Furthermore, the specimen TLJ-60-FO-SFRC2 without additional reinforcement sustained a higher peak load than the RC specimen, indicating that SFRC may be able to replace conventional reinforcement. However, this observation is based on the comparison of merely two tests, and the sudden brittle failure of the specimen TLJ-60-FO-SFRC2 raises concerns about its applicability in structural elements such as tunnel linings.

A comparison of the crack width development of the joint tests is only possible for the TLJ-40 specimens, as for the RC specimen with TLJ-60 no crack measurements are available (cracks occurred on the opposite face of the DIC system). The comparison of the TLJ-40 specimens reveals (i) significant scatter among the two RC specimens and (ii) similar or higher load levels at the same crack widths in the SFRC specimens.

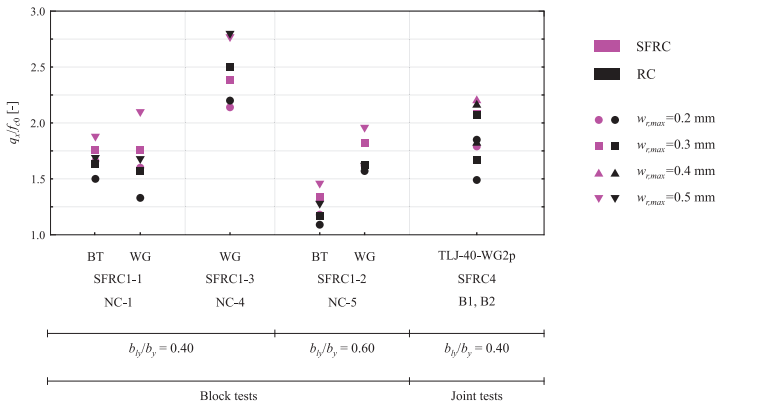

Fig. 6.8 - Load levels for a given crack width for SFRC and RC specimens of block and joint tests. RC specimens from Morger et al. [3], [15].

6.4 Modelling

In this section, the modelling of strip-loaded SFRC is discussed separately for hybrid-reinforced (Section 6.4.1) and purely fibre-reinforced (Section 6.4.2) specimens. In both cases, the residual tensile strength of the SFRC ($\sigma_{t,f}$) obtained from the three-point bending tests (see Appendix 6.A.3) is considered, and it is assumed that this value is representative for the strip-loaded specimens. If this condition cannot be guaranteed, for example due to unfavourable casting conditions, fibre distribution and orientation factors reducing the contribution of the steel fibres are required to predict the load-bearing capacity with the proposed models. Indeed, selecting pertinent fibre distribution and orientation factors is crucial for structural design. Codes such as *fib* Model Code 2020 [14] and EN 1992-1-1:2023 [22] provide guidance for common cases; a discussion on their background (see e.g. [23] for an overview) is beyond the scope of this article.

6.4.1 Hybrid reinforcement

For the hybrid-reinforced specimens, where the confining reinforcement controls the crack width development of the concrete within the reinforcement, it is proposed to superimpose the confining stresses provided by the reinforcement σ_{conf} with the residual fibre tensile strength $\sigma_{t,f}$ of the SFRC according to Eq. (6.1). The resulting stresses ($\sigma_{conf,hyb}$) can then be used as input in mechanically sound models established for RC elements subjected to strip loading that account for load dispersion and passive confinement, such as the Multi-Wedge (MW) [15] or Dual-Wedge (DW) [2], [3] stress fields (see Fig. 6.9a and b). Thereby, $\sigma_{t,f}$ is determined for a crack width $w = 1$ mm, as it is assumed that this crack width occurs at full activation of the conventional confining reinforcement. This assumption may be

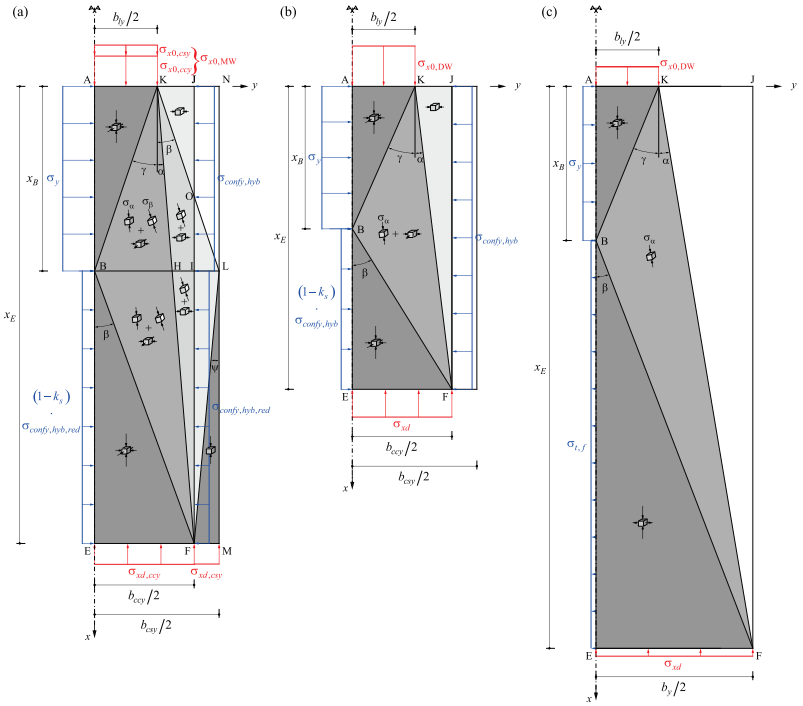

Fig. 6.9 - Models for strip-loaded SFRC: (a) Multi-Wedge stress field for hybrid-reinforced specimens, (b) Dual-Wedge stress field for hybrid-reinforced specimens, and (c) Dual-Wedge stress field for SFRC specimens without additional reinforcement. (a) and (b) drawn to scale for the specimen WG-SFRC1-1 and (c) for the specimen TLJ-40-FO-SFRC2. Only one symmetrical half is shown, and transverse stresses are exaggerated compared to vertical stresses. (a) and (b) with the same scaling to allow a direct comparison.

verified by investigating the strains of the confining reinforcement at the peak load of hybrid-reinforced specimens, for example using fibre optical measurements as presented in Morger and Kaufmann [24]. However, the $\sigma_{t,f}$-w diagrams in Appendix 6.A.3 show that a 0.5 mm variation in w does not substantially impact the value of $\sigma_{t,f}$. The load is dispersed within the width of the reinforcement b_{csy} or within the confined concrete width b_{ccy} for the Multi-Wedge or the Dual-Wedge stress field, respectively (see Fig. 6.9). The resistance of the unconfined zone of the joint test specimens is determined accounting for the uniaxial concrete compressive strength f_{c0} within the area inside the reinforcement $A_{cs} = b_{csy} \cdot b_{csz}$, as proposed in Morger et al. [15]. For the definition of all input parameters of the stress fields as well as the procedure to determine σ_{x0}, the reader is referred to Markić et al. [2] and Morger et al. [3], [15]. Note that σ_{x0} can only be applied within the confined concrete length in the longitudinal direction (b_{ccz}). The loaded area outside b_{ccz}, if present, can only sustain f_{c0} (DW, see[3]) or $\sigma_{x0,csz}$ (MW, considering

Table 6.3 - Parameters of MW and DW stress fields and comparison with the experimental data.

Specimen	MW and DW			MW					DW					$q_{u,exp}/q_{u,model}$	
	b_{ccy}	b_{ccz}	$q_{u,unconf}$	σ_{x0}	$\sigma_{x0,cz}$[(1)]	$\sigma_{xd,cc}$	x_E	$q_{u,conf}$	σ_{x0}	σ_{xd}	x_E	$q_{u,conf}$	MW	DW
	[mm]	[mm]	[MPa]	[MPa]	[MPa]	[MPa]	[mm]	[MPa]	[MPa]	[MPa]	[mm]	[MPa]	[-]	[-]
BT-SFRC1-1	203.2	350.8	-	100.1	55.6	50.6	510	90.3	97.9	67.4	338	87.3	1.15	1.19
WG-SFRC1-1	203.2	378.3	-	100.4	58.9	50.8	510	93.8	98.2	67.6	338	90.5	1.19	1.23
BT-SFRC1-2	223.5	409.3	-	104.4	62.7	85.9	525	100.6	104.5	98.2	433	99.6	0.94	0.95
WG-SFRC1-2	223.5	426.0	-	104.9	70.1	86.3	524	103.0	105.0	98.7	433	102.1	1.09	1.10
WG-SFRC1-3	239.0	429.2	-	158.2	74.2	84.5	493	154.3	163.5	95.7	367	158.2	1.21	1.18
TLJ-40-WG2p-SFRC4	222.3	580.0	98.6	109.8	56.1	57.2	410	104.1	114.2	71.9	354	107.0	1.13	1.13
TLJ-60-WG1p-SFRC4	201.2	574.9	65.7	73.0	55.3	60.6	405	70.9	71.7	74.8	-[(2)]	70.6	1.21	1.21
												Mean	1.13	1.14
												COV [%]	8.41	8.36

(1): Computed with $\sigma_{cc} = \sigma_{conf,hyd}/5$, see Morger et al. [15].
(2): No load dispersion possible since $b_{ty} > b_{ccy}$.

longitudinal load dispersion, see [15]). Consequently, the load-bearing capacity $q_{x,u}$ is determined as a weighted average of these stresses with their respective areas, as presented in Morger et al. [3], [15].

Table 6.3 summarises the parameters of the two stress fields and compares the predicted load-bearing capacities with the experimental data of the hybrid-reinforced specimens. Note that the calculations of the models were carried out without considering a concrete brittleness factor and accordingly reducing the concrete compressive strength, as often used in current codes, for example. $\eta_{cc} = (30/f_{c0})^{(1/3)} \leq 1$ according to SIA 262 [25]. The comparison shows that the two models predict similar and, apart from the specimen BT-SFRC1-2, safe ($q_{x,u,exp}/q_{x,u,model} \geq 1$) values of the load-bearing capacity. Note that slightly unsafe predictions were also obtained for the RC specimen equivalent to BT-SFRC1-2 with a wide load application area and bent tie reinforcement (BT-NC-5 in [3]). For the SFRC joint tests, both models predict that the unconfined zone governs the load-bearing capacity, i.e., $q_{x,u,model}$ is limited by $q_{x,u,unconf}$, corresponding to the load $A_{cs} \cdot f_{c0}$ (uniaxial compressive strength within the reinforcement) divided by the joint area [15]. For the specimen TLJ-40-WG2p-SFRC4, this is in accordance with the experimental observations; for TLJ-60-WG1p-SFRC4, the failure mode was not clearly identified.

Overall, superimposing the confining stresses of the conventional reinforcement σ_{conf} with the residual tensile strength of the SFRC $\sigma_{t,f}$ (see Eq. (6.1)) at a crack opening of 1 mm and applying the sum $\sigma_{conf,hyb}$ as confining stress in models considering load dispersion and passive confinement appears reasonable. This also indirectly demonstrates that conventional confining reinforcement can be partially substituted by SFRC.

On a side note, the comparison between MW and DW shows that for low conventional confining ratios (BT-SFRC1-1 and WG-SFRC1-1) accompanied by small confined concrete widths b_{ccy}, the MW predicts higher load-bearing capacities σ_{x0} by spreading the load within b_{csy} and not only b_{ccy} as proposed for the DW by activating the confining reinforcement over a larger height x_E (see Fig. 6.9a vs. Fig. 6.9b, or Table 6.3).

6.4.2 SFRC without additional reinforcement

The DW stress field in its simplest form (see Fig. 6.9c) is proposed to model the load dispersion of strip-loaded purely fibre-reinforced specimens; essentially this corresponds to a classical case of partial area loading, where the bursting force is resisted by the SFRC residual tensile strength $\sigma_{t,f}$. The latter is defined here for a crack width of 0.5 mm based on the recommendation of Trabucchi et al. [12], which is in good agreement with the experimentally observed crack widths in the purely fibre-reinforced specimens. Confinement by the SFRC is neglected since the experiments clearly showed brittle tensile failures in the absence of conventional confining reinforcement, which is in line with the observation that $\sigma_{t,f}$ is commonly well below the concrete tensile strength (see $\sigma_{t,f}$ vs. f_{ct} in Appendix 6.A). On the other hand, the full specimen width b_y is used for load dispersion, rather than limiting it to b_{csy} (MW) or b_{ccy} (DW), respectively, as in the hybrid-reinforced specimens. Note that the stress field assumes activation of uniform tensile stresses $\sigma_{t,f}$ over the height from point B to E ($x_E - x_B$), which requires stress redistributions after occurrence of initial concrete cracks.

Despite that confinement by SFRC is neglected, the load-bearing capacity predicted by the DW stress field at the load introduction will often be higher than the uniaxial concrete compressive strength f_{c0} due

Table 6.4 - Parameter of DW stress field and comparison with experimental data of purely fibre-reinforced specimens.

Specimen	x_B [mm]	x_E [mm]	DW σ_{x0} [MPa]	$q_{x,u,exp}/q_{x,u,model}$ [-]
FO-SFRC1-1	126	525	65.5	1.18
TLJ-40-FO-SFRC2	172	627	58.1	1.25
TLJ-40-FO-SFRC3	176	565	66.3	1.15
TLJ-60-FO-SFRC2	241	641	52.3	1.29
			Mean	1.22
			COV [%]	5.23

to load dispersion in the transverse y-direction and resulting geometrical confinement, i.e., favourable transverse compressive stresses σ_y within the wedge ABK. Accordingly, principal compressive stresses in the longitudinal z-direction not smaller than σ_y are required inside ABK to comply with the underlying modified Coulomb failure criterion (see e.g. [3]). Such compressive stresses can be generated by (i) load application areas not expanding over the entire specimen length b_z (allowing load dispersion in the longitudinal direction, analogously to the transverse direction), (ii) restraint provided by the impediment of the concrete expansion at the load introduction by the unloaded shoulders (see e.g. [6]; the shoulders are consequently subjected to tension that can be resisted by $\sigma_{t,f}$), (iii) conventional longitudinal reinforcement (as in RC specimens), or (iv) externally applied compression. Quantifying these effects, which depend on the geometrical configuration and may require optimisation, is not straightforward and beyond the scope of this article. However, if the required longitudinal compressive stresses cannot be ensured, predicted load-bearing capacities above f_{c0} need to be reduced in design.

Table 6.4 compiles the parameters of the DW stress field and the comparison with the experimental data. The model predicts the load-bearing capacity on the safe side for all tests. Note that the predictions of the DW, which are all above f_{c0}, were obtained without checking the required longitudinal confining stresses; the even higher experimental failure loads indicate that sufficient longitudinal confining stresses could be activated in the given geometrical configuration to ensure that the transverse direction was governing. According to the DW model, both wedges ABK and BEF are predicted to fail simultaneously, which was achieved by optimising the height x_E of the joint tests (corresponding to 565 mm, 627 mm and 641 mm, respectively, see Table 6.4) to maximise the load-bearing capacity: Increasing x_E reduces the geometrical confinement of the top wedge but at the same time decreases the bursting force while increasing the bursting resistance by activating $\sigma_{t,f}$ over a larger height ($x_E - x_B$) of the bottom wedge. In the specimen FO-SFRC1-1, x_E is limited by the specimen height such that the bottom wedge BEF governs, while the top wedge ABK has reserve capacity.

In the light of the experimentally observed lack of ductility, and considering that the DW stress field assumes activation of uniform tensile stresses up to the height x_E, further investigations are required to validate the model for its application to the design of tunnel lining segments, despite the satisfactory correlation with the experimental data (note that the scatter of the comparison of the model with the experimental data is smaller than the scatter of the material tests – this is not investigated further in this article). This could include limiting the height x_E of the stress field up to which uniform residual tensile stresses are assumed to account for limited load distribution and varying crack openings over the specimen height, resulting in lower predictions of the load-bearing capacity. Such further investigations

as well as comparison with empirical and semi-empirical design approaches [11], [12] are, however, beyond the scope of this article.

6.5 Conclusion

This article investigates the load-bearing behaviour of strip-loaded SFRC with and without additional reinforcement. Eleven experiments on strip-loaded SFRC specimens out of two campaigns investigating strip loading in block specimens and longitudinal joints of tunnel lining segments are presented. Seven specimens contained additional conventional confining reinforcement (hybrid-reinforced specimens), while the remaining four were purely fibre-reinforced. The experimental results highlight different failure modes for the hybrid and purely fibre-reinforced specimens: The hybrid-reinforced specimens failed in a ductile manner, while the purely fibre-reinforced specimens experienced a roughly linear elastic behaviour with pronounced softening (block test) or brittle failure (joint tests) despite displacement-controlled loading in a stiff testing machine. Although the purely fibre-reinforced specimens exhibited brittle failure, failure loads higher than the load at which surface cracks first appeared were observed, indicating that the fibres were activated, and likely hindering the growth of initial (micro-)cracks. Compared to RC block specimens, most hybrid-reinforced SFRC block specimens exhibited higher load-bearing capacities and increased ductility. The same holds for the joint tests as long as the unconfined zone did not govern failure. Note that with a higher content of conventional reinforcement, the effect of the fibres reduces. The crack widths on the specimen surface were measured with DIC. The reinforced SFRC specimens experienced smaller crack widths at the same load level than similar RC specimens with moderate conventional confining reinforcement ratios. For higher confinement, no beneficial effect of the fibres on the crack widths was observed.

Furthermore, the article presents modelling approaches for strip-loaded hybrid and purely steel fibre reinforced concrete. For hybrid-reinforced specimens, it is proposed to linearly superimpose the confining stresses provided by conventional reinforcement with the post-cracked residual tensile strength of the SFRC. These stresses are subsequently applied to mechanically sound models established for RC elements subjected to strip loading that account for load dispersion and passive confinement, such as the Multi-Wedge [15] or Dual-Wedge [2], [3] stress fields. The residual tensile strength is determined for a crack width of 1 mm according to the linear model of *fib* Model Code 2020 [14], based on standard material tests with prismatic SFRC beams subjected to three-point bending according to EN 14651 [16]. The comparison of the experimental results with the predictions of the two stress fields shows good agreement. Even though only seven tests were available, the data set contained two different reinforcement types (BT and WG), different conventional reinforcement ratios, and varying load application widths, providing a substantial validation. In addition, all hybrid-reinforced specimens exhibited ductile failures. Consequently, the models can be recommended as a valid basis for design.

For the SFRC specimens without additional conventional reinforcement controlling crack growth, the simplest Dual-Wedge stress field [2] is proposed to account for load dispersion. The residual tensile strength of the SFRC, determined here for a crack width opening of 0.5 mm, is assumed to equilibrate the bursting stresses. The model predictions are on the safe side compared to the experimental results, and the stress field is a useful tool to trace the force flow. Nevertheless, the brittle failure mode of the

joint tests and a related possible size effect require further investigation for successful model validation. This might include limiting the height x_E of the stress field up to which uniform residual tensile stresses are assumed to account for limited load distribution and varying crack openings over the specimen height, resulting in lower predictions of the load-bearing capacity.

All proposed modelling approaches rely on a pertinent description of the mechanical properties of the SFRC within the structural member. For the residual tensile strength, the orientation and distribution of the fibres are of great importance. Accordingly, adequate reduction factors must be applied to the residual tensile strength if the fibre orientation or distribution in the specimens differs from that in the material characterisation tests used to determine the mechanical properties.

In conclusion, SFRC can enhance the load-bearing behaviour of strip-loaded concrete and minimise crack widths. SFRC is particularly efficient for hybrid-reinforced specimens when combined with low conventional confining reinforcement ratios. Consequently, SFRC is a viable option for the design of precast tunnel lining segments, as it allows the required conventional reinforcement of the longitudinal joints to be reduced while providing further beneficial effects, such as higher robustness. The load-bearing capacity of the hybrid-reinforced specimens can be reliably determined using the proposed modelling approach. However, the application of strip-loaded SFRC specimens without additional conventional reinforcement in design requires further investigation, particularly regarding a potential size effect related to the brittle failure mechanism, despite the promising modelling approaches.

Acknowledgements

The authors gratefully acknowledge the support by: The Swiss Federal Roads Office and the Swiss Federal Office of Transport for partially funding this work (Project AGT 2019/001). Robert Widmann for his support at testing at Empa testing hall. The staff of the IBK structures lab at ETH Zurich for their support during the preparation of the block specimens. The staff of the Empa testing hall for their support during the conduction of the experiments. Marti Tunnel AG for producing the joint specimens of the experimental campaign.

Appendix 6.A Mechanical properties of SFRC

6.A.1 SFRC properties of block tests

Table 6.A.1 compiles the mean values, the number of tested samples, and the coefficients of variation of the mechanical properties of the SFRC of the block tests. Standard cylinders with a diameter of 150 mm and a height of 300 mm were used to determine the cylinder compressive strength f_{c0} and the Young's modulus E_c (secant modulus at a stress of roughly $0.3 \cdot f_{c0}$). The cube compressive strength $f_{c,cube}$ was determined from standard cubes of 150 mm side length. The tensile strength f_{ct} was determined indirectly using double punch tests on half standard cylinders loaded with 37.5 mm diameter steel punches [26], [27].

Table 6.A.1 - Mechanical properties of SFRC of block tests.

Batch	f_{c0} [MPa]	$f_{c,cube}$ [MPa]	f_{ct} [MPa]	E_c [GPa]
SFRC1	50.1 (5, 2.0%)	55.8 (3, 0.7%)	3.9 (4, 3.5%)	34.3 (5, 6.7%)

6.A.2 SFRC properties of joint tests

Table 6.A.2 compiles the information of the concrete cores sampled from the joint specimens to determine the concrete compressive strength f_{c0}. The cores were taken from the less damaged specimen of the test on the opposite side of the longitudinal joint. The $f_{c0,i}$ values were calculated by multiplying the strength of the cores ($f_{c,core,i}$) by the core length factor *CLF* according to SN EN 13791:2019 [28], and their mean is used as the cylindrical compressive strength f_{c0} with standard deviation (s) and coefficient of variation (COV). No other reduction factors were applied.

Table 6.A.2 - Concrete compressive strength of joint tests determined on cored concrete samples.

Batch	Investigated specimen	Age [days]	$\rho_{c,core,i}$ [kg/m^3]	$f_{c,core,i}$ [MPa]	$d_{core,i}$ [mm]	$h_{core,i}$ [mm]	*CLF* [-]	$f_{c0,i}$ [MPa]	f_{c0} [MPa]	$s(f_{c0})$ [MPa]	COV(f_{c0}) [-]
SFRC2	TLJ-40-FO-SFRC2	247	2359	53.9	80.4	80.2	0.82	44.1	**42.3**	1.19	2.8%
			2365	50.6	80.4	80.0		41.3			
			2371	51.4	80.3	80.3		42.0			
		260	2357	41.1	80.0	160.2	1.00	41.1			
			2330	42.8	80.5	160.3		42.7			
SFRC3	TLJ-40-FO-SFRC3	371	2380	58.0	80.4	79.9	0.82	47.4	**46.7**	1.50	3.2%
			2366	55.1	80.4	79.9		45.0			
			2373	58.5	80.4	79.9		47.8			
SFRC4	TLJ-40-WG2p-SFRC4	297	2380	58.8	80.4	79.8	0.82	48.0	**47.6**	1.32	2.8%
			2374	58.0	80.4	79.8		47.3			
			2368	55.4	80.4	79.8		45.2			
			2369	49.2	80.5	159.7	1.00	49.1			
			2357	47.7	80.6	159.6		47.6			
			2363	48.5	80.5	159.7		48.4			

Furthermore, Table 6.A.3 presents the concrete compressive strength f_{c0} determined on standard cylinders and Table 6.A.4 shows the tensile strength f_{ct} determined indirectly using double punch tests for batch SFRC2.

Table 6.A.3 - Concrete compressive strength determined with standard cylinders for batch SFRC2.

Batch	Age [days]	ρ_c [kg/m^3]	$f_{c0,i}$ [MPa]	f_{c0} [MPa]	$s(f_{c0})$ [MPa]	COV(f_{c0}) [-]
SFRC2	218	2361	40.9	**42.0**	0.97	2.3%
		2347	41.0			
	233	2353	42.3			
		2351	43.1			
	245	2347	42.5			

Table 6.A.4 - Concrete tensile strength determined with standard half cylinders for batch SFRC2.

Batch	Age [days]	ρ_c [kg/m^3]	$f_{ct,i}$ [MPa]	f_{ct} [MPa]	$s(f_{ct})$ [MPa]	COV(f_{ct}) [-]
SFRC2	233	2319	3.1	**3.58**	0.34	9.5%
		2350	3.9			
	245	2344	3.7			
		2333	3.6			

6.A.3 Post-cracking properties of SFRC

Fig. 6.A.1 presents the results of the notched prismatic SFRC beams (150·150·550 mm^3) subjected to three-point bending according to EN 14651 [16] for the four batches. The top row plots the residual flexural tensile strength f_R against the crack mouth opening displacement *CMOD*. In the bottom row, the residual tensile strength $\sigma_{t,f}$ determined with the linear model of *fib* Model Code 2020 [14] as well as *fib* Model Code 2010 [29] is plotted against the crack width opening w. Table 6.A.5 depicts the values of the residual flexural tensile strengths f_{R1}, f_{R2}, f_{R3}, and f_{R4} corresponding to a *CMOD* of 0.5 mm, 1.5 mm, 2.5 mm, and 3.5 mm, respectively.

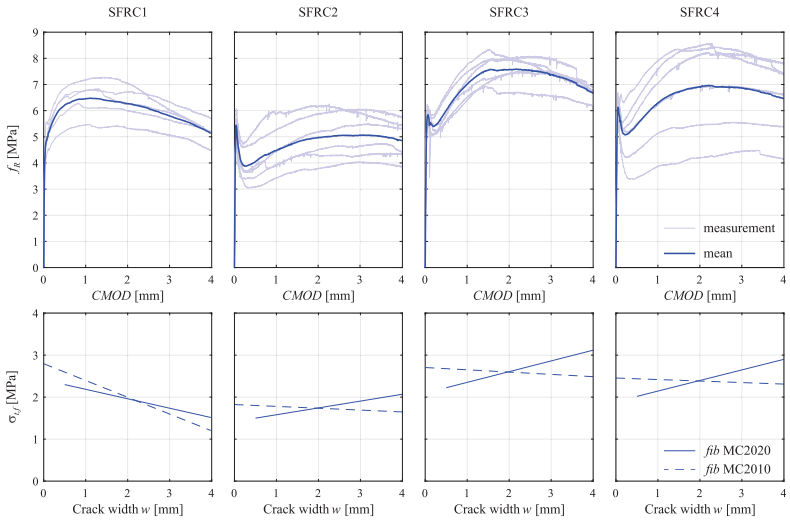

Fig. 6.A.1 - Classification of residual post-cracking strength of different SFRC batches.

Table 6.A.5 - Residual flexural tensile strength of different SFRC batches with coefficient of variation in brackets.

Batch	f_{R1} [MPa]	f_{R2} [MPa]	f_{R3} [MPa]	f_{R4} [MPa]
SFRC1	6.21 (0.11)	6.39 (0.11)	6.07 (0.09)	5.53 (0.08)
SFRC2	4.05 (0.21)	4.81 (0.19)	5.05 (0.18)	5.03 (0.16)
SFRC3	6.01 (0.08)	7.55 (0.08)	7.54 (0.07)	7.13 (0.06)
SFRC4	5.45 (0.24)	6.71 (0.26)	6.91 (0.24)	6.70 (0.23)

Notation

Latin letters

$A_{cs} = b_{csy} \cdot b_{csz}$	Concrete area inside the confining reinforcement
b_{ccy}, b_{ccz}	Confined concrete width and length
$b_{csy} = b_y - 2 \cdot c_{nom} - Ø_{conf}$ $b_{csz} = b_z - 2 \cdot c_{nom} - Ø_{conf}$	Maximum width and length of confining reinforcement (dimension between centre lines)
b_{ly}, b_{lz}	Width and length of loaded area
b_y, b_z	Width and length of concrete block
CLF	Core length factor
$CMOD$	Crack mouth opening displacement, measured on notched SFRC prisms
c_{nom}	Concrete cover
d_{core}	Diameter of cored concrete sample
D_{max}	Maximum aggregate size
f_{c0}	Uniaxial concrete cylinder compressive strength
$f_{c,cube}$	Uniaxial concrete cube compressive strength
f_{ct}	Concrete tensile strength
$f_{R1}, f_{R2}, f_{R3}, f_{R4}$	Residual flexural tensile strength of SFRC corresponding to $CMOD$ of 0.5 mm, 1.5 mm, 2.5 mm and 3.5 mm
f_{sy}	Yield stress of reinforcing steel
h	Specimen height (in axial x-direction)
h_{core}	Height of cored concrete sample
h_{joint}	Joint height (half of shoulder distance)
h_{tot}	Total height of joint tests consisting of two half specimens placed on each other
$k_s \in [0,1]$	Parameter indicating the part of $\sigma_{confy,hyb,red}$ resp. $\sigma_{confy,hyb}$ available to equilibrate the bursting stresses for Multi-Wedge or Dual-Wedge stress field
$N_{x,u}$	Peak axial force
q_x	Average axial stress across loaded area
$q_{x,u}$	Load-bearing capacity = min($q_{x,u,conf}$, $q_{x,u,unconf}$), average axial stress across loaded area at peak load
$q_{x,u,conf}$	Load-bearing capacity of confined zone (referred to loaded area)
$q_{x,u,unconf}$	Load-bearing capacity of unconfined zone (referred to loaded area)
s_x, s_y, s_z	Spacing of confining reinforcement in respective directions
s_{x1}	Distance in x-direction between load introduction and first reinforcement layer
$s_{y,avg}, s_{z,avg}$	Average confining reinforcement spacing in lateral y- and z-direction
$s_{y,max}, s_{z,max}$	Maximum confining reinforcement spacing in lateral y- and z-direction
w	Crack width of SFRC
$w_{r,max}$	Maximum crack width on specimen surface
x	Loading direction (axial, vertical)
x_B	Height of top wedge of Multi-Wedge or Dual-Wedge stress field
x_E	Height of Multi-Wedge or Dual-Wedge stress field

$x_{E,max}$	Confined height
y	Lateral transverse direction
z	Lateral longitudinal direction

Greek letters

α	Inclination angle of diagonal compressive strut of Multi-Wedge or Dual-Wedge stress field
β	Inclination angle of trapezoidal compressive strut of Multi-Wedge stress field
γ	Inclination angle of top wedge of Multi-Wedge or Dual-Wedge stress field
δ_x	Compression in axial x-direction
η_{cc}	Strength reduction factor to account for higher-strength concrete brittleness
$\sigma(U,V)$	Standard deviation of displacements in lateral and vertical direction
σ_α	Compressive stress in diagonal strut with inclination α of Multi-Wedge or Dual-Wedge stress field
σ_β	Compressive stress in trapezoidal strut with inclination β of Multi-Wedge stress field
σ_{conf}	Confining stress provided by reinforcement
$\sigma_{conf,hyb}$	Combined confining stress provided by reinforcement and SFRC (hybrid reinforcement)
$\sigma_{confy}, \sigma_{confz}$	Confining stress in the transverse and longitudinal direction
$\sigma_{confy,hyb}, \sigma_{confz,hyb}$	Combined confining stress in the transverse and longitudinal direction (hybrid reinforcement)
$\sigma_{confy,red}, \sigma_{confy,hyb,red}$	Reduced transverse confining stress (conventional or hybrid reinforcement)
$\sigma_{t,f}$	Post-cracked residual tensile strength of SFRC
σ_{x0}	Axial stress across the loaded area within b_{ccz} determined with Multi-Wedge or Dual-Wedge stress field
$\sigma_{x0,ccy}, \sigma_{x0,csy}$	Axial stress across the loaded area within b_{ccz} for load dispersion within b_{ccy} or $b_{csy} - b_{ccy}$ determined with Multi-Wedge stress field
$\sigma_{x0,csz}$	Axial stress across the loaded area outside b_{ccz} for load dispersion within $b_{csz} - b_{ccz}$, see Morger et al. [15]
σ_{xd}	Axial stress after load dispersion determined with Dual-Wedge stress field
$\sigma_{xd,ccy}, \sigma_{xd,csy} = f_{c0}$	Axial stress after load dispersion within b_{ccy} or $b_{csy} - b_{ccy}$ determined with Multi-Wedge stress field
σ_y	Horizontal principal confining stress
$\rho_{c,core}$	Density of cored concrete sample
ω_y, ω_z	Transverse and longitudinal mechanical reinforcement ratio
$\tilde{\omega}_{y,hyb}, \tilde{\omega}_{z,hyb}$	Transverse and longitudinal hybrid mechanical reinforcement ratio

Special characters

$Ø_s$	Diameter of reinforcing steel

References

[1] H. P. Spieth, 'Das Verhalten von Beton unter hoher örtlicher Pressung', *Beton- und Stahlbetonbau*, vol. 56, no. 11, pp. 257–263, 1961.

[2] T. Markić, F. Morger, and W. Kaufmann, 'Partially loaded areas in reinforced concrete: Mechanical modelling', *Engineering Structures*, vol. 271, p. 114938, Nov. 2022, doi: 10.1016/j.engstruct.2022.114938.

[3] F. Morger, A. Kenel, and W. Kaufmann, 'Strip loading in reinforced concrete: Mechanical modeling and experimental validation', *Structural Concrete*, vol. 27, pp. 163–192, 2026, doi: 10.1002/suco.70154.

[4] T. Markić, F. Morger, and W. Kaufmann, 'Partially loaded areas in reinforced concrete: experimental campaign and model validation', *Engineering Structures*, vol. 273, p. 114905, Dec. 2022, doi: 10.1016/j.engstruct.2022.114905.

[5] G. Schmidt-Thrö, M. Smarslik, B. Tabka, W. Scheufler, O. Fischer, and P. Mark, 'Experimental analysis of concrete elements under partial area strip loading', *Civil Engineering Design*, vol. 1, no. 1, pp. 28–38, 2019, doi: 10.1002/cend.201900001.

[6] T. Markić, W. Kaufmann, and A. Amin, 'Stress field solution for strip loaded reinforced concrete blocks', *Engineering Structures*, vol. 171, pp. 911–920, 2018, doi: 10.1016/j.engstruct.2018.03.027.

[7] ACI Committee 533, *Guide for Precast Concrete Tunnel Segments (ACI 533.5R-20)*. Farmington Hills, MI: American Concrete Institute, 2020.

[8] G. Tiberti, A. Conforti, and G. A. Plizzari, 'Precast segments under TBM hydraulic jacks: Experimental investigation on the local splitting behavior', *Tunnelling and Underground Space Technology*, vol. 50, pp. 438–450, Aug. 2015, doi: 10.1016/j.tust.2015.08.013.

[9] A. Conforti, G. Tiberti, and G. A. Plizzari, 'Splitting and crushing failure in FRC elements subjected to a high concentrated load', *Composites Part B: Engineering*, vol. 105, pp. 82–92, Nov. 2016, doi: 10.1016/j.compositesb.2016.08.032.

[10] I. Trabucchi, G. Tiberti, A. Conforti, F. Medeghini, and G. A. Plizzari, 'Experimental study on Steel Fiber Reinforced Concrete and Reinforced Concrete elements under concentrated loads', *Construction and Building Materials*, vol. 307, p. 124834, Nov. 2021, doi: 10.1016/j.conbuildmat.2021.124834.

[11] S. Plückelmann, R. Breitenbücher, M. Smarslik, and P. Mark, 'Aufnehmbare Teilflächenspannung von hochfestem Stahlfaserbeton', *Beton- und Stahlbetonbau*, vol. 114, no. 9, pp. 653–662, 2019, doi: 10.1002/best.201900015.

[12] I. Trabucchi, G. Tiberti, and G. A. Plizzari, 'A model for predicting the splitting bearing capacity of Fiber Reinforced Concrete elements under partially loaded areas', *Structural Concrete*, vol. 24, no. 1, pp. 1271–1281, 2023, doi: 10.1002/suco.202200010.

[13] H. Aoude, 'Structural behaviour of steel fibre reinforced concrete members', Doctoral Thesis, McGill University, Montreal, Canada, 2007.

[14] International Federation for Structural Concrete (fib), *Model Code for Concrete Structures 2020*, Lausanne, 2024.

[15] F. Morger, A. Kenel, and W. Kaufmann, 'Experimental and theoretical investigation of longitudinal tunnel lining joints with confining reinforcement', *Structural Concrete*, 2026, doi: 10.1002/suco.70453.

[16] EN 14651:2005, *Test method for metallic fibered concrete - Measuring the flexural tensile strength (limit of proportionality (LOP), residual)*, Brussels, Belgium, 2005.

[17] F. Morger, A. Kenel, and W. Kaufmann, 'Passive confinement of reinforced concrete members revisited', *Structural Concrete*, vol. 25, no. 6, pp. 4283–4299, 2024, doi: 10.1002/suco.202400209.

[18] J. Mata-Falcón, S. Haefliger, M. Lee, T. Galkovski, and N. Gehri, 'Combined Application of Distributed Fibre Optical and Digital Image Correlation Measurements to Structural Concrete Experiments', *Engineering Structures*, vol. 225, p. 111309, Dec. 2020, doi: 10.1016/j.engstruct.2020.111309.

[19] N. Gehri, J. Mata-Falcón, and W. Kaufmann, 'Automated crack detection and measurement based on digital image correlation', *Construction and Building Materials*, vol. 256, p. 119383, 2020, doi: 10.1016/j.conbuildmat.2020.119383.
[20] N. Gehri, J. Mata-Falcón, and W. Kaufmann, 'Refined extraction of crack characteristics in Large-scale concrete experiments based on digital image correlation', *Engineering Structures*, vol. 251, p. 113486, 2022, doi: 10.1016/j.engstruct.2021.113486.
[21] T. Böhme, M. Empelmann, and M. Wichers, 'Emsquerung für die Erdgasleitung A660. Einsatz von stahlfaserbewehrten Tübbingen', *Beton- und Stahlbetonbau*, vol. 104, no. 12, pp. 882–889, 2009, doi: 10.1002/best.200900052.
[22] EN 1992-1-1:2023, 'Eurocode 2 - Design of concrete structures - Part 1-1: General rules and rules for buildings, bridges and civil engineering structures', Brussels, 2023.
[23] F. Medeghini, G. Tiberti, J. Guhathakurta, S. Simon, G. A. Plizzari, and P. Mark, 'Fiber orientation and orientation factors in steel fiber-reinforced concrete beams with hybrid fibers: A critical review', *Structural Concrete*, vol. 26, no. 1, pp. 481–500, 2025, doi: 10.1002/suco.202400461.
[24] F. Morger and W. Kaufmann, 'Experimental investigation of welded reinforcement grids for partial area loading', in *Proceedings of the 15th fib PhD Symposium in Civil Engineering*, Fédération Internationale du Béton (fib), 2024. doi: https://doi.org/10.3929/ethz-b-000711139.
[25] SIA, *Swisscode SIA 262: Concrete Structures*, Zurich, Switzerland., 2013.
[26] W. F. Chen, 'Double Punch Test for Tensile Strength of Concrete', *ACI Journal*, vol. 67, no. 12, pp. 993–995, 1970.
[27] P. Marti, 'Size Effect in Double-Punch Tests on Concrete Cylinders', *Materials Journal*, vol. 86, no. 6, pp. 597–601, 1989, doi: 10.14359/2261.
[28] SIA, *SN EN 13791:2019: Assessment of in-situ compressive strength in structures and precast concrete components*, Zurich, 2021.
[29] International Federation for Structural Concrete (fib), *Model Code for Concrete Structures 2010*, Berlin, Germany, 2013.

7 Concluding remarks

This chapter summarises the theoretical and experimental investigations on passive confinement and strip loading, with a focus on the longitudinal joints of tunnel lining segments subjected to high compressive forces. It gives an overview of the most important findings and concludes the thesis by outlining directions for future research.

7.1 Summary

The aim of this thesis was to advance the knowledge of the load-bearing behaviour of strip-loaded reinforced concrete (RC) and steel fibre reinforced concrete (SFRC) with substantial passive confinement in order to propose efficient and mechanically sound design approaches for longitudinal joints of tunnel lining segments. This objective was addressed by a combination of experimental and theoretical investigations. As a starting point, a novel confinement model consistently describing the load dispersion of activated confining forces in the concrete was developed, and the activation of welded grid confining reinforcement was experimentally investigated by fibre optical measurements. To study the load bearing behaviour of strip loading, two experimental campaigns were conducted: one on blocks (block tests) and one on large-scale specimens with longitudinal joints representing tunnel lining segments (joint tests) made of RC and SFRC with substantial confining reinforcement. Based on the experimental findings, mechanically sound stress field models that consider both load dispersion (geometrical confinement) as well as confining reinforcement (passive confinement) were developed. The models were successfully validated against the experimental results and can thus be recommended as a valid basis for design, enabling the construction of more efficient tunnel lining segments. The proposed models stand out due to their mechanical consistency and the ability to track the entire load path, while the provided simplifications facilitate their application in engineering practice.

The thesis is divided into three main parts. In the first main part (Chapters 2 and 3), the passive confinement model was developed and the load-bearing behaviour of welded grid as confining reinforcement was experimentally investigated. In the second main part (Chapters 4 and 5), the block and joint tests were presented. In addition, the Dual-Wedge stress field [1] was further developed for the application of wide strip loading and the Multi-Wedge stress field was introduced as an appropriate model for the design of longitudinal tunnel lining joints. In the last main part (Chapter 6), experimental tests on strip-loaded SFRC were presented and the stress fields were extended for the application with SFRC.

Chapter 1 contextualised the thesis by providing an overview of (i) the importance of an efficient design of longitudinal tunnel lining joints and (ii) their current design approaches related to strip loading along with the problem statement and research objectives. It is well known that load dispersion and confining reinforcement increase the load-bearing capacity of concrete subjected to compressive loading. However, most current design approaches for strip loading either build on the semi-empirical square-root

equation to account for the beneficial effect of load dispersion or consider solely the confining reinforcement. Most current guidelines do not allow these two effects to be combined, leading to overly conservative designs of longitudinal tunnel lining joints. Moreover, experimental data on strip loading with substantial confining reinforcement is scarce, preventing a solid validation of design approaches that consider the combined effect of load dispersion and passive confinement.

Chapter 2 reviewed the state of the art on passive confinement of reinforced concrete, presenting the design approaches of current guidelines (Eurocode 2 – Design of concrete structures [2], SIA 262:2013 Concrete Structures [3] and *fib* Model Code for Concrete Structures 2010 [4]) to determine the confined concrete area and the confining stresses of activated reinforcement. Furthermore, a new model for passive confinement of rectangular cross-sections was introduced, which can also be consistently applied to circular cross-sections. In comparison to the previous models, the new model describes the entire three-dimensional force flow of the confining forces in the concrete and ensures equilibrium. The confining forces are spread by compression-only shells in the shape of paraboloids, whose form ensures uniformly distributed deviation forces corresponding to the confining stresses. At the same time the geometry of the paraboloids, defined by the reinforcement spacings and an initial inclination of the lateral and diagonal parabolas of 45°, determines the confined concrete volume, where a triaxial compressive stress state is present. The governing cross-section with the smallest confined concrete area lies in the centre between two adjacent confining reinforcement layers. For the sake of simplicity, it was proposed to approximate the governing confined concrete area by the largest enclosed rectangle. The parabolic shape of the shells causes thrust forces, which impacts the determination of the confining stresses. The proposed model and its simplification were compared to the design approaches proposed by current guidelines, and both were successfully validated against experimental data from literature. The simplified new model is a valuable alternative to existing models in current guidelines as (i) it is mechanically more consistent, (ii) its application is more straightforward, and (iii) it allows for a comprehensive treatment of rectangular and circular cross-sections using the same equations. The simplification of the confined concrete area and the determination of the confining stresses accounting for the thrust force was applied in the models developed in the following chapters.

Chapter 3 presented an experimental investigation of welded reinforcement grids applied as confining reinforcement in concrete members subjected to strip loading. Welded reinforcement grids offer several advantages over conventional bent tie reinforcement. They simplify the reinforcement assembly, reduce time and costs in the prefabrication process and facilitate concrete casting by avoiding congestion. In order to increase the knowledge on the load-bearing behaviour of the welded reinforcement grids and their interaction with the surrounding concrete, fibre optical measurements along several reinforcing bars were conducted. Based on these measurements and the characteristics of the bare reinforcing bars, the normal stresses and the curvature of the reinforcing bars could be inferred. It could be shown that the transverse reinforcing bars reached the yield stress and could consequently be fully activated through anchorage by two longitudinal reinforcing bars connected with welded cross joints SF50. Furthermore, the measurements yielded insight into the load transfer between reinforcement and surrounding concrete, which led to the proposal to assume the position of the outer welded cross joint between the transverse and longitudinal reinforcing bars as the location of the discrete load introduction point of the confining force. This location is required to determine the governing confined concrete area. The longitudinal reinforcing bars of the welded grids experienced pronounced lateral bending due to the direct

load introduction at the welded cross joints but were nonetheless able to provide the required confinement in their direction.

Chapter 4 described the load-bearing behaviour of strip loading in RC, highlighting the beneficial effects of lateral confining stresses provided by load dispersion and confining reinforcement on the concrete compressive strength. In addition, recently proposed design approaches (the Dual-Wedge stress field [1], the geometric and passive confinement model [5] and the square-root equation according to DAUB [6]) were presented and discussed in detail, and extended if necessary. A simplification of the Dual-Wedge stress field based on a parametric study was introduced, and the determination of the confinement parameters was elaborated for regular and irregular reinforcement spacings. Furthermore, an experimental campaign of 15 concrete blocks subjected to strip loading with substantial confining reinforcement placed over the entire specimen height, carried out in the course of this thesis, was presented (block tests). The investigated parameters included (i) the reinforcement ratio and type, (ii) the width and position of the loaded area, and (iii) the concrete compressive strength. Digital image correlation was applied to determine surface crack widths. The experimental results showed that with the minimum reinforcement ratio, a ductile behaviour occurs and that the load-bearing capacity can be substantially increased with confining reinforcement. Furthermore, the performance of different reinforcement types (bent ties, welded grids and double-headed bars) was similar, indicating that welded grids can be a viable alternative to bent ties. The tests confirmed that the geometrical confinement decreases with a larger loaded width or eccentric loading, thereby reducing the maximum stress that can be applied at the load introduction. The experimental results were also used to compare the different model approaches for strip loading, corroborating the hypothesis that the load-bearing capacities predicted by the models accounting for load dispersion and passive confinement were in good agreement with the tests and allow for an efficient design, whereas the square-root approach proposed in DAUB was generally very conservative. The simplification of the Dual-Wedge stress field stood out for its ease of use and lowest coefficient of variation. Furthermore, the experimental tests indicated that for normal strength concrete the crack widths do not govern the design, which may however be the case for high strength concrete.

Chapter 5 presented an experimental campaign investigating the structural behaviour of tunnel lining segments with longitudinal joints in nine specimens (joint specimens) with pronounced passive confinement. Each specimen consisted of two identical RC segments placed on top of each other with a reduced contact area – corresponding to the longitudinal joint – compared to the full cross-section. The investigated parameters included (i) the geometry of the longitudinal joint, (ii) the reinforcement ratio (iii) the reinforcement layout (confinement over the full specimen height or only parts adjacent to the joint which resulted in a confined and unconfined zone), and (iv) centric and eccentric loading. The experimental results yielded valuable insight into the mechanical behaviour, confirming that passive confinement can considerably increase the load-bearing capacity. The results also highlighted the importance of considering – where provided – both the unconfined zone as well as the guiding rod groove. All specimens exhibited a certain amount of ductility, with the specimens failing in the unconfined zone exhibiting a less ductile behaviour than those failing in the confined zone. Based on the experimental observations, modelling approaches for the confined and unconfined zones were proposed. In the unconfined zone only the uniaxial concrete compressive strength within the area inside the confining reinforcement was considered, which reflected the observed spalling of the cover concrete in the confined zone that extended into the unconfined zone. For the confined zone, the Multi-Wedge stress field, an extension of

the Dual-Wedge stress field, was introduced. While the Dual-Wedge stress field only accounts for the confined concrete area (within the smallest cross-section defined by the paraboloids dispersing the confining forces), the Multi-Wedge stress field disperses part of the load from the joint to the larger area within the confining reinforcement in the confined zone, thereby ensuring a consistent transition to the adjacent unconfined zone. The Multi-Wedge stress field was further extended to consider a guiding rod groove, proposing three different variants that predict higher load-bearing capacities with increasing complexity of the stress field. The comparison of the experimental data with the Multi-Wedge stress field, as well as the design approaches presented in Chapter 4 considering load dispersion and confining reinforcement, showed good agreement as long as the potential limitation of the load-bearing capacity by the unconfined zone was considered. Furthermore, the crack widths and joint closings were measured with digital image correlation. The crack widths did not govern the design of the test specimens since passive confinement activation and associated lateral expansion was limited either by the reinforcement ratio or the governing unconfined zone.

Chapter 6 focused on the behaviour of strip loading in SFRC. Eleven tests on strip-loaded SFRC were conducted, including seven tests investigating the load-bearing behaviour of specimens with additional pronounced confining reinforcement (hybrid-reinforced specimens) and four tests on purely fibre-reinforced specimens. The tests were carried out as part of the two experimental campaigns presented in Chapters 4 and 5. The experimental results were compared to the results of RC specimens without fibres, showing that steel fibre reinforcement was able to enhance the load-bearing capacity of strip-loaded reinforced concrete and minimise crack widths. It was proposed to account for the effect of SFRC in the confined zone of hybrid-reinforced elements by superimposing the confining stresses provided by conventional reinforcement with the residual tensile strength of the SFRC. The resulting stresses can then be used as input parameters in mechanically sound models established for RC elements subjected to strip loading that account for load dispersion and confining reinforcement, such as the Multi-Wedge or Dual-Wedge stress fields. The uniaxial compressive strength in the unconfined zone, if present, is not affected by the SFRC. Comparison of the modelling approaches with the experimental results of the hybrid specimens showed good agreement. For the purely fibre-reinforced specimens, a simple modelling approach based on the Dual-Wedge stress field considering only the residual tensile strength of the SRFC was proposed. This modelling approach was promising, but uncertainty arises regarding brittle failures and a possible size effect of purely fibre-reinforced specimens.

7.2 Conclusion

The Multi-Wedge and Dual-Wedge stress fields, combined with the new confinement model, realistically account for the combined effects of load dispersion and confining reinforcement in strip loading. The models build on a sound mechanical basis satisfying equilibrium and the failure criteria of concrete and reinforcing steel. The model predictions align with the load-bearing behaviour observed in extensive experimental campaigns of block and joint tests. In particular, for longitudinal joints of tunnel lining segments – where an unconfined zone adjacent to the confined joint zone is common – the Multi-Wedge stress field is the only design approach that enables consistently tracing the entire load path. Applying the stress fields enables full exploitation of the load-bearing capacity of strip-loaded RC members.

Additionally, welded grid reinforcement and SFRC provide further potential to a more efficient design of tunnel lining segments.

7.2.1 Passive confinement

The key findings of the first part of the thesis are:

- The review of the state of the art of confining reinforcement confirms the basic principles of confining reinforcement. However, current design approaches determine the confined concrete area semi-empirically and disregard the dispersion of the confining forces when defining the confining stresses.
- A mechanically consistent model describing the three-dimensional load dispersion of activated confining reinforcement was developed: Parabolic shells spread the confining forces and enable the determination of the governing confined concrete area and the confining stresses based on equilibrium and the failure criteria of the concrete and the reinforcing steel. The model accounts for the dependency of the confining stresses on the axial and lateral spacings, the steel properties and the cross-section of the reinforcement and has been successfully validated against experimental data from literature. The application of the proposed simplification – used to determine the governing confined concrete area – is straightforward and thus recommended for use in engineering practice; in fact, it has already been adopted in the newest version of the Swiss design code for concrete structures [7].
- The load-bearing behaviour of welded grid reinforcement employed as confining reinforcement was investigated experimentally. The transverse reinforcing bars of the grids were fully activated by two longitudinal bars welded to it on both sides with a nominal shear strength factor of 0.5 (SF50). The longitudinal bars provided anchorage of the transverse bars and confinement in the longitudinal direction. Their stress state was complex due to the shear forces and bending moments caused by the transverse bar anchorages. Hence, no specific design proposals for varying parameters could be made based on the given experimental results.
- For application of welded grids in engineering practice, it is recommended to assume the position of the outer welded cross joints between the transverse and longitudinal reinforcing bars as the location of the discrete load introduction points to determine the governing confined concrete area, if the geometrical placing of the longitudinal bars does not considerably vary from the welded grids investigated in this thesis.

7.2.2 Strip loading in reinforced concrete

The key findings of the second part of the thesis are:

- The experimental investigations of strip-loaded RC blocks provided valuable further insights into their structural behaviour. The two most relevant findings are: (i) higher amounts of confining reinforcement can substantially increase the load-bearing capacity, and (ii) geometrical confinement decreases with larger loaded width or eccentricity, resulting in reduced maximum

contact stresses that can be applied at the load introduction (but still higher compressive forces in case of a larger contact area).

- The Dual-Wedge stress field has been refined for application of strip loading with large load application widths and pronounced confining reinforcement. Improving the model with regards to the confined concrete area and the effect of irregular confining reinforcement spacings resulted in accurate load-bearing predictions, as confirmed by the experimental results. The simplification of the model provides similar predictions, while being significantly easier to apply. The simplification is thus recommended as a tool for engineering practice.
- A series of large-scale tests on RC specimens investigating the load-bearing behaviour of longitudinal tunnel lining joints was conducted. The most relevant findings are: (i) higher amounts of confining reinforcement can substantially increase the load-bearing capacity as long as the unconfined zone does not govern failure, and (ii) specimens with guiding rod grooves or joint eccentricities can sustain higher contact stresses (but still lower compressive forces due to the smaller loaded area).
- The Dual-Wedge stress field was extended to account for an unconfined zone adjacent to the confined zone and the impact of a guiding rod groove, resulting in the Multi-Wedge stress field. The Multi-Wedge stress field disperses the load within the reinforcement in the confined zone (rather than only within the confined concrete area) and therefore allows a consistent transition to the unconfined zone. For the unconfined zone, the uniaxial concrete compressive strength should be accounted for only within the area of the confining reinforcement due to concrete cover spalling progressing from the confined zone.
- The stress field solutions with their extensions provide a safe and efficient design considering the combined effect of load-dispersion and passive confinement. They are the only design approaches that enable one to track mechanically consistently the entire load path.
- The occurring crack widths and joint closing were experimentally related to the load-bearing capacity. In most cases, the crack widths did not govern the design, except for specimens with high concrete strength or high confining stresses. Joint closings of up to 1 mm can be expected at serviceability limit state.

7.2.3 Strip loading in steel fibre reinforced concrete

The key findings of the third part of the thesis are:

- The influence of SFRC on strip loading with and without additional conventional confining reinforcement was investigated experimentally and compared to the behaviour of RC specimens without steel fibres. Accordingly, SFRC can enhance the load-bearing behaviour of strip-loaded concrete and minimise crack widths. SFRC is particularly efficient in combination with low conventional reinforcement ratios. Purely fibre-reinforced specimens exhibited a brittle failure, however, the failure load was higher than the load at which surface cracks were initially observed.

- Superposition of the confining stresses provided by the reinforcement and the residual SFRC tensile strength is proposed for the design of the hybrid specimens based on the Multi-Wedge and Dual-Wedge stress fields.
- For the purely fibre-reinforced specimens, no specific recommendations can be made based on the limited experimental data due to the brittle failure and related potential size effect.

7.3 Recommendations for future research

The findings of this thesis improve the understanding of passive confinement and strip loading applied to longitudinal joints of tunnel lining segments and facilitate their more efficient design. However, the following main knowledge gaps require further investigation:

- The passive confinement model has been validated against experimental data from 40 tests on RC members subjected to compressive loading by comparing the predicted normal force against the obtained peak normal force. In these tests, the load-bearing capacity not only depended on the concrete strength increase due to passive confinement, but also on other factors such as the compressive strength of to the concrete within the reinforcement as well as to the cover concrete, and axial reinforcement. Consequently, the impact of the passive confinement on the load-bearing capacity was limited and its quantification subject to uncertainties in the other contributing factors. For a more accurate validation of the confinement model, experimental data on compression members with low uniaxial concrete compressive strength, minimal concrete cover and no (or not continuous) axial reinforcement would be required. Such a specimen design would also reduce the required capacity of the testing machine – which is often a limiting factor in such tests – allowing to test larger specimens and therefore the impact of various lateral reinforcement spacings and specimen cross-sections.
- The welded grid reinforcement has been investigated with fibre optical measurements merely in one specimen. The application of two fibre optical sensors per investigated reinforcing bar yielded valuable insight. However, the obtained data was not sufficient to propose a design approach for the reinforcing bars in longitudinal direction, which are subjected to shear forces and bending moments due to the anchorage of the transverse reinforcing bars in addition to the normal forces required to provide confinement in the longitudinal direction. Further fibre optical measurements may allow to determine the loading of the longitudinal bars by quantifying and reducing the scatter of the bending moments and shear forces (determined as second and third derivative, respectively, of the measured bar curvature). Furthermore, additional experimental data is required to investigate the impact of the reinforcing bar diameter and the reinforcement spacings on the load-bearing behaviour of the welded grids.
- More tests on strip-loaded specimens made of high strength concrete would be desirable since for two out of three high strength concrete specimens, the load-bearing capacity predictions are unsafe and the crack widths govern the design. Applying a concrete brittleness factor and reducing the concrete compressive strength accordingly, as often used in current codes (e.g. $\eta_{cc} = (30/f_{c0})^{(1/3)} \leq 1$ according to [3]), would result in safe predictions of all high strength

specimens. However, the load-bearing capacity predictions for the normal strength specimens would become more conservative.

- In current codes the brittleness factor (e.g. $\eta_{cc} = (30/f_{c0})^{(1/3)} \leq 1$ according to [3]) has a substantial impact on the design concrete compressive strength. For typical characteristic concrete compressive strengths in segmental linings of 50…60 MPa a reduction in the design concrete compressive strength of 15%…20% results. As mentioned above, the load-bearing capacity predictions for the normal strength specimens with the different model approaches were on the safe side despite neglecting the brittleness factor. This indicates that the brittleness factor currently used is conservative for strip loading of confined and unconfined concrete. Further research, targeting a less conservative factor, would thus have a significant impact on the design of concrete structures such as lining segments.
- The investigation of the block tests in Chapter 4 revealed that among specimens with nearly equal transverse mechanical reinforcement ratio, those having a higher longitudinal mechanical reinforcement ratio exhibited higher load-bearing capacities. According to the modified Coulomb failure criterion incorporated in the stress fields, a higher principal compressive stress in longitudinal than in transverse direction does not increase the load-bearing capacity since only the minimum (lateral) and maximum (axial) principal compressive stresses govern failure. The difference in the load-bearing capacity can likely be attributed to the shorter confined concrete length b_{ccz}, which results for the specimens with lower longitudinal reinforcement ratio as the reinforcement diameter was kept constant. This effect is accounted for in the modelling with the Dual-Wedge and Multi-Wedge stress fields. However, comparing the predictions of the Dual-Wedge stress field with the experimental results indicates that specimens with higher longitudinal reinforcement are more conservative, implying an effect of the principal compressive stress in longitudinal direction when exceeding the minimum principal compressive stress in transverse direction (e.g. WG-NC-2 vs. WG-NC-3 or BT-NC-5 vs. WG-NC-5) on the load-bearing capacity. This effect of the intermediate principal stress could be investigated further using failure criteria that consider all three principal stresses (e.g. [8] or [9]).
- The Dual-Wedge and Multi-Wedge stress fields determine a height of the confined zone (x_E) required to mobilise the full load-bearing capacity. Generally, the Multi-Wedge stress field requires a greater confinement height to achieve its maximum load-bearing capacity than the Dual-Wedge stress field, for which even smaller confinement heights than provided in the experiments are predicted. Accordingly, the Dual-Wedge stress field indicates that reduced confinement heights may be sufficient. Since the influence of varying the confinement height has not been examined experimentally, further experimental investigations are thus required for its validation.
- The Multi-Wedge stress field was extended to account for the effect of a guiding rod groove, proposing three different variants. The comparison of the variant predicting the highest load-bearing capacity with the experimental result of the one specimen containing a guiding rod groove shows that the model is promising. However, relying on only one test is not sufficient to successfully validate the model. More tests with guiding rod grooves are thus required, particularly on specimens with varying reinforcement ratios and joint geometries.

- The serviceability criteria of crack width and joint closing were only investigated experimentally. The joint closing may be predicted analytically by considering the stress-strain relationship of confined concrete and assuming linear load dispersion e.g. over the confined concrete height. The occurrence of cracks on the lateral surfaces is related to the degree of lateral expansion and the concrete tensile strength, whose large scatter makes it difficult to accurately predict the crack widths as highlighted by the substantial difference in crack widths obtained for the similar specimens TLJ-40-WG2p-B1 and TLJ-40-WG2p-B2 in Chapter 5. Therefore, a simple (analytical or empirical, e.g. building on [10]) design proposal should be developed that takes into account the tensile strength of the concrete and its scatter, the thickness of the concrete cover and the confining reinforcement content.
- The investigation of the creep behaviour of specimen TLJ-60-WG2f-B4 in Chapter 5 revealed pronounced creep deformation under an average stress at the joint of $0.81 \cdot f_{c0}$. However, current design guidelines for tunnel lining segments (e.g. [6], [11]) do not account for the effects of creep. Lanig [12] examined the long-term behaviour of concrete under multiaxial stress states. Nevertheless, further research is required to determine whether and how the influence of creep, and long-term effects in general, can be effectively incorporated into the design of longitudinal joints of segments with pronounced confining reinforcement.
- The purely fibre-reinforced joint specimens failed in a brittle manner and revealed a potential size effect. Although failure did not occur at the load at which surface cracks were initially observed, further experimental large-scale investigations are required to assess whether purely fibre-reinforced segments provide a viable solution for the design of longitudinal joints.

References

[1] T. Markić, F. Morger, and W. Kaufmann, 'Partially loaded areas in reinforced concrete: Mechanical modelling', *Engineering Structures*, vol. 271, p. 114938, Nov. 2022, doi: 10.1016/j.engstruct.2022.114938.

[2] EN 1992-1-1:2023, 'Eurocode 2 - Design of concrete structures - Part 1-1: General rules and rules for buildings, bridges and civil engineering structures', Brussels, 2023.

[3] SIA, *Swisscode SIA 262: Concrete Structures*, Zurich, Switzerland, 2013.

[4] International Federation for Structural Concrete (fib), *Model Code for Concrete Structures 2010*, Berlin, Germany, 2013.

[5] C. Proksch-Weilguni, M. Decker, and J. Kollegger, 'Load distribution and passive confinement in reinforced concrete: Development of a mechanical model', *Engineering Structures*, vol. 304, p. 117562, Apr. 2024, doi: 10.1016/j.engstruct.2024.117562.

[6] German Tunnelling Committee (ITA-AITES), *Empfehlungen für den Entwurf, die Herstellung und den Einbau von Tübbingringen*, Deutscher Ausschuss für unterirdisches Bauen e. V. (DAUB), 2024.

[7] SIA, *Swisscode SIA 262: Concrete Structures*, Zurich, Switzerland, 2025.

[8] N. S. Ottosen, 'A Failure Criterion for Concrete', *Journal of the Engineering Mechanics Division*, vol. 103, no. 4, pp. 527–535, Aug. 1977, doi: 10.1061/JMCEA3.0002248.

[9] K. J. Willam and E. P. Warnke, 'Constitutive model for the triaxial behaviour of concrete', *IABSE reports of the working commissions*, vol. 19, p. 1, 1974, doi: 10.5169/seals-17526.

[10] G. Schmidt-Thrö, 'Zum Tragverhalten der Tübbinglängsfuge', Doctoral Thesis, Technische Universität München, 2019.

[11] ACI Committee 533, *Guide for Precast Concrete Tunnel Segments (ACI 533.5R-20)*. Farmington Hills, MI: American Concrete Institute, 2020.

[12] N. Lanig, 'Langzeitverhalten von Beton bei mehrachsiger Beanspruchung', Doctoral thesis, Technische Universität München, 1988.

B. Ringfugen – Ungerissene linear elastische Modellierung (Cedrus)

Scheibenbeanspruchung Ringfugen
Linear-elastische Modellierung

Page 1
08.12.25, 11:47

ETHZ Institut für Baustatik und Konstruktion — Fabian Morger

Cedrus-9 - Rel. 251 (1)

Structure — Scale 1 :25.0

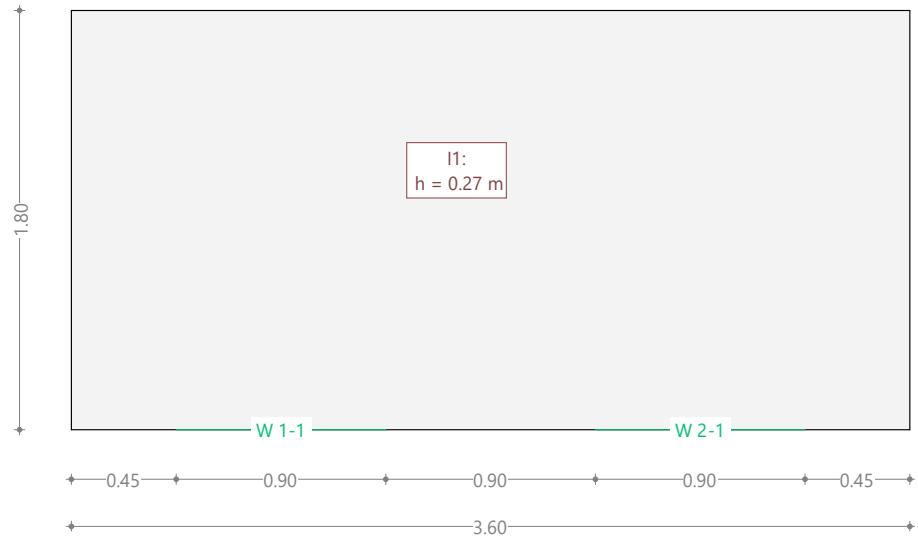

Loading Jacks — Scale 1 :25.0 (-0.20,-0.18..3.78,2.38)

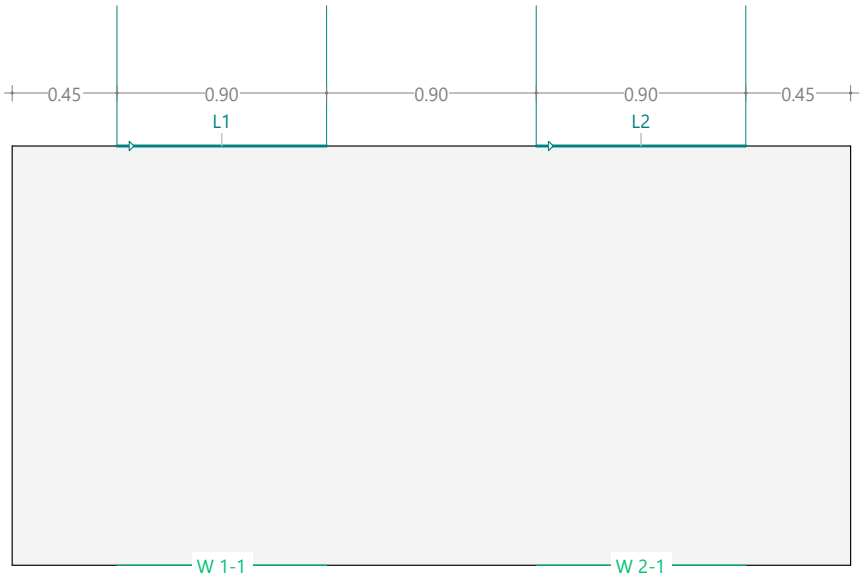

L1 = L2 = 5111.1 kN/m → 4.6 MN

Limited Student Version - not for professional use

Nr.:

C:\Users\morgerf\AppData\Local\

Scheibenbeanspruchung Ringfugen Linear-elastische Modellierung	Page 2 08.12.25, 11:47
ETHZ Institut für Baustatik und Konstruktion — Fabian Morger	Cedrus-9 - Rel. 251 (1)

Principal stress: Loading Jacks — Scale 1 :25.0

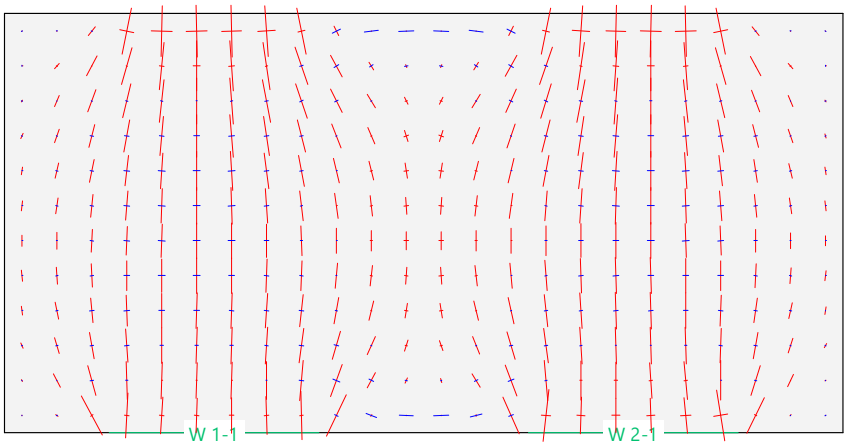

Stresses σx [N/mm2], Equidistance: 1.00 [N/mm2], Reference line: 0.00
Loading Jacks — Scale 1 :25.0

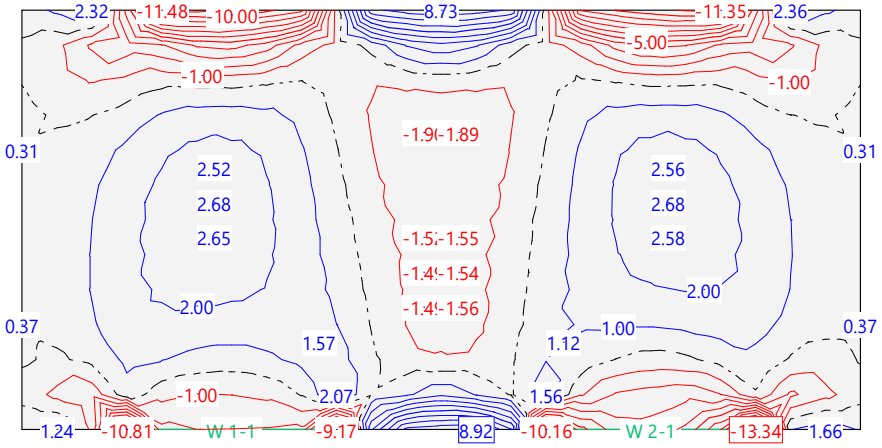

Limited Student Version - not for professional use

Nr.:

C:\Users\morgerf\AppData\Local\

Scheibenbeanspruchung Ringfugen Linear-elastische Modellierung	Page 3 08.12.25, 11:47
ETHZ Institut für Baustatik und Konstruktion Fabian Morger	Cedrus-9 - Rel. 251 (1)

Stresses σy [N/mm2], Equidistance: 1.00 [N/mm2], Reference line: 0.00
Loading Jacks

Scale 1 :25.0

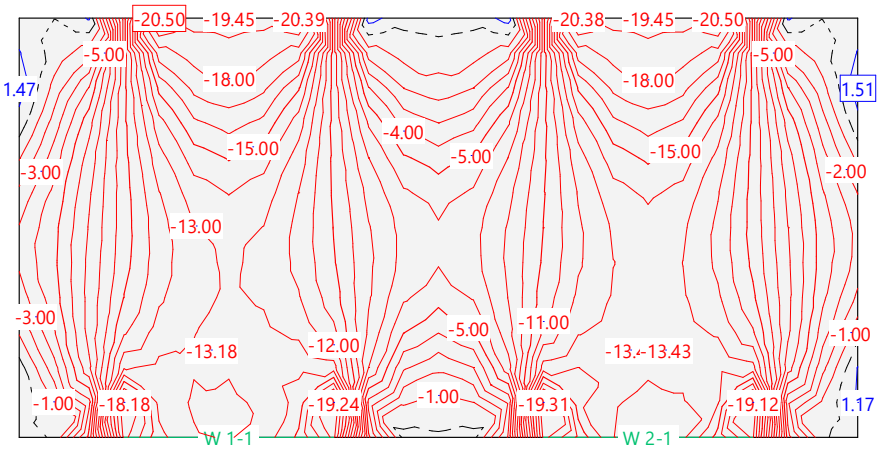

Stresses τxy [N/mm2], Equidistance: 0.50 [N/mm2], Reference line: 0.00
Loading Jacks

Scale 1 :25.0

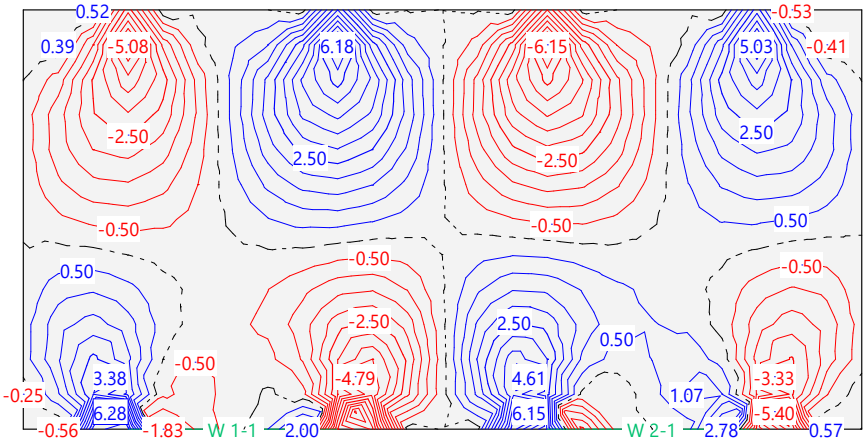

Limited Student Version - not for professional use

	Nr.:

C:\Users\morgerf\AppData\Local\

Scheibenbeanspruchung Ringfugen Linear-elastische Modellierung		Page 4 08.12.25, 11:47
ETHZ Institut für Baustatik und Konstruktion	Fabian Morger	Cedrus-9 - Rel. 251 (1)

Sections

Scale 1 :25.0

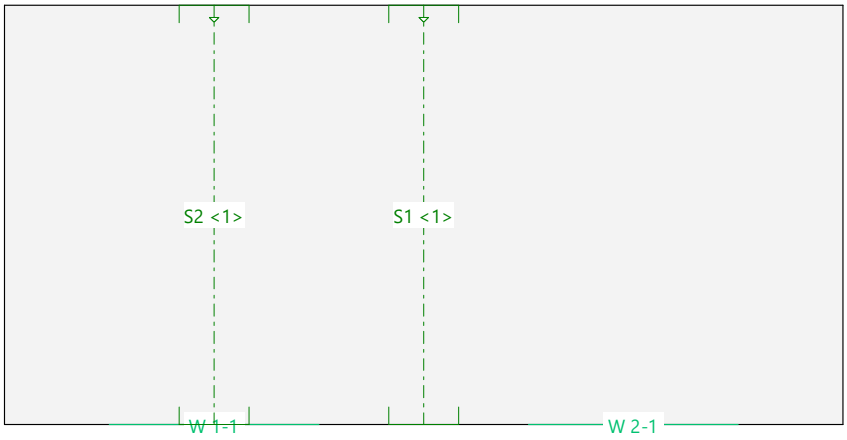

Sections

Section: S1 (1.80,1.80 - 1.80,0.00)

Membrane stresses normal to section, Loading Jacks

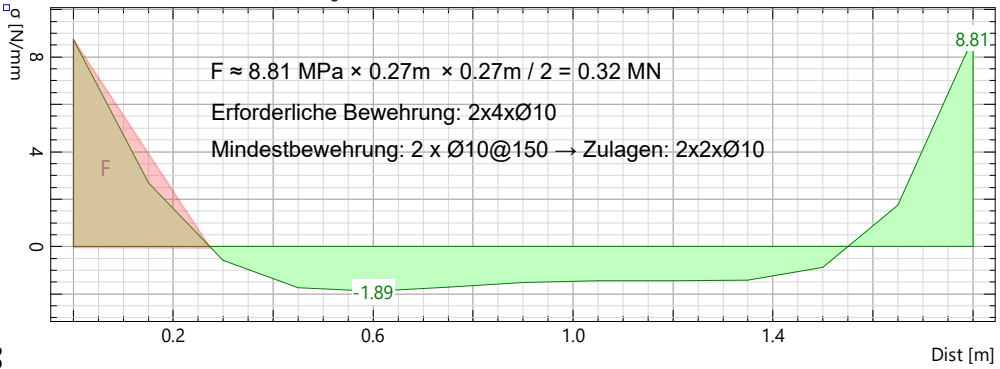

Limited Student Version - not for professional use

	Nr.:

C:\Users\morgerf\AppData\Local\

Sections

Section: S2 (0.90,1.80 - 0.90,0.00)

Membrane stresses normal to section, Loading Jacks

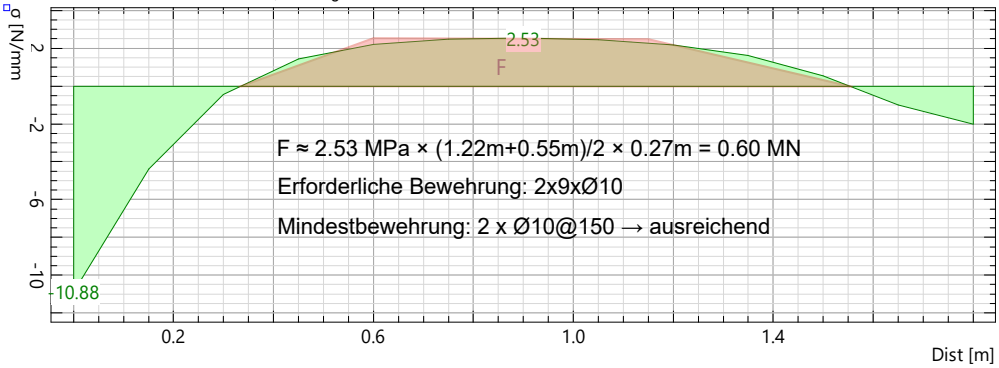

F ≈ 2.53 MPa × (1.22m+0.55m)/2 × 0.27m = 0.60 MN

Erforderliche Bewehrung: 2x9xØ10

Mindestbewehrung: 2 x Ø10@150 → ausreichend

Limited Student Version - not for professional use

Nr.:

C:\Users\morgerf\AppData\Local\

C. Ringfugen – Nichtlineare Modellierung (IDEA StatiCa Detail)

Project: **Scheibenbeanspruchung Ringfugen**
Project no:
Author: **Fabian Morger**

Project data

Project name	Scheibenbeanspruchung Ringfugen
Project number	
Author	Fabian Morger
Description	
Date	17.10.2025
Design code	EN

Materials

Concrete

Name	f_{ck} [MPa]	$f_{ctk,0.05}$ [MPa]	f_{ctm} [MPa]	E_{cm} [MPa]	ν [-]	φ_{perm}	φ_{pres}
C55/67	55.0	3.0	4.2	38214.2	0.20	0	2.5
	ε_{c2} = 22.0 1e-4, ε_{cu2} = 500.0 1e-4, Diagram type: Parabolic φ_{perm}: 0.00 φ_{pres}: 2.50						

Reinforcement

Name	f_{yk} [MPa]	k [-]	E_s [MPa]	Unit mass [kg/m^3]	ε_{uk} [1e-4]	Surface
B 500B	500.0	1.08	200000.0	7850	500.0	Ribbed
	ε_{st} = 500.0 1e-4, ε_{sc} = 500.0 1e-4,					

Scheibenbeanspruchung Ringfugen

Description: Mindestbewehrung mit Zulagen basierend auf linear elastischer Analyse.

Project: Scheibenbeanspruchung Ringfugen
Project no:
Author: Fabian Morger

Geometry

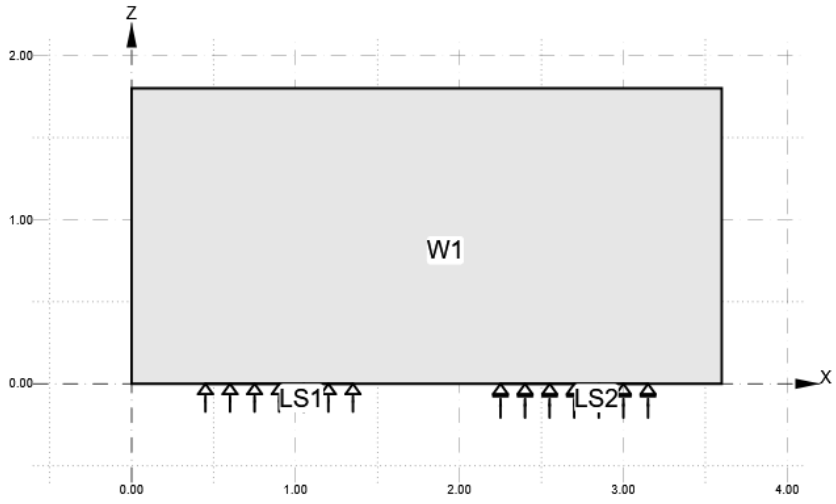

Overview table

Name	Type	Properties	Position
W1	Wall	General; T: 0.27 m; Material: C55/67	
LS1	Line support	X; Z (Pressure only); Local; L: 0.90 m	M: W1, Edge 1; Part of edge; From beginning; X: 0.45 m
LS2	Line support	Z (Pressure only); Local; L: 0.90 m	M: W1, Edge 1; Part of edge; From end; X: 0.45 m

Loads

LC1, LC2

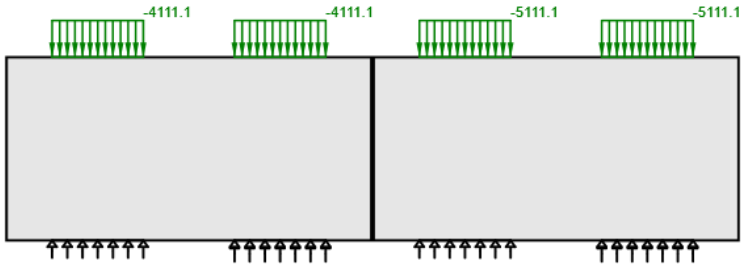

Project: Scheibenbeanspruchung Ringfugen
Project no:
Author: Fabian Morger

C1, C2

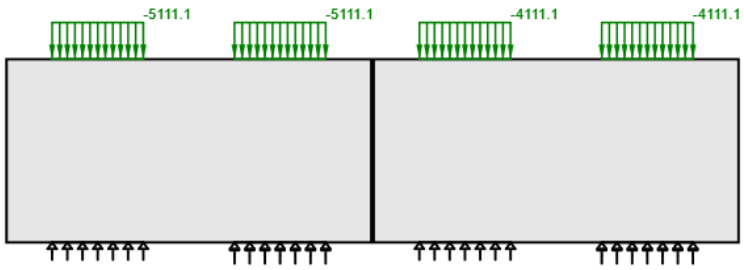

Load case LC1 - Permanent

Line loads

Name	Begin [kN/m]	End [kN/m]	Direction	Position	Length [m]
LL1	-4111.1	-4111.1	Global Z	W1: Edge 3 Position on edge: 0.45 m	0.90
LL2	-4111.1	-4111.1	Global Z	W1: Edge 3 Position on edge: 0.45 m	0.90

Load case LC2 - Permanent

Line loads

Name	Begin [kN/m]	End [kN/m]	Direction	Position	Length [m]
LL3	-5111.1	-5111.1	Global Z	W1: Edge 3 Position on edge: 0.45 m	0.90
LL4	-5111.1	-5111.1	Global Z	W1: Edge 3 Position on edge: 0.45 m	0.90

Combination

Name	Type	Content
C1	ULS	LC2
C2	SLS - Characteristic	LC1

Project: Scheibenbeanspruchung Ringfugen
Project no:
Author: Fabian Morger

Reinforcement

Scheme of reinforcement

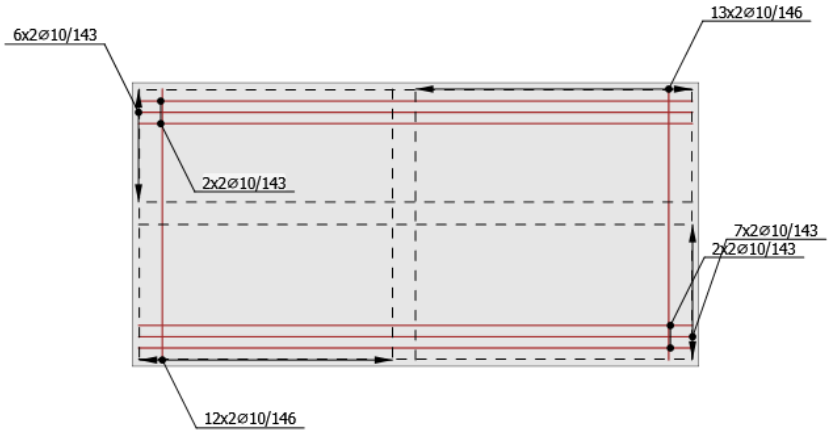

Concrete: C55/67; Steel: B 500B

Project: Scheibenbeanspruchung Ringfugen
Project no:
Author: Fabian Morger

Results

ULS - Summary

Stress flow

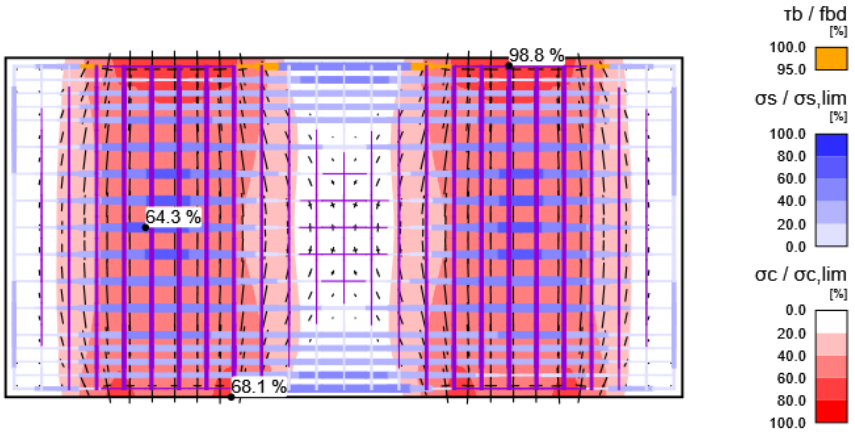

Above yield	Compression	Explanation
		Thickness proportional to force

Summary of reactions and applied loads: C1, Load increment: G100.0%

Type	F_x [kN]	F_z [kN]	M_y [kNm]
Summary of reactions	0.0	9200.0	16560.0
Summary of applied load	0.0	-9200.0	-16560.0
Check of equilibrium	0.0	0.0	0.0

Project: Scheibenbeanspruchung Ringfugen
Project no:
Author: Fabian Morger

IDEA StatiCa
Calculate yesterday's estimates

ULS - Strength

Detailed concrete strength results: C1, Load increment: G100.0%

Directions of principal stresses

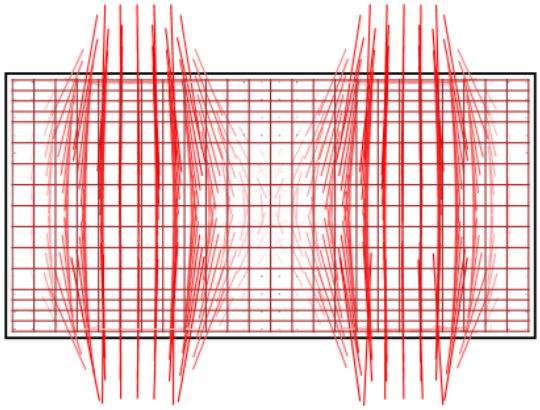

Reinforcement stress - σ_s [MPa]

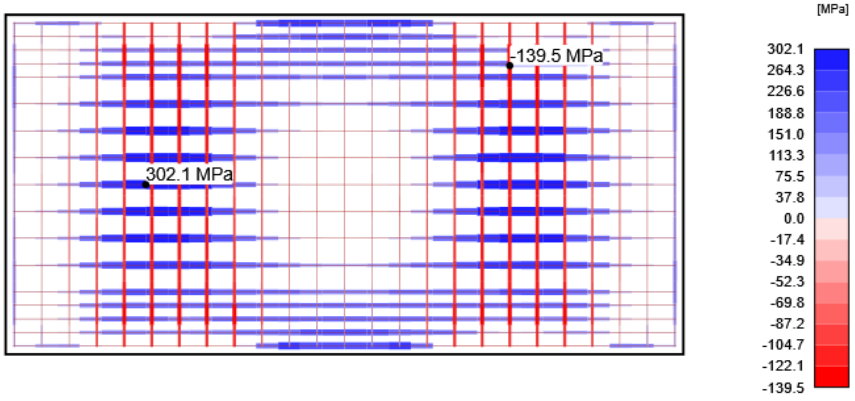

6 / 9

Project: Scheibenbeanspruchung Ringfugen
Project no:
Author: Fabian Morger

IDEA StatiCa
Calculate yesterday's estimates

SLS - Stress

Detailed concrete stress results: C2, Load increment: G100.0%

Reinforcement stress - σ_s [MPa]

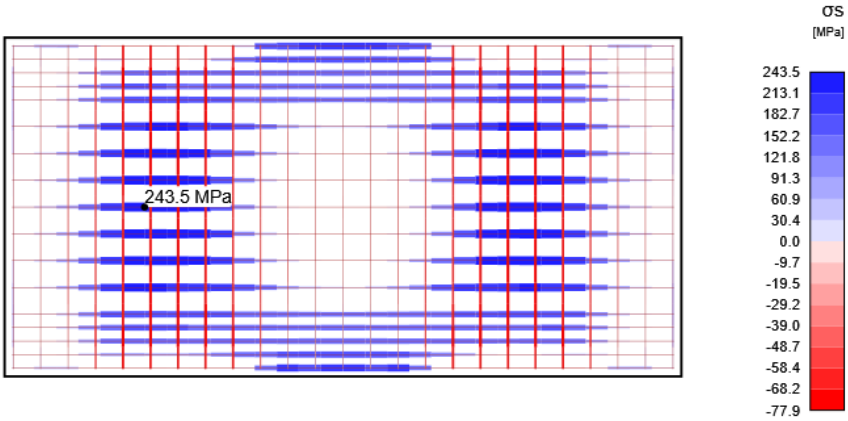

Crack width - w [mm]

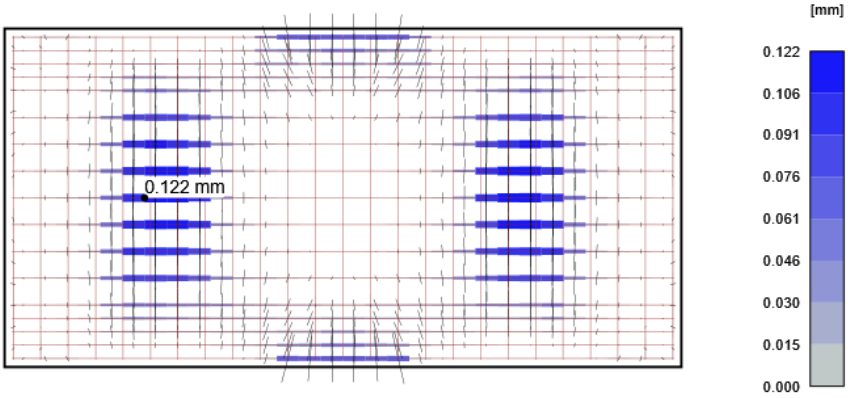

7 / 9

Project: Scheibenbeanspruchung Ringfugen
Project no:
Author: Fabian Morger

Bill of material

Items numbering

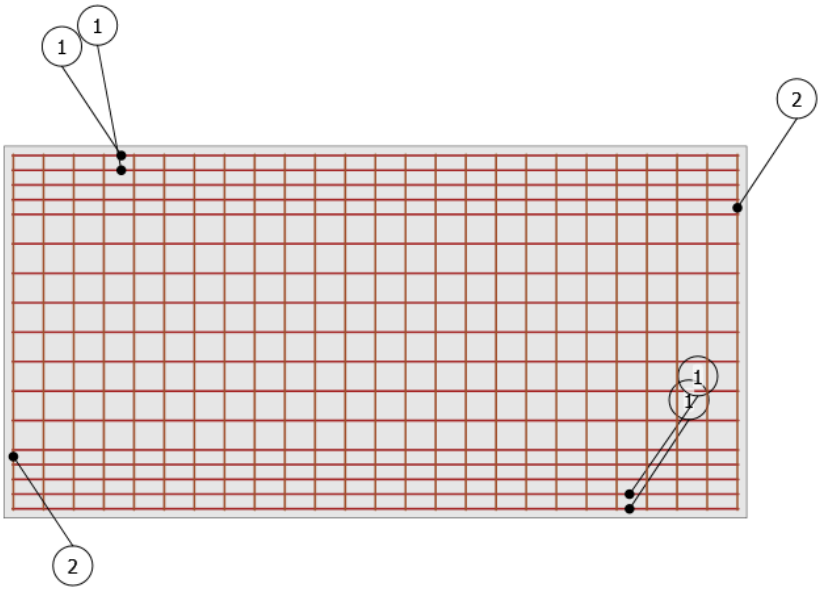

8 / 9

Project: Scheibenbeanspruchung Ringfugen
Project no:
Author: Fabian Morger

Brief reinforcement bar table

Index	Φ [mm]	Material	Items	Length [mm]	Weight [kg]	Total length [m]
1	10	B 500B	34	3520	2	119.68
2	10	B 500B	50	1720	1	86.00

Detailed reinforcement bar tables

Parameter	Value	Shape
Index	1	
Φ [mm]	10	
Material	B 500B	
Number of items	34	
Length [mm]	3520	
Weight [kg]	2	
Total length [m]	119.68	

Parameter	Value	Shape
Index	2	
Φ [mm]	10	
Material	B 500B	
Number of items	50	
Length [mm]	1720	
Weight [kg]	1	
Total length [m]	86.00	

Software info

Application	IDEA StatiCa Detail
Version	25.0.4.1234
Developed by	IDEA StatiCa®

Projektabschluss

Schweizerische Eidgenossenschaft
Confédération suisse
Confederazione Svizzera
Confederaziun svizra

Eidgenössisches Departement für
Umwelt, Verkehr, Energie und Kommunikation UVEK
Bundesamt für Strassen ASTRA

FORSCHUNG IM STRASSENWESEN DES UVEK

Version vom 09.10.2013

Formular Nr. 3: Projektabschluss

erstellt / geändert am: 27.02.2026

Grunddaten

Projekt-Nr.: AGT2019/001

Projekttitel: Tragverhalten und Bemessung von Tübbingfugen

Enddatum: 31.05.2026

Texte

Zusammenfassung der Projektresultate:

Bei der Bemessung von vorfabrizierten Stahlbetontübbingen spielen die Längs- und Ringfugen eine zentrale Rolle. Erstere werden insbesondere bei Tunnels unter hohen Ringnormalkräften massgebend für die Abmessung der Segmentdicke, wodurch eine effiziente Bemessung einen beträchtlichen Einfluss auf Tunnelbauprojekte haben kann. Das vorliegende Projekt fokusierte sich auf die Untersuchung des Tragwiderstands der Längsfugen und deren Modellierung unter Berücksichtigung einer im Fugenbereich neuartig angeordneter Umschnürungsbewehrung. Ergänzend wurde die nummerische Modellierung der Ringfugen untersucht.

Die Resultate aus den Versuchen und theoretischen Untersuchungen zu den Längsfugen zeigen, dass Umschnürungsbewehrung den Tragwiderstand der Längsfugen günstig beinflusst. Bei Tübbingen mit einer auf den Fugenberich begrenzten Umschnürungsbewehrung kann der Tragwiderstand der Längfugen mit höheren Bewehrungsgehalten gesteigert werden, solange die nicht umschnürte Zone Tragreserven besitzt, sprich die einachsige Betonfestigkeit nicht überschritten wird. Mit den im Projekt entwickelten und experimentell validierten Spannungsfeldern kann der Tragwiderstand der Längsfugen mechanisch konsistent ermittelt werden. Dieses Vorgehen ist durch heutige Normenwerke abgedeckt, so dass die Anwendung der Spannungsfelder in der Praxis zulässig ist.

Aus dem Projekt haben sich zudem weitere Erkenntnisse zum allgemeinen Traglastverhalten der Längsfugen ergeben. So hat sich gezeigt, dass eine geschweisste Leiterbewehrung als Umschnürungsbewehrung verwendet werden kann und vergleichbare oder höhere Tragwiderstände als eine konventionelle Bügel- oder Dübelbewehrung erzeugt. Weiter konnte experimentell gezeigt werden, dass durch Zugabe von Stahlfasern zur Betonmischung der Tragwiderstand von hybrid bewehrten Tübbingen (konventionelle Stabbewehrung + Faserbewehrung) gesteigert und die Rissweiten reduziert werden können, speziell für Tübbinge mit geringem konventionellem Stabbewehrungsgehalt. Der Einfluss von faserbewehrten Beton kann mit den entwickelten Spannungsfeldern berücksichtigt werden. Zuletzt wurde der Einfluss einer Anordung eines Führungsstabes in der Längsfuge aufgezeigt und die Spannungsfelder wurden für dessen Berücksichtigung weiterentwickelt.

Bei den Ringfugen zeigten die nummerischen Untersuchungen, dass (i) eine nichtlineare Modellierung einen Mehrwert zur häufig durchgeführten linear elastische Modellierungen bietet, da zusätzlich Informationen zu den Rissweiten resultieren, und (ii) die Gefahr von Rissen aufgrund von Versätzen nicht durch Bewehrung verhindert werden kann, so dass der genauen Tübbingplatzierung grosse Bedeutung zukommt.

Schweizerische Eidgenossenschaft
Confédération suisse
Confederazione Svizzera
Confederaziun svizra

Eidgenössisches Departement für
Umwelt, Verkehr, Energie und Kommunikation UVEK
Bundesamt für Strassen ASTRA

Zielerreichung:

Es ist gelungen, die mechanischen Grundlagen zur Berücksichtigung einer Umschnürungsbewehrung zur Ermittlung des Tragwiderstands der Längsfugen zu erarbeiten. Dies bietet den Ingenieuren in der Praxis eine zusätzliche Bemessungsvariante für die Längsfugen, dies vor allem für Tübbinge mit hoher Normalkraftbeanspruchung. Im Vergleich zum bestehenden empirischen Bemessungsansatz in der DAUB-Richtlinie, der keine Umschnürunbgsbewehrung berücksichtigt, sind die quantitativen Vorteile einer Umschnürungsbewehrung projektspezifisch mit den zur Verfügung gestellten Hilfsmitteln (Spannungsfelder und eine Vereinfachung davon) zu untersuchen, da keine pauschalen Aussagen getroffen werden können.

Obwohl mit den experimentellen und theoretischen Untersuchungen wesentliche, neue Erkenntnisse zum Stand der Forschung im Bereich der Längsfugen beigetragen wurden, verbleiben nach wie vor Wissenslücken, insbesondere zur Untersuchung der Gebrauchstauglichkeit und der Langzeiteffekte, der Eignung von rein faserbewehrten Tübbingen, der Validierung der Modelle für Führungsstäbe sowie eine Bemessungsgrundlage für geschweisste Leiterbewehrung. Weiter wäre ein direkter experimenteller Vergleich zwischen Tübbingen mit Umschnürungsbewehrung und bemessen mit den Spannungsfeldern sowie Tübbingen ohne Umschnürung und bemessen nach der DAUB-Richtlinie wünschenswert.

Folgerungen und Empfehlungen:

Die entwickelten und experimentell validierten Spannungsfelder ermöglichen eine mechanisch fundierte Bemessung der Längsfugen unter Berücksichtigung der Umschnürungsbewehrung. Die Spannungsfelder sind normkonform (SIA 262:2025 oder EN 1992.1.1:2023), so dass sie für die direkte Anwendung in der Praxis geeignet sind. In der Bemessung ermöglicht die Vereinfachung des Spannungsfelds eine Vorbemessung, während die Anwendung der Spannungsfelder für die detailliertere Bemessung verwender werden sollen.

Für die Ringfugen wird empfohlen, die häufig angewendete linear elastische Modellierung mit einer nichtlinieren Modellierung zu ergänzen und Schäden durch Versätze bauspezifisch durch genaues Platzieren der Tübbinge zu verhindern.

Wie bei der Zielereichung bereits aufgezählt, besteht weiterhin Forschungsbedarf bezüglich den Längsfugen.

Publikationen:

ETH-Dissertation:
F. Morger, «Passive Confinement and Strip Loading in Longitudinal Tunnel Lining Segment Joints», 2025. doi: 10.3929/ethz-c-000796399.

Journal-Publikationen:
- F. Morger, A. Kenel, und W. Kaufmann, «Passive confinement of reinforced concrete members revisited», Structural Concrete, Bd. 25, Nr. 6, S. 4283–4299, 2024, doi: 10.1002/suco.202400209.
- F. Morger, A. Kenel, und W. Kaufmann, «Strip loading in reinforced concrete: Mechanical modeling and experimental validation», Structural Concrete, Bd. 27, S. 163–192, 2026, doi: 10.1002/suco.70154.
- F. Morger, A. Kenel, und W. Kaufmann, «Experimental and theoretical investigation of longitudinal tunnel lining joints with confining reinforcement», Structural Concrete, 2026, doi: 10.1002/suco.70453.
- F. Morger, A. Kenel, und W. Kaufmann, «Strip loading in steel fiber reinforced concrete: Experimental and theoretical investigation», Structural Concrete, 2025, doi: 10.1002/suco.70339.

Konferenz-Publikationen:
- F. Morger und W. Kaufmann, «Design of longitudinal tunnel lining joints - experimental investigation on partially loaded reinforced concrete blocks», in Proceedings of the 14th fib PhD Symposium in Civil Engineering, Fédération Internationale du Béton (fib), 2022, S. 467–474. doi: 10.3929/ethz-b-000572924.
-F. Morger und W. Kaufmann, «Experimental investigation of welded reinforcement grids for partial area loading», in Proceedings of the 15th fib PhD Symposium in Civil Engineering, Fédération Internationale du Béton (fib), 2024. doi: https://doi.org/10.3929/ethz-b-000711139.

Der Projektleiter/die Projektleiterin:

Name: Kaufmann Vorname: Walter

Amt, Firma, Institut: ETH Zürich, Institut für Baustatik und Konstruktion

Unterschrift des Projektleiters/der Projektleiterin:

Schweizerische Eidgenossenschaft
Confédération suisse
Confederazione Svizzera
Confederaziun svizra

Eidgenössisches Departement für
Umwelt, Verkehr, Energie und Kommunikation UVEK
Bundesamt für Strassen ASTRA

FORSCHUNG IM STRASSENWESEN DES UVEK
Formular Nr. 3: Projektabschluss

Beurteilung der Begleitkommission:

Beurteilung:

Bei maschinellen Tunnelvortrieben mit Tübbingausbau ist oft die Tragfähigkeit der Längsfugen der Tübbinge massgebend für die Bemessung. Die Bemessung erfolgt üblicherweise mit empirischen Ansätzen. Als Massnahme bei ungenügender Tragfähigkeit wird meist die Tübbingdicke vergrössert. Die damit verknüpfte Vergrösserung des Ausbruchsdurchmessers führt sowohl zu einem Mehrausbruch wie auch zu einem Mehrverbrauch an Beton und Perlkies/Mörtel für die Tübbinge bzw. Ringspaltverfüllung. Eine genauere Bemessung der Längsfugen und gegebenenfalls Anordnung einer Umschnürungsbewehrung im Fugenbereich können somit zur Kostenreduktion beitragen.
Im Rahmen des Forschungsprojekts 2019/001 wurde mit Fokus auf die Tragsicherheit ein mechanisch konsistentes Berechnungsmodell für die Tragfähigkeit von Tübbinglängsfugen mit Umschnürungsbewehrung entwickelt und anhand von Laborversuchen validiert. Das Forschungsprojekt hat gezeigt, dass mit dem neuen Modell unter Umständen deutlich höhere Tragwiderstände nachgewiesen werden können. Es ist allerdings nicht möglich, pauschale Aussagen zum Optimierungspotential zu machen. Ob durch die Umschnürung ein erhöhter Tragwiderstand gegenüber den bisher üblichen empirischen Ansätzen nachgewiesen werden kann, hängt vom konkreten Anwendungsfall ab.

Umsetzung:

Die Umsetzung erfolgte, abgesehen von äusseren Faktoren wie Corona-Pandemie und Wartungsarbeiten an der Presse, weitgehend nach Programm. Zusammen mit der Begleitkommission wurden im Verlauf des Forschungsprojekts verschiedene Anpassungen diskutiert und beschlossen, welche den weiteren Projektverlauf beeinflussten und teilweise zu zusätzlichem Zeitbedarf führten. Die Begleitkommission wurde jederzeit über den Projektfortschritt informiert und aktiv in Entscheidungsprozesse miteinbezogen.

weitergehender Forschungsbedarf:

- Die Gebrauchstauglichkeitsgrenze konnte nur experimentell untersucht werden. Hier wären im Rahmen weiterer Forschung für die Praxis belastbare Richtwerte bzw. Bemessungsregeln zu definieren.
- Rein faserbewehrte Tübbinge finden in der Praxis breite Anwendung, ihre Fugentragfähigkeit ist aber bisher nur unzureichend untersucht worden. Der einizge im Rahmen des Forschungsprojekts durchgeführte Versuch zeigte ein ungünstiges Nachbruchverhalten. Diesbezüglich besteht somit weiterer Forschungsbedarf.
- Im Vergleich zur empirischen DAUB-Richtlinie wurden teilweise auch tiefere Tragfähigkeiten ermittelt. Es wäre daher genauer zu untersuchen, ob die DAUB-Richtlinie für gewisse Fälle (z.B. schmale Tübbingfuge) nicht auf der unsicheren Seite liegt.

Einfluss auf Normenwerk:

Die Berechnung der wirksamen umschnürten Fläche auf Basis der vorhandenen Umschnürungsbewehrung hat bereits Eingang in die SIA 262:2025 gefunden (4.2.1.9). Ebenfalls erlaubt SIA 262:2025 eine Überlagerung der Effekte der geometrischen Lastausbreitung und der passiven Umschnürung durch Bewehrung (4.2.1.13). Die normative Basis für die Anwendung des neuen mechanisch konsistenten Bemessungsmodells für die Tragfähigkeit der Tübbinglängsfugen ist damit vorhanden.

Der Präsident/die Präsidentin der Begleitkommission:

Name: Crapp Vorname: Remo

Amt, Firma, Institut: Lombardi SA Ingegneri Consulenti, Giubiasco

Unterschrift des Präsidenten/der Präsidentin der Begleitkommission: